University of Strathclyde

Department of Pure and Applied Chemistry

2D and 3D Optical Imaging of SERS Nanotags Intracellularly

By

Sarah McAughtrie

A thesis submitted to the Department of Pure and Applied Chemistry, University of Strathclyde, in fulfilment of the requirements for the degree of Doctor of Philosophy.

July 2014

This thesis is the result of the author's original research. It has been composed by the author and has not been previously submitted for examination which has led to the award of a degree. The copyright of this thesis belongs to the author under the terms of the United Kingdom Copyright Acts as qualified by University of Strathclyde Regulation 3.50. Due acknowledgement must always be made of the use of any material contained in, or derived from, this thesis.

Signed:

Date:

Previously published material:

1. After initial submission of the thesis a large proportion of the material contained within the introduction formed part of the review – '*Surface Enhanced Raman Spectroscopy (SERS): Potential Applications for Disease Detection and Treatment*' - Pg. 271 – 284.

2. The 3D data contained within Chapter 4, Section 4.3 was published prior to the completion of this thesis – *'3D Optical Imaging of Multiple SERS Nanotags in Cells'* – Pg. 250 – 256. I was responsible for all aspects of the research and the preparation of the publication. Katherine Lau collected the data at Renishaw plc.

Signed:

Date:

Acknowledgement

I would firstly like to thank my supervisors Professor Duncan Graham and Dr. Karen Faulds for their endless help, support and advice over the last three and half years. I've had some fantastic opportunities while working in the group and while others have grudged the 'absences' without them we wouldn't have had the facilities or opportunities that we did. I would also like to thank Dr. Alastair Wark and Professor Ewen Smith for all their help and science discussions. Thanks to Renishaw plc for funding and assistance, in particular, Dr. Katherine Lau and the other members of the spectroscopy division.

To all the members, past and present, of the Centre for Molecular Nanometrology A.K.A the Ramanators you've always made it a fabulous place to work. In particular, special thanks and appreciation go to Alan 'falcon punch, true fact' Hutton and Kirsten 'Mulvoid infiltrator' Gracie, we made it pals, we made it! For Dr. Derek 'ethanol saturated' Craig and Dr. Mhairi 'RSC wino' Harper, whose banter, advice and the Laurieston made the last six months bearable. Derek, I cry with laughter every time I think of you spraying your entire body with ethanol in preparation for cell culture. Mhairi, how we did not receive lifetime bans from the RSC I will never know but Danny Gleeballs and Jenny Tails never did receive their mail. To the ragers Dr. Stacey 'loud hailer' O'Donnell, Dr. Kristy 'CHIP, CHIK, INN' McKeating and Rachel 'cock?....bar' Norman thanks for all the wild nights in 'The Ark' and for destroying my ability to drink white wine for 7 months. To the 1st year trio of Jon 'DJ Jizzy Jon' Simpson, Chris 'gun show' Steven and Julie 'kleptomaniac' Docherty for being great desk buddies and all the injections of positivity in the last six months. For Dr. Lee 'Karen hugger' Barrett and Dr. Sam 'MILF' Mabbott whose conjugation and statistical advice, and banter in general has been invaluable. Finally, I would like to thank some legendary Ramanators Dr. Jen 'Bayden Wood's shoes' Dougan, Dr. Jane 'Pat Butcher' Wotherspoon, Dr. Eleanore 'is that your *** face' Irvine, Sarah 'undercarriage' Rooney, Dr. Kirsty 'Hercule Poirot' Wilson and last but not least my favourite desk sharer of all time Dr. Danny 'for the spanking, I sleep with it in' van Lierop, all of you have made the experience epic!

To my family, in particular my big sister Kay and my partner in crime/wee bro Robert 'fatty' McAughtrie for laughing at my craziness and who without you both I would be

lost. To my mum and dad who because of the time and family commitments didn't necessarily follow the paths they would have chosen for themselves and because of this made sure we all reached for the stars. Finally, to Barry who followed me home from New Zealand and now I can't get rid of….jokes! Thank you for everything –for all the tea, dinners and for more than tolerating the writing up hysteria. Thank you all, for always being my biggest fans and without your love and support I would never have made it to the end.

Last but not least, Callum, Sophie, Oliver, Euan, Thomas, Lillie and Reegan I hope I make you proud!

'Science…it is therefore the highest form of creative art.'

C.V. Raman.

Abstract

Adoption of a multi-marker nanotag approach will led to better disease characterisation whilst simultaneously enabling targeting of multiple disease markers or organelles. The employed nanotag method controllably aggregated nanoparticles with 1,6-hexamethylene diamine (1,6-HMD), before polymer coating with polyvinylpyrrolidone (PVP) and labelling with small molecule reporters; 4-mercaptopyridine (MPY), 5,5'-dithiobis(2-nitrobenzoic acid) (DTNB), 4-nitrobenzenethiol (NBT) and 2-naphthalenethiol (2-NPT). Within a multiple component suspension reporters were identified by their unique peak and when present within single cells or populations they were additionally identified using component direct classical least squares (DCLS). Within a single cell three of the four components (MPY, DTNB and NBT) were positively identified.

2D SERS imaging can monitor nanotag uptake but it provides no conclusive evidence of cellular inclusion. The simultaneous determination of cellular uptake and nanotag identification was however achieved using combined 3D Raman and SERS imaging. Three of the four components were detected within a single cell and by combining 2D sections from the 3D images it was possible to determine their intracellular location. Determination of intracellular localisation was achieved using principal component analysis (PCA) since it resulted in the resolution of a subcellular compartment.

However, the ultimate success of the system will only be realised when active targeting is demonstrated. Nanotags were functionalised with peptide sequences specific for the endoplasmic reticulum (ER) and trans-Golgi network (TGN). Both nanotag systems were found to locate within lipid rich regions of the cell but they could not be positively confirmed as the ER or TGN. To identify these structures and confirm localisation, further chemometric methods must be investigated including hierarchical cluster analysis (HCA).

In conclusion, the SERS nanotags were suitable imaging agents for 2 and 3D cell interrogation. 3D imaging simultaneously permitted organelle resolution and the intracellular localisation of the SERS nanotags. Targeting systems were developed and

in future work their localisation within organelles will be confirmed by the application of advanced chemometric methods.

Abbreviations

Ag – silver

ATP – 2-aminothiophenol

Au - gold

CCD – charge coupled device

CEA – carcinoembryonic antigen

CHO – Chinese hamster ovarian

CPPs – cell penetrating peptides

CTCs – circulating tumour cells

DCLS – direct classical least squares

dH_2O – distilled water

DLS – dynamic light scattering

DMEM – Dulbecco's Modified Eagle Medium

DPN – dip-pen nanolithography

DPX - distyrene-plasticiser-xylene

DTNB – 5,5'-dithiobis(2-nitrobenzoic acid)

EGFR – epidermal growth factor receptor

ELISA – enzyme linked immunosorbent assay

ER – endoplasmic reticulum

FBS – foetal bovine serum

FT – Fourier transform

HBSS - Hank's balanced salt solution

HCA – hierarchical cluster analysis

HEPES - 4-(2-hydroxyethyl)-1-piperazineethancesulfonic acid

HGNs – hollow gold nanospheres

1,6-HMD – 1,6-hexamethylene diamine

ICAM1 – intercellular adhesion molecule 1

IR – infrared

LUT – look up table

MALDI – matrix-assisted laser desorption ionisation

MBA – 4-mercaptobenzoic acid

MCR-ALS – multivariate curve resolution – alternating least squares

MES - 2-(N-morpholino)ethanesulfonic acid

MPY – 4-mercaptopyridine

MUA – mercaptoundecanoic acid

MUC4 – mucin protein

N.A. – numerical aperture

NaCl – sodium chloride

NBT – 4-nitrobenzenethiol

NIR – near infrared

NLS – nuclear localisation sequence

2-NPT – 2-naphthalenethiol

OSCC – oral squamous cell carcinoma

PBS – phosphate buffered saline

PCs – principal components

PCA – principal component analysis

PDDA - poly(diallyldimethylammonium) chloride

PEG – polyethylene glycol

PEI - polyethylenimine

PMA – poly(isobutylene-alt-maleic anhydride)

PLGA – poly(D,L-lactide-co-glycolide)

PSA – prostate specific antigen

PVP – polyvinylpyrrolidone

Rf – retardation factor

RME – receptor mediated endocytosis

RNS – reactive nitrate species

ROS – reactive oxygen species

RPMI – Rosewell Park Memorial Institute Medium

RRS – resonance Raman spectroscopy

SEHGNs – silica encapsulated hollow gold nanospheres

SEHRS – surface enhanced hyper Raman scattering

SEM – scanning electron microscopy

SERS – surface enhanced Raman spectroscopy

SERS-403 – 5-(4-pyridyl)-1,3,4-oxadiazole-2-thiol

SERRS – surface enhanced resonance Raman spectroscopy

SESORS – surface enhanced spatially offset Raman spectroscopy

SIM – structured illumination microscopy

SORS – spatially offset Raman spectroscopy

STED – stimulated emission depletion microscopy

STEM – scanning transmission electron microscopy

SV40 – simian virus 40

TAT – transactivator of transcription

TBE – Tris Borate EDTA

TEM – transmission electron microscopy

TGN – trans-Golgi network

TLC – thin layer chromatography

X-Gal – 5-bromo-4-chloro-3-indolyl-β-D-galactopyranoside

Contents

Chapter 1 Introduction

When the pioneers of Raman spectroscopy initially conceived the technique in 1923[1] and latterly demonstrated it in 1928[2] it is unlikely that they had any inclination of the future impact or bio-diagnostic applications the method would find. This is due in part to instrumental improvements and successive developments of the original technique most notably surface enhanced Raman spectroscopy (SERS)[3-5] and surface enhanced resonance Raman spectroscopy (SERRS).[6] Since then Raman and SERS have become invaluable analytical techniques for a whole host of applications including *in vitro*,[7-9] *ex vivo* and *in vivo* bio-sensing,[10-12] bio-diagnostics,[13-15] explosives detection,[14] the analysis of illicit[16, 17] and pharmaceutical drugs,[18] the identification of environmental pollutants,[19, 20] the aging and authentication of historic artefacts[21, 22] and the control and monitoring of industrial processes.[23]

In recent years, Raman and SERS have been exploited in the fields of intracellular, tissue and *in vivo* imaging.[7-11, 24] The ability to measure spectroscopic signatures within these matrices are extremely powerful applications of the techniques not least because sensitive and reliable imaging is required for a whole host of diagnostic and therapeutic applications.[10] When used in conjunction with chemometric methods greater levels of information can be extracted, conclusions can be drawn with statistical significance and the true potential of the techniques can be realised. Should the advancement of Raman and SERS as diagnostic imaging techniques continue at the current pace there will be huge potential to revolutionise the ability to detect, treat and manage disease.

The next sections will look at the theory of Raman spectroscopy, cell structure and the vast array of biodiagnostic applications now fulfilled by Raman and SERS.

1.1 Spectroscopy

Spectroscopy is a broad scientific division encompassing a wide range of analytical techniques including fluorescence, infrared (IR) absorption and Raman scattering. However, the underlying objective of any spectroscopic technique remains the same and is concerned with the measurement of discrete amounts of energy that are interchanged between the interrogated system and the electromagnetic radiation.[25] During the interaction process energy can be absorbed, emitted or scattered and the

two predominant methods by which molecular vibrations are detected are IR and Raman.[25, 26] Both of these techniques allow for structural resolution since the produced spectral signatures are characteristic of the molecular components present.[25]

In IR spectroscopy the process is characterised by the absorption of a photon, the energy of which exactly equal corresponds to the discrepancy between the ground and first vibrational level.[25] When this occurs the molecule is promoted to a vibrationally excited stated and in accordance with this promotion a peak will appear in the spectra. The peak position directly corresponds to the energy which has been absorbed and as molecular constituents appear at characteristic regions in the spectral range the chemical structure can be readily elucidated.[25] Raman spectroscopy is complementary to IR and unlike the latter technique scattering rather than absorption is measured.

1.1.1 Raman Spectroscopy

Raman spectroscopy is concerned with measuring the light which is scattered as a result of the irradiating laser interacting with the analyte molecule. During this interaction the light source can polarise the electron cloud of the molecule and when this situation arises a virtual state is formed.[25] However, this state has a limited lifetime, a direct result of its unstable nature and the photon responsible for polarisation is almost instantaneously scattered.[25, 26] Much of the scattered light will be radiated at the same wavelength as that of the irradiating laser, the energy has not changed and this elastic process is known as Rayleigh scattering.[25, 26] However, if during the interaction, motion of the nucleus occurs, the photon is radiated at a different wavelength and the phenomenon of Raman scattering arises.[25, 26]

This inelastic process can be subdivided into two distinct classes known as Stokes and anti-Stokes and these are classified according to whether the molecule was originally in the ground or vibrationally excited state (**Figure 1.1**).[25, 26] Stokes scattering arises when a molecule which was initially in the ground vibrational state relaxes back to a vibrational level of higher energy (**Figure 1.1**). Anti-stokes scattering occurs when a molecule which was initially in a vibrationally excited state relaxes back to the ground vibrational state. (**Figure 1.1**).[25, 26]

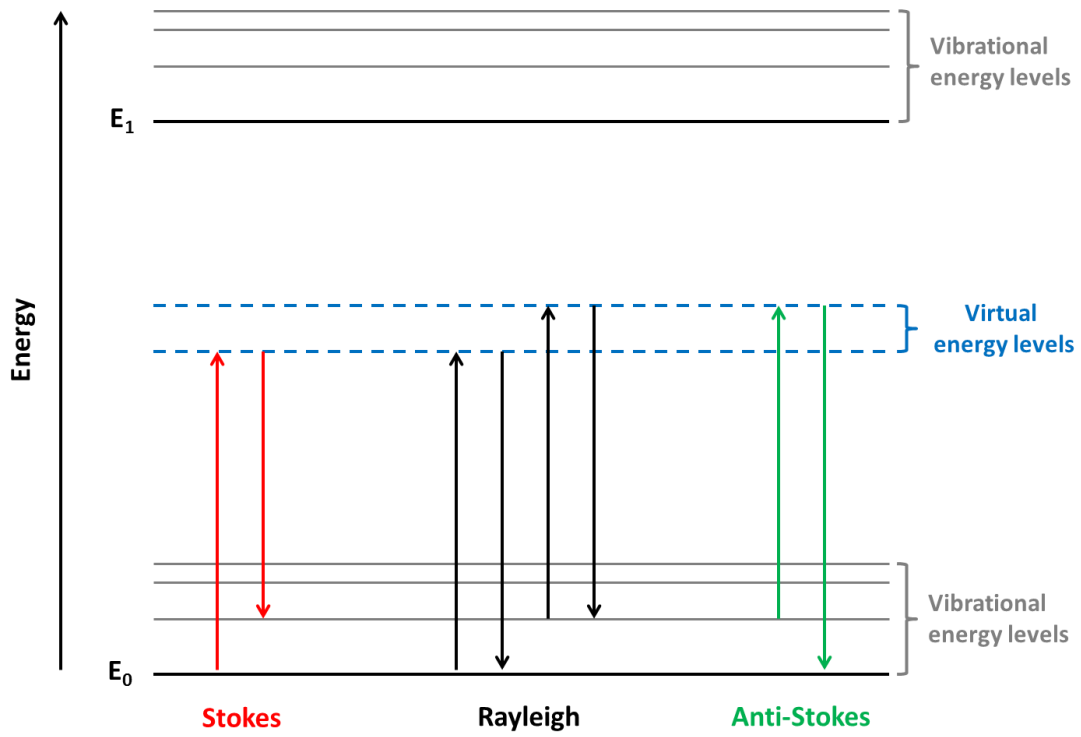

Figure 1.1: Jablonski diagram indicating the transitions between energy levels when light is scattered.

Under normal experimental conditions the proportion of molecules which possess vibrational energy will be minimal and most will be found in the ground vibrational state.[25, 26] This explains why anti-Stokes is the weaker of the two processes and why Stokes scattering is typically measured during a spectral acquisition.[25] Deviations from standard conditions such as a temperature rise will increase the proportion of molecules which reside in the vibrationally excited state and the Boltzmann equation can be implemented to derive the occupation of the two vibrational energy levels.[25]

$$\frac{N_n}{N_m} = \frac{g_n}{g_m} exp\left[\frac{-(E_n - E_m)}{kT}\right]$$

Equation 1[25]

Where:

N_n = the number of molecules in the excited vibrational energy level

N_m = the number of molecules in the ground vibrational energy level

g = the degeneracy of the levels of n and m

E_n-E_m = difference in energy between the vibrational energy levels

k = Boltzmann constant 1.3807×10^{-23} JK^{-1}

T = Temperature K

Key to the proliferation of Raman spectroscopy for the analysis of biological challenges *in vitro*, *ex vivo* and *in vivo* are the features of non-invasivity and the provision of molecularly specific spectra. However, the obvious disadvantage with its implementation is that it can be quite insubstantial, especially when considering that approximately only one for every one million photons are Raman scattered.[25] This weak effect can be negated by successive developments of the original technique including resonance Raman spectroscopy (RRS), SERS and SERRS.

1.1.2 Resonance Raman Spectroscopy (RRS)

The first of the enhancements to the original technique is relatively straightforward and simply involves considered selection of the irradiating laser line such that it corresponds to electronic transition of the interrogated analyte, this is known as RRS.[25] Under these circumstances the molecule undergoes a transition to an excited electronic vibrational level and employment of this method can result in enhancements in the range of 10^3-10^4.[25]

The obvious advantages of this method over conventional Raman are that electronic and vibrational information are simultaneously obtained and the selective enhancement of certain bands results in simplified spectra which are easier to interpret.[25] However, problems surrounding fluorescence and sample degradation must also be considered when implementing this technique.[25]

1.1.3 Surface enhanced Raman Spectroscopy (SERS)

Significant spectral enhancements are also observed if analyte molecules are adsorbed onto a roughened metal surface and this phenomenon is known as surface enhanced Raman scattering (SERS).[3-6] Fleishmann *et al.* unwittingly demonstrated this in 1974 when an increase in signal intensity was observed from pyridine molecules adsorbed on a roughened silver electrode.[3] The increase in Raman signal was initially ascribed to an increased surface area but subsequent studies by the Van Duyne group and Albrecht

et al. empirically determined that this could not account for the enhancements which were observed.[4, 5] The exact mechanistic details of the enhancement remains unknown but within the research community it is widely accepted that the enhancement arises from combined electromagnetic and chemical effects.

1.1.3.1 Electromagnetic Enhancement

The conduction electrons on a metal surface collectively move following laser irradiation and this movement is known as surface plasmon oscillation.[25] On a smooth metal surface the conduction electrons will only oscillate in a parallel direction but roughening of the surface allows for the plasmons to additionally oscillate in the perpendicular direction and scattering can now occur.[25, 27] The surface associated electromagnetic fields are now substantially enhanced intensifying the polarisation experienced by the plasmons and any adsorbed molecule.[25] This leads to significant improvements in the scattering efficiency.

1.1.3.2 Chemical Enhancement

Chemical enhancement proceeds via the development of new electronic states which form as the analyte molecule adsorbs onto the metal surface.[27] Under these conditions a series of charge transfer reactions can occur whereby the charge is transferred from the metal to the analyte and then back again before scattering occurs from the metal surface.[25, 27] The newly formed electronic states and the subsequent charge transfer reactions additionally intensify the polarisation of the system and again significant enhancements in the scattering can occur.[27]

1.1.3.3 Suitable SERS substrates

Suitable SERS substrates include metallic - electrodes,[3-6] coated spheres,[28] planar surfaces[29] and nanoparticles in a range of configurations including spheres, rods and shells.[10, 30, 31] An equally vast array of suitable metals have been investigated and include Au,[32] Ag,[32] Cu,[33, 34] Al,[34] In,[34] Na,[34] Li[34] and K[34] but colloidal suspensions prepared by the citrate reduction of Au and Ag salts are undoubtedly the most prolifically used of all the substrates.[32, 35]

In terms of intracellular imaging their small size, large surface-to-volume ratio and their unique chemical, physical, electronic and optical properties pinpoint their allure and implementation. Nanoparticle surfaces are also readily amenable to

functionalisation via reporter and bio- molecules resulting in the production of novel, sensitive, selective, chemical and biological sensing nanoscaffolds.

In specific relation to their unique optical properties and as discussed previously in section 1.1.3.1 the collective movement of the conduction electrons is known as surface plasmon oscillation. Specifically, this process is characterised by the electron cloud being displaced relative to the nuclei but restorative forces in accordance with the repulsion experienced by the electrons and the nuclei arise and collective oscillation results. [36] This can be tracked by monitoring the plasmon band which will vary depending on the nanoparticle system and the dielectric constant of the metal and the surrounding 'solvent' system.[36, 37]

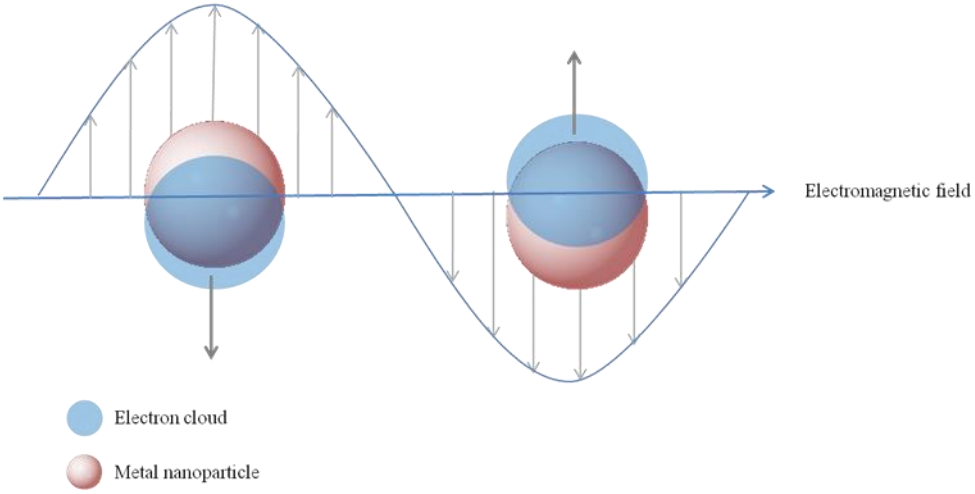

Figure 1.2: The electromagnetic fields which are formed by the surface plasmons are strongly enhanced and the experienced displacement of the nanoparticle electron cloud is shown.

SERS enhancement values are reported as 10^6 but this can be augmented by nanoparticle aggregation which further increases the electromagnetic fields. [38, 39] The most intense of which are thought to arise in the interstitial spaces between particles.[38] Manipulation of this effect can be artificially attained by the use of aggregating agents such as sodium chloride,[38, 40] poly(L-lysine)[34] and spermine.[41] However, artificial aggregation is undesirable for cell based applications, primarily because it is uncontrolled and the structural size must be tightly regulated in order to maintain uptake. The packaging of nanoparticles into endosomes can induce aggregation to a certain extent but it is unlikely that the same enhancement will be attained.[24]

1.1.4 Surface enhanced Resonance Raman Spectroscopy (SERRS)

SERRS was first demonstrated experimentally by Stacy *et al*. in 1983. This final modification of the original Raman technique involves analyte adsorption onto a roughened metal surface and the analyte is also characterised by an electronic transition which corresponds to the frequency of the employed laser.[6, 25] Implementation of the dual modes of enhancement leads to significant increases in scattering efficiency in the 10^{10}-10^{14} range.[6, 25] Fluorescence issues associated with the resonance technique are negated by the incorporation of a metallic scaffold which effectively quenches any fluorescence. Similarly, as a direct result of the conferred enhancement, concerns regarding sample degradation can now be managed effectively by limiting the measurement acquisition and the laser power.[6]

1.1.5 Raman Imaging

Instrumental improvements have undoubtedly revolutionised Raman spectroscopy as a fundamental analytical technique. The development of sophisticated systems coupled to moveable stages and microscopes more akin to a biological laboratory have seen a further reinvigoration of the technique. The result being that Raman spectroscopy has found application in a vast array of research fields and most significantly in *in vitro, ex vivo* and *in vivo* imaging for the detection and characterisation of diseases.

For fast, low-resolution imaging, the optical set up of the system is designed to produce a laser line on the sample. The sample is then effectively rastered by the laser through movement of the motorised stage beneath the objective.[42] The data, which is generated for the entire line at each step, within the predetermined sampling area is simultaneously recorded by the detector.[42] The obvious disadvantage of the method is that the collected images are of low resolution but the speed by which they can be collected can offset this.[43]

Similarly, for the generation of high resolution images, the optical set up generates a laser spot on the sample. Again, the motorised stage moves beneath the objective such that the laser spot interrogates at every defined step of the pre-determined sampling area.[42] Unlike line mapping, a single spectrum is collected from each point on the map as the spot moves across the sample. The obvious advantage is that the images are of

higher resolution than those generated by line mapping but the speed at which images can be acquired is sacrificed.[42, 44]

1.2 The Cell

1.2.1 Basic Cell Structure and Organelles

Cells are the basic units of all living organisms and the way in which they are structurally organised can be used to differentiate them into two main types; prokaryotic and eukaryotic. All single celled organisms such as bacteria and archaea are examples of prokaryotic cells and they are distinguished from eukaryotic cells by the absence of a nucleus and other membrane bound organelles.[45]

Eukaryotic cells are more highly organised and are the structural building blocks of all other forms of life. The outer wall of a eukaryotic cell is composed of a phospholipid bilayer in which cholesterol, carbohydrates, glycol- and integral proteins are all embedded.[45] The phospholipid bilayer essentially consists of hydrophilic head and hydrophobic tail regions and it is this membrane which is responsible for the regulation of components into and out of the cell. Cholesterol is interspaced between the phospholipids in mammalian cells in order to strengthen the bilayer. Integral proteins are also interspaced throughout the bilayer and the quantity and type ultimately determines the role of the membrane.[45] The outer surface of the bilayer is also randomly impregnated with glycoproteins and carbohydrates which are specifically for identification purposes, for example in blood typing.[45] If the identity of the carbohydrates and glycoproteins present on the cell surface is known then they can be specifically targeted with nanoparticle systems.[45] This has recently been employed for the differentiation between cancerous and non-cancerous prostate cells.[46]

Within the cell the most important of the organelles is arguably the nucleus especially when considering the residence of the majority of the genetic material within its structure (**Figure 1.3**).[45, 47] Entry into the nucleus is permitted by way of the nuclear envelope which itself consists of a double membrane. In the interior of the nucleus, chromatin can be found which is comprised of protein and DNA. The nucleolus also resides within the nucleus and is the site of ribosome synthesis (**Figure 1.3**).[45]

The endoplasmic reticulum (ER) is a membrane bound organelle within the cell which consists of two well-defined sections namely the smooth and the rough ER (**Figure 1.3**). The two surfaces are distinguished by their action and appearance, with ribosomes patterning the surface of the rough ER.[45] Protein synthesis is initiated within the rough ER whilst enzymes within the smooth are responsible for lipid synthesis, carbohydrate metabolism and drug detoxification.[45] Adjacent to the ER is the Golgi apparatus which is the logistic centre of the cell. It is responsible for the sorting, modification and distribution of products from the ER (**Figure 1.3**). The trans-Golgi network (TGN) is the distribution centre and vesicles can bud from its surface to transport cargo to the specified locations.[45]

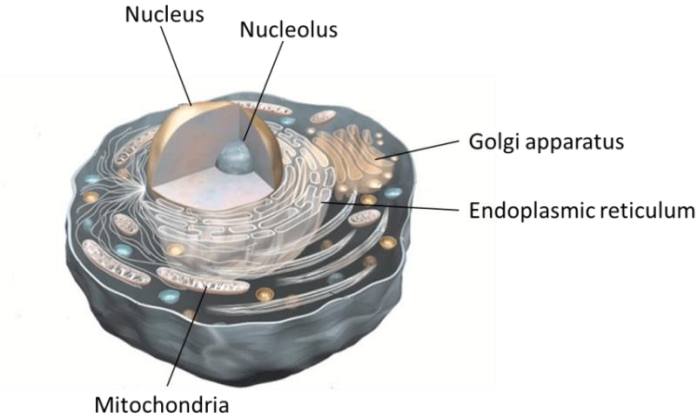

Figure 1.3: Eukaryotic cell structure – the principle cell organelles have been identified and include the nucleus, nucleolus, Golgi apparatus, endoplasmic reticulum and mitochondria. Image modified and reprinted.[48]

The mitochondria are also membrane bound organelles and they are considered to be the powerhouses of the cell since oxidative phosphorylation, the process by which ATP is generated, occurs within the inner membrane space.[49] Mitochondria are characterised by two phospholipid membranes the outer of which is smooth but the inner is highly folded and these invaginations are known cristae.[45] Within the boundaries of the cristae fatty acid oxidation and the citric acid cycle take place.[45, 49]

1.2.2 Cell Lines and Research

The cell lines which are selected for use in research are often dependent on the lines a laboratory has access to and is licensed to culture. Macrophage and dendritic cells derived from Balb/c mice and the immortal epithelial cell lines, HeLa and Chinese Hamster Ovarian (CHO) cells, were of interest for this research.

Dendritic and macrophage cells derived from Balb/C mice are phagocytic cells which engulf a vast array of foreign material non-discriminately.[50] This non-specific uptake of material defines their suitability for use in nanoparticle uptake studies. The oldest and most commonly used cell line is the HeLa named after the patient, Henrietta Lacks, from which they were originally derived. HeLa cells are robust, proliferate at an abnormally rapid rate and are easy to culture hence their use in a research environment. Similarly, CHO cells also demonstrate an ease of culture and although they proliferate at a lower rate than HeLa cells they are also ideally suited for research purposes.

1.3 Cellular Uptake of Nanoparticles and Delivery Strategies

Before any intracellular investigation can be commenced nanoparticles must navigate the plasma membrane and enter cells.[24, 51] Internalisation can occur by numerous pathways for example functionalisation with ligands which will interact directly with membrane receptors[7] or indirectly through electrostatic or hydrophobic mechanisms between the particles and the plasma membrane.[51]

1.3.1 Endocytosis

Nanoparticle introduction is predominantly thought to occur by endocytosis but this is a broad term which encompasses a range of distinct pathways.[51] The simplest and least sophisticated method by which this occurs involves consumption of the particle by the plasma membrane.[24] Once the particle has been engulfed, the portion of the membrane surrounding the particle detaches resulting in endosome formation.[52] This is beneficial because the nanoparticle has successfully transversed the membrane but it is now trapped within an endosome. In order to reach other parts of the cell it must escape otherwise the risk of recycling and ultimately removal from the cell exists.[24] This method of incorporation encompasses phagocytosis and macropinocytosis (**Figure 1.4**) and it is employed by dendritic and macrophage cells which non-discriminately consume material from the extracellular fluid.[50]

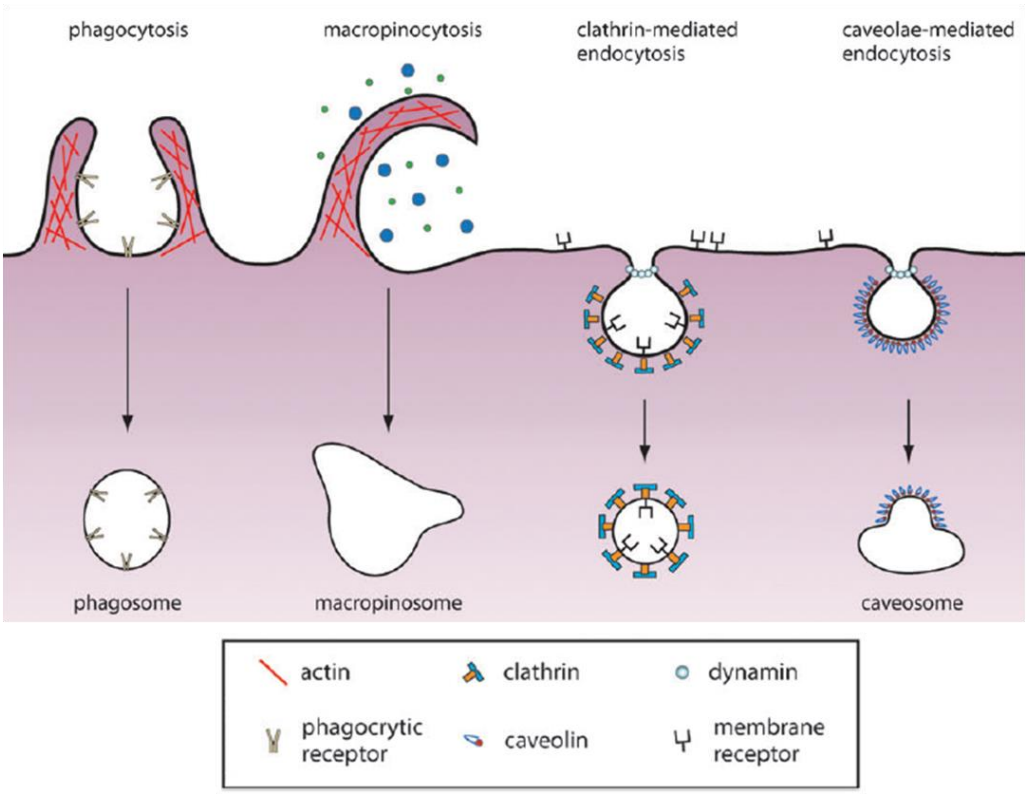

Figure 1.4: Mechanistically distinct endocytic pathways; endocytosis by membrane invagination - phagocytosis and macropinocytosis, receptor mediated endocytosis - clathrin-mediated and caveolae-mediated endocytosis.[51] Reproduced and adapted from[51] with permission of The Royal Society of Chemistry.

Clathrin-mediated, caveolae-mediated and lipid-raft dependent[53] are all examples of direct endocytosis which are thought to take advantage of the cell membrane receptors.[51] Clathrin mediated is the best documented and characterised of the three processes. In simplistic terms, nanoparticles functionalised with ligands bind to the plasma membrane resulting in a surge of clathrin receptors. This surge continues as the membrane infolds on itself with the final result being a clathrin decorated vesicle as a result of enzymatic membrane cleavage (**Figure 1.4**).[51, 54]

The mechanistic details of the other receptor mediated pathways are not as well documented but induction of the caveolae-mediated path may be size and not ligand dependant (**Figure 1.4**). Internalisation of fluorescent latex beads occurred by clathrin mediated pathways when the particles were < 200 nm but as particles were increased to 500 nm the adoption of the caveolae mediated pathway dominated.[55] Caveolae

endocytosis was also considered to be the dominate method by which viruses (e.g. Simian virus 40 (SV 40)) navigate across the cell membrane.[55, 56 57] Entry via this method ensures avoidance of the endolysosomal pathway and thus virus survival. However, the same research group also concluded that the virus could cross the cell membrane more efficiently when the cells were lacking in caveolae.[58 57]This highlights the difficulty in determining the exact method of uptake and the elucidation of the exact mechanistic details.

Endocytosis mediated by lipid-rafts (regions embedded with glycol and lipo proteins) in the plasma membrane, as the name suggests, take advantage of ligand receptor interactions between proteins and functionalised nanoparticles. This recognition system is useful in surface targeting and also in intracellular delivery of drug conjugates.[46, 59] Partlow *et al*. demonstrated that phospholipid coated nanoparticles, which were also functionalised with a ligand for specific receptor targeting, used this method of cell entry, undergoing lipid exchange and fusion reactions with the cell membrane.[59] Such systems can additionally be functionalised with lipophilic drugs which will partition into the lipid layer, thus facilitating drug transport into cells.[59] Infection agents can also manipulate lipid-rafts in the plasma membrane to ensure their uptake.[51, 60]

Regardless of the exact method of endocytosis it has been actively demonstrated that several mechanisms can operate simultaneously to facilitate transport across the cell membrane. In one study where clathrin-mediated endocytosis was found to be the pre-dominant method of uptake, nanoparticle inclusion continued to occur even when this pathway was inhibited.[61] Subsequent inhibition of macropinocytosis but not clathrin mediated processes also resulted in reduced nanoparticle inclusion. This suggests that the particles were taken into the cell by both clathrin mediated and macropinocytosis processes.[61] Similarly, Ochsenkuhn *et al*. demonstrated that when inhibitors to energy-dependent, lipid-raft and clathrin mediated methods of uptake were deployed nanoparticle uptake did not decrease indicating that endocytosis alone was not responsible for cellular inclusion.[53] It was postulated that the particles interacted with the membrane in such a way that a form of 'passive diffusion' was responsible for their uptake.[53]

1.3.2 *In situ* Synthesis of Nanoparticles

Au and Ag nanoparticles can also be synthesised *in situ* by the introduction of their salts into cells. For example, Au^{3+} and Ag^{+} salts which are consumed by the cell are reduced intracellularly to form nanoparticles.[24, 62-65] This method of synthesis is particularly advantageous for Au since the nuclei[63] has been reached in several human cells lines and in bacterial cells access to the cytoplasm is readily achievable.[62] Unsurprisingly and presumably because of their bactericidal action Ag nanoparticles cannot be synthesised within bacterial cells but they can be produced intracellularly in fungi.[66] The main advantage of this method is its simplicity since nuclear targeting can be difficult to achieve even with highly designed nuclear targeting conjugates. However, since the method is reliant on the native cell chemistry there is no control over nanoparticle growth or potential adulterants. In some instances this has led to biofouling of the nanoparticle surface and the formation of small particles, which because of their small size are unsuitable for imaging purposes.[63, 65]

1.3.3 Physical Methods of Introduction

As a guaranteed method of cellular introduction nanoparticles can be physically introduced into the cell by using either microinjection or electroporation.[51] Microinjection uses a glass micropipette with a fine tip for nanoparticle delivery in a manner analogous to that used in *in vitro* fertilisation.[51] With electroporation holes are temporarily generated within the plasma membrane by the application of a voltage.[51] The obvious advantages of both methods are that a higher concentration of nanoparticles can be incorporated than can be achieved by uptake, the methods are compatible with a host of cell lines and most importantly the nanoparticles have not been endocytosed and therefore are free to access regions of the cell which may have been previously prohibited by endosome enclosure.[51] However, both methods require sophisticated experimental setups, a certain degree of technical training and they are not in any way representative of actual cellular uptake.[51]

1.3.4 Biochemical Manipulation for Improved Cellular Delivery

The concept of functionalising nanoparticles with ligands to manipulate receptors on the cell membrane has already been discussed (see section 1.3.1). However, this can be extended further to facilitate optimal uptake by the cell and even nanoparticle escape from vesicles and passage across organelle membranes.[51, 67] In the most elegant and

sophisticated of the examples the targeting moiety can initially be hidden from the cell with exposure resulting after successful passage through the cell membrane. [67] This Trojan horse approach is mutually beneficial since the targeting entity is protected when crossing the membrane and similarly uptake is not retarded by its presence.

A commonly used method for increasing uptake across the cell membrane involves functionalisation or coating of the nanoparticles with cationic molecules. To date positively charged small molecules,[8] liposomes,[68] polymers[69] and cell penetrating peptides (CPPs), rich in the positively charged residues arginine and lysine, [7, 47, 70-72] have all been employed to enhance uptake. Cell uptake is thought to be enhanced by the electrostatic attraction between particles which are positively charged and the phospholipid membrane which is negatively charged. It was postulated that through this interaction nanoscale holes formed in the membrane.[51] Lin *et al.* recently determined this experimentally whereby the structure of the cell membrane was simulated using dipalmitoylphosphaticlylcholine as lipid molecules. Hole formation depended on the size of the targeting entity and its shape but positively charged nanoparticles directly transversed the membrane.[73] It is now thought that positively charged particles bind to negatively charged proteins in the lipid bilayer and as more positively charged molecules approach the membrane, the local electric field changes resulting in the spontaneous formation of a membrane hole and transport of the positively charged molecules into the cell.[73] Cationic particles continue to participate in conventional endocytosis but this offers one theory as to why uptake is greater for cationic molecules.

For organelle specific targeting the nanoparticles must be functionalised with an entity which has an affinity for surface antigens or membrane receptors on the organelle.[51, 74] As mentioned earlier Trojan horse approaches are elegant examples of navigating nanoparticles across the plasma membrane. Such approaches include protective encapsulation of nanoparticles in degradable polymers (degradation is usually environmentally led) and this surface layer facilitates transport across the plasma membrane whilst ensuring protection of the targeting moiety.[51] Kim *et al.* demonstrated this principle whereby quantum dots were functionalised with targeting antibodies before polymer coating with poly(D,L-lactide-co-glycolide) (PLGA).[67] Once inside the cells the endosome pH altered the charge of the polymer, negotiating particle release from the endosome, before cytosol mediated degradation occurred facilitating

release and initiating the targeting capability of the quantum dots.[67] Similar approaches can also be achieved with CPPs and Jin *et al.* demonstrated this principal with peptide and drug functionalised micellar nanoparticles.[75] The driving force for this demonstration results from the fact that positively charged amino acids on peptide sequences can frequently participate in non-specific interactions. However conversion of these side chains to non-interacting equivalents ensures that their targeting capability is maintained while cell uptake is achieved. As with the former example environmentally led pH changes restored the peptide to its original conformation allowing for controlled, target specific, drug delivery.[75]

1.4 Nanoparticles and Cell Toxicity

Nanotechnology, specifically nanoparticle derived biomedical and biodiagnostic applications have increased exponentially in recent years.[76] Intrinsically linked to this growth is an imperative need for the determination of nanoparticle toxicity, in particular, for those systems which are destined for medical use.[76] Any issues surrounding safety must be predetermined via initial *in vitro* and subsequent *in vivo* studies but fortunately the range of toxicity tests and the toxicological parameters for which they test, is vast.[76] For example, they can be used to determine compromised cell and lysosome membranes, impairment of mitochondrial and cell metabolism as well detecting any indicators of membrane apoptosis.[77]

As mentioned previously Au and Ag nanoparticles are some of the most prolifically used scaffolds and as a result the discussion will be restricted to Au and Ag.[76-84] When considering Au and Ag nanoparticles, Au is widely considered to be the more biocompatible of the two but at the cellular level negative effects can still elicited. For example, when Au nanoparticles were introduced to lung fibroblasts *in vitro* a concentration dependant inhibition of cell proliferation was found in addition to gene damage, specifically for those genes associated with maintaining genomic stability and the repair of damaged DNA.[80] Similarly, the introduction of Au nanoparticles into dermal fibroblasts again resulted in reduced cell proliferation and a reduction in protein and collagen synthesis.[85] However, despite the induced damage it was discovered that the cells could recover following nanoparticle removal.[85] In contradiction to the two previous studies it was found that when Au nanoparticles of varying size and surface functionalisation were applied to human leukaemia cells none

of the particle arrangements were toxic.[78] [79] Similarly when Au nanoparticles were introduced into macrophage immune effector cells they did not display any toxicological effects and were actually found to reduce the reactive oxygen (ROS) and nitrate species (RNS).[86]

To fully understand nanoparticle toxicity consideration must also be given to the functionalisation agent since it is this moiety which will ultimately be presented to and interact with the cell membrane. Goodman *et al.* found that nanoparticles functionalised with cationic linkers were more toxic than their anionic functionalised analogues. However, this increased toxicity is not necessarily a representative or comparable effect and may result from an increased uptake of the cationic particles due to their favourable electrostatic interactions with the plasma membrane.[83] Consideration of this effect should be given especially since cationic scaffolds are frequently employed because of this enhanced translocation.[8, 73]

Murphy *et al.* were also keen to highlight the need for discrimination between toxicity and cellular impairment.[78] Many of the employed tests only monitor for specified toxicological parameters which may not be reflective of conditions associated with impaired viability.[78] This principle was demonstrated when citrate reduced nanoparticles were exposed to dermal fibroblasts. In the cells where nanoparticles were found their localisation was associated with the disappearance of actin stress fibres thus effectively minimising the capability of the cell to adhere, grow and synthesise proteins.[87]

As with Au and depending on the circumstances Ag nanoparticles can also elicit a toxicological response.[77] For example, in macrophage cells a plethora of responses were induced following uptake, including impaired mitochondrial function and the induction of responses associated with free radical and cytokine synthesis. The worst of the effects induced damage resulting in apoptotic cell death.[88]

Similarly, as with the Au particles surface functionalisation can have a significant effect on the measured response. Ahmed *et al*. demonstrated that when unfunctionalised and polysaccharide coated silver nanoparticles were introduced into two different cell lines the elicited response was greatest for the functionalised particles.[84] This response manifested itself in the form of damage to the cellular DNA, the most extreme of which

resulted in apoptosis.[84] In a separate study the opposite effect was found and increasing surface functionalisation effectively reduced the toxicity of the system.[89] Nanoparticles were functionalised with mercaptoundecanoic acid (MUA), MUA and poly(isobutylene-alt-maleic anhydride) (PMA), MUA-PMA and 1 PEG and MUA-PMA-saturated with PEG and the later nanoparticles exhibited the lowest toxicity.[89] These studies highlight the variability that can be obtained and how the measured toxicity is highly specific to each system.

Size dependant toxicity was also demonstrated by silver nanoparticles when they were introduced into alveolar macrophages.[81] The toxicity manifested itself in the form of oxidative stress and a significant increase in ROS was observed, as the nanoparticles were decreased in size from 30-15 nm.[81] Oxidative stress of this kind is alarming since irreversible cell damage can result and at particularly elevated levels apoptosis will occur.[81] When size dependant effects were studied further similar results were observed for macrophage cells. The toxicity response was again in the form of oxidative stress and was greatest for the smallest nanoparticles (20 nm *c.f.* 80 and 113 nm).[90] In the same study Park *et al.* also directly compared macrophage and fibroblast cells. The toxicity effects were found to be more pronounced for the fibroblasts, further highlighting differential responses between cell lines.[90]

The toxic effects and/or cellular impairment displayed by Au and Ag nanoparticles is highly variable and a full understanding of the threat can only be achieved when consideration is given to the particle size, shape, surface functionalisation and the specific cell line in question since all can influence the toxicity displayed.[78, 91] With this in mind it would be prudent to incorporate toxicological studies as part of the standard experimental remit for any new body of research.[78]

1.5 *In vitro, Ex vivo* and *In vivo* Applications of Raman and SERS

1.5.1 Raman Spectroscopy and Cells

Raman spectroscopy is a non-destructive and non-invasive analysis technique which is ideally suited for studying cellular structure and monitoring cellular events relating to cell health and viability.[92-94] Alternatives to Raman spectroscopy for monitoring cellular structure include fluorescence, scanning electron microscopy (SEM), cryoelectron microscopy and X-ray diffraction and topography.[94, 95] However, none of these

techniques can offer the molecularly rich and biochemically specific information provided by Raman. The techniques are also invasive and the processes of sample preparation including staining, fixation or freezing can destroy or distort the cell and the spectral information which is obtained.[94] Instrumental improvements have also ensured that Raman spectroscopy can be used in a number of configurations to accumulate the information which is required. For example, the attainment of a live cell image does not require the same resolution as an image detailing organelle structure. As such the laser power, spatial resolution and acquisition time can all be tuned accordingly.[96]

From the outset the resolution of cell organelles by Raman spectroscopy may seem like a trivial matter especially when considering the sophisticated applications of the technique for *in vivo* disease detection.[97, 98] However, organelle resolution and structural characterisation of the cell are equally important for the determination of disease. The architecture of the cell can be altered considerably during processes such as differentiation,[93] mitosis and apoptosis[99] and uncontrolled division and cell death can be indicative of pathosis, including tumour growth, inflammation, HIV infection and neurodegeneration diseases such as Parkinson's and Alzheimer's.[94] Therefore, documentation of this can allow for characterisation of the cell cycle, cell health and viability.[99] As with many applications of Raman the employment of chemometric methods has permitted the resolution of cell organelles. From large identifiable structures such as the nucleus[92] to much smaller membrane bound vesicles[93] and organelles like the mitochondria.[99] The implementation of fluorescent stains in conjugation with Raman imaging has resulted in a sophisticated publication to differentiate between the major cell organelles including the nucleus, mitochondria, ER and the Golgi apparatus. (**Figure 1.5**)[94] The fluorescent stains delineated the organelle boundaries such that the Raman spectra could be extracted from these locations to determine organelle specific spectra (**Figure 1.5**).[94] This is a critical step forward since these membrane bound organelles, with the exception of the nucleus, are structural similar and difficult to differentiate between. The confident spectral resolution of these organelles under 'normal' circumstances will be essential for monitoring any changes in cellular organisation that occurs as the result of disease processes.[94] The advent of 3D Raman cell imaging, which has also resulted in the resolution of cell organelles, will also undoubtedly be important in the abovementioned scenarios where the cell

architecture changes.[95, 100] 3D tissue imaging will also be useful for monitoring changes as a result of infection or injury.[100]

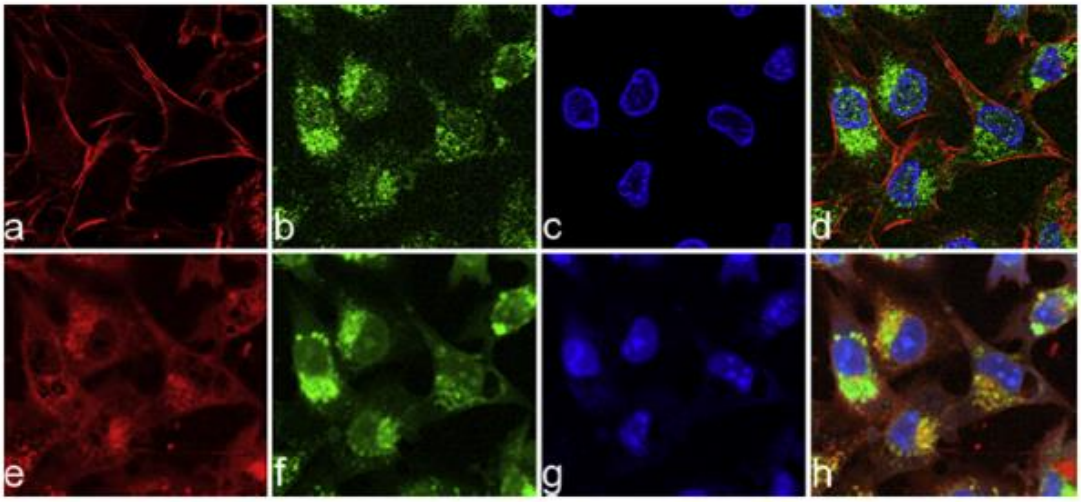

Figure 1.5: Comparison between the immunofluorescent images and false colour images created using organelle specific Raman spectra. a)-d) immunofluorescent and e)-h) Raman images corresponding to the cytoskeleton a) and e), Golgi b) and f), nuclei c) and g) and composite image d) and h).[94] Modified and reprinted from Biophysical Journal, Vol. 102, K. Klein, A.M. Gigler, T. Aschenbrenner, R. Monetti, W. Bunk, F. Jamitzky, G. Morfill, R.W. Stark and J. Schlegel, Label-Free Live-Cell Imaging with Confocal Raman Microscopy, 360-368, (2012), with permission from Elsevier.

Raman spectroscopy can additionally be used to give an indication towards cell health - readily differentiating between healthy and diseased cells based on their spectral signatures.[101] Live and dead cells can be distinguished based on DNA peaks at 782, 788 and 1095 cm^{-1} but most notably by the peak at 788 cm^{-1}. In dead cells this peak was found to reduce significantly in intensity.[102] The authors also observed that spectral variations were apparent in cells at various phases of their life cycle .[102] Cell death in response to an external stimulant was also monitored and the same reduction in the peak at 788 cm^{-1}, which is characteristic for DNA, was observed for the dead cells.[103] The authors noted that this could provide a method to evaluate toxicity in response to the effects of an external stimulant (i.e. nanoparticles) and as a non-destructive method for determining cell viability.[102, 103] Indeed, cell stress as a result of exposure to an external stimulant was latterly measured in this way. Changes were observed in the Raman spectra and morphological changes were evident in the white light and false colour Raman images when cells were exposed to the lysis agent Triton X-100. In the

highly stressed cells morphological changes in the false colour maps were indicative of apoptosis, including contraction of the cell and nuclear attrition.[104] Cell stress can additionally be monitored by Raman by way of autophagy – a survival mechanism whereby cells package material into vesicles known as autophagosomes in response to toxins, famine and as a method by which to remove degraded cellular components.[105] Similarly, the process of apoptosis can be followed using Raman and it was found that DNA specific bands increased in intensity in accordance with condensation of the nucleus.[106] The oxygen status (oxygenated vs. deoxygenated) of single red blood cells was also determined by Raman spectroscopy and this may prove to be diagnostically important for pathosis which afflict erythrocytes.[107]

Cells can also be readily distinguished on the basis of their phenotypic differences and this has been used to discriminate between bone[108] and lung cells,[109] and more importantly in terms of disease diagnosis between cancerous and non-cancerous cells.[110, 111]

In order to direct the differentiation of stem cells there is a need to determine the initial cellular status. This can currently be achieved by immunohistochemical methods but it represents an invasive method of analysis.[112] However, Raman spectroscopy in conjunction with chemometric methods represents a non-invasive alternative by which to discriminate between differentiation statuses. [112, 113] The authors found that the spectral differences could be attributed to compositional variations in the protein and DNA.[113] The spectral determination of RNA content has also been validated as a method for distinguishing between undifferentiated and differentiated stem cells.[114]

1.5.2 Raman Spectroscopy and *ex vivo/in vivo* Applications

1.5.2.1 Breast Cancer

The incidence of breast cancer in the UK accounts for the greatest proportion of all cancer diagnosis and like all forms of the disease there is a demand for sensitive, selective and non-invasive detection.[98] The feasibility of using Raman spectroscopy to detect breast cancer was first demonstrated experimentally in 1991. Alfano *et al.*, employed Fourier transform (FT) Raman spectroscopy and postulated that the spectral variations between cancerous and non-cancerous tissues could be implemented as a method for disease diagnosis.[115] Confocal Raman measurements also demonstrated the

ability to distinguish between healthy, benign and malignant tissue samples. In this particular study the compositional differences were investigated and the changes were used to successfully determine the pathology of the tissues which ranged from healthy to fibrous to cancerous.[116] Further technical progressions and a subsequent adaptation of the original Raman technique also led to the development of spatially offset Raman spectroscopy (SORS). This has a demonstrated ability to differentiate between calcifications associated with cancerous and non-cancerous tissues at a depth of 8.7 mm.[117] The authors reported that this could be used to complement the current clinical method of detection, mammography, whilst simultaneously demonstrating the potential to minimise the number of invasive biopsies.[117] Successive developments and the implementation of an advanced transmission Raman setup increased the thickness of tissue through which cancerous and non-cancerous samples could be differentiated.[118] The depth of detection was increased to 27 mm with anything above 20 mm being classified as clinically significant for *in vivo* detection. This further highlights the applicability and relevance of implementing the technique in a clinical environment.[118] More recently SORS has been investigated as a possible method for analysing the boundary surrounding the area from where diseased breast tissue has been removed.[119] Reappearance is usually in close proximity to the original site of cancerous growth therefore there is a critical need to characterise the remaining tissue to ensure that all the diseased sections are removed whilst minimising the loss of healthy tissue.[119]

This is in no way an exhaustive review of the implementation of Raman spectroscopy in the diagnosis of breast cancer but it does highlight the possibility of using the method to do so and the potential for it to be applied in a clinical setting.

1.5.2.2 Skin Cancer

The non-invasive nature of Raman spectroscopy also lends itself for implementation in the diagnosis of skin cancer, especially considering that the current diagnostic method primarily involves invasive biopsy procedures.[120] In a study analysing 453 samples including melanomas, carcinomas and the non-cancerous skin lesions keratosis and nevi the technique successfully discriminated between malignant and benign lesions.[120] In addition to diagnosis it is suggested that Raman could be implemented to accurately determine tumour boundaries in a manner analogous to that described for breast

cancer in the previous section.[97] As with breast cancer there is a real need for the thorough ablation of the malignancy whilst minimising the removal of healthy tissue. [97]

1.5.2.3 Prostate Cancer

The detection of prostate cancer *via* Raman spectroscopy was initially determined *in vitro* by Crow *et al.*[121] It was found that it was possible to differentiate between cancerous and non-cancerous samples and within the cancerous sample set it was also possible to differentiate specimens based on their differential levels of aggressiveness.[121] The authors noted that distinguishing between samples in this manner would lend the technique for application in tissue grading.[121] Later studies also investigated whether the same principles could be applied for the differentiation of representative prostate cancer cell lines. As with the tissue samples, it was found that Raman was a suitable method for cell line discernment. [122] Subsequent studies looked at the feasibility of using a fibre optic probe system for the diagnosis and it was found that it was possible to distinguish between malignant and benign samples with a reasonably high level of accuracy.[123] Implementation of the fibre optic probe was a significant step forward and its design was such that it could easily be coupled to current endoscopes, highlighting the ease of implementation for clinical studies.[123]

1.5.2.4 Bladder Cancer

In a manner analogous to that described for the detection of prostate cancer it was possible to use Raman spectroscopy for the differentiation of malignant, inflamed and normal bladder samples.[124] *In vitro* fibre optic probe analysis was also performed and again it was possible to distinguish between those samples which were malignant and those which were benign with a reasonably high level of accuracy.[123] As with the prostate cancer discussed above the use of a fibre optic probe highlighted the potential to rapidly implement the technique for analysis *in vivo*.[123] Successful *in vivo* analysis has taken place and it was possible to distinguish regions of the bladder that were cancerous from those which were normal.[125, 126]

1.5.2.5 Cervical Cancer

Cervical cancer is currently detected via screening and histopathology methods which can lead to erroneous results since they are reliant on human collection and interpretation.[127, 128] However, initial results based on the use of Raman spectroscopy for the diagnosis of cervical cancer were particularly encouraging and not only was it

possible to distinguish cancerous from non-cancerous tissue but abnormalities such as inflammation and metaplasia could be readily differentiated from the actual cancerous samples.[128] Despite these promising results the data was collected *in vitro* and the authors warned that the method was not yet suitable for extension *in vivo* because of the extended acquisition times.[128] However, subsequent *in vivo* experiments were successful at differentiating between cancerous, non-cancerous and altered tissue samples. Nonetheless, the initial sample set was small and again the diagnostic acquisition times were long (1-3 min).[129] In accordance with instrumental developments, in particular miniaturisation which resulted in a portable system and in compliance with application in a clinical setting much shorter acquisition times (5s c.f. 90s) were implemented.[129, 130] In this much larger clinical study it was possible to differentiate between the tissues which ranged from normal to benign to dysplastic. The tissue was also graded with higher sensitivity and specificity by the spectroscopic method than was achieved by the histopathology expert.[130]

1.5.2.6 Colorectal Cancer

The current methods for screening of colorectal disease are not necessarily fit for purpose since many of the indistinct lesions escape detection and for those patients who present with several lesions multiple biopsies can be somewhat unfeasible.[131] As a result of this, analysis and biopsy using *in vivo* Raman spectroscopy has become an appealing replacement especially since multiple lesions could be characterised without the need for tissue removal.[131] Several groups have looked at methods for distinguishing between normal, altered but non-cancerous and cancerous polyps. Each group found it was possible to differentiate between the tissue grades with high specificity and sensitivity.[132, 133] Similarly, when a probe based system was tested *in vivo* cancerous polyps were identified with high sensitivity, specificity and accuracy.[134]

1.5.2.7 Alternative Disease Based Detection Systems

In addition to the other forms of cancer discussed, cancer of the oesophagus is another area which has been intensely studied.[98] As with many of the disease processes outlined it was possible to diagnose and classify tumours with high sensitivity and specificity when *in vitro* samples were analysed by Raman spectroscopy.[135] Successful *in vivo* studies have also been performed[136] but some leaders in the field report that there is still a real need to substantiate the capacity of the technique to grade tissues *in vivo* and in general there is a need to make the technique more robust in terms of

repeatability especially when considering the variability in instrument setups.[98] A proof of concept study also investigated the possibility of detecting brain tumours, *in vivo*, in mice models.[137] The authors reported that the tumours could be located with an accuracy of approximately 250 μm and while principally a demonstration of what could be achieved, the authors emphasised the possibility of using Raman spectroscopy for brain analysis and tumour detection in a live subject.[137]

Raman spectroscopy is not limited to the detection of cancer and research has postulated that the method could be used for the characterisation and monitoring of atherosclerotic plaques.[138] In the UK alone coronary heart disease and the conditions which stem from it cost an estimated £19 billion.[139] This is clearly an extensive and significant problem and Raman was found to be a suitable method by which plaque deposits could be distinguished and their size determined.[138] The effects of statin drug treatment were also tracked, and in mice that were provided a cholesterol rich diet, the statins successfully minimised plaque formation.[138] Whilst this remains a proof of principal study there is potential for extension to studies in man and although not demonstrated, remote sensing could be achieved with a fibre optic probe system.[138]

Similarly, Raman spectroscopy has been implemented to monitor organ rejection in patients following transplant procedures.[140, 141] While not directly involving the detection of disease, it is possible that the processes which led to transplant were the result of disease, for example, coronary heart or chronic kidney disease and these studies demonstrate the application of Raman for monitoring subsequent disease effects. In the particular instances of heart and kidney transplant the confirmation of rejection requires an invasive biopsy procedure and the observation of an elevated serum creatinine level, respectively.[140, 141] However, the rejection of heart tissues can be characterised by serotonin biomarkers, which can be detected using Raman, presenting a viable non-invasive alternative to biopsy.[141] While the methods for monitoring kidney rejection do not require the same invasive procedures, by the time detection of serum creatine is confirmed significant deterioration of the organ can have occurred. [140] Raman spectroscopy was employed as a method to differentiate between T-cells which were produced in response to different stimuli (i.e. in response to rejection and under normal circumstances).[140] These were selected as biomarkers for monitoring the rejection response since the process is primarily characterised by T-cells. The technique was found to be suitable for differentiating between normal cells and those

which are characteristic of a rejection response.[140] It should be noted that the T-cells were not directly obtained from a patient undergoing rejection but rather the cells were artificially modelled to be representative. Raman spectroscopy therefore represents a viable alternative by which rejection could be monitored.

1.5.2.8 Summary

Raman spectroscopy has found application in a wide variety of medical and research fields because it offers a non-invasive, non-destructive and molecularly specific method by which considerable information can be gained. Instrumental improvements and thoughtful design has led to a whole range of suitable configurations, including portable fibre optic probe based systems, for analysis in a variety of settings. Although it is an inherently weak process with careful consideration and optimisation of the employed laser power and acquisition time clinical relevant signals can be achieved from a whole host of biological matrices. Central to all of the discussed applications is the implementation of chemometric methods and it is these which are responsible for the elucidation of information hidden within the Raman spectra. Chemometric methods also allow conclusions to be drawn with statistical significance.

1.5.3 SERS and *In vitro* Investigations

1.5.3.1 SERS and Intracellular Investigations of Cell Components

Raman spectroscopy is routinely used for the analysis of cell structure and highly detailed images can be obtained.[93] However, since it is an inherently weak process intracellular signals can be enhanced by the incorporation of metallic nanoparticles.[52, 142] The SERS based method is advantageous since it can provide information relating to the intracellular localisation of the nanoparticles and also about any intrinsic bands which may be selectively enhanced by their presence.[24]

The cellular composition can also be derived by the analysis of intrinsic cell bands.[142] Kneipp *et al.* demonstrated this by measuring signals in live cells from protein, amino acid, DNA and RNA components.[142] Additionally, they determined that by measuring representative spectral peaks of both protein and DNA it was possible to determine their co-localisation.[142] Protein was identified by phenylalanine at ~1004 cm^{-1} and DNA by the band at ~1120 cm^{-1}. The determination of these signals not only allowed for the elucidation of the cellular components but the method demonstrated how the signals

changed throughout the cells and ultimately where co-localisation occurred.[142] However, the obvious drawback of this method is that it does not provide a picture of the cell in its entirety since nanoparticles are not disseminated throughout cells in a uniform fashion.[24]

Whilst probing the intracellular composition is undoubtedly interesting nanoparticle incorporation can also be used to monitor cell events such as endocytosis. For example, cells can be monitored throughout the period of uptake and the temporal spectral changes can be used to provide information about the cellular environment.[52, 143] When epithelial and macrophage cells were exposed to gold nanoparticles the SERS spectra changed with time, increasing in intensity as endocytosis progressed and as increasing numbers of nanoparticles were packaged into vesicles.[8, 52] Significant spectral differences were observed between the two cell lines following vesicle enclosure and as might be expected, this indicated that the two cells lines subjected the nanoparticles to distinctly different, cell specific, endosome treatment.[52]

The introduction of metallic nanoparticles can be further used to assess life cycle stage and to differentiate between cancerous and non-cancerous cells thus providing means by which to assess health.[24, 144, 145] For example, when silver nanoparticles were introduced into cancerous and non-cancerous tissue samples spectral variations allowed for their discrimination.[24, 144] This method of differentiation is analogous to many of those discussed in the previous section (section 1.5.2) with the exception that the signals are now enhanced by nanoscaffolds.[24] Programmed cell death can also be monitored through the appearance of DNA bands in the spectra. At present, nuclear penetration or targeting can be difficult to achieve and as a result only a few DNA bands are typically observed when unfunctionalised nanoparticles are present in healthy cells. However, in apoptotic cells the nucleus condenses and then fragments, and DNA bands can be measured throughout the cell.[145] While apoptosis can be monitored via intracellularly located nanoparticles the SERS effect can be manipulated in an alternative fashion to provide a label-free method by which to also monitor apoptosis.[146] Jiang *et al.* directly formed silver nanoparticles on the surface of silicon wafers which were subsequently used as attachment surfaces for cell growth.[146] Cell death, as with the intracellular method, was monitored via DNA spectral variations, further highlighting the applicability of SERS for measuring cell life cycle stage.[146]

1.5.3.2 SERS Nanotags

To actively image and/or target and detect disease *in vitro*, *ex vivo* and *in vivo* the sophistication of the implemented 'nanotag' systems varies. For example, *in vitro* methods have employed unfunctionalised nanoparticles for simple sensing applications, including the monitoring of enzyme activity [147] or in the determination of intracellular components.[142]. Whilst more sophisticated systems range from metallic nanoparticles labelled with reporter molecules [7, 8, 148-150] to even more complicated systems with mixed reporter monolayers [151], dually functionalised systems consisting of reporter molecules and membrane penetrating or targeting antibodies [9, 152, 153], peptides [7, 70, 71] or oligomers.[154] To minimise or prohibit degradation from the surrounding environment nanotag structures can be afforded a certain degree of stability by silica [10, 12, 39] or polymer encapsulation. [9, 155, 156] The incorporation of polyethylene glycol (PEG) again offers protection from the chemical and physical environment, minimisation of non-specific binding [157] and, depending on the terminal functionality, PEG is also readily amenable for bioconjugation to a range of targeting ligands. [158]

1.5.3.3 SERS Nanotags and pH Sensing

Intracellular pH probes have also been developed by labelling metallic nanoparticles with pH sensitive molecules such as mercaptobenzoic acid and mercaptopyridine. Ratiometric peak variations at known pH values can be used to construct pH calibrations to allow for intracellular predictions of pH.[159-162] Knowledge of the intracellular pH is beneficial for many reasons particularly because it can be used to decipher the cell specific endocytic pathway and it can also be used to design more robust and elegant nanotags capable of escaping the endolysosomal pathway. The endocytic pathway in HeLa cells has already been deciphered using this method.[160] Pallaoro *et* al., found that the intracellular pH was predominantly pH 4-5 with a few locations registering pH values of 6 and even less measuring pH 7-8. On the basis of these pH values it was concluded that clathrin mediated endocytosis was the predominant method of uptake since the pH of endosomes generated by this pathway are typically between pH 4-5. Endosomes formed by caveolae mediated endocytosis or macropinocytosis tend to have a higher pH.[160] In addition to determining the specific method of endocytic uptake intracellular pH measurements can also monitor the progress of pH sensitive nanotags along the endolysosomal pathway in accordance with endosome maturation.[163]

Complementary to pH measurements is the ability to monitor the intracellular redox potential. Knowledge of this is important because it can vary at different stages of the cell cycle and in response to toxins.[164] Extremes of redox potential, in particular, highly oxidising environments, are often indicative of underlying disease conditions.[164] In one study, redox responsive small molecules were used to label gold nanoshells and their ability to measure the intracellular redox potential was demonstrated.[164] Auchinvole *et al.* also reported that the redox sensors could also be developed further to target specific organelles in order to monitor their modes of redox regulation.[164]

1.5.3.4 SERS Nanotags and *In vitro* Applications for the Detection of Disease

SERS based nanotags have been used in a variety of different formats for the *in vitro* detection of disease. In some of the earliest examples, functionalised nanoparticles and nanotags were not employed for the detection of disease, instead metallic surfaces were used to exploit the SERS effect. In one such system used for the detection of glucose, spheres were coated in a layer of silver for the provision of the SERS enhancement and they were subsequently functionalised with both decanethiol and mercaptohexanol.[28] Dual functionalisation with molecules of varying chain length results in hole formation between the different chains, actively providing a region into which the glucose molecules can enter and the response can be measured via SERS.[28] With the implementation of the system it was possible to quantitatively detect glucose and the majority of the measurements were detected within levels which were considered to be medically relevant.[28] The authors also reported that the system worked effectively even when interfering analytes were present.[28] Detecting glucose in real-time is of huge importance for diabetes sufferers who currently check their levels via pin prick blood tests. With this method of monitoring huge variations in glucose levels are often missed and in order to improve disease management, there is a real need for accurate continuous monitors.[28] Later work by the same group has strived to further develop this method for *in vivo* sensing.[165-167] In the initial stages the sensors (as described above) were implanted into animal models and the glucose levels were successfully measured via SERS and surface enhanced spatially offset Raman spectroscopy (SESORS) respectively.[165-167]. (SESORS shall be discussed further in section 1.5.4.1). In the most recent developments, the same sensor has been investigated via animal implementation.[167] The device was found to actively work over 17 days and more importantly the authors reported that between days 6 and 17, the measured glucose levels were found to lie within the clinically relevant levels.[167] This

elegant and sophisticated example is a significant step forward in the development of a method by which diabetes sufferers could monitor and control their condition more accurately.[167] A similar format was also used to monitor lactate quantitatively.[168] Variations in lactate levels can be indicative of trauma in a number of medical conditions and as with glucose monitoring the ability to measure lactate in real time would further improve the clinical care offered to patients suffering from a range of conditions.[168]

In other examples, the SERS enhancement was achieved using metallic nanoparticles. Using this format and a nanofluidic device Chou *et al.* demonstrated the detection of the β-amyloid peptide, which is a key component in plaques in sufferers of Alzheimer disease.[169] β-amyloid detection was achieved by concentrating the nanoparticles and target molecules within the device, irradiating with a laser and monitoring the SERS signal.[169] To demonstrate the sensitivity of the detection system the author's added additional proteins of similar and different conformations. Analysis of the SERS signals found that it was possible to discriminate between the different protein forms,[169] in particular, α-helices could be discriminated from β-sheets and between the different β-sheet forms discrimination was also possible.[169] Having a method by which to characterise the disease process is hugely beneficial and it could be used as a method to monitor disease development.[169]

Unfunctionalised nanoparticles have also been used to monitor enzyme activity intracellularly.[147] This is relevant in terms of disease detection since some notable diseases, including cystic fibrosis, Parkinson's and Alzheimer's are all characterised by some form of abnormal enzyme activity.[147] In the study Au nanoparticles were incorporated by cell populations alongside the colourless substrate X-Gal, where upon internalisation it was enzymatically transformed by β-galactosidase enzymes to 5,5'-dibromo-4,4'-dichloroindigo. This transformation was characterised by the appearance of a peak in the SERS spectra at 598 cm^{-1} and a blue colour which was indicative of the turnover of the substrate by the enzyme (**Figure 1.6**).[147] The conversion was specific to the enzyme as confirmed when known enzyme inhibitors were introduced (**Figure 1.6**) and the corresponding reduction in the measured SERS signal.[147] High resolution analysis of single cells and cell populations suggested that enzyme action was localised in specific cellular compartments which were proposed to be endosomes.[147] The authors expressed a desire to quantify enzyme levels within these compartments,

particularly in response to different disease stimuli and states since it is hoped that such knowledge will facilitate the development of suitable treatments.[147]

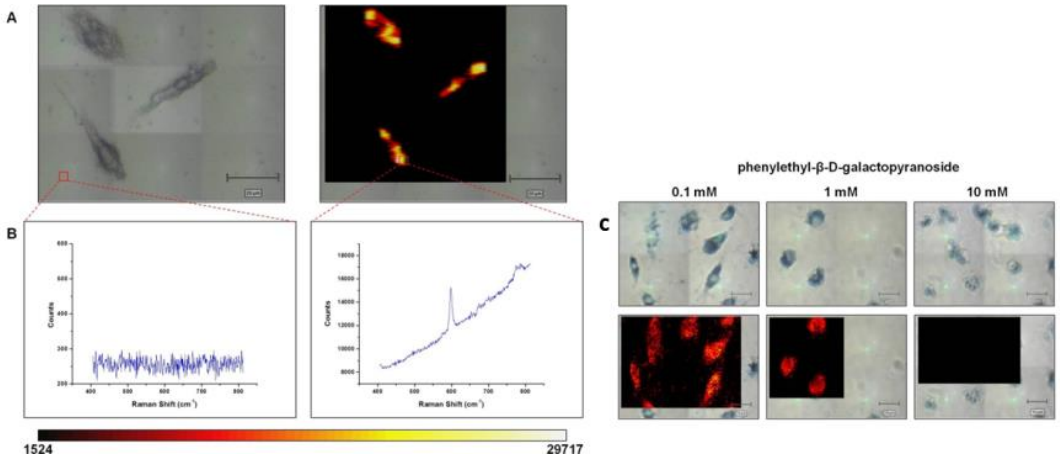

Figure 1.6: Intracellular conversion of X-Gal to the blue coloured product 5,5'-dibromo-4,4'-dichloro indigo by the enzyme β-galactosidase – A) white light and false colour image based on the 5,5'-dibromo-4,4'-dichloro indigo peak at 598 cm^{-1}, B) corresponding spectra from the highlighted areas and the associated false colour LUT bar and C) the effect of an enzyme inhibitor on the measured SERS signals.**[147]** Reproduced by permission of the RSC.

More recently systems for disease detection have looked at functionalised nanotags.[170-172] In one immunoassay, the detection of the carcinoembryonic antigen (CEA), a marker frequently used for the detection of lung cancer, was achieved using a combination of hollow gold nanospheres (HGNs) and magnetic beads.[172] Porter *et al.* also implemented an immunoassay format for the detection of the pancreatic cancer marker, MUC4.[170] This marker is suitable for detecting cancer since it appears to be absent in healthy and pancreatitis-suffering populations.[170] Detection was achieved using SERS via gold nanoparticles which were labelled with a reporter molecule and an antibody specific for the marker. SERS was critical for the detection of disease, especially as the authors noted that conventional immunoassay formats had failed to detect the protein in human sera.[170] In an extension of this initial work Porter *et al.* developed an immunoassay system which could simultaneously detect two markers of pancreatic cancer.[171] The detection of multiple disease markers is a key step in the future of disease diagnosis since it is rare for disease processes to be represented or characterised by a single indicator.[10] In addition, the detection of multiple aspects of a disease will undoubtedly lead to better personalised medicine and immunoassays could be extended to detect a plethora of diseases simultaneously.

Cell based detection is a vast field and in particular research has centred on detecting breast cancer.[173, 174] One of the earliest studies employed SERS dots (a form of silica encapsulated nanotags) functionalised with breast cancer (HER2) or leukaemia specific antibodies (CD10).[173] Antibody functionalisation was required so that the dots would bind specifically to the corresponding cell line and when the conjugates were incubated with different cell populations this specificity was observed.[173] HER2-functionalised dots only bound to the breast cancer cells and similarly the CD10 functionalised dots bound only to the leukaemia cells.[173] SERS signals were not observed when either of the antibody functionalised nanotags was incubated with the control cell population.[173] This initial study highlighted the possibility of screening cell populations for cancerous and non-cancerous cells and, provided that each subset of dots was labelled with a distinct reporter and an antibody, a range of disease could be detected simultaneously. The authors also reported that the method could potentially be implemented as an alternative to the radioactive tagging of cells and tissues.[173]

Later, studies took advantage of the same binding relationship between HER2 antibodies and the corresponding receptors on cell membranes.[30, 31] However, rather than focusing on spherical shaped nanostructures rods and HGNs were investigated as alternative imaging scaffolds.[30, 31] In both instances, recognition via the specific antibody-antigen interaction was achieved and brighter images were observed (**Figure 1.7**).[30, 31] The increased SERS intensity in the false colour images were not the result of any improvement in the binding efficiency but were a direct result of the enhanced optical properties demonstrated by both the rods and HGNs (**Figure 1.7**).[30, 31] The authors suggested that both systems are extremely sensitive imaging agents and when designing a disease detection system consideration should also be given to the imaging scaffold especially if the disease target is present at low concentrations.[30, 31]

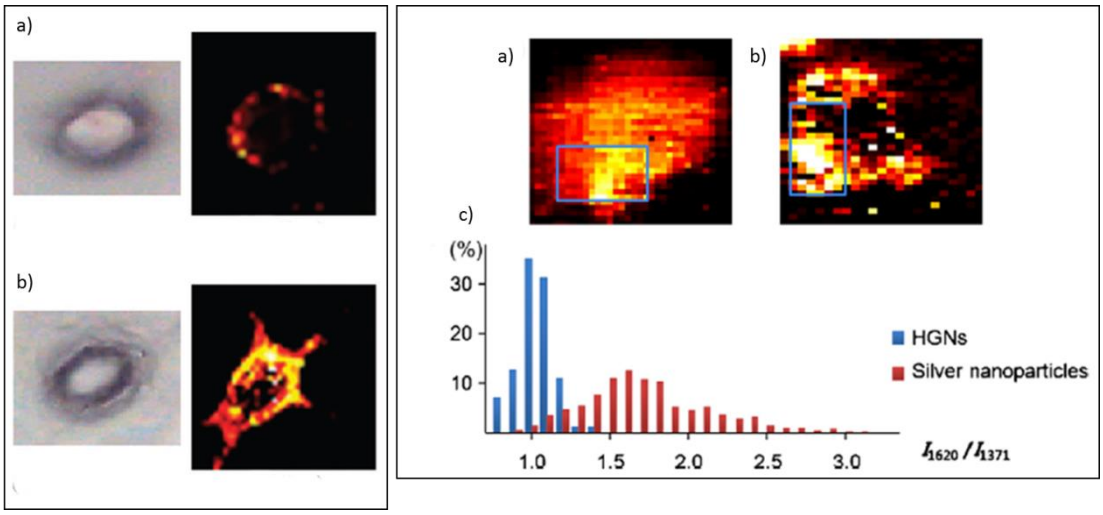

Figure 1.7: Left Panel – differential levels of binding between a)gold nanospheres and b)rods functionalised with HER2 antibody and exposed to MCF7 cells overexpressing HER2.[30] Right panel – differential levels of binding between a) HGNs and b) silver nanoparticles functionalised with HER2 antibody and exposed to MCF7 cells overexpressing HER2, c)intensity ratios for the peaks at I_{1620}/I_{1371} for the crystal violet reporter.[31] Reprinted with permission from Elsevier.

In a recent study antibody-antigen interactions were also studied as means for differentiating between disease states.[152] The development of the nanostructures involved the labelling of silver nanoparticles with reporter molecules, and HER2 antibodies were subsequently conjugated via the terminal carboxylic acid group on the reporter.[152] The functionalised nanostructures were then exposed to two cell lines (SKBR3 and MCF7) which demonstrated a differential level of HER2 expression.[152] In the SKBR3 cell line which exhibits a high level of HER2 expression the SERS signal was observed by the authors to be 3-4 times greater than in MCF7 cells, which have a low level of expression.[152] Although significantly greater levels of data would need to be collected from cells, at a number of different disease stages, this preliminary study highlights the implementation of SERS nanotags for the categorisation of cancerous disease states. The principles of the study are not limited to cancer and any other condition which exhibits differential levels in the expression of disease markers could be analysed and graded in an analogous manner.

In the most recent study implementing breast cancer cell lines, the cell phenotype was determined from specific antibody-antigen interactions occurring between nanostructures labelled with antibodies and antigen receptors present on cell

surfaces.[175] This was achievable because each of the nanostructures was labelled with a different reporter molecule and thus different SERS signals were measured (**Figure 1.8**).[175] The false colour SERS maps were subsequently used as a method to quantify the level of biomarker expression since the SERS intensity is a direct measure of the concentration of biomarker.[175]

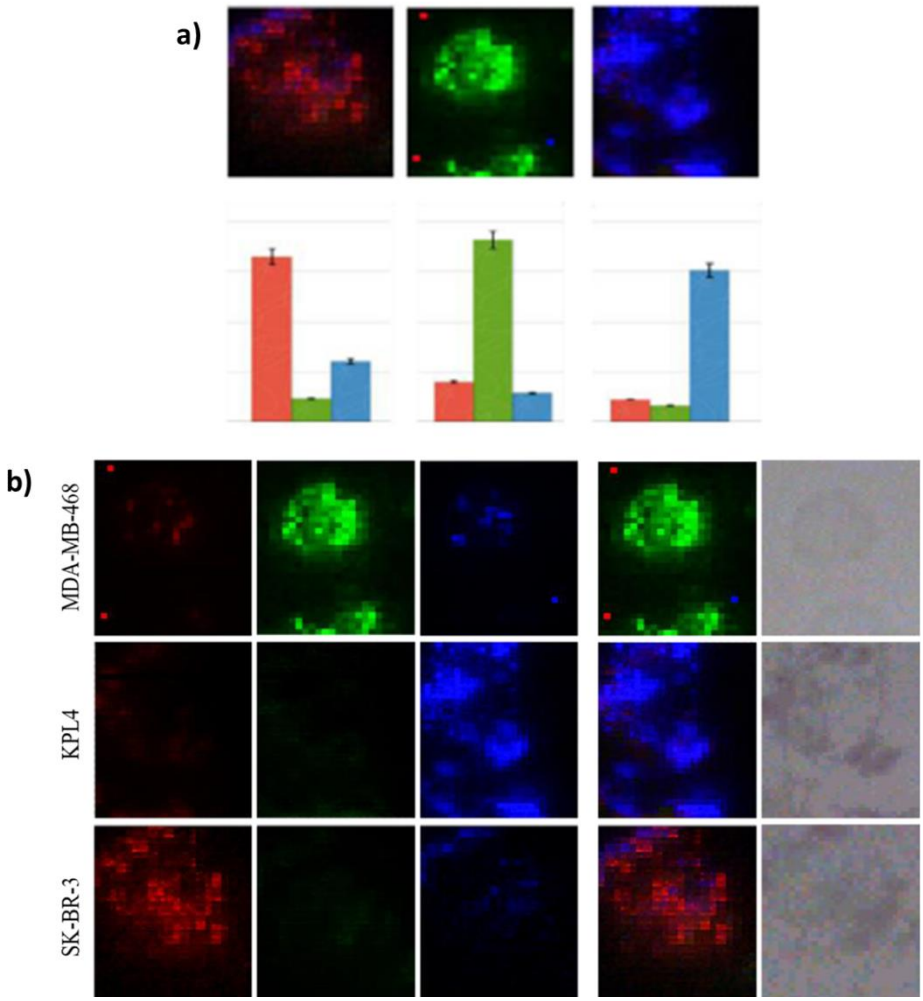

Figure 1.8: Silica encapsulated hollow gold nanoshells (SEHGNs) used to phenotypically identify cancerous cell lines and determine the level of antigen expression in each cell line – a) SEHGNs were applied to the different cell lines and each of the cell types were identified based on the signal from the specific reporter molecules and b) SERS mapping images of the corresponding cell lines were measured at 1650 cm ^{1} (RBITC), 1619 cm^{-1} (MGITC) and 1490 cm^{-1} (RuITC) for the SK-BR-3, KPL4 and MDA-MB-468 cell line specific reporter molecules.[175] Modified and reprinted with permission from Elsevier.

Biomarker or protein expression can also be used to differentiate cancerous from non-cancerous cells.[176] In prostate cancer cells neuropilin-1 is overexpressed and, on the basis of this knowledge, selective SERS nanotags were constructed for differentiating between cell lines.[176] To actively target cancerous cells or more specifically the receptors, nanotags were functionalised with a peptide with a specific affinity for neuropilin.[176] Control nanotags were functionalised with the HIV transactivator of transcription (TAT) peptide sequence and these nanotags had the ability to bind to both cells lines.[176] In order to positively identify the cancerous cells, the ratio of the SERS signal from each of the reporters was calculated.[176] The cancerous cells should have a high contribution from the reporter on the specific targeting nanotags whilst the non-cancerous cells should have a high contribution from the reporter on the control system.[176] This was found to be true and this represents a viable method for differentiating between the two cell lines.[176] Prostate cancer cells can also be positively identified from interactions between imaging agents and surface carbohydrates.[46] For example, PC3 cancerous cells exhibit elevated levels of sialic residues on their surface.[46] These can be actively targeted with nanostructures functionalised with the lectin, *Triticum vulgaris*, which is known to have a specific affinity for these glycans.[46] Craig *et al.* demonstrated this lectin-glycan interaction and in doing so successfully distinguished cancerous PC3 cells from the non-cancerous PNT2A cells.[46]

Further applications involving the detection of cancerous cells have centred on circulating tumour cells (CTCs). Unlike other applications, which might be concerned with the primary detection of cancer, CTCs are particularly aggressive and are associated with the initiation of further cancerous growth.[153, 177] During an initial study the CTCs were exposed to antibody functionalised nanotags and magnetic beads. The nanotags whilst simultaneously binding to the CTCs acted as the reporter component and similarly, the magnetic beads whilst capable of binding to the cancer cells, were also incorporated so that the samples could be concentrated via a magnet.[153] The implementation of this method has resulted in successful detection of CTCs via SERS and detection was also achievable with high sensitivity and specificity when whole blood was employed.[153] In a subsequent study by Wang *et al.* a similar method was employed but the incorporation of magnetic beads was substituted for a physical separation step.[177] Initially, the blood was separated by centrifugation and, because of their low density, CTCs were removed from the upper portion of the container with relative ease.[177] CTCs were then incubated with nanotags for a specified period and

after this any unbound nanotags were also removed by centrifugation prior to the SERS analysis.[177] Both methods were found to allow for the sensitive and selective detection of CTCs.[153, 177]

In a final example of SERS based disease detection *in vitro*, targeting of stem cells was investigated. Although this is not strictly a method for the detection of disease, stem cells have an important role in disease research.[178] In this study nuclear targeting SERS nanotags were deployed to ascertain the differences between differentiated and undifferentiated stem cell populations.[178] The cells were analysed by SERS and spectral information was extracted. Principal component analysis (PCA) was employed and it revealed that there were distinct differences between the two stem cell forms with regards to the organisation of the nucleus. These changes were suitably distinct and allowed for cell identification.[178]

1.5.4 SERS and *Ex vivo/In vivo* Applications for the Detection of Disease

1.5.4.1 Tissue Imaging and Disease Detection

The use of SERS for disease related tissue imaging was initially performed by Schlucker *et al.* in 2006.[179] Their SERS based detection system consisted of gold nanoparticles conjugated to an antibody via a small molecule reporter and this was used to actively detect prostate specific antigen (PSA) in tissue samples.[179] In a later study the same group extended this to monitor PSA expression in tissues.[158] This predominantly occurs in the epithelium of the prostate and when incubated with functionalised nanoshells, the localised expression was confirmed by SERS signals arising from the specific nanoshell antibody-tissue antigen interaction. This interaction was particularly evident in the false colour SERS maps (**Figure 1.9**).[158] Determining the localisation of other components within the tissues is not isolated to biomarkers of disease and the group successfully determined the localisation of the tumour suppressor p63, in non-cancerous tissue.[180] Elucidation of this was again determined by SERS signals arising from the specific interaction between the detection system and the tissue.[180]

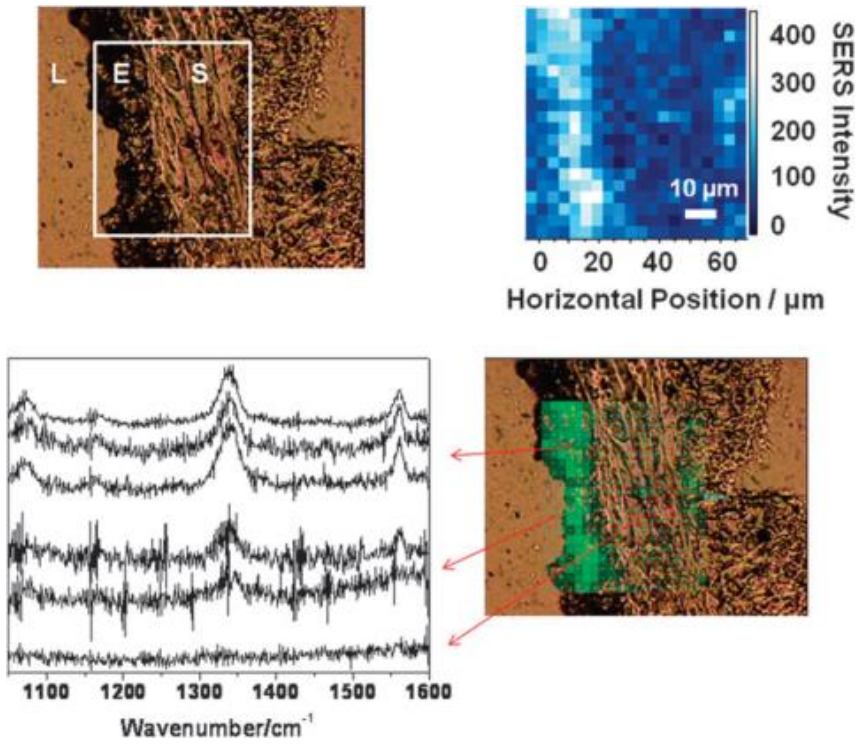

Figure 1.9 Detection of PSA *ex vivo* – top: bright field microscope image of a prostate tissue section. The grid shows the locations at which Raman spectra were acquired in a point mapping experiment. The false colour SERS image shows that the characteristic signal of the SERS-labelled antibody is observed selectively in the epithelium. Reproduced from[158] with permission from the PCCP Owner Societies.

Whilst detection systems like this might seem trivial, they are actually of huge importance for the characterisation of disease in tissue. In all of the examples discussed, the measured signals arise from the SERS reporters. However, a second laser line could be employed at a frequency where the nanotags are not SERS active but where intrinsic Raman signals from the tissues dominate. This would allow biochemically characteristic information to be obtained from the tissues and the false colour SERS images could be used to delineate the boundaries between the regions where, for example, PSA expression is high and low. This would provide further information which is biochemically representative of the disease biomarkers. Whilst areas of protein expression can be imaged using traditional immunohistochemical methods, no biochemical information is obtained. Additionally, conventional fluorophores have broad absorption and emission bands so the staining of multiple areas is difficult. However, when employing either Raman and/or SERS imaging, the

spectral bands are narrow and not limited in terms of the tissue regions or receptors which could be targeted simultaneously. This is particularly important as the documentation of disease processes progresses towards the detection of multiple markers.[10]

Manipulation of the antibody-antigen interaction has also been exploited for the determination of nasopharyngeal cancer in tissue samples.[181] As with most of the discussed samples, antibody functionalised SERS nanotags were exposed to tissues.[181] Clinical samples were analysed and directly compared with the tissue which had been analysed via a traditional immunohistochemical method. SERS analysis was found to considerably exceed the conventional method.[181] In total, there were 34 cancerous and 20 non-cancerous tissue samples and the SERS detection method correctly identified 33 of the cancerous samples whilst the traditional method only identified 22.[181] Negative samples were correctly identified by both methods.[181] As with the previous examples, the above discussed advantages of the SERS method are equally applicable to this study.[181]

SORS has been previously discussed as a method for disease detection in section 1.5.2.1. SORS has also been developed to incorporate a surface enhanced method known as surface enhanced spatially offset Raman spectroscopy (SESORS).[182] The key feature and main advantage of this technique is that it can measure Raman or SERS signals through medically relevant tissue depths.[182] This is of huge importance since it actively demonstrates non-invasive detection of disease.[182] In one of the latest studies cumulative SERS signals were measured from four different SERS nanotags which were located within tissue at a depth of 20 mm.[182] Even more significantly, it was possible to measure SERS signals through 50 mm of tissue.[182] This study highlights the possibility of implementing SERS and their nanotags for use *in vivo.*

In a subsequent study the method was also investigated in specific relation to a disease process osteoporosis.[183] This is a progressive bone disease which can be treated with drugs known as bisphosphonates.[183] The disease itself was not investigated but rather the study was designed to replicate drug distribution and investigate its localisation.[183] In order to do this, the drug was conjugated to SERS nanotags and subsequently incubated with representative bone samples. The bones were then transplanted into a tissue mass and the samples were analysed.[183] It was possible to detect the drug-

nanotag conjugates at a depth of 20 mm and although this study did not involve the direct detection of the disease it is nonetheless important because it actively demonstrates the ability to monitor drug distribution non-invasively.[183] This therefore highlights the suitability of SERS as a key process in the treatment of disease.

1.5.4.2 *In vivo* Imaging and Disease Detection

One of the most recognisable and well documented examples of *in vivo* SERS imaging is undoubtedly the study by Qian *et al.*,[11] where tumours were successfully targeted with an antibody functionalised gold nanoparticle system *in vivo*.[11] The nanotag conjugates were introduced into the mice model via tail injection and they were successfully translocated to tumour locations.[11] Successful targeting was demonstrated via monitoring of the SERS signals and those measured from the tumour regions of the mouse were found to be representative of the reporter from the SERS nanotags (**Figure 1.10**).[11] This study actively demonstrated that the nanoparticles were able to travel through the animal model and reach their targets.[11] It was also critical for demonstrating the success and application of SERS for monitoring such interactions *in vivo*.

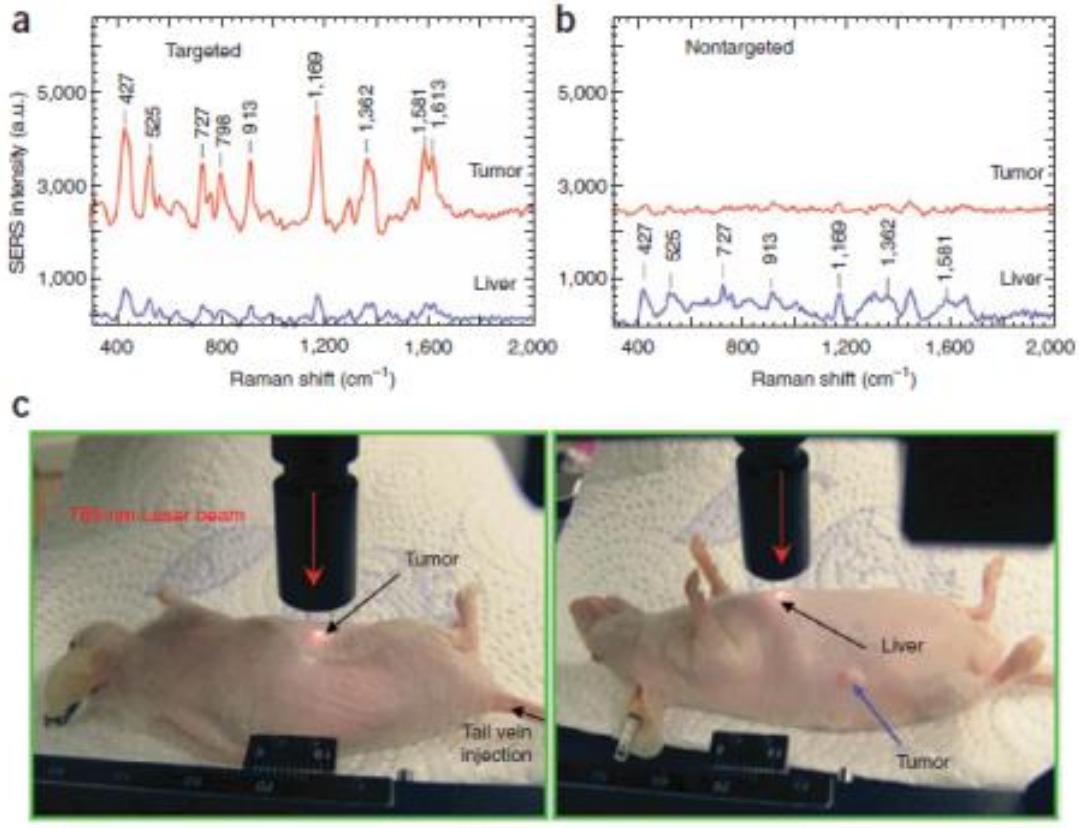

Figure 1.10: *In vivo* cancer targeting and surface enhanced Raman detection by using ScFv-antibody conjugated gold nanoparticles that recognise the tumour biomarker EGFR. (a,b) SERS spectra obtained from the tumour and the liver locations by using targeted (a) and nontargeted (b) nanoparticles. Two nude mice bearing human head-and-neck squamous cell carcinoma (Tu686) xenograft tumour (3-mm diameter) received 90 μL of ScFv EGFR-conjugated SERS tags or pegylated SERS tags (460 ρM). The particles were administered via tail vein single injection. SERS spectra were taken 5 h after injection. (c) Photographs showing a laser beam focusing on the tumour site or on the anatomical location of liver. *In vivo* SERS spectra were obtained from the tumour site (red) and the liver site (blue) with 2-s signal integration and at 785 nm excitation. The spectra were background subtracted and shifted for better visualisation. The Raman reporter molecule is malachite green, with distinct spectral signatures as labelled in a and b. Laser power, 20 mW. Reprinted by permission from Macmillan Publishers Ltd. Nature Biotechnology,**[11]** (2008).

In vivo imaging of SERS nanotags has also been applied for the observation of inflammation and again, while not a disease process, it is of relevance since any change can be indicative of infection and underlying disease conditions.[184] Nanotags were functionalised with antibodies which have a specific affinity for the identified inflammation biomarker, intracellular adhesion molecule 1 – (ICAM-1-). The nanotags specifically targeted inflammation *in vitro*, *ex vivo* and *in vivo*.[184] When the effectiveness of the SERS approach was directly compared with the conventional fluorescence method it was also found to be significantly more sensitive.[184]

Whilst the previous examples have demonstrated active *in vivo* disease targeting, a multi marker approach is considered to be beneficial, especially if multiple disease aspects are to be detected simultaneously.[10] It is hoped that by analysing disease processes or even multiple different diseases it will lead to better characterisation and personalised medicine.

With the advent of superior nanotag systems, which display excellent stability and are optically 'hot', the possibility of multiplexed imaging *in vivo* has become a real possibility.[10, 12] Zavaleta *et al*., showed in early experiments that it was possible to simultaneously detect two different nanotags within a live subject. This was latterly extended to include the simultaneous detection of ten different nanotags (**Figure 1.11**).[10, 12] This was a crucial step forward for multiplexed detection *in vivo*, actively demonstrating the potential to detect multiple pathosis or different elements of disease

simultaneously.[10] In a further extension of the work and in terms of true multiplexing and the confident identification of nanotags present within a specified location, it was possible to positively identify four nanotags in a multiplexed scenario.[10]

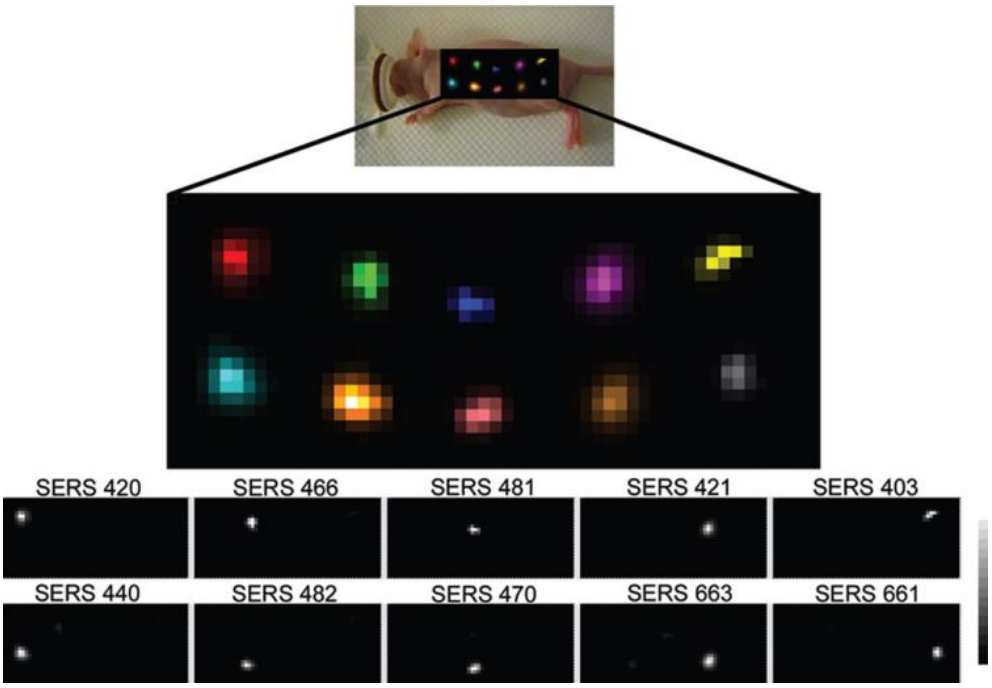

Figure 1.11: Evaluation of multiplexing 10 different SERS nanoparticles *in vivo*. Raman map of 10 different SERS particles injected subcutaneously in a nude mouse. Grayscale bar to the right depicts the Raman intensity, where white represents the maximum intensity and black represents no intensity. **[10]** C.L. Zavaleta, B.R. Smith, I. Walton, W. Doering, G. Davis, B. Shojaei, M.J. Natan, S.S. Gambhir, Proc. Natl. Acad. Sci. USA., 106 (2009), 13511-13516. Copyright (2009) National Academy of Sciences of the United States of America.

Further *in vivo* applications have been demonstrated by Maiti *et al.*[185-187] In the first of their *in vivo* experiments nanotags were injected into a mouse model and successfully imaged using SERS.[185] The only difference being that the antibody functionalised nanotags were actively bound to cancerous cells prior to their introduction, highlighting the opportunity to successfully image the nanotags *in vivo* even after participation in a disease recognition event.[185] In an extension to this work nanotags functionalised with antibodies, which had a specific affinity for the receptors in the xenograft, were found to translocate to the xenograft site following introduction into the animal.[186] Thus the conjugates participated in antibody-antigen recognition and signals representative of the reporter molecule were measured at the xenograft site.[186] However, when nanotags were introduced into mice bearing xenografts of the non-

cancerous cell population SERS signals were not measured in accordance with the absence of a specific binding event.[186]

In the most recent of their work, the group elegantly demonstrated the selectivity of their targeting nanotags.[187] In this study the xenograft was composed of oral squamous cell carcinoma (OSCC) cells which exhibit a differential level of expression of EGFR and HER2. EGFR receptors are present at a much higher levels than HER2 receptors on the surface of the cells.[187] In accordance with the expressed receptors three nanotags were injected into the tail of the animal subject, two of which had been functionalised with the EGFR specific antibody and the remaining nanotag was functionalised with the HER2 antibody.[187] The signals which were measured from the site of the xenograft were in accordance with the two nanotags functionalised with the specific antibody and two different reporter molecules. There was no contribution from the nanotag functionalised with the HER2 antibody (**Figure 1.12**). This study represents one of the first true, targeted, *in vivo* multiplexing examples, and this is an important step forwards in terms of striving towards the deliverable of comprehensively characterising and detecting multiple aspects of disease.[187]

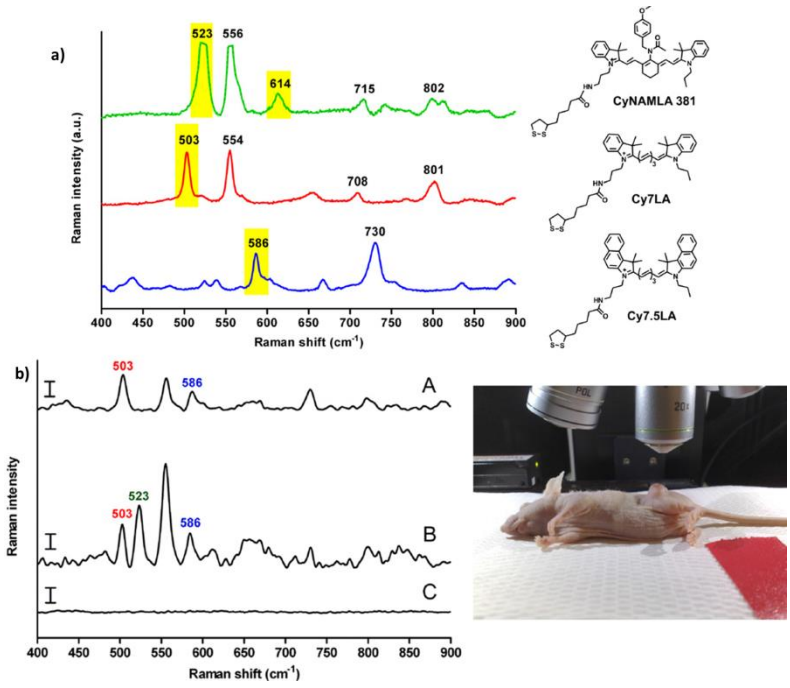

Figure 1.12: *In vivo* multiplex detection in xenograft tumour – a) Normalised SERS spectra of CyNAMLA-381, Cy7LA and Cy7.5LA after chemisorption of AuNPs and b) – A: SERS spectra from tumour site (peaks obtained at 503 and 586 cm^{-1} from two EGFR positive nanotags, Cy7LA and

Cy7.5LA), B: SERS spectra from liver site (peaks obtained at 503, 523 and 586 cm^{-1}) from two EGFR nanotag Cy7LA, Cy7.5 and anti-HER2 nanotag CyNAMLA-381) and C: SERS spectra from dorsal region. [187] Modified and reprinted with permission from Elsevier.

Chapter 2 Aims

This thesis aims to develop analytical examples which demonstrate the power of SERS and in particular combined Raman and SERS for cellular imaging and analysis. The main areas of research aimed to:

Develop and implement suitable nanotag systems for the analysis of single cells and cell populations in a multiple component manner. Detecting multiple nanotags within a single cell or cell population has important implications for targeting applications including the targeting of multiple cell organelles and for intracellular drug delivery. A multi marker approach is also thought to be critical for the comprehensive characterisation of disease processes.

Develop the best process in terms of instrumentation and chemical reporting for the production of 3D images of single cells. As a standalone application 3D Raman imaging has important implications for understanding architectural and compositional changes between healthy and diseased samples. However, if used in parallel with SERS (2D and 3D), for the tracking of multiple nanotags, it is thought that the combination will allow for the simultaneous confirmation of cellular uptake and nanotag identification.

Develop a range of targeting nanotags which when functionalised with biomolecules can target multiple cell receptors or organelles. Analysis will involve 2D and 3D Raman imaging to confirm localisation and for organelle targeting uptake of the nanotags within the correct organelle.

Chapter 3 Development and Imaging of Multiple SERS Nanotags in Cells

3.1 Introduction

'*It is recognised that no single targeting agent can provide the information needed to characterise or detect a specific disease process'.*[10] As a result, research in the field of *in vitro*, *ex vivo* and *in vivo* imaging, using SERS nanotags, has focused on the development of multi-marker approaches with the prognosis for earlier detection, better characterisation and with the ultimate aim of improving the sensitivity and specificity by which diseases are detected. [7-10] In the specific case of cancerous cells, there are multiple reports of single target detection methods[11, 30, 31, 152, 153, 173] and although the ability to detect multiple targets has been demonstrated in solution[188, 189] this has yet to be extended *in vitro* and *in vivo.* In addition to disease detection, the potential also exists for nanotags/nanoprobes to aid in the treatment of disease, for example as drug transport agents.[7, 190] Nanoparticles used in chemotherapy treatment can deliver a payload specifically to diseased cells with the result of improving efficacy whilst concomitantly minimising deleterious effects since targeting can be localised to the diseased region.[7, 190] If this approach were extended to multiple targets within a single cell, then multi-marker nanotags would undoubtedly improve the detection, treatment and management of disease.

Nanotags or nanoprobes for biomedical research can be synthesised by a variety of methods, the most simple of which involve labelling metallic nanoparticles with reporter molecules.[7, 8, 143, 149, 150] More complicated systems can additionally involve mixed monolayers of reporter[151] and membrane penetrating or targeting antibodies,[9, 152, 153] peptides[7, 70, 71] or oligomers.[154] Robust and chemically resistant systems can be created by silica[10, 12, 191] or polymer encapsulation.[9, 155] Regardless of the synthesis method, effective implementation requires confirmation of cell uptake as well as an understanding of their subsequent intracellular dissemination.[7, 8]

With the multi-marker, cellular uptake and intracellular distribution criterion in mind this chapter will investigate suitable systems for the development of a range of multi-marker nanotags and their subsequent cellular detectability.

3.2 Multiple Component System – Commercial System

3.2.1 Commercial SERS Nanotags

Initial investigations into multi-marker cellular imaging agents were carried out using commercially available SERS nanotags (Nanoplex Biotags – Cabot Corporation). These were selected on the basis that they have demonstrated applications as biological contrast agents[10, 12] whilst their overall structure is reported to be biocompatible, physically and chemically durable.[10] These are important factors which need to be considered when selecting cellular imaging agents since they must remain detectable following cell uptake, be non-toxic to the cell and resistant to the intracellular environment. These nanotags had the added advantage that they were SERS active in the near-infrared (NIR) window thus when considering further applications such as *in vivo* studies they were ideally suited to the analysis matrix.[10, 12] Outside of the NIR window tissue auto-fluorescence becomes an increasingly dominant problem.[10]

The nanotags consisted of a gold nanoparticle core onto which the Raman active molecules were adsorbed and this core was coated with silica to make the nanotags physically and chemically robust (**Figure 3.1**). The nanotags obtained were denoted as SERS 403, 420, 421 and 440. These were differentiated based on the Raman active molecule adsorbed onto the gold nanoparticle core and for SERS 403, 420, 421 and 440 were 5-(4-pyridyl)-1,3,4-oxadiazole-2-thiol, 4,4'-dipyridyl, d8-4,4'-dipyridyl and trans-1,2-bis(4-pyridyl)-ethylene respectively (**Figure 3.1**).

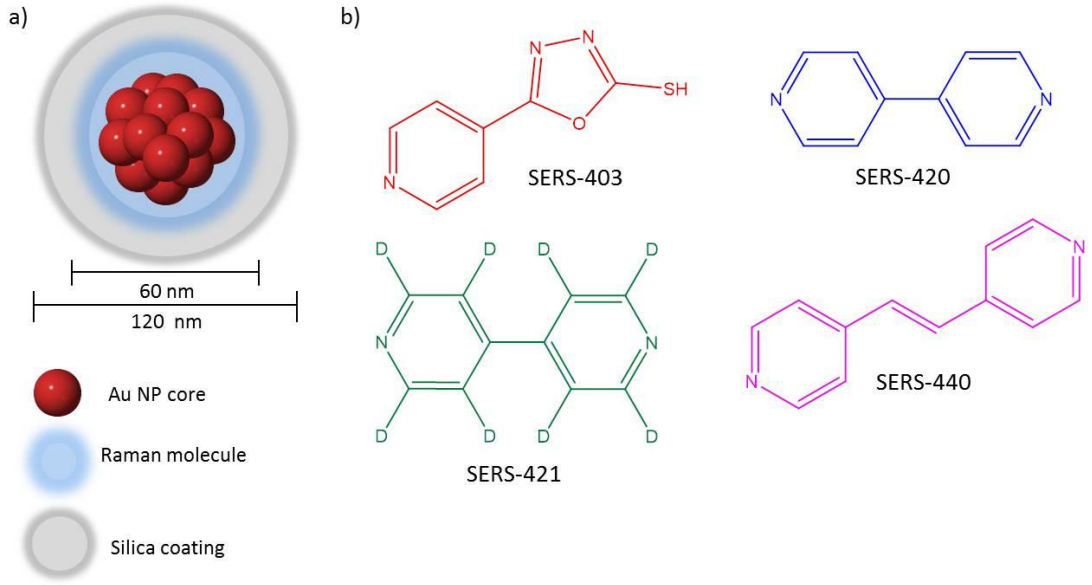

Figure 3.1: Commercial SERS nanotags – a) nanotag structure and b) Raman active molecules adsorbed onto the Au nanoparticle core for the range of SERS nanotags investigated in the study.[10]

3.2.2 Characterisation of the Commercial SERS Nanotags

3.2.2.1 Stability Measurements

To determine the stability of the commercial nanotags in solution, analyses were performed using extinction spectroscopy and dynamic light scattering (DLS). The extinction measurements were made in distilled water (dH_2O) whilst the DLS measurements were additionally performed in the serum free cell media Rosewell Park Memorial Institute Medium (RPMI). The results from the extinction spectroscopy suggested that the commercial nanotags were stable, monodisperse and SERS-403, 420, 421 and 440 had a λ_{max}= 548, 555, 545 and 547 nm respectively (**Figure 3.2**). SERS-420 appeared to be less stable than the other three nanotags as exemplified by a red shift and broadening of the plasmon band (**Figure 3.2**). However, this reduced stability was not considered to be a significant hindrance to further solution or cellular studies since it wasn't particularly extensive and it is possible that SERS-420 has a propensity to form larger aggregates. Attempts were also made to measure the extinction spectra in RPMI cell media to determine if this induced any aggregation. Unfortunately because of the presence of phenol red, a colour changing pH indicator used to monitor cell viability during culture, extinction measurements were not possible as the broad absorbance

band of phenol red obscured the extinction profile of the nanotags. To measure the effects of the cell media this study would need to be repeated in media free of phenol red which wasn't an option at the time.

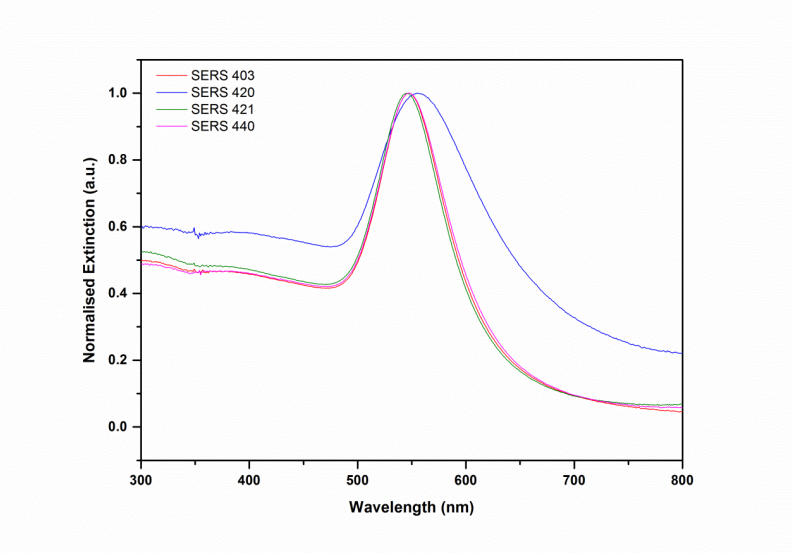

Figure 3.2: Extinction spectroscopy analysis of the commercial nanotags dispersed in dH_2O. The λ_{max} = 548, 555, 545 and 547 nm for SERS-403, 420, 421 and 440 respectively.

DLS was used to obtain size and Zeta potential measurements for each sample and the principles of the measurements are as follows. When particles within a solution are illuminated with light, scattering occurs generating an interference pattern.[192] Brownian motion is assumed for the particles and any motion will cause a change in the interference pattern or more specifically, the intensity changes which appears to cause an overall change in the pattern.[192] This intensity change is used to calculate the particle size. Surrounding each of the particles in solution is an electrical double layer which consists of two distinct parts namely the Stern and diffuse layer.[192] The division between these layers influences the movement of the ions associated with a particle, such that ions close to the division move with the particle whilst those away from the division do not.[192] The potential measured at the division is known as the Zeta potential. Zeta potential measurements are used as a measure of colloidal stability and in general values greater than -30 mV or + 30 mV are considered to be stable and non-aggregated.[192]

The nanotags were reported to have an overall size of ~120 nm,[10, 12] however, with the exception of the SERS-403 nanotags (153 nm), the DLS size measurements revealed

that they were slightly smaller ~ 100 nm (99, 96 and 111 nm for SERS-420, 421 and 440 respectively) (**Figure 3.3**). However, these values were in good agreement with the provided data sheets and any variability from the average reported value (~ 120 nm) might be due to variation in the silica shell thickness.

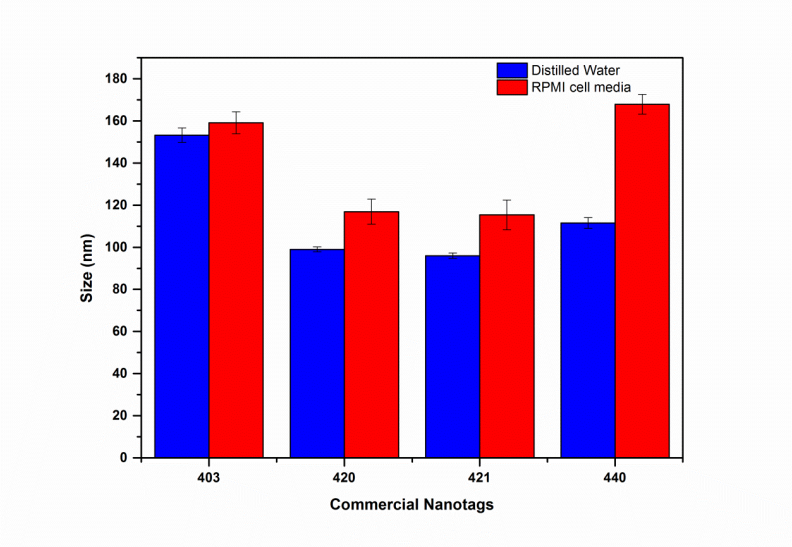

Figure 3.3: DLS size measurements for the commercial nanotags when dispersed in dH_2O and RPMI cell media. Measurements were made in triplicate, the average value is shown and the error bars represent the standard deviation of the triplicate measurements.

When dispersed in the cell media the size of the nanotags was observed to increase and this was most pronounced for SERS-440 (**Figure 3.3**) which exhibited a ~ 50 nm increase. For the remaining nanotags the increase was around ~ 20 nm. Typically when dispersed in cell media, a corona, which is comprised of the main media components (e.g. protein and sugar), can enshrine the surface of the nanoscaffold.[193, 194] Therefore, this size increase was not necessarily representative of aggregation. The media however was serum free hence corona formation was unlikely to be extensive but as the serum was additionally supplemented with L-glutamine and it is possible that the free amine groups on the amino acid interacted with the silica shell. Regardless of whether 'true' aggregation or corona formation was taking place the overall size of the nanotags as measured in the cell media was not considered to be detrimental to cellular uptake. Although smaller particles can demonstrate higher levels of uptake[195] particles ~1000 nm have also been shown to be viable.[196] Particles in the same size range as the nanotags used in the study have further been shown to be taken up by both endocytic[197] and passive diffusion mechanisms[53] thus the size range exhibited was

unlikely to be prohibitive to cellular uptake. The stabilisation of the gold nanoparticle core by the silica shell was apparent in the Zeta potential measurements (**Figure 3.4**).

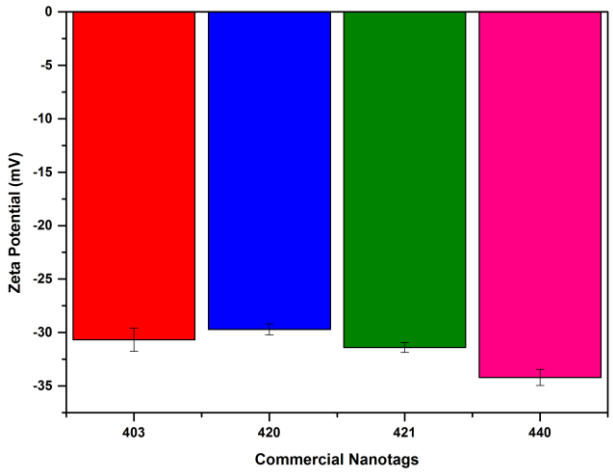

Figure 3.4: Zeta potential measurements for the commercial nanotags dispersed in distilled water. Measurements were made in triplicate, the average value is shown and the error bars represent the standard deviation of the triplicate measurements.

Large negative values (- 30 mV) indicative of stabilisation were measured for each of the commercial nanotags and were -30.6, -29.7, -31.4 and -34.2 for SERS-403, 420, 421 and 440 respectively (**Figure 3.4**).[192] Attempts were also made to measure the Zeta potential in the cell media to determine if this induced any instability resulting in aggregation. However, when the Zeta potential of the cell media was measured it was found to be ~ -9 mV and successive Zeta potential measurements of the nanotags suspended in the cell media were also found to be ~ -9 to -11 mV. This suggested that the measurements were representative of the cell media rather than the influence and interaction between the media and the nanotags. This was not surprising since the cell media contained components (amino acids, vitamins and ions) which themselves can be prone to electrostatic or charge repulsion or attraction between particles. Several studies have reported Zeta potential measurements of nanotags in cell media[198, 199] but typically the tags were left to interact with the media before centrifugation and resuspension in a buffer suitable for measuring Zeta potential. This assumes that interactions and any electrostatic binding which take place between the media and the nanotags are maintained following resuspension. This was not considered to be representative of the environment to which the nanotags were actually exposed and as

such measurements were not performed in this way. Overall, on the basis of the extinction (**Figure 3.2**) and Zeta potential (**Figure 3.4**) measurements performed in dH_2O and the size measurements performed in dH_2O and cell media (**Figure 3.3**) the nanotags were considered to be stable, monodisperse and of a size suitable for cellular uptake.

3.2.2.2 Spectroscopic Measurements

A unique SERS signal was observed for each of the commercial nanotags (**Figure 3.5**) and the predominant molecular vibrations arose from the pyridyl and oxadiazole ring systems (**Figure 3.1**, **Figure 3.5** and **Table 3.1**).

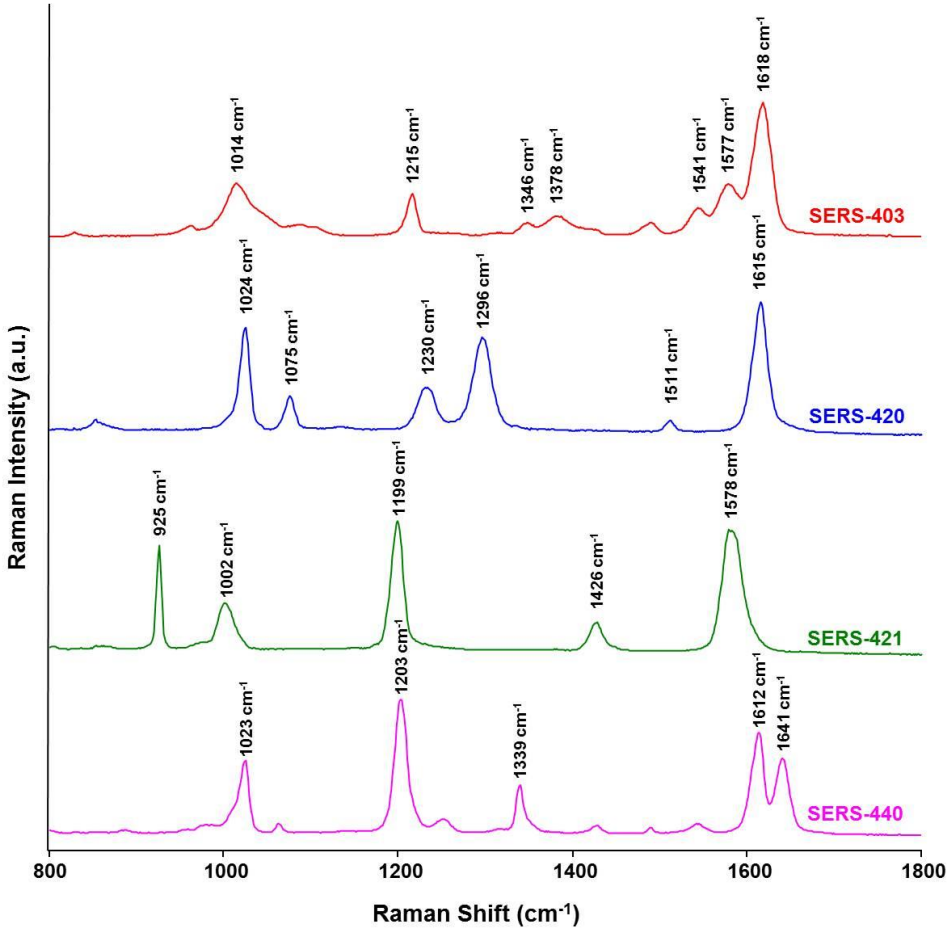

Figure 3.5: Control SERS spectra for the commercial nanotags SERS-403, 420, 421 and 440 shown in red, blue, green and magenta respectively. Spectra were offset for illustrative purposes and no major peaks were observed below 800 cm^{-1} or above 1800 cm^{-1} hence the spectra were truncated accordingly. (λ_{ex} = 785 nm, 100% (0.45 W), extended scan, 10s, 800-1800 cm^{-1})

The main molecular vibrations have been assigned (**Table 3.1**). A number of smaller peaks were observed in the fingerprint region but these were not considered to be sufficiently intense for identification purposes. Molecular vibrations were not observed above 1800 cm^{-1} hence the spectra were truncated accordingly (**Figure 3.5**).

Table 3.1: Peak assignments for the predominant molecular vibrations for each commercial nanotag.[200-202]

Commercial Nanotag	Observed Peak Position (cm^{-1})	Assignment
SERS-403	1618	υ_{ring}
	1577	ring stretch
	1541	ring in plane deformation, υ(C-N)
	1378	δ(CH)
	1346	δ(CH)
	1215	inter ring stretch
	1014	υ_{ring}
SERS-420	1615	υ_{ring}
	1511	υ_{ring}, δ(CH)
	1296	υ_{ring}, δ(CH), inter ring stretch
	1230	δ(CH)
	1075	υ_{ring}, δ(CH)
	1024	υ_{ring}, δ(CH), ring deformation
SERS-421	1578	υ_{ring}
	1426	δ(CH), ring stretch
	1199	Inter ring stretch
	1002	ring breathing
	925	δ(CH)
SERS-440	1641	υ(C=C)
	1612	υ(C-C), δ(CH)
	1339	δ(CH), δ(C-C)
	1203	υ(ring-C), δ(CH)
	1023	ring in plane deformation (ring breathing), γ(CH), γ(C=C)

3.2.3 Multiple Component Capability

Prior to any cell investigations the suitability of the SERS nanotags as multi-markers for disease detection was investigated in solution. With a total of 4 nanotags there were 11 (6 duplex, 4 triplex and 1 fourplex) possible combinations which were pre-mixed and analysed. Some degree of spectral overlap was expected since the Raman reporters were similar in structure, predominantly consisting of bi-pyridyl ring systems (**Figure 3.1**). However, for all the solutions analysed it was possible to deconvolve the spectra by eye and identify the specific combination of nanotags present. For the purposes of subsequent experiments, the mixed suspensions were referred to as multiple component samples since they were not true examples of a multiplex. In a true multiplex it is expected that all the peaks from the contributing reporters will be found in the overall combined spectrum. This is true for the solution samples but in some of the later cell experiments the nanotags were often found in discrete locations so there was no overall 'multiplex' spectrum.

Although a multivariate analysis method was used to identify the specific combination of nanotags present in the cell experiments the multiple component criteria was defined such that there must be at least one unique peak identifiable for each of the SERS nanotags. In the specific case of the fourplex, the highest achievable multi-marker system, unique peaks were found at ~1296 cm^{-1}, ~925 cm^{-1} and ~1641 cm^{-1} for SERS-420, 421 and 440 respectively. Although there was no single peak unique to SERS-403 it was readily identifiable from the triplet of peaks produced at ~1541, 1577 and 1618 cm^{-1} (**Figure 3.6**).

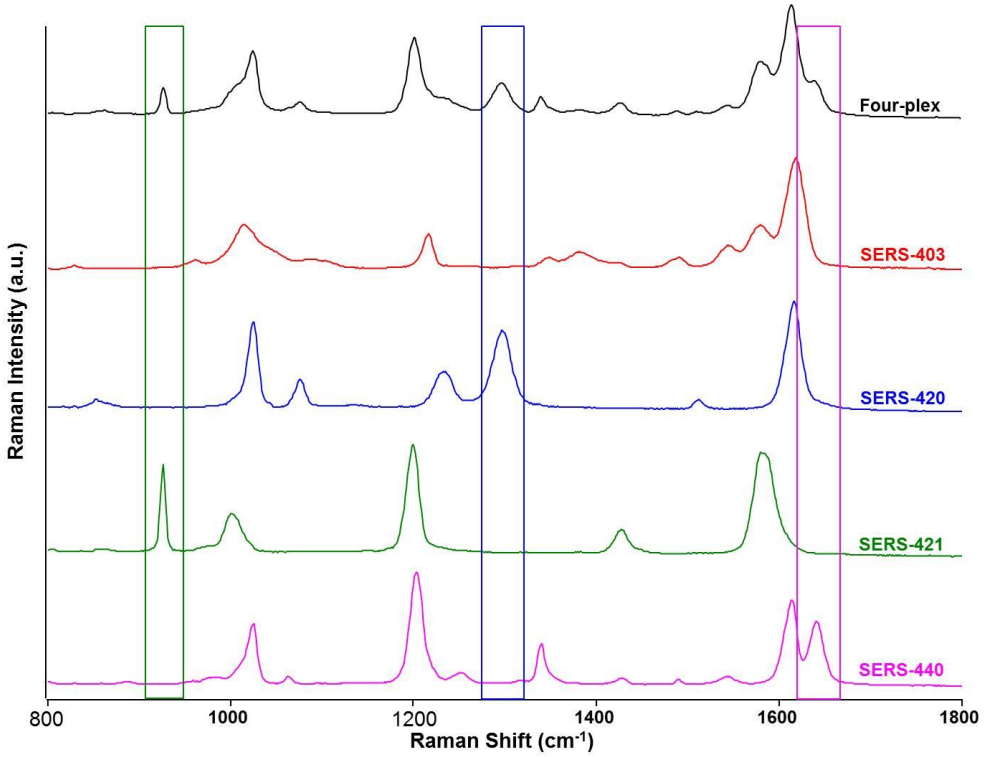

Figure 3.6: Representative spectra for the fourplex solution sample and control spectra for the commercial nanotags. Spectral contributions from each of the commercial nanotags are readily identifiable within the multiple component spectra. (λ_{ex} = 785 nm, 100% (0.45 W), extended scan, 10s, 800-1800 cm^{-1}).

Although a broad spectral range was observable during the measurement of solution samples instrumental constraints relating to the charge coupled device (CCD) chip and the grating combination (1200 l/mm) meant that only a very narrow spectral range ~400 cm^{-1} was observable when mapping. As a result of this it was decided to concentrate on a spectral region where peaks from all four nanotags were present and could readily be differentiated from one another. The region from ~ 1540 – 1650 cm^{-1} was selected and considering the highest achievable multiple component sample – the fourplex – it was possible to differentiate between each of the four nanotags as follows. SERS-403 was readily identifiable from the triplet of peaks produced at ~1541, 1577 and 1618 cm^{-1}. SERS-420 gave rise to a peak ~1615 cm^{-1} and was differentiated from SERS-403, which produced a peak in the same region at ~1618 cm^{-1}, by the occurrence of the triplet of peaks (**Table 3.2**). SERS-440 also produced a peak ~1612 cm^{-1} and this was differentiated from SERS-420 by the doublet of peaks in the SERS-440 spectrum at

~1612 and 1641 cm^{-1}, this peak was unique to SERS-440. SERS-421 produced a peak ~ 1578 cm^{-1} and this was differentiated from SERS-403, which also produced a peak in this region ~1577 cm^{-1}, again by the occurrence of the triplet of peaks (**Table 3.2**).

Table 3.2: Key identification peak(s) for each SERS nanotag suspension in the spectral region ~1540 – 1650 cm^{-1}.

Nanoparticle suspension	Key Identification Peak(s) (cm^{-1})
SERS-403	Triplet, ~1541, 1577 and 1618
SERS-420	~1615
SERS-421	~1578
SERS-440	Doublet, ~ 1612 and 1641

3.2.4 *In vitro* Analysis of the Commercial Nanotags

Following on from the success of the multiple component solution study - where it was possible to identify the specific combination of nanotags present within any given multiple component sample – the nanotags were applied individually to cell populations (macrophage and dendritic cells derived from Balb/C mice). In these experiments all 11 of the possible multiple component combinations were applied to the cells. Macrophage and dendritic cells were chosen for this study and, as the Greek name for macrophage cells 'large eaters' suggests, the cells readily engulf nutrients, debris and pathogens presented in the extracellular fluid. The cultured cells were incubated with the appropriate nanoparticle solution (100 µL, 0.5× concentration – diluted from 20× stock concentration) for 90 min. Following incubation, the cells were washed four times with 1× phosphate buffered saline (PBS, pH 7.6) to remove extracellular nanoparticles before fixation with methanol. After fixation the cells were washed with PBS, dH_2O and air dried before mounting onto microscope slides.

Samples were interrogated by Raman mapping using a Renishaw inVia Raman spectrometer/ Leica DMI 5000 M inverted microscope. A 785 nm laser diode excitation source was used and cell samples were imaged using a Leica 100× LWD (0.75 N.A.) objective. A grating of 1200 lines / mm was used with a RenCam CCD (400 × 576 pixels). Some of the measurements were performed at Renishaw plc, Gloucestershire, UK using a Renishaw inVia Raman spectrometer / Leica DM 2500 M microscope. Again a 785 nm laser diode excitation source was used and cell samples were imaged under

immersion in a saline solution using an Olympus 50× (0.75 N.A.) water immersion objective. A grating of 1200 lines / mm was used with a RenCam CCD (1040 x 256 pixels). The superior CCD chip on the system at Renishaw allowed for a larger spectral range (1000 cm^{-1} *c.f.* 400 cm^{-1}) to be observed and in the following discussion of the data the specific system used will be identified. Line mapping and high resolution images were collected with a StreamLine™ and StreamLineHR™ Raman mapping system and the experimental conditions are summarised in **Table 3.3**. The principles of StreamLine and StreamLineHR mapping are described in section 1.1.5.[42]

Table 3.3: Experimental parameters for cell mapping using the systems available at Strathclyde University and Renishaw, plc.

Laser excitation (nm)	Laser line line or edge	Spectral range (cm^{-1})	Laser power (% and W)
785 – Strathclyde	line	1434-1774	100% -0.29
785 – Strathclyde	edge	1434-1774	100% -0.45
785 – Renishaw	line	607-1720	100% - N.A.
785 – Renishaw	edge	607-1720	100% -0.13

Acquisition and analysis of the collected data was performed using the Windows-based Raman Environment (WiRE™ - Renishaw plc) 3.4 software package. Within the software the data can be used to generate false colour SERS map images using uni-variate or multivariate analysis methods.[203, 204] Uni-variate methods can be used to generate a whole array of different images including signal to baseline maps whereby increases in signal intensity over a defined spectral range are monitored. Similarly, peak intensity maps can be generated by monitoring the signal intensity at a particular wavenumber. For this study however, the false colour SERS images were generated using the multivariate analysis method - component direct classical least squares (DCLS). This method is typically employed when '*reference spectra are available for all of the components and involves fitting the unknown data (collected during mapping) to a linear combination of the specified component spectra (the reference spectra for each of the commercial nanotags). If there is a good spectral fit between the reference and the collected spectra a false colour is assigned and each reference spectrum is used to create separate false colour images*'.[204] In the following images the blue trace represents the reference spectrum whilst the red trace is an isolated spectrum from the map.

Associated with each false colour image is a look up table (LUT) and the minimum and maximum values of the LUT give an indication towards the degree of spectral fit.

3.2.5 Detectability of the Commercial Nanotags in Cells

3.2.5.1 StreamLine Measurements of the Commercial Nanotags in Cells

In all instances it was possible to identify the commercial nanotag or combination of nanotags applied to a cell population. When individual suspensions of the nanotags were applied each appeared to be successfully taken up within a single cell (**Figure 3.7** - **Figure 3.10**) and component DCLS correctly identified the individual nanotag present (**Figure 3.7** - **Figure 3.10**).

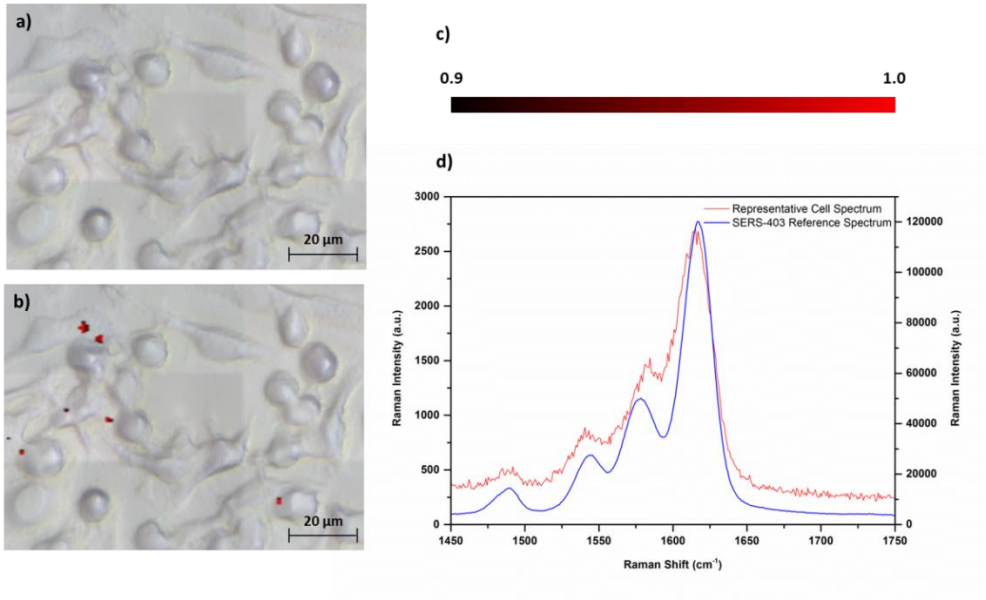

Figure 3.7: False colour SERS map image and representative spectrum for SERS-403 nanotags applied to a macrophage cell population. a) white light image, b) false colour SERS map image c) LUT colour bar and d) representative SERS spectrum for SERS-403 – the cell spectrum is plotted on the primary y-axis and the reference on the secondary y-axis. (StreamLine - λ_{ex} = 785 nm, 100% (0.29 W), spectral range 1434-1774 cm^{-1}, step size x,y 1.0 µm, 0.5 µm, 2s acquisition).

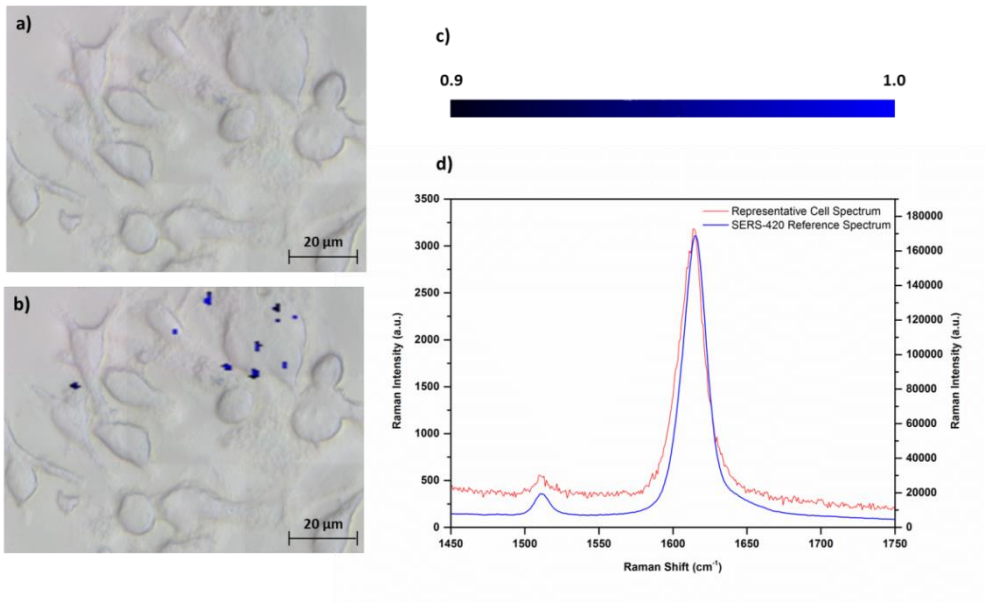

Figure 3.8: False colour SERS map image and representative spectrum for SERS-420 nanotags applied to a macrophage cell population. a) white light image, b) false colour SERS map image c) LUT colour bar and d) representative SERS spectrum for SERS-420 - the cell spectrum is plotted on the primary y-axis and the reference on the secondary y-axis. (StreamLine - λ_{ex} = 785 nm, 100% (0.29 W), spectral range 1434-1774 cm^{-1}, step size x,y 1.0 µm, 0.5 µm, 2s acquisition).

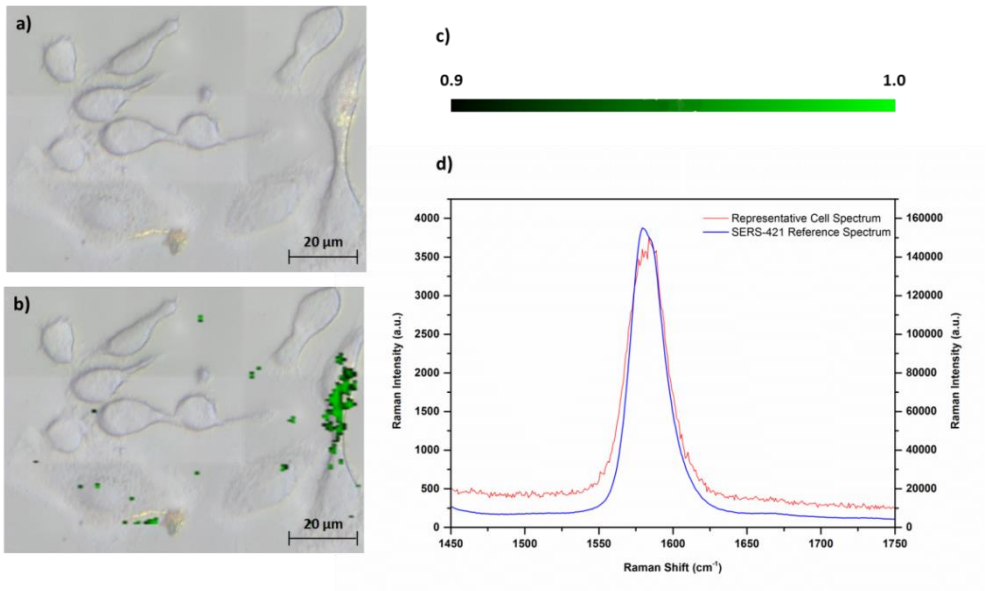

Figure 3.9: False colour SERS map image and representative spectrum for SERS-421 nanotags applied to a macrophage cell population. a) white light image, b) false colour SERS map image c) LUT colour bar and d) representative SERS spectrum for SERS-421 - the cell spectrum is plotted

on the primary y-axis and the reference on the secondary y-axis. (StreamLine - λ_{ex} = 785 nm, 100% (0.29 W), spectral range 1434-1774 cm^{-1}, step size x,y 1.0 µm, 0.5 µm, 2s acquisition).

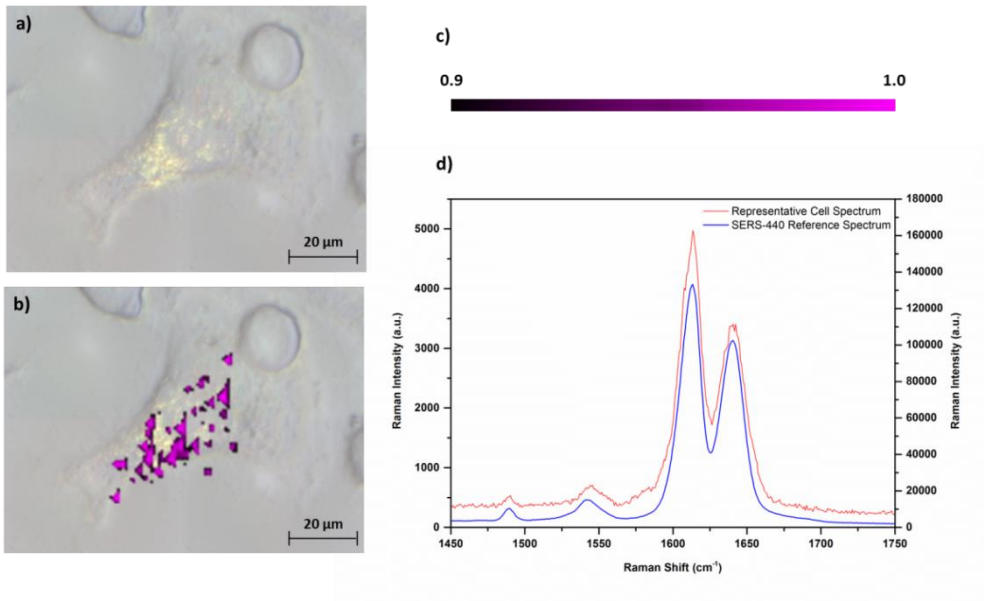

Figure 3.10: False colour SERS map image and representative spectrum for SERS-440 nanotags applied to a macrophage cell population. a) white light image, b) false colour SERS map image c) LUT colour bar and d) representative SERS spectrum for SERS-440 - the cell spectrum is plotted on the primary y-axis and the reference on the secondary y-axis. (StreamLine - λ_{ex} = 785 nm, 100% (0.29 W), spectral range 1434-1774 cm^{-1}, step size x,y 1.0 µm, 0.5 µm 2s).

The measurements were performed using the StreamLine mapping system at Strathclyde and due to instrumental constraints StreamLineHR images were not obtained when the measurements were initially made. The 785 nm laser line requires a pinhole to generate a laser spot for high resolution mapping and this was not initially fitted on the instrument. Nonetheless, all of the commercial nanotags were detectable within a single cell (**Figure 3.7** - **Figure 3.10**). The measurable SERS signal of the cell associated nanotags was reduced when compared with the reference spectrum (**Figure 3.7- Figure 3.10**)**.** This however was not an effect of cell uptake and was a direct result of the cell applied nanotag suspension being diluted from a 20× stock concentration to 0.5× working concentration. It was expected that this 40× dilution would result in a 40-fold reduction in the measured signal and this was consistent with the observations made (**Figure 3.7**- **Figure 3.10**)**.** In the different examples the nanotags were not taken up uniformly across the cells and this may differ depending on cell fitness and their propensity to incorporate the nanotags.

Consistent with the false colour images was a degree of non-specific binding (**Figure 3.7- Figure 3.10**). Signals were measured from the nanotags out with the cell boundaries but this was to be expected, to a certain extent, since the nanotags were not functionalised with any directing moiety and were not specifically targeting a cell component or membrane. The images also do not offer any definitive proof of cellular uptake and it can be argued that the nanotags were bound to the cell surface. Uptake by the cell could be confirmed by Transmission Electron Microscopy (TEM), depth profiling in the z-direction or 3D imaging to determine the location of the nanotags relative to the cell. It is however, reasonable to assume cellular uptake and there are several instances within the literature where uptake has not been confirmed by a supplementary method.[7, 8, 205] In addition, this preliminary study was designed to determine if the commercial nanotags were suitable as cell bio-imaging agents. Their suitability has been determined and in further studies conclusive proof of uptake using 3D imaging would be investigated.

3.2.5.2 StreamLineHR Water Immersion Measurements of the Commercial Nanotags in Cells

In the initial stages of the investigation the absence of a pinhole prohibited StreamLineHR measurements and the inverted microscope system prevented water immersion measurements. As a result of this a selection of samples were analysed at Renishaw using an upright microscope fitted with a pinhole which allowed for both high resolution and water immersion measurements to be made. The use of a water immersion objective has several advantages - namely the minimisation of refraction which can occur at the sample-air interface[206, 207] and a reduction in the power density which is important when directly interrogating the cell since it can reduce any sample degradation.[208]

Due to time constraints it was only possible to analyse a single duplex sample to which SERS-403 and SERS-421 commercial nanotags had been applied (**Figure 3.11**). However, component DCLS was able to resolve the individual nanotags which were present and it was also possible to observe cumulative SERS signals – that is SERS signals from all the nanotags found within a specified location (**Figure 3.11i-k**).

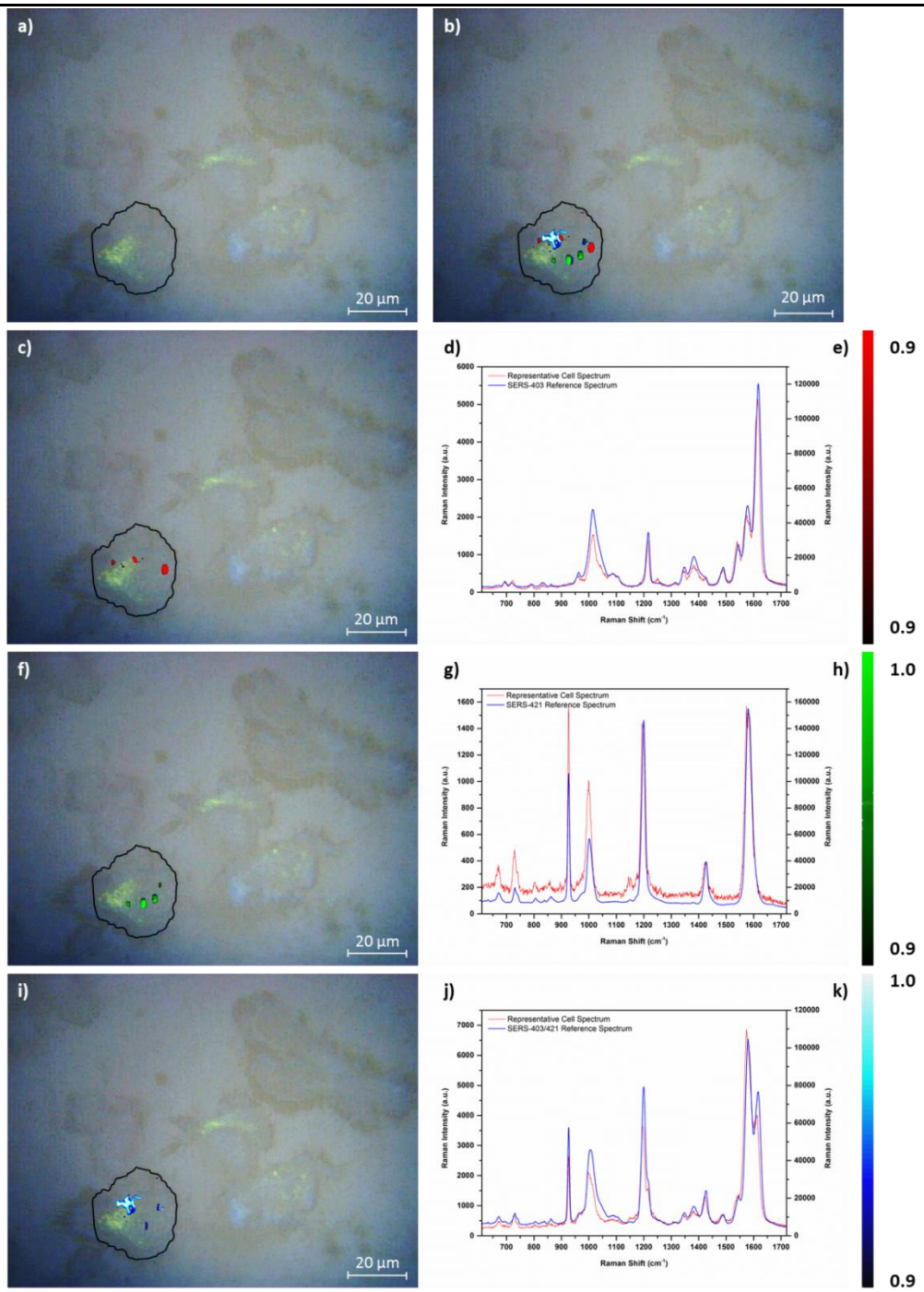

Figure 3.11: False colour SERS map image and representative spectrum for SERS-403 and 421 nanotags applied to a macrophage cell population. a) white light image, b) complete false colour SERS map image and false colour SERS map image, representative cell spectrum and LUT colour bar for c)-e)SERS-403, f)-h)SERS-421 and i)-k) cumulative SERS-403/421 respectively. The cell spectrum is plotted on the primary y-axis and the reference on the secondary y-axis (StreamLineHR - λ_{ex} = 785 nm, 100% (0.13 W), spectral range 607-1720 cm^{-1}, step size x,y 0.2 µm, 0.2s).

Both SERS-403 (**Figure 3.11c-e**) and SERS-421 (**Figure 3.11f-h**) were detectable within a single cell and when identified individually the nanotags were found in discrete cellular locations. The exact location of the nanotags within the cell was unknown but this could be achieved by interrogating the cells with a laser wavelength which allows for the visualisation of the intrinsic Raman cell signals. Cell signals can be observed with a 785 nm laser but the employed laser power (100% - 0.13 W) and acquisition time (0.2 s) were optimised for visualisation of the nanotags and not the cell. Although the positioning of the nanotags relative to the cell components would have provided valuable information, this was outside the scope of the study since the initial goal was to determine the suitability of the nanotags as cellular imaging agents. Surface functionalisation has also been observed to influence cellular uptake[7] however the positioning of the nanotags in discrete cellular locations was unlikely to be influenced by this since the silica shell of the commercial nanotags, rather than the reporter molecule, was presented to the cell surface. Their occurrence in distinct cell positions was also not influenced by any targeting moiety since the nanotags were unfunctionalised.

Interestingly, it was also possible to observe cumulative SERS signals from both the SERS-403 and SERS-421 commercial nanotags when they were found within the same single location (**Figure 3.11i-k**). When the nanotags were located close together, they were also found in a discrete cellular location from where the nanotags were found individually (**Figure 3.11b**). In the instances of co-localisation it was probable that the nanotags were internalised simultaneously.

Consistent with the examples where the nanotags were applied to the macrophage cells individually (**Figure 3.7- Figure 3.10**) the images provided no evidence of cellular uptake. As stated earlier the preliminary goal of the investigation was to determine if the nanotags were suitable cellular imaging agents. This has been determined and in future studies definitive proof of cellular uptake would be obtained.

3.2.5.3 StreamLineHR Measurements of the Commercial Nanotags in Cells

With the addition of a pinhole to the system at Strathclyde it was possible to perform StreamLineHR measurements and some of the samples initially analysed by the StreamLine system were re-interrogated. However, the use of an inverted microscope

still prohibited the use of a water immersion objective. The samples which were re-analysed included dendritic cells to which all four nanotags had been applied. As with the previous examples it was possible to observe and identify the exact combination of SERS nanotags which had been applied (**Figure 3.12**).

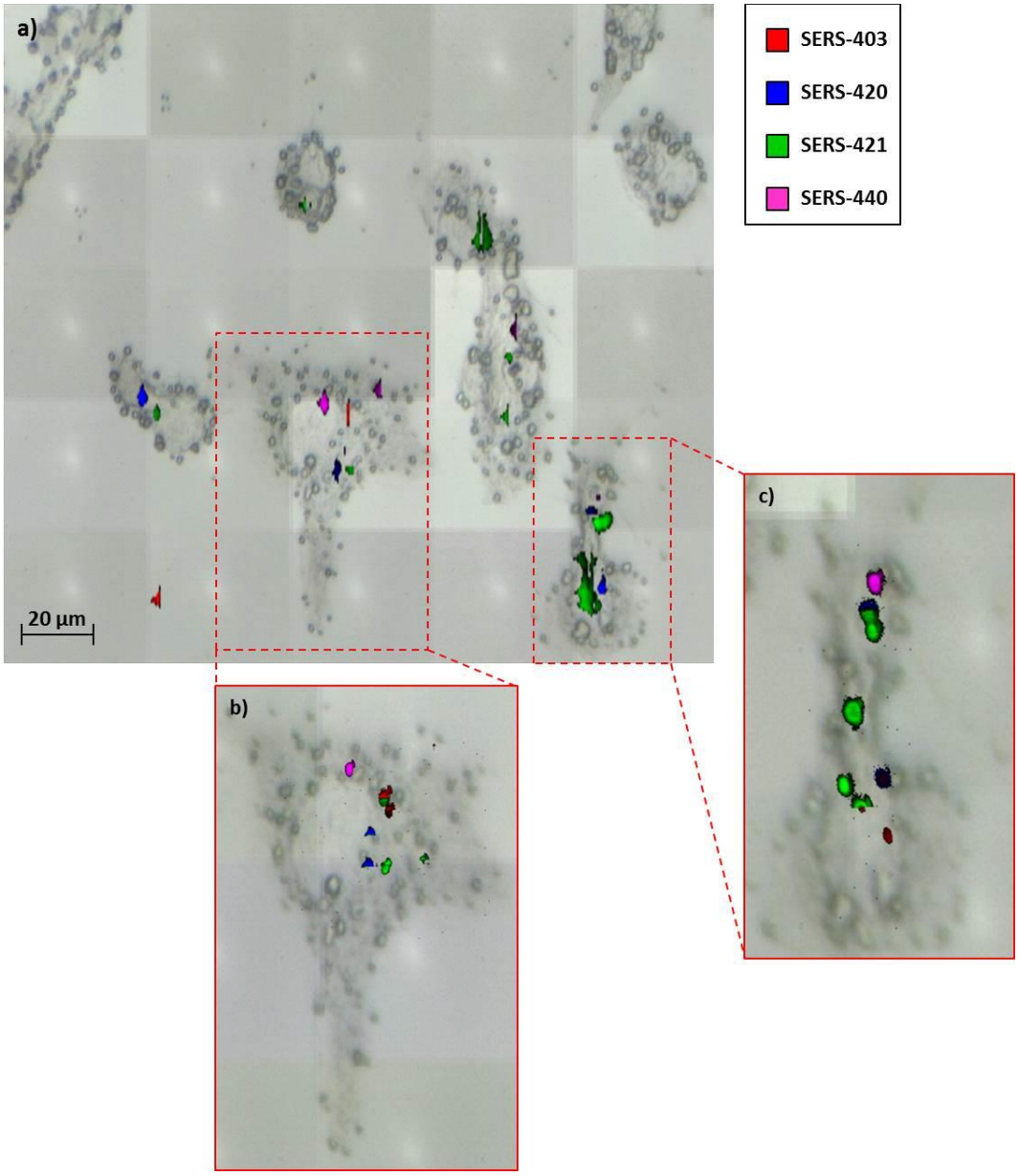

Figure 3.12: False colour SERS maps images of all four commercial nanotags applied to a dendritic cell population. a) StreamLine image of a dendritic cell population and b-c) StreamLineHR images of the highlighted cells. (StreamLine -λ_{ex} = 785 nm, 100% (0.29 W), spectral range 1434-1774 cm^{-1}, step size x,y 0.3 µm, 0.5 µm, 5s and StreamLineHR - λ_{ex} = 785 nm, 100% (0.45 W), spectral range 1439-1774 cm^{-1}, step size x,y 0.1 µm, 0.1s).

In this particular example a cell population was initially analysed using the StreamLine method to rapidly determine which cells had taken up the SERS nanotags. From the StreamLine image it can be seen that five cells had internalised the nanotags to varying degrees (**Figure 3.12a**). SERS-420 and SERS-421 were found in all 5 cells and only one of the cells was found to contain all four nanotags (**Figure 3.12a**). As with some of the other examples there was a certain degree of non-specific binding but again the nanotags were not functionalised with any targeting moiety and this was to be expected.

Re-analysing two of the nanotag positive cells with the StreamLineHR method had a drastic effect on the resolution (**Figure 3.12a** *c.f.* **Figure 3.12b, c**). In the StreamLine image the nanotags were quite columnar and not particular spherical. This is a direct result of mapping using a non-confocal laser line rather than a spot. Implementation of a confocal method and a laser spot resulted in false colour images where the nanotags were well resolved and spherical. In addition, in the StreamLine image only SERS-420 and SERS-421 nanotags were visible within the cell on the right (**Figure 3.12c**). However, when the cell was interrogated with the high resolution method it was apparent that all four nanotags were actually present within this single cell. This highlights the benefits of imaging with a confocal system where the laser is focused into a tight spot and each point on the map is individually interrogated with this area.

In the final example a single dendritic cell to which all four nanotags had been applied was analysed using the StreamLineHR method. All four nanotags were successfully identified using component DCLS (**Figure 3.13**). As with the previous examples, each of the nanotags were found within discrete cellular locations but to a lesser extent than the duplex sample (**Figure 3.11** *c.f.* **Figure 3.13**). However, there was no consistency to where the nanotags were found and they did not cluster within specific regions of the cell (**Figure 3.13**). Determining the exact cellular positioning was out with the scope of this preliminary study and as mentioned earlier, a 40-fold reduction in signal intensity was expected as result of diluting the nanotags to a 0.5× working concentration. In this example however, signals from the nanotags decreased up to 300-fold when compared with the reference (**Figure 3.13d, j and m**). This may suggest that these nanotags were present at a greater depth within the cell and this might provide evidence of uptake. However, this would need to be confirmed be a secondary method.

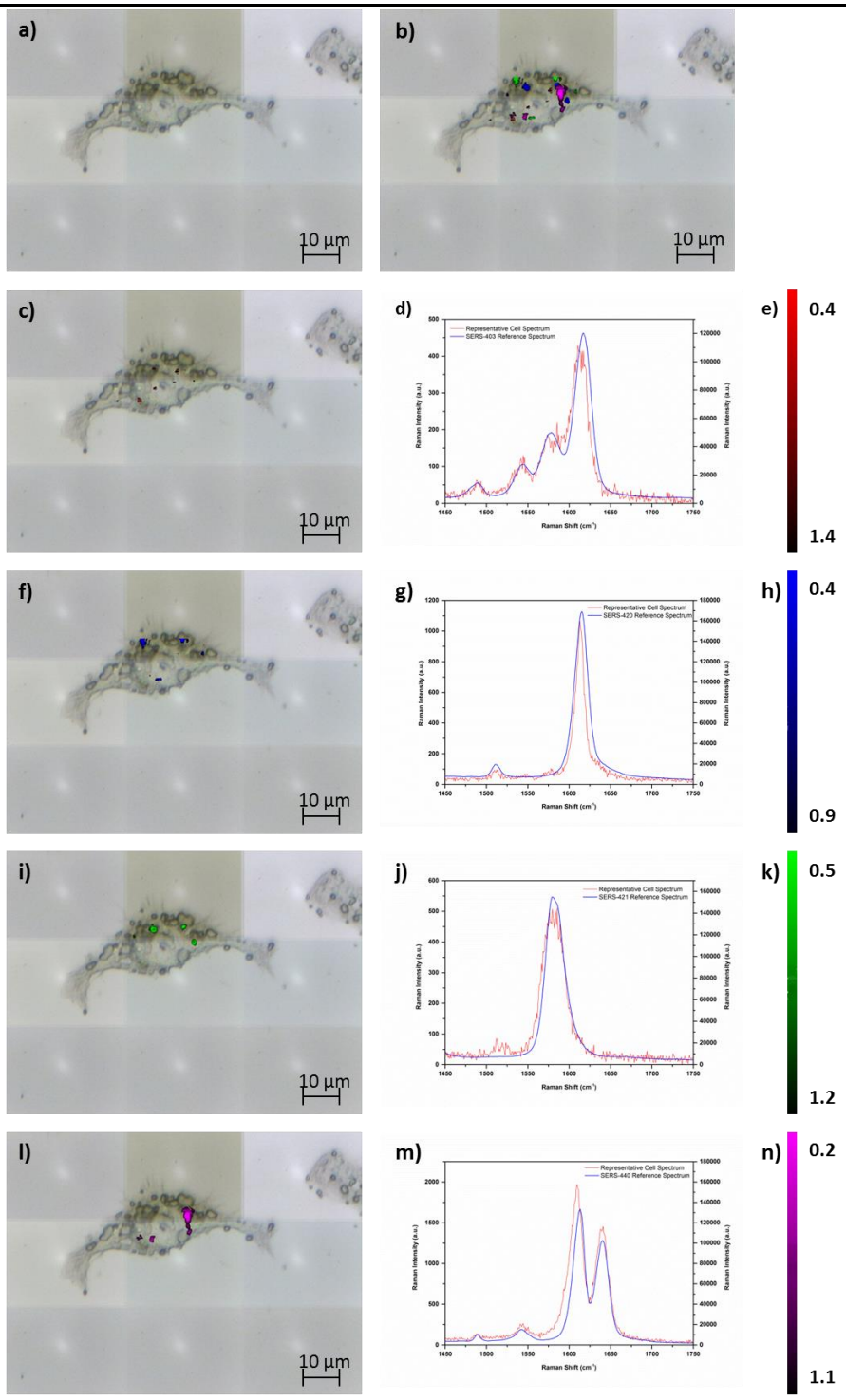

Figure 3.13: False colour SERS map images of all four nanotags applied to a dendritic cell population. a) white light image, b) complete false colour SERS map image, c-e), f)-h), i)-k) and l)-n) false colour SERS map image, representative cell spectrum and LUT colour bar for SERS-403,420,421 and 440 respectively. The cell spectrum is plotted on the primary y-axis and the reference on the secondary y-axis (StreamLineHR - λ_{ex} = 785 nm, 100% (0.45 W), spectral range 1434-1774 cm^{-1}, step size x,y 1.0 µm, 0.2s)

It does however highlight the need to use robust SERS nanotags which can still be detected within cells should uptake result in such a reduction in signal intensity.

3.2.5.4 Conclusions and Commercial Issues

The commercial nanotags were found to be suitable multi-marker cell imaging agents. When analysed individually and as multiple component samples, both in suspension and when applied to cells, it was possible to identify the specific combination of nanotags present. Cumulative SERS signals were also detectable and the benefits of StreamLineHR imaging were demonstrated. High resolution mapping provided superior resolution of the nanotags and revealed further information which was lacking when the StreamLine method was employed (**Figure 3.11**). Common to all of the samples were issues with non-specific binding, a need for definitive proof of cellular uptake and an indication of nanotag localisation relative to the major cell organelles. The next stages of investigation would have considered functionalising the nanotags with targeting moieties, determining cellular uptake by depth profiling and 3D mapping techniques and imaging in 2D with a secondary laser to measure the intrinsic Raman cell signals. This in combination with chemometric methods would hopefully result in the resolution of cell organelles to give an indication of the cellular localisation of the nanotags.

Unfortunately the nanotags were a commercial product and as sponsorship was provided by another commercial company there was a conflict of interest in implementing these nanotags in further studies. As a result their use had to be suspended.

3.3 Investigations of Suitable Nanotag Systems

Investigations were commenced into alternative nanotag systems for use as multi-marker cellular imaging agents. One of the first systems investigated involved functionalising a range of silver (Ag) and gold (Au) nanoparticles with small molecule reporters. Such systems were selected as they had demonstrated applications as individual cell imaging agents[7, 8, 209] but this had not yet been extended to a multi-marker approach.

Ag citrate, hydroxylamine, borohydride and Au citrate nanoparticles were functionalised with 4-mercaptobenzoic acid (MBA), 4-mercaptopyridine (MPY) and 2-aminothiophenol (ATP) (10 µL, 10 mM stock concentration, 0.1 mM final concentration) and analysed accordingly (**Figure 3.14**).

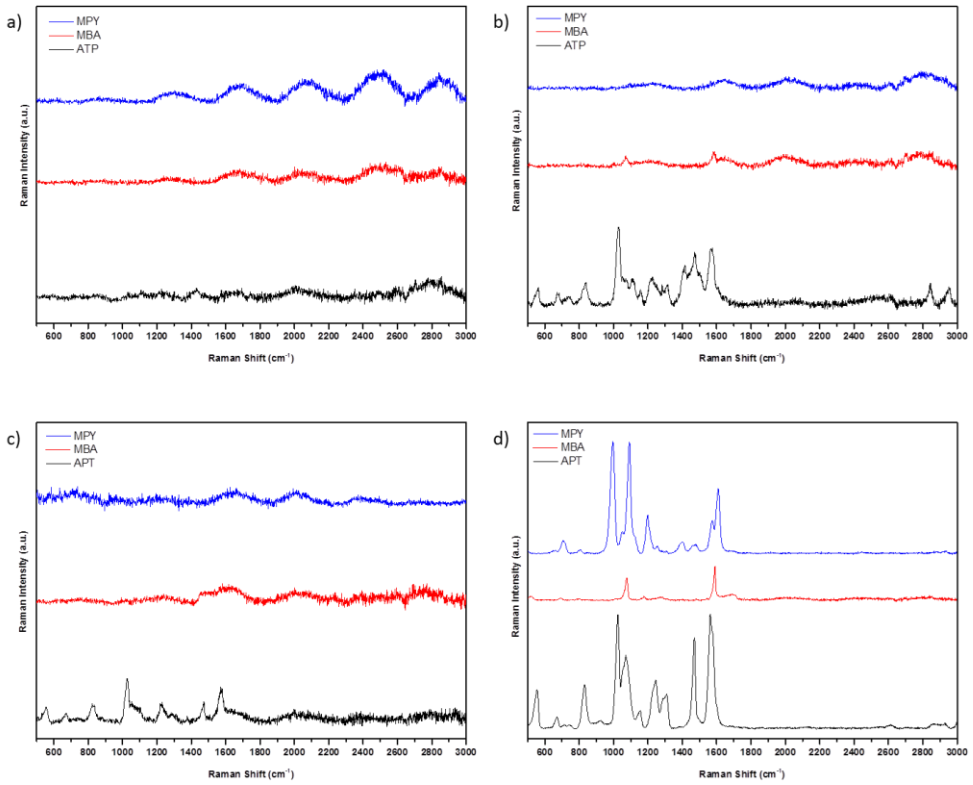

Figure 3.14: Spectral analysis of a) Ag citrate, b) hydroxylamine, c) borohydride and d) Au citrate nanoparticles functionalised with a range of small molecule reporters. (Single scan – λ_{ex}= 633 nm, 100% (~6.6 mW), spectral range 100-3200 cm^{-1}, 10s).

When the Ag citrate nanoparticles were analysed no measurable signals from the small molecule reporters were observable. Analysis of the hydroxylamine and borohydride nanoparticles showed that the only conjugates from which a signal was obtained was from those functionalised with APT (**Figure 3.14**). In contrast signals were measured from all of the small molecule functionalised Au nanoparticles (**Figure 3.14**). The intense signals measured from the Au conjugates were a direct result of nanoparticle aggregation and this was so extensive that visible particles formed within the solutions within 24 h.

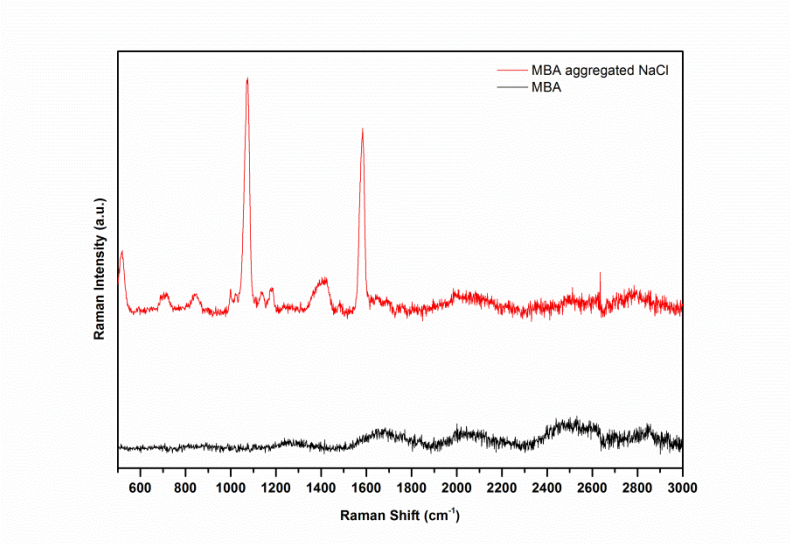

Figure 3.15: Ag citrate nanoparticles functionalised with MBA- the black trace is representative of nanoparticles without aggregation and the red trace is representative of MBA functionalised nanoparticles which have been aggregated with 2M NaCl. (Single scan – λ_{ex}= 633 nm, 100% (~6.6 mW), spectral range 100-3200 cm^{-1}, 10s).

Measurable signals were observed from the remaining Ag citrate (**Figure 3.15**), hydroxylamine and borohydride nanoparticles provided that the solutions were aggregated with a 2 M salt solution (NaCl). The aggregation exhibited by the Au citrate conjugates, and the uncontrolled aggregation achieved by the addition of salt, was however, considered to be detrimental since the initial 'homogeneity' of the nanoparticle suspension was destroyed and aggregate formation in this manner is highly irreproducible.[38, 39] Uncontrolled aggregation of this manner would be highly undesirable for conjugates that were to be used in cellular studies since aggregation could continue to an extent where the nanoparticles/nanotags were no longer eligible for cell uptake. However, without some method of aggregation the conjugates were not suitable as multi-marker imaging agents as no measurable signals were obtained.

The Au core was central to the success of the commercial nanotags and similarly the salt induced formation of aggregates was key to the success of the conjugates described above. From this, and the previous investigations with the commercial nanotags, it was clear that some form of induced, but controlled aggregation, was necessary. Based on this information an already published method was investigated.[9] This system involved 'controlled' aggregation of Ag citrate nanoparticles with a cross-linking agent before

polymer coating and labelling with various small molecule reporters.[9] The multiple component capabilities of the nanotags had been investigated to the extent of a triplex solution dried on a glass microscope slide and in another study some of the nanotags had been functionalised with cell surface binding antibodies for cellular studies. However, their use as multi-marker intracellular imaging agents had not been investigated.

3.4 Optimisation of the Selected Nanotag System

Prior to the commencement of any multiple component capability studies in solution or within cell populations it was necessary to optimise the synthesis of the nanotags.

3.4.1 1,6-Hexamethylenediamine (1,6-HMD) Optimisation

It is well known that the strength of the SERS signal can be enhanced by the aggregation of nanoparticles.[38, 39] This phenomenon arises because the reporter molecules can reside in the interstices between two particles and at these intersections the electromagnetic fields are considerably augmented.[38, 39] As discussed previously, uncontrolled aggregation can be detrimental but some form of 'controlled' aggregation was considered to be necessary for the development of robust and optically strong nanotags, especially for use in intracellular studies. In order to achieve 'controlled' aggregation the cross-linking agent 1,6-hexamethylenediamine (1,6-HMD) was employed.[9] Cross-linking occurs via the terminal amine groups and each terminus binds to separate nanoparticles bringing them in close proximity with one another.[9]

During the initial stages a wide range of 1,6-HMD concentrations (0.1 – 1 mM final concentrations) were investigated in order to select the optimum for controlled aggregation (**Figure 3.16a** and **b**). From the results of the extinction spectroscopy measurements it was observed that when the concentration was increased above 0.4 mM a broad band, indicative of aggregation, in particular cluster or aggregate formation, began to arise between 600 – 800 nm and this was especially pronounced for 0.8 – 1 mM concentrations (**Figure 3.16b**). In addition, there was a broadening of the plasmon band and this was most pronounced for the higher concentrations of 1,6-HMD (**Figure 3.16a** and **b**). There was also significant dampening of the plasmon band

(λ_{max} = 405 nm) for concentrations above 0.7 mM and this was again indicative of aggregation (**Figure 3.16a**) in particular sedimentation.

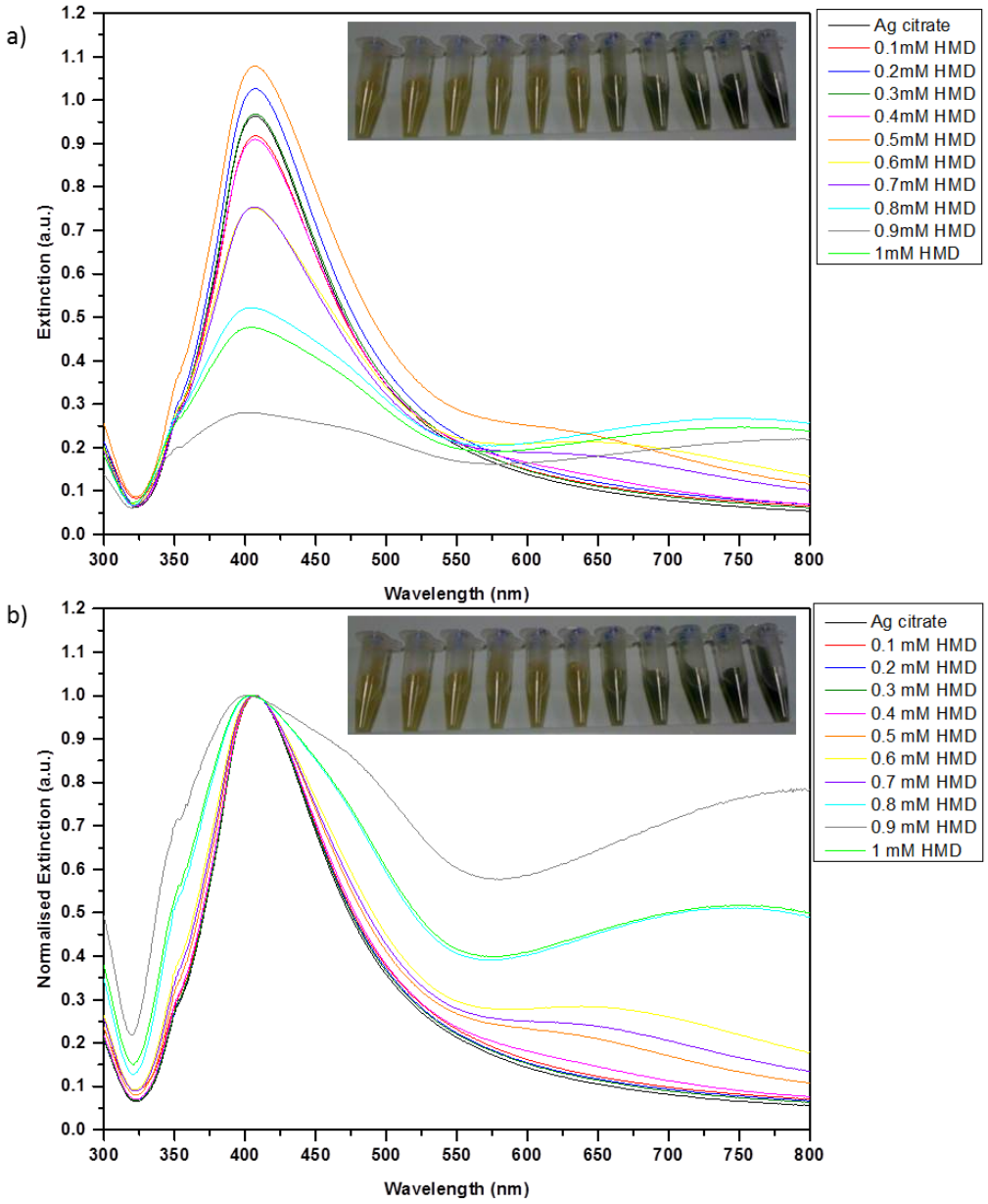

Figure 3.16: 1,6-HMD optimisation – a range of 1,6-HMD concentrations (0.1-1 mM) were investigated as controlled aggregating agents. a) non-normalised extinction spectra and b) normalised extinction spectra. Dampening of the main plasmon band at ~ 400 nm was obvious in the non-normalised spectrum whilst any blue or red shift was more easily visualised in the normalised spectrum. Insert a) and b) from left to right; Ag citrate colloid, Ag citrate colloid aggregated with 0.1 mM – 1 mM 1,6-HMD respectively.

Although band broadening and dampening were observed the λ_{max} did not shift significantly between the samples. For example, Ag citrate λ_{max} = 406 nm *c.f.* 0.9 mM HMD λ_{max} = 403 nm. For 0.6 – 1 mM concentrations there was an immediate colour change from yellow to dark green suggesting that aggregation was progressing rapidly. While the 0.1 – 0.5 mM concentrations all retained the yellow colour of the bare citrate colloid suggesting that aggregation was more controlled and not as rapid.

Based on the extinction data and the visual observations, significant aggregation occurred within the 0.5 – 1 mM solutions. Such significant and rapid aggregation was undesirable since larger aggregates would be unable to penetrate cell walls and external membranes. Additionally, the dramatic colour changes observed suggested that these solutions would not be stable over longer periods of time. As a result it was decided to only proceed with 0.1 and 0.2 mM 1,6-HMD concentrations. Although 0.3 and 0.4 mM concentrations demonstrated an extinction profile similar to that of the bare citrate colloid, the solutions changed colour from yellow to dark green, after a couple of hours, raising concerns regarding their long term stability.

To determine how the aggregation process progressed with time the nanoparticles were cross-linked with 0.1 and 0.2 mM 1,6-HMD and monitored over 12 h (**Figure 3.17**).

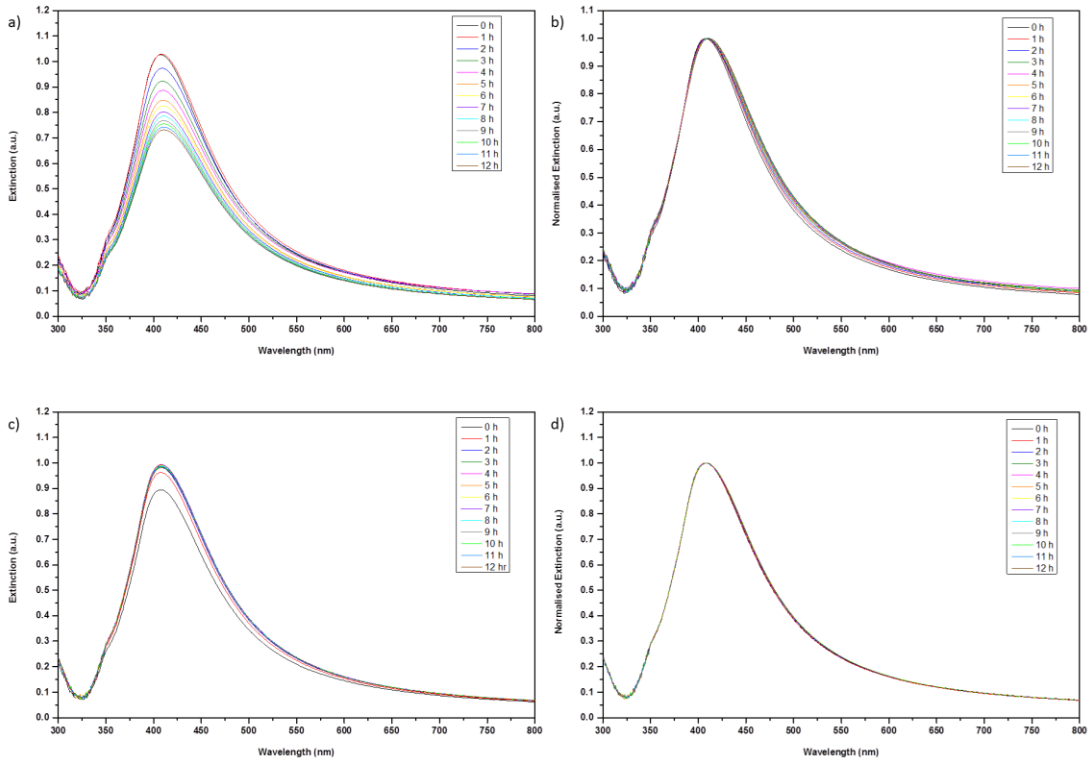

Figure 3.17: 1,6-HMD optimisation study – Ag citrate nanoparticles were controllably aggregated with a)-b)0.1 and c)-d)0.2 mM 1,6-HMD and monitored over a 12h period. The data was both non-normalised and normalised. Dampening of the plasmon band was obvious in the non-normalised spectrum whilst any blue or red shift was more easily visualised in the normalised spectrum.

When aggregated with 0.1 mM HMD over a 12 h time period the plasmon band was observed to dampen as the time progressed (**Figure 3.17**). The λ_{max} values for the 0.1 mM samples were not observed to shift significantly (λ_{max} = 408 - 411) but a very slight red shift and broadening of the plasmon band was observed which became more evident with increasing time increments (**Figure 3.17**). This would suggest that aggregation continued to progress with time and since there was nothing to slow this reaction this was to be expected. However, unlike the samples where larger concentrations of 1,6-HMD were employed (**Figure 3.16**) aggregation did not appear to be particularly rapid or extensive.

Unlike the 0.1 mM 1,6-HMD sample the 0.2 mM sample did not give any indication that aggregation was progressing with time (**Figure 3.17**). When the data was normalised

all of the samples retained approximately the same profile as that of the bare citrate colloid and the λ_{max} values were not observed to shift, remaining at λ_{max} = 408 nm and any signs of peak broadening were very slight (**Figure 3.17**). This was surprising since it was expected that aggregation would increase with increasing concentration of the aggregating agent especially since aggregation was continuing at the lower concentration of 1,6-HMD.

It was decided that either a 0.1 or 0.2 mM concentration of 1,6-HMD could be used to controllably aggregate the nanoparticles. Based on the extinction data (**Figure 3.16** and **Figure 3.17**) it was determined that it might be more prudent to opt for the 0.2 mM concentration since the solutions appeared to demonstrate a greater stability over time. In addition, at this concentration samples should achieve maximum levels of aggregation without any loss of stability and more extensive 'controlled' aggregation should, in theory, lead to greater signal enhancement.

3.4.2 Polyvinylpyrrolidone (PVP) Optimisation

Polymer encapsulation has traditionally been used as a method for protection and stabilisation in nanotag systems;[39] preventing reporter molecules from desorbing whilst simultaneously preventing any adulterants or interfering agents from adsorbing onto the nanotag surface.[39] Encapsulation agents can include bio[210] and organic[211] polymers and inorganic materials such as silica.[10, 39] Silica is often favoured as it confers physical durability whilst simultaneously protecting the nanotags from the chemical environment and as a result silica coated nanotags tend to have an extended shelf life.[10, 39] In this system polymer encapsulation was dually functional in that it dampened the induced aggregation whilst simultaneously offering a degree of protection to the nanotags.[9]

As with the optimisation of 1,6-HMD, various concentrations of PVP were initially investigated. Ag citrate nanoparticles were aggregated with 0.1 and 0.2 mM 1,6-HMD and after a recommended aggregation period of 3 min,[9] although samples can demonstrate stability over longer periods of time (**Figure 3.17**), PVP was added to dampen the reaction and stabilise the nanoparticle aggregates.

In the case of the 0.1 mM 1,6-HMD samples, PVP concentrations ranging from 0 – 22.7 µM were investigated (**Figure 3.18**).

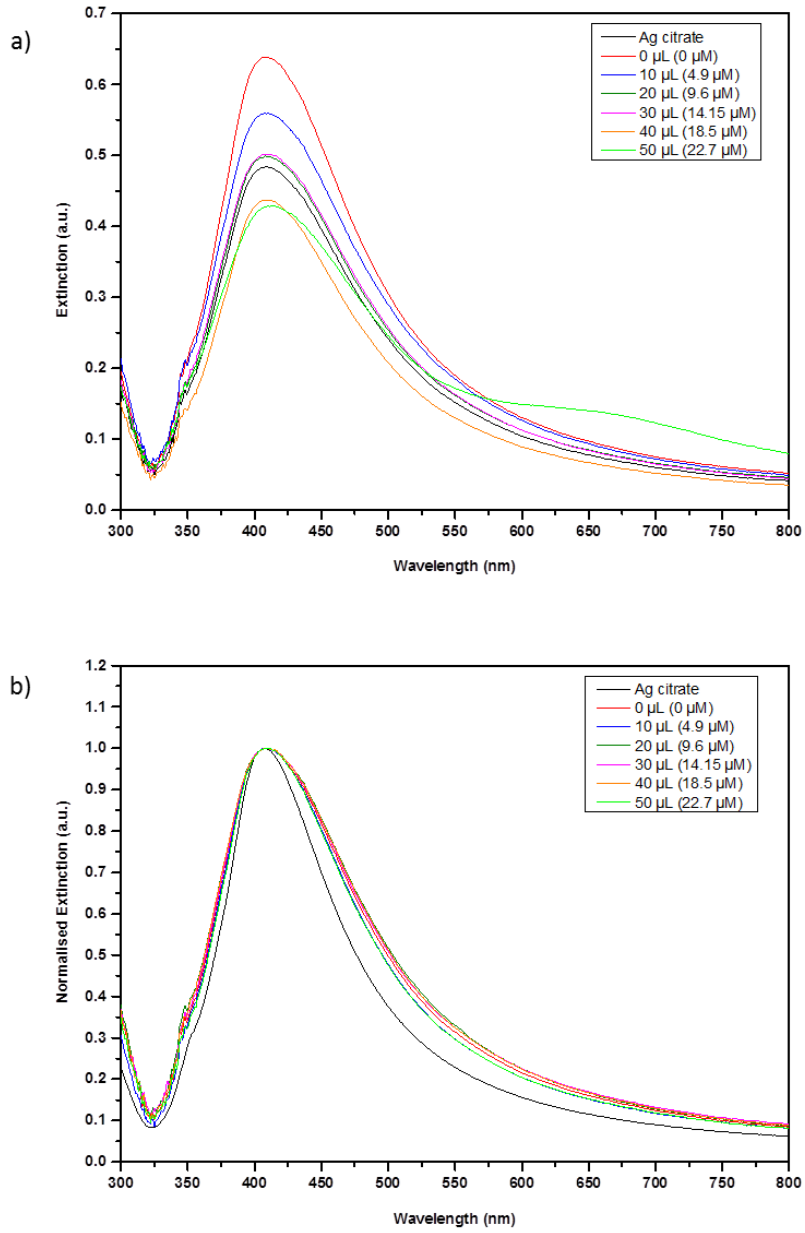

Figure 3.18: PVP optimisation – Ag citrate was cross-linked with 0.1 mM 1,6-HMD before PVP was applied to dampen the aggregation reaction. Various volumes (0 – 50 µL) were investigated and the concentrations shown in brackets refer to the final concentration (PVP stock - 10 mg/mL, 250 µM) added to samples. The data was a)non-normalised and b)normalised.

In the non-normalised data set the plasmon band was observed to decrease for the highest concentrations of PVP (**Figure 3.18**). This was surprising as it was expected

that the higher concentrations of PVP would be the most successful at dampening the aggregation. However, when the data was normalised red shifting (λ_{ex} = 408 - 410 nm) and broadening of the plasmon band was apparent for all of the concentrations when compared directly to the bare citrate colloid (**Figure 3.18**). This broadening was least prominent for the highest concentration of PVP. When only considering the samples to which PVP had been applied, this red shift and broadening was very slight and there was no obvious correlation between increasing PVP concentration and stability (**Figure 3.18**). This small difference between the samples suggests that aggregation at a 0.1 mM 1,6-HMD concentration was not particularly extensive or rapid and even small concentrations of PVP were sufficient to dampen the aggregation.

When the same concentration series, 0 – 22.7 μM, was repeated with samples that had been aggregated with 0.2 mM 1,6-HMD they were observed to visibly aggregate over time suggesting that the PVP concentrations were not sufficient to dampen the aggregation reaction. As a result higher concentrations 30.7 – 41.7 μM, of PVP were applied (**Figure 3.19**).

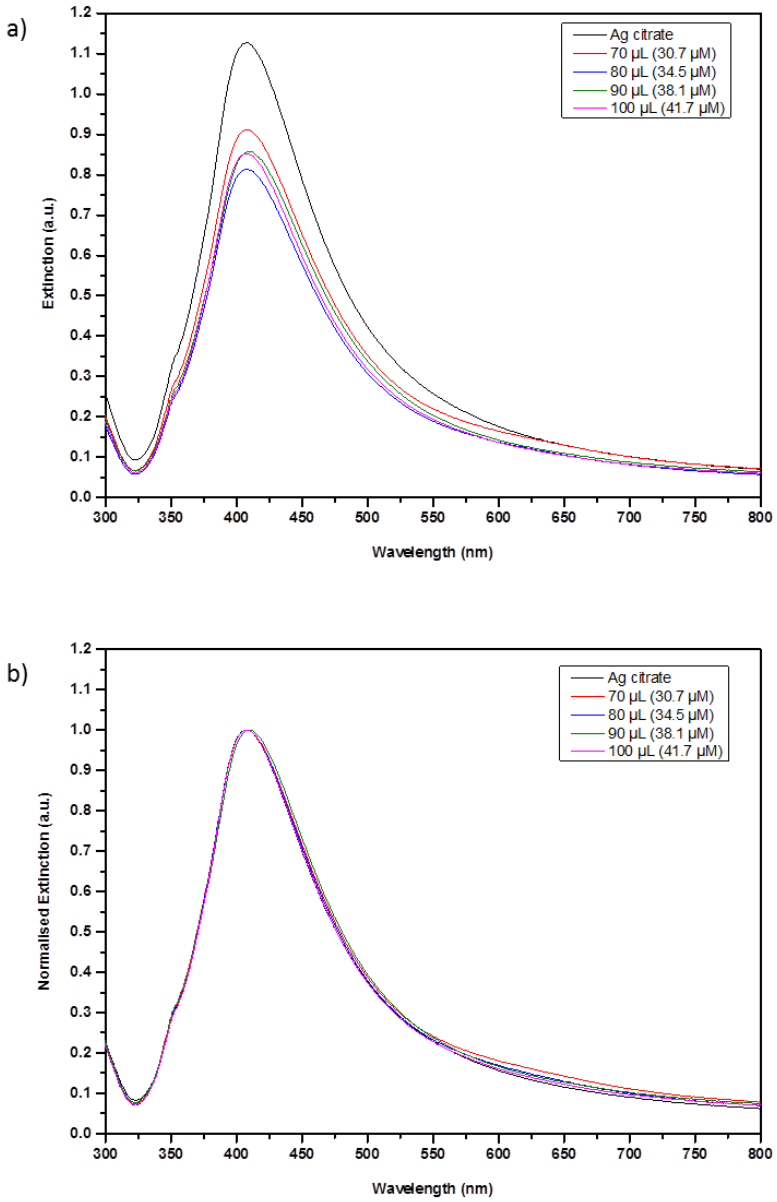

Figure 3.19: PVP optimisation – Ag citrate colloid was cross-linked with 0.2 mM 1,6-HMD before PVP was applied to dampen the aggregation reaction. Various volumes (70 – 100 µL) were investigated and the concentrations shown in brackets refer to the final concentration (PVP stock - 10 mg/mL, 250 µM) added to samples. The data was both a) non-normalised and b) normalised.

When the non-normalised extinction data were analysed a dampening in the plasmon band was observed and this was most pronounced for the 34.5 µM PVP sample and least pronounced for the lowest concentration of PVP (**Figure 3.19**). Analysis of the

normalised extinction data revealed a very slight broadening of the plasmon band but the λ_{max} of 408 nm was not observed to shift when compared with the colloid standard (λ_{max} = 408 nm). When comparing the samples to which the PVP had been applied, the broadening of the plasmon band was greatest for the sample to which the lowest concentration of PVP (30.7 μM) was applied and least for the sample to which the highest concentration (41.7 μM) was applied. In fact, the broadening of the plasmon band decreased with increasing PVP concentration suggesting that there was a correlation between the PVP concentration and sample stability.

Although the initial stability demonstrated by the 0.2 mM 1,6-HMD, 41.7 μM PVP sample was promising, it was necessary to determine the longer term stability therefore the sample was monitored over a 12 h period (**Figure 3.20**).

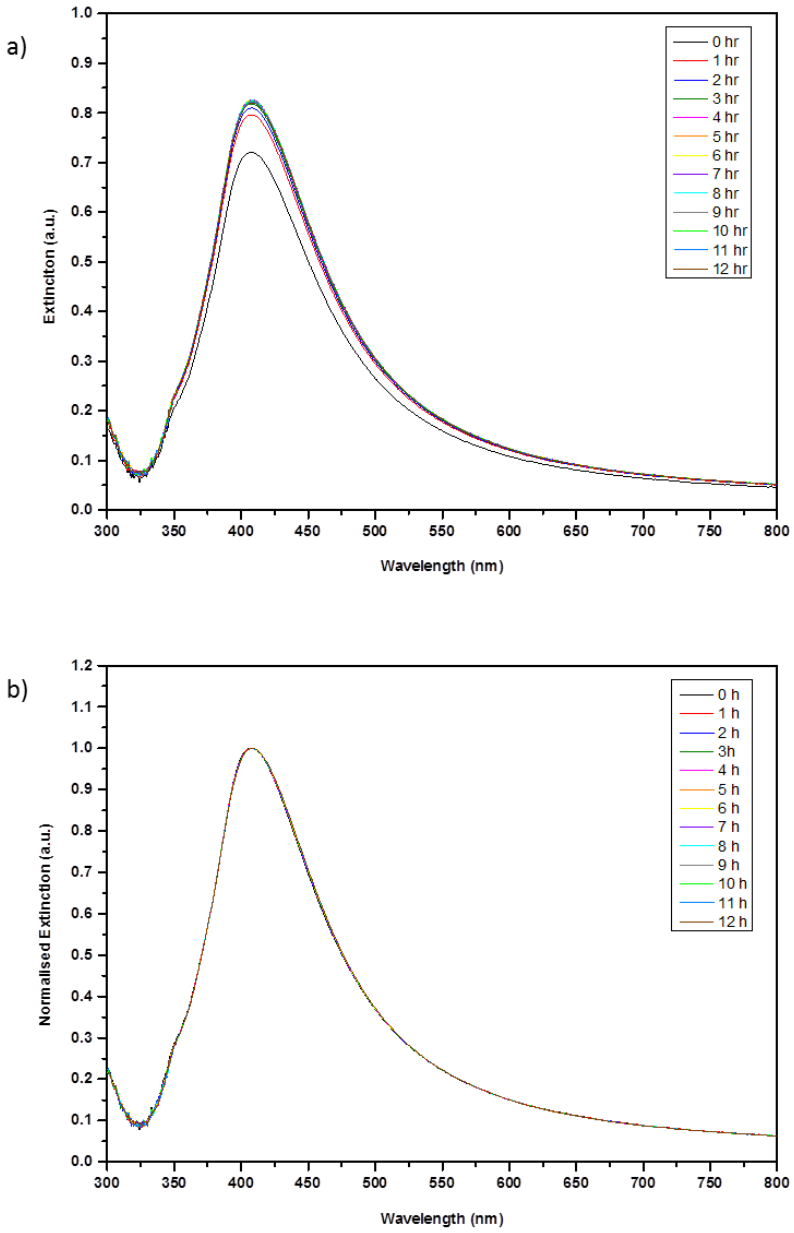

Figure 3.20: PVP optimisation- Ag citrate colloid controllably aggregated with 1,6-HMD and polymer wrapped with 41.7 µM PVP. The dampening of the aggregation process was monitored over a 12 h period. The data was both a) non-normalised and b)normalised.

In the non-normalised extinction data, the intensity of the plasmon band of all the samples to which PVP was added increased above that of the 0 h sample (**Figure 3.20**). In the normalised extinction data the plasmon band of the samples were not found to change, there was no band broadening or red shifting or any general indication that the PVP had not dampened or at least dramatically slowed the induced aggregation (**Figure**

3.20). Based on these results it was decided to proceed with a final 1,6-HMD concentration of **0.2 mM** and a final PVP concentration of **41.7 µM**. Although 0.1 mM 1,6-HMD can probably achieve sufficient levels of aggregation, the 0.2 mM samples, for unknown reasons, appeared to be more stable, both initially and over longer periods of time (**Figure 3.18** c.f. **Figure 3.19**, **Figure 3.20**). By selecting the higher of the two 1,6-HMD concentrations it was hoped that controlled aggregation could be achieved resulting in significant signal enhancement, and by polymer wrapping with 41.7 µM PVP, all of this could be accomplished without any observable loss of sample stability.

The nanotag samples were also analysed by scanning electron microscopy (SEM) to determine the full extent of aggregation induced by the addition of 1,6-HMD and to further determine if the subsequent PVP quenching reaction had indeed been successful.

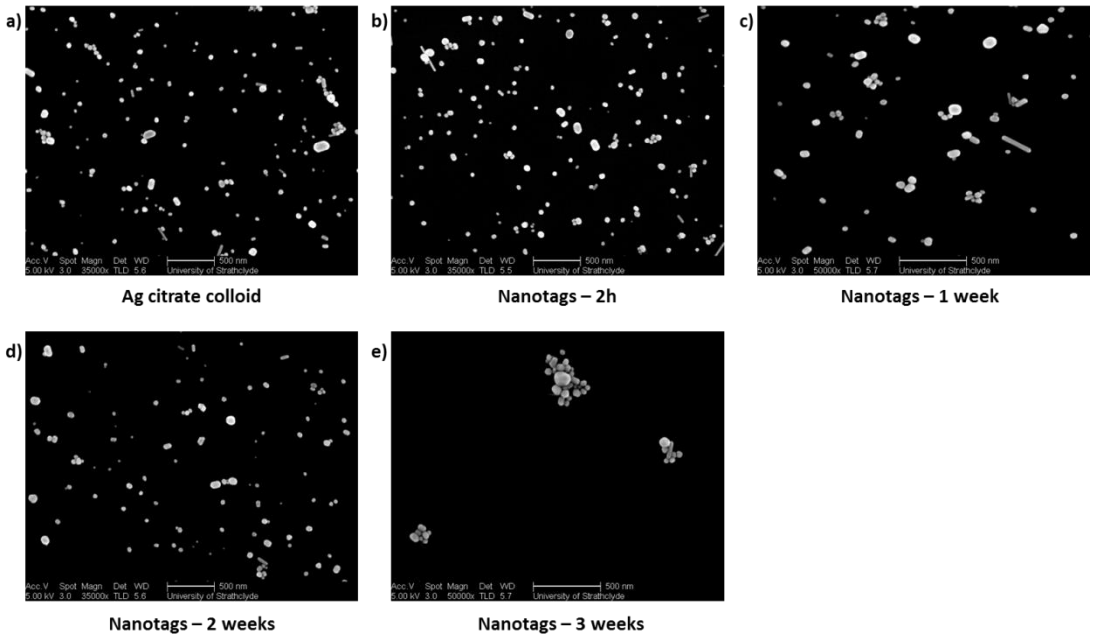

Figure 3.21: SEM images of the nanotags - a) Ag citrate nanoparticles, b)-e) Ag citrate nanoparticles aggregated with 0.2 mM 1,6-HMD and polymer wrapped with 41.7 µM PVP analysed after 2h, 1 week, 2 weeks and 3 weeks respectively. Scale 500 nm.

The SEM images show that the citrate colloid wasn't particularly homogenous and consisted of a mixture of single nanoparticles, larger aggregates and some rods (**Figure 3.21a**). The 1 and 2 week old and the 2h nanotag samples were relatively similar, again

consisting of single nanoparticles, some rods but mainly dimers, trimers and small clusters (**Figure 3.21b-d**). This was to be expected since the samples were subject to 'controlled' aggregation and the ultimate aim was the formation of small clusters since these scaffolds can provide large enhancements in signal, whilst still being capable of cell penetration. However, the 3 week old nanotag sample consisted of considerably larger clusters (~ 200 nm) suggesting that the PVP was not entirely capable of stopping the aggregation reaction and it only slowed the aggregation over time. Although such extensive aggregation is clearly undesirable in terms of cell penetration, it was not particularly rapid. Therefore provided the samples were renewed every 2 weeks, the benefits of controlled aggregation could be reaped without any detrimental effect on their ability to be taken up by cells.

3.4.3 Small molecule selection

The range of molecules available for use as reporters[212-215] in SERS studies is vast. For example, fluorescent labels can be purchased commercially (e.g. ROX, HEX, FAM, TET, Cy3 and TAMRA)[216, 217] or dyes can be synthesised with specific chemical moieties known to give strong SERS signals.[212-215, 218, 219] Within the research group at the Centre for Molecular Nanometrology numerous dyes have been synthesised for reporter use, most notably benzotriazole azo dyes[212-215] and more recently squaraine[218] and cyanine[219] type reporters. However, commercial dyes can be expensive and dye synthesis time consuming and complicated. Therefore, a range of small molecules were selected as reporters for this particular study. The molecules were selected on the basis that no synthesis was required, they were inexpensive, readily available, gave strong SERS signals, nanoparticle conjugation was extremely straightforward and if required their chemical structures were such that subsequent functionalisation with biomolecules would be relatively simple to achieve.

4-mercaptobenzoic acid (MBA), 4-mercaptopyridine (MPY), 5,5'-dithiobis(2-nitrobenzoic acid) (DTNB), 4- nitrobenzenethiol (NBT), 5-(4-pyridyl)-1,3,4-oxadiazole-2-thiol (SERS-403) and 2-napthalenthiol (2-NPT) were selected. The molecules were all similar in structure consisting of benzene, pyridine and/or oxadiazole ring systems, a terminal thiol or di-sulfide linkage and carboxylic acid and/or nitro group side chains (**Figure 3.22**).

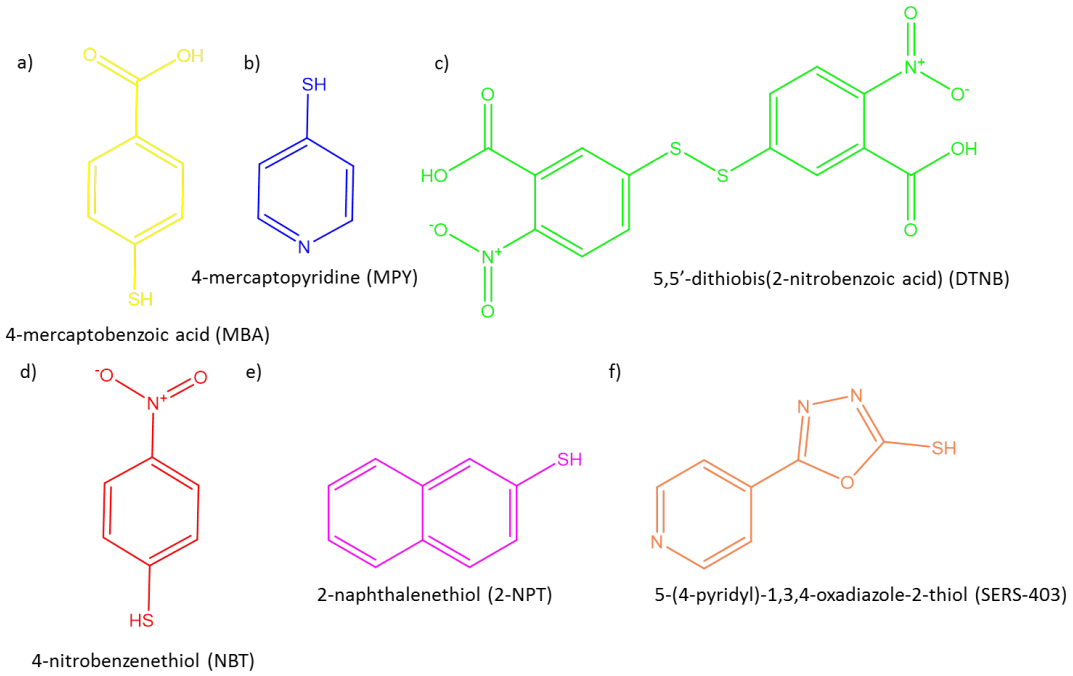

Figure 3.22: Small molecule reporters used in the study – a) 4-mercaptobenzoic acid (MBA), b) 4-mercaptopyridine (MPY), c) 5,5'-dithiobis(2-nitrobenzoic acid) (DTNB), d) 4-nitrobenzenethiol (NBT), e) 2-naphthalenethiol (2-NPT) and f) 5-(4-pyridyl)-1,3,4-oxadiazole-2-thiol (SERS-403).

A unique SERS signal was observed for each of the small molecules when adsorbed on the Ag nanotag scaffold. As the molecules were non-resonant with the exciting laser line (633 nm) there was no resonance contribution and the signal enhancement resulted solely from their adsorption onto the nanotag surface. The predominant molecular vibrations arose from the aromatic or hetero rings and the carboxylic acid or nitro group side chains. The spectra for each of the small molecule labelled nanotags was measured in water and also when the nanotags were re-suspended in cell media (**Figure 3.23** and **Figure 3.24**). As shall be discussed later (see section 3.4.4) some modification to the nanotag synthesis took place in order to improve the stability, whereby the nanotag scaffolds were additionally labelled with a thiol-terminated polyethylene glycol (PEG). Following the addition of PEG to the surface of the nanotags the same predominant molecular vibrations were apparent. In the case of MPY labelled nanotags a doublet of peaks was observable ~ 1001 and 1017 cm^{-1}. However when the nanotags were additionally labelled with PEG a single peak was observed at ~1002 cm^{-1}. This wasn't considered to be an effect of PEG addition since a single peak was

sometimes observable when there is no PEG present on the surface and this was thought to be a batch specific effect. The SERS spectra for each of the small molecule/PEG labelled nanotags was also measured in water and also when re-suspended in cell media (**Figure 3.25** and **Figure 3.26**). The predominant molecular vibrations have been assigned (**Table 3.4**) and for completeness the spectra were measured for all the nanotags at 532 nm and 785 nm (see **Appendix I-Appendix IV**) as were control spectra for each of the small molecule reporters (**Appendix V**).

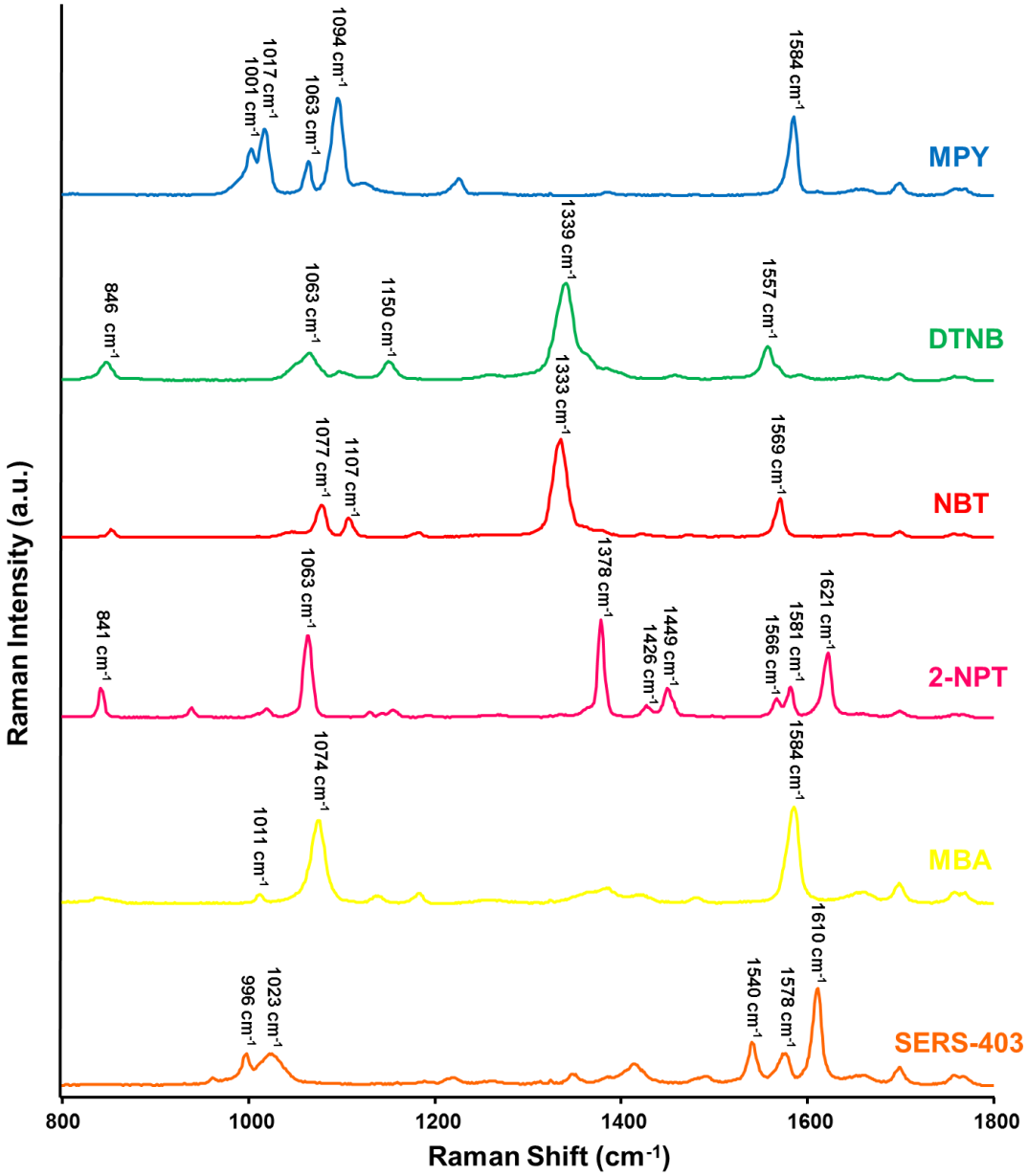

Figure 3.23: Representative SERS spectra for each of the small molecule labelled nanotags. Spectra were offset for illustrative purposes and as no major peaks used for identification were

observed below 800 cm^{-1} or above 1800 cm^{-1} the spectra were truncated accordingly (λ_{ex} = 633 nm edge, 10% (0.66 mW), 10s, extended scan, 800-1800 cm^{-1}).

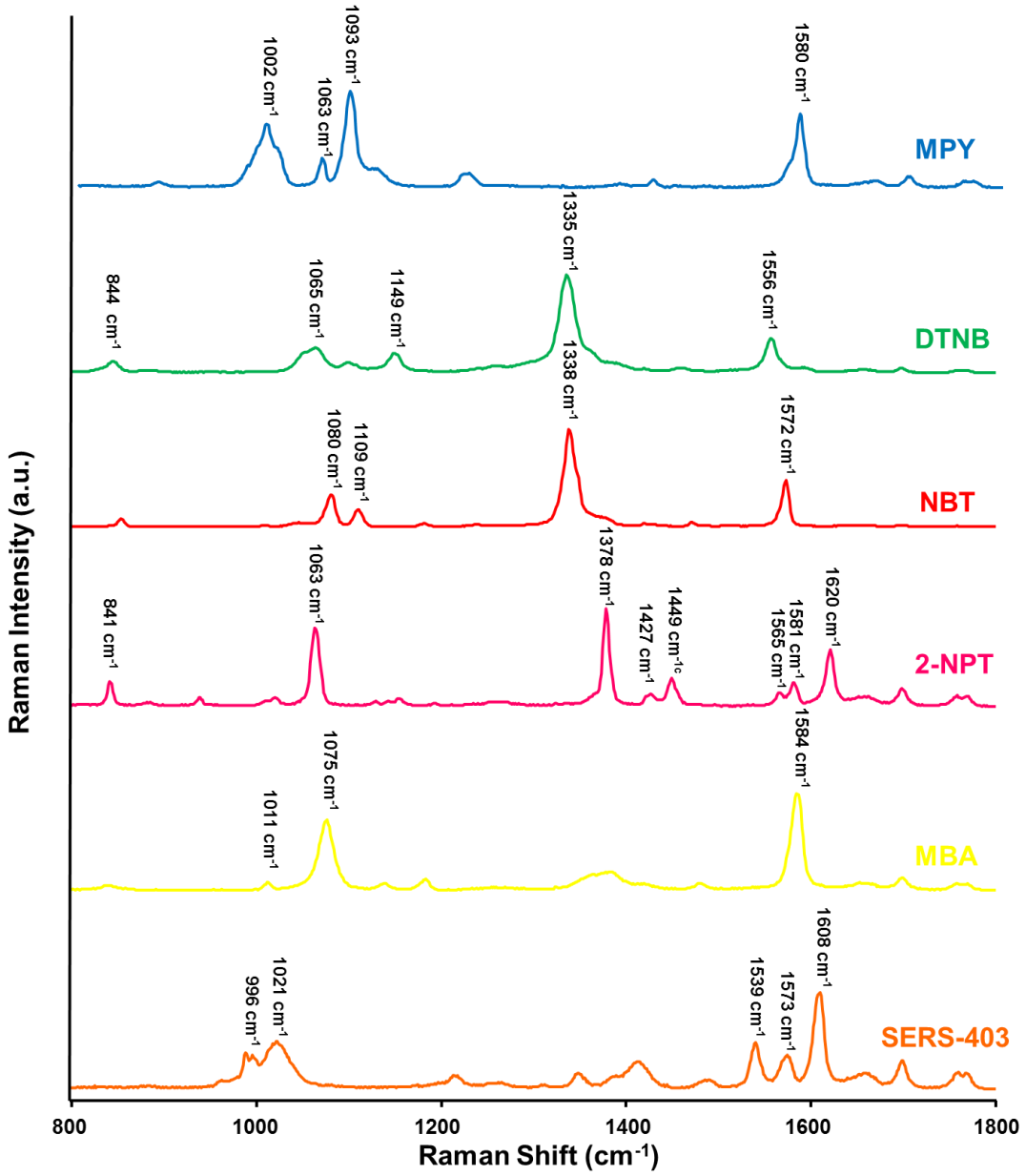

Figure 3.24: Representative SERS spectra for each of the small molecule labelled nanotags when resuspended in cell media. Spectra were offset for illustrative purposes and as no major peaks used for identification were observed below 800 cm^{-1} or above 1800 cm^{-1} the spectra were truncated accordingly (λ_{ex} = 633 nm edge, 10% (0.66 mW), 10s, extended scan, 800-1800 cm^{-1}).

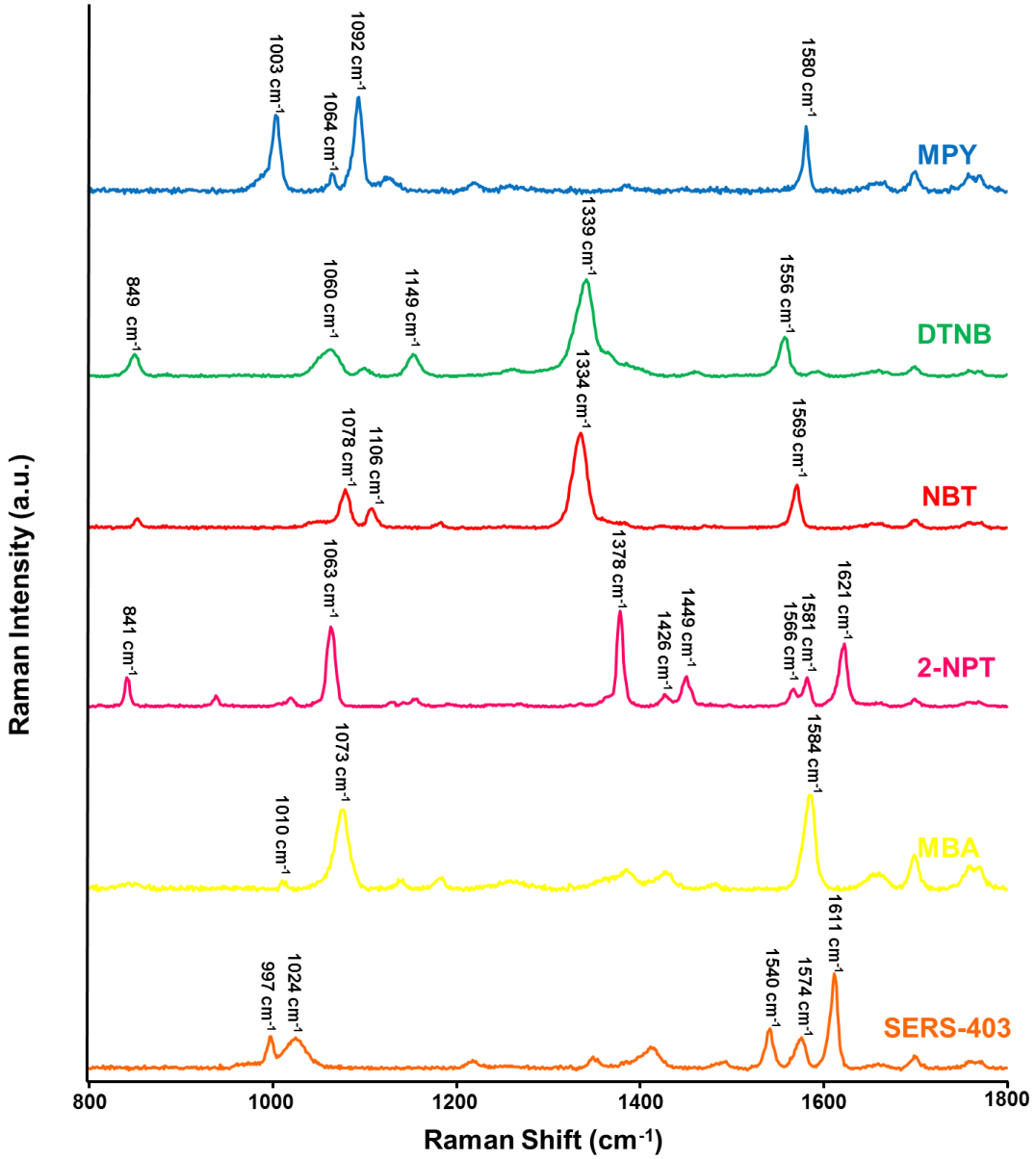

Figure 3.25: Representative SERS spectra for each of the small molecule/PEG nanotags. Spectra were offset for illustrative purposes and as no major peaks used for identification were observed below 800 cm^{-1} or above 1800 cm^{-1} the spectra were truncated accordingly (λ_{ex} = 633 nm edge, 10% (0.66 mW), 10s, extended scan, 800-1800 cm^{-1}).

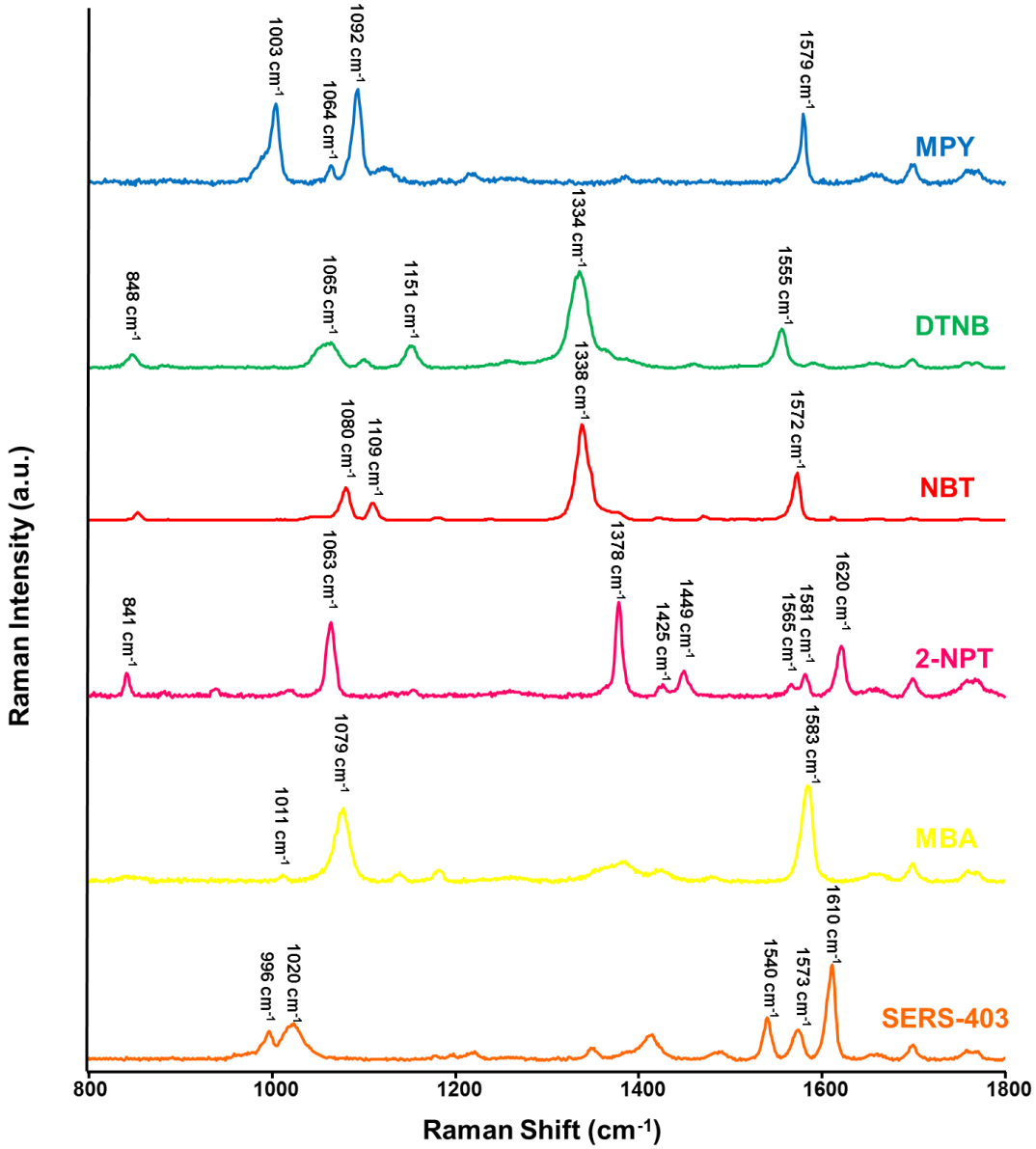

Figure 3.26: Representative SERS spectra for each of the small molecule/PEG nanotags when resuspended in cell media. Spectra were offset for illustrative purposes and as no major peaks used for identification were observed below 800 cm^{-1} or above 1800 cm^{-1} the spectra were truncated accordingly (λ_{ex} = 633 nm edge, 10% (0.66 mW), 10s, extended scan, 800-1800 cm^{-1}).

Table 3.4: Peak assignments for the predominant molecular vibrations for each of the small molecule labelled and small molecule/PEG labelled nanotags analysed as pure suspensions and when resuspended in cell media.[159, 200-202, 220-225]

Small molecule labelled nanotag	Observed Peak Position (cm^{-1})	Assignment
MPY	~ 1001 -1004	ring breathing
	~ 1063 – 1064	β(CH)
	~ 1092 - 1094	ring breathing/C-S
	~ 1579 - 1584	υ(C-C)
DTNB	~844 - 849	in plane symmetric δNO_2^-
	~ 1060 - 1065	β(CH)
	~ 1097 - 1099	ring breathing
	~ 1149 – 1151	δ(C-H), δ(C-C)
	~ 1334 – 1339	$\upsilon_s NO_2^-$
	~ 1555 - 1557	υ(C-C)
NBT	~ 852 - 853	in plane symmetric δNO_2^-
	~ 1077 – 1080	in plane δ(C-H) mode, δ(C-C)
	~ 1106 – 1109	in plane δ(C-H) mode
	~ 1333 – 1338	$\upsilon_s NO_2^-$
	~ 1569 - 1572	υ(C-C)
2-NPT	~ 841	C-H twist
	~ 1063	δ(C-H)
	~1378	υ_{ring}
	~ 1425 – 1427	υ_{ring}
	~ 1449	υ_{ring}
	~1565	υ_{ring}
	~1581	υ_{ring}
	~1620	υ_{ring}
MBA	~1010-1011	υ_{ring}
	~ 1073 – 1079	υ(C-C)
	~ 1182 - 1184	-
	~ 1583 – 1584	υ(C-C)
SERS-403	~ 996 -997	ring breathing
	~ 1018 - 1024	υ_{ring}
	~ 1539 – 1540	ring in plane deformation υ(C-N)
	~ 1573 - 1578	υ_{ring}
	~ 1608 - 1611	υ_{ring}

Common to all of the small molecule reporters was a terminal thiol or a disulfide linkage in the case of DTNB (**Figure 3.22**). Conjugation to the nanotags was therefore straightforward and resulted in the adsorption of the thiols onto the surface of the nanotags. There is some debate as to whether DTNB adsorbs via the disulfide bond or breaks apart and adsorbs by a single thiol. Regardless of the mechanism of attachment it was still possible to differentiate between each of the individually labelled nanotags (**Figure 3.23** - **Figure 3.26**).

3.4.4 Optimised Nanotag system

The final step in the development of the complete nanotag system was the addition of the reporter molecules. Some degree of optimisation was necessary as addition of too low a concentration of reporter resulted in little or no signal and similarly addition of too much can result in further aggregation.[9] This is likely to be due to the thiol functionalised small molecules having a greater affinity for the nanotag surface resulting in displacement of the stabilising polymer.[9] In addition, some of the spectra obtained from the SERS labels were significantly more intense than others. Therefore, the concentrations of the reporter molecules were required to be optimised to prevent the spectral signal of the less intense reporter molecules becoming obscured at the chosen excitation wavelength.

The final optimised nanoprobe system (**Figure 3.27**) consisted of Ag citrate nanoparticles 'controllably' aggregated with **0.2 mM** (final concentration) 1,6-HMD, polymer coated with **41.7 µM** (final concentration) PVP and labelled with either **10 µM** (final concentration) of MBA, NBT, SERS-403 or 2-NPT or **50 µM** (final concentration) of MPY or DTNB.

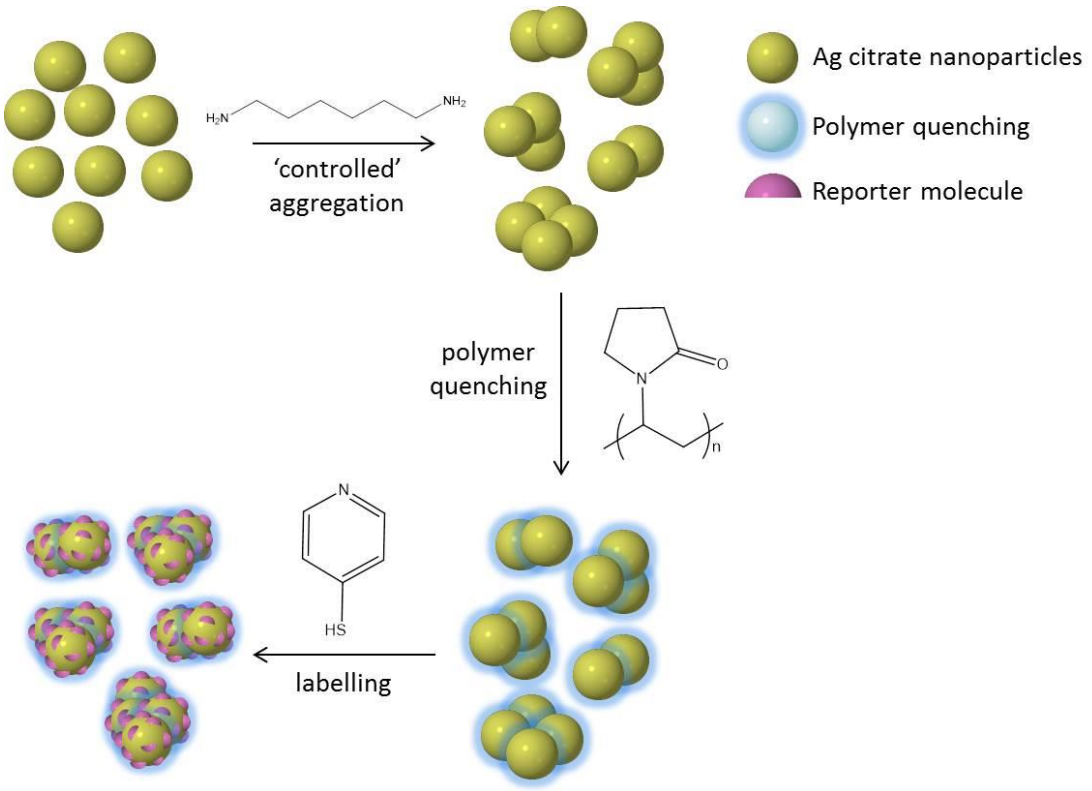

Figure 3.27: Optimised nanotag system - samples were controllably aggregated with 1,6-HMD, then polymer wrapped with PVP before labelling with the small molecule reporters.[9]

As mentioned in section 3.4.3, there were some issues regarding the stability of the nanotags. This was obvious following the nanotag purification process (nanotags were centrifuged, the supernatant was removed and the pellet was resuspended) as on a few occasions the nanotags were visibly aggregated. As a result of this a further stabilisation step was incorporated via the addition of a thiol-terminated PEG molecule.[9, 11] The other end was carboxylic acid terminated and this was considered to be ideal for future bio-molecule conjugations. For this system the nanotag scaffolds were prepared as previous which involved controlled aggregation with **0.2 mM** (final concentration) 1,6-HMD, polymer coating with **41.7 µM** (final concentration) PVP followed by the addition of **2 nM** (final concentration) carboxymethyl-polyethylene glycol-thiol (COOH-PEG-SH – ~ 5000MW). This solution was allowed to agitate for 30 min before the small molecule reporter was added at **200 µM** (final concentration) and again this solution was allowed to agitate for 30 min before a final addition of **20 µM** (final concentration) COOH-PEG-SH. The PEG molecule was added sequentially in

increasing concentrations since adding the molecule at an initially high concentration completely blocked the surface and prevented the small molecule from adsorbing. With this system the concentration of the small molecules were not optimised to compensate for those reporters which were more efficient. However the gain in stability offset this.

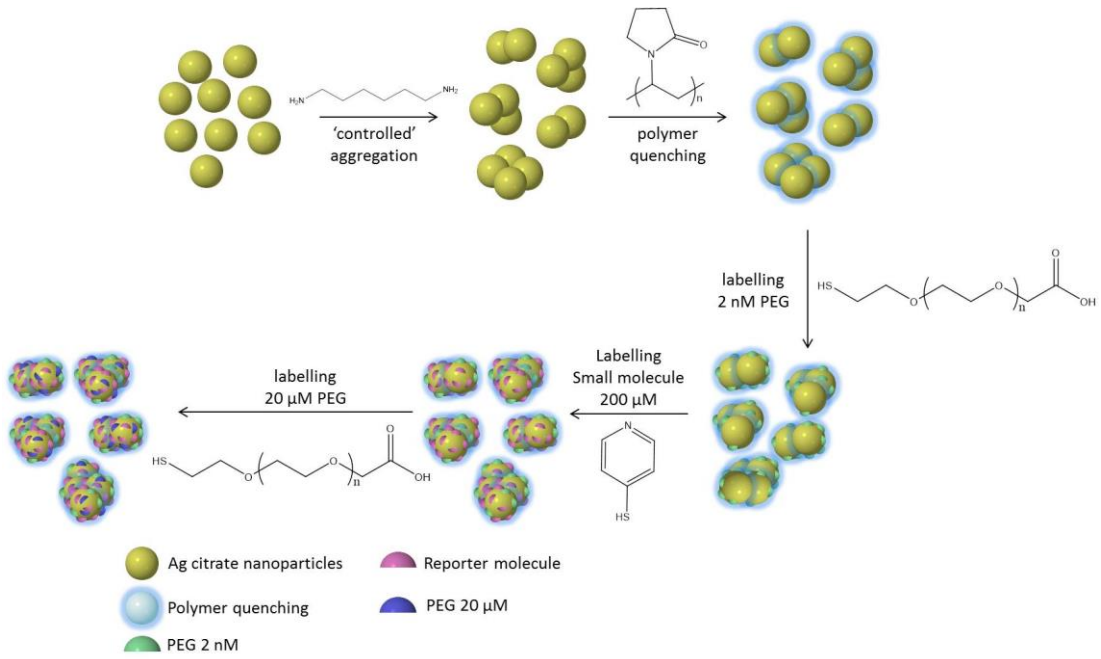

Figure 3.28: Optimised nanotag system additionally stabilised with COOH-PEG-SH - samples were controllably aggregated with 1,6-HMD, then polymer wrapped with PVP before stabilisation with PEG, labelling with a small molecule reporter and a final PEG stabilisation step.

3.4.5 Stability of the Optimised Nanotag Systems

To determine the stability of the two nanotag systems, analyses were performed using extinction spectroscopy and DLS. The extinction measurements were carried out in distilled water (dH_2O) whilst the DLS measurements were additionally performed in the cell media Dulbecco's Modified Eagle Medium (DMEM). The results from the extinction spectroscopy reveal varying degrees of stability between and within the two nanotags sets (**Figure 3.29**). For the small molecule labelled nanotags there was a dampening of the plasmon band for the nanotags labelled with DTNB, 2-NPT and MBA when compared with the bare Ag colloid standard (**Figure 3.29**). Aggregation associated with the dampening of the plasmon band was expected since the small molecule reporters displace the stabilising PVP polymer layer when adsorbing on to

the surface.[9] If the displacement of the PVP was extensive it was possible that further aggregation could have occurred. When compared with the nanotag standard however the dampening wasn't particularly extensive and the aggregation obviously results from a combination of both the method of nanotag synthesis and the subsequent labelling of the nanotags with the small molecule reporters (**Figure 3.29a**).

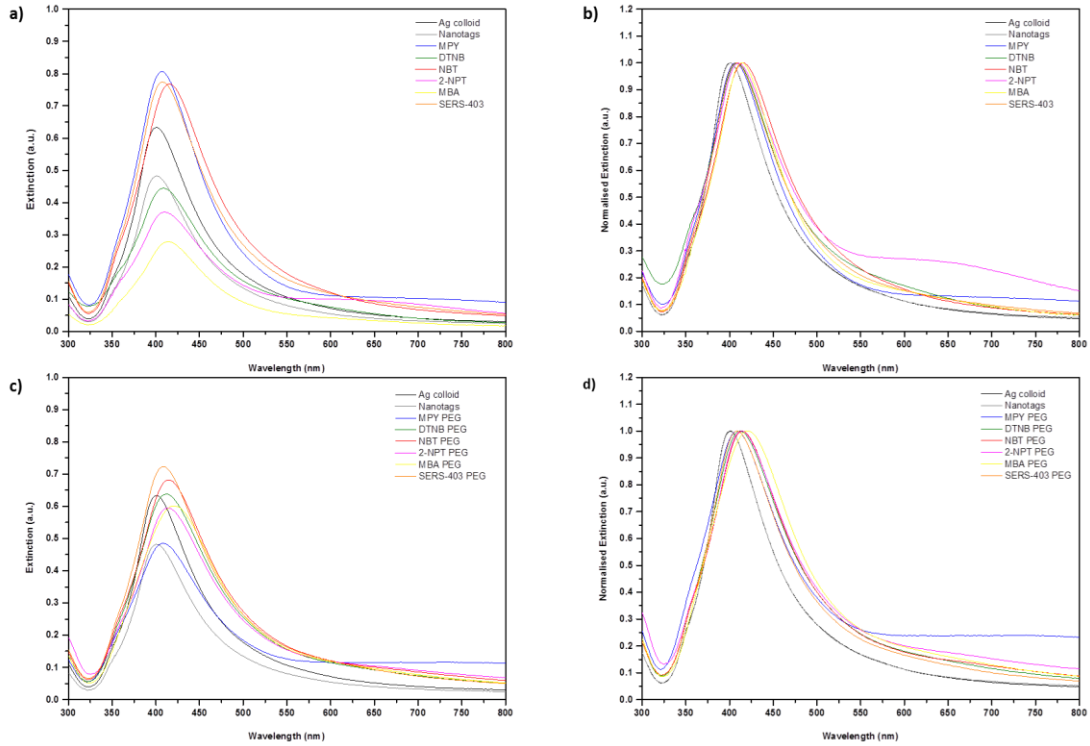

Figure 3.29: Extinction spectroscopy analysis of the small molecule labelled nanotags and the small molecule/PEG labelled nanotags a)-b) non-normalised and normalised data for the small molecule labelled nanotags and c)-d) non-normalised and normalised data for the small molecule/PEG labelled nanotags.

Analysis of the normalised data set revealed a broadening of the plasmon band and a red shift for each of the small molecule labelled nanotags (**Figure 3.29b**). A broad band also began to appear between 600-800 nm and this was particularly pronounced for the MPY and 2-NPT nanotags. This was consistent with the aggregation indicated by the dampening of the plasmon band for the 2-NPT nanotags but no other visible signs of aggregation were observed for the MPY nanotags. Red shifting was also expected to a certain extent and whilst it can be indicative of aggregation, it is also associated with

further functionalisation of the structures, such as labelling with a reporter molecule, due to a change in the overall size of the nanostructure.

In contrast, the non-normalised extinction data for the PEG functionalised nanotags would suggest that they were more stable than the small molecule only labelled nanotags (**Figure 3.29a** and **c**). The plasmon band when compared directly with the Ag citrate control decreased for the MPY labelled nanotags but this was again to a level which was comparable with the nanotag standard suggesting that any aggregation was the result of the synthesis method. In the normalised data set, broadening of the plasmon band and red shifting was observed for all of the nanotags (**Figure 3.29**). Red shifting was again consistent with functionalisation of the nanotag surface with both the small molecule reporter and PEG. The observed red shifts were greatest for the dually functionalised nanotags and this was consistent with labelling the nanotag surface with a larger molecule such as PEG (**Table 3.5**).

Table 3.5: Extinction spectroscopy measurements for the small molecule labelled nanotags and the small molecule/PEG labelled nanotags.

Nanotag sample	λ_{max}	Extinction (a.u.)
Ag colloid	400	0.633
Nanotag	400	0.482
MPY nanotags	407	0.806
MPY/PEG nanotags	408	0.485
DTNB nanotags	408	0.444
DTNB/PEG nanotags	412	0.638
NBT nanotags	415	0.768
NBT/PEG nanotags	415	0.682
2-NPT nanotags	410	0.371
2-NPT/PEG nanotags	414	0.595
MBA nanotags	414	0.280
MBA/PEG nanotags	420	0.602
SERS-403 nanotags	407	0.774
SERS-403/PEG nanotags	409	0.723

The broadening of the main plasmon band and the appearance of a broad band between 600 - 800 nm was most apparent for the MPY/PEG labelled nanotags and was

consistent with the aggregation indicated by the dampening of the plasmon band. Attempts were also made to measure the extinction spectra in DMEM cell media to determine if this induced any aggregation. Unfortunately as discussed in section 3.2.2.1 it wasn't possible to measure the extinction profiles due to the presence of phenol red in this media and this study would need to be repeated with phenol red free cell media.

In general, the PEG functionalised nanotags were larger in size than the nanotags which were solely functionalised with the small molecule reporters (**Figure 3.30**). NBT/PEG and MBA/PEG functionalised nanotags were exceptions to this rule and the reasons for this were unclear. It is possible that aggregation following addition of the small molecule reporter led to an increase in size for the small molecule only functionalised nanotags. It was however, expected that the PEG functionalised nanotags would be larger in size due to the presence of the large PEG (~ 5000 MW) molecule on the surface.

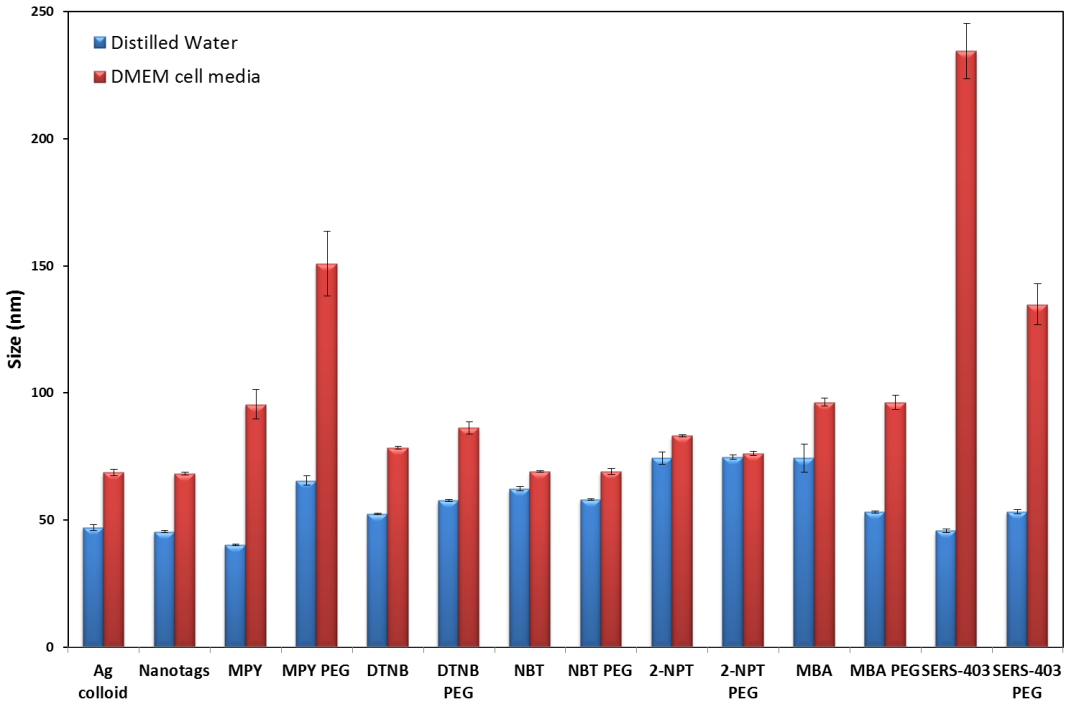

Figure 3.30: DLS size measurements for the small molecule labelled nanotags and the small molecule/PEG labelled nanotags when dispersed in distilled water and the cell media DMEM. Measurements were made in triplicate, the average value is shown and the error bars represent the standard deviation of the triplicate measurements.

Common to all of the nanotags was an increase in size when dispersed in the cell media (**Figure 3.30**). This was most prolific for both MPY and SERS-403 nanotag systems. In the case of the MPY nanotags an increase in size of ~ 55 nm and ~ 86 nm was observed for the two nanotags systems respectively. The SERS-403 nanotags exhibited an increase in size of ~ 200 nm and ~ 82 nm for the two nanotag systems respectively (**Figure 3.30**). For the remaining nanotags the increase in size ranged from ~ 9 - 43 nm (**Figure 3.30**). As discussed earlier, a corona comprising of media components can enshrine the nanotag[193, 194] so the size increase was not necessarily representative of aggregation. Unlike the previous example (see section 3.2.2.1), the media used in this study was additionally supplemented with foetal bovine serum (FBS) which tends to form the majority of the protein corona.[226] The formation of this corona is important because not only does it alter the size of the nanotags but it can additionally alter the method of cellular uptake since it is the corona itself which is presented to the cell for interaction.[53, 198, 226]. Regardless of whether 'true' aggregation or corona formation was taking place, the overall size of the nanotags in the cell media was again not considered to be detrimental to cellular uptake. Particles in the same size range as the nanotags used in the study have been shown to be taken up by both endocytic[197] and passive diffusion mechanisms[53] thus the size range exhibited was unlikely to be prohibitive to cellular uptake. With the exception of the SERS-403 labelled nanotags, all of the nanotags were considerably smaller than their commercial counterparts (**Figure 3.3** *c.f.* **Figure 3.30**) which proved to be excellent multi-marker cell imaging agents.

The Zeta potential data of all the nanotags were considered to be relatively stable (**Figure 3.31**) as a result of their large negative Zeta values. The Ag citrate standard demonstrated the greatest negative charge but this was to be expected since some level of change in the surface charge would undoubtedly be introduced by controllably aggregating the nanotags. With the exception of the MPY labelled nanotags all of the dually functionalised nanotags exhibited larger Zeta values and this was consistent with the stabilisation provided by the addition of PEG to their surface (**Figure 3.31**).[9, 11] Attempts were made to measure the Zeta potential of the nanotags when dispersed in the cell media but because of the electrostatic nature of the compounds within the media itself this was not possible. Other groups have measured the Zeta potential of nanoparticles/nanotags following exposure to cell media but as this was not

considered to be representative of the actual incubation process between the nanotags and the media this was not attempted.

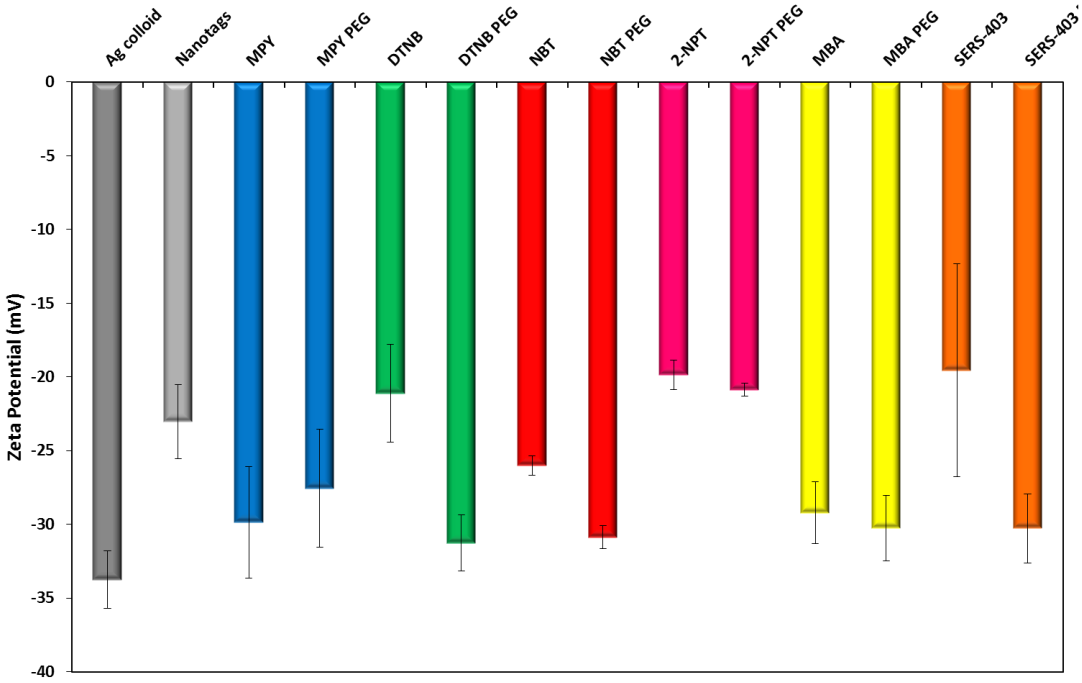

Figure 3.31: Zeta potential measurements for the small molecule labelled nanotags and the small molecule/PEG labelled nanotags. All of the nanotags were dispersed in dH_2O. Measurements were made in triplicate, the average value is shown and the error bars represent the standard deviation of the triplicate measurements.

Overall, on the basis of the extinction (**Figure 3.29**) and Zeta potential (**Figure 3.4**) measurements performed in dH_2O and the size measurements performed in dH_2O and cell media (**Figure 3.30**) the two nanotag systems were considered to be relatively stable and of a suitable size for cellular uptake. There was some concern regarding the small molecule labelled nanotags, in particular those labelled with DTNB, 2-NPT and SERS-403 but analysis of the size and Zeta data did not suggest that the nanotags were particularly large or unstable. The extinction spectra for SERS-403 did not suggest any signs of aggregation but they exhibited the lowest Zeta potential and increased in size dramatically when dispersed in cell media (**Figure 3.29** - **Figure 3.31**). However, the size of the nanotags was not considered to be a concern for cell uptake since larger systems have successfully transversed the membrane by both endocytic[197] and passive diffusion mechanisms.[53] The size of the particles may influence uptake rate, as will the

formation of any protein corona on the nanotag surface, and this should be considered during mapping analysis.

3.5 Development of a Multiple Component System

With a suitable alternative nanotag system in place the next step of the investigation involved developing a suitable multiple component system. For the cell investigations it was unclear whether the nanotags would cluster together or be found in discrete cell locations. In the advent that they were found together and the possibility of multiple component signals arising it was necessary to determine which of the individually labelled nanotags could be combined but still be individually identified within a multiple component suspension.

Although there were a total of 6 nanotag labels the initial investigations were only carried out with 4 of those labels (MBA, MPY, DTNB and NBT) since it was believed that a multiple component could be generated with these four labels. In order to test the multiple component capability of the nanotags all 11 possible combinations (6 duplex, 4 triplex and 1 fourplex) were premixed and analysed. Some degree of spectral overlap was expected since the small molecules were all reasonably similar in structure; consisting of an aromatic or hetero ring system, terminal thiol or disulfide linkage and carboxylic acid and/or nitro group side chains (**Figure 3.22**). As will be seen in later data sets, component DCLS was used to identify each of the nanotags and deconvolve the spectra. However, in order to increase the confidence in the final multiple component suspension the multiple component criteria defined that there must be at least one peak unique to each reporter.

From the 6 possible duplex combinations all were found to be suitable for multiple component analysis (MBA+MPY, MBA+DTNB, MBA+NBT, MPY+DTNB, MPY+NBT and DTNB+NBT – data not shown). Despite the success of the duplex combinations higher multiple component combinations were desired and therefore the investigation focused on achieving triplex and higher multiple component samples.

From the 4 possible triplex combinations 3 were found to be suitable for multiple component analysis; MBA+MPY+DTNB, MBA+MPY+NBT and MPY+DTNB+NBT. For the MBA+MPY+DTNB triplex solution unique peaks were found at ~ 1334 cm^{-1} $\upsilon(NO_2)$,[223] ~

1180 cm^{-1} δ(C-C)[159] and ~1000 cm^{-1} (ring breathing)[220, 227] for DTNB, MBA and MPY respectively (**Figure 3.32**). However, the MBA identification peak at ~1180 cm^{-1} was relatively low in intensity ~ 1000 a.u. (**Figure 3.32**) compared to other peaks in the spectrum and therefore this peak may not be identifiable when the multiple component suspension was applied to cells.

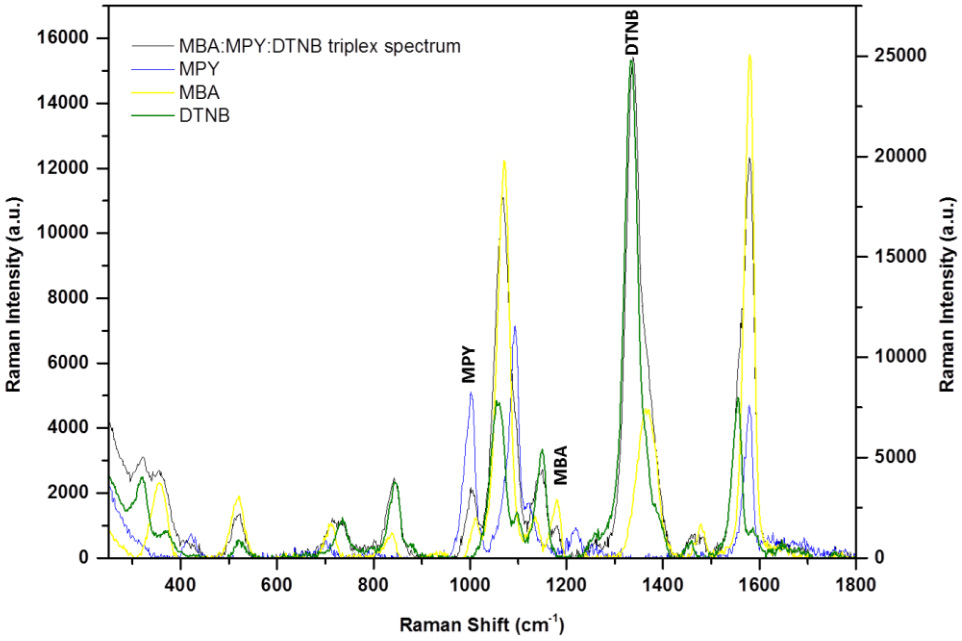

Figure 3.32: MBA+MPY+DTNB triplex sample – the triplex solution (black line) was plotted on the primary y-axis and the solution standards MBA (yellow line), MPY (blue line) and DTNB (green line) were plotted on the secondary y-axis. The unique peaks were labelled with the appropriate small molecule abbreviation. No major peaks were observed below 250 cm^{-1} or above 1800 cm^{-1} hence the spectrum was truncated accordingly (λ_{ex} = 633 nm edge, 50% (3.3 mW), 10s, extended scan, 0-3200 cm^{-1}).

From the previous study with the commercial nanotags, it was observed that in some instances (**Figure 3.13**) a 100-300 fold decrease in signal intensity occurred following cell uptake. If this occurred it may not be possible to detect the MBA component and as a result it was decided not to progress with this triplex in further cell investigations. Unfortunately, as with many of the multiple component samples analysed, the major spectral peaks did not meet the multiple component criteria and thus could not be

selected for identification because of the high degree of spectral overlap between each of the nanotags.

Similarly for the MBA+MPY+NBT triplex solution unique peaks were found at ~ 1180 cm^{-1} υ(C-C)[159] ring, ~1001 cm^{-1} (ring breathing)[220] and 1331 cm^{-1} $\upsilon(NO_2)$[223] for MBA, MPY and NBT respectively (**Figure 3.33**). However the unique identification peak for MBA was again relatively low in intensity and this might not be identifiable following cell uptake. Therefore, it was decided not to progress with this triplex for further cell investigation.

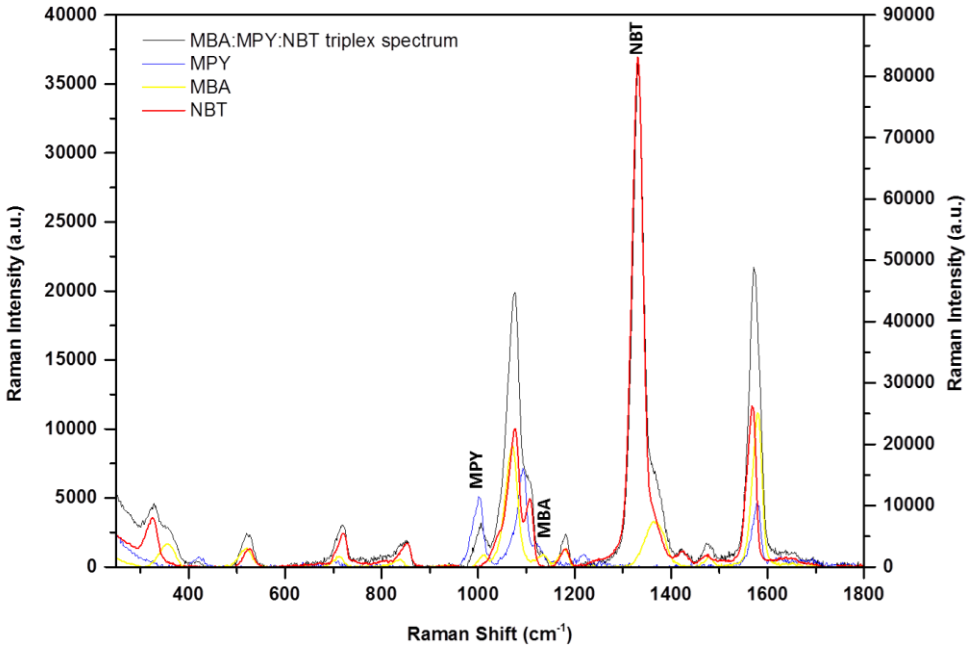

Figure 3.33: MBA+MPY+NBT triplex sample – the triplex solution (black line) was plotted on the primary y-axis and the solution standards MBA (yellow line), MPY (blue line) and NBT (red line) were plotted on the secondary y-axis. The unique peaks were labelled with the appropriate small molecule abbreviation. No major peaks were observed below 250 cm^{-1} or above 1800 cm^{-1} hence the spectrum was truncated accordingly (λ_{ex} = 633 nm edge, 50% (3.3 mW), 10s, extended scan, 0-3200 cm^{-1}).

For the triplex solution MPY+DTNB+NBT, unique peaks were found at ~1075 cm^{-1} δ(C-C)[223]. ~1150 cm^{-1} δ(C-C)[221] and ~ 1001 cm^{-1}(ring breathing mode)[220] for NBT, DTNB and MPY respectively (**Figure 3.34** and **Figure 3.35**). Although the MPY identification

peak at ~1001 cm^{-1} was relatively low in intensity ~5000 a.u. it was hoped that this peak would still be identifiable when the sample was applied to cells. Even if a 10 fold decrease in signal intensity arose the peak should still have an intensity ~500 a.u., thus it should be distinct from the baseline and satisfy the 3× signal-to-noise threshold for a peak to be considered to be 'real'.

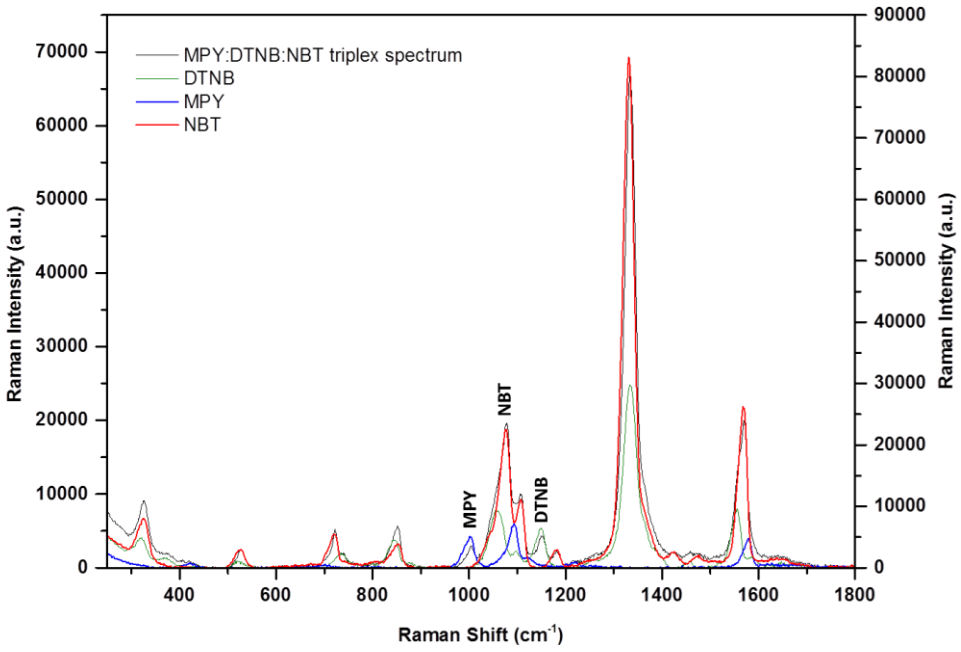

Figure 3.34: MPY+DTNB+NBT triplex sample – the triplex solution (black line) was plotted on the primary y-axis and the solution standards MPY (blue line), DTNB (green line)and NBT (red line) were plotted on the secondary y-axis. The unique peaks were labelled with the appropriate small molecule abbreviation. No major peaks were observed below 250 cm^{-1} or above 1800 cm^{-1} hence the spectrum was truncated accordingly (λ_{ex} = 633 nm edge, 50% (3.3 mW), 10s, extended scan, 0-3200 cm^{-1}).

The key identification peaks for the triplex (MPY+DTNB+NBT) occurred within a small range (980-1160 cm^{-1}) (**Figure 3.35**) and this was ideal when considering the instrumental constraints at the initial time of analysis. The grating combination and the CCD (400 × 576) only allowed for a very small spectral range to be analysed when mapping ~ 400 cm^{-1}. Thus for this particular triplex, the key identification peaks could be observed simultaneously rather than performing multiple maps of the same area using different spectral ranges. Based on the success of the triplex in solution (**Figure**

3.34 and **Figure 3.35**) and the potential to rapidly observe the key identification peaks, provided that cell uptake was successful, it was decided to progress with this triplex for cellular investigations.

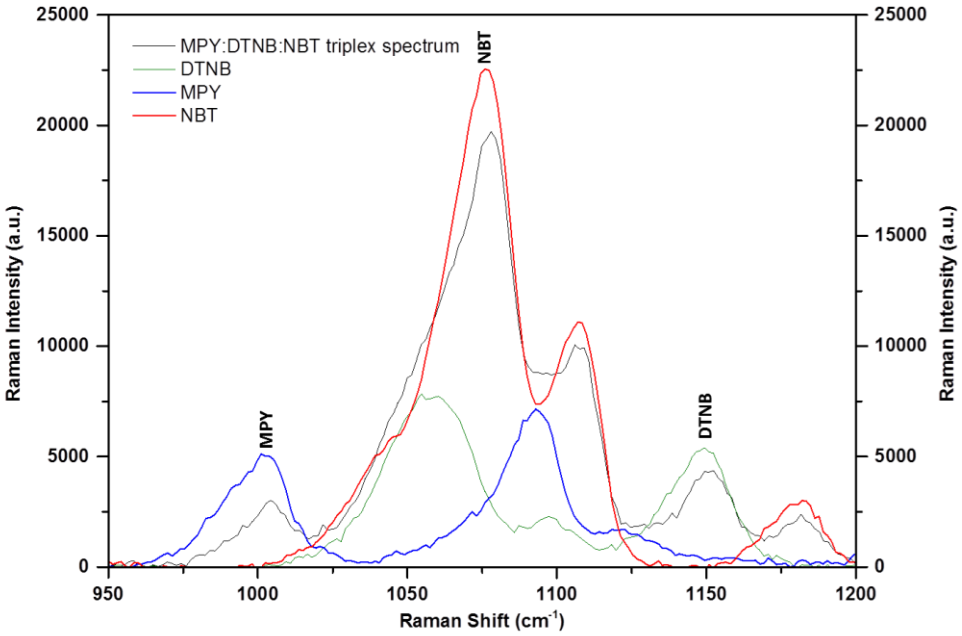

Figure 3.35: MPY+DTNB+NBT triplex sample – distinguishing peaks. The enlarged spectral area depicts individually unique peaks for MPY, DTNB and NBT. The unique peaks were labelled with the appropriate small molecule abbreviation. (λ_{ex} = 633 nm edge, 50% (3.3 mW), 10s, extended scan, 0-3200 cm^{-1}).

There was only one possible higher multiple component combination MBA+MPY+DTNB+NBT and this was not found to be suitable for multiple component analysis since there was considerable spectral overlap between the four reporter molecules. There were no peaks uniquely distinct to MBA, DTNB and NBT and there was only one unique MPY peak (~ 415 cm^{-1}). In the hope of achieving a higher multiple component sample two further SERS labels, 2-NPT and SERS-403, were incorporated into the investigation. Each of the labels were individually and cumulatively added to the three successful triplexes already discussed (MBA+MPY+DTNB, MBA+MPY+NBT and MPY+DTNB+NBT). However, SERS-403 overlapped considerably with MPY, thus it was not suitable for incorporation in any of the triplexes and 2-NPT overlapped considerably with MBA thus it was only suitable for incorporation in the final triplex.

The removal of SERS-403 labelled nanotags also eliminated any concerns about the dramatic increase in size following exposure to the cell media. The incorporation of 2-NPT into the final triplex MPY+DTNB+NBT did however lead to a successful fourplex. Unique peaks were found at ~ 1621 cm^{-1} υ(C-C)ring,[25, 224] ~1075 cm^{-1} δ(C-C),[223] ~ 1150 cm^{-1} δ(C-C)[221] and ~1001 cm^{-1} (ring breathing mode)[220] for 2-NPT, NBT, DTNB and MPY respectively (**Figure 3.36**). The doublet of peaks arising ~ 1075 cm^{-1} which has already been identified as a unique peak and at ~1108 cm^{-1} was further used for identification of NBT.

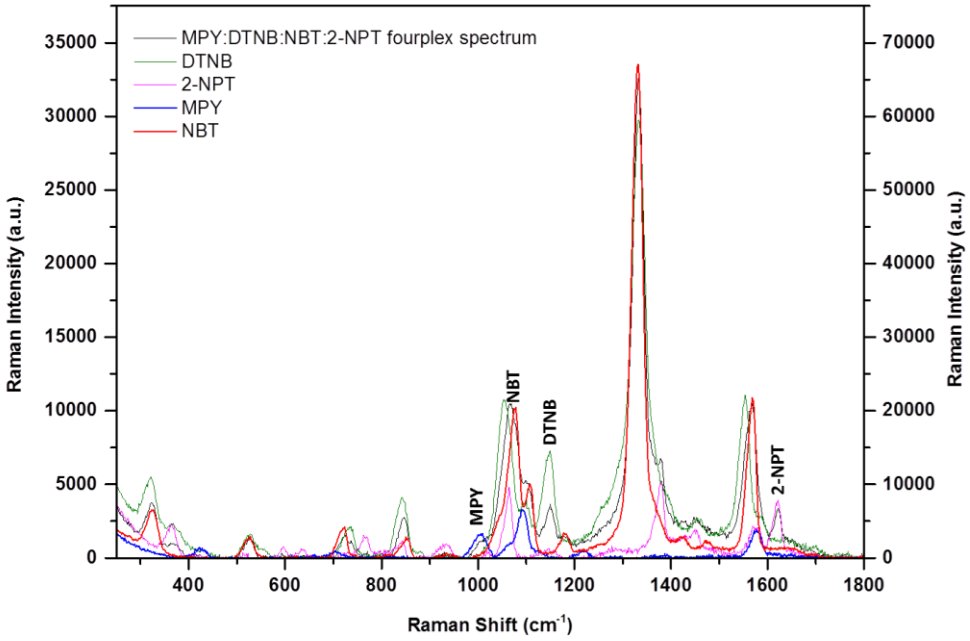

Figure 3.36: MPY+DTNB+NBT+2-NPT fourplex sample – the fourplex solution (black line) was plotted on the primary y-axis and the solution standards MPY (blue line), DTNB (green line), NBT (red line) and 2-NPT (magenta line) were plotted on the secondary y-axis. The unique peaks were labelled with the appropriate small molecule abbreviation. No major peaks were observed below 250 cm^{-1} or above 1800 cm^{-1} hence the spectrum was truncated accordingly (λ_{ex} = 633 nm edge, 50% (3.3 mW), 10s, extended scan, 0-3200 cm^{-1}).

As with the MPY identification peak (~ 1001 cm^{-1}) the 2-NPT identification peak was relatively low in intensity ~ 8000 a.u. (**Figure 3.36**) and again if a 10-fold decrease in signal intensity arose upon applying the nanotags to the cells the peak should still have

an intensity ~ 800 a.u. and be distinct from the baseline whilst satisfying the signal-to-noise criteria.

However, unlike the triplex sample, provided that cellular uptake was successful, identification of all four unique peaks would only be possible by mapping the same area twice because of the instrumental limitations (i.e. the CCD range). Any cell population subject to the fourplex multiple component solution would be mapped once by centring at 1100 cm^{-1} for identification of MPY, DTNB and NBT and again while centred at 1600 cm^{-1} for identification of the 2-NPT peak (**Figure 3.36**). Although this was potentially more time consuming, the possibility of ultimately implementing and detecting four unique nanotags will compensate for the loss of speed.

The triplex MPY+DTNB+NBT and the fourplex MPY+DTNB+NBT+2-NPT were both considered to be suitable multiple component samples for multi-marker cell imaging and will be investigated further in cellular studies.

3.5.1 Principal Component Analysis (PCA) of the Fourplex

It was clear that this study would benefit from chemometric analysis since this would aid in the differentiation between the individually labelled nanotag suspensions and in the development of a superior multiple component sample. However, it was still considered to be important to have at least one peak unique to each of the small molecule reporters, to increase the confidence and to have a second method for differentiating between the nanotags. Principal component analysis (PCA) was carried out and it was found that it was possible to identify each of the individually labelled nanotags when they were part of a fourplex multiple component sample (**Figure 3.37**).

PCA analysis was performed by Dr. Sam Mabbott.

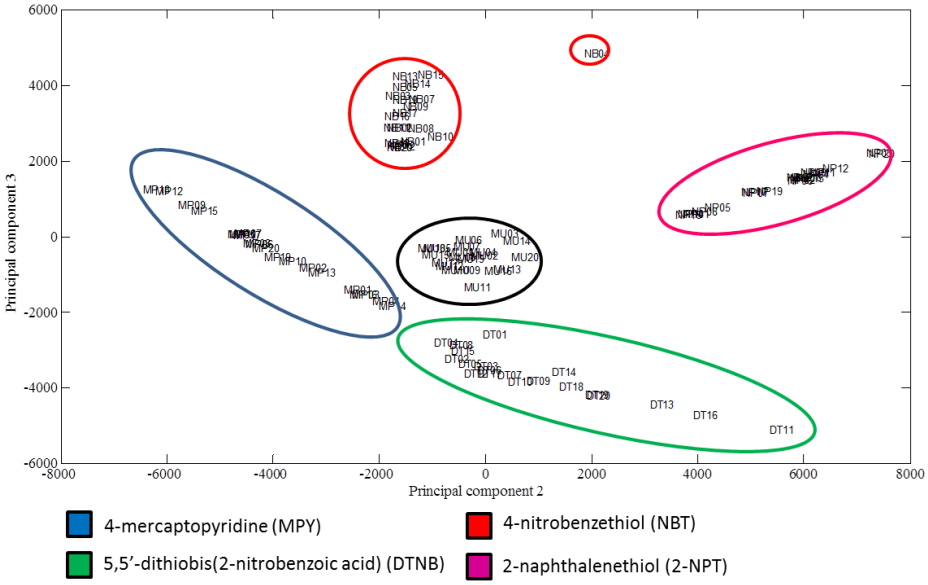

Figure 3.37: PCA of each of the individually labelled nanotag suspensions and fourplex multiple component samples. The multiple component samples containing equally proportions all four of the individually labelled nanotags are delineated by a black circle.

Spectral variations and thus the required information were identified by the implementation of PCA which reduces the dimensionality of the data.[41, 101] By doing this the system is considerably simplified and variations are represented by principal components (PCs). 20 replicates of each of the individually labelled nanotags were analysed as were 20 replicates of the fourplex multiple component sample. From the PCA plot it can be seen that the multiple component samples lie in the middle, delineated by the black circle, whilst each of the individually labelled nanotag suspension, which are also delineated by an appropriately coloured circle, are found in discrete locations around the central multiple component sample. This separation confirmed that it was possible to differentiate between each of the individual components within a multiple component sample. For the NBT labelled samples there was an outliner and this was probably due to spectral variation between this sample and the others analysed, such as a cosmic ray or it may have been aggregated to a greater extent.

3.6 Detectability of SERS Nanotags in Cell Populations and Single Cells

3.6.1 *In vitro* Analysis of the SERS Nanotags

Following on from the success of the multiple component study – where a successful fourplex was developed – the nanotags were applied individually to cell populations (HeLa) to evaluate their detectability and to demonstrate proof-of-concept. In addition the triplex MPY+DTNB+NBT and the fourplex MPY+DTNB+NBT+2-NPT were also applied since these were previously found to be the most suitable multi-markers for cellular imaging. The cultured cells were incubated with the appropriate nanotag solution (100 µL) for 1h. Following incubation, the cells were washed 4× with 1× PBS (pH 7.6) to remove extracellular nanotags before fixation with paraformaldehyde. After fixation the cells were washed with PBS, dH_2O and air dried before mounting onto microscope slides.

Samples were interrogated by Raman mapping using a Renishaw inVia Raman spectrometer/ Leica DMI 5000 M inverted microscope. A 633 nm HeNe excitation source was used and cell samples were imaged using a Leica 100× LWD (0.75 N.A.) objective. A grating of 1800 lines / mm was used with a RenCam CCD (400 × 576 pixels). The principles of StreamLine™ and StreamLineHR™ mapping in addition to the method of false colour image generation are discussed in section 3.2.4.

3.6.2 Detectability of the Individual SERS Nanotag Suspensions in Cell Populations

When each of the small molecule labelled nanotag suspensions were applied individually to HeLa cells they were detectable within the population and they were positively identified by component DCLS (**Figure 3.38** - **Figure 3.41**). The measurements were performed using the StreamLine mapping system as at the initial time of measurement the instrument wasn't optimised for high resolution mapping.

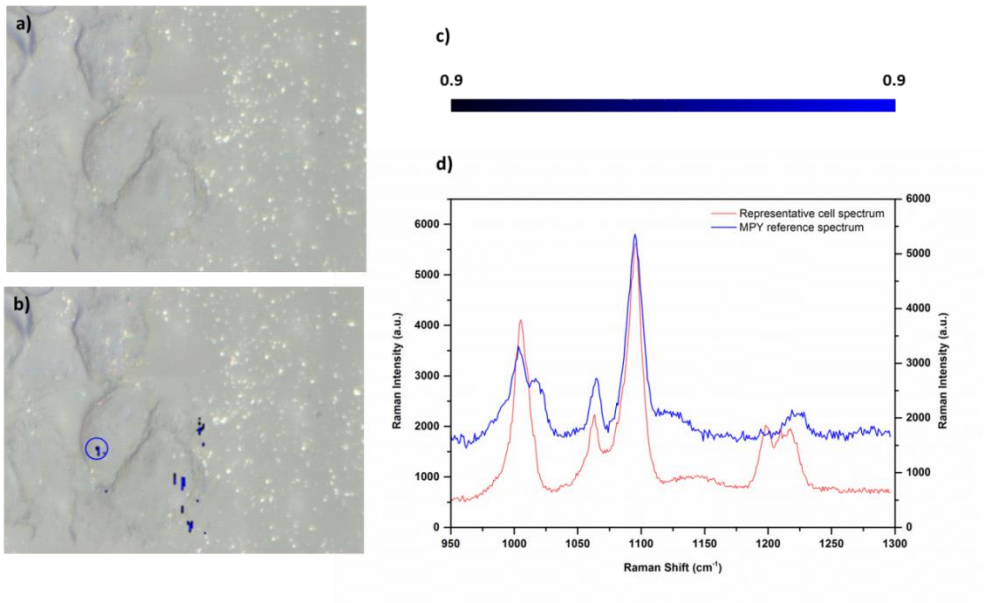

Figure 3.38: False colour SERS map image and representative spectrum for MPY labelled nanotags applied to a HeLa cell population. a) white light image, b) false colour SERS map image c) LUT colour bar and d) representative SERS spectrum for MPY labelled nanotags - the cell spectrum is plotted on the primary y-axis and the reference on the secondary y-axis. (StreamLine - λ_{ex} = 633 nm, 100% (~ 6 mW), spectral range 914-1296 cm^{-1}, step size x,y 0.5 µm 5s).

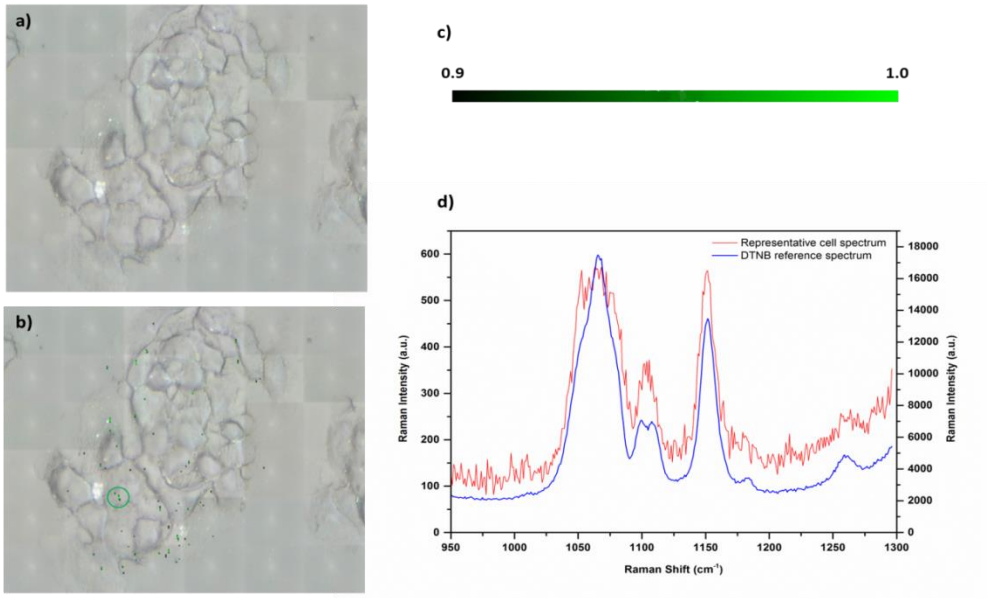

Figure 3.39: False colour SERS map image and representative spectrum for DTNB labelled nanotags applied to a HeLa cell population. a) white light image, b) false colour SERS map image c) LUT colour bar and d) representative SERS spectrum for DTNB labelled nanotags - the cell spectrum is plotted on the primary y-axis and the reference on the secondary y-axis.

(StreamLine - λ_{ex} = 633 nm, 100% (~ 6 mW), spectral range 914-1296 cm^{-1}, step size x,y 0.5 µm 5s).

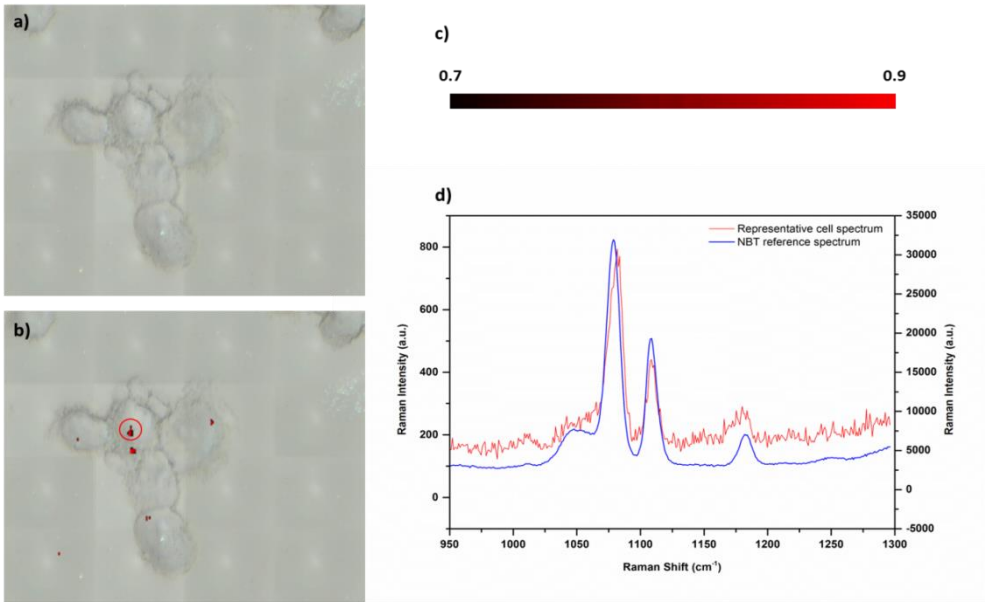

Figure 3.40: False colour SERS map image and representative spectrum for NBT labelled nanotags applied to a HeLa cell population. a) white light image, b) false colour SERS map image c) LUT colour bar and d) representative SERS spectrum for NBT labelled nanotags - the cell spectrum is plotted on the primary y-axis and the reference on the secondary y-axis. (StreamLine - λ_{ex} = 633 nm, 100% (~ 6 mW), spectral range 914-1296 cm^{-1}, step size x,y 0.5 µm 5s).

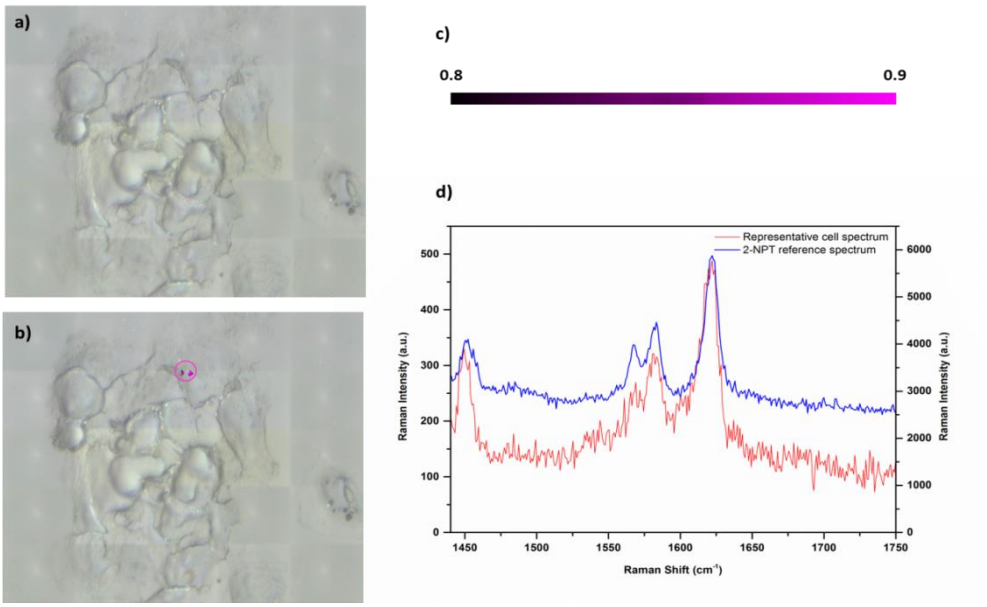

Figure 3.41: False colour SERS map image and representative spectrum for 2-NPT labelled nanotags applied to a HeLa cell population. a) white light image, b) false colour SERS map image

c) LUT colour bar and d) representative SERS spectrum for 2-NPT labelled nanotags - the cell spectrum is plotted on the primary y-axis and the reference on the secondary y-axis. (StreamLine - λ_{ex} = 633 nm, 100% (~ 6 mW), spectral range 914-1296 cm^{-1}, step size x,y 0.5 μm 5s).

In all instances there was a significant reduction in the signal measured from the cell associated nanotags when compared with the reference spectrum but since there were a reduced number of nanotags in the laser path when compared to the solution samples, as well as a risk of background fluorescence interference from the biological samples, this was to be expected to a certain extent. In addition, it was possible that the reduction in signal intensity was a direct result of cellular uptake and the signal measured was coming from nanotags located at depth within the cell (**Figure 3.38**-**Figure 3.41**).

In the MPY, DTNB and NBT samples (**Figure 3.38**-**Figure 3.40**) there were areas where signal was measured outside of the cell perimeters and again this was expected to a certain degree since the nanotags were not functionalised with any targeting moiety and thus were not specifically targeting a cell component or cellular membrane. A certain amount of non-specific binding may also be attributed to the method of cell preparation since cells were grown on glass microscope cover-slips to which the nanotags have an affinity and can easily bind. Although washing steps may help remove the unbound or non-endocytosed nanotags, it was not an entirely efficient process.

As with the commercial nanotag examples, and based on these images alone, it can be argued that the nanotags were simply attached to the cell surface. However, in the initial stages of the investigation the preliminary aim was to find suitable multi-marker nanotags for cellular imaging. The nanotags can be detected individually when applied to a cell population and have thus satisfied the criteria. The strength of the method will be increased, however, if cellular uptake can be actively demonstrated. Uptake into the cell could be confirmed by TEM or a depth profile SERS map image. With depth profiling methods the mapping stage is lowered or raised beneath the objective such that the depth at which the laser penetrates the cell is altered. This measures how the signal from the cell associated nanotag changes with depth. Collection of such data would also permit construction of 3D map images but at this stage of the investigation

depth profiling and 3D imaging were limited by the instrumentation available. Ideally depth profiling would be carried out using a water immersion objective and a system immersed in water so that the refractive index of the cell and the medium are closely matched.[207] This is particularly important since when using metallurgic objectives in air since the refractive index mismatch can hinder the correct reconstruction of the final image.[206, 207] The inverted microscope system unfortunately limited 'true' immersion imaging.

In the cell images the nanotags were found to lie around the cell periphery and none of the nanotags were found within the middle of the cells (**Figure 3.38**-**Figure 3.41**). The images provide no indication as to the exact intracellular location of the nanotags but if the cells were imaged with an alternative laser line (532 nm and 785 nm) intrinsic Raman cell signals could be observed and the major cellular components distinguished. This could provide an indication as to their localisation,[93] which may be directly related to their chemical functionality,[8] and potentially provide evidence of endosome inclusion since this is characterised by a high lipid content.[93] Due to instrumental constraints and the laser wavelengths available at the time of the initial investigation this was not possible but will be investigated in future chapters. When individually applied to cell populations all four nanotags were identified within their respective population. This was promising for the multiple component sample and suggested that the nanotags could be suitable as multi-marker cell imaging agents.

3.6.3 Detectability of the Developed Triplex in a Cell Population

When the triplex sample was applied to a cell population and analysed (MPY+DTNB+NBT) it was only possible to identify two of the three nanotags within the triplex (**Figure 3.42**). Signals were measurable from the MPY (**Figure 3.41c-e**) and NBT (**Figure 3.42f-h**) components but not from the DTNB. The reason as to why the DTNB signal was not measurable in any of the samples was unknown but it is possible that the DTNB nanotags aggregated resulting in clusters too large for cellular uptake. It was also possible that the interior cell pH altered the system but this was considered to be unlikely since DTNB was readily detectable when it was applied individually to a cell population (**Figure 3.39**) and, unlike the MPY or MBA[159, 160] nanotags, it did not demonstrate any pH sensitivity. Similarly, although caution was advised regarding the MPY identification peak, it may have been prudent to also exercise the same caution

about the DTNB identification peak. When measured in solution, the unique identification peak of MPY had an intensity of ~ 5000 a.u. thus if a 10-100 fold decrease in signal intensity did occur, as had been observed with the commercial nanotags, this may explain why no measurable DTNB signals were observed. However, this is again unlikely since strong signals were measured from the individually labelled DTNB nanotags (**Figure 3.39**).

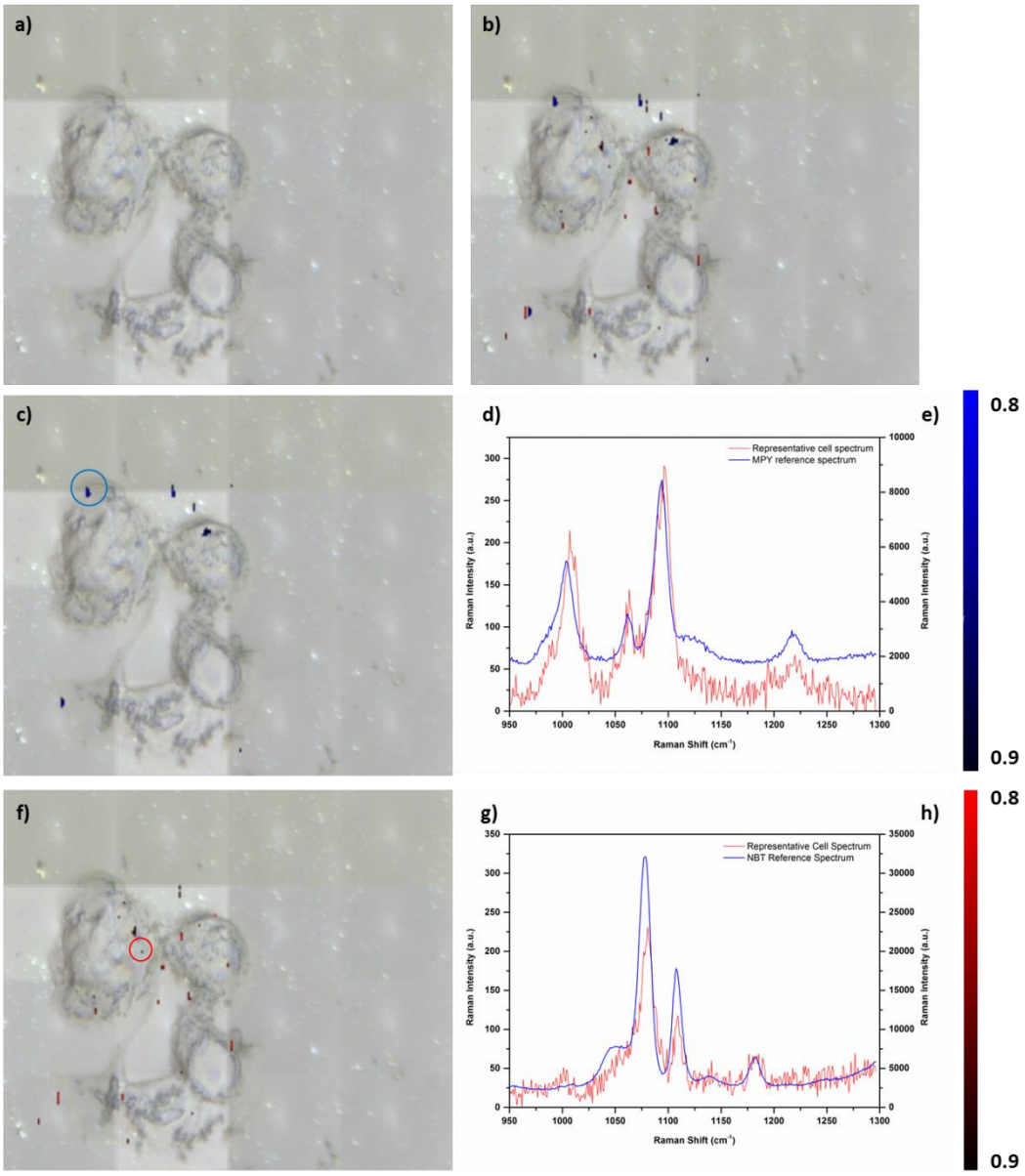

Figure 3.42: False colour SERS map image and representative spectrum for the triplex (MPY+DTNB+NBT) applied to a HeLa cell population. a) white light image, b) complete false colour SERS map image. c)-e) and f)-h) false colour SERS map image, representative SERS

spectrum and LUT colour bar for MPY and NBT labelled nanotags respectively. The cell spectrum is plotted on the primary y-axis and the reference on the secondary y-axis. (StreamLine - λ_{ex} = 633 nm, 100% (~ 6 mW), spectral range 914-1296 cm^{-1}, step size x,y 0.5 μm 5s).

The lack of signal was also not thought to be cell line specific since the DTNB nanotags were readily imaged when applied individually to a HeLa population. One plausible explanation as to the lack of observable DTNB signal may be the method of mapping analysis since the triplex sample was interrogated using the StreamLine method rather than in combination with the StreamLineHR method. It was possible that if the slide sample had been analysed using the high resolution method, signals from the DTNB component would have been observable since each point on the map would have been interrogated with a focused laser spot rather than a laser line. In addition, the StreamLineHR method allows more detailed refined information to be obtained and is particularly useful for samples where the signal strength has been found to be poor when mapping using the conventional StreamLine method. This was found to be the case when imaging the commercial nanotags in cells (**Figure 3.12**).

One interesting feature to note from the false colour SERS map image was the absence of any cumulative triplex signals. It was unclear when the multiple component study was initiated whether individual signals from the nanotags or cumulative signals from the triplex would arise. In the previous study with the commercial nanotags, it was possible to observe individual and cumulative signals from each of the applied nanotags even in regions where only one nanotag had been previously thought to exist (**Figure 3.11**). Therefore, if the samples were reanalysed with the high resolution method it may have been possible to observe cumulative spectra and the spectral profiles typical of the multiple component sample in question will prove to be useful.

As with the other cell samples, there was a significant reduction in the signals measured from the nanotags inside the cell, there was evidence of non-specific binding and again the nanotags were found on the periphery of the cell. These issues have been discussed in the previous section and attempts will be made to address these. However, the ability to detect two of the three nanotags is a step-wise progression towards the development of suitable multi-marker system for cellular imaging.

3.6.4 Detectability of the Developed Fourplex in a Cell Population

When the fourplex sample (MPY+DTNB+NBT+2-NPT) was applied to a HeLa cell population and analysed it was possible to identify three out of the four nanotags within the multiple component sample.

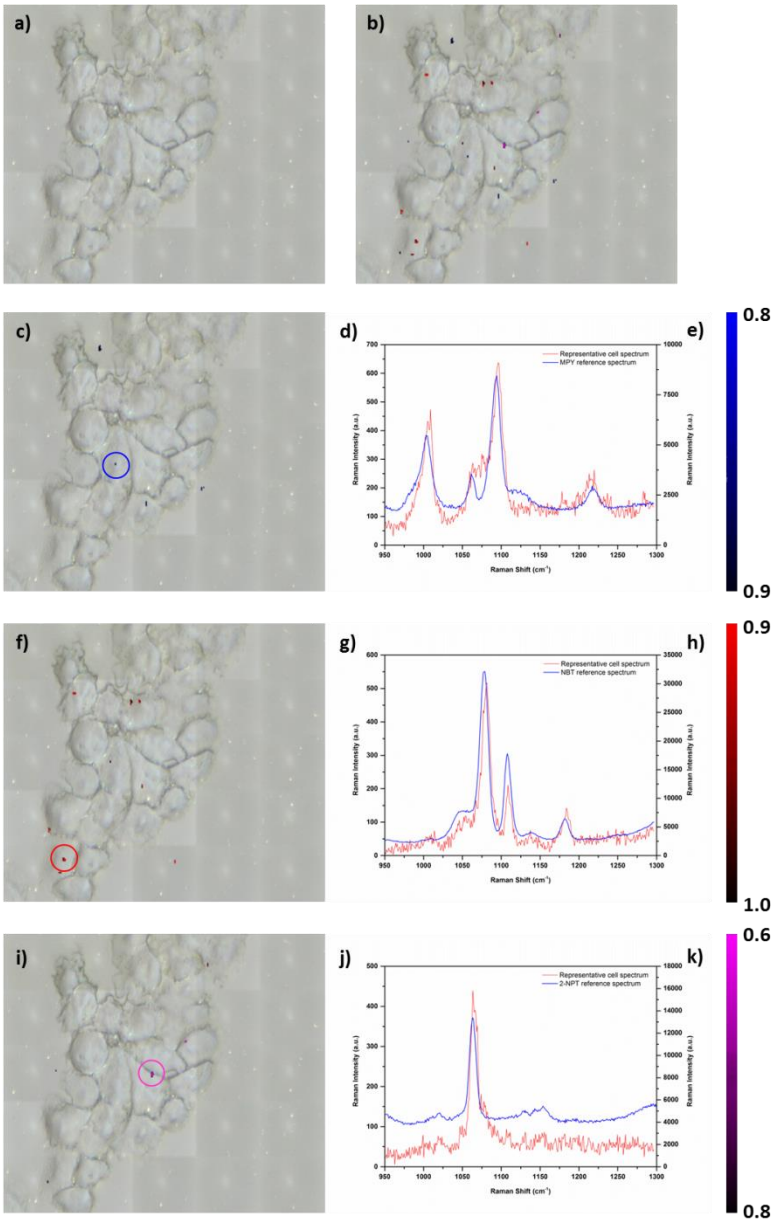

Figure 3.43: False colour SERS map image and representative spectrum for the fourplex (MPY+DTNB+NBT+2-NPT) applied to a HeLa cell population. a) white light image, b) complete false colour SERS map image. c)-e), f)-h) and i)-k) false colour SERS map image, representative SERS spectrum and LUT colour bar for MPY, NBT and 2-NPT labelled nanotags respectively. The cell spectrum is plotted on the primary y-axis and the reference on the secondary y-axis.

(StreamLine - λ_{ex} = 633 nm, 100% (~ 6 mW), spectral range 914-1296 cm^{-1}, step size x,y 0.5 µm 5s).

Signals were measurable from the MPY, NBT and 2-NPT components and, as with the triplex sample, no signal was measurable from the DTNB component (**Figure 3.42** c.f. **Figure 3.43**). Although DTNB labelled nanotags were not observed, a successful triplex multiple component sample was developed for the multi marker imaging of cells. As stated earlier, it would have been necessary to map the same cell population twice in order to identify the unique 2-NPT identification peak because of the limitations of the CCD. However, as no cumulative cell signals arose and component DCLS matches the reference spectrum with the data collected during mapping, in this instance it was possible to use the peak at ~1063 cm^{-1} for positive identification of 2-NPT. The reasons for the absence of any measurable DTNB signals were given in section 3.6.2 and it is most likely that this particular batch of DTNB labelled nanotags were unstable or aggregated extensively and become too large for cell uptake.

As with the previous examples, there was a significant reduction in the signals measured from the nanotags inside the cell when compared with their appropriate reference. This may be indicative of cell uptake reflecting the depth at which the nanotags are found within the cell however, this would need to be confirmed with a secondary method. The labelled nanotags in this particular example were all found within individual cells and this may be related to their chemical functionality. However, it was expected that all of the small molecule reporters would be negatively charged to a certain extent at this pH. Therefore this would not influence cell uptake and if a protein corona formed around the nanotags then their location within distinct and different cells may be entirely random.

Although a successful triplex had been developed and detected within a cell population this was comparable with the maximum number of components that could be detected within a single cell or cell population[150, 221] at the time of the investigation. However, one of the primary aims was to increase the number of components that could be detected within a single cell or cell population. With this in mind the fourplex was introduced into two further cell lines to determine if it was possible to detect four

individually labelled nanotags within a single cell and that uptake was dependant on cell line.

3.6.5 Detectability of the Developed Fourplex in a Single Cell

3.6.5.1 Macrophage Cells

The developed fourplex was applied to a macrophage cell population since macrophage cells are well known to engulf material within the extracellular fluid, thus this non-discriminative method of phagocytosis is an ideal mechanism. Within a single cell it was possible to detect all four of the individually labelled nanotags from the multiple component sample (**Figure 3.44**). The DTNB and 2-NPT labelled nanotags were found within the macrophage cell and signal from the MPY and NBT nanotags appeared to come from the cell membrane or from the periphery of the cell (**Figure 3.44**).

Unfortunately the cell was imaged using the StreamLine method rather than a combination of both the StreamLine and the StreamLineHR. This method allows more detailed refined information to be obtained and the strength of the technique was demonstrated when analysing the commercial nanotags. In the StreamLine map of the cell associated commercial nanotags it was only possible to see two of the four components within a single cell however when the sample was reanalysed using the high resolution method it was possible to observe signal from all four components (**Figure 3.12**). Although the MPY and NBT nanotags appear on the periphery of the macrophage cell, analysis with the high resolution method may have revealed a different pattern of distribution as with the commercial nanotags (**Figure 3.12**). Despite all four nanotags not being directly located within a single cell this example does demonstrates the potential for all four to be found within a single cell and suggests that it would be possible to target four different cellular components (i.e. 3 organelles and 1 membrane).

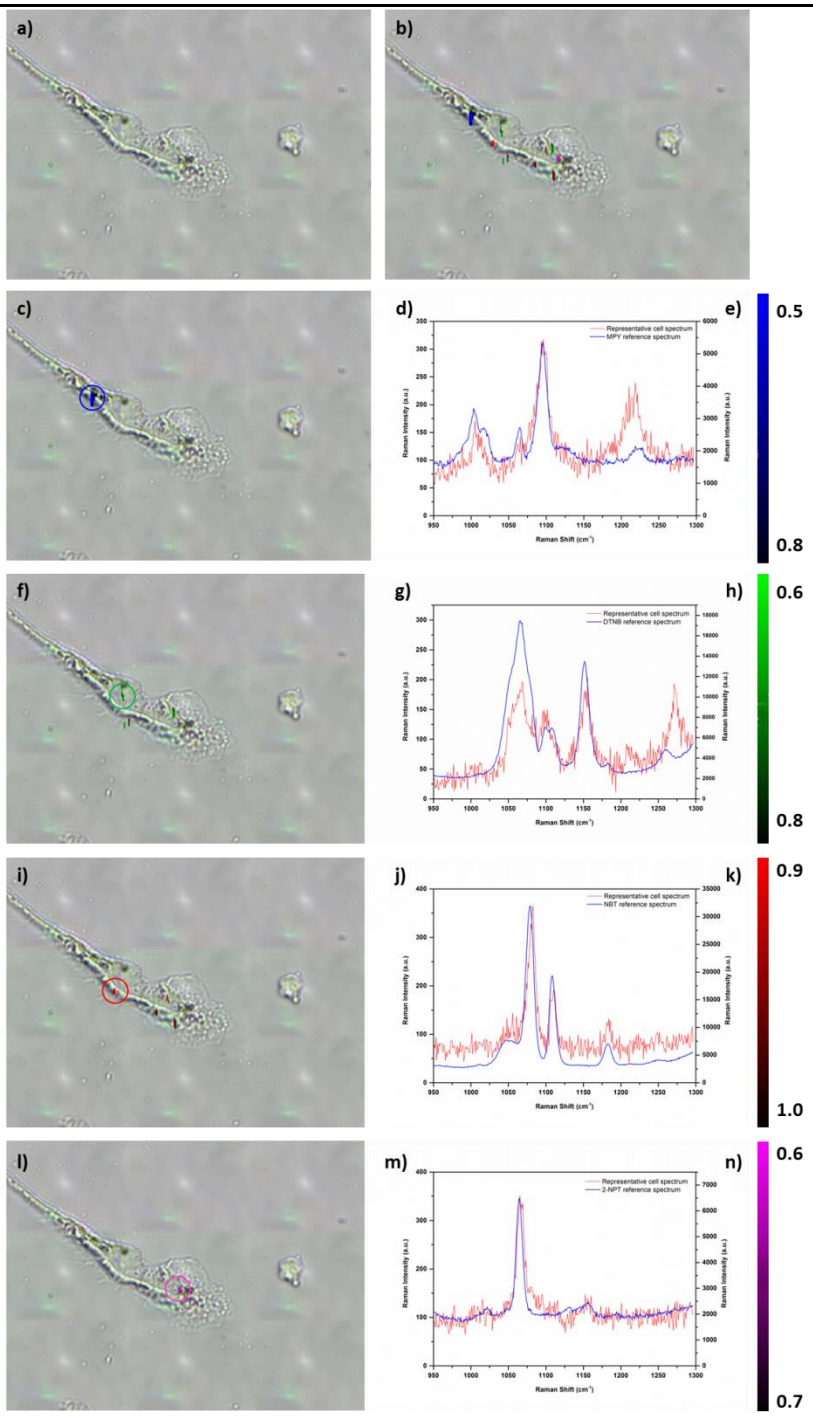

Figure 3.44: False colour SERS map image and representative spectrum for the fourplex (MPY+DTNB+NBT+2-NPT) applied to a macrophage cell population. a) white light image, b) complete false colour SERS map image. c)-e), f)-h), i)-k) and l)-n) false colour SERS map image, representative SERS spectrum and LUT colour bar for MPY, DTNB, NBT, and 2-NPT labelled nanotags respectively. The cell spectrum is plotted on the primary y-axis and the reference on the secondary y-axis. (StreamLine - λ_{ex} = 633 nm, 100% (~ 6 mW), spectral range 914-1296 cm^{-1}, step size x,y 0.3 µm, 0.5 µm 5s).

Although signals from the DTNB labelled nanotags were measured within the boundary of the macrophage cell but not within the HeLa cell this was not thought to be the result of a cell-line specific interaction. Signal from the DTNB labelled nanotags could be measured within the HeLa cells when they were applied individually and it was only when they were part of a multiple component suspension did it become problematic to observe any signal. This could be attributed to a number of things including a possible interaction with the other nanotags or that the particular batch of nanotags could have simply been aggregated to an extent which negated cell uptake. Whilst it was not thought to be cell line specific, the macrophage cells probably did have a greater propensity to incorporate extracellular material than the HeLa cells. In this particular sample, 2-NPT was again identified using the peak at ~1063 cm^{-1}. This was not the unique identification peak determined during the multiple component study but component DCLS adequately elucidated it from the spectral profile of the other nanotags.

The next stage of investigation would have involved looking at the macrophage cells as a suitable cell line for investigating the uptake of the fourplex while definitively determining cellular incorporation and localisation of the nanotags relative to the cell organelles. Unfortunately access to the macrophage cells ceased and it was necessary to looks at an alternative cell line to ultimately determine if the fourplex could indeed be detected within a single cell.

3.6.6 Chinese Hamster Ovarian (CHO) Cells

In a final attempt to detect all four components within a single cell the fourplex was applied to a CHO population. In the StreamLine image of a single cell it was possible to confidently detect three of the components (**Figure 3.45**). MPY was found on the periphery of the cell and may not be cell associated while DTNB and NBT were located within the cell boundary (**Figure 3.45**). 2-NPT was also identified on the periphery of the cell, however, it demonstrated a poor spectral fit with the reference spectrum so it was not included(**Figure 3.45**). Similarly, when the cell was re-analysed using the StreamLineHR method it was confidently concluded that two out of the three components were present within a single cell (**Figure 3.46**). MPY and NBT demonstrated a good spectral fit with their reference spectrum while DTNB and 2-NPT did not (**Figure 3.46**). Common to the StreamLine NBT spectrum and StreamLineHR

NBT and DTNB spectra were the appearance of some additional peaks (**Figure 3.45** and **Figure 3.46**).

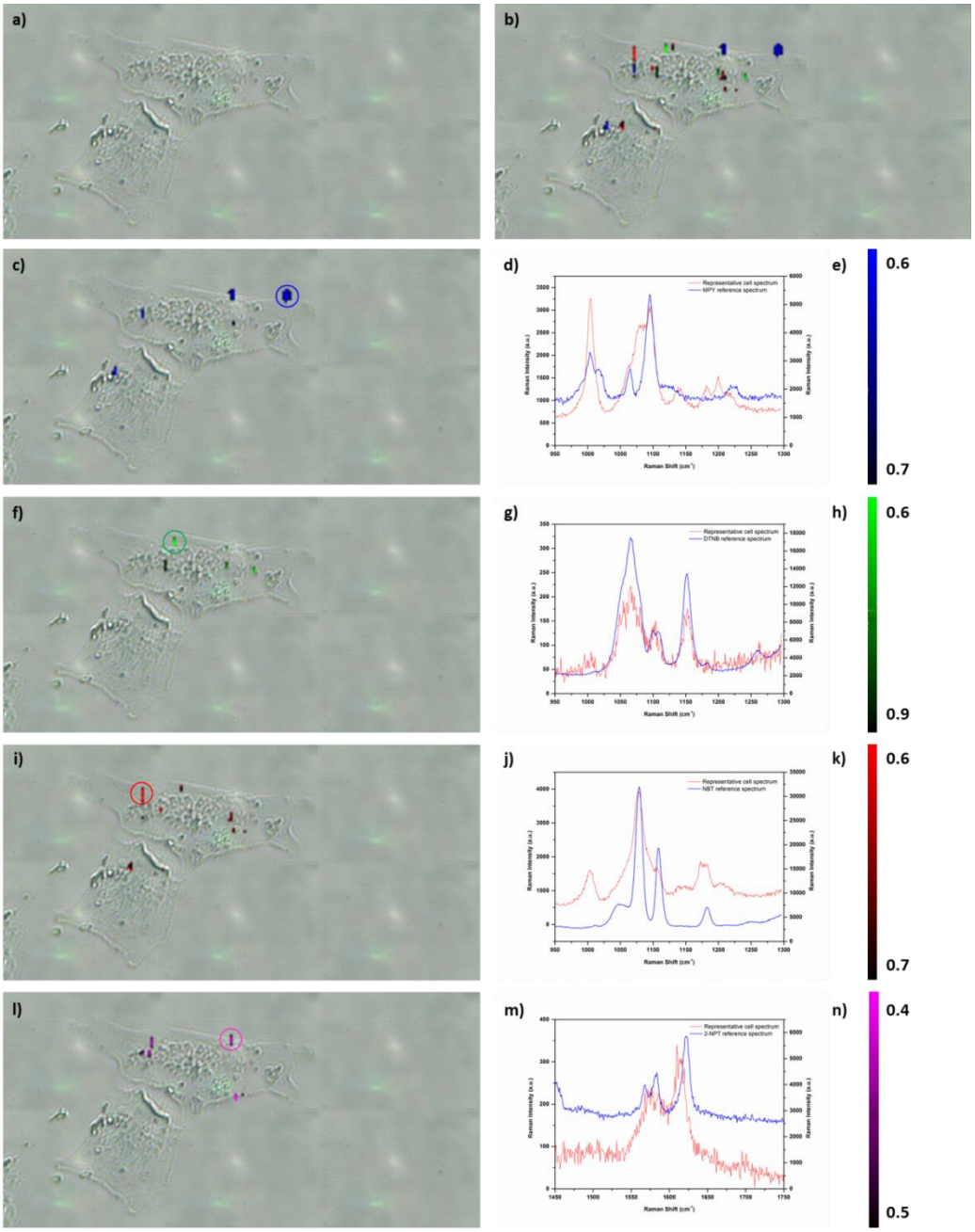

Figure 3.45: False colour SERS map image and representative spectrum for the fourplex (MPY+DTNB+NBT+2-NPT) applied to a CHO cell population. a) white light image, b) complete false colour SERS map image. c)-e), f)-h), i)-k) and l)-n) false colour SERS map image, representative SERS spectrum and LUT colour bar for MPY, DTNB, NBT and 2-NPT labelled nanotags respectively. The cell spectrum is plotted on the primary y-axis and the reference on the secondary y-axis. (StreamLine - λ_{ex} = 633 nm, 100% (~ 6 mW), spectral range 914-1296 cm^{-1}, step size x,y 0.5 µm 5s).

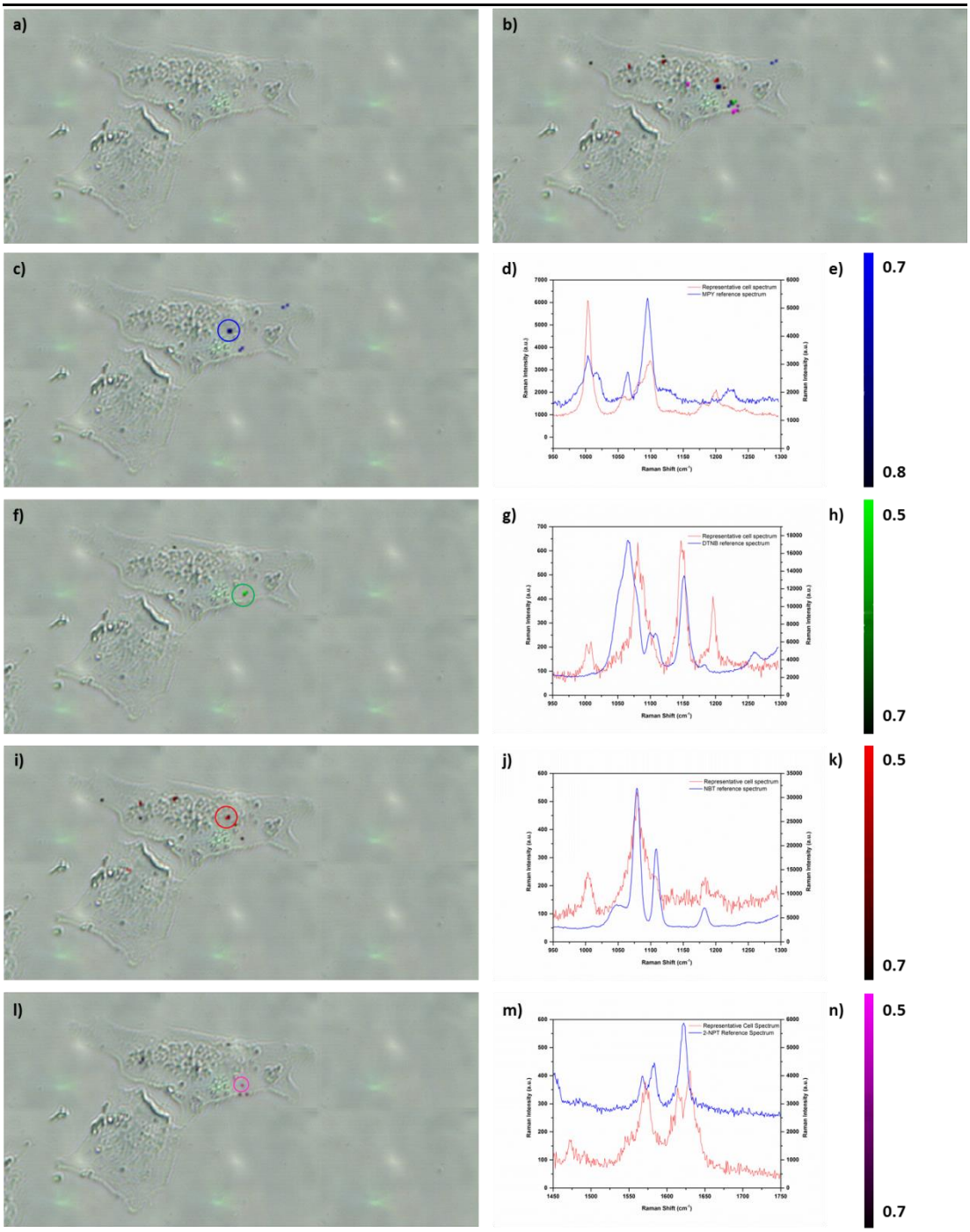

Figure 3.46: False colour SERS map image and representative spectrum for the fourplex (MPY+DTNB+NBT+2-NPT) applied to a CHO cell population. a) white light image, b) complete false colour SERS map image. c)-e), f)-h), i)-k) and l)-n) false colour SERS map image, representative SERS spectrum and LUT colour bar for MPY, DTNB, NBT and 2-NPT labelled nanotags respectively. The cell spectrum is plotted on the primary y-axis and the reference on the secondary y-axis. (StreamLineHR - λ_{ex} = 633 nm, 5% (~ 0.33 mW), spectral range 914-1296 cm^{-1}, step size x,y 0.5 µm 3s).

These peaks have potentially arisen as a result of two different processes. It is probable that these are cell enhanced vibrations as a result of certain molecules being in close proximity to the nanotag surface. If this process occurred it would suggest that either the nanotag surface wasn't covered with a monolayer of molecules or some of the molecules present on the nanotag surface have desorbed and allowed the native cellular constituents access to the metal surface. However, when bare unlabelled nanotags were incubated with cells and analysed no intrinsic cell signals were observed (**Figure 3.47**).

The unlabelled nanotags had been prepared using the small molecule only procedure however no reporter was added so that the surface was accessible to the cell surface and intracellular molecules. The nanotags were then incubated according to the standard protocol whereby they were incubated with cells grown on a coverslip for 1 h and then washed and fixed accordingly. In an effort to minimise non-specific binding, a second method of incubation was also performed whereby the nanotags were added and incubated in a flask with the cells for 24h. The cells were then washed and tryptanised and this was thought to be a superior method for the removal of any remaining unbound and extracellular nanotags.[209] The cells were then grown on coverslips for 24 h before being washed and fixed accordingly.

During the analysis of both the pre-incubated and non-preincubated control samples no intrinsic Raman cell signals were observed for any of the cells analysed (**Figure 3.47**). 20 cells were analysed for each method of incubation and it is fair to assume that within a group of 40 randomly selected cells that some form of nanoparticle uptake would have taken place. Although no intrinsic cell signals were measured from the control samples, it is reasonable to assume that there was potentially a risk of enhancing some cells bands especially since nanoparticles and tag based systems have been routinely used to probe the intracellular environment.[52, 145, 148, 149, 205]

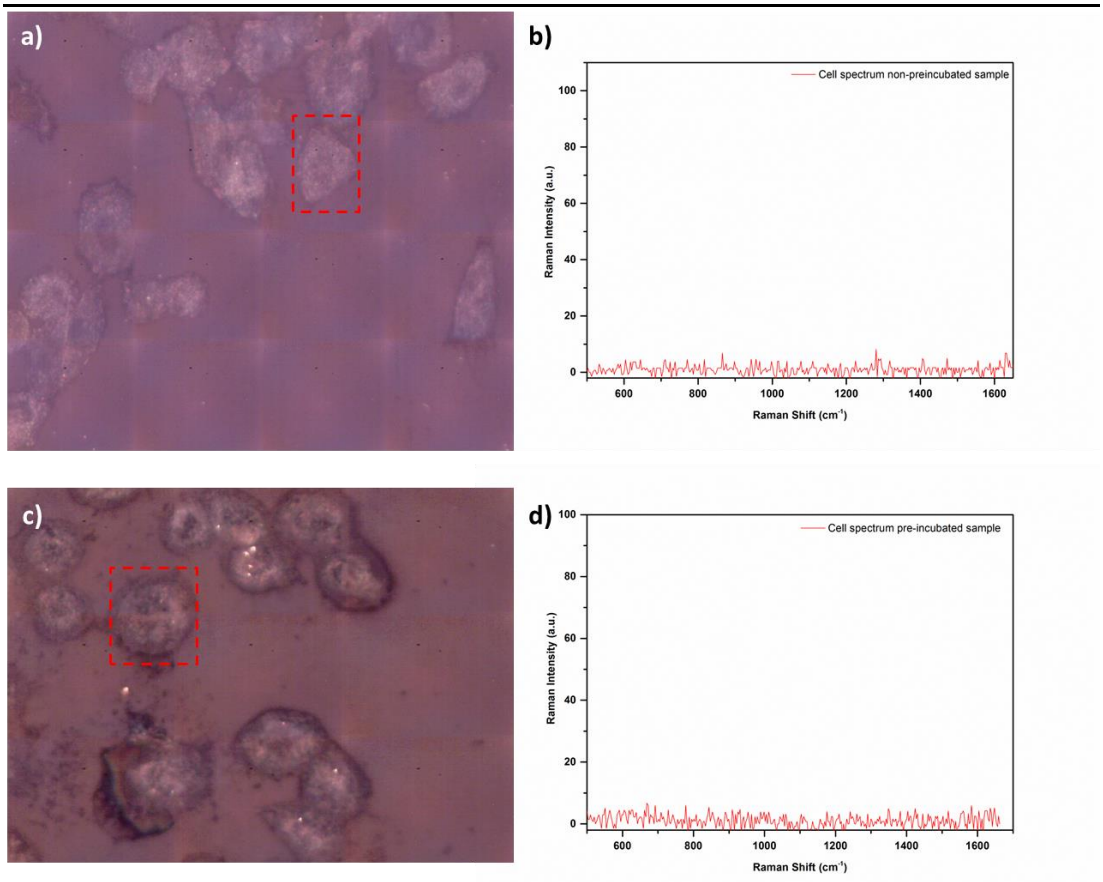

Figure 3.47: Control cells which have been exposed to nanotags without any label to determine the influence cell surface and intracellular molecules have on the spectra produced – a) white light image of cell population subject to the standard nanotag incubation procedure and the cell within the dashed red rectangle was mapped, b) representative cell spectrum from the mapped cell, c) white light image of cell population pre-incubated with the nanotag suspensions and the cell within the dashed red rectangle was mapped and d) representative cell spectrum from the mapped cell. (StreamLineHR - λ_{ex} = 633 nm, 100% (~ 6.6 mW), spectral range 478-1661 cm^{-1}, step size x,y 0.5 µm 0.5s).

In the second instance the additional peaks may also be due to cumulative SERS signals, that is a contribution to the overall SERS signal from each of the nanotags present within a specified location. In the StreamLine and StreamLineHR image there was an additional band present in the NBT spectrum at ~ 1000 cm^{-1} which could be attributed to MPY since it was in close proximity to the representative NBT cell signal on both occasions (**Figure 3.48a,b** and **c**). Similarly, in the case of the DTNB StreamLineHR spectrum there were additional peaks at ~1002 cm^{-1} and 1081 cm^{-1}, the unique

identification peaks for MPY and NBT, which were also in close proximity to the representative DTNB cell signal (**Figure 3.48b**).

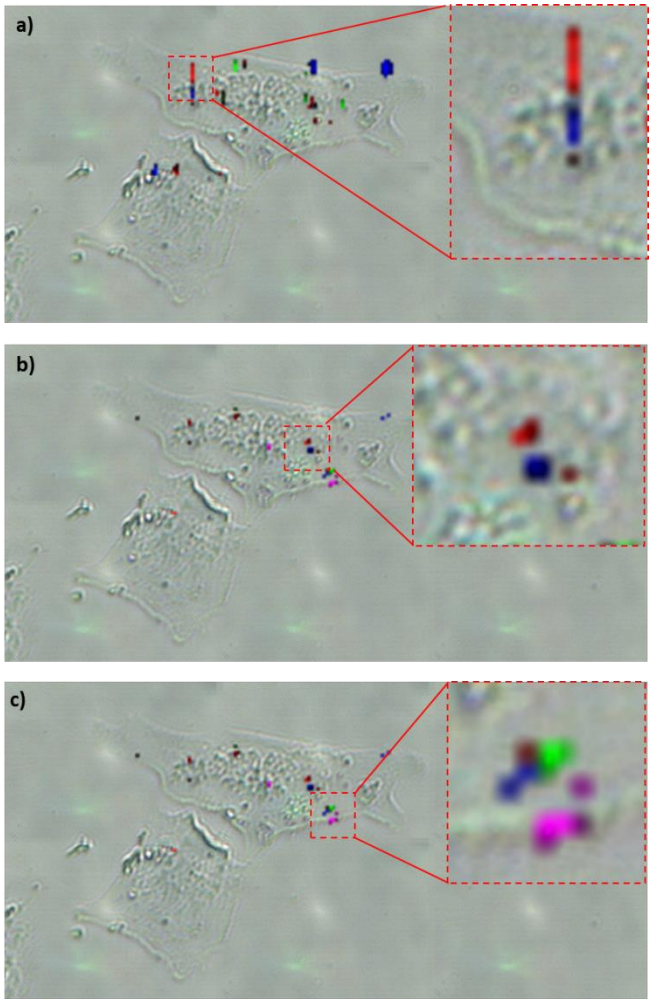

Figure 3.48: Cumulative SERS signals – additional features in the SERS spectrum could be due to the close proximity between differently labelled nanotags. NBT and MPY were in close proximity to one another in the a) StreamLine and b) StreamLineHR false colour image and c) DTNB was in close proximity to both MPY and NBT in the StreamLineHR image.

Although this was not the typical cumulative spectra expected from this specific combination of nanotags (based on the multiple component study) the exact spectrum produced will vary depending on the local environment and also the contribution from each component present within a specified location.[9] Regardless of the method by which these additional features appear in the spectrum, the LUT filters were typically set at high levels (equivalent to ~ 70-100%) to ensure the best possible fit between the reference spectrum and the observed cell signal. However it is important to be aware of

such interference potential within the spectrum. Overall it is proposed that it is possible to detect three out of the four nanotags when a multiple component suspension was applied to a CHO cell population.

3.7 Toxicity of SERS Nanotags

The toxicity of the SERS nanotags towards CHO cells was investigated using the PEG nanotags. All of the previous examples of cell mapping experiments were carried out using the small molecule functionalised nanotags. Both nanotag systems were not investigated as both methods of incubation – 1) directly on to the coverslips and 2) direct flask incubation with the cells were trialled. In order to do this a vast amount of consumables and cells were required therefore it was not considered to be cost effective to investigate both. It is however noted that the PEG functionalisation might aid in biocompatibility and does not represent the toxicity that might be induced by the small molecule only labelled nanotags.

The toxicity of the nanotags towards the cells was investigated using an alamarBlue® assay.[228] Addition of the reagent to the nanotag/cell populations results in the active ingredient, resazurin (blue), being reduced to a red fluorescent compound resorufin, following cell internalisation.[228] Turnover of the reagent should only continue as long as cells are viable and therefore, the fluorescence signal should increase over time. The overall fluorescence intensity is proportional to the number of living cells.[228] In addition to the alamarBlue® assay, cell health was monitored using a SYTOX® green nucleic acid stain.[229] This reagent will only enter cells with impaired or damaged membranes where it subsequently binds to nucleic acids.[229] If the cells are healthy the stain will not cross the plasma membrane.[229]

As mentioned above, the cells were incubated with the nanotags via two different methods of incubation. Typically, only 100 μL of the nanotags were added however, in order to assess the effects of the nanotags and determine whether a larger volume could be used, 100-300 μL were investigated. For the alamarBlue® assay a large number should be produced by the fluorimeter since the cells should be healthy and continually producing resorufin.

In the first example the results are somewhat variable but it was instantly clear that the MPY labelled nanotags displayed the greatest toxicity towards the cells when added directly onto the cells grown on coverslips (**Figure 3.49**).

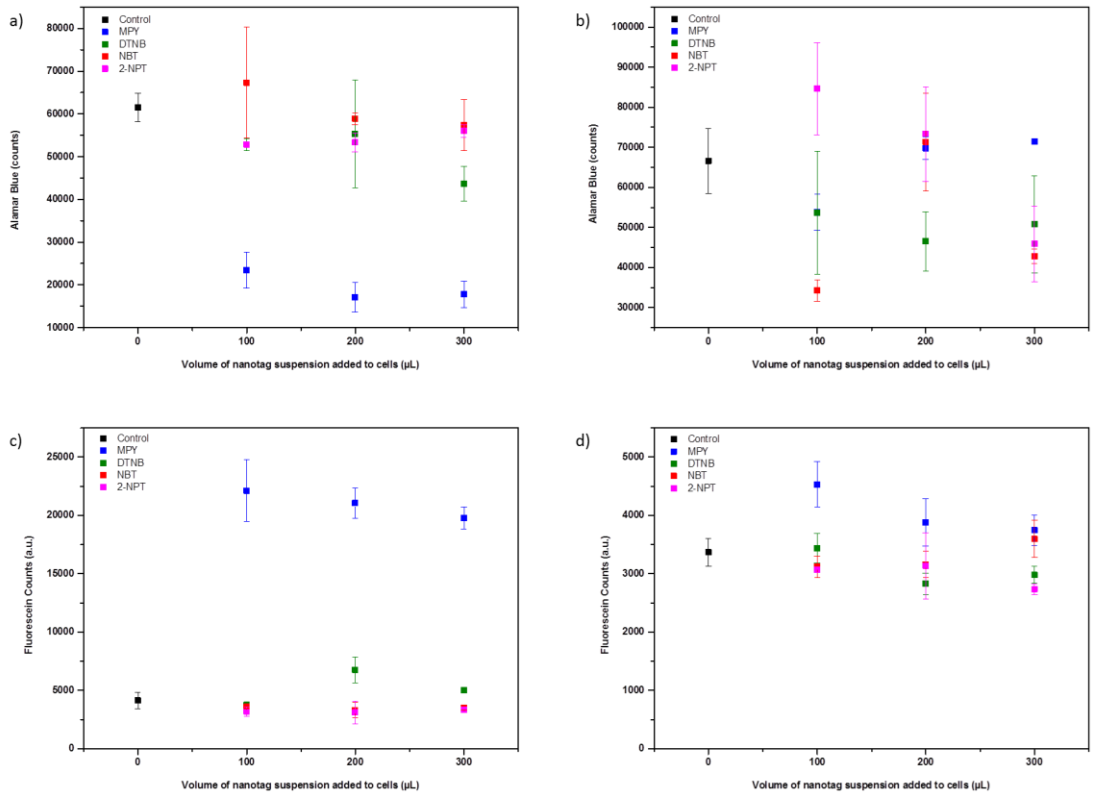

Figure 3.49: Toxicity tests for the PEG labelled nanotags – a) and c) the nanotags were incubated directly with cells grown on coverslips for 1 h b) and d) or with cells in a flask for 24 h. The cell viability was evaluated using AlamarBlue® and SytoxGreen®. The error bars represent the standard deviation of three replicate measurements.

A reduction in cell viability was demonstrated for the DTNB labelled nanotags at all volumes and at a level below that of the control sample. In the case of NBT and 2-NPT, a reduction in viability was observed initially but the number of viable cells increased at the highest concentration of nanotags, but remaining at a level below that of the control. With the exception of the MPY nanotags, the reduction in cell viability was minimal and although the introduction of the nanotags was expected to interfere with the cell viability it wasn't particularly prolific (**Figure 3.49**).

When the nanotags were incubated directly with the cells in the flask the results were somewhat more variable. With the exception of MPY, all of the remaining nanotags at the highest concentration produced less fluorescence than the control sample. There was however no clear relationship between increasing concentration of nanotags and cell viability except for the nanotags labelled with 2-NPT and MPY, which decreased and increased with increasing concentration of the nanotags respectively. With the exception of MPY, the effects on the cell viability were more obvious with this incubation method but again cell viability wasn't particularly affected.

For the SytoxGreen® assay unlike the alamarBlue®, a small number should be produced by the fluorimeter since this is a direct measure of the number of compromised cells within a sample. Again with the exception of MPY, the other small molecules did not seem to compromise the viability of the cells. MPY when compared with the control sample exhibited a significant increase in the fluorescence produced and thus the number of compromised cells.

When the MPY and NBT samples were incubated with the cells in the flask the fluorescein counts in the Sytox Green assay were only marginally larger than the count produced by the control sample. While the counts for the remaining nanotags decreased with increasing concentration. This would suggest that this method of incubation was suitable and the nanotags have little effect on the cell viability.

Overall, toxicity results suggested that either method was suitable for the incubation of the nanotags. However the method of flask incubation may be more suitable for nanotags functionalised with MPY. On the whole the small molecule reporters and nanotags in general didn't seem to be particularly toxic towards the CHO cells. There was some variation between the nanotags and the standard, but this was to be expected due to the introduction of a foreign based material.

3.8 Conclusions

In the initial stages a range of commercial nanotags were investigated and trialled as potential multi marker cellular imaging agents. The commercial nanotags performed exceptionally and it was possible to readily identify the specific combination of nanotags present within a solution or cell population. All four of the nanotags could be

found within a single cell. However, for commercial reasons the use of the nanotags in further studies was prohibited.

In an effort to find suitable alternatives for the multi marker imaging of cells, a range of silver nanoparticle suspensions labelled with small molecules reporters were investigated. Unfortunately, this had limited success and strong SERS signals were only measured if the suspensions were physically aggregated or self-aggregated uncontrollably. Based on these results, and the principles behind the commercial nanotags, it was realised that a nanotag system was required whereby some form of 'controlled' aggregation took place but not to the extent that the nanotags would no longer be viable for cell uptake.

A method was found within the literature whereby silver citrate nanoparticles were controllably aggregated with 1,6-HMD, polymer coated with PVP and labelled with a range of small molecule reporters.[9] This system had been used previously to target cell surface receptors but it had not been fully exploited for use as multi markers for cell imaging. It was necessary to optimise the concentration of 1,6-HMD, PVP and select appropriate small molecule reporters.

The nanotags were tested in solution to determine if a new multiple component system could be developed whereby four components of a single cell, cell population or tissue structure could eventually be targeted simultaneously. A successful triplex and fourplex system were developed. The triplex and fourplex were tested in HeLa cells and this produced varying results but when the fourplex was extended to CHO and macrophage cells it was possible to detect three, potentially four and all four of the nanotags within a single cell respectively. Between the different cell populations there was some spectral variation in the signals measured from each of the individually labelled nanotags and this was likely to be due to variations in the microenvironment of each cell type. Variation in nanoparticle treatment by different cell lines, including endosome enclosure has been documented.[52] At the time of the study the maximum number of nanotags which could be simultaneously detected within a single cell was three[150, 230] and although approaches suggested the use of four or five different multi markers this was only demonstrated with a cell population[231] or on cell surfaces[149] or with an *in vitro* duplex[221] and not with single cells. Whilst this can in no way compete

with the number of nanotags which could be simultaneously detected *in vivo at* the time of the study, an increase in the ability to map single cell, cell populations and tissues with a multi marker approach was achieved.

Common to all of the images discussed in this chapter there was a real need to confirm cellular uptake and this will be investigated in the later chapters using combined 3D Raman and SERS imaging. In addition to this, the intracellular location of the nanotags could be investigated further using an alternative laser line to determine the localisation of the nanotags relative to the major cell organelles. This would also determine if the functional group on the small molecule reporter influences the method of uptake or directs the nanotags to a specific intracellular location.

Chapter 4 3D Optical Imaging of Multiple SERS Nanotags in Cells

4.1 Introduction

The application of Raman and surface enhanced Raman spectroscopy (SERS) to complex biological and medical samples has increased dramatically in recent years. This is due in part to improvements in instrument sensitivity but also because both represent a non-destructive method by which considerable information can be gained. Raman spectroscopy also has the added advantage of being a non-invasive analysis method. Whilst the Raman spectra of biological samples are often complex, subtle changes between samples can be readily elucidated by the incorporation of multivariate analysis methods. For example, Raman spectroscopy has been used to identify cell components[92] and to discriminate between cancerous and normal cells,[232] cancer cells with differing phenotype[233] and in distinguishing human embryonic stem cells from differentiated cells.[234] In the case of SERS, unfunctionalised nanoparticles have been used to obtain information about cell compartments,[142] endocytosis,[52] as well as cell health[144] and viability.[145] Function specific SERS nanotags have also been designed for the molecular profiling of single cells,[52] intracellular pH sensing[160] and *in vivo* tumour targeting and detection.[10, 11]

However, despite the advanced applications[52, 92, 142, 144, 145, 232-234] of both Raman and SERS spectroscopies there are limited examples of sophisticated 3D imaging within the literature to accompany these applications.[100] This is surprising considering that imaging in 3D can be relatively simple to achieve using depth profiling methods (i.e. the same area is mapped sequentially at different z-levels) and post collection image processing applications such as ImageJ and Volocity™. 3D imaging also has the potential to provide a wealth of information which could be critical to the detection of disease states. For example, the 3D imaging of cells and tissues can enable the resolution of cell organelles which represents a non-invasive technique for studying cell construction,[100] and this could be beneficial for interrogating changes in cellular architecture between diseased and healthy samples. Combining 3D Raman with 3D SERS imaging offers the possibility of tracking nanotags functionalised with organelle targeting moieties or

drug molecules. Imaging in this manner would not only provide non-destructive evidence of cellular uptake, but would provide evidence that the tags are being directed to their intended targets.

One of the most notable difficulties regarding the imaging of intracellular SERS active nanotags is undoubtedly in determining cellular inclusion. Whilst 2D[7, 8] imaging is considered a straightforward approach to monitoring the uptake and localisation of nanotags, this cannot be considered as conclusive evidence of cellular inclusion. Internalisation has traditionally been confirmed by depth profiling in the z-direction or transmission electron microscopy (TEM), TEM however, can require convoluted sample preparation; image acquisition can be expensive and the technique ultimately results in cell destruction so live cell imaging is impossible to achieve. Whilst conventional TEM imaging can provide evidence of cellular inclusion, confocal scanning transmission electron microscopy (STEM)[235], as well as X-ray diffraction[236] and topography,[237] and ion-abrasion scanning electron microscopy (SEM)[238] can all be used to generate 3D cell images. Excellent resolution (nm range c.f. μm range for Raman spectroscopy) and comparable acquisition times can be achieved. However, no biochemical information is obtained, some of the techniques are destructive and 3D image generation is reliant on the post processing of 2D images.

Comparisons are frequently made between fluorescence and Raman spectroscopies and with the advent of fluorescent approaches such as stimulated emission depletion (STED) microscopy[239] and structured illumination microscopy (SIM),[240] which offer excellent enhancements in resolution (~ 30 nm in the x, y and z directions cf. μm),[239] comparisons between the two types of spectroscopy for 3D cell image generation are likely to continue. Fluorescent microscopy can offer fast acquisition times, since the collection of a full vibrational spectrum is not required, but there are a number of disadvantages associated with the technique namely that biochemical imaging of the cell contents is prohibited, staining is required to resolve the cell organelles and the post processing of 2D image stacks is required to generate the final 3D image. Fluorophores are also prone to bleaching which is problematic if they are to be used for 3D imaging since this is reliant on the collection of sequential z-sections and any bleaching will prohibit complete 3D reconstruction.[241] The broad absorption and emission bands associated with fluorophores also limit the number of components

which can be identified simultaneously. In addition, visualisation of multiple fluorophores often requires multiple excitation sources.

Whilst Raman and SERS are currently limited by long acquisition times (hours *cf.* seconds) and the spatial resolution that they can offer, many of the issues surrounding the other techniques are circumnavigated. For example, both methods are non-destructive whilst Raman is also non-invasive. Vast amounts of biochemically specific information can be obtained with respect to the cell and since Raman and SERS active labels produce sharp (nm width) molecularly specific bands, multiple components within a single sample are readily identifiable. With these advantages in mind this chapter will discuss the concept and development of combined 3D Raman and SERS imaging for the simultaneous confirmation of cellular inclusion and multiple component detection. This method removes the need for expensive TEM imaging and avoids the required post collection processing of each individual image. Using this technique the entire volume of the cell is collected at once, hence all the collected data can be processed and analysed as one data set, and both uni-variate and multivariate analyses can be applied to the entire volume simultaneously.

4.2 Proof of Concept - 3D Raman and SERS Imaging of Cells and Nanotags

Multiple component cell samples were prepared by incubating a suspension containing four different nanotags (4-mercaptopyridine (**MPY**), 5,5'-dithiobis(2-nitrobenzoic acid) (**DTNB**), 4-nitrobenzenethiol (**NBT**) and 2-naphthanlenethiol (**2-NPT**) labelled nanotags) with Chinese Hamster Ovarian (CHO) cells according to the standard protocol (see section 8.4.1). Prior to the collection of any 3D data, samples were mapped in 2D (StreamLine™, StreamLineHR™ - Renishaw inVia Raman spectrometer / Leica DM 2500 M microscope) to rapidly identify cells which had incorporated the nanoparticle suspension and in which all four or multiple components could be identified. A 633 nm laser (HeNe) excitation source was used and cell samples were imaged under immersion in a saline solution using an Olympus 50× (N.A. 0.75) water immersion objective. A grating of 1800 lines/mm was used with a RenCam CCD (1046 × 256 pixels). As discussed in Chapter 3, nanotags were identified by a two-fold process whereby each of the components was identified by a unique peak and component

direct classical least squares (DCLS) multivariate analysis. Following the identification of a multiple component positive cell, the sample was interrogated by depth profiling at different z-depths to roughly determine the cell thickness and the z-slices from which data should be collected.

Imaging of the cell in 3D was achieved using a 532 nm laser (Cobalt) excitation source and 3D imaging of the nanotags was achieved using a 633 nm laser (HeNe) excitation source. Cells were imaged under immersion as described above and the grating and CCD remained the same.

Acquisition and analysis of the collected data was performed using the WiRE 3.4 software package. All PCA analysis was completed in WiRE and the conditions used are discussed. The 3D images were created using the WiRE VolumeViewer software. The 3D Raman cell and SERS nanotag images were taken directly from the VolumeViewer software as were the 2D sections for the Raman cell and SERS nanotag images. The individual 2D sections were then combined into a single image using a GNU image manipulation programme.

4.2.1 Spatial and Depth Resolution

When employing a confocal configuration it is important to define the spatial and depth resolution especially since instrumental improvements, in some instances, have ensured operation at or close to the diffraction limit. Theoretical values of the spatial and depth resolution can be calculated using equation 2 and 3, respectively.[206, 242]

$$\frac{0.61\lambda}{NA}$$

Equation 2

$$\frac{4n\lambda}{NA^2}$$

Equation 3 [206, 242]

Where:

λ = laser wavelength (nm)

NA = numerical aperture of the microscope objective
n = refractive index of the sample

When imaging cells in 3D, under immersion in a saline solution (n = 1.33), using a 532 nm laser and a microscope objective with a 0.75 N.A. the theoretical spatial and depth resolution were calculated to be 0.43 μm and 5.03 μm respectively. Similarly, when imaging nanotags in cells in 3D, using the above conditions, the theoretical spatial and depth resolution were calculated to be 0.51 μm and 5.99 μm respectively.

4.2.2 3D Raman Imaging of Cells

3D Raman cell images were generated using volume mapping; a confocal configuration that allows layers of Raman images to be rapidly collected. With the employment of this method there is no need for post collection image processing since the entire volume is collected at once. The step sizes in the x and y direction can also be defined independently from the step size in the z direction and for this particular data set the step sizes in the x, y and z directions were set at 1 μm and the z range was defined as ± 5 μm from the point of focus when the cell was observed under white light illumination (set as z=0). The cell sample was imaged under immersion in a saline solution using a 50× (N.A. 0.75) water immersion objective and a 532 nm laser (100 mW). At this wavelength intrinsic Raman signals from cell components such as proteins, amino acids, lipids and DNA can be readily observed. [52, 142] There is little interference from the SERS nanotags and the cell structure can be readily elucidated.

Following data collection, false colour 3D Raman images were constructed by performing univariate data analysis based on signal to baseline maps, whereby increases in signal intensity over a defined spectral range were monitored. False colour Raman images were generated for the CH wagging of proteins and lipids (1426-1472 cm^{-1}), amino acids (1412-1425 cm^{-1}), $\delta(CH_3)_{asymm}$ and $\upsilon(COO^-)$, and specifically for the ring breathing mode of the amino acid phenylalanine (998-1008 cm^{-1}, ~1001 cm^{-1}).[52, 142] These spectral regions were selected on the basis that proteins, lipids and amino acids are found throughout the cell and in the case of proteins/lipids are integral components of the cell membrane. Any cell peak consistently found within the Raman spectra, provided that it is sufficiently intense, can be used to generate false colour

images. Of the images generated, none apart from the ring breathing mode of phenylalanine were found to delineate the cell (**Figure 4.1**).

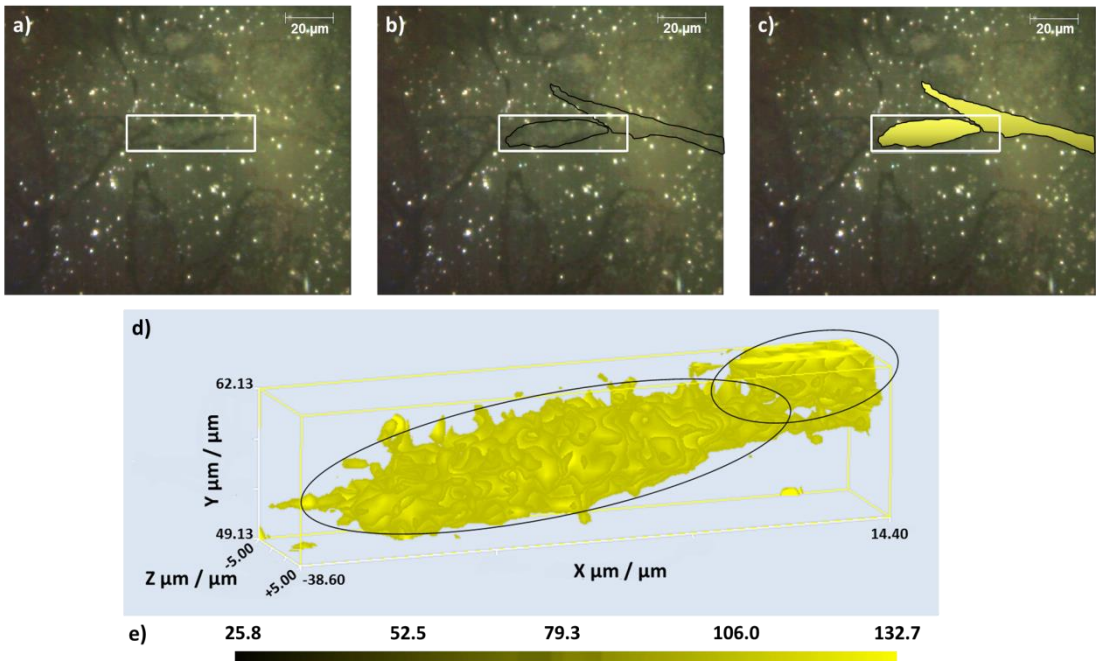

Figure 4.1: White light and false colour volume 3D Raman images of the mapped cells – a) white light image of the mapped cells, the area within the white rectangle was analysed during mapping, the cells are outlined in black in b) and the mapped cell areas are distinguished with a gradient fill in yellow in c). d) False colour 3D Raman cell image generated using the phenylalanine peak at ~1001 cm^{-1} and e) LUT colour bar. (StreamLineHR λ_{ex} = 532 nm, 100% (100 mW), spectral range 834-1681 cm^{-1}, step size x,y,z 1.0 µm, 10s).

Phenylalanine is found ubiquitously in the cell and as a result is an excellent marker for cell delineation (**Figure 4.1**). This is the first representation of a 3D Raman cell image in which no operator post processing of the individual 2D z-slices is required for the production of the final 3D image. The contouring reflects the variation in signal intensity in different regions of the cell (**Figure 4.1d**). Although the false colour image is based on the phenylalanine band (~ 1001 cm^{-1}) other spectral bands representative of general cell contents appear in the spectrum. These include the amide III protein band,[243] CH_3/CH_2 lipid twisting or bending modes,[243] CH_2CH_3 lipid deformations,[244] and amide I protein bands[243] at 1243, 1310, 1452 and 1655 cm^{-1} respectively[243, 244] (**Figure 4.2**). Although these peaks appear in the representative cell spectra they were not consistently apparent and thus could not be used to resolve the cell structure.

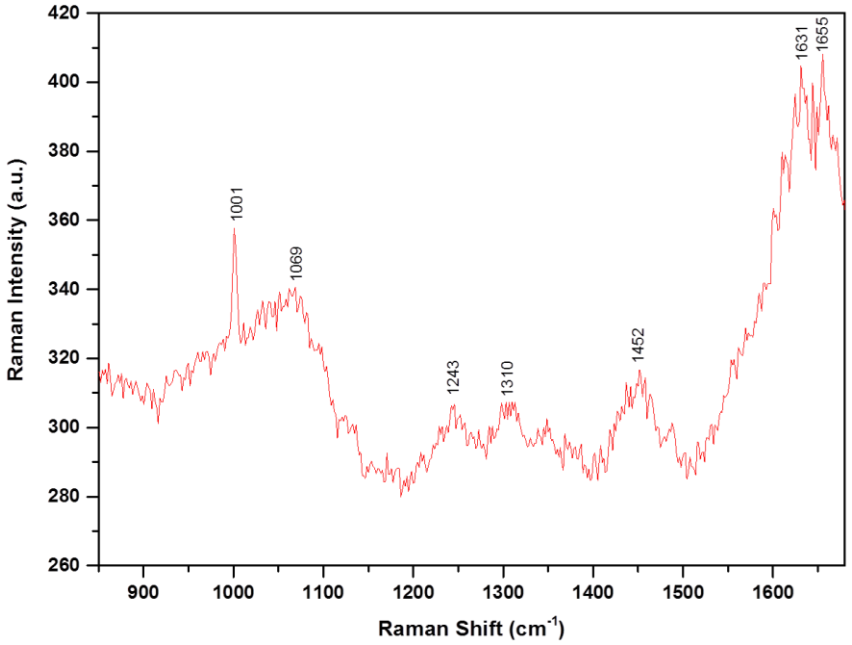

Figure 4.2: Representative Raman spectrum for the imaged cell. (StreamLineHR λ_{ex} = 532 nm, 100% (100 mW), spectral range 834-1681 cm^{-1}, step size x,y,z 1.0 µm, 10s)

4.2.3 3D SERS Imaging of Nanotags

The 3D SERS nanotag image was acquired prior to any cell data and by mapping exactly the same area as outlined for the 3D Raman cell image (**Figure 4.1a** and **Figure 4.3a**). The step sizes in the x, y and z direction were set at 1 µm and again the z range was defined as ± 5 µm from the point of focus when the cell was observed under white light illumination (set as z=0). The only difference between the two data sets was the laser line used to provide the excitation, a 633 nm laser excitation was used to obtain the SERS image. At this wavelength the signals from the small molecule reporters can be readily visualised and using the employed laser power and acquisition time intrinsic Raman signals from the cell were minimal. It should be noted that the molecules were non-resonant with the exciting laser line therefore there was no additional resonance contribution from the molecule and the signal enhancement resulted solely from their interaction with the nanoparticle surface.

Following data collection the false colour SERS nanotag image was generated by performing multivariate data analysis in the form of component DCLS. As discussed

previously (see Chapter 3) the DCLS method allows the measured solution spectra for each component to be compared directly with every data point collected during mapping analysis. If a match was found to occur between the reference and the collected data a 'false' colour was assigned in that location and each of the reference spectra were assigned to a separate false colour (**Figure 4.3**). MPY, DTNB, NBT and 2-NPT are shown in blue, green, red and magenta respectively (**Figure 4.3**).

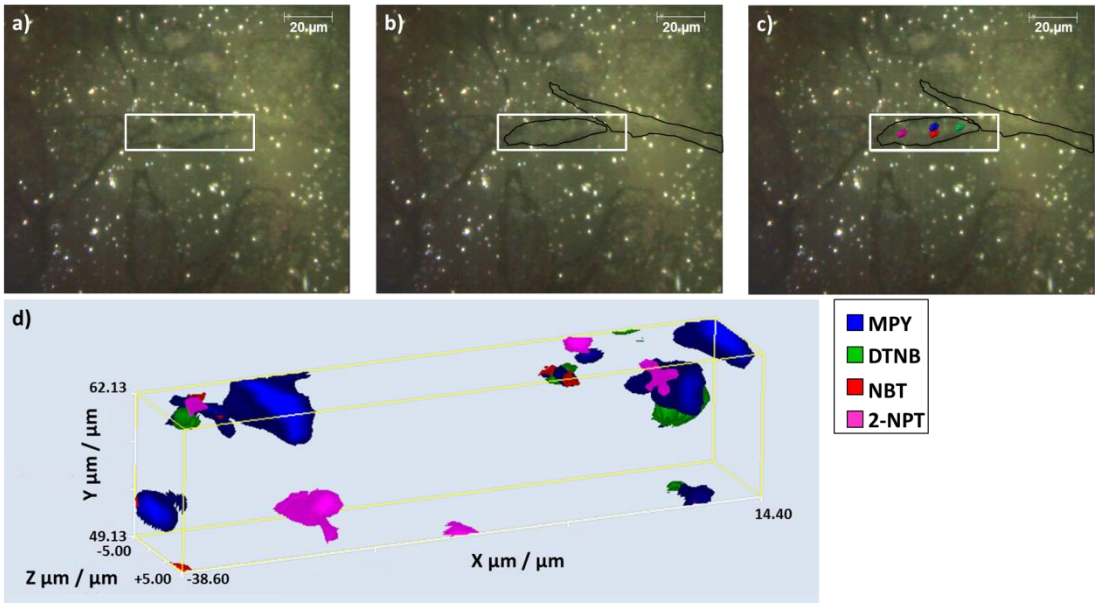

Figure 4.3: White light and false colour volume 3D SERS images of the mapped cells – a) white light image of the mapped cells, the area within the white rectangle was analysed during mapping, the cells are outlined in black in b) and the nanotags are highlighted with shapes of appropriate colour in c). d) False colour 3D SERS nanotag image generated using the solution standards for each of the individually labelled nanotags – MPY, DTNB, NBT and 2-NPT are shown in blue, green, red and magenta respectively. (StreamLineHR – λ_{ex} = 633 nm, 100% (9 mW), spectral range 936-1702 cm^{-1}, step size x,y,z 1.00µm, 0.1s).

Based on the spectral matches assigned by the component DCLS all four nanotags can be readily identified in the 3D image (**Figure 4.3**). Viewing the image in 3D however does not allow for visualisation of the spectral assignment and positive intracellular nanotag identification can only be ascertained by analysing the data in 2D (see section 4.2.3). In the 3D image the nanotags appear quite columnar and not spherical as envisaged. This may be due to the step sizes and the numerical aperture of the objective used. It was thought that the resolution could be improved by using smaller step sizes and an objective with a higher numerical aperture. There was also very little

co-localisation between the nanotags which was surprising considering the suspension applied to the cell population contained equal proportions of all four nanotags. Their occurrence in distinct spatial locations may however, be correlated to their chemical functionality and it has been demonstrated that nanoparticles/nanotags were preferentially taken up into cells in the following order - positively, negatively, unlabelled and neutrally charged species[8] (**Figure 4.3**). However, it was expected that all the nanotags would be negatively or neutrally charged under the conditions used and if a protein corona forms around the nanotags it is this surface which is presented to the cell. With these conditions it would be expected that there would be little difference in the uptake of the differently labelled nanotags.

4.2.4 Combined 3D Raman and SERS Imaging of SERS Nanotags in Cells

Whilst it is possible to collect individual 3D Raman and SERS images separately they provide no evidence of cellular uptake or allow for definitive nanotag identification. In order to confirm uptake it was necessary to combine the two data sets (**Figure 4.4**) and this was possible because they had been collected from exactly the same area and volume. The corresponding z-slices from both data sets were extracted and combined in both 2 (**Figure 4.5**) and 3 dimensions (**Figure 4.6**). The 2D slices were extracted directly from the Volume Viewer software and they were combined by overlaying the two images using a GNU image manipulation programme. The images can be directly overlaid because they were taken from exactly the same area and were exactly the same size. The individual 2D slices were also combined in Volocity to generate the 3D image. The relevant intracellular z-slices were ascertained by viewing the 3D volume cell map along the z-direction. From this angle the only z-slices which were of relevance were z-slices +1.00 to -2.00. When viewed in this way the width of the cell can be observed and the z-slices within the middle of the cell can instantly be determined.

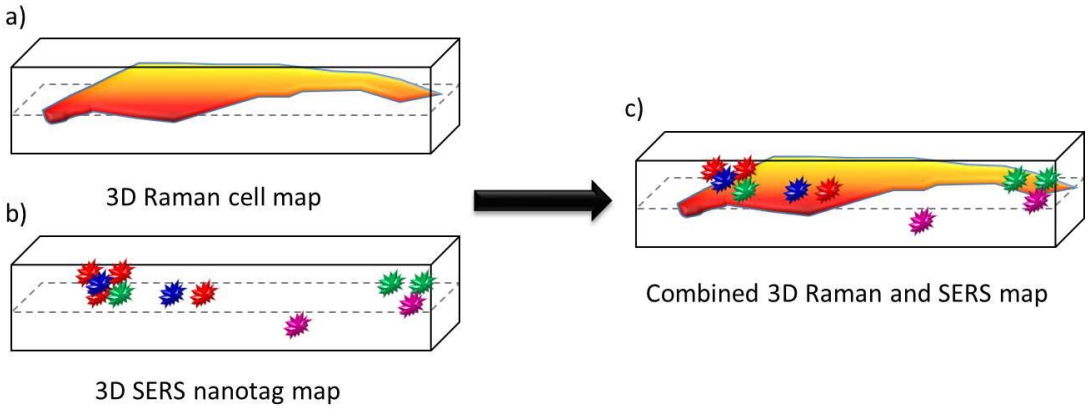

Figure 4.4: Schematic illustrating how the two data sets are combined. a) Schematic of volume 3D Raman cell map, b) schematic of volume 3D SERS nanotag map and c) combined 3D volume Raman cell and SERS nanotag map.

On the basis of the combined z-slices alone it was apparent that MPY and 2-NPT labelled nanotags can be observed in all of the relevant z-slices (**Figure 4.5 a-d**). 2-NPT appears to be located intracellulary in all four z-slices whilst MPY appears on the periphery of the larger cell and within the smaller cell which has been mapped. NBT and DTNB tags were observed intracellularly in z-slice +1.00 and 0.00 and z-slice 0.00 respectively (**Figure 4.5 a-b**). There was also a degree of non-specific binding which was apparent in all of the z-slices. This was to be expected to a certain degree since the nanotags were not functionalised with any specific targeting moiety. The nanotags which were located intracellularly can also be visualised (**Figure 4.6**) and non-specific binding was also apparent in this image (**Figure 4.6**).

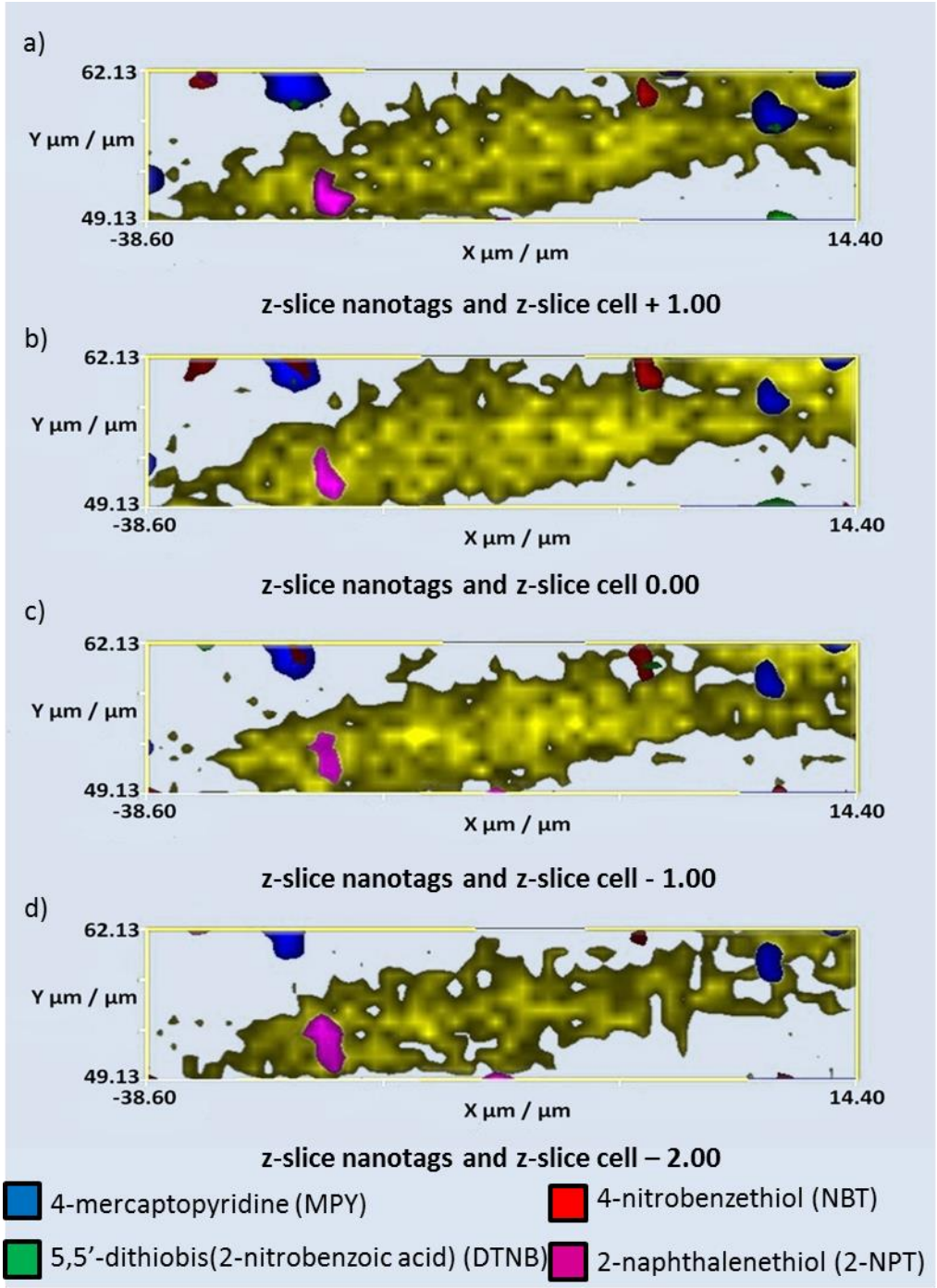

Figure 4.5: Images from each plane of the 3D volume Raman cell and SERS nanotags maps can be extracted and these can be combined in 2D – a) z-slice nanotags and cell +1.00, b) z-slice nanotags and cell +0.00, c) z-slice nanotags and cell -1.00 and d) z-slice nanotags and cell -2.00. MPY, DTNB, NBT and 2-NPT are shown in blue, green, red and magenta respectively.

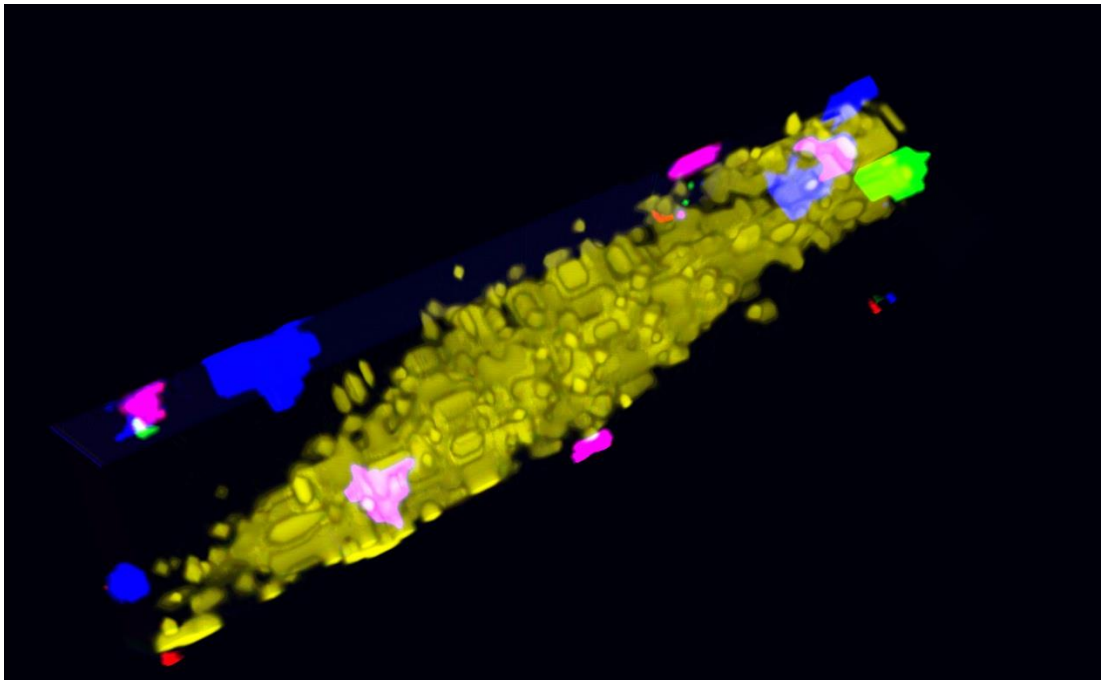

Figure 4.6: Combined 3D volume Raman cell and SERS Nanotag map generated by combining the individual 2D slices in Volocity.

Although the component DCLS has assigned matches in the highlighted locations (**Figure 4.5**) it was necessary to view the data on moveable plane slices within the volume. When viewed in this way the corresponding spectrum for a selected position was displayed and this can be extracted and compared alongside the reference spectrum. This allows the operator to check the spectral assignment and make any adjustments such as increasing the limits so that the false colours are representative of the nanotags found within a specified location.

Analysis of z-slice +0.00 where all four nanotags were located revealed a good spectral fit for MPY labelled nanotags (**Figure 4.7a, b and d**). The MPY unique identification peak at ~1004 cm^{-1} was visible. There was a reasonable fit for the NBT labelled nanotags and the unique identification peak for NBT at ~1078 cm^{-1} was visible. However, some peaks were absent from the NBT spectra most notably the peak ~1333 cm^{-1}. The reasons for this absence were unclear but it is possible that the intracellular environment,[245] depending on the location of the nanotag, selectively enhances or diminishes certain peaks. Such spectral changes are often apparent with pH sensitive

molecules such as MBA or MPY, where depending on the pH, the molecules can be protonated or unprotonated and give rise to different spectral signatures.

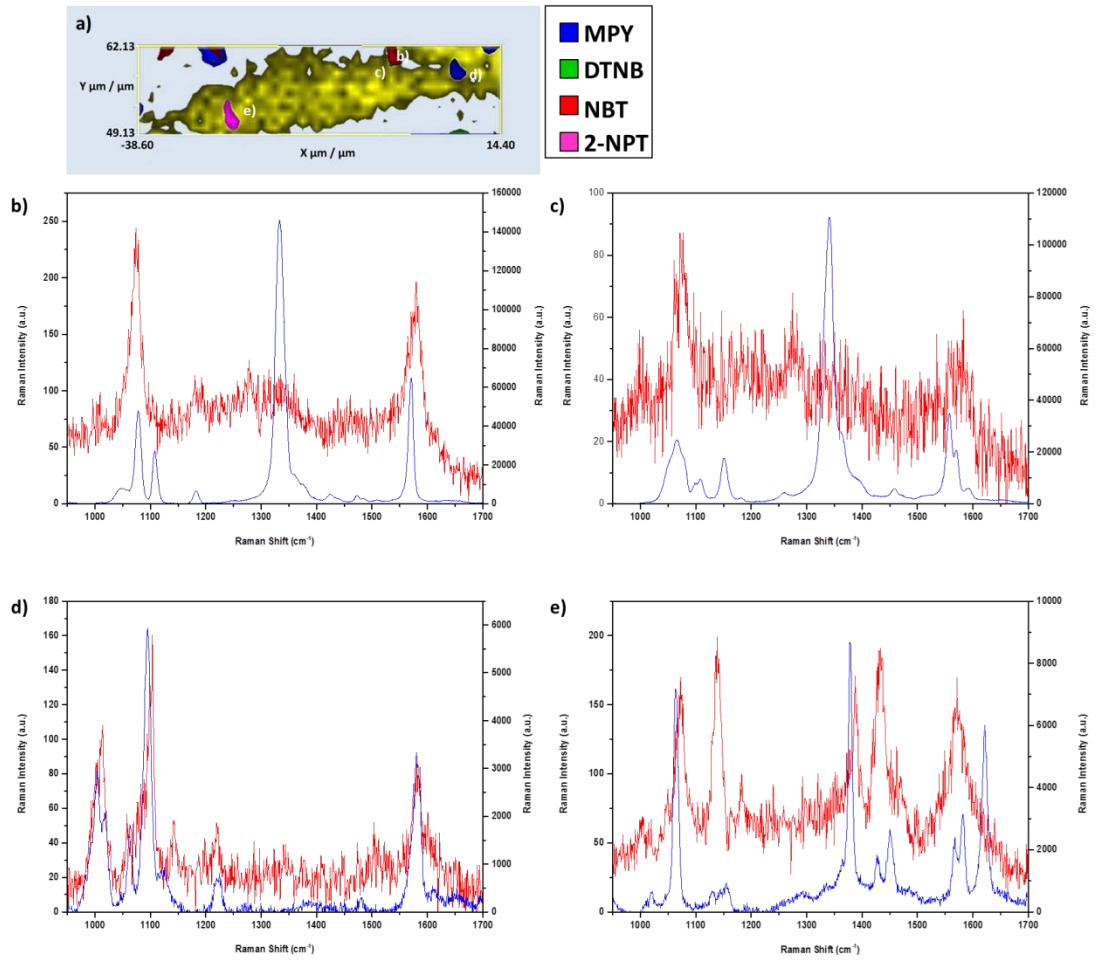

Figure 4.7: z-slice 0.00 and the corresponding spectral assignments for each of the labelled nanotags. a) False colour image for z-slice 0.00, spectral assignments for b) NBT, c) DTNB, d) MPY and e) 2-NPT. MPY, DTNB, NBT and 2-NPT are shown in blue, green, red and magenta respectively. The cell spectrum is plotted on the primary y-axis and the reference on the secondary y-axis.

Similarly, spectral variations both in terms of intensity and frequency can also be observed depending on how the molecule orientates itself on the surface of a nanoscaffold. This can give rise to different spectral signatures and the enhancement of certain vibrational modes[246] It was also possible that these bands were enhanced cell bands hence the poor spectral fit with the reference spectra. In order for this situation to arise the small molecules would have had to desorb from the surface in order to

allow the native cellular constituents access to the metal surface. As discussed in Chapter 3 no intrinsic cell signals were observed in the control samples but there was always a possibility that some cell bands might be enhanced.

The spectral fit for DTNB and 2-NPT nanotags was poor (**Figure 4.7a, c and e**). Representative spectra assigned as a good fit for DTNB (**Figure 4.7c**) were similar to that assigned to NBT (**Figure 4.7a**) and this may be due to the problems associated with differentiating between the two labels. During a separate statistical study into developing a multiple component system with a greater number of reporters multivariate curve resolution-alternating least squares (MCR-ALS) suggested that might it be difficult to distinguish between NBT and DTNB (data not shown). The fact that the two labels (NBT and DTNB) always have a close proximity to each other in the false colour image would further suggest that this was the case. However, this study was completed at a later date than the 3D analysis and provided that their unique peaks feature in the spectrum it should be possible to differentiate between the two. The assignment of representative spectra for 2-NPT was based on spectral matches at ~1426 and ~1566-1582 cm^{-1} but the overall fit was very poor and would suggest that some operator supervision was required for positive intracellular identification of the nanotags. This involved increasing the limits on the LUT so that the assigned false colours were representative of regions where a good spectral match occurred between the measured and the reference spectrum.

The data was subject to further operator supervision and based on this it can be confidently concluded that only MPY nanotags were located intracellularly (**Figure 4.8**). This was determined in the usual two-fold manner from their unique peak and DCLS multivariate analysis (**Figure 4.7d**). MPY was identified from its unique peak at ~1004 cm^{-1} and in addition to this there was a good spectral fit between the MPY reference spectrum (blue trace) and the signal measured from within the cell (red trace) (**Figure 4.7d**).

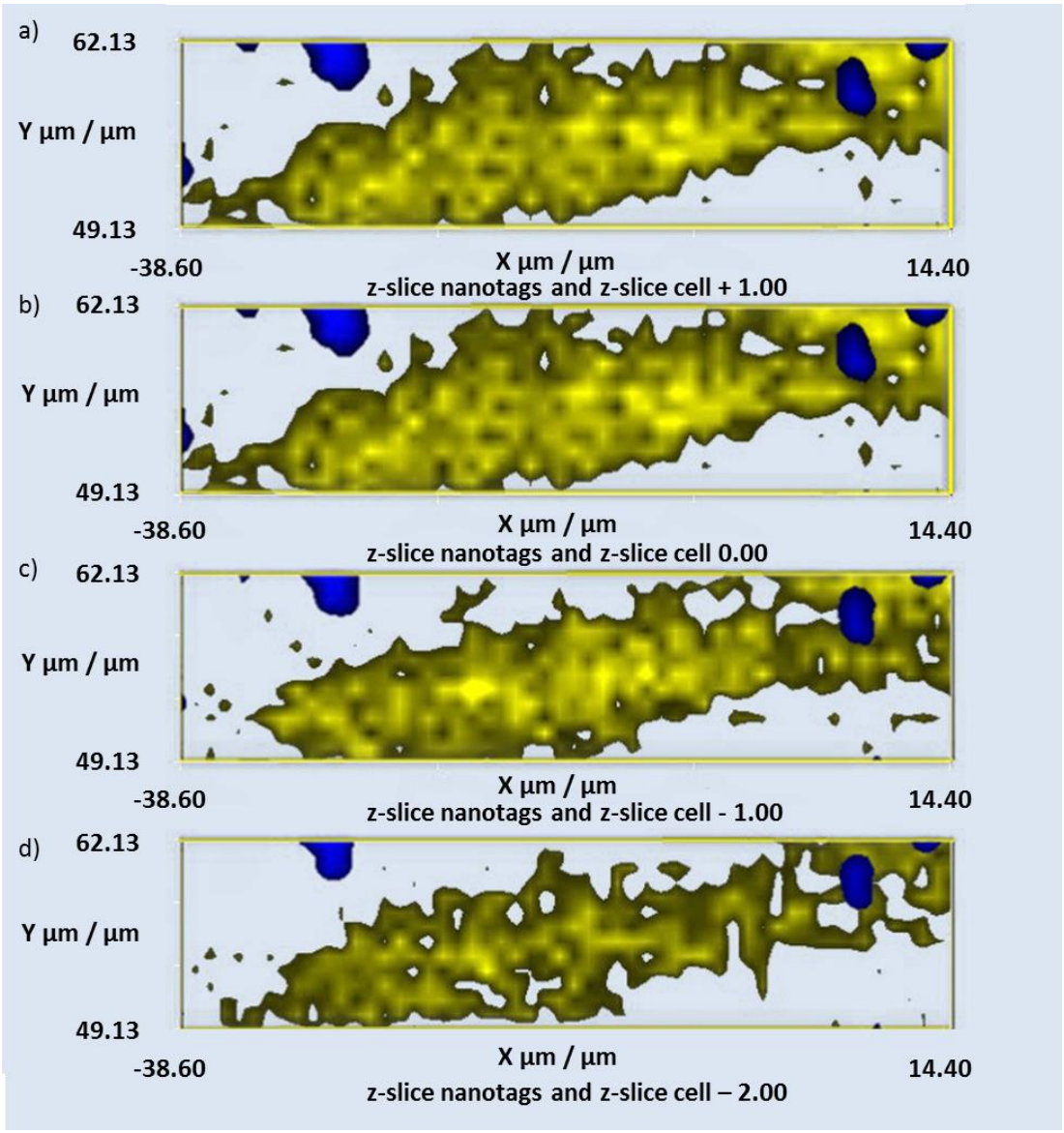

Figure 4.8: Images from each plane of the 3D volume Raman cell and SERS nanotags maps after operator supervision. Individual z-slices can be extracted and these can be combined in 2D – a) z-slice nanotags and cell +1.00, b) z-slice nanotags and cell +0.00, c) z-slice nanotags and cell -1.00 and d) z-slice nanotags and cell -2.00. MPY was shown in blue.

Although only one nanotag was located intracellularly this proof-of-concept data set was invaluable for several reasons. It demonstrated that it was possible to image cells and SERS nanotags in 3D and these images represent the first 3D images of their kind. Whereby, no operator post processing of individual 2D z-slices was required for the production of the final 3D image. Provided that data was collected from the same area

and same volume, it was possible to combine the two data sets in both 2 and 3 dimensions. Combining the data in this way permitted non-destructive evidence of cellular uptake whilst simultaneously permitting the identification of the SERS nanotags.

4.3 Confocal 3D Raman and SERS Imaging of Cells and Nanotags

Despite the advantages demonstrated by the proof of concept data set the resolution of the nanotags was poor as was the signal strength. This data set also provided no indication of the localisation of the nanotags in relation to any major cell organelle. In an effort to improve the image quality a number of steps were taken. Firstly a microscope objective with a higher numerical aperture (60× - N.A. 1) was employed, since this concomitantly resulted in an increase in the one half angular aperture, allowing for the collection of light from a wider angular range and thus resulting in the production of higher resolution images. The calculated theoretical values for the spatial and depth resolution also increased under these conditions (see section 4.2.1). When imaging the cells by Raman using a 532 nm laser, the spatial resolution increased from 0.43 to 0.32 μm whilst the depth resolution increased from 5.03 to 2.83 μm. Similarly, when analysing the nanotags, using a 633 nm laser, the spatial resolution increased from 0.51 to 0.39 μm whilst the depth resolution increased from 5.99 to 3.37 μm. The step sizes in the x and y directions (0.8 μm and 0.5 μm *c.f.* 1.00 μm) were reduced for both the cell and the nanotag map in an effort to gain more detailed information again with higher resolution. As well as these improvements made to the data collection, the data was also analysed by multivariate methods to determine if there were any spectral variations which could be ascribed to specific cell organelles. [247] Multivariate data analysis methods were also applied to the previous data set but because of the weak cell signals and poor resolution no significant differences were found to occur. In addition, the nanotags in this data set were pegylated according to the standard protocol (see section 8.4.2) and this may have aided in the uptake of the nanotags into the cell.

4.3.1 3D Raman Imaging of Cells

As with the previous data set, a multiple component positive cell was initially identified by mapping in 2D and 3D. The sample was then analysed by depth profiling to

determine a rough indication of the cell thickness and the z-range from which z-slices should be collected. The 3D Raman cell image was then collected by mapping the area highlighted within the red rectangle (**Figure 4.9a-c**). The sample was imaged under immersion in a saline solution using an Olympus 60× (N.A. 1) water immersion objective and a 532 nm (100 mW) laser excitation. For this particular data set the step size in the x and y directions were set at 0.8 μm and in the z direction it was set at 1 μm. The z-range was defined as ±3 μm from the point of focus when the cell was observed under white light illumination (set as z=0). However, when the volume 3D cell map was collected it was found that only certain z-slices were of relevance. This was ascertained by viewing the 3D volume cell map along the z-direction. From this angle it was apparent that the spectra from above z-slice +2.00 and below z-slice +0.00 were not of relevance. In light of this the 3D cell map was recollected from z-slice +2.00 to +0.00.

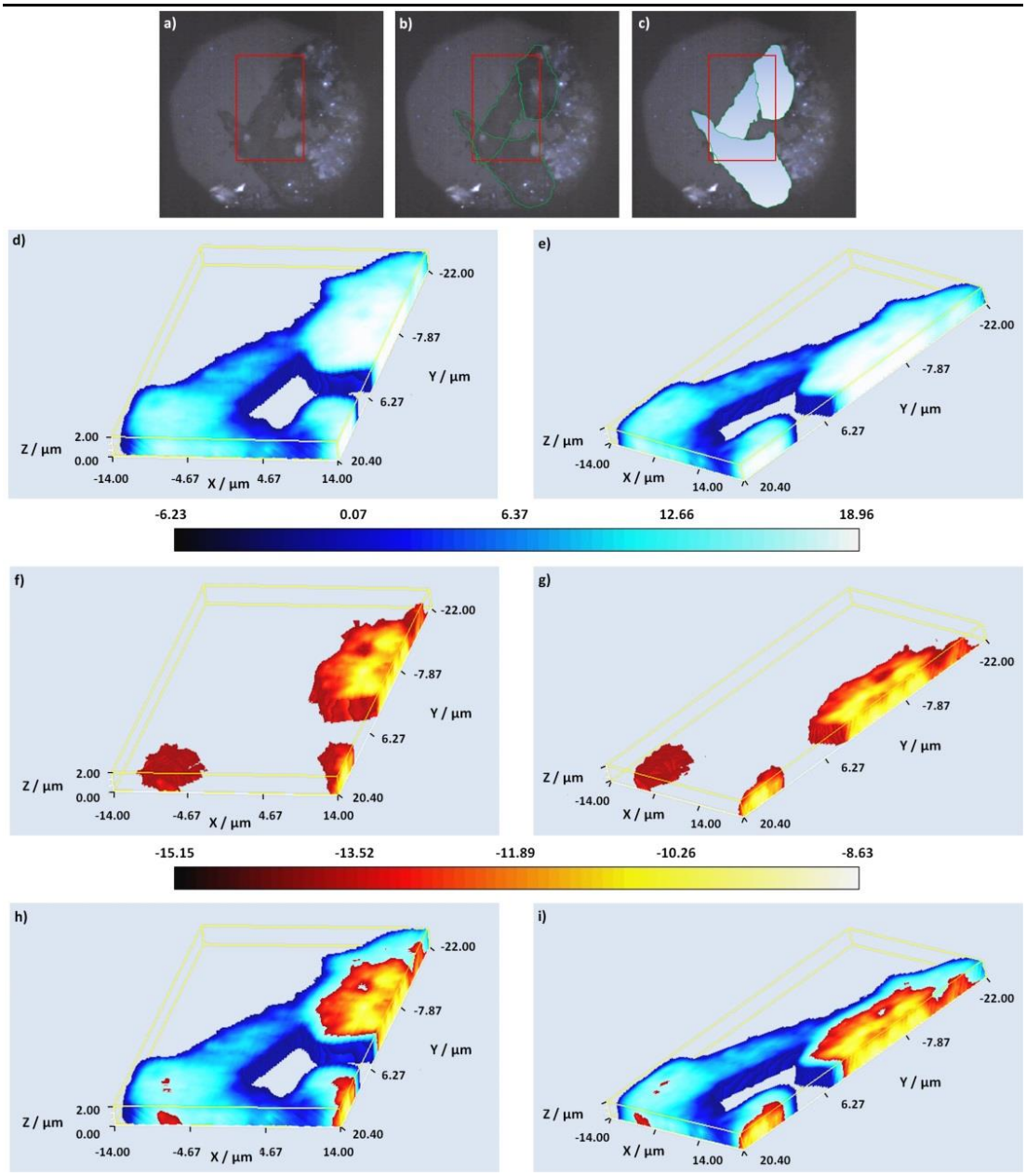

Figure 4.9: White light and false colour volume 3D Raman images of the mapped cells - a) white light image of the mapped cells, the cells are outlined in green in b) and the mapped cell areas are distinguished with a gradient fill in blue in c). In a)-c) the red box indicates the complete 3D Raman analysed area. d)-e) False colour 3D Raman cell image generated using PC2 displayed at different angles. f)-g) False colour 3D Raman nuclei image generated using PC1 displayed at different angles. h)-i) Combined false colour 3D Raman cell and nuclei images presented at different angles. In d)-g) the false colour scale bar is shown below the images. (StreamLineHR - λ_{ex} = 532 nm, 100% (100 mW), spectral range 743-1600 cm^{-1}, step size x,y 0.8 µm and z 1.0µm, 2s).

Following data collection, the false colour Raman 3D images were constructed by initially performing univariate analysis based on signal to baseline maps. As with the previous data set a signal to baseline map was generated specifically for the ring breathing mode of the amino acid phenylalanine (998-1008 cm-1, ~1004 cm^{-1})[52, 142] and this was found to clearly define the cell structure (data not shown). No other cell signals were found to be sufficiently intense to delineate the cell or resolve any major cell organelle. In an attempt to determine the localisation of the SERS nanotags in relation to the cell organelles principal component analysis (PCA – normalised, not mean centred) was applied to determine if there were any spectral variations, which could be ascribed to specific cell organelles.[247] The PCA conditions included spectrum centring and normalisation. Mean centring was not applied since the band positions were sufficiently different to distinguish the two PC's chemically (**Figure 4.10b and d**). The main advantages of the conditions are that the loadings reflect the baseline offset, the background and the appearance of a typical spectrum.

For the analysed cells two principal components (PCs) explained 86.5% of the variance in the data with PCs 1 and 2 representing the cell contents (**Figure 4.10**). Analysis of the PC loadings (**Figure 4.10d**) and the band assignments (**Table 4.1**) revealed that PC2 was collectively characterised by Raman bands which could be attributed to protein, lipid and nucleic acids but most notably by peaks at 1004 cm^{-1}, 1245cm^{-1} and 1451 cm^{-1} assigned to phenylalanine,[243, 248] the amide III (protein) band[249] and the CH_2CH_3 deformation of protein and lipid.[244] PC2 therefore represents the general cellular regions and this was consistent with the raw Raman spectra (**Figure 4.10c**). As with the signal-to-baseline map generated for the ring-breathing mode of phenylalanine PC2 clearly defines the structure of the mapped cells (**Figure 4.9d, e, h and i**).

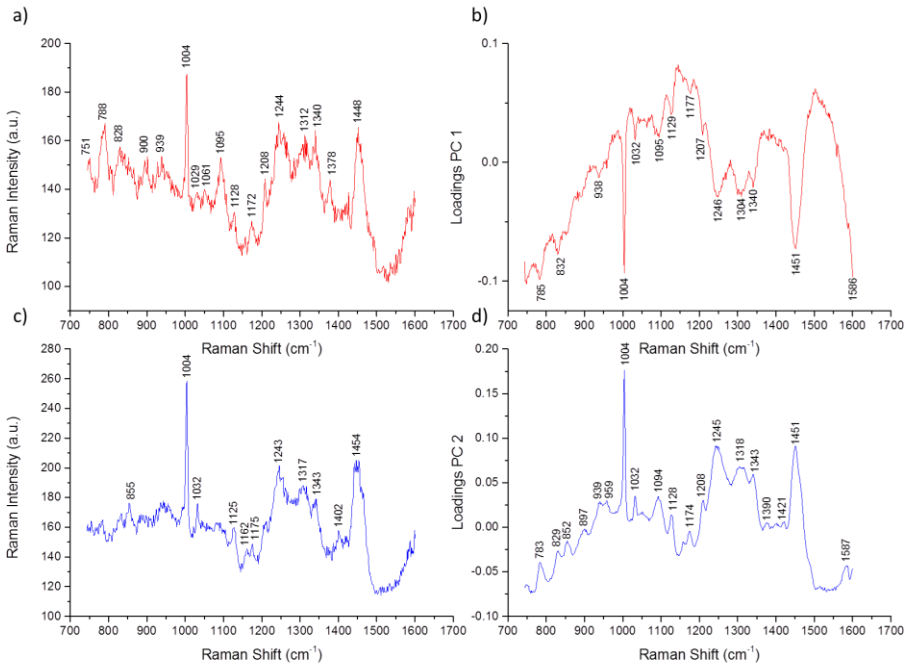

Figure 4.10: Representative Raman spectra and the corresponding PC loadings for the cells and the nuclei. a) A representative Raman spectrum measured from the nuclei, b) PC 1 loadings which distinguishes the nuclei, c) representative Raman spectrum measured from the cells and d) PC 2 loadings which distinguishes the cells.

Table 4.1: Peak position and tentative assignments of the main peaks found in the principal component (PC) loadings for each PC shown in the volume 3D map.[52, 243, 244, 248-256]

Peak position (cm^{-1})	Assignment
783	DNA
785	νO-P-O stretch DNA
829	O-P-O stretch DNA/RNA
	ring breathing tyrosine
832	tyrosine, ν_{asym}OPO
852	proline/tyrosine
897	-
938/939	νC-C, peptide
959	-
1004	phenylalanine
1032	CH_2CH_3 collagen and phospholipids, phenylalanine
1094/1095	DNA, νC-N lipid
1128	C-N (proteins), C-O (carbohydrates)
1174	phenylalanine, tyrosine
1177	tyrosine, cytosine, guanine
1207/1208	phenylalanine
1245/1246	amide III
1304	CH_2 deformation (lipid) adenine/cytosine
1318	guanine (DNA/RNA)
1340	-
1421	adenine, guanine ring breathing modes of DNA/RNA
1451	CH_2CH_3 deformation
1586/1587	phenylalanine

In contrast to PC2, the PC1 domain contains negative scores and is thus characterised by negative peaks in the loadings. PC1 is characterised by a combination of peaks which can be ascribed to nucleic acids, nucleotides, amino acids and protein. These peaks include phenylalanine peaks at 1004cm^{-1} [52, 243, 248] and the CH_2CH_3 deformation of protein at 1451 cm^{-1} (**Figure 4.10b** and **Table 4.1**).[244] The PC loadings therefore suggest that PC1 represents domains which were biochemically distinct from the main cell structure and based on the loadings it was proposed that PC1 represents the cell nuclei

(**Figure 4.9f-i**). This assignment was consistent with the raw Raman spectra from the nuclei, specifically the DNA peaks at 751 cm^{-1} and 788 cm^{-1} (**Figure 4.10a** and **Table 4.1**).[250, 251] When PC1 and PC2 were combined they were found to delineate the general cell contents and the nuclei (**Figure 4.9h, i**). This data set highlights how PCA can be used to delineate cell organelles from the main cell structure.

4.3.2 3D SERS Imaging of Nanotags

The 3D SERS nanotag image was collected prior to the collection of any cell data and by mapping exactly the same area as previously outlined (**Figure 4.9 a-c**). The step sizes in the x and y direction were set at 0.5 µm and 1 µm in the z direction. The z range was defined as ± 3 µm from the point of focus when the area was viewed under white light illumination. The false colour SERS 3D images were constructed by performing multivariate data analysis in the form of component DCLS. In contrast to the previous data set, where the nanotags appeared quite columnar and large (**Figure 4.3**), the nanotags in this image were well resolved and spherical (**Figure 4.11**).

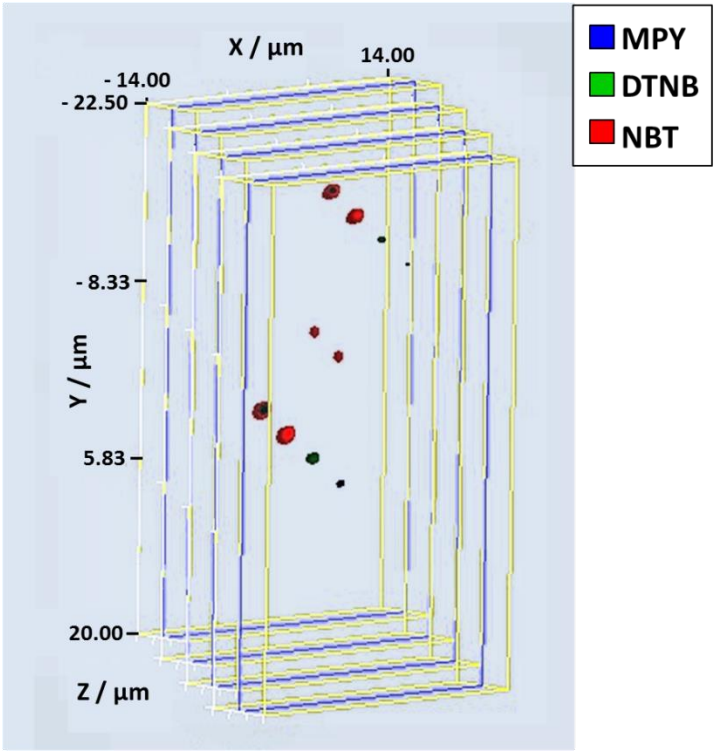

Figure 4.11: False colour 3D SERS nanotag image generated using the solution standards for each of the individually labelled nanotags. The rear rectangle is the complete false colour SERS nanotag image, the consecutive rectangles show each of the individual false colour images and

are shown for NBT (red), DTNB (green) and MPY(blue) respectively. (StreamLineHR - λ_{ex} = 633 nm, 1% (0.09 mW), spectral range 934-1720 cm^{-1}, step size x,y 0.5 μm and z 1.0μm, 0.5s)

In this data set the nanotags were not found in discrete locations but instead were found to co-localise together. A degree of co-localisation was to be expected since equal proportions of the nanotags were in the suspension applied and it was speculated that they would be taken up together. This co-localisation was attributed to the improvement in objective and the smaller step size used, since both allow for more highly resolved images to be obtained. This co-localisation may also be due to the pegylation of the nanotags. The PEG molecule is quite large (MW=5000) and it may surround the reporter molecule such that it is the PEG molecule which is presented to the cell surface rather than the reporter functionality.[11] This would explain why all three nanotags are co-localised within a single location.

In accordance with the co-localisation observed it was necessary to show the data in 'exploded' form so that each of the individually labelled nanotags could be visualised (**Figure 4.11**). In the back rectangle the complete false colour SERS map image is shown for all nanotags visually present within a specified location. The successive false colour SERS map images then show the localisation of the NBT, DTNB and MPY labelled nanotags respectively. In both of the collected data sets 2-NPT was not found intracellulary. The reasons for this are unclear but if 2-NPT has a propensity to remain extracellulary the possibility of using this nanotag as an external standard exists. 2-NPT labelled nanotags tend to be larger in size than the other labelled nanotags (**Figure 3.30**) which might explain why it was not located intracellularly however, this increased size was not thought to prohibit cell uptake.

4.3.3 Confocal Combined 3D Raman and SERS Imaging of SERS Nanotags in Cells

The two independently collected 3D data sets were then combined in 2 dimensions for the determination of cellular uptake and multiple component detection (**Figure 4.12**). As stated previously the z-range was defined as ± 3 μm from the point of focus for the nanotag map but the data was recollected from +2.00-0.00 for the cell map. Despite this it was still possible to combine the relevant z-slices in 2D to ascertain cellular uptake and the combined cell and nanotag z-slices are presented in **Figure 4.13**. The x,y step

size in the cell map was set at 0.8 µm and in the nanotag map it was set at 0.5 µm. As a result of the smaller step size used (0.5 µm *cf.* 0.8 µm) the SERS image was collected at 0.5 µm higher in the y direction than the Raman cell image. In order to account for this 0.5 µm discrepancy the SERS image was offset from the Raman image by 0.5 µm and this was accurately determined by pixel count.

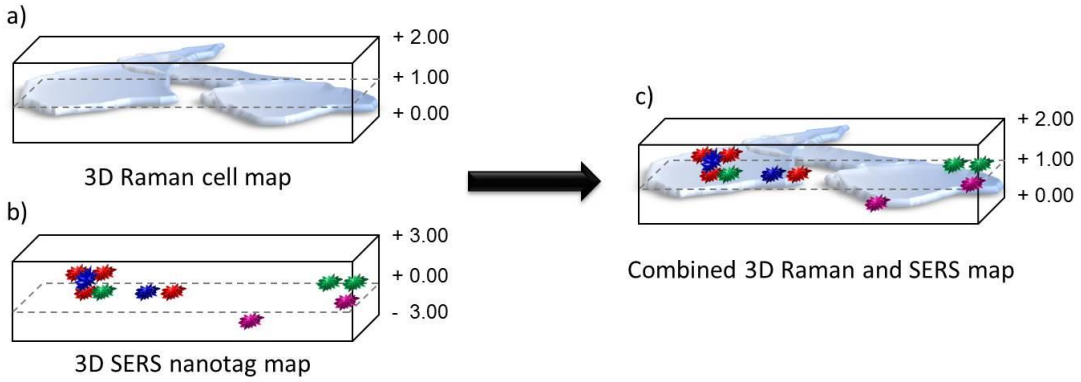

Figure 4.12: Schematic illustrating how the two data sets are combined. a) Schematic of volume 3D Raman cell map, b) schematic of volume 3D SERS nanotag map and c) combined 3D volume Raman cell and SERS nanotag map.

On close inspection of the combined z-slices we can instantly determine that three out of the four nanotags – MPY, DTNB and NBT labelled nanotags, which are shown in blue, green and red respectively, within the multiple component suspension are located within cells (**Figure 4.13**). In z-slice +2.00 only NBT labelled nanotags were observed (**Figure 4.13a**) whilst in z-slice +1.00 only NBT and DTNB labelled nanotags were found (**Figure 4.13b**) and in z-slice +0.00 three out of the four nanotags, MPY, DTNB and NBT, were observed. (**Figure 4.13c**).

On the basis of these images (**Figure 4.13a-c**) it is quite difficult to observe the three nanotags located within the cells because of the co-localisation observed and because the false colours have been set to reflect the spectral intensity measured. In theory, co-localisation may be expected since the suspension applied to the cell population contained equal proportions of the four individually labelled tags which were well mixed. Thus there was an equal probability of each nanotag within the suspension being internalised simultaneously. In terms of the false colours these could have been

enhanced to facilitate discrimination between the three nanotags but this would not have been representative of the measured SERS response.

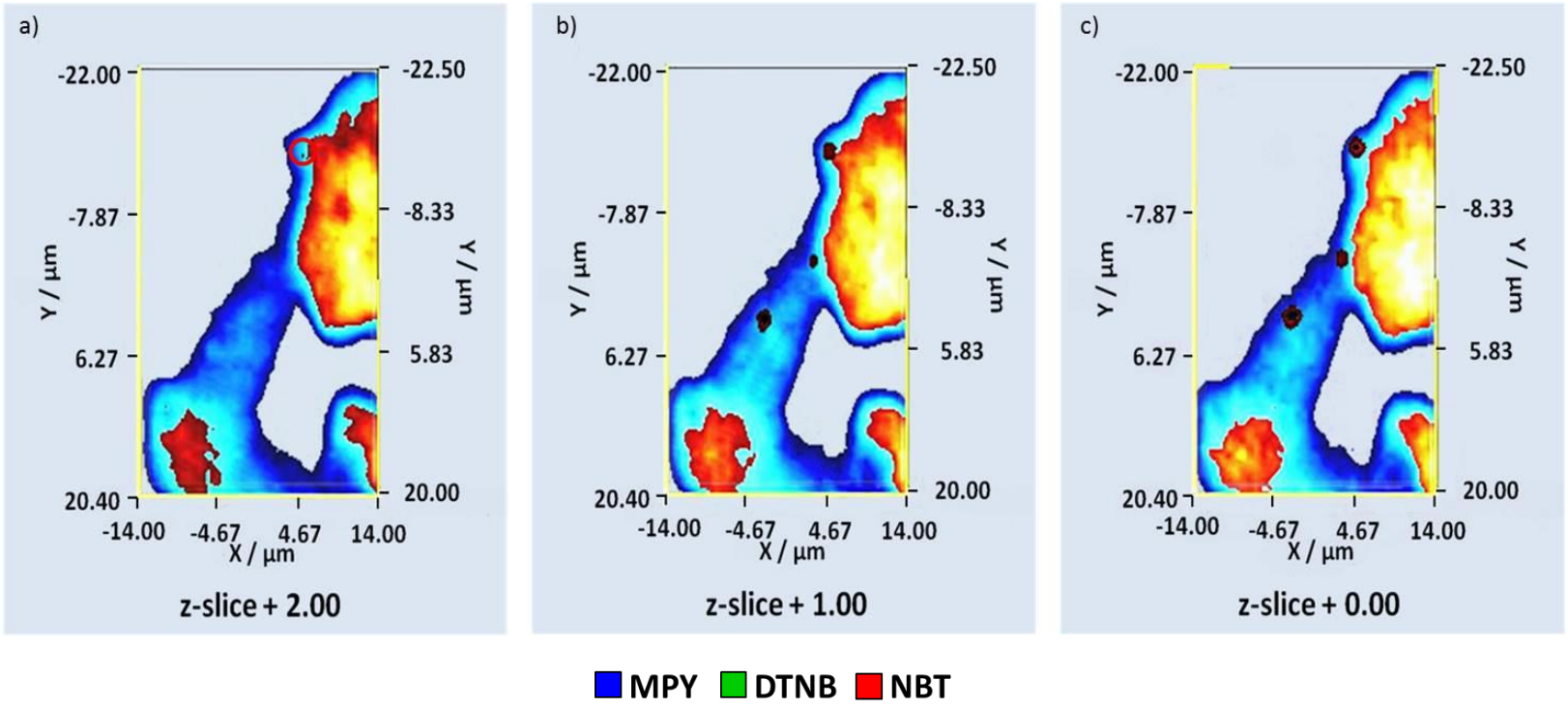

Figure 4.13: Images from each plane of the 3D volume Raman cell and SERS nanotag maps can be extracted and these can be combined in 2D – a) z-slice nanotags and cell +2.00, in this z-slice the signal is considerable weaker than those obtained from the other z-slices and as such the corresponding false colour is considerably smaller hence it is highlighted with an appropriately coloured circle, b) z-slice nanotags and cell +1.00 and c) z-slice nanotags and cell +0.00. MPY, DTNB, NBT labelled nanotags are shown in blue, green and red respectively.

In order to observe the three individually labelled nanotags, z-slice +0.00 has been enlarged (**Figure 4.14a-c**). The three nanotags were found in both the top and bottom spot of z-slice +0.00 but again because of the co-localisation and the false colour settings it remains quite difficult to see all three within the top spot. However, in the bottom spot all three can be clearly visualised.

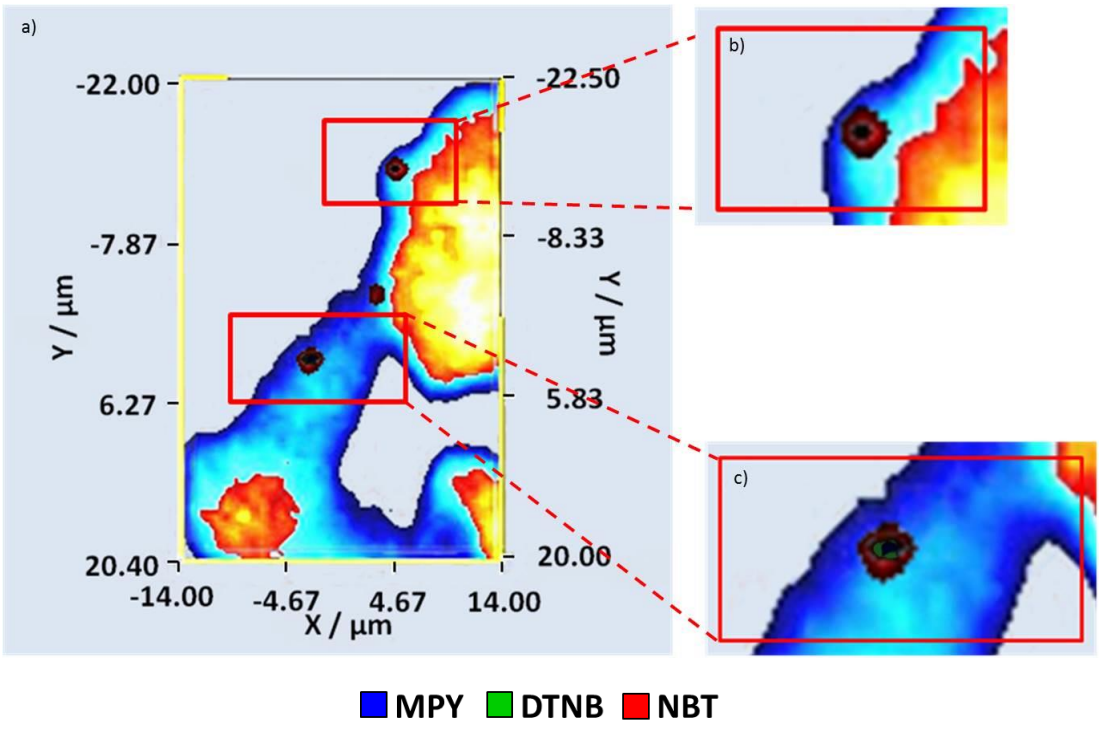

Figure 4.14: Enlarged image of z-slice +0.00 – a) 2D z-slice nanotags and cell +0.00, b) and c) enlarged areas from the top and bottom clusters respectively, z-slice +0.00 which shows three of the four nanotags within a single area and a single cell.

Each of the components was identified by their unique peak and component DCLS analysis. Unique peaks were found at ~1004 cm^{-1}, 1150 cm^{-1}, 1084cm^{-1} and 1450 cm^{-1} or ~ 1620cm^{-1} for MPY, DTNB, NBT and 2-NPT respectively. As discussed earlier the component DCLS assigns a false colour if a match was found to occur between the reference spectra and the collected data. This requires a degree of operator supervision and in order to further confirm the spatial positioning of the components, the data was viewed on moveable plane slices within the volume. When viewed in this way the corresponding spectra for a selected position were also displayed and these can be extracted and visually compared with standard spectra from the nanotag suspensions.

For z-slice +0.00 representative SERS spectra were extracted for each of the three locations where the nanotags were found (**Figure 4.15b-d**). In accordance with the co-localisation observed cumulative SERS signals concomitantly arise from the nanotags. That is, we observe SERS signals from all of the nanotags which are found within a specified location (**Figure 4.15b-d**). In all instances the unique peak for the appropriate nanotag has been labelled with the corresponding abbreviation and peak position and the minor peaks have also been tentatively assigned to a small molecule reporter and labelled with an asterisk of corresponding colour (**Figure 4.15b-d**). For the top spot in z-slice +0.00 MPY, NBT and DTNB were identified at ~1006 cm^{-1}, 1081cm^{-1} and ~1158 cm^{-1} respectively. In the top cluster DTNB makes more of a contribution to the shoulder ~ 1150 cm^{-1} but it has been identified at ~ 1158 cm^{-1} since it is reasonable to assume that some peak shifting occurred. For the middle spot, NBT was identified at ~1079 cm^{-1}. Contributions from MPY and DTNB labelled nanotags were also identified in the middle spot however these were masked by the red NBT false colour and the NBT labelled nanotags gave rise to the predominant signals in this region. MPY, NBT and DTNB were identified at ~1009 cm^{-1}, ~1079 cm^{-1} and ~1147 cm^{-1} in the bottom cluster. 2-NPT was also identified at ~1445 cm^{-1} in the bottom spot although no false colour has been assigned to 2-NPT at that particular location. As this failed to meet the two fold identification criteria this assignment to 2-NPT was very tentative.

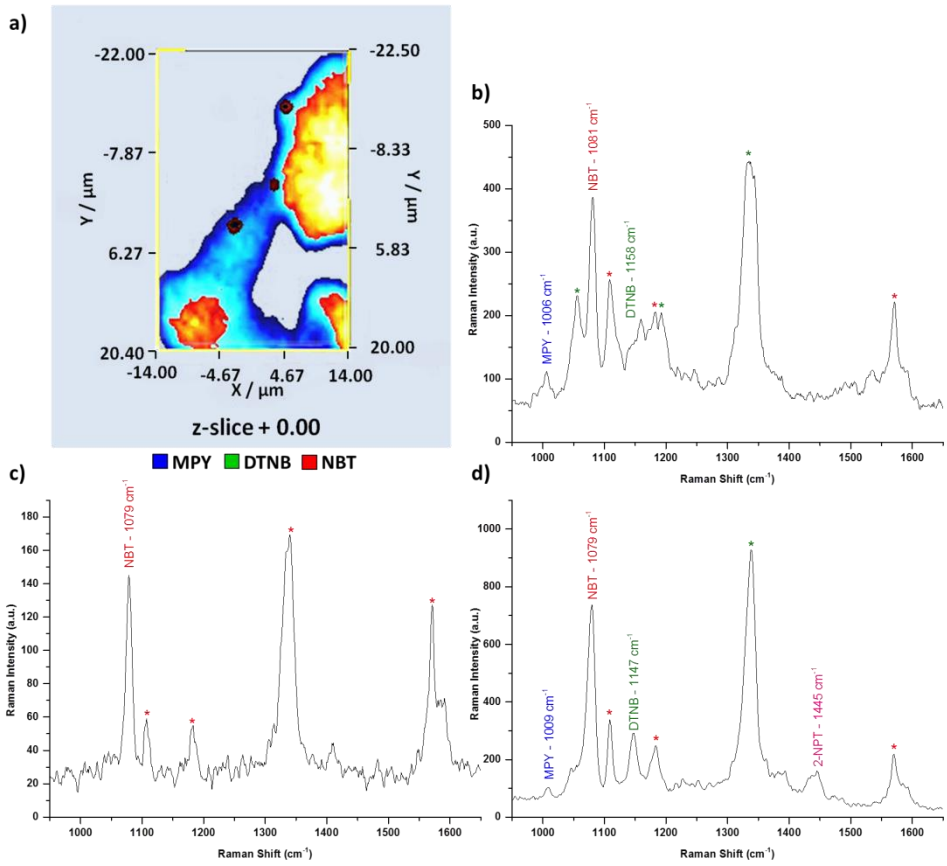

Figure 4.15: a) Enlarged image of z-slice +0.00 and representative SERS spectra obtained for the b) top, c) middle and d) bottom false colour clusters.

The contribution, each of the individually labelled nanotags made to the cumulative cell signals in the top and the bottom spot is also shown (**Figure 4.16**). The signals from the two locations vary but this was to be expected and will be dependent on the contribution each of the individually labelled nanotags make in the specified location.[9]

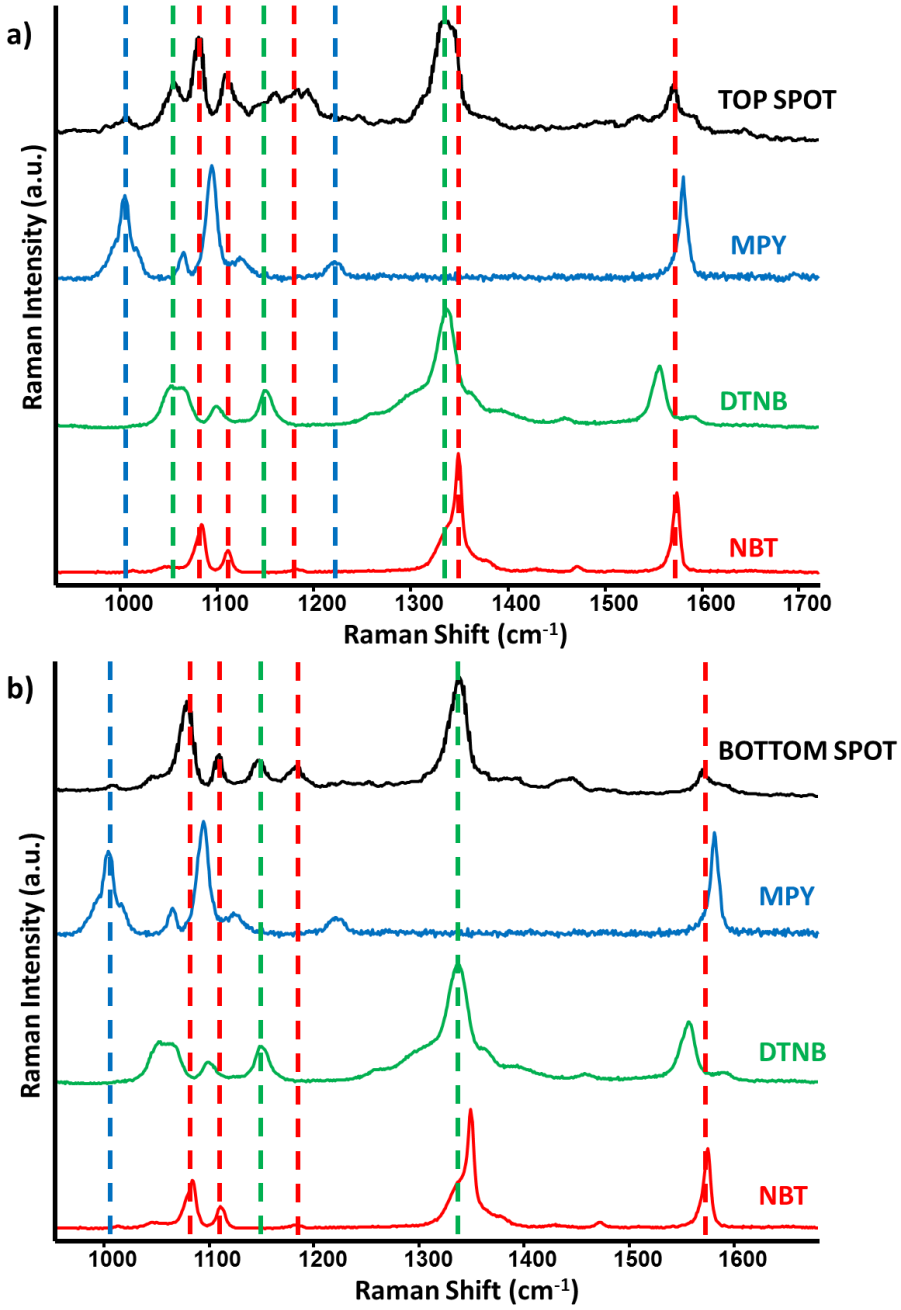

Figure 4.16: The contribution each of the individually labelled nanotags make to the cumulative SERS signal – a) cumulative signal from the top spot and b) cumulative signal from the bottom spot.

Some peak shifting was observed when the cell spectra were compared with the solution standards. For example, the unique identification peak for NBT was found at ~1084 cm^{-1} in solution but it was found to occur intracellularly at ~ 1079 and 1081 cm^{-}

[1]. This was to be expected and probably resulted from the local intracellular environment. Peaks can also be selectively enhanced or can diminish demonstrating variations in both signal intensity or frequency depending on where the nanotag is located and the intracellular environment to which it is exposed.[245]

In the specific case of the representative spectrum for the bottom spot (**Figure 4.15d**) this demonstrated a good spectral fit with a representative multiple component solution standard for the 'triplex' - MPY, DTNB and NBT. The DCLS was performed using the individual solution standards rather than the multiple component standard, as it was deemed to be the most appropriate method of determining the combination of nanotags present. Nonetheless this has been included as further confirmatory evidence that all three nanotags were present within that specified location.

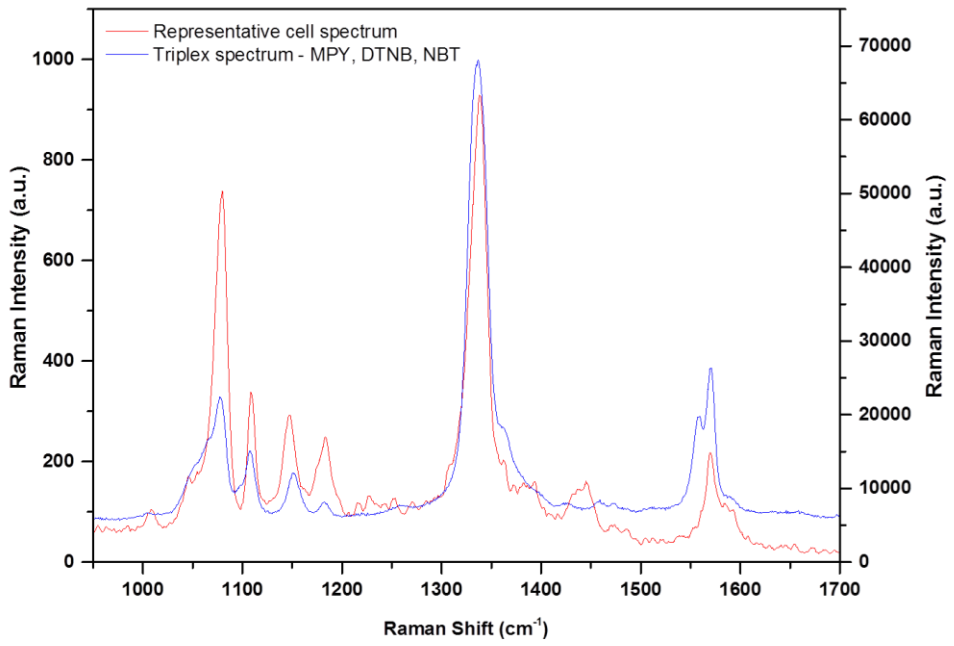

Figure 4.17: Spectral profiles for the representative cell spectrum in the bottom spot and the triplex solution standard spectrum for MPY, NBT and DTNB labelled nanotags. The representative cell spectrum was plotted on the primary y-axis and the triplex spectrum on the secondary y-axis.

Similarly, analysis of a further representative multiple component solution standards for the 'triplex' – MPY, DTNB and NBT over the range 950-1200 cm^{-1} reveals the

individual peaks of the small molecule reporters which would typically be responsible for the representative/cumulative SERS spectra that were observed. The sole contribution from MPY was the peak ~1004 cm^{-1}, NBT was responsible for the doublet of peaks at ~1084 cm^{-1} and 1110 cm^{-1} whilst DTNB was responsible for the shoulder on the peak ~1084cm^{-1} and the main peak at ~1150cm^{-1}. Again, this is further confirmatory evidence that all three nanotags were present within the specified locations.

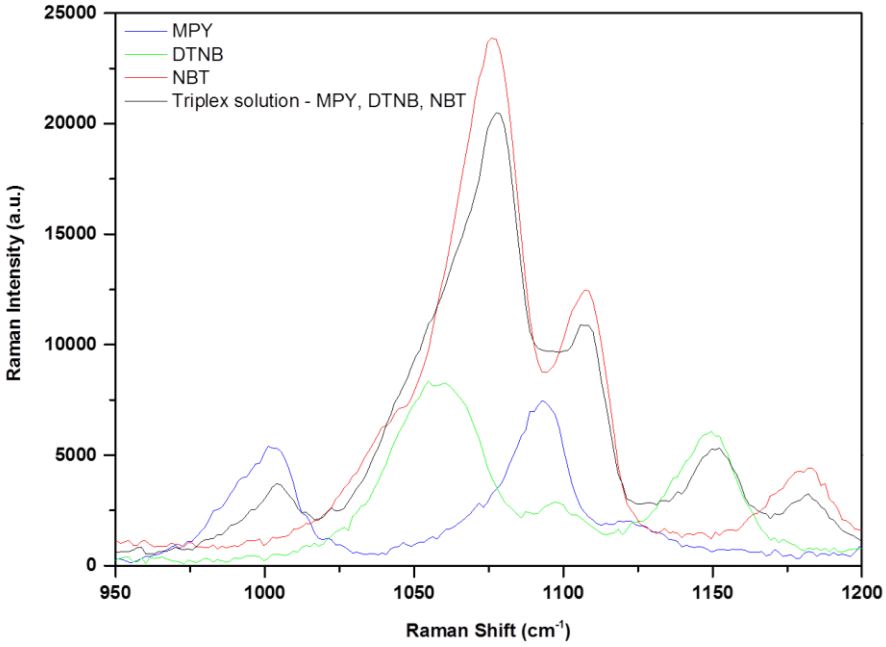

Figure 4.18: Spectral profiles for a representative 'triplex' solution - MPY, DTNB and NBT and the individually labelled nanotag solutions - MPY, DTNB and NBT respectively. This highlights the contribution each small molecule reporter makes to the representative/cumulative cell spectrum. The triplex solution spectrum was plotted on the primary y-axis and the individual solution spectra were plotted on the secondary y-axis.

Finally, it should be noted that none of the nanotags penetrated the nuclei (**Figure 4.13 - Figure 4.15**) and they presumably resided in the cytoplasm or endosome compartments. This was to be expected since the nanotags were not functionalised with targeting moieties specific for this or any other cell organelle. Based on this information, these unfunctionalised nanotags could be used as controls to distinguish between targeting and non-targeting nanotags when organelle targeting is attempted.

4.4 Conclusions

Studies have reported the production of 3D cell images[100] but these have relied on depth profiling methods and the post processing of 2D image stacks. In this study the entire volume was collected, no operator processing of individual 2D stacks was required and the entire volume was analysed as a single data set. The advantage of applying statistical evaluation to the entire volume is that the trends in the data are explained in the x, y and z directions simultaneously, as opposed to applying multivariate analysis to each plane and reassembling plane images as a block which only takes trends in the x and y directions into account.[100]

The study also demonstrated how it was possible to combine the 3D Raman and SERS images, provided that they had been collected from the same area and volume, and this represents a non-destructive alternative to TEM imaging for the simultaneous confirmation of cellular inclusion and multiple component detection. Three out of the four components of the suspension were detected, and by extracting and combining 2D slices from the 3D images it was possible to determine the intracellular location of the nanotags.

It was also possible to define a subcellular compartment in 3D without the need for any special sample preparation (i.e. staining). The resolution of further cell organelles[100] is expected and the ability to detect such structures whilst maintaining the integrity of the cell will undoubtedly be of benefit to the detection of disease processes in which the architecture of the cell changes considerably. The adoption of a multi-marker approach is also critical if disease states are to be fully characterised or multiple cell organelles are to be targeted. Hence, the ability to detect these multi-markers in 3 dimensions is of huge importance for a whole host of applications including cellular disease or tumour detection and the delivery of drugs and their subsequent fate within the cells. This work also has implications for the application of combined 3D Raman and SERS imaging to living cells.

Chapter 5 The Development of Organelle Targeting Nanotags

5.1 Introduction

The development of multi-marker nanotags for imaging purposes and their subsequent demonstration of cellular uptake are undoubtedly important precedents in the advancement of a system designed for disease detection. However, the ultimate success of the system will only be realised when specific intracellular targeting is achieved. Nanotags can be readily functionalised with a whole host of targeting moieties including oligonucleotides,[154] antibodies[11] and cell penetrating peptides (CPPs).[70, 71] However, widespread antibody use in targeting applications may be hindered by their large size which will influence their transport across cell membranes and mobility within the cell.[11, 257] In addition, there is always a danger that they may elicit an immune response.[11, 257] In contrast, CPPs are considerably smaller, uptake has been demonstrated with several different cell lines and their risk of eliciting an immune response is minimal.[257] This flexibility may explain the increased use of CPPs in intracellular targeting experiments.[7, 70, 71, 258, 259]

Nuclear targeting has been widely demonstrated in a host of cell lines using the HIV transactivator of transcription (TAT) sequence, [7, 47, 258] the SV-40 nuclear localisation sequence (NLS)[70, 71] and a combination of adenoviral receptor mediated endocytosis (RME) and NLS sequences.[71] Attention is usually focused on nuclear targeting due to the localisation of genetic material within its structure and especially since accessing this information is thought to be important for the phenotypic determination of disease, the discovery of novel therapeutic agents and in the development of antisense therapy.[47] In addition to nuclear targeting the endoplasmic reticulum,[74] Golgi apparatus[74] and mitochondria[260] have also been successful reached using CPPs. In the case of mitochondrial targeting, the anticancer drug doxorubicin was targeted to the mitochondria using a CPP where it inhibited DNA topoisomerase and damaged mitochondrial DNA.[260] Unlike the nuclear targeting equivalents a reduced efficacy and a susceptibility to cellular expulsion was not exhibited when the conjugates were exposed to drug resistant cells.[260] The authors reported that this potentially represents

a more viable route for targeting cancerous cells. In addition to this cancer treatment, Copolovici *et al*. have reported, in a recent review, CPP conjugation to treatment agents including drug molecules, oligonucleotides and larger, more complex proteins for the possible treatment of muscular dystrophy, strokes, antiprion treatment for diseases of the nervous system as well as antiviral and antibacterial applications.[261]

The elegant and sophisticated applications described above demonstrate how the native cell logistics for protein cataloguing can be manipulated by CPPs to actively target cell organelles. This manipulation will be investigated in an attempt to target the endoplasmic reticulum (ER), the trans-Golgi network (TGN) and the cell nucleus. Whilst the final applications may lack the finesse of those mentioned above, the ability to reach these cell organelles will potentially facilitate the comprehensive detection of diseases, organelle specific drug delivery and pH sensing.

5.2 Organelle Specificity of the Peptide Sequences

Peptide sequences were obtained from the literature with a demonstrated targeting ability to the ER,[74] TGN[74] and the nucleus.[71] However, the peptide sequences were originally tested in rat-1 fibroblasts and HepG2 cell lines. In order to determine organelle specificity for the Chinese hamster ovarian (CHO) cell line, used in this study, a preliminary fluorescence investigation was carried out.

5.2.1 Peptide Sequences

The ER was demonstrated to be targetable[74] provided that the amino acid sequence lysine-aspartic acid-glutamic acid-leucine (**KDEL**) was part of the peptide sequence. **KDEL** is a retention signal associated with proteins of the ER and incorporation of this sequence ensures interaction with ER receptors.[74] Similarly the TGN was demonstrated to be targetable[74] provided that the amino acid sequence serine-aspartic acid-tyrosine-glutamine-arginine-leucine (**SDYQRL**) was part of the peptide sequence. **SDYQRL** is a retention signal of proteins found within the TGN and again it can interact with receptors in this location.[74] With regards to the nuclear targeting, there were several sequences to choose from including the TAT and NLS sequences.[258] [7, 70, 71] Both have been investigated in relation to nuclear targeting in SERS based studies,[71, 72] and the final sequences selected were the adenoviral NLS and the adenoviral RME sequences.

Although the nanotags used in the study are capable of cellular uptake, for nuclear targeting it has been demonstrated that using a combination of both sequences leads to elevated levels of nuclear uptake.[71] When functionalised solely with NLS sequences, nanoparticles have difficulty entering the cell[71] and in initial experiments NLS functionalised nanoparticles had to be introduced using microinjection to guarantee cellular entry.[262]

Common to all of the final complete peptide sequences was the incorporation of the pentapeptide cysteine-alanine-leucine-asparagine-asparagine (**CALNN**)[259] on the N-terminus. This was primarily incorporated because of the presence of the thiol on the side chain of the terminal cysteine residue, which was crucial for binding to the nanotag surface. However, the CALNN offered other advantages including the potential to aid in nanotag binding via the amine group on the N-terminus.[259]

The full peptide sequences are shown (**Figure 5.1** and **Figure 5.2**) and in addition to the CALNN commonality, glycine residues were added between the targeting amino acid sequences and the CALNN tether to act as spacer groups (**Figure 5.1** and **Figure 5.2**). The ER targeting sequence has a net negative charge of -1 at pH 7, due to the presence of the positively charged lysine residue and the two negatively charged aspartic and glutamic acid residues. The TGN targeting sequence has a net neutral charge due to the presence of negatively and positively charged residues; aspartic acid and arginine. In contrast both of the peptide sequences required for targeting the nucleus have a net positive charge of 3. The NLS was comprised of three positively charged residues; two arginine and one lysine whilst the RME sequence was comprised of six positively charged lysine and three negatively charged residues; two glutamic and one aspartic acid. CPPs which are rich in positively charged residues (arginine and lysine) can rapidly translocate across cell membranes, presumably because of the differences in charge, but functionalisation of citrate reduced nanoparticles can prove difficult due to the unfavourable electrostatic interactions.

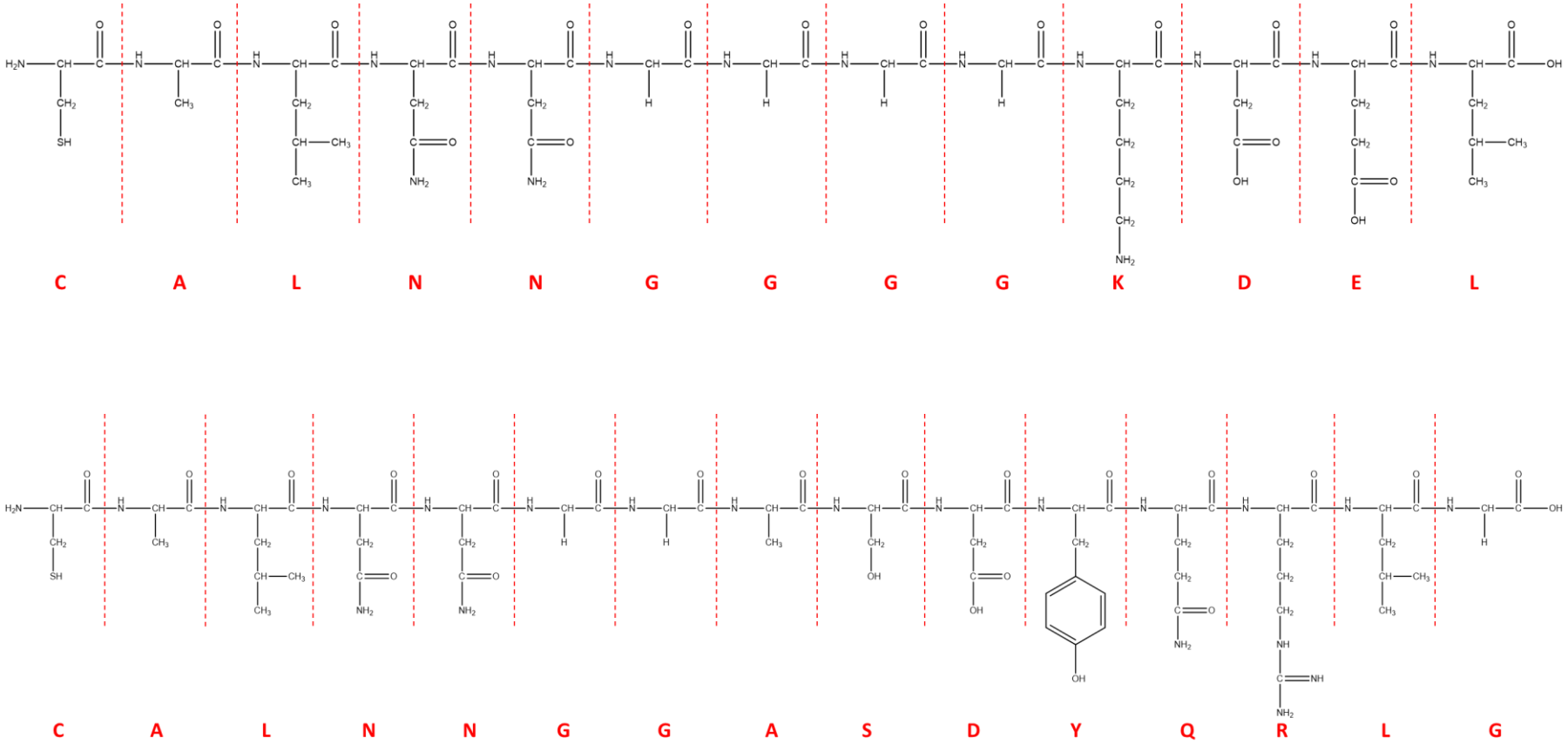

Figure 5.1: Targeting peptide sequences – upper: structure of the peptide sequence for targeting the ER and lower: structure of the peptide sequence for targeting the TGN. The single letter code for each amino acid is shown below each sequence.[74, 259]

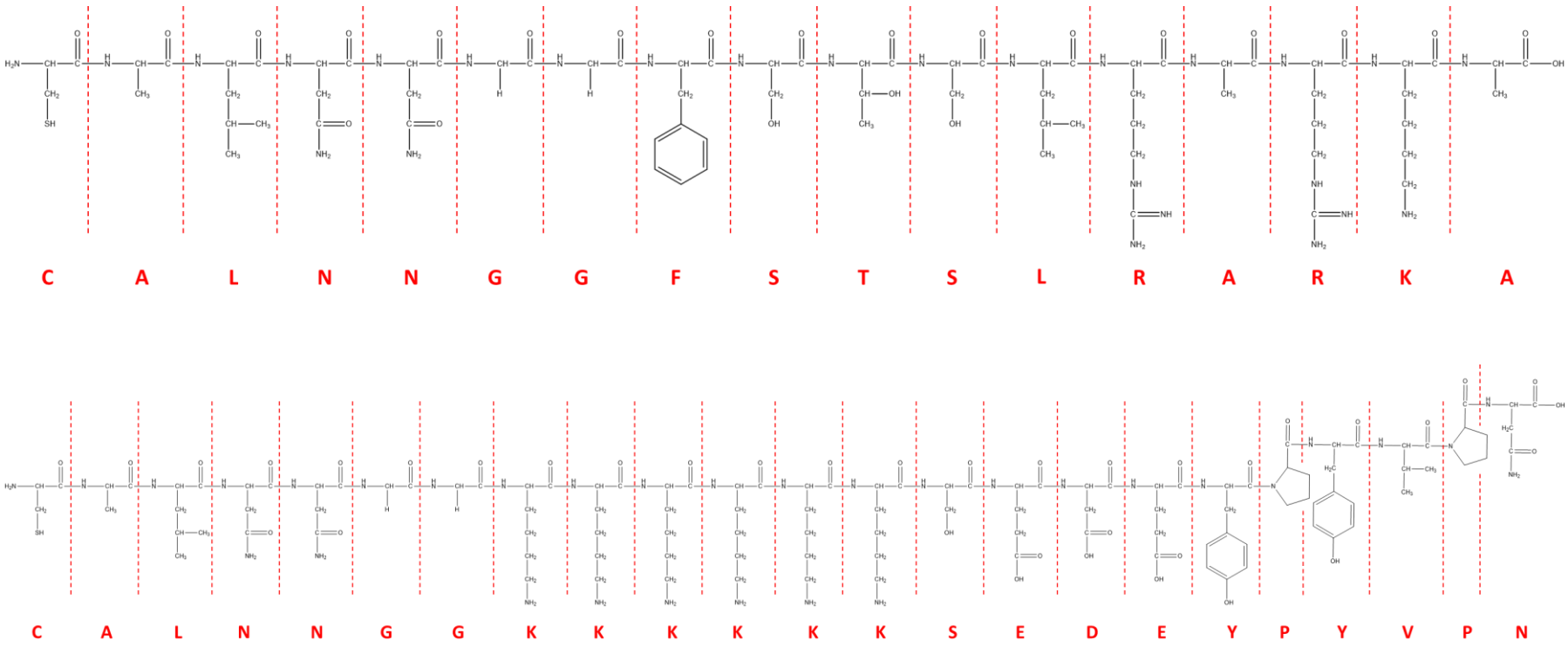

Figure 5.2: Targeting peptide sequences – upper: structure of the peptide sequence for the NLS and lower: structure of the peptide sequence for the RME. The single letter code for each amino acid is shown below each sequence.[71, 259]

5.2.2 Fluorophore Conjugation

To test the organelle specificity of the peptide sequences in the CHO cell line each of the sequences were conjugated to a fluorophore. The peptide sequences should translocate the fluorophore to the correct organelle compartment and when counterstained with an organelle specific dye, co-localisation should be observed. This method of testing organelle specificity had already been demonstrated using the ER and the TGN sequences,[74] however the method was reduced to a single step reaction with the fluorophore. A Texas Red® C_2 maleimide was selected since its reacts selectively with thiols in the presence of amine groups to form a thioether. Therefore, each of the peptide sequences bearing a thiol on the cysteine side chain could be readily conjugated to the maleimide (**Figure 5.3**).

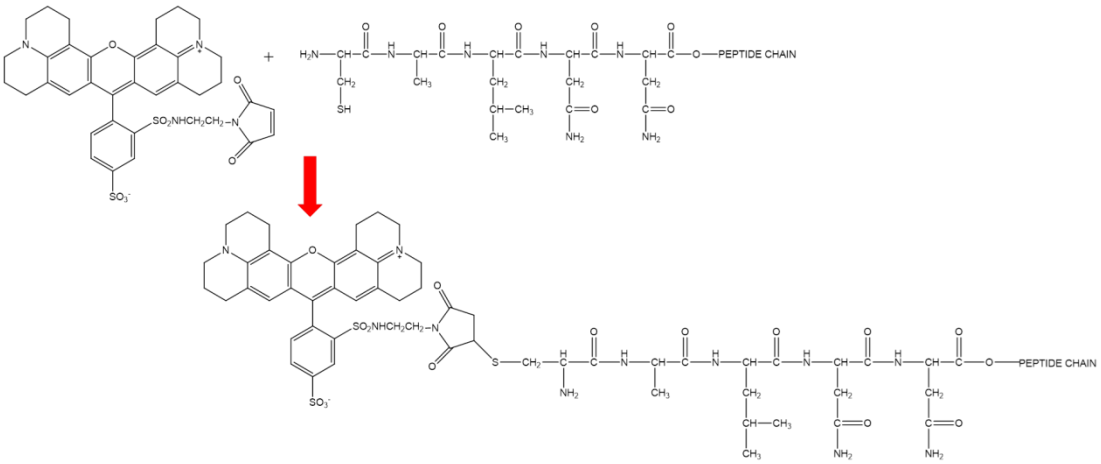

Figure 5.3: Reaction between Texas Red® C_2 maleimide and the thiol group on the peptide sequence to form a thioether.

Conjugation was achieved by adding the maleimide (20× molar excess) drop wise to the peptide and leaving the reaction to agitate overnight. In order to retrieve the dye peptide conjugate from any unreacted dye or peptide it was necessary to perform a simple extraction using a mixture of chloroform, water and acetic acid. The unreacted dye partitioned into the chloroform extract while the dye-peptide conjugate and any unreacted peptide partitioned into the water phase.[74] Conjugation was initially determined using thin layer chromatography (TLC) (chloroform:methanol:acetic acid:water – 25:15:3:2 v/v)[74] and after the water extract was dried, matrix-assisted laser desorption ionisation (MALDI) mass spectrometry was performed for the pure dye, each of the peptide sequences and the dye-peptide conjugates. There were two

peptide sequences for nuclear targeting and both were required for successful cell entry. However, since simultaneous, dual functionalisation, of the fluorophore could not be achieved, neither of the nuclear peptide sequences were conjugated to the fluorophore.

The initial TLC results suggested that conjugation had been successful since all of the dye peptide conjugates had a lower retardation factor (Rf) when compared with the pure dye and extracts 1 and 6 (**Table 5.1**).

Table 5.1: TLC analysis for each of the dye-peptide conjugates compared with the pure dye and extracts 1 and 6.

Peptide	Dye (Rf)	Extract 1 (Rf)	Extract 6 (Rf)	Dye/Peptide (Rf)
ER	0.97	0.97	0.97	0.61
TGN	0.96	0.96	0.96	0.61

Similarly, MALDI analysis confirmed that conjugation had been successful based on the masses measured. Singly charged masses of 728.89, 1247.40 and 1538.55 m/z were identified in the MALDI-MS analysis of the pure dye, the ER and the TGN peptide sequences respectively. Ions with 1972.33 and 2265.25 m/z corresponding to the dye-ER and dye-TGN conjugates were evident in the MALDI-MS spectrum obtained for each of the respective conjugates. The MALDI spectra are shown (**Appendix VI** - **Appendix X**).

5.2.3 Detection of the Organelle Specific Peptide Sequences in Cells

Following on from the successful conjugation of each peptide sequence to the fluorophore, the dye-peptide conjugates were incubated with the CHO cells for varying periods of time (0-30 min). The time increments were based on a previous study where it was determined that sufficient uptake occurred within 16 min.[74] After incubation with the dye-peptide conjugates the cells were washed twice with PBS (1×) and then stained with the appropriate organelle specific counterstain. The cells were then washed, fixed and analysed using a fluorescent microscope with the appropriate filters.

5.2.3.1 ER Specific Peptide Sequences and Cell Experiments

The ER was counterstained with ER tracker green which consisted of a green-fluorescent BODIPY® FL dye and glibenclamide. Key to the function of this fluorophore was the glibenclamide which functions by binding to the abundant potassium channels in the ER in particular the sulphonylurea receptors.[263] In order to analyse the ER samples the fluorescent filter cubes FITC 3540B-NTE(organelle specific stain) and TEXAS RED 4040B–NTE (dye/peptide conjugate) were used alongside a Nikon Eclipse LV100 microscope and a Photometrics CoolSNAP HQ camera. The images were collected using Metamorph® Microscopy Automation and Image Analysis Software.

The collected images revealed co-localisation of the stains between 15-25 min (**Figure 5.4**).

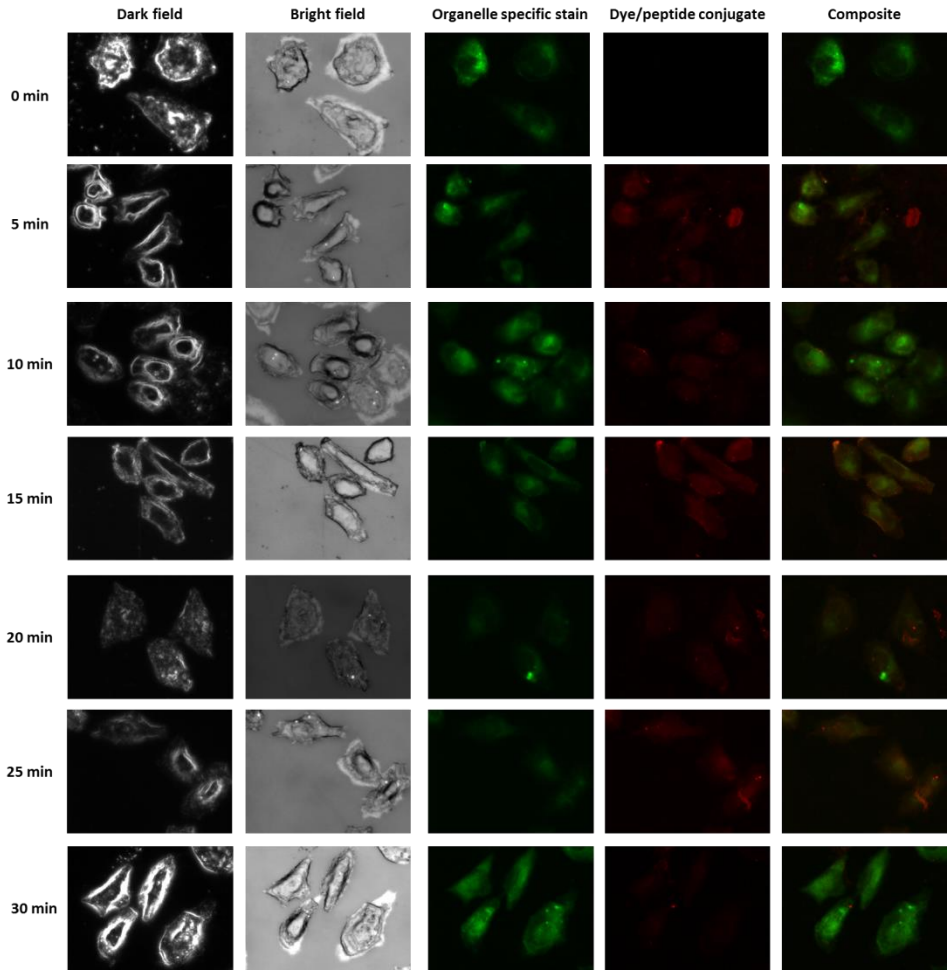

Figure 5.4: Images representative of the dye/ER peptide conjugate – the dark field, the bright field, the organelle specific stain, the dye/peptide conjugate and the composite images are shown.

This was apparent from the orange colour in the composite images (**Figure 5.4**). Co-localisation was still visible at 30 min but the intensity of the dye/peptide conjugate was lower and because of the contrast between the two stains it was more difficult to observe. The observed co-localisation would suggest that the peptide sequence for the ER does indeed target the correct cell organelle and that this peptide sequence was appropriate for targeting in the CHO cell line.

5.2.3.2 TGN Specific Peptide Sequences and Cell Experiments

The TGN was counterstained with BODIPY® FL C_5-ceramide which consisted of a green-fluorescent dye. Key to the function of the fluorophore was the ceramide which is typically synthesised in the ER before it is transported to the TGN where it is converted into sphingomyelin.[264] Ceramide is useful for staining the TGN since it will accumulate in the structure in preparation for bioconversion. In order to analyse the TGN samples the same equipment and procedures as in section 5.3.2.1 were used.

Unfortunately when the samples were analysed using the appropriate filter for the dye/peptide conjugate no selective staining of the TGN was observed. This would suggest that the peptide had in this instance not successfully transported the dye to the specified cell organelle. As a result of this the staining procedure was repeated on a separate occasion and the same outcome was achieved. The only staining pattern that was visible was that of the organelle specific stain (**Figure 5.5**). While this would suggest a lack of organelle specificity by the peptide sequence the reasons for the absence of any dye/peptide staining may not be as obvious. In the first instance it is possible that conjugation to the fluorophore had hindered the targeting capability of the peptide sequence. However, conjugation of a similar sequence to a fluorophore did not influence its targeting capability in any way and the sequence still directed the fluorophore to the TGN.[74] In the same study the fluorophore conjugated peptide was incubated with the cell line at 37 ˚C and since successful targeting of the organelle was demonstrated the same procedure was followed in this study. However, the standard procedure for counterstaining with the organelle specific stain used a distinctly different procedure and initially involved incubating the stain with the cells at 4 ˚C for 30 min before further incubation at 37 ˚C. It was possible that incubation at this initial lower temperature was critical to the successful staining of the organelle and it is an aspect of the study which would need to be investigated further. It is also possible that

this peptide takes longer to diffuse to its target. Despite the demonstrated lack of organelle specificity the peptide sequence will be investigated further in the subsequent nanotag studies.

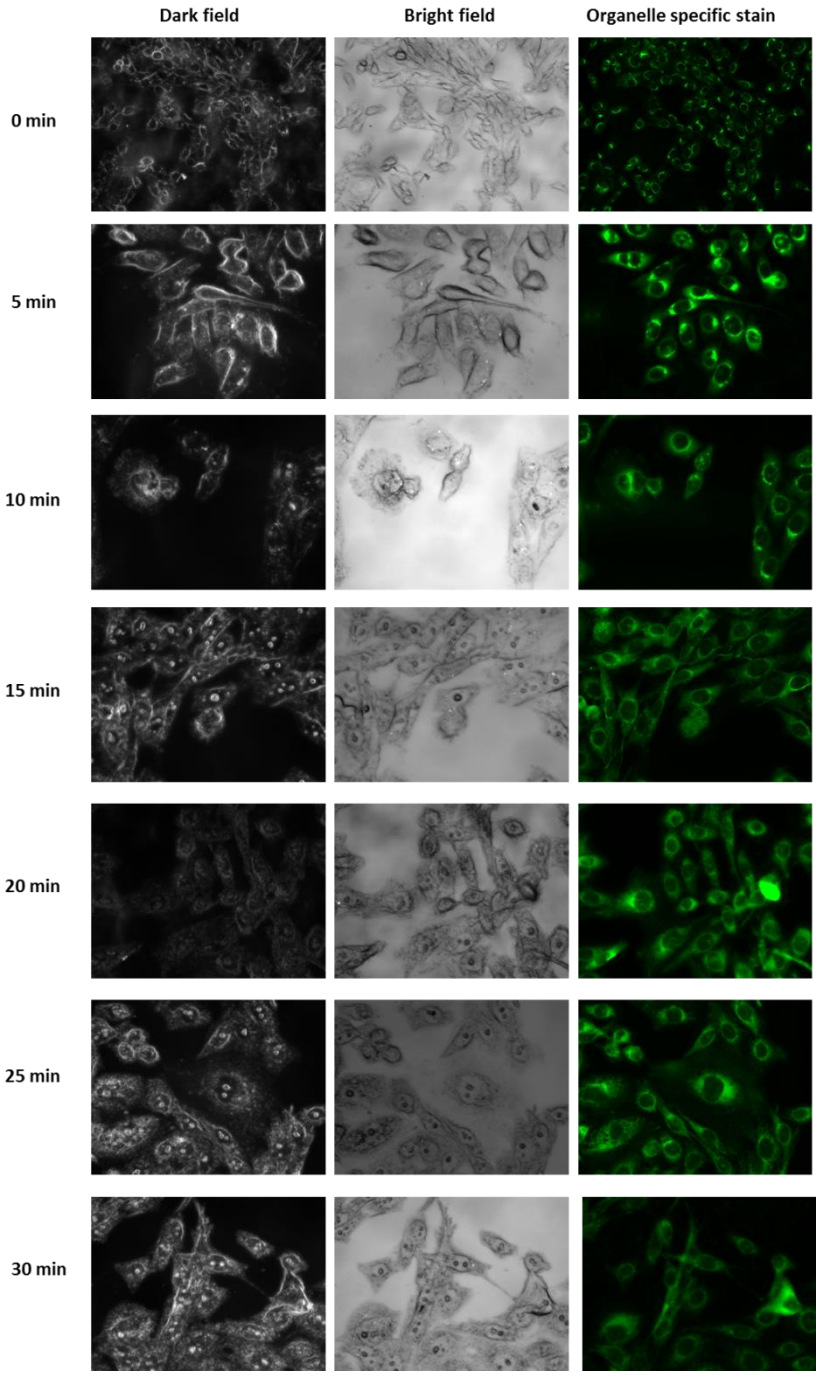

Figure 5.5: Images representative of the dye/TGN peptide conjugate – the dark field, the bright field and the organelle specific stain are shown. No fluorescence was observed for the dye/TGN peptide conjugate hence it is not shown.

5.3 Synthesis of Peptide Functionalised SERS Nanotags for Organelle Targeting

It was not anticipated that there would be any difficulty functionalising the existing nanotag system with either the ER or TGN specific peptide sequences since they were negatively and neutrally charged respectively. However, both of the nuclear targeting sequences were positively charged and there was concern that this would aggregate the negatively charged nanotag system because of unfavourable electrostatic attractions.

5.3.1 Synthesis and Characterisation of Endoplasmic Reticulum (ER) and trans-Golgi Network (TGN) Targeting Nanotags

5.3.1.1 Synthesis of the Nanotags - Standard Protocol

The nanotag synthesis method (see section 8.4.2 and 8.4.3) was followed whereby the nanotags were sequentially functionalised with 2 nM PEG, 200 μM of reporter and finally with 20 μM PEG. However, the PEG was replaced with appropriate peptide sequence. The peptide adsorbs onto the nanotag via the thiol on the terminal cysteine side chain. In order to compare the stability, small molecule, PEG and a combination of small molecule/PEG functionalised nanotags were synthesised alongside the peptide analogues. The stability of the nanotags was then determined by UV-vis spectroscopy and DLS.

Analysis of the non-normalised data for the ER functionalised nanotags revealed that when this synthesis method was used the ER only functionalised nanotags were the most unstable as exhibited by a dampening and broadening of the plasmon band (**Figure 5.6**). In contrast the TGN only functionalised nanotags were more stable and there were no obvious signs of aggregation (**Figure 5.6**). This difference in stability between the two peptide functionalised nanotags may be due to the differences in charge between the two peptide sequences. The ER peptide has a net negative charge and it was likely that some level of repulsion was experienced between the peptide and the negatively charged nanotag surface. This may limit the amount of peptide that covers the surface and stabilises the nanotag aggregate. The TGN peptide however has a net neutral charge and therefore experiences no repulsion. There was no inhibition of this peptide from approaching the surface and stabilising the nanoaggregates.

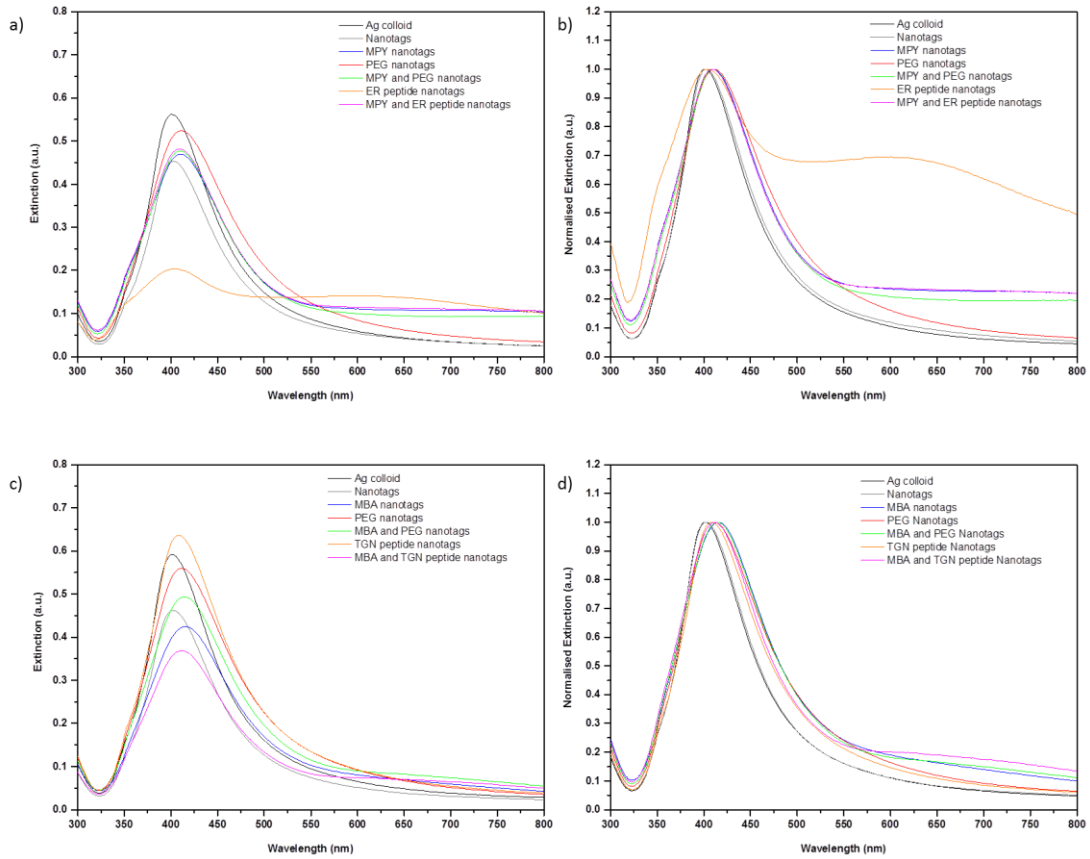

Figure 5.6: Extinction spectroscopy analysis of the peptide labelled nanotags compared with small molecule/PEG labelled nanotags. The data for both the a)-b)ER and the c)-d)Golgi peptide functionalised nanotags are shown. Both the non-normalised and the normalised data are shown.

Analysis of the size data for the ER labelled nanotags also confirmed that the tags solely functionalised with the ER peptide increased the most in size (**Figure 5.7**). This suggested that peptide conjugation had not stabilised the nanotag surface. However for all of the nanotags within the ER and TGN peptide data sets none of the nanotags increased above a size, which would cause concern regarding cellular uptake (**Figure 5.7**). Similarly, analysis of the Zeta data suggested that none of the nanotags were particularly unstable or unsuitable for further cell experiments (**Figure 5.7**).

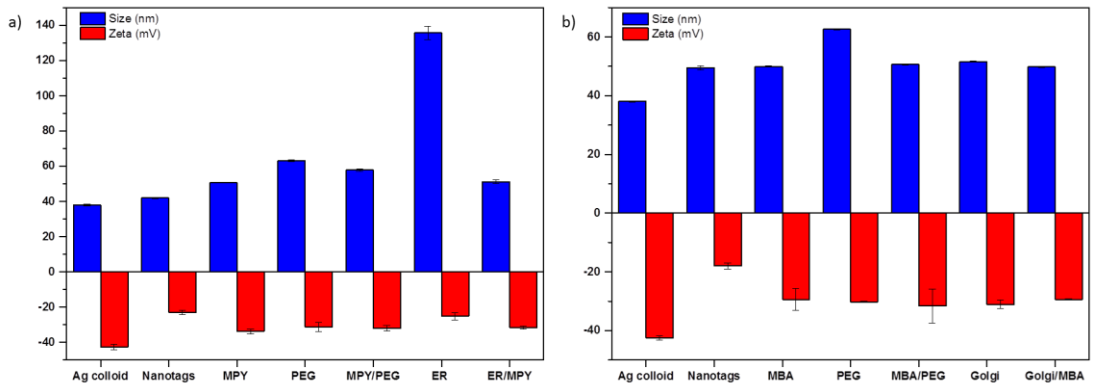

Figure 5.7: DLS size and Zeta measurements for the peptide labelled nanotags and the small molecule/PEG labelled nanotags when dispersed in distilled water – a) ER peptide and b) TGN peptide. The measurements were made in triplicate, the average is shown and the error bars are represented by the standard deviation of the triplicate measurements.

5.3.1.2 Simplification of the Nanotag Synthesis

Although the size and stability of the nanotags described in section 5.3.1.1 were not of concern, the synthesis method required sequential addition of the components and it was thought that this method could be simplified by the single addition of both the peptide and the small molecule simultaneously. In order to limit competitive binding between the peptide and the small molecule reporter, they were both added simultaneously to achieve a final concentration of 1 μM. By adding the peptide at an initially higher concentration (1 μM *c.f.* 2 nM) it was postulated that the nanotag surface would be stabilised rapidly and to a greater extent. Analysis of the results, in particular the nanotags functionalised solely with the ER peptide, showed a marked improvement in stability. There was some dampening of the plasmon band but there was no red shifting and minimal band broadening (**Figure 5.8**). The same was true for the nanotags functionalised with the TGN peptide.

It should be noted that a different batch of citrate reduced silver nanoparticles was used for the preparation of these conjugates and it was found to be more monodisperse (**Figure 5.7** *c.f.* **Figure 5.9**). Although this undoubtedly contributed to the additional stability observed it was unlikely that this was the sole reason.

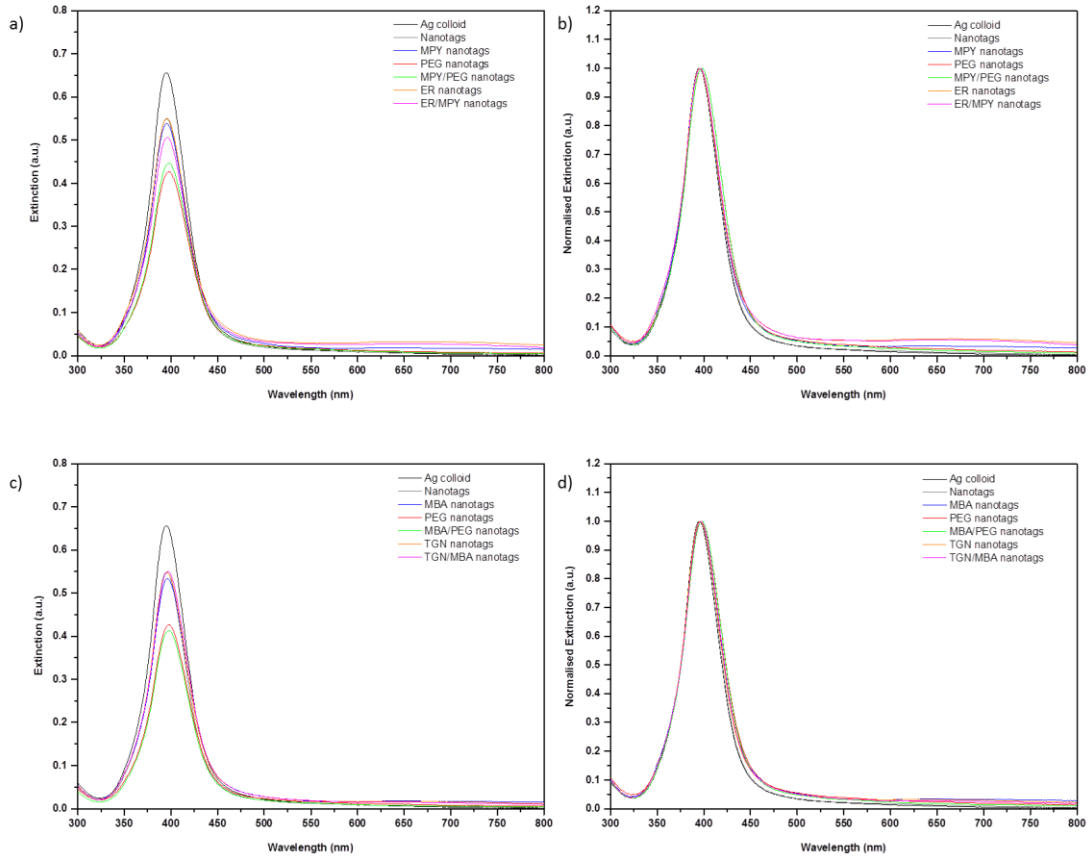

Figure 5.8: Extinction spectroscopy analysis of the peptide labelled nanotags compared with small molecule/PEG labelled nanotags when the peptide and reporter were added to the nanotags simultaneously. The data for both the a)-b)ER and the c)-d) TGN peptide functionalised nanotags is shown. Both the non-normalised and the normalised data are also shown.

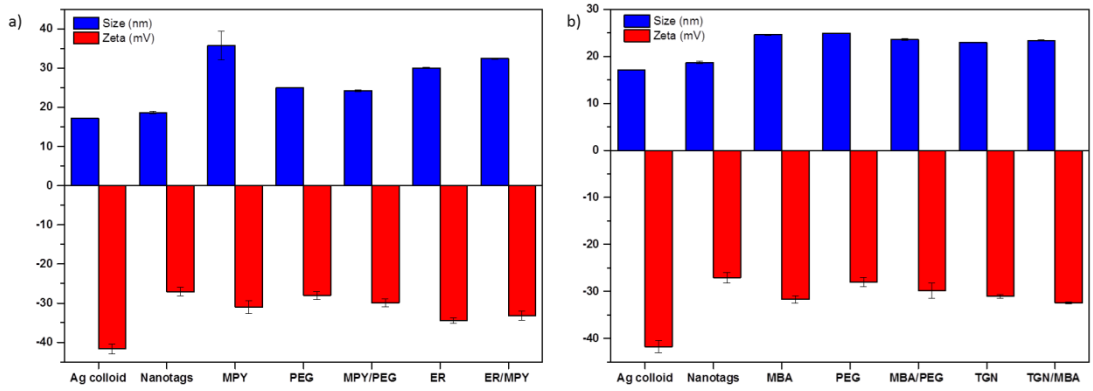

Figure 5.9: DLS size and Zeta measurements for the peptide labelled nanotags and the small molecule/PEG labelled nanotags when labelled simultaneously with the peptide and small molecule reporter. Samples were dispersed in distilled water – a) ER peptide and b) TGN

peptide. The measurements were made in triplicate, the average is shown and the error bars are represented by the standard deviation of the triplicate measurements.

The size and Zeta potential measurements also showed a marked improvement for both the ER and TGN labelled nanotags (**Figure 5.9**). A reduction in size was observed for all of the synthesised conjugates but this may have been the result of using a nanoparticle suspension with a smaller size distribution (17 nm *c.f*. 38 nm). Similarly, an increase in the Zeta potential was observed for all of the conjugates (**Figure 5.9**) and this again may have been due to the more monodisperse colloid. However, it was also attributed to the initial elevated level of peptide stabilising the nanotag aggregates more rapidly and to a greater extent.

To confirm functionalisation of the nanotag surfaces with the peptide sequences gel electrophoresis was used. This technique separates proteins based on their size and charge and it has been previously used for the detection of nanoparticle protein binding.[265, 266] The peptide only functionalised nanotags should exhibit a difference in electrophoretic mobility in comparison to the small molecule only and the unfunctionalised nanotags and nanoparticles. The same should also be true for nanotags dually functionalised with the appropriate small molecule reporter and peptide and small molecule/PEG conjugates. The analysed solutions were prepared by centrifuging at 5000 rpm for 10 min followed by resuspension in 50 μL of 10 mM phosphate buffer (pH 7.6). 10 μL of these resuspended solutions were removed and mixed with 1 μL of 6× loading buffer. The solutions were added to a 1 % agarose gel and a voltage (160 mV) was applied. The peptide only functionalised nanotags travelled in the gel (**Figure 5.10** – **lane 9** and **10**) as did the dually functionalised peptide small molecule nanotags (**Figure 5.10 – lane 11** and **12**). The peptide only nanotags travelled a greater distance than the non-modified nanotags and nanoparticles but to a lesser extent than the dually functionalised nanotags (**Figure 5.10**). In conjunction with the other characterisation data it can be concluded that peptide functionalisation of the nanotags had been successful.

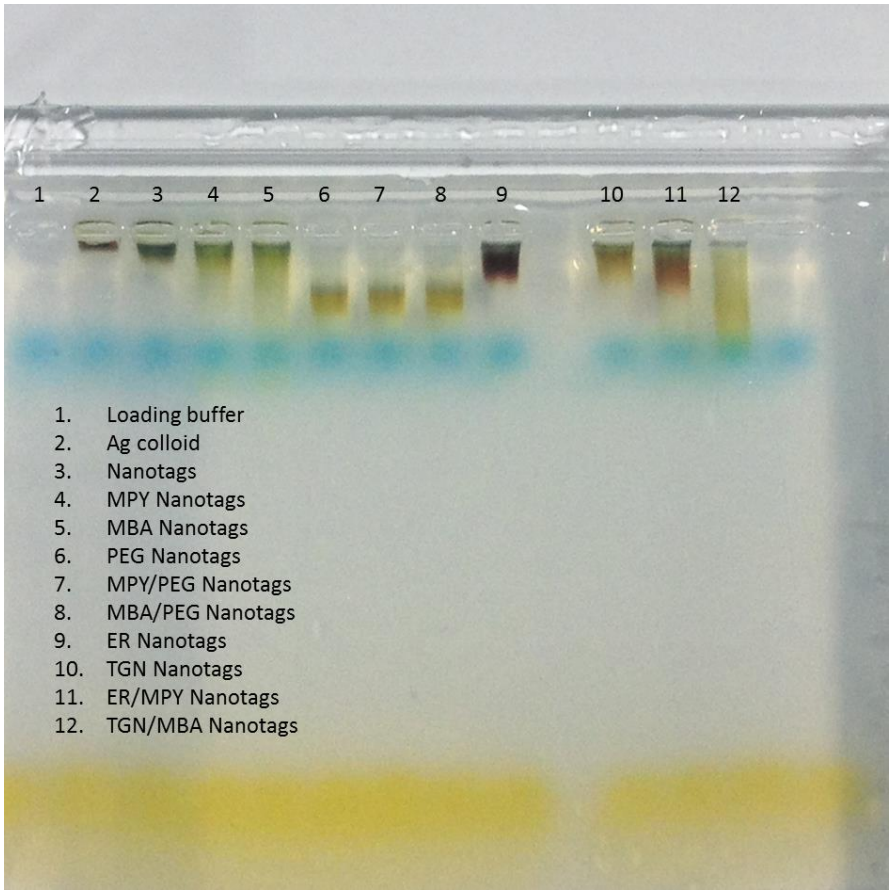

Figure 5.10: Gel electrophoresis analysis of the peptide functionalised conjugates. (1 % agarose gel ran in 1× TBE buffer for 30 min at 160 V).

5.3.1.3 Final Optimised Synthesis of ER and TGN Nanotags

In a final modification to the nanotag synthesis the concentration of small molecule reporter added to the nanotag surface was increased. In the initial cell experiments the concentration of small molecule added to the nanotags was either 10, 50 or 200 μM (see section 3.4.4) depending on the method of synthesis. With the previous synthesis method the small molecule was added at a concentration of 1 μM, but to ensure that the nanotags were detectable within cell populations, the concentration was increased to 10 μM. To prevent the small molecule from competitively occupying the nanotag surface the peptide was added 30 min before the reporter to ensure stabilisation and adequate coverage of the nanotag surface.

The ER and TGN functionalised nanotags exhibited a red shift (λ_{max} = 400 c.f. λ_{max} = 411) when compared to the colloid and nanotag standard but this may have been due to functionalisation of the nanotag surface resulting in an increase in size (**Figure 5.11**). There were no obvious signs of aggregation such as significant dampening of the plasmon and band broadening (**Figure 5.11**).

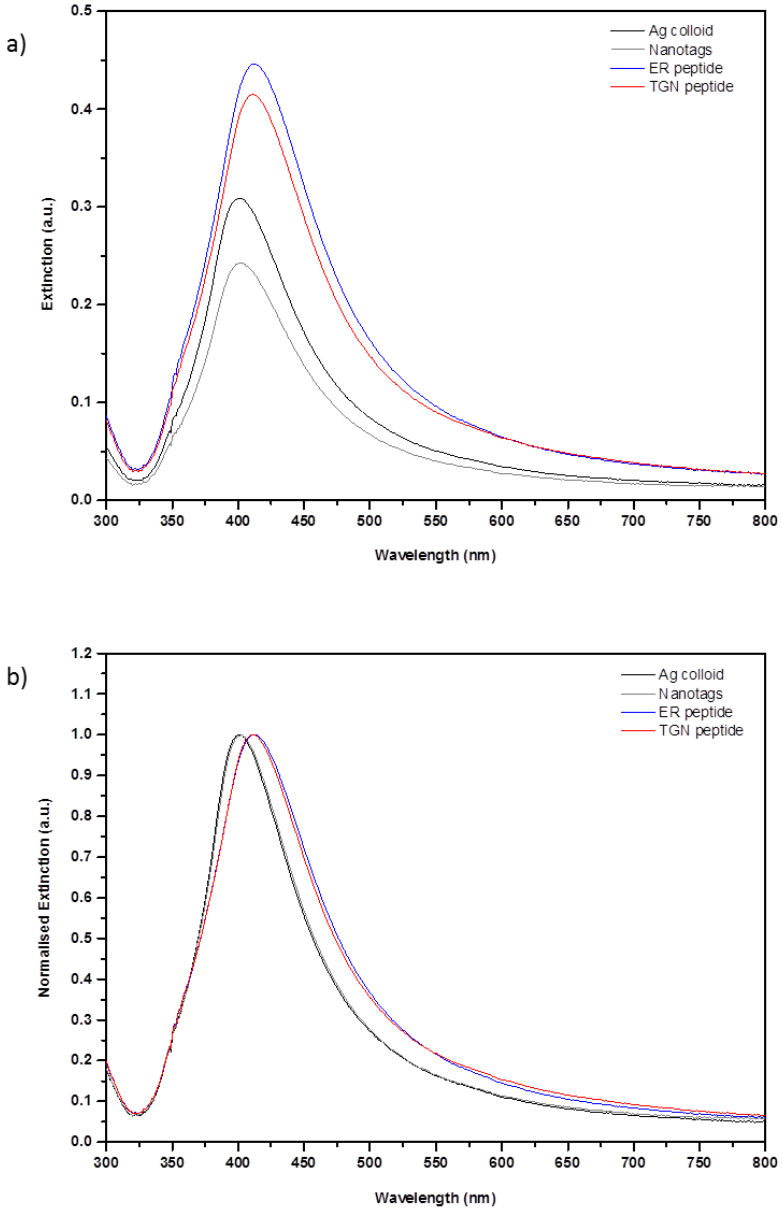

Figure 5.11: Extinction spectroscopy analysis of the peptide/small molecule labelled nanotags - The peptide (1 μM) and small molecule reporter (10 μM) were added sequentially. The ER peptide nanotags were labelled with NBT and the TGN peptide nanotags were labelled with MBA. Both the a)non-normalised and the b) normalised data are shown.

Similarly, when the nanotags were functionalised with the peptide sequences and the small molecule reporters an increase in size was observed but this was consistent with functionalising the surface and the Zeta potential indicated that they were of reasonable stability (**Figure 5.12**). The final optimised peptide nanotag system involved labelling the nanotags with the appropriate peptide (**1 μM**) then this solution was left to agitate for 30 min before the small molecule reporter was added (**10 μM**).

It should be noted that a further batch of nanoparticles was used in this study as the monodisperse colloid used in section 5.3.1.2 did not exhibit good long term stability.

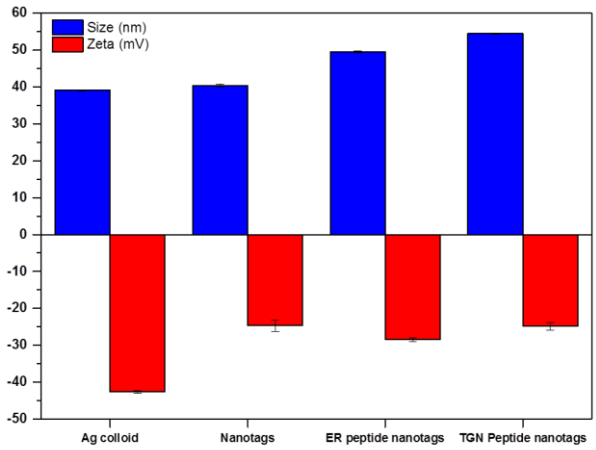

Figure 5.12: DLS size and Zeta measurements for the peptide/small molecule labelled nanotags. The peptide (1 μM) and small molecule reporter (10 μM) were added sequentially. Samples were dispersed in distilled water. The measurements were made in triplicate, the average is shown and the error bars are represented by the standard deviation of the triplicate measurements.

5.3.2 Synthesis and Characterisation of Nuclear Targeting Nanotags

5.3.2.1 Synthesis of the Nanotags - Standard Protocol

As with the ER and TGN targeting nanotags, the original synthesis method (see section 3.4.4) - whereby the nanotags were sequentially functionalised with 2 nM PEG, 200 μM of reporter and finally with 20 μM PEG was employed. However, the PEG was removed from the system and replaced with the nuclear targeting peptide sequences. The stability of the peptide functionalised nanotags was compared with the small molecule/PEG system.

As expected all of the nanotags which were to be functionalised with the positively charged peptide sequences either aggregated to the extent that they were completely colourless (NLS nanotags), or to a level where it was obvious that significant aggregation had occurred (i.e. dampening of the plasmon and band broadening) (**Figure 5.13**). For the nuclear 'functionalised' nanotags, significant band broadening and red shifting was apparent (**Figure 5.13**). The samples to which the small molecule had been added displayed a greater level of stability however, it wasn't sufficient to prevent the unfavourable electrostatic interactions occurring between the largely cationic peptides and the anionic nanotags (**Figure 5.13**).

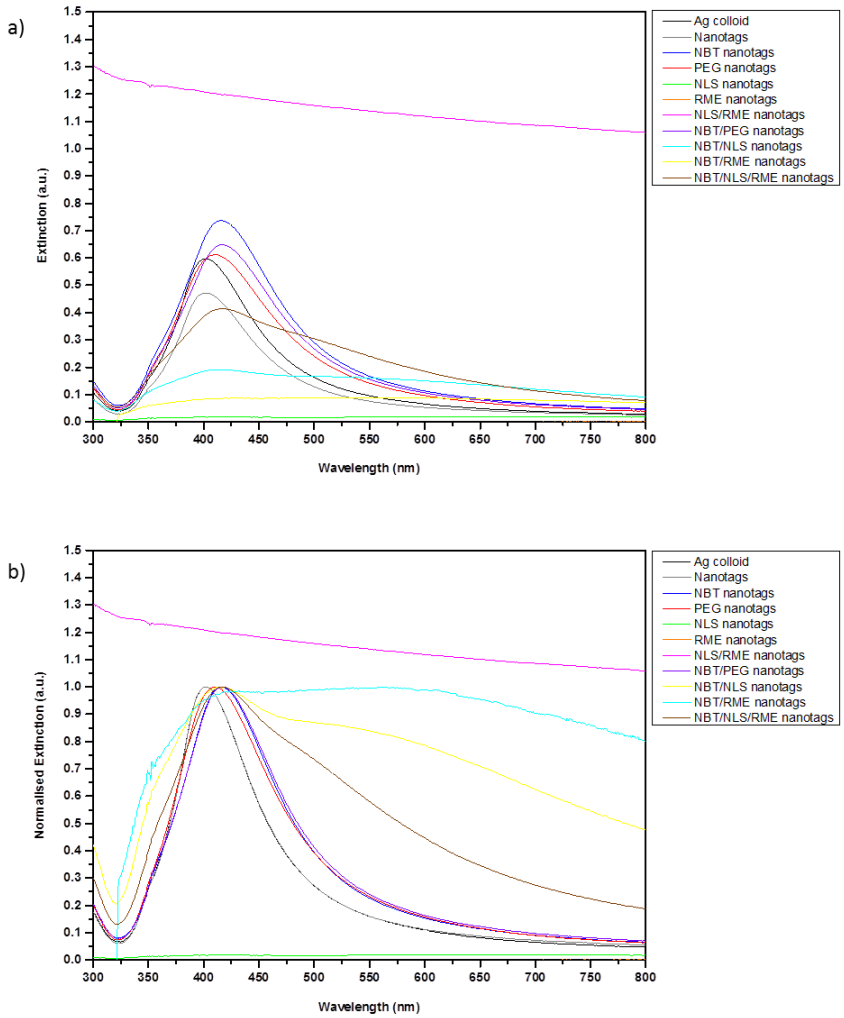

Figure 5.13: Extinction spectroscopy analysis of the nuclear peptide labelled nanotags compared with small molecule/PEG labelled nanotags. Both the a) non-normalised and the b) normalised data are shown.

5.3.2.2 Increased Peptide Concentration

The unfavourable electrostatic interactions between the peptide sequences and the nanotags were undoubtedly the source of the observed aggregation. However, it was necessary to demonstrate this unequivocally and to determine that the aggregation wasn't simply due to an insufficient concentration of peptide to stabilise the nanotag surface. In addition the concentrations of peptide used for nanoparticle functionalisation varied widely in the literature ranging from 0.2 μM – 0.17 mM.[11, 257, 259] When the concentrations of the peptides were increased electrostatic induced aggregation occurred as expected. As the aggregation was so extensive no empirical data was collected.

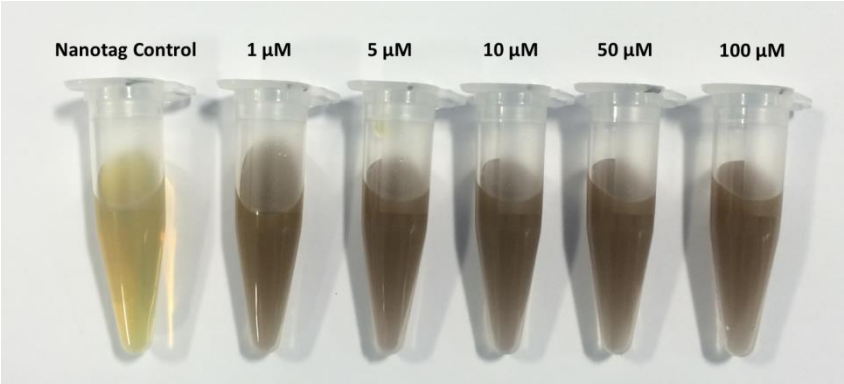

Figure 5.14: Nanotags were dually functionalised with the NLS and RME nuclear targeting peptide sequences. The displayed concentrations indicate the final concentrations of both peptide sequences.

5.3.2.3 Decreased Peptide Concentration

As the unfavourable electrostatic interactions were unavoidable, adding the peptide at lower concentrations seemed a viable route for successful functionalisation. The original synthesis procedure was followed but when it came to the final peptide addition the concentrations were reduced from 20 μM – 2 nM. The levels of aggregation were also investigated for nanotags solely and dually functionalised with each of the peptide sequences. In all instances aggregation was evident before centrifugation, the suspensions changed colour and visible aggregates were obvious, when the peptide was added at concentrations of 20 μM, 2μM and 0.2 μM (**Figure 5.15**).

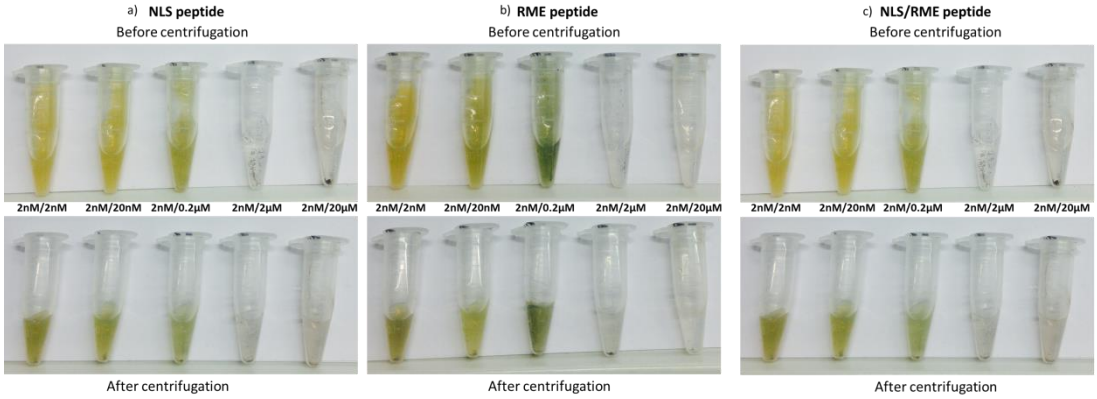

Figure 5.15: Concentration study for the functionalisation of the nanotags with nuclear targeting peptides. The final peptide addition was reduced from 20 μM to 2 μM, 0.2 μM, 20 nM and 2 nM – a) NLS peptide, b) RME peptide and c) combined NLS/RME sequence.

After centrifugation and resuspension aggregation was evident in all of the samples but to a lesser extent in those to which the peptide had been added at 20 nM and 2 nM during the final addition (**Figure 5.15**). This was based on observations made by eye and the resulting colour of the solution. Only the 20 μM, 20 nM and 2 nM dually functionalised samples were analysed further. As expected the sample to which the highest concentration of peptide was added displayed the greatest amount of aggregation as indicated by the colourless solution (**Figure 5.16 NLS/RME sample 20 μM**). However, even in the samples where the lowest concentrations of peptide had been added the plasmon dampened significantly and there was further evidence of aggregation in the form of band broadening and a blue shift (**Figure 5.16 NLS/RME samples 20** and **2 nM**). In the samples which were dually functionalised with the peptide sequences and the small molecule reporter, an additional level of stability appeared to be conferred by the addition of the small molecule (**Figure 5.16**). There was some red shifting and band broadening but not to the same extent as those nanotags only functionalised with the peptide.

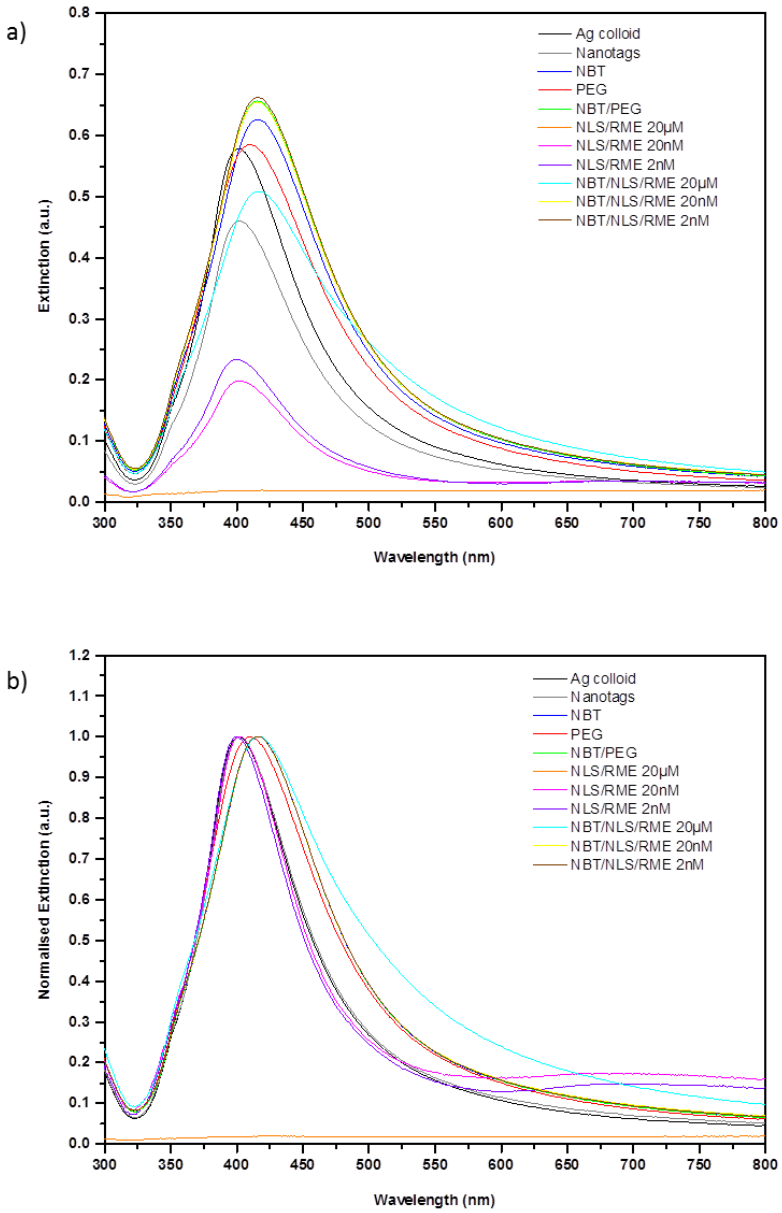

Figure 5.16: Extinction spectroscopy analysis of the nuclear peptide labelled nanotags when the concentration of the nuclear peptides was lowered. Both the a) non-normalised and the b) normalised data are shown.

The influence of the electrostatic interactions was clearly visible when the size of the nanotags was measured and this was greatest for the sample to which the highest concentration of peptide had been added (**Figure 5.17**).

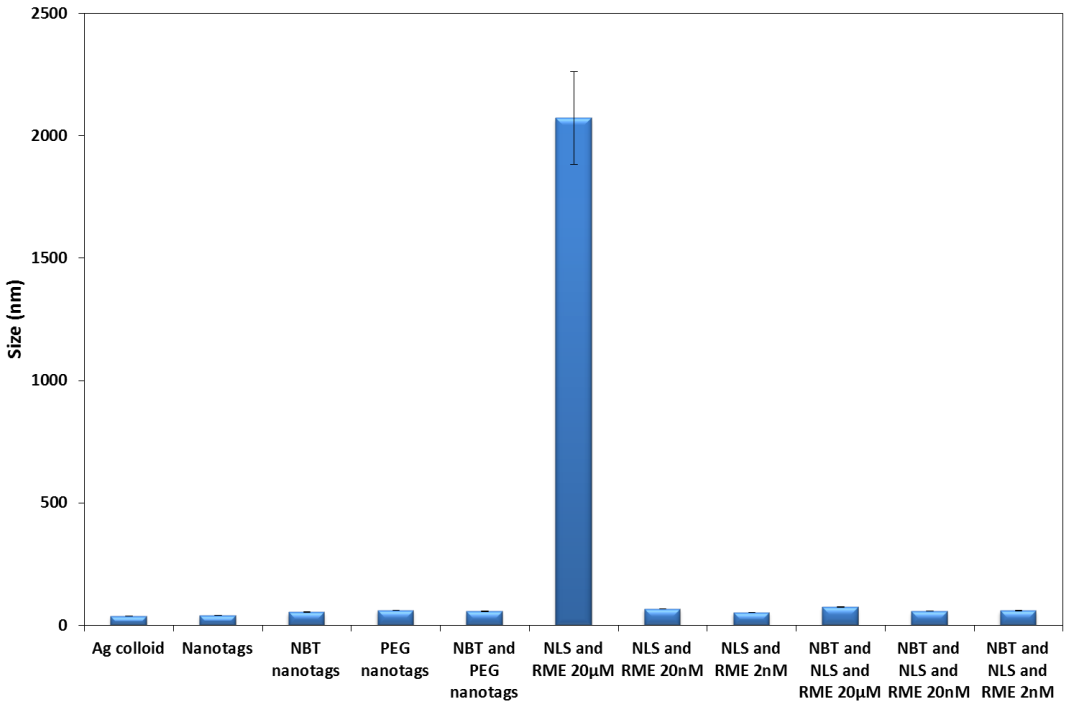

Figure 5.17: DLS size measurements for the nuclear peptide and peptide/small molecule labelled nanotag concentration study. The measurements were made in triplicate and the average is shown. The error bars are represented by the standard deviation of the triplicate measurements.

When this sample was removed from the data set the size of the remaining nanotags were within a range which would be considered suitable for cell uptake (**Figure 5.18**).

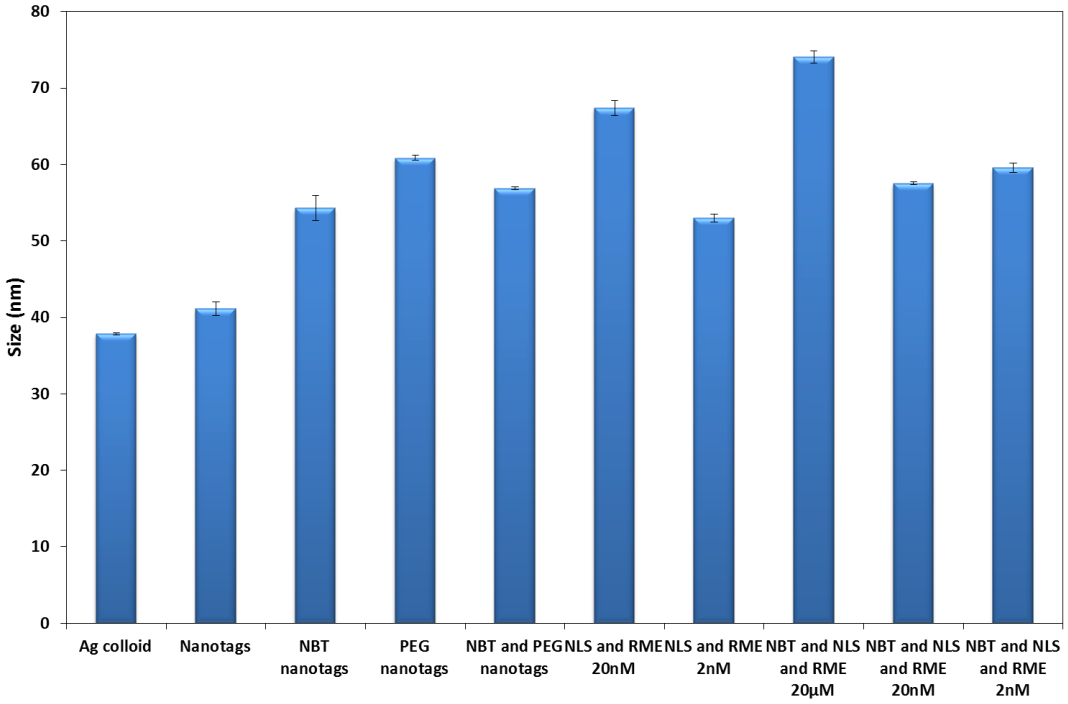

Figure 5.18: DLS size measurements for the nuclear peptide and peptide/small molecule labelled nanotag concentration study – the outlier from the previous data set was removed. The measurements were made in triplicate and the average is shown. The error bars are represented by the standard deviation of the triplicate measurements.

Similarly, when the Zeta potential measurements were analysed the stability of the nanotags were also within a range which would be considered suitable for further cell studies (**Figure 5.19**). Labelling the nanotags with much lower concentrations of the peptides represents a viable route for generating nuclear targeting nanotags. However, there were concerns regarding the longer term stability of nanotags functionalised in this manner especially since following centrifugation a notable colour change was observed.

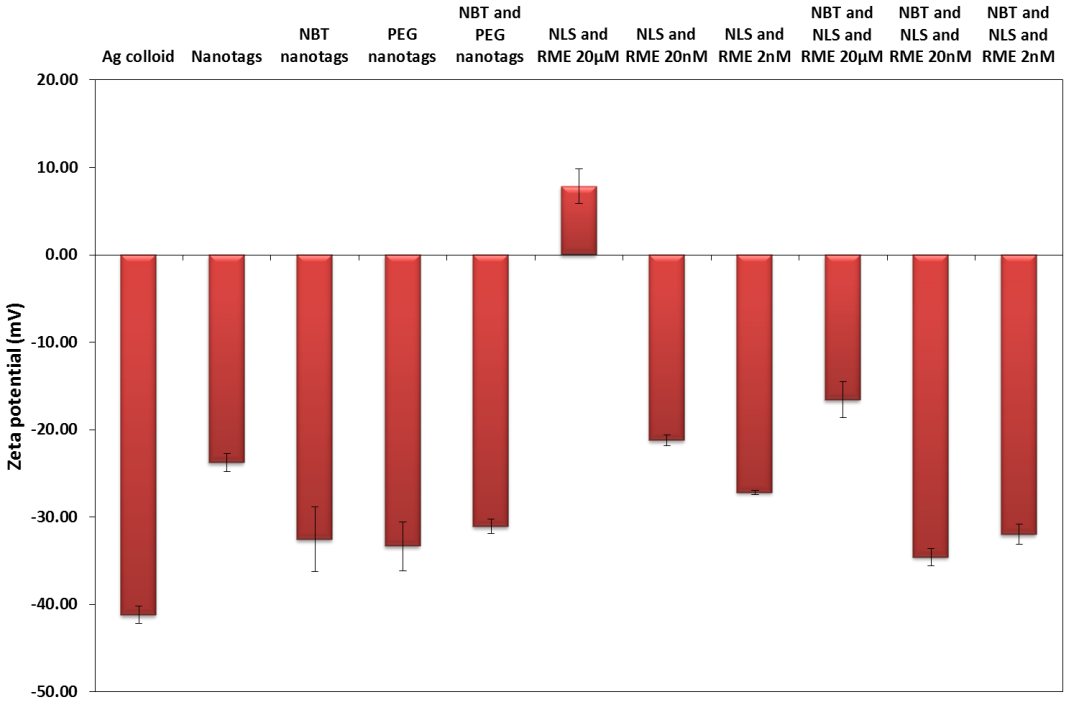

Figure 5.19: DLS Zeta measurements for the nuclear peptide and peptide/small molecule labelled nanotag concentration study. The measurements were made in triplicate and the average is shown. The error bars are represented by the standard deviation of the triplicate measurements.

5.3.2.4 Positively Charged Nanoparticles

In an effort to circumvent the electrostatic interactions between the nanotags and the peptides, polyethylenimine (PEI) was added to the surface of citrate capped nanoparticles and to the pre-formed nanotags to create positively charged surfaces. This should eliminate any unfavourable electrostatic interactions upon addition of the peptide sequences however, unfavourable electrostatic attractions between the colloid and the PEI shall also exist. These attractions can be minimised by adding the PEI at low concentrations. However, even when PEI was added at very low concentrations aggregation was observed (**Figure 5.20**). When PEI was added at 2 $x10^{-6}$ % no visible aggregation occurred but the particles retained their negative surface charge when the Zeta potential was measured. Altering the surface charge was not considered to be a viable route for the generation of nuclear targeting nanotags.

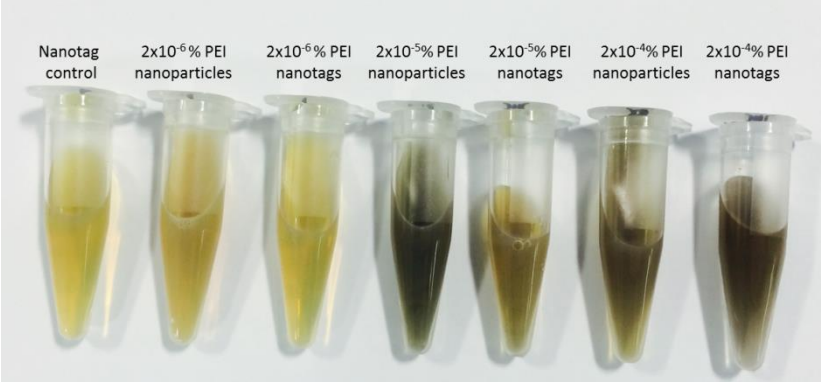

Figure 5.20: Concentration study for the functionalisation of nanoparticles and nanotags with PEI.

5.3.2.5 Bioconjugation of Peptide to Ligand Functionalised Nanotags

In a further attempt to generate nuclear targeting nanotags, the nanotags were functionalised with two PEG molecules of varying length (PEG_{635} an PEG_{5000}). The PEG molecules were thiol terminated at one end, for nanotag attachment and carboxylic acid terminated at the other, for bioconjugation. It has been demonstrated that positively charged nuclear targeting sequences can be conjugated to the carboxylic acid of the PEG molecule via amino groups on the peptide by aqueous carbodiimide chemistry.[70] However, upon addition of the peptide sequences aggregation of the nanotag suspensions occurred (**Figure 5.21**).

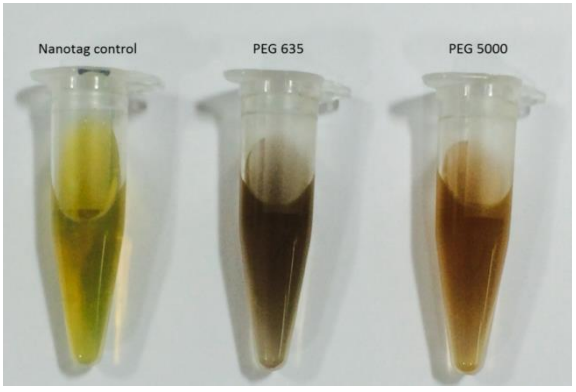

Figure 5.21: Bioconjugation of the nuclear targeting peptides via a PEG linker molecule.

5.3.2.6 Pre-stabilisation of the Nanotags Prior to Peptide Addition

The final method investigated for the generation of nuclear targeting nanotags involved pre-stabilisation of the nanotag surface with a PEG (PEG_{5000}) molecule prior to the

addition of the peptides. The order of molecule addition was also investigated since the PEG can rapidly occupy the surface and it has been observed that some additional stability can also be conferred by the addition of the small molecule reporter. For both methods the molecules were added sequentially at 10 min intervals to a final concentration of 1 μM. For method 1, addition was in the following order; PEG, NBT, peptide and for method 2 PEG, peptide, NBT. Simultaneous addition was also investigated but these nanotags were found to aggregate with time indicating that the nanotag surface must be pre-stabilised before peptide addition.

For both methods of addition a dampening of the plasmon band was observed as was a red shift (**Figure 5.22**). However, with the exception of the dampening of the plasmon band there were no other signs of significant aggregation.

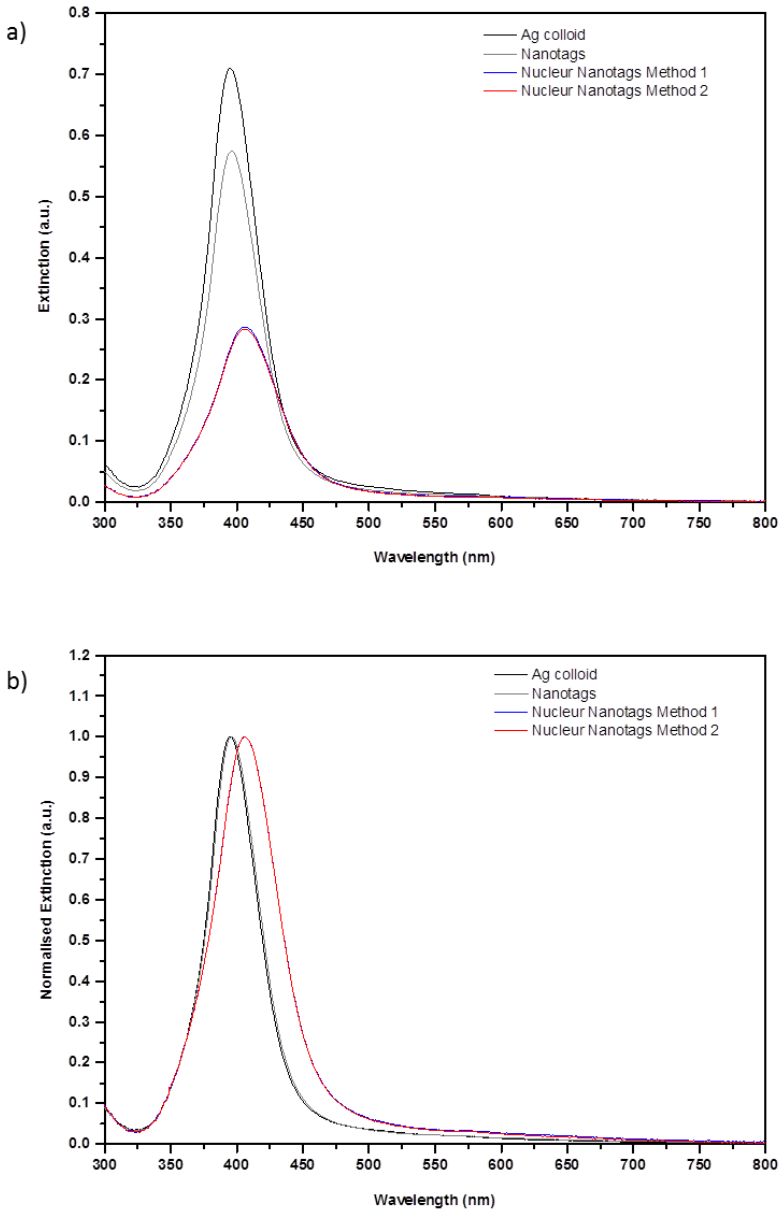

Figure 5.22: Extinction spectroscopy analysis of the nuclear peptide labelled nanotags when pre-stabilised with PEG. Both the a)non-normalised and the b) normalised data are shown.

The size and Zeta measurements were also within the limits considered acceptable for cell uptake and exposure to the cell environment. The nanotags increased in size as a result of surface functionalisation and did not show any signs of significant instability (**Figure 5.23**). The concern regarding this method of synthesis was that the large PEG molecule had potentially blocked the surface of the nanotag and prohibited the peptide from adsorbing. In addition, if adsorption had occurred there was concern that the PEG

molecule would enshrine the considerably smaller peptide resulting in a reduction of its biological activity.

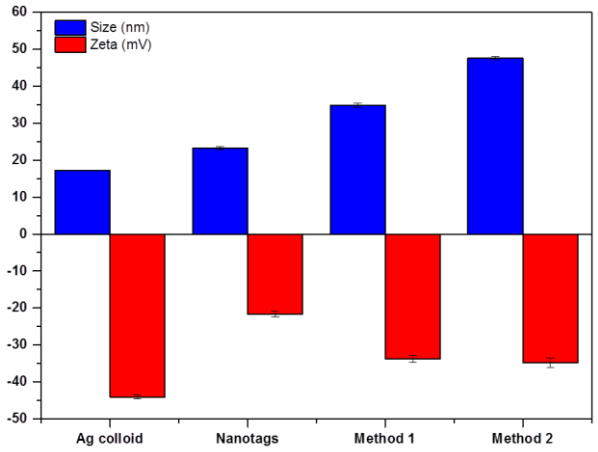

Figure 5.23: DLS size and Zeta measurements for the nuclear targeting nanotags prestabilised with PEG. Samples were dispersed in distilled water. The measurements were made in triplicate, the average is shown and the error bars are represented by the standard deviation of the triplicate measurements.

5.3.2.7 Conclusions

To date a satisfactory nuclear targeting nanotag system has not been developed. A potential candidate which could be investigated further includes the system where lower concentrations of peptides were used to functionalise the surface. By minimising the peptide available the level of unfavourable electrostatic interactions were minimised. However, there were concerns regarding the long term stability of these nanotags and this system is only viable for short periods of time since the low concentrations of peptide were not sufficient to stabilise the nanotag aggregates in the long term. Pre-stabilising the nanotag surface with a PEG molecule presents another viable option. However, subsequent functionalisation of the nanotag surface by the peptide must be demonstrated and the biological activity of the peptide must not be hindered by the bulky PEG molecule. Other options which could be considered include conversion of the amine groups on the lysine residues to succinyl amides, since this would remove the issue of unfavourable electrostatic interactions and permit conjugation to the nanotag surface.[75] Once inside the cell and presented to an acidic

environment the targeting functionality of the peptide could be restored.[75] However, at this stage there is always the risk that aggregation could occur.

5.4 *In vitro* Analysis of the Targeting Nanotag Systems

A stable nuclear targeting nanotag system was not developed and as a result only the ER and TGN targeting nanotags (5.3.1.3) were carried forward to the *in vitro* studies. The ER targeting nanotags were labelled with (4-nitrobenzenethiol) NBT and the TGN targeting nanotags were labelled with (4-mercaptobenzoic acid) MBA. The targeting samples were made up individually and added to cell populations. An equal proportion of both the ER and TGN nanotags were also pre-mixed and added to cells to form the multiple component sample.

5.4.1 2D Raman and SERS Imaging

Samples were interrogated by Raman mapping using a Renishaw inVia Raman spectrometer/Leica DM 2500 M microscope. For the Raman measurements a 532 nm laser (Cobalt) excitation source was used and the cell samples were imaged under immersion in a saline solution using an Olympus 60× (N.A. 1) water immersion objective. A grating of 1800 lines / mm was used with a RenCam CCD (1046 × 256 pixels). For the SERS measurements a 633 nm (HeNe) excitation source was used and cells were also imaged under immersion.

Acquisition and analysis of the collected data was performed using the WiRE 4 software package. All PCA analysis was performed in WiRE and a number of pre-processing steps can be incorporated including mean centring, spectrum centring and normalisation. False colour Raman maps were generated using PCA[204] and false colour SERS maps were generated using component DCLS.[204]

5.5 Targeted 2D Optical Imaging of ER Targeting SERS Nanotags in Cells

Individual cell samples were prepared with ER and TGN nanotags and a multiple component sample with a combination of ER and TGN targeting nanotags were also prepared. As an initial starting point the ER targeting nanotag samples were analysed.

5.5.1 2D Raman Imaging of Cells

Once a nanotag positive cell had been identified from the NBT reporter on the surface of the nanotag, the cell can be imaged using the 532 nm laser. At this excitation intrinsic Raman signals of the cell can be collected. Following data collection and as discussed in Chapter 4 false colour Raman maps can be constructed using univariate or multivariate analysis. As it was important to determine the localisation of the SERS nanotags in relation to the cell organelles, particularly the ER, PCA was applied to the data to determine if there were any spectral variations which could be ascribed to specific cell organelles.[247] PCA conditions included mean centring and no scaling. Mean centring was employed so that the main differences between the spectra could be observed especially since the majority of the spectra in the sample were similar and had a large offset from zero in the y-axis (**Figure 5.24**).

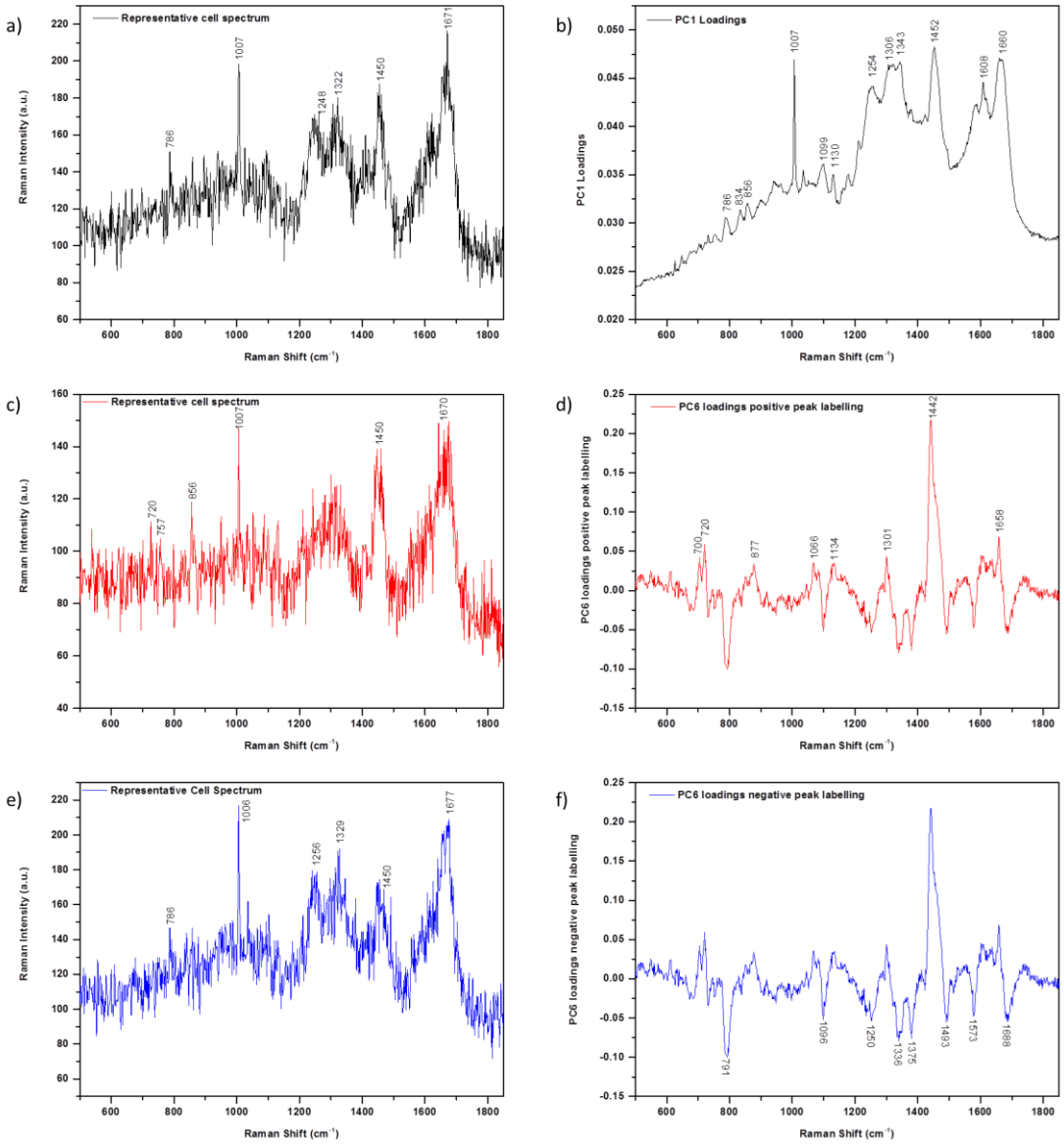

Figure 5.24: Representative Raman Spectra and the corresponding PC loadings for the cell, lipid rich regions and the nuclei. a) A representative Raman spectrum measured from the general cell contents, b) PC 1 loadings which distinguish the general cell contents, c) representative Raman spectrum measured from the lipid rich cell regions, d) PC 6 loadings positive peak labelling which distinguish the lipid rich regions, e) representative Raman spectrum measured from the nuclei and f) PC 6 loadings negative peak labelling which distinguish the nuclei.

Scaling was not applied since it was desired that the processed data reflected the differences between the spectra. For the analysed sample, eight principal components (PCs) explained 93.7% of the variance in the data set, with PC 1 representing the

general cell contents and both the positive and negative loadings of PC 6 representing lipid rich cell regions and the nuclei of the cell respectively.

When comparing the PC loadings and the band assignments (**Table 5.2**), PC 1 explained 91.4% of the variance in the data. PC 1 was collectively characterised by Raman bands attributed to protein, lipid and nucleic acids but most notably by peaks ascribed to the ring breathing mode of phenylalanine (1007 cm^{-1})[243, 248] and the CH_2CH_3 deformation of protein and lipid bands.[244] PC 1 represents the general cellular regions and this is consistent with the raw Raman spectrum. The PC 1 false colour image clearly defines the structure of the mapped cells (**Figure 5.25d**).

Table 5.2: Peak positions and tentative assignments of the main peaks found in the principal component (PC) loadings for each PC shown in the 2D and 3D volume cell maps.[92, 243, 244, 248, 249, 251-256, 267-271]

Peak position (cm^{-1})	Assignment
549	cholesterol
704	cholesterol/fatty acids
720	DNA, C-N phospholipid head phosphatidyl choline
732	
752-753	DNA
786	DNA
787	nucleic acids
791-792	υO-P-O DNA
833-834	υO-P-O DNA, tyrosine
856	hydroxyproline
876	υ(C-C), hydroxyproline
1006,1007	phenylalanine
1066	fatty acids
1096, 1097	phosphodioxy groups (PO_2^-)
1099	υ(C-N)
1130	υC-C, phospholipid
1134	phenylalanine
1211	phenylalanine, tyrosine
1249	
1250	guanine, cytosine
1254	C-N in plane

1301	lipids CH vibration, fatty acids
1336	DNA polynucleotide chain
1342	guanine (DNA/RNA)
1343	CH_3CH_2
1375	adenine, guanine, thymine
1377	
1441	CH_2 scissoring/CH_3 bending in lipids and protein
1442	fatty acids
1452	CH_2CH_3
1489,1490	DNA
1493	DNA
1573	guanine, adenine
1578	guanine, adenine
1606	phenylalanine
1608	cytosine
1656	C=O, C=C lipids
1658	amide I
1660	amide I
1671	cholesterol
1688	amide I

PC 6 explained 4.44% of the variance in the data. Its characteristics were explained by the positive peaks in the PC loadings which have been ascribed to lipids and fatty acids but most notably by the phosphatidyl choline peak at 720 cm^{-1} lipid peak at 1301 cm^{-1} and the fatty acid peak at 1442 cm^{-1} (**Table 5.2**).[251, 267] The ER is typically associated with a high lipid content[93] and the close proximity to the nucleus and the size of this region suggested that it may represent the ER. In addition, the presence of phosphatidyl choline is particularly diagnostic of membrane bound organelles. However, it is possible that this region may also represent other lipid rich organelles including the Golgi, mitochondria, lysosomes and other intracellular vesicles.[99, 272] All of these have membranes which predominantly consist of phospholipids, therefore they are spectrally similar, and difficult to differentiate between.[99] Nonetheless PC 6 positive domains represented lipid rich regions of the cell (**Figure 5.25e**).

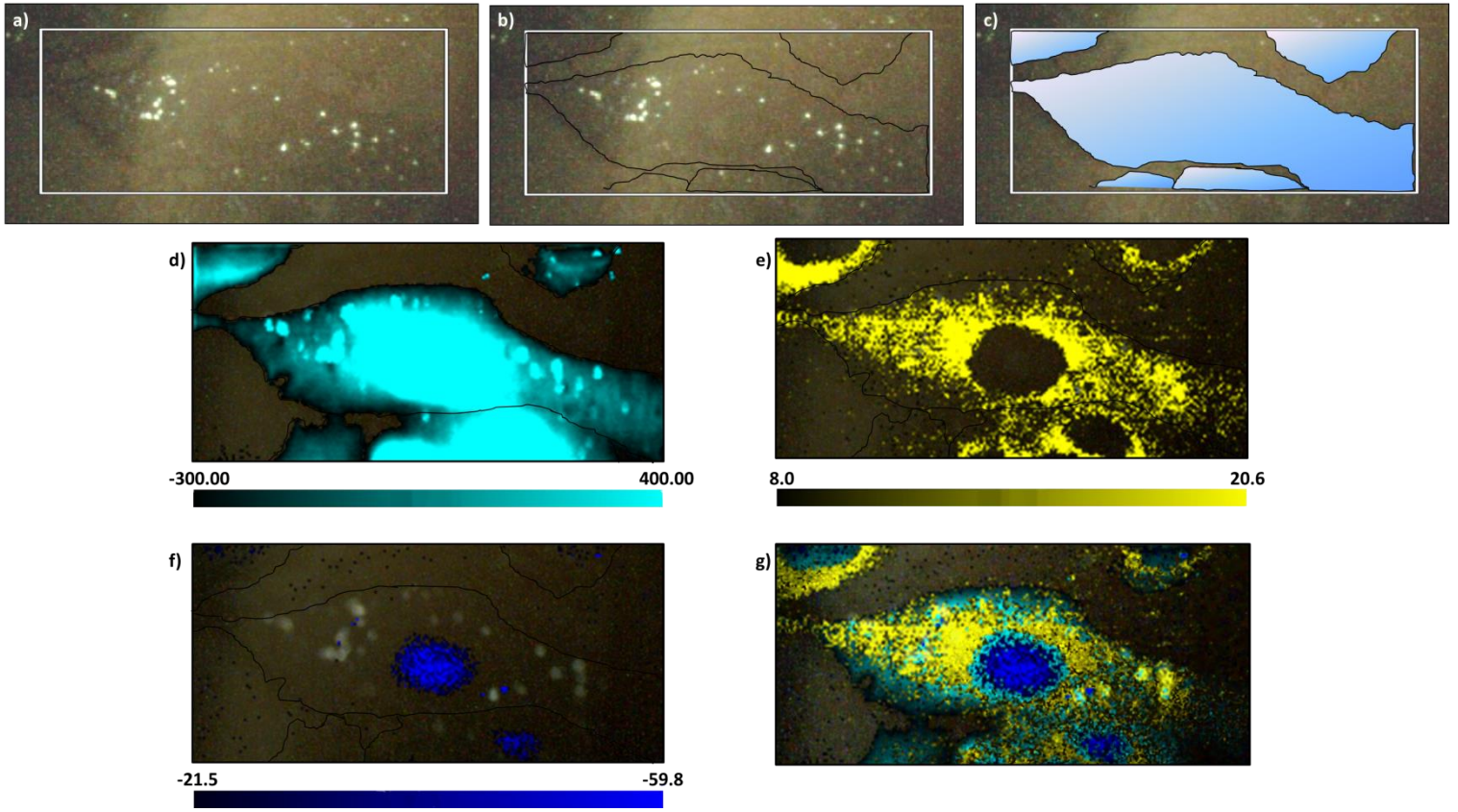

Figure 5.25: White light and false colour Raman map images – a) white light image of the mapped cells, the cells are outlined in black in b) and are distinguished with a gradient fill in blue in c). In a)-c) the white box indicates the imaged area. d)-g) False colour Raman map images generated using PC1 and PC6 loadings and the complete false colour Raman map image. In d)-f) the false colour scale bar is shown below the images. (StreamLineHR – λ_{ex} = 532 nm, 50% (50 mW), spectral range 478-1880 cm^{-1}, step size x,y 0.5 µm, 0.8s)

The PC 6 negative domains were described by negative peaks in the loadings which have been ascribed to DNA, phosphodioxy groups and nucleotides at 791, 1096 and 1336 cm^{-1} respectively (**Table 5.2** and **Figure 5.24f**).[253, 268] The negative PC loadings suggest that the PC 6 negative domains represented regions which were biochemically distinct from the main cell structure and based on the loadings it was proposed that these domains represent the cell nuclei (**Figure 5.25f**). This was consistent with the raw Raman spectra specifically the DNA band at 786 cm^{-1} (**Figure 5.24e**).

The final combined PC image which represents the general cell contents, lipid rich regions and the cell nuclei is shown (**Figure 5.25g**).

5.5.2 2D SERS Imaging of Nanotags

The 2D SERS image was obtained prior to the collection of any cell data and involved mapping the area highlighted within the white rectangle with a 633 nm excitation source (**Figure 5.26**).

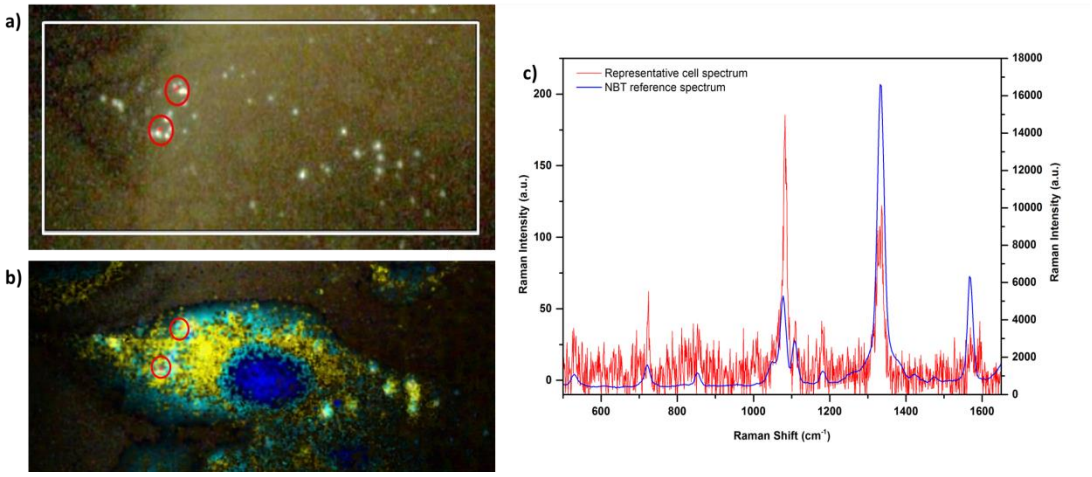

Figure 5.26: False colour SERS nanotag map – a) false colour SERS NBT ER peptide nanotag image, b) combined false colour Raman and SERS map image and c) representative NBT spectrum measured from within the cell. (StreamLineHR – λ_{ex} = 633 nm, 5% (~ 0.45 mW), spectral range 493-1648 cm^{-1}, step size x,y 0.5 µm, 0.3s).

The false colour SERS map was generated by performing component DCLS using the reference standard for the nanotags dually labelled with the ER targeting peptide and the small molecule NBT. From the false colour SERS map NBT signals were found in two locations within the cell and a representative spectrum was also observed (**Figure**

5.26a and **c**). The false colour SERS nanotag map can be overlaid with the false colour Raman cell map because both images were collected from exactly the same region (**Figure 5.26c**).

When the two images were overlaid the ER labelled nanotags were found within the lipid rich regions of the cell which potentially could be the ER (**Figure 5.26c**). However, it was possible that these lipid rich regions could be indicative of any lipid rich organelle or vesicle. Similarly, it has been demonstrated that NBT labelled nanotags can transverse the cell membrane (**Figure 4.12** - **Figure 4.14**) and when they did so they were located within the general contents of the cell. It was possible that in this previous data (section 4.3) set the nanotags were located within lipid rich regions but they were simply not resolved by the PCA. In addition, in this particular data it was not possible to determine whether the cell associated nanotags were located within the cell or were bound to the cell surface. It was demonstrated in the fluorescence analysis that the peptide sequence did translocate the fluorophore to the correct organelle. Provided that the bioactivity of the peptide was retained, there was no reason to assume that the same targeting effect could not be achieved with the peptide labelled nanotags.

In order to definitively determine the intracellular location of the nanotags and for the resolution of further cell organelles, particularly those of similar composition, it might be necessary to look at other methods of multivariate analysis including cluster analysis.[93] This has permitted the cellular resolution of the nucleus, cytoplasm, ER, cell vesicles and the membrane.[93] In another elegant example, Raman spectra were correlated with immunofluorescent stains to build up a database of organelle specific spectra. This allowed for the identification of the nucleus, ER, Golgi and mitochondria.[94] Determining organelle specific spectra is probably one of the few ways of definitively determining and demonstrating organelle specific targeting.

5.6 3D *In Vitro* Analysis of the Targeting Nanotag Systems

5.6.1 3D Raman and SERS Imaging

Samples were interrogated by Raman mapping using a Renishaw inVia Raman spectrometer/Leica DM 2500 M microscope. For the Raman measurements, a 532 nm laser (Cobalt) excitation source was used and cell samples were imaged under

immersion in a saline solution using an Olympus 60× (N.A. 1) water immersion objective. A grating of 1800 lines / mm was used with a RenCam CCD (1046 × 256 pixels). For the SERS measurements a 633 nm (HeNe) excitation source was used and cells were imaged under immersion as described above. The z range was collected from +6.00 to -1.00 from the point of focus when the cell was observed under white light illumination (set as z=0).

Acquisition and analysis of the collected data was performed using the WiRE 4 software package. All PCA analysis was performed in WiRE and a number of pre-processing steps can be incorporated including mean centring, spectrum centring and normalisation. False colour Raman maps were generated using PCA analysis and false colour SERS maps were generated using component DCLS.[204] The volume 3D Raman cell and 3D SERS nanotag images were taken directly from the WiRE Volume Viewer Software. The 2D slices for the Raman images of the cell and the 2D slices for the SERS images of the nanotags were also taken directly from the Volume Viewer Software. The individual 2D slices were then combined into a single image using a GNU image manipulation programme.

5.7 Targeted 3D Optical Imaging of Multiple Targeting SERS Nanotags in Cells

In order to maximise the information gained it was decided to analyse the multiple component sample to which both the TGN and ER functionalised nanotags had been applied.

5.7.1 3D Raman Imaging of Cells

As with previous samples a multiple component positive cell was identified from the signals of the small molecule reporters on the surface of the nanotags. In this instance the TGN targeting nanotags were functionalised with MBA and the ER targeting nanotags were functionalised with NBT. Following identification of the multiple component positive cell, the sample was interrogated by depth profiling at different z-depths to roughly determine the cell thickness and the z-slices from which data should be collected.

The 3D Raman cell image was then collected by mapping the area highlighted within the white rectangle (**Figure 5.28a-b**). As mentioned in 5.6.1 the sample was imaged under immersion and for this particular data set the step size in the x and y directions were set at 0.5 μm and in the z direction at 1.0 μm. The z –range was defined as +6.00- -1.00 μm from the point of focus when the cell was observed under white light illumination (set as z = 0). Following data collection, the false colour 3D Raman images were constructed using PCA since it was necessary to determine the localisation of the nanotags relative to the cell organelles and especially since the resolution of the ER and the Golgi was required. The PCA conditions included spectrum centring, normalisation and mean centring. Mean centring was applied because the primary interest was in the differences between the spectra and also because the raw spectra appeared similar and had an offset from zero in the y-axis (**Figure 5.27**).

For the analysed cells ten PCs explained 16.4 % of the variance in the data with PC 1 and both the positive and negative loadings of PC 4 representing the general cell contents, the lipid rich cell regions and the cell nuclei respectively. PC1 explained 11.5% of the variance in the data and analysis of the PC loadings (**Figure 5.27b**) and the band assignments (**Table 5.2**) revealed that PC 1 was collectively characterised by Raman bands which could be ascribed to proteins, lipids and DNA. Most notably by the ring breathing mode of phenylalanine at 1007 cm^{-1},[243, 248] the CH_2CH_3 deformation of protein and lipid at 1452 cm^{-1} [244] and the lipid band of cholesterol at 1671 cm^{-1}. PC 1 represents the general cellular regions and this is consistent with the raw Raman spectra (**Figure 5.27a**). When PC 1 was used in the generation of the 3D cell image it was found to clearly define the structure of the mapped cells (**Figure 5.28c** and **d**).

PC 4 explained 0.24 % of the variance in the data. Its characteristics were explained by the positive peaks in the PC loadings which have been ascribed to lipids most notably by the cholesterol and fatty acid peaks at 549 and 704 cm^{-1},[268] the lipid peak at 1301 cm^{-1}, the CH_2 scissoring/CH_3 bending lipid peak at 1441 cm^{-1} and the C=O, C=C stretch at 1656 cm^{-1} (**Figure 5.27c** and **d**).[244, 248, 269] As discussed in section 5.5.1., this lipid rich region could represent either the ER or the Golgi but considering the size and location it could potentially represent any/or all of the organelles or vesicles of high lipid content (**Figure 5.28e** and **f**). Nonetheless PC 4 positive loadings represent the lipid rich regions of the cell.

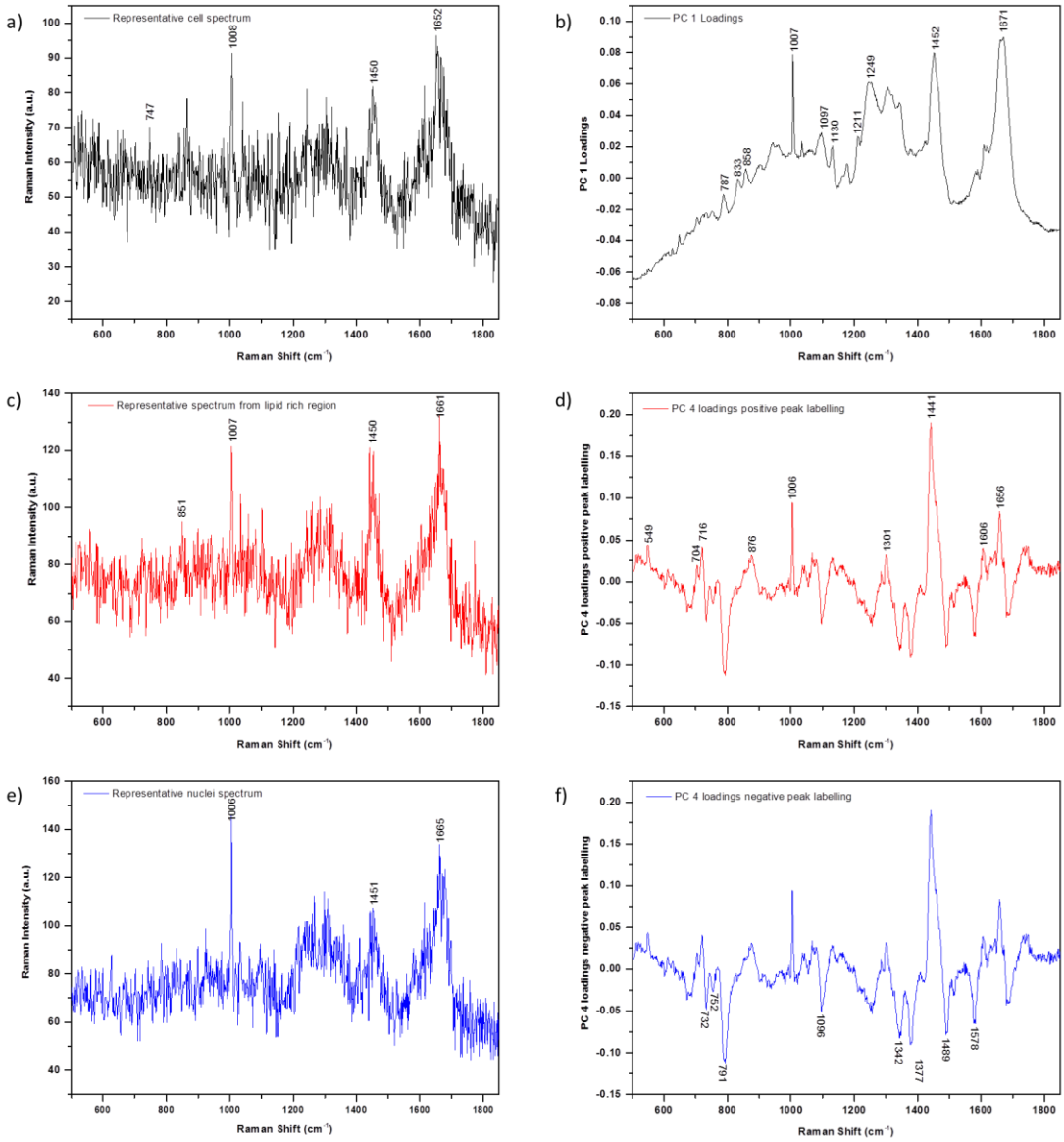

Figure 5.27: Representative Raman Spectra and the corresponding PC loadings for the cell, lipid rich regions and the nuclei. a) A representative Raman spectrum measured from the general cell contents, b) PC 1 loadings which distinguish the general cell contents, c) representative Raman spectrum measured from the lipid rich cell regions, d) PC 4 loadings positive peak labelling which distinguish the lipid rich regions, e) representative Raman spectrum measured from the nuclei and f) PC 4 loadings negative peak labelling which distinguish the nuclei.

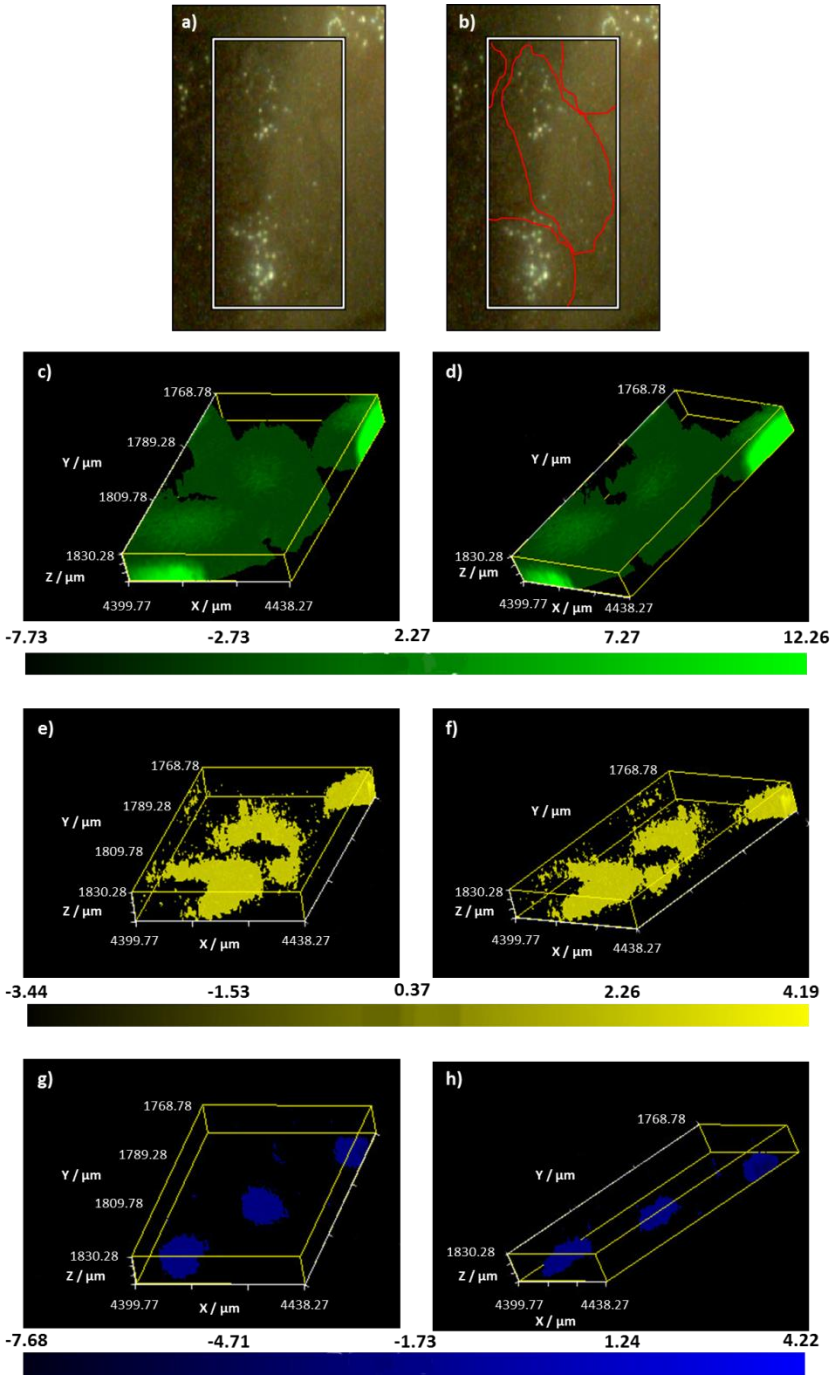

Figure 5.28: White light and false colour volume 3D Raman images of the mapped cells – a) white light image of the mapped cells, the cells are outlined in red. In a) and b) the white box indicates the complete 3D Raman analysed area. c) and d) False colour 3D Raman cell image generated using PC 1 displayed at different angles. e) and f) False colour 3D Raman lipid rich image generated using PC 4 positive loadings displayed at different angles. g) and h) False colour 3D Raman nuclei image generated using PC 4 negative loadings displayed at different angles. In c)-h) the false colour scale bars are shown below the images. (Volume StreamLineHR

– λ_{ex} = 532 nm, 50% (~ 50 mW), spectral range 478-1880 cm^{-1}, step size x,y - 0.5 µm, z - 1 µm, 1s).

The PC 4 negative domains were described by negative peaks in the loadings and have been ascribed to DNA, phosphodioxy groups and nucleotides. The DNA peaks occurred at 752 and 1489 cm^{-1}, while the stretching mode of the phosphodiester backbone was found at 791 cm^{-1}.[248, 270] The band for the phosphodioxy groups occurred at 1096 cm^{-1} and nucleotide bands were found at 1342 and 1578 cm^{-1} (**Figure 5.27e** and **f**).[251, 268] Based on these band assignments it was proposed that the negative PC loadings represented the cell nuclei and when these loadings were used in the 3D Raman false colour image they were found to delineate the cell nuclei (**Figure 5.28g** and **h**).

5.7.2 3D SERS Imaging of the Targeting Nanotags

The 3D SERS nanotag image of the targeting nanotags was generated prior to the collection of any cell data by mapping exactly the same area as highlighted (**Figure 5.28a** and **b**), but using a 633 nm laser excitation instead. The false colour SERS nanotag map was generated by performing component DCLS on the collected volume and although the multiple component sample was analysed signals from only one of the peptide functionalised nanotag was found within this particular cell (**Figure 5.29**). These signals were measured from the MBA/TGN peptide functionalised nanotags (**Figure 5.29**).

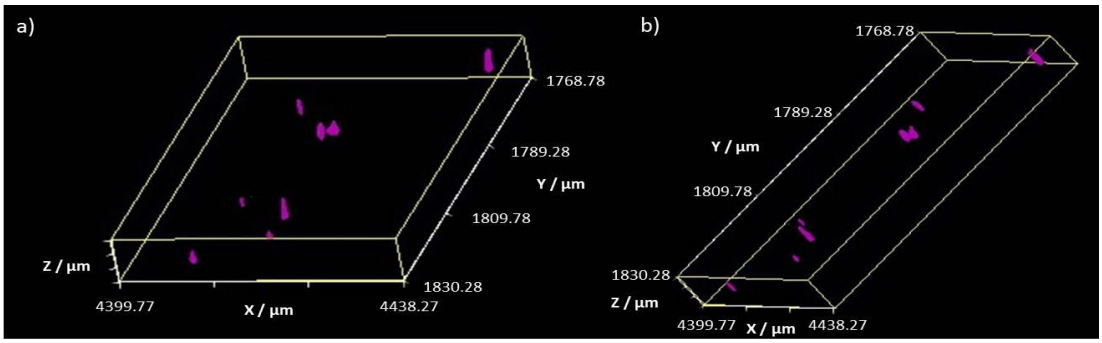

Figure 5.29: False colour 3D SERS nanotag image displayed at different angles – the magenta colour corresponds to the MBA/TGN targeting functionalised nanotags. (Volume StreamLineHR – λ_{ex} = 633 nm, 5% (~ 0.45 mW), spectral range 493-1648 cm^{-1}, step size x,y - 0.5 µm, z – 1 µm, 0.3s).

5.7.3 Combined 3D Raman and SERS Targeted Imaging

The two independently collected 3D data sets were then combined in 2 dimensions for the determination of cellular uptake and localisation of the nanotags relative to the cell organelles which had been resolved. On close inspection of the z-slices it was possible to determine that the MBA/TGN functionalised nanotags were found within the cell since signals were found within all of the z-slices except z-slice +6.00 (**Figure 5.30b-g**). The nanotags were predominantly located in lower z-slices and within the lipid rich regions of the cell. There were some nanotags which were found out with this location and it was possible that these had just entered the cell, but had not had time to actively target the TGN (**Figure 5.30**). None of the nanotags were found within the nucleus but this was to be expected since they were not actively targeting this organelle. The cell on the lower left hand side of the image also appeared to be undergoing mitosis as indicated by the double nucleus (**Figure 5.30e-g**).

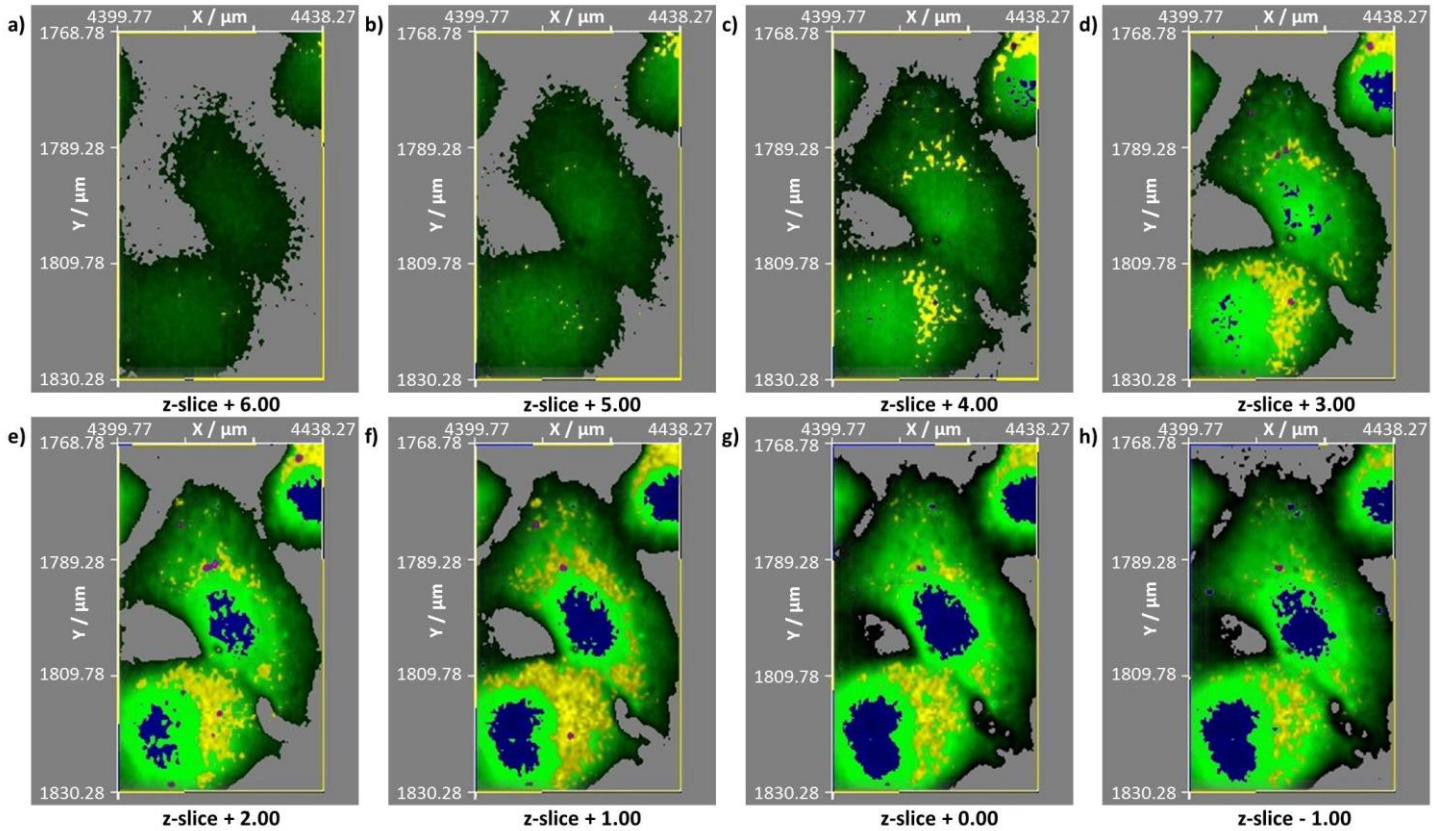

Figure 5.30: Combined 3D volume Raman cell and SERS nanotag maps, images from each plane can be extracted and these can be combined in 2D – a)-g) z-slice cell and nanotag +6.00 - -1.00 respectively. The general cell contents are shown in green, the lipid rich regions in yellow and the cell nuclei in blue. The nanotags are shown in magenta.

Z-slice +1.00 has been enlarged since this was considered to be a z-slice from within the middle of the cell and in which the nanotags can be found within several locations. Representative spectra for the MBA/TGN functionalised nanotags were extracted from two of these locations (**Figure 5.31**).

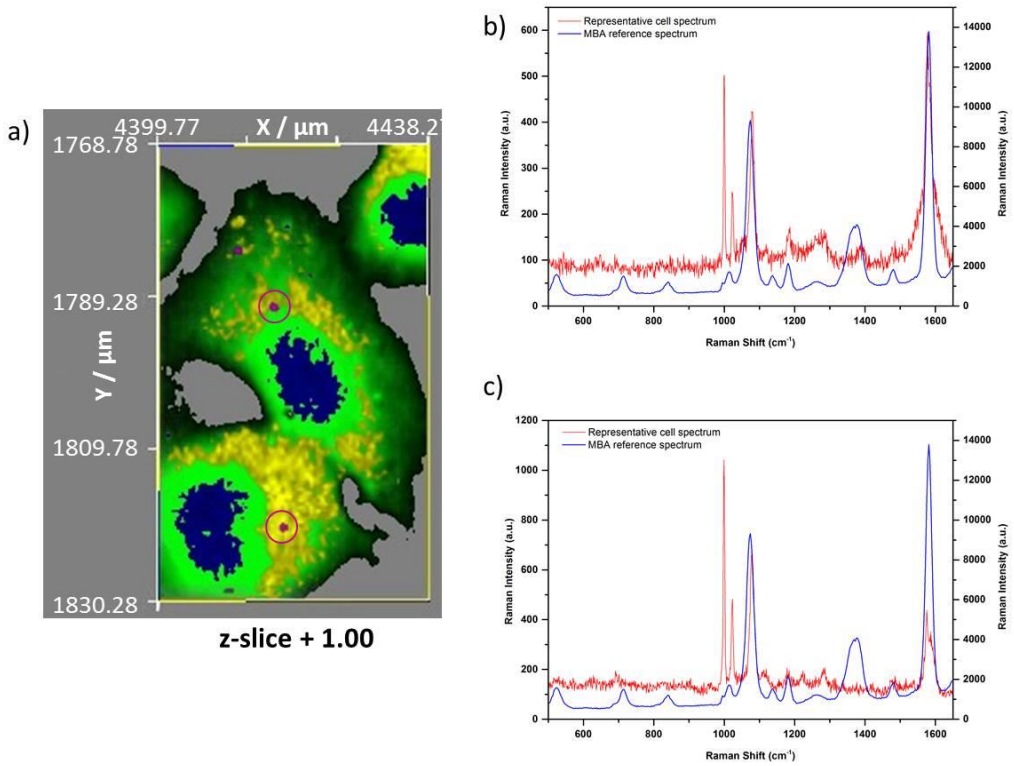

Figure 5.31: Enlarged image of z-slice +1.00 and representative SERS spectra from the areas encircled – a) 2D z-slice nanotag and cells +1.00, b) representative SERS spectrum from the top spot and c) representative SERS spectrum from the bottom spot.

In both the upper and lower locations from where the representative cell spectra have been extracted, there was a reasonable fit with the solution standard (**Figure 5.31b** and **c**). In both instances there appeared to be enhancement of the two bands at ~1000 cm^{-1} and more obviously the absence of the broad peak at ~ 1372 cm^{-1}. It is proposed that the absence of this peak may be due to intracellular pH changes. The presence and absence of this peak has been measured at different pH values when MBA has been adsorbed on Ag nanoaggregates using surface enhanced hyper Raman scattering (SEHRS).[159] Although this technique is different from the method employed here it offers one plausible suggestion as to the absence of this peak. In addition, pH changes were consistent with the shifting of the peak at ~1074 cm^{-1} to ~1080 cm^{-1}. The

technique was also extended to pH measurements in cells and it was found that based on these measurements, most of the particles had accumulated inside lysosomes.[159] The variation in the techniques mean that no conclusive results can be drawn, but it can be suggested that based on the spectra measured, the targeting nanotags were actually found within lipid rich vesicles rather than a lipid rich organelle such as the Golgi. The TGN in CHO cells has a reported pH of ~6[273] and if the nanotags were found within this organelle the peak at 1372 cm^{-1} would be apparent in the SERS spectra.[159] With the absence of any corroborating fluorescence data it is also difficult to suggest that the nanotags would be expected to target or reside in the TGN and based on the current data, it is very difficult to demonstrate targeting of the nanotags to specific cell organelles.

As discussed in section 5.5.2, it was difficult to differentiate between lipid rich organelles such as the ER, the Golgi, the mitochondria and lipid rich vesicles. In order to definitively determine the intracellular location of the nanotags, without employing other techniques, the use of cluster analysis[93] or the creation of an organelle specific spectral databases will undoubtedly become essential. Until then it will be very difficult to demonstrate organelle specific targeting.

5.8 Conclusions

The demonstrated intracellular detectability of the developed nanotag system in 3D was an important precedent. However, if the nanotags are to be suitable multi-markers for the detection of disease processes or drug delivery vehicles then a targeting ability has to be actively proven. In an attempt to demonstrate a targeting ability, it was decided to take advantage of the cell logistics for protein cataloguing and peptide sequences suitable for the targeting of the ER, TGN and the nucleus found within the literature.[71, 72, 74]

The peptide sequences had been tested in cell lines different to those used in this study and in an effort to determine the organelle specificity of the sequences for the specific cell line used each peptide was conjugated to a fluorophore. If the peptide sequence had a targeting ability to the organelle then it was expected that it would translocate the fluorophore to the appropriate cell compartment and when counterstained with an organelle specific stain, co-localisation of the fluorophores would be observed.

Organelle specificity was only demonstrated for the ER peptide sequence, the TGN sequence didn't exhibit any organelle specificity. This may have been due to the method of incubation, however despite the lack of demonstrated organelle specificity it was decided to use the peptide sequence to generate targeting nanotags.

The nanotags were easily functionalised with the ER and the TGN peptide sequences but with the positively charged nuclear targeting sequences it was difficult to create stable nuclear targeting nanotags. As a result of this, only the ER and TGN targeting nanotags were taken forward for cellular studies. This was disappointing since a nuclear targeting nanotag system would have provided the 'gold standard' since, in both 2 and 3D, the nucleus can be readily resolved by Raman spectroscopy.

Due to instrumental time constraints it was only possible to analyse one sample in 2D and a further sample in 3D. In an effort to maximise the information gathered an ER targeting nanotag sample was analysed in 2D and the nanotags were found within the lipid rich regions of the cell. Similarly when a multiple component sample which had been exposed to nanotags functionalised with the ER and the TGN peptide sequences was analysed in 3D, only the TGN labelled nanotags were found within the particular cell analysed but again these were located within the lipid rich regions. Differentiating between organelles and vesicles which are both rich in lipids is a notoriously difficult problem. Whilst the fluorescence data corroborated that the ER peptide sequence was capable of targeting the ER no such data was available for the TGN peptide sequence. In both instances it was difficult to definitively determine whether the nanotags had reached their intended destinations or whether they were located within a lipid rich vesicle like an endosome or lysosome.

To resolve organelles and vesicles of similar composition, such as the ER, the Golgi, the mitochondria, endosomes and lysosomes it may be necessary to employ multivariate methods such as hierarchical cluster analysis or develop a database of organelle specific spectra using the boundaries from immunofluorescent stains as a guidance to the organelle location.[93, 94]

Chapter 6 Conclusions

In the initial stages of investigation a range of commercial nanotags were investigated as suitable multi marker imaging agents for *in vitro* experiments. These nanotags performed excellently both in suspension and in cell experiments. In each instance it was possible to identify the specific combination of nanotags that were present. The nanotags were identified from the unique combination of peaks produced by each of the reporter molecules and using the multivariate analysis method, component DCLS, it was possible to positively identify each of the nanotags present within a multiple component sample. The maximum number of components which could be detected in a single cell was four nanotags. However, this was the maximum which was applied to the cell populations and it is likely that further components could be detected within a single cell if the number of individually labelled nanotags was increased. The next stage of investigation would have involved imaging the cells and nanotags in 3D but, unfortunately for commercial reasons, further work with the nanotags could not be continued.

Additional investigations were required to find suitable imaging alternatives. A range of colloidal materials were labelled with small molecule reporters but variable results were obtained. With the Ag nanoparticle suspensions measurable signals were only observed when the suspensions were forcibly aggregated with a salt agent, whilst the Au suspensions aggregated uncontrollably with addition of the small molecule reporters. Uncontrolled aggregation is undesirable for cell investigations since excessively large aggregates are incapable of crossing cell membranes. However, it was clear than some form of aggregation would need to be implemented if optically strong imaging agents were to be developed. Within the literature a method for 'controllably' aggregating the nanotags was found.[9] The nanoparticles were cross-linked with 1,6-HMD and the aggregation reaction was subsequently dampened by the addition of the polymer, PVP.[9] At this stage the nanotags could be labelled with virtual any reporter molecule but a range of small molecules were implemented. It was necessary to optimise several conditions and the final nanotag system consisted of Ag citrate controllably aggregated with 0.2 mM 1,6-HMD, polymer coated with 41.7 μM PVP and labelled with either 10 μM MBA, NBT, SERS-403 and 2-NPT or 50 μM MPY or DTNB.

Additional stability was added to the system by the introduction of PEG. The nanotag stock solution was prepared as previously described and PEG was then added at 2 nM. This solution was agitated for 30 min before the small molecule reporters were added at 200 μM and again the solution was allowed to agitate for 30 min before the final addition of PEG at 20 μM. Purification of both nanotag systems was achieved by centrifuging at 5000 rpm for 10 min, supernatant removal and pellet resuspension with dH_2O.

A multiple component sample consisting of MPY, DTNB, NBT and 2-NPT labelled nanotags was developed for cell investigations. Each of the individually labelled nanotags was identified by their unique peak and component DCLS analysis. In the final cell studies it was possible to identify 3 components (MPY, DTNB and NBT) of the multiple component sample within a cell. At the time this marked an increase in the number of nanotags which could be detected simultaneously within a single cell.

Nanotag uptake and intracellular localisation can be difficult to determine without using conventional techniques such as TEM. The concept of combined 3D Raman and SERS imaging was proposed as an alternative for the simultaneous identification of multiple components and confirmation of cellular uptake. A proof of concept experiment was devised and it was determined that it was possible to combine the 3D Raman cell map with the 3D SERS nanotag map for nanotag identification and confirmation of cell uptake. However, it was only possible to identify one nanotag confidently within a single cell and the resolution of the nanotags was poor. In an effort to improve the resolution and the number of nanotags identifiable numerous improvements were made. The nanotags were PEGylated to improve stability and the images were collected with a microscope objective with a higher N.A. This can allow for the collection of higher resolution images since it is possible to collect the light from a wider angular range. With these improvements it was possible to detect three nanotags (MPY, DTNB and NBT) within a single cell in 3D, thus confirming identification and uptake. The nanotags were found to co-localise with one another and in accordance with this co-localisation cumulative cell signals arose. That is SERS signals from each of the nanotags within a specified location were observed. The application of PCA also resulted in the resolution of a major cell organelle without the need for any cell staining or any other specialised sample preparation. The ability to detect multiple imaging

agents within a single cell in 3D will be invaluable for range of applications where disease states or processes are to be detected and characterised fully.

The development of multi-marker nanotags and their subsequent detection in 3D were key steps in the progression of a system which could potentially be used for *in vivo* disease detection. However, until sensitive and selective targeting can be demonstrated the system is limited in the applications to which it can be applied. In order to specifically target cell organelles the nanotags were functionalised with peptides, each of which had a reported specificity towards a particular cell organelle (ER, TGN and nucleus). The nanotags were successfully functionalised with the ER and TGN sequences but unfortunately they could not be functionalised with the nuclear sequences. This was due to unfavourable electrostatic attractions between the positively charged peptide sequences and the negatively charged nanotags. The ER functionalised nanotags were applied to a cell population and when they were analysed in 2D they were located within lipid rich regions of the cell. Similarly, when cells exposed to ER and TGN functionalised nanotags were analysed in 3D, the TGN nanotags were also located within lipid rich regions of the cell. However, it was impossible to definitively determine if these lipid rich regions were the ER and TGN since a range of organelles including the ER, TGN, mitochondria and other vesicles are known to be lipid rich. In order to determine specific organelle targeting the implementation of further chemometric methods will be required to resolve organelles of similar composition.

Chapter 7 Future Work

In the 2D cell experiments it was clear that the uptake of the nanotags wasn't uniform across the cell population and the investigation could benefit from an uptake study. This is important for many reasons especially as it could potentially provide the optimum concentration at which the nanotags should be applied to the cell population so that their uptake is more uniform across individual cells and the entire population. The uptake study could be performed for each of the individually labelled nanotags and for the multiple component samples, to determine if the uptake within the mixed sample is competitive, co-operative or independent. With some careful manipulation the method of uptake (i.e. clathrin or caveolae endocytosis) could also be determined and this could benefit the targeting experiment. Depending on the method of uptake the nanotags may become trapped within the endolysosomal network. Knowledge of this could allow for the design of more sophisticated nanotags capable of escaping this pathway and directly reaching their targets.

For the 3D cell experiments further data could be collected for the nanotags in cells to determine how representative the current data sets are. Further comparisons should be made between the PEG and normal nanotags to determine if pegylation is responsible for the improved uptake and co-localisation. 3D Raman imaging is a useful technique for studying cellular architecture and this could be expanded to study several processes where the cell architecture is known to change considerably such as mitosis and apoptosis or between undifferentiated and differentiated stem cells. In addition, since the cellular architecture can change considerably between diseased and healthy cells, 3D Raman imaging could be used to provide an understanding of these changes. Drug delivery and the subsequent effect on the cell architecture could also be studied in this way. Similarly, the process of drug delivery and distribution throughout a cell could be monitored using the 3D methods.

For the targeting experiments there is a real need to develop a nuclear targeting system. This represents the 'gold standard' since selective targeting of this organelle can be readily confirmed by resolution of the nucleus by Raman spectroscopy. One possible option is to coat gold nanoparticles with PEI since in a previous study they did

not aggregate excessively. This would provide a positive surface for the peptide to bind to and the unfavourable electrostatic attractions would be eliminated. The resolution of further cell organelles is required and additional chemometric methods should be investigated for this purpose, in particular cluster analysis. The development of an organelle specific Raman database is another possible option for the resolution of the organelles. Until organelle specific data has been obtained and in the absence of any corroborating fluorescence data, specific organelle localisation of the targeting nanotags will be difficult to confirm. If organelle targeting can be demonstrated this method could be adapted to measure organelle or vesicle pH. MBA and MPY are both pH sensitive molecules and the ratiometric change indicated by their spectral profiles can be used as a measure of pH. Knowledge of both could be helpful in the design of more suitable nanotags, especially if they are presented with extremes of pH. For example, the nanotags could be coated with a protective layer which facilitates passage across the cell membrane whilst protecting the targeting entity. This protective layer could be tuned so that it degrades at a specific point exposing the targeting moiety and allowing the nanotag to continue on its targeting journey.

Chapter 8 Experimental

8.1 Instrumentation

UV-Visible Absorption Spectroscopy

- Varian Cary® 300 Bio UV-visible spectrophotometer

Dynamic light scattering and Zeta potential measurements

- Malvern Zetasizer Nano Zs

SEM Imaging

- Sirion 200 Schottky field emission electron microscope

Raman and SERS Imaging

- Strathclyde – Renishaw inVia Raman spectrometer/Leica DMI 5000 M inverted microscope
- Renishaw plc – Renishaw inVia Raman spectrometer/Leica DM 2500 M microscope

Lasers

- 532 nm excitation – Argon ion laser
- 633 nm excitation – HeNe laser
- 785 nm excitation – Laser diode

Fluorescence Microscopy

- Nikon Eclipse LV100 microscope and Photometrics CoolSNAP HQ camera
- Semrock FITC 350B-NTE filter cube
- Semrock TEXAS RED 4040B-NTE filter cube
- Metamorph® Microscopy Automation and Image Analysis Software

8.2 Buffer Preparation

8.2.1 Phosphate Buffer (60 mM)

0.02880 g of NaH_2PO_4 and 0.3407 g of Na_2HPO_4 were individually dissolved in 40 mL dH_2O. The desired pH solution was prepared by mixing various ratios of the two salt solutions. Working concentrations of the buffer were prepared by diluting the stock with dH_2O.

8.2.2 HEPES Buffer (1M)

23.8 g of 4-(2-hydroxyethyl)-1-piperazineethancesulfonic acid (HEPES) powder was dissolved in 70 mL dH_2O. NaOH (1 M) was used to pH adjust the solution to pH 7.5. The volume was increased to 100 mL with dH_2O. Working concentrations of the buffer were prepared by diluting the stock with dH_2O.

8.2.3 MES Buffer (0.5 M)

9.76 g of 2-(N-morpholino)ethanesulfonic acid (MES) powder was dissolved in 80 mL dH_2O. NaOH (1 M) was used to pH adjust the solution to pH 6.0. The volume was increased to 100 mL with dH_2O. Working concentrations of the buffer were prepared by diluting the stock with dH_2O.

8.3 Colloidal Suspensions

8.3.1 Commercial SERS Nanotags

SERS nanotags (Nanoplex Biotags – Cabot Corporation) were used as supplied (20×). For the cell experiments the nanotags were diluted to a working concentration (0.5×) using dH_2O, 125 µL (20×) in 5 mL dH_2O.

8.3.2 Preparative Steps for Colloid Synthesis

Prior to any colloid preparation the appropriate glassware; 3 parallel necked round bottom flask (1 L), 500 mL glass beaker, glass link stirrer, thermometer, 500 mL and 10 mL measuring cylinders were soaked in aqua regia ($HCl:HNO_3$, 3:1 v/v) for 1-2 h. The glassware was then rinsed with dH_2O into a large beaker. The rinsing's were neutralised with sodium carbonate before being washed down the sink with excess water.

8.3.3 Preparation of Citrate Reduced Silver Colloid

Citrate reduced Ag colloid was prepared according to the Lee and Meisel method[32] whereby 90 mg of silver nitrate was added to 500 mL dH_2O and heated until boiling. Upon boiling a 1% aqueous solution of sodium citrate (100 mg in 10 mL dH_2O) was added and boiling was maintained for 1 h. The solution was allowed to cool and continuous stirring was maintained throughout.

8.3.4 Preparation of Hydroxlamine Reduced Silver Colloid

Sodium hydroxide (0.01199 g) and hydroxylamine hydrochloride (0.0104 g) were added to 90 mL dH_2O and stirred vigorously. Silver nitrate (0.0169 g in 10 mL dH_2O) was added to the mixture and the solution was left to stir for 15 min. [274]

8.3.5 Preparation of Borohydride Reduced, Citrate Stabilised Silver Colloid

A solution of sodium citrate (0.00306 g in 396 mL dH_2O, 0.3 mM) and sodium borohydride (0.01497 g in 396 mL dH_2O, 1 mM) were vigorously stirred on an ice bath for 1 h prior to the rapid addition of silver perchlorate monohydrate (0.009012 g in 4 mL dH_2O, 0.01 M).[275] The solution was continuously stirred for 1 h to ensure the preparation of monodisperse colloids. A colour change is observed on addition of the silver salt, from colourless to a vivid yellow colour.

8.3.6 Preparation of Citrate Reduced Gold Colloid

Citrate reduced Au colloid was prepared according to the method described by Turkevich, Stevenson and Hillier[35] whereby 50 mg of sodium tetrachloroaurate was added to 500 mL dH_2O and heated until boiling. Upon boiling a 1% aqueous solution of sodium citrate (75 mg in 7.5 mL dH_2O) was added and boiling was maintained for 15 min. After this the solution was allowed to cool and continuous stirring was maintained throughout.

8.4 Nanotag Preparation

8.4.1 Nanotag System

The nanotag stock solution was prepared by reacting 10 mL Ag citrate colloid with 10 µL 1,6 –HMD (0.0232 g in 1 mL dH_2O, 0.2 M) for 3 min. 2 mL PVP (50 mg in 5 mL dH_2O,

10 mg/ mL or 250 μM) was added to slow down the aggregation. 999 or 995 μL aliquots were removed and labelled with the appropriate small molecule reporter at the appropriate concentration (see below). The individual nanotag suspensions were left to agitate overnight and the samples were purified by centrifuging at 5000 rpm for 10 min. The supernatant was removed and the pellet was re-suspended by the addition of 1 mL dH_2O.

8.4.1.1 Small Molecule Reporter Concentrations

10 μM final concentration

MBA (1 μL (10 mM), 0.0077 g in 5 mL MeOH)

NBT (1 μL (10 mM), 0.0077 g in 5 mL MeOH)

SERS-403 (1 μL (10 mM), 0.0089 g in 5 mL in MeOH)

2-NPT (1 μL (10 mM), 0.0080 g in 5 mL in MeOH)

50 μM final concentration

MPY (5 μL (10 mM), 0.0055 g in 5 mL in MeOH)

DTNB (5 μL (10 mM), 0.0198 g in 5 mL in MeOH)

The final optimised nanotag system consisted of Ag citrate colloid aggregated with **0.2 mM** (final concentration) 1,6-HMD, polymer coated with **41.7 μM** (final concentration) PVP and labelled with either **10 μM** (final concentration) of MBA, NBT, SERS-403 or 2-NPT or **50 μM** (final concentration) of MPY or DTNB.

8.4.2 Stabilised Nanotag System

The nanotag stock solution was prepared as described in section 8.4.1 940 μL aliquots were removed and labelled with 20 μL carboxymethyl-polyethylene glycol-thiol (COOH-PEG-SH - ~ 5000 MW, 0.0025 g in 500 μL dH_2O, 2 nM final concentration). This solution was allowed to agitate for 30 min before 20 μL of the appropriate small molecule reporter (10 mM stock solutions see above, 200 μM final concentration) was added and this solution was allowed to agitate for 30 min before a final 20 μL addition of COOH-PEG-SH (20 μM final concentration). The individual nanotag suspensions were left to agitate overnight and the samples were purified by centrifuging at 5000 rpm for 10 min. The supernatant was removed and the pellet was re-suspended by the addition of 1 mL or 500 μL dH_2O.

8.4.3 ER and TGN Peptide Stabilised Nanotag Systems

The nanotag stock solution was as described in section 8.4.1. 970.2 µL aliquots were removed and labelled with 9.8 µL of either the ER (0.1 mM solution diluted from 1 mM stock solution - 0.00125 g in 1 mL dH_2O) or the TGN (0.1 mM solution diluted from 1 mM stock solution – 0.00154 g in 1 mL dH_2O) peptide. The final peptide concentration was 1 µM. The solution was allowed to agitate for 30 min before 20 µL of the appropriate small molecule reporter (1 mM solution diluted from the 10 mM stock solution) was added. The stock solutions for the small molecule reporters are listed in section 8.3.1.1 and the final reporter concentrations was 10 µM. The individual nanotag suspensions were left to agitate overnight and the samples were purified by centrifuging at 5000 rpm for 10 min. The supernatant was removed and the pellet was re-suspended by the addition of 1 mL or 500 µL dH_2O.

8.4.4 Nuclear Peptide Stabilised Nanotag System

8.4.4.1Nucleur Peptide Stabilised Nanotags – refer to section 5.3.2.1 – 5.3.2.3

Nanotags were initially stabilised with nuclear peptide sequences according to the standard protocol described in section 8.3.2 with the exception that PEG was replaced with pre-mixed solutions of both nuclear peptides at the specified concentrations (section 5.3.2.1). Increased and decreased peptide concentrations of the nuclear peptides were investigated. For the experiments using elevated concentrations of the nuclear peptides (section 5.3.2.2) the nanotags were only labelled with the peptide sequences to give final peptide concentrations ranging from 1 – 100 µM on the nanotag surface. For the decreased peptide concentration experiments (section 5.3.2.3) the nanotags were prepared according to the procedure described in section 8.3.2 but the PEG was replaced with pre-mixed solutions of both nuclear peptides and for the final peptide addition the concentrations ranged from 20 µM – 2 nM.

8.4.4.2 Positively Charged Nanoparticles/Nanotags – refer to 5.3.2.4

Nanotags were prepared according to the procedure described in section 8.3.2 but the PEG was replaced with pre-mixed solutions of both nuclear peptides at the specified concentrations. Polyethylamine (PEI) was added to the surface of unfunctionalised nanoparticles and the prepared nanotags to give final concentrations ranging from 2×10^{-4} - 2×10^{-6} %. PEI solutions were prepared by diluting the 2 % stock solution (0.1 g in 1 mL) with dH_2O.

8.4.4.3 Bioconjugation of the Peptide – refer to 5.3.2.5

Nanotags were prepared according to the protocol described in section 8.3.2. 950.4 µL aliquots were removed and were labelled with 9.6 µL small molecule reporter (1 mM diluted from 10 mM stock to give 10 µM final concentration). Samples were left to agitate for 10 min before 40 µL PEG (PEG_{635} or PEG_{5000} 1 mM to give 40 µM final concentration) was added and samples were left overnight. Nanotags were purified by centrifuging at 5000 rpm for 10 min, the supernatant was removed and the pellet was re-suspended with 40 µL NHS (1 mg/mL in 10 mM MES buffer) and 20 µL EDC (1 mg/mL in 10 mM MES buffer). The sample volume was increased to 1 mL with 10 mM MES buffer. The samples were allowed to agitate for 30 min at room temperature before the sample was centrifuged at 5000 rpm for 10 min. The supernatant was removed and the pellet was re-suspended with 10 µL NLS/RME combined peptide sequences (1 mM – 10 µM final concentration) and the sample volume was increased to 1 mL with 10 mM HEPES buffer. Samples aggregated upon peptide addition and full re-suspension.

8.4.4.4 Prestabilisation of the Nanotag Surface - refer to 5.3.2.6

Nanotags were prepared according to the protocol described in sections 8.3.2. 940 µL aliquots were removed and were labelled with either 20 µL PEG_{5000} or the nuclear peptide sequences (1 µM). Samples were left agitating for 10 min before 20 µL of the appropriate small molecule reporter was added (1 µM). Samples were again left to agitate for a further 10 min. In the final addition step 20 µL PEG_{5000} or the nuclear peptide sequences whichever had not been added in the first addition were added to the nanotag suspension. The individual nanotag suspensions were left to agitate overnight and the samples were purified by centrifuging at 5000 rpm for 10 min. The supernatant was removed and the pellet was re-suspended by the addition of 1 mL dH_2O.

8.5 Cell Preparation

8.5.1 Preparation of Materials for Cell Culture

Phosphate buffered saline (PBS) for cell culture was prepared by dissolving a PBS Dulbecco A tablet in 100 mL dH_2O which had been sterilised by autoclaving. The PBS solution was also autoclaved prior to use.

8.5.2 Macrophage and Dendritic Cell Preparation

Macrophage and dendritic cells obtained from Balb/C mice were routinely grown in Rosewell Park Memorial Institute (RPMI) medium supplemented with L-glutamine (1 %) and penicillin/streptomycin (1 %) at 37 ˚C in a humidified 5 % CO_2 atmosphere. After reaching confluence, cells were harvested and seeded at 2 × 10^5 cells per well in a 24-well sterile tissue culture plate to which 13 mm round glass coverslips had been previously applied. The cells were incubated overnight at 37 ˚C, 5 % CO_2 in order to allow the cells to adhere to the coverslips. The appropriate nanotag solutions were added to the cells and incubated for 90 min. Following incubation and in order to remove any extracellular material the cells were washed four times with PBS before fixation with methanol. After 15 min the coverslips were washed consecutively with PBS and dH_2O. After fixation the coverslips were air dried for ~ 2 h before being mounted on labelled slides using distyrene-plasticiser-xylene (DPX) mountant.

8.5.3 HeLa and CHO Cell Preparation

HeLa and CHO cells were grown in Dulbecco's Modified Eagle Medium (DMEM) with heat-inactivated foetal bovine serum (10 %), L-glutamine (1 %) and penicillin/streptomycin (1 %) at 37 ˚C in a humidified 5% CO_2 atmosphere. After reaching confluence, cells were harvested and seeded at 2 × 10^5 cells per well in a 24-well sterile tissue culture plate to which 13 mm round glass coverslips had been previously applied. The cells were incubated overnight at 37 ˚C, 5 % CO_2 in order to allow the cells to adhere to the coverslips. The appropriate nanotag solutions were added to the cells and incubated for 1 h. Following incubation and in order to remove any extracellular material the cells were washed four times with PBS before fixation with paraformaldehyde (4 %). After 15 min the coverslips were washed consecutively with PBS and dH_2O. After fixation the coverslips were air dried for ~ 2 h before being mounted on labelled slides using DPX mountant.

Glass microscope slides and coverslips can interfere with spectral measurements and for the 3D data sets cells were grown on CaF_2 windows. The same procedure as used for the preparation of the coverslip samples was adhered too including the fixation protocol but there was no need for sample mounting.

In a further modification and for the minimisation of non-specific binding the cells were cultured as above but upon reaching confluence the cells (0.5 mL, 4 × 10^6 cells per mL) were transferred to a T25 tissue culture flask with 5 mL of the appropriate media and 100 μL of the appropriate nanotag suspension. The flask was left for 24 h and after this the cells were washed with the remaining cell media by gently agitating the flask for 5 min. The cell media was discarded and the cells were washed with PBS (1 mL) for a further 5 min, the PBS was discarded and the wash procedure repeated. The cells were removed from the flask with trypsin (2 mL) and this reaction was quenched by the addition of cell media (3 mL). 2 mL aliquots were removed and incubated with CaF_2 windows for 24 h. Following incubation the cells were washed four times with PBS before fixation with paraformaldehyde (4 %). After 15 min the coverslips were washed consecutively with PBS and dH_2O. After fixation the coverslips were air dried for ~ 2 h before being mounted on labelled slides using DPX mountant.

8.5.4 Cell preparation for Toxicity Testing

8.5.4.1 Replicating Direct Nanotag Incubation on Coverslips

CHO cell samples were prepared according to the procedure described above whereby cells were seeded at 2 × 10^5 cells per well in a 24-well sterile tissue culture plate. 300, 200 or 100 μL of the appropriate nanotag suspension was added for 1 h and a portion of this cell/nanotag mixture was removed and added to a 96-well plate for analysis on the fluorimeter. Samples were prepared in triplicate for each of the nanotag concentrations and for each of the nanotag labels including a multiple component sample. AlamarBlue® reagent was added to each well and samples were incubated at 37 ˚C for 4 h. After 4 h the produced fluorescence was measured. To the same wells Sytox® Green was added and samples were incubated for 10 min at 37 ˚C and the fluorescence signal was also measured.

8.5.4.2 Replicating Nanotag Incubation in Culture Flasks

Nanotag samples prepared by directly incubating the nanotags in tissue culture flasks with the cells were prepared according to the procedure described in section 8.5.3. Upon reaching confluence the cells (0.5 mL, 4 × 10^6 cells per mL) were transferred to a T25 tissue culture flask with 5 mL of the appropriate media and 300, 200 or 100 μL of the appropriate nanotag suspension. The flask was left for 24 h and after this the procedure as described in section 8.5.3 was replicated. Aliquots were removed and

added to a 96-well plate for analysis on the fluorimeter. Samples were prepared in triplicate for each of the nanotag concentrations and for each of the nanotag labels including a multiple component sample. AlamarBlue® reagent was added to each well and samples were incubated at 37 ˚C for 4 h. After 4 h the produced fluorescence was measured. To the same wells Sytox® Green was added and samples were incubated for 10 min at 37 ˚C and the fluorescence signal was measured.

8.6 Stability and Characterisation Measurements

8.6.1 UV-Visible Absorption Spectroscopy

UV-visible absorption spectra were measured on the instrument listed in section 8.1 using 1 cm path length cells. A dH_2O blank was run prior to any sample analysis to establish a baseline. Sample analysis was carried out with an appropriate volume of the colloidal suspension diluted to 2 mL with dH_2O. UV-visible spectra were normalised to the absorption maxima.

8.6.2 Dynamic Light Scattering (DLS) and Zeta potential

DLS measurements were recorded using the instrument listed in section 8.1 using 1 cm path length cell. DLS was used to determine the size of the nanoparticles within the suspension and to observe the size effects of functionalising the nanoparticle surface. Sample analysis was carried out with 1 mL of the appropriate suspension diluted to 2 mL with dH_2O.

Zeta potential measurements were carried out in an identical manner to the DLS except a 1 cm path length dip cell was used with 600 µL of the appropriate sample.

8.6.3 SEM Imaging

Silicon wafers were cleaned using water and ethanol before being dried under nitrogen flow. Wafers were placed in an oxygen plasma cleaner for 60 s before treatment with poly(diallyldimethylammonium) chloride (PDDA) (50 µL) – (30 µL PDDA in 1 mL 1 mM NaCl). The PDDA provides a positive surface to which the negatively charged nanoparticles can adhere. Wafers were left for 30 min before being washed with distilled water and dried under nitrogen flow. 50 µL of sample was deposited on to a wafer and allowed to rest for 30 min. The solution was then removed and the wafers

were again washed with distilled water and dried under nitrogen flow. The samples were analysed using the instrumentation outlined in section 8.1.

8.6.4 Gel Electrophoresis

1 g agarose was dissolved in 100 mL Tris Borate EDTA (TBE) buffer (1× diluted from 10 × stock) by heating. The gel solution was cooled, poured and allowed to set. The gel was added to the electrophoresis tank, the tank was filled and the gel was completely covered with 1× TBE buffer. The samples were prepared according to the particular method of nanotag preparation and were purified by centrifuging at 5000 rpm for 10 min. The supernatant was removed and the pellet was re-suspended with 50 µL phosphate buffer (10 mM, pH 7.6). A 10 µL aliquot was removed and mixed with 1 µL 6× loading buffer, the sample was then loaded into a well in the gel. A 160 mV voltage was applied to the gel and the gel was run for ~ 30 min.

8.7 Spectroscopic Measurements and Imaging

8.7.1 Solution Measurements of the SERS Nanotags

Solution measurements of the commercial SERS nanotags were made using a 785 nm probe system and 1 cm path length cells. The exact experimental conditions are specified in figure captions. Both static and extended scans were performed.

Synthesised nanoparticle suspensions were analysed using a Renishaw inVia Raman spectrometer / Leica DMI 5000 M microscope and a 633 nm laser excitation source. Aliquots of the appropriate solution were added to glass vials and analysed with the inverted laser system. The exact experimental conditions are specified in figure captions and both static and extended scans were performed.

8.7.2 2D SERS Imaging of Nanotags and Cells

Fixed cell samples were imaged in 2D according to the experimental conditions specified in the figure captions. Line mapping and high resolution imaging were performed according to the standard protocols described in TM10 – StreamLine imaging[43] and TM9 – StreamLineHR imaging technical notes.[44] The instrumental setup used (see section 8.1) is specified in the main body of the text.

8.7.3 Volume 3D Raman Imaging of Cells

Multiple component positive cells were imaged in 3D according to the standard protocol described in TM11 – 3D Imaging,[276] using the conditions and setup specified in the figure captions and the main body of the text. For the observation of intrinsic Raman cell signals a 532 nm laser excitation source was used.

8.7.4 Volume 3D SERS Imaging of Nanotags

Multiple component positive cells were imaged in 3D according to the standard protocol described in TM11 – 3D Imaging,[276] using the conditions and setup specified in the figure captions and the main body of the text. For the observation of SERS specific nanotag signals a 633 nm laser excitation source was used.

8.7.5 Production of 3D Volume Images and 2D z-slice Images

Volume 3D Raman cell and SERS nanotag images were extracted directly from the WiRE (version 3.4 or 4.0) Volume Viewer Software. Images were cropped with Microsoft Office Picture Manager and the original labels on the x, y and z axes were replaced with textboxes in Microsoft Office PowerPoint to increase clarity.

The 2D slices for the Raman images of the cell and the 2D slices for the SERS images of the nanotags were taken directly from the Volume Viewer software. Images were cropped with Microsoft Office Picture Manager and the original labels on the x, y and z axes were replaced using textboxes in Microsoft Office PowerPoint to increase the clarity. The individual 2D slices were then combined into a single image using a GNU image manipulation programme.

8.7.6 Data Analysis

False colour Raman and SERS map images were derived using a number of uni-variate and multivariate analysis methods according to the standard protocols described in TM14 – Multi-file data analysis (uni-variate)[203] and TM15 – Multi-file data analysis (multivariate).[204] The data analysis methods were in-built to the WiRE software and were accessed using the same interface as that employed for data collection. Signal to baseline maps as the name suggests is a method by which to monitor signal intensity within a specified range, the limits of which are set by the operator.

Component DCLS SERS map images were derived and are typically used '*when reference spectra are available for all of the components in the multiple component sample (i.e. the solution standards). The DCLS method involves fitting the unknown data (collected during mapping) to a linear combination of the specified component spectra (the reference spectra for each of the nanotag suspensions). If there is a good spectral fit between the reference and the collected spectra a false colour is assigned and each reference spectrum is used to create separate false colour images. Associated with each false colour image is a look up table (LUT) and the minimum and maximum values of the LUT can give an indication towards the degree of spectral fit'.*[204]

PCA derived Raman cell images were created using the in-built WiRE chemometrics package. With this function there are a number of pre-processing steps which can be applied and include scaling and mean centring. The other PCA parameters such as the number of PCs are selected by the operator. The employed conditions are dependent on the data set and will vary from scenario to scenario.[204]

8.8 Preparation of Fluorescent Peptide Sequences and Fluorescence Microscopy Measurements

8.8.1 Fluorophore Conjugation

4.5 µL of the appropriate peptide (100 µM) was added to 495.5 µL HEPES buffer (100 mM). To this 100 µL Texas Red® C2 maleimide fluorophore was added dropwise whilst the solution was stirred. This mixture was left to react at 4 ˚C overnight. The sample was purified by solvent extraction whereby the peptide/dye mixture was added to the solvent mixture (2 mL chloroform, 1 mL dH_2O and 50 µL acetic acid) in a 25 mL separating flask. The mixture was vigorously agitated in order to separate the free dye from the peptide/dye conjugate and in order to separate the individual components into their respective phases. The unreacted dye partitioned into the chloroform phase whilst the peptide partitioned into the water phase. The chloroform extract was run-off, collected and the extraction was repeated 6×. The remaining extract was removed.

The purity of the conjugates was verified by TLC on silica 60 plates using a suitable solvent system (chloroform:methanol:acetic acid:water – 25:15:3:2 v/v). The water

extract was dried and conjugation was confirmed by MALDI mass spectrometry which was performed by technical staff (**Appendix VI** - **Appendix X**).

8.8.2 ER Specific Peptide Sequences and Cell Experiments

The ER peptide/dye extract was diluted to 5 mg/mL (594 µL peptide/dye extract in 8 mL 406 µL 100 mM HEPES) and 1 mL aliquots were incubated with CHO cells grown on CaF_2 windows (see section 8.4.3) for specified periods of time (0 – 30 min) at 37 ˚C, 5 % CO_2. The cells were washed 2× with PBS and the cells were counter stained with 1 mL aliquots of ER tracker™ Green (1 µM final concentration – 10 µL (1 mM) in 9 mL 990 µL Hank's balanced salt solution (HBSS)) at 37 ˚C, 5 % CO_2 for 30 min. After this the cell stain was removed and the cells were washed twice with 1× PBS for 5 min. The cells were fixed with paraformaldehyde (4 %) at 37 ˚C for 2 min. After fixation the cells were consecutively washed with 1× PBS and dH_2O for 5 min intervals. The samples were left to air dry and were then analysed using the instrumentation and filter sets specified in section 8.1.

8.8.3 TGN Specific Peptide Sequences and Cell Experiments

The TGN peptide/dye extract was diluted to 5 mg/mL (594 µL peptide/dye extract in 8 mL 406 µL 100 mM HEPES) and 1 mL aliquots were incubated with CHO cells grown on CaF_2 windows (see section 8.4.3) for specified periods of time (0 – 30 min) at 37 ˚C, 5 % CO_2. The cells were washed with HBSS and the cells were counter stained with 1 mL aliquots of Golgi BODIPY® FL C_5-ceramide (5 µM - 10 µL in 1 mL HBSS diluted from 0.5 mM stock solution) at 4 ˚C for 30 min. After this the cell stain was removed and the cells were washed 2× with ice cold media (DMEM) before fresh media was added and the samples were incubated for a further 30 min at 37 ˚C. The media was removed and the cells were fixed with paraformaldehyde (4 %) at 37 ˚C for 2 min. After fixation the cells were consecutively washed with 1× PBS and dH_2O for 5 min intervals. The samples were left to air dry and were then analysed using the instrumentation and filter sets specified in section 8.1.

Chapter 9 References

1. A. Smekal, *Naturwissenschaften*, **1923**, 11, 873-875.
2. C. V. Raman and K. S. Krishnan, *Nature*, **1928**, 121, 501-502.
3. M. Fleischmann, P. J. Hendra and A. J. McQuillan, *Chemical Physics Letters*, **1974**, 26, 163 - 166.
4. D. L. Jeanmaire and R. P. Van Duyne, *Journal of Electroanalytical Chemistry*, **1977**, 84, 1-20.
5. M. G. Albrecht and J. A. Creighton, *Journal of the American Chemical Society*, **1977**, 99, 5215-5217.
6. A. A. Stacy and R. P. Van Duyne, *Chemical Physics Letters*, **1983**, 102, 365-370.
7. M. K. Gregas, J. P. Scaffidi, B. Lauly and T. Vo-Dinh, *Applied Spectroscopy*, **2010**, 64, 858 - 866.
8. M. K. Gregas, F. Yan, J. Scaffidi, H.-N. Wang and T. Vo-Dinh, *Nanomedicine: Nanotechnology, Biology and Medicine*, **2011**, 7, 115-122.
9. G. B. Braun, S. J. Lee, T. Laurence, N. Fera, L. Fabris, G. C. Bazan, M. Moskovits and N. O. Reich, *The Journal of Physical Chemistry C*, **2009**, 113, 13622-13629.
10. C. L. Zavaleta, B. R. Smith, I. Walton, W. Doering, G. Davis, B. Shojaei, M. J. Natan and S. S. Gambhir, *Proceedings of the National Academy of Sciences of the United States of America*, **2009**, 106, 13511-13516.
11. X. Qian, X.-H. Peng, D. O. Ansari, Q. Yin-Goen, G. Z. Chen, D. M. Shin, L. Yang, A. N. Young, M. D. Wang and S. Nie, *Nature Biotechnology*, **2008**, 26, 83-90.
12. S. Keren, C. Zavaleta, Z. Cheng, A. de la Zerda, O. Gheysens and S. S. Gambhir, *Proceedings of the National Academy of Sciences of the United States of America*, **2008**, 105, 5844-5849.
13. Y. C. Cao, R. Jin and C. A. Mirkin, *Science*, **2002**, 297, 1536-1540.
14. F. T. Docherty, P. B. Monaghan, C. J. McHugh, D. Graham, W. E. Smith and J. M. Cooper, *Sensors Journal IEEE*, **2005**, 5, 632-640.
15. F. T. Docherty, M. Clark, G. McNay, D. Graham and W. E. Smith, *Faraday Discussions*, **2004**, 126, 281-288.
16. K. Faulds, W. E. Smith, D. Graham and R. J. Lacey, *Analyst*, **2002**, 127, 282-286.
17. S. Mabbott, A. Eckmann, C. Casiraghi and R. Goodacre, *Analyst*, **2013**, 138, 118-122.

18. C. McLaughlin, D. MacMillan, C. McCardle and W. E. Smith, *Analytical Chemistry*, **2002**, 74, 3160-3167.
19. R. A. Alvarez-Puebla, J. D. S. dos Santos and R. F. Aroca, *Analyst*, **2007**, 132, 1210-1214.
20. M. Mulvihill, A. Tao, K. Benjauthrit, J. Arnold and P. Yang, *Angewandte Chemie International Edition*, **2008**, 47, 6456-6460.
21. F. R. Perez, H. G. M. Edwards, A. Rivas and L. Drummond, *Journal of Raman Spectroscopy*, **1999**, 30, 301-305.
22. J. Zuo, C. Xu, C. Wang and Z. Yushi, *Journal of Raman Spectroscopy*, **1999**, 30, 1053-1055.
23. J. P. Besson, P. W. B. King, T. A. Wilkins, M. McIvor and N. Everall, *European Patent Application*, **1996**.
24. K. Willets, *Analytical and Bioanalytical Chemistry*, **2009**, 394, 85-94.
25. E. Smith and G. Dent, *Modern Raman Spectroscopy - A Practical Approach*, Wiley-Blackwell, **2004**.
26. E. C. Le Ru and P. G. Etchegoin, *Principles of Surface-Enhanced Raman Spectroscopy*, Elsevier, 1st edn., **2009**.
27. K. Faulds, A. Hernandez-Santana and W. E. Smith, in *Spectroscopic Properties of Inorganic and Organometallic Compounds*, eds. J. Yarwood, R. Douthwaite and S. Duckett, Royal Society of Chemistry, 2010, DOI: 10.1039/9781849730853, ch. 1, pp. 1-21.
28. O. Lyandres, N. C. Shah, C. R. Yonzon, J. T. Walsh, M. R. Glucksberg and R. P. Van Duyne, *Analytical Chemistry*, **2005**, 77, 6134-6139.
29. K. F. Gibson, D. Correia-Ledo, M. Couture, D. Graham and J.-F. Masson, *Chemical Communications*, **2011**, 47, 3404-3406.
30. H. Park, S. Lee, L. Chen, E. K. Lee, S. Y. Shin, Y. H. Lee, S. W. Son, C. H. Oh, J. M. Song, S. H. Kang and J. Choo, *Physical Chemistry Chemical Physics*, **2009**, 11, 7444-7449.
31. S. Lee, H. Chon, M. Lee, J. Choo, S. Y. Shin, Y. H. Lee, I. J. Rhyu, S. W. Son and C. H. Oh, *Biosensors and Bioelectronics*, **2009**, 24, 2260-2263.
32. P. C. Lee and D. Meisel, *The Journal of Physical Chemistry*, **1982**, 86, 3391-3395.
33. L.-P. Ding and Y. Fang, *Spectrochimica Acta Part A: Molecular and Biomolecular Spectroscopy*, **2007**, 67, 767-771.

34. C. H. Munro, W. E. Smith, M. Garner, J. Clarkson and P. C. White, *Langmuir*, **1995**, 11, 3712-3720.
35. J. Turkevich, P. C. Stevenson and J. Hillier, *Discussions of the Faraday Society*, **1951**, 11, 55-75.
36. K. L. Kelly, E. Coronado, L. L. Zhao and G. C. Schatz, *The Journal of Physical Chemistry B*, **2002**, 107, 668-677.
37. G. Mie, *Annalen der Physik*, **1908**, 330, 377-445.
38. R. Jin, *Angewandte Chemie International Edition*, **2010**, 49, 2826-2829.
39. S. Schlucker, *ChemPhysChem*, **2009**, 10, 1344-1354.
40. D. Cunningham, R. E. Littleford, W. E. Smith, P. J. Lundahl, I. Khan, D. W. McComb, D. Graham and N. Laforest, *Faraday Discussions*, **2006**, 132, 135-145.
41. K. Gracie, E. Correa, S. Mabbott, J. A. Dougan, D. Graham, R. Goodacre and K. Faulds, *Chemical Science*, **2014**, 5, 1030-1040.
42. Renishaw, StreamLine™ Plus: Raman chemical imaging just got faster, Accessed 24/06/2014, 2014.
43. Renishaw, TM10 - StreamLine Imaging, inVia User Guide, 2014.
44. Renishaw, TM9 - StreamLineHR imaging, inVia User Guide, 2014.
45. N. A. Campbell, J. B. Reece and L. G. Mitchell, *Biology*, Addison Wesley World Student Series, 5th edn., **1999**.
46. D. Craig, S. McAughtrie, J. Simpson, C. McCraw, K. Faulds and D. Graham, *Analytical Chemistry*, **2014**, 86, 4775-4782.
47. J. M. de la Fuente and C. C. Berry, *Bioconjugate Chemistry*, **2005**, 16, 1176-1180.
48. Invitrogen, Imaging Cell Structure - Organelle Stain Selection Guides http://www.lifetechnologies.com/uk/en/home/life-science/cell-analysis/cell-structure.html
49. L. Stryer, *Biochemistry*, W.H. Freeman and Company, New York, USA, 4th Edition edn., **1999**.
50. S. T. Reddy, A. Rehor, H. G. Schmoekel, J. A. Hubbell and M. A. Swartz, *Journal of Controlled Release*, **2006**, 112, 26-34.
51. L. Y. T. Chou, K. Ming and W. C. W. Chan, *Chemical Society Reviews*, **2011**, 40, 233-245.
52. J. Kneipp, H. Kneipp, M. McLaughlin, D. Brown and K. Kneipp, *Nano Letters*, **2006**, 6, 2225-2231.

53. M. A. Ochsenkühn, P. R. T. Jess, H. Stoquert, K. Dholakia and C. J. Campbell, *ACS Nano*, **2009**, 3, 3613-3621.
54. S. A. Mousavi, L. Malerød, T. Berg and R. Kjeken, *Biochemical Journal*, **2044**, 377, 1-16.
55. J. Rejman, V. Oberle, I. S. Zuhorn and D. Hoekstra, *Biochemical Journal*, **2004** 377, 159-169.
56. L. Pelkmans, J. Kartenbeck and A. Helenius, *Nature Cell Biology*, **2001**, 3, 473-483.
57. T.-G. Iversen, T. Skotland and K. Sandvig, *Nano Today*, **2011**, 6, 176-185.
58. E. M. Damm, L. Pelkmans, J. Kartenbeck, A. Mezzacasa, T. Kurzchalia and A. Helenius, *Journal of Cell Biology*, **2005**, 168, 477-488.
59. K. C. Partlow, G. M. Lanza and S. A. Wickline, *Biomaterials*, **2008**, 29, 3367-3375.
60. J. Gruenberg and F. G. van der Goot, *Nature Reviews Molecular Cell Biology*, **2006**, 7, 495-504.
61. C. Greulich, J. Diendorf, T. Simon, G. Eggeler, M. Epple and M. Köller, *Acta Biomaterialia*, **2011**, 7, 347-354.
62. R. M. Jarvis, N. Law, I. T. Shadi, P. O'Brien, J. R. Lloyd and R. Goodacre, *Analytical Chemistry*, **2008**, 80, 6741-6746.
63. A. Shamsaie, M. Jonczyk, J. Sturgis, J. Paul Robinson and J. Irudayaraj, *Journal of Biomedical Optics*, **2007**, 12, 020502-020502-020503.
64. D. Mandal, M. Bolander, D. Mukhopadhyay, G. Sarkar and P. Mukherjee, *Applied Microbiology and Biotechnology*, **2006**, 69, 485-492.
65. Anshup, J. S. Venkataraman, C. Subramaniam, R. R. Kumar, S. Priya, T. R. S. Kumar, R. V. Omkumar, A. John and T. Pradeep, *Langmuir*, **2005**, 21, 11562-11567.
66. P. Mukherjee, A. Ahmad, D. Mandal, S. Senapati, S. R. Sainkar, M. I. Khan, R. Parishcha, P. V. Ajaykumar, M. Alam, R. Kumar and M. Sastry, *Nano Letters*, **2001**, 1, 515-519.
67. B. Y. S. Kim, W. Jiang, J. Oreopoulos, C. M. Yip, J. T. Rutka and W. C. W. Chan, *Nano Letters*, **2008**, 8, 3887-3892.
68. W.-K. Rhim, J.-S. Kim and J.-M. Nam, *Small*, **2008**, 4, 1651-1655.
69. M. A. Herrero, F. M. Toma, K. T. Al-Jamal, K. Kostarelos, A. Bianco, T. Da Ros, F. Bano, L. Casalis, G. Scoles and M. Prato, *Journal of the American Chemical Society*, **2009**, 131, 9843-9848.

70. W. Xie, L. Wang, Y. Zhang, L. Su, A. Shen, J. Tan and J. Hu, *Bioconjugate Chemistry*, **2009**, 20, 768-773.
71. A. G. Tkachenko, H. Xie, D. Coleman, W. Glomm, J. Ryan, M. F. Anderson, S. Franzen and D. L. Feldheim, *Journal of the American Chemical Society*, **2003**, 125, 4700-4701.
72. A. G. Tkachenko, H. Xie, Y. Liu, D. Coleman, J. Ryan, W. R. Glomm, M. K. Shipton, S. Franzen and D. L. Feldheim, *Bioconjugate Chemistry*, **2004**, 15, 482-490.
73. J. Lin and A. Alexander-Katz, *ACS Nano*, **2013**, 7, 10799-10808.
74. E. H. W. Pap, T. B. Dansen, R. van Summeren and K. W. A. Wirtz, *Experimental Cell Research*, **2001**, 265, 288-293.
75. E. Jin, B. Zhang, X. Sun, Z. Zhou, X. Ma, Q. Sun, J. Tang, Y. Shen, E. Van Kirk, W. J. Murdoch and M. Radosz, *Journal of the American Chemical Society*, **2012**, 135, 933-940.
76. M. Tarantola, D. Schneider, E. Sunnick, H. Adam, S. Pierrat, C. Rosman, V. Breus, C. Sönnichsen, T. Basché, J. Wegener and A. Janshoff, *ACS Nano*, **2008**, 3, 213-222.
77. M. Mahmoudi, K. Azadmanesh, M. A. Shokrgozar, W. S. Journeay and S. Laurent, *Chemical Reviews*, **2011**, 111, 3407-3432.
78. C. J. Murphy, A. M. Gole, J. W. Stone, P. N. Sisco, A. M. Alkilany, E. C. Goldsmith and S. C. Baxter, *Accounts of Chemical Research*, **2008**, 41, 1721-1730.
79. E. E. Connor, J. Mwamuka, A. Gole, C. J. Murphy and M. D. Wyatt, *Small*, **2005**, 1, 325-327.
80. J. J. Li, L. Zou, D. Hartono, C. N. Ong, B. H. Bay and L. Y. Lanry Yung, *Advanced Materials*, **2008**, 20, 138-142.
81. C. Carlson, S. M. Hussain, A. M. Schrand, L. K. Braydich-Stolle, K. L. Hess, R. L. Jones and J. J. Schlager, *The Journal of Physical Chemistry B*, **2008**, 112, 13608-13619.
82. H. K. Patra, S. Banerjee, U. Chaudhuri, P. Lahiri and A. K. Dasgupta, *Nanomedicine: Nanotechnology, Biology and Medicine*, **2007**, 3, 111-119.
83. C. M. Goodman, C. D. McCusker, T. Yilmaz and V. M. Rotello, *Bioconjugate Chemistry*, **2004**, 15, 897-900.
84. M. Ahamed, M. Karns, M. Goodson, J. Rowe, S. M. Hussain, J. J. Schlager and Y. Hong, *Toxicology and Applied Pharmacology*, **2008**, 233, 404-410.

85. T. Mironava, M. Hadjiargyrou, M. Simon, V. Jurukovski and M. H. Rafailovich, *Nanotoxicology*, **2010**, 4, 120-137.
86. R. Shukla, V. Bansal, M. Chaudhary, A. Basu, R. R. Bhonde and M. Sastry, *Langmuir*, **2005**, 21, 10644-10654.
87. N. Pernodet, X. Fang, Y. Sun, A. Bakhtina, A. Ramakrishnan, J. Sokolov, A. Ulman and M. Rafailovich, *Small*, **2006**, 2, 766-773.
88. R. P. Singh and P. Ramarao, *Toxicology Letters*, **2012**, 213, 249-259.
89. E. Caballero-Díaz, C. Pfeiffer, L. Kastl, P. Rivera-Gil, B. Simonet, M. Valcárcel, J. Jiménez-Lamana, F. Laborda and W. J. Parak, *Particle & Particle Systems Characterization*, **2013**, 30, 1079-1085.
90. M. V. D. Z. Park, A. M. Neigh, J. P. Vermeulen, L. J. J. de la Fonteyne, H. W. Verharen, J. J. Briedé, H. van Loveren and W. H. de Jong, *Biomaterials*, **2011**, 32, 9810-9817.
91. N. Khlebtsov and L. Dykman, *Chemical Society Reviews*, **2011**, 40, 1647-1671.
92. C. Krafft, T. Knetschke, A. Siegner, R. H. W. Funk and R. Salzer, *Vibrational Spectroscopy*, **2003**, 32, 75-83.
93. C. Krafft, T. Knetschke, R. H. W. Funk and R. Salzer, *Vibrational Spectroscopy*, **2005**, 38, 85-93.
94. K. Klein, Alexander M. Gigler, T. Aschenbrenner, R. Monetti, W. Bunk, F. Jamitzky, G. Morfill, Robert W. Stark and J. Schlegel, *Biophysical Journal*, **2012**, 102, 360-368.
95. S. McAughtrie, K. Lau, K. Faulds and D. Graham, *Chemical Science*, **2013**, 4, 3566-3572.
96. R. J. Swain and M. M. Stevens, *Biochemical Society Transactions*, **2007**, 35, 544-549.
97. K. Kong, C. J. Rowlands, S. Varma, W. Perkins, I. H. Leach, A. A. Koloydenko, A. Pitiot, H. C. Williams and I. Notingher, *Journal of Molecular Structure*, **2014**.
98. C. Kallaway, L. M. Almond, H. Barr, J. Wood, J. Hutchings, C. Kendall and N. Stone, *Photodiagnosis and photodynamic therapy*, **2013**, 10, 207-219.
99. C. Matthäus, T. Chernenko, J. A. Newmark, C. M. Warner and M. Diem, *Biophysical Journal*, **2007**, 93, 668-673.
100. K. Majzner, A. Kaczor, N. Kachamakova-Trojanowska, A. Fedorowicz, S. Chlopicki and M. Baranska, *Analyst*, **2013**, 138, 603-610.

101. I. Notingher, G. Jell, P. L. Notingher, I. Bisson, O. Tsigkou, J. M. Polak, M. M. Stevens and L. L. Hench, *Journal of Molecular Structure*, **2005**, 744-747, 179-185.
102. I. Notingher, S. Verrier, S. Haque, J. M. Polak and L. L. Hench, *Biopolymers*, **2003**, 72, 230-240.
103. S. Verrier, I. Notingher, J. M. Polak and L. L. Hench, *Biopolymers*, **2004**, 74, 157-162.
104. C. Krafft, T. Knetschke, R. H. W. Funk and R. Salzer, *Analytical Chemistry*, **2006**, 78, 4424-4429.
105. S. O. Konorov, M. A. Jardon, J. M. Piret, M. W. Blades and R. F. B. Turner, *Analyst*, **2012**, 137, 4662-4668.
106. A. Zoladek, F. C. Pascut, P. Patel and I. Notingher, *Journal of Raman Spectroscopy*, **2011**, 42, 251-258.
107. B. R. Wood and D. McNaughton, *Journal of Raman Spectroscopy*, **2002**, 33, 517-523.
108. I. Notingher, G. Jell, U. Lohbauer, V. Salih and L. L. Hench, *Journal of Cellular Biochemistry*, **2004**, 92, 1180-1192.
109. R. J. Swain, S. J. Kemp, P. Goldstraw, T. D. Tetley and M. M. Stevens, *Biophysical Journal*, **2010**, 98, 1703-1711.
110. E. Gazi, A. D. Ward, N. W. Clarke, T. J. Harvey, R. D. Snook, P. Gardner, E. C. Faria, M. D. Brown and A. Henderson, *Journal of Biomedical Optics*, **2008**, 13, 064004-064004-064012.
111. T. J. Harvey, C. Hughes, A. D. Ward, E. C. Faria, A. Henderson, N. W. Clarke, M. D. Brown, R. D. Snook and P. Gardner, *Journal of Biophotonics*, **2009**, 2, 47-69.
112. A. Downes, R. Mouras, P. Bagnaninchi and A. Elfick, *Journal of Raman Spectroscopy*, **2011**, 42, 1864-1870.
113. H. G. Schulze, S. O. Konorov, N. J. Caron, J. M. Piret, M. W. Blades and R. F. B. Turner, *Analytical Chemistry*, **2010**, 82, 5020-5027.
114. I. Notingher, I. Bisson, A. E. Bishop, W. L. Randle, J. M. P. Polak and L. L. Hench, *Analytical Chemistry*, **2004**, 76, 3185-3193.
115. R. R. Alfano, C. H. Liu, L. Sah, W., H. R. Zhu, D. L. Akins, J. Cleary, R. Prudente and E. Cellmer, *Lasers in the Life Sciences*, **1991**, 4, 23-28.
116. K. E. Shafer-Peltier, A. S. Haka, M. Fitzmaurice, J. Crowe, J. Myles, R. R. Dasari and M. S. Feld, *Journal of Raman Spectroscopy*, **2002**, 33, 552-563.

117. N. Stone, R. Baker, K. Rogers, A. W. Parker and P. Matousek, *Analyst*, **2007**, 132, 899-905.
118. N. Stone and P. Matousek, *Cancer Research*, **2008**, 68, 4424-4430.
119. M. D. Keller, E. Vargis, N. de Matos Granja, R. H. Wilson, M.-A. Mycek, M. C. Kelley and A. Mahadevan-Jansen, *Journal of Biomedical Optics*, **2011**, 16, 077006-077006-077008.
120. H. Lui, J. Zhao, D. McLean and H. Zeng, *Cancer Research*, **2012**, 72, 2491-2500.
121. P. Crow, N. Stone, C. A. Kendall, J. S. Uff, J. A. M. Farmer, H. Barr and M. P. J. Wright, *British Journal of Cancer*, **2003**, 89, 106-108.
122. P. Crow, B. Barrass, C. A. Kendall, M. Hart-Prieto, M. Wright, R. Persad and N. Stone, *British Journal of Cancer*, **2005**, 92, 2166-2170.
123. P. Crow, A. Molckovsky, N. Stone, J. S. Uff, B. Wilson and L.-M. WongKeeSong, *Urology*, **2005**, 65, 1126-1130.
124. P. Crow, J. S. Uff, J. A. Farmer, M. P. Wright and N. Stone, *BJU International*, **2004**, 93, 1232-1236.
125. M. C. M. Grimbergen, C. F. P. van Swol, R. O. P. Draga, P. van Diest, R. M. Verdaasdonk, N. Stone and J. H. L. R. Bosch, **2009**, 7161, 716114-716114-716116.
126. R. O. P. Draga, M. C. M. Grimbergen, P. L. M. Vijverberg, C. F. P. v. Swol, T. G. N. Jonges, J. A. Kummer and J. L. H. Ruud Bosch, *Analytical Chemistry*, **2010**, 82, 5993-5999.
127. D. I. Ellis and R. Goodacre, *Analyst*, **2006**, 131, 875-885.
128. A. Mahadevan-Jansen, M. F. Mitchell, N. Ramanujamf, A. Malpica, S. Thomsen, U. Utzinger and R. Richards-Kortumt, *Photochemistry and Photobiology*, **1998**, 68, 123-132.
129. U. Utzinger, D. L. Heintzelman, A. Mahadevan-Jansen, A. Malpica, M. Follen and R. Richards-Kortum, *Applied Spectroscopy*, **2001**, 55, 955-959.
130. A. Robichaux-Viehoever, E. Kanter, H. Shappell, D. Billheimer, H. Jones, 3rd and A. Mahadevan-Jansen, *Applied Spectroscopy*, **2007**, 61, 986-993.
131. Q. Tu and C. Chang, *Nanomedicine: Nanotechnology, Biology and Medicine*, **2012**, 8, 545-558.
132. E. Widjaja, W. Zheng and Z. Huang, *International Journal of Oncology*, **2008**, 32, 653-662.

133. A. Beljebbar, O. Bouché, M. D. Diébold, P. J. Guillou, J. P. Palot, D. Eudes and M. Manfait, *Critical Reviews in Oncology/Hematology*, **2009**, 72, 255-264.
134. A. Molckovsky, L. M. Wong Kee Song, M. G. Shim, N. E. Marcon and B. C. Wilson, *Gastrointestinal Endoscopy*, **2003**, 57, 396-402.
135. C. Kendall, N. Stone, N. Shepherd, K. Geboes, B. Warren, R. Bennett and H. Barr, *The Journal of Pathology*, **2003**, 200, 602-609.
136. M. S. Bergholt, W. Zheng, K. Lin, K. Y. Ho, M. Teh, K. G. Yeoh, J. B. Y. So and Z. Huang, *Technology in Cancer Research and Treatment*, **2011**, 10, 103-112.
137. M. Kirsch, G. Schackert, R. Salzer and C. Krafft, *Analytical and Bioanalytical Chemistry*, **2010**, 398, 1707-1713.
138. S. W. E. van de Poll, T. J. Römer, O. L. Volger, D. J. M. Delsing, T. C. Bakker Schut, H. M. G. Princen, L. M. Havekes, J. W. Jukema, A. van der Laarse and G. J. Puppels, *Arteriosclerosis, Thrombosis, and Vascular Biology*, **2001**, 21, 1630-1635.
139. B. H. Foundation, Cardiovascular Disease Statistics - http://www.bhf.org.uk/heart-health/heart-statistics.aspx, Accessed 23/06/2014, 2014.
140. K. L. Brown, O. Y. Palyvoda, J. S. Thakur, S. L. Nehlsen-Cannarella, O. R. Fagoaga, S. A. Gruber and G. W. Auner, *Cytometry Part A*, **2009**, 75A, 917-923.
141. Y. G. Chung, Q. Tu, D. Cao, S. Harada, H. J. Eisen and C. Chang, *Clinical and Translational Science*, **2009**, 2, 206-210.
142. K. Kneipp, A. S. Haka, H. Kneipp, K. Badizadegan, N. Yoshizawa, C. Boone, K. E. Shafer-Peltier, J. T. Motz, R. R. Dasari and M. S. Feld, *Applied Spectroscopy*, **2002**, 56, 150-154.
143. J. Kneipp, H. Kneipp, W. L. Rice and K. Kneipp, *Analytical Chemistry*, **2005**, 77, 2381-2385.
144. S. C. Pînzaru, L. M. Andronie, I. Domsa, O. Cozar and S. Astilean, *Journal of Raman Spectroscopy*, **2008**, 39, 331-334.
145. H.-W. Tang, X. B. Yang, J. Kirkham and D. A. Smith, *Applied Spectroscopy*, **2008**, 62, 1060-1069.
146. X. Jiang, Z. Jiang, T. Xu, S. Su, Y. Zhong, F. Peng, Y. Su and Y. He, *Analytical Chemistry*, **2013**, 85, 2809-2816.
147. R. Stevenson, S. McAughtrie, L. Senior, R. J. Stokes, H. McGachy, L. Tetley, P. Nativo, J. M. Brewer, J. Alexander, K. Faulds and D. Graham, *Analyst*, **2013**, 138, 6331-6336.

148. J. Kneipp, H. Kneipp, B. Wittig and K. Kneipp, *Nanomedicine: Nanotechnology, Biology and Medicine*, **2010**, 6, 214-226.

149. D. C. Kennedy, K. A. Hoop, L. L. Tay and J. P. Pezacki, *Nanoscale*, **2010**, 2, 1413-1416.

150. N. M. S. Sirimuthu, C. D. Syme and J. M. Cooper, San Francisco, California, USA, **2012**, 8234, 82340F-82347.

151. M. Gellner, K. Kömpe and S. Schlücker, *Analytical and Bioanalytical Chemistry*, **2009**, 394, 1839-1844.

152. J. Yang, Z. Wang, S. Zong, C. Song, R. Zhang and Y. Cui, *Analytical and Bioanalytical Chemistry*, **2012**, 402, 1093-1100.

153. M. Y. Sha, H. Xu, M. J. Natan and R. Cromer, *Journal of the American Chemical Society*, **2008**, 130, 17214-17215.

154. D. A. Giljohann, D. S. Seferos, P. C. Patel, J. E. Millstone, N. L. Rosi and C. A. Mirkin, *Nano Letters*, **2007**, 7, 3818-3821.

155. X. Tan, Z. Wang, J. Yang, C. Song, R. Zhang and Y. Cui, *Nanotechnology*, **2009**, 20, 445102.

156. A. F. McCabe, C. Eliasson, R. Arun Prasath, A. Hernandez-Santana, L. Stevenson, I. Apple, P. A. G. Cormack, D. Graham, W. E. Smith, P. Corish, S. J. Lipscomb, E. R. Holland and P. D. Prince, *Faraday Discussions*, **2006**, 132, 303-308.

157. S. Yu, S. B. Lee, M. Kang and C. R. Martin, *Nano Letters*, **2001**, 1, 495-498.

158. C. Jehn, B. Kustner, P. Adam, A. Marx, P. Strobel, C. Schmuck and S. Schlucker, *Physical Chemistry Chemical Physics*, **2009**, 11, 7499-7504.

159. J. Kneipp, H. Kneipp, B. Wittig and K. Kneipp, *Nano Letters*, **2007**, 7, 2819-2823.

160. A. Pallaoro, G. B. Bruan, N. O. Reich and M. Moskovits, *Small*, **2010**, 6, 618-622.

161. C. E. Talley, L. Jusinski, C. W. Hollars, S. M. Lane and T. Huser, *Analytical Chemistry*, **2004**, 76, 7064-7068.

162. J. Scaffidi, M. Gregas, V. Seewaldt and T. Vo-Dinh, *Analytical and Bioanalytical Chemistry*, **2009**, 393, 1135-1141.

163. J. Kneipp, H. Kneipp, B. Wittig and K. Kneipp, *The Journal of Physical Chemistry C*, **2010**, 114, 7421-7426.

164. C. A. R. Auchinvole, P. Richardson, C. McGuinnes, V. Mallikarjun, K. Donaldson, H. McNab and C. J. Campbell, *ACS Nano*, **2011**, 6, 888-896.

165. D. A. Stuart, J. M. Yuen, N. Shah, O. Lyandres, C. R. Yonzon, M. R. Glucksberg, J. T. Walsh and R. P. Van Duyne, *Analytical Chemistry*, **2006**, 78, 7211-7215.

166. J. M. Yuen, N. C. Shah, J. T. Walsh, M. R. Glucksberg and R. P. Van Duyne, *Analytical Chemistry*, **2010**, 82, 8382-8385.
167. K. Ma, J. M. Yuen, N. C. Shah, J. T. Walsh, M. R. Glucksberg and R. P. Van Duyne, *Analytical Chemistry*, **2011**, 83, 9146-9152.
168. N. C. Shah, O. Lyandres, J. T. Walsh, M. R. Glucksberg and R. P. Van Duyne, *Analytical Chemistry*, **2007**, 79, 6927-6932.
169. I. H. Chou, M. Benford, H. T. Beier, G. L. Coté, M. Wang, N. Jing, J. Kameoka and T. A. Good, *Nano Letters*, **2008**, 8, 1729-1735.
170. G. Wang, R. J. Lipert, M. Jain, S. Kaur, S. Chakraboty, M. P. Torres, S. K. Batra, R. E. Brand and M. D. Porter, *Analytical Chemistry*, **2011**, 83, 2554-2561.
171. J. H. Granger, M. C. Granger, M. A. Firpo, S. J. Mulvihill and M. D. Porter, *Analyst*, **2013**, 138, 410-416.
172. H. Chon, S. Lee, S. W. Son, C. H. Oh and J. Choo, *Analytical Chemistry*, **2009**, 81, 3029-3034.
173. J.-H. Kim, J.-S. Kim, H. Choi, S.-M. Lee, B.-H. Jun, K.-N. Yu, E. Kuk, Y.-K. Kim, D. H. Jeong, M.-H. Cho and Y.-S. Lee, *Analytical Chemistry*, **2006**, 78, 6967-6973.
174. K. K. Maiti, A. Samanta, M. Vendrell, K.-S. Soh, M. Olivo and Y.-T. Chang, *Chemical Communications*, **2011**, 47, 3514-3516.
175. S. Lee, H. Chon, J. Lee, J. Ko, B. H. Chung, D. W. Lim and J. Choo, *Biosensors and Bioelectronics*, **2014**, 51, 238-243.
176. A. Pallaoro, G. B. Braun and M. Moskovits, *Proceedings of the National Academy of Sciences*, **2011**, 108, 16559-16564.
177. X. Wang, X. Qian, J. J. Beitler, Z. G. Chen, F. R. Khuri, M. M. Lewis, H. J. C. Shin, S. Nie and D. M. Shin, *Cancer Research*, **2011**, 71, 1526-1532.
178. A. Huefner, W.-L. Kuan, R. A. Barker and S. Mahajan, *Nano Letters*, **2013**, 13, 2463-2470.
179. S. Schlücker, B. Küstner, A. Punge, R. Bonfig, A. Marx and P. Ströbel, *Journal of Raman Spectroscopy*, **2006**, 37, 719-721.
180. M. Schutz, D. Steinigeweg, M. Salehi, K. Kompe and S. Schlucker, *Chemical Communications*, **2011**, 47, 4216-4218.
181. Y. P. Chen, X. W. Zheng, G. Chen, C. He, W. F. Zhu, S. Y. Feng, G. Xi, R. Chen, F. H. Lan and H. S. Zeng, *International Journal of Nanomedicine*, **2011**, 2012, 73-82.
182. N. Stone, M. Kerssens, G. R. Lloyd, K. Faulds, D. Graham and P. Matousek, *Chemical Science*, **2011**, 2, 776-780.

183. H.-n. Xie, R. Stevenson, N. Stone, A. Hernandez-Santana, K. Faulds and D. Graham, *Angewandte Chemie International Edition*, **2012**, 51, 8509-8511.
184. R. McQueenie, R. Stevenson, R. Benson, N. MacRitchie, I. McInnes, P. Maffia, K. Faulds, D. Graham, J. Brewer and P. Garside, *Analytical Chemistry*, **2012**, 84, 5968-5975.
185. K. K. Maiti, U. S. Dinish, C. Y. Fu, J.-J. Lee, K.-S. Soh, S.-W. Yun, R. Bhuvaneswari, M. Olivo and Y.-T. Chang, *Biosensors and Bioelectronics*, **2010**, 26, 398-403.
186. A. Samanta, K. K. Maiti, K.-S. Soh, X. Liao, M. Vendrell, U. S. Dinish, S.-W. Yun, R. Bhuvaneswari, H. Kim, S. Rautela, J. Chung, M. Olivo and Y.-T. Chang, *Angewandte Chemie International Edition*, **2011**, 50, 6089-6092.
187. K. K. Maiti, U. S. Dinish, A. Samanta, M. Vendrell, K.-S. Soh, S.-J. Park, M. Olivo and Y.-T. Chang, *Nano Today*, **2012**, 7, 85-93.
188. H.-N. Wang and T. Vo-Dinh, *Nanotechnology*, **2009**, 20, 065101.
189. H. Chon, S. Lee, S.-Y. Yoon, S.-I. Chang, D. W. Lim and J. Choo, *Chemical Communications*, **2011**, 47, 12515-12517.
190. G. F. Paciotti, L. Myer, D. Weinreich, D. Goia, N. Pavel, R. E. McLaughlin and L. Tamarkin, *Drug Deliv*, **2004**, 11, 169-183.
191. W. E. Doering and S. Nie, *Analytical Chemistry*, **2003**, 75, 6171-6176.
192. *Zetasizer Nano Series User Manual*, Malvern Instruments, **2009**.
193. I. Lynch, T. Cedervall, M. Lundqvist, C. Cabaleiro-Lago, S. Linse and K. A. Dawson, *Advances in Colloid and Interface Science*, **2007**, 134–135, 167-174.
194. Z. Zeng, J. Patel, S.-H. Lee, M. McCallum, A. Tyagi, M. Yan and K. J. Shea, *Journal of the American Chemical Society*, **2012**, 134, 2681-2690.
195. F. Lu, S.-H. Wu, Y. Hung and C.-Y. Mou, *Small*, **2009**, 5, 1408-1413.
196. W. Liu, X. Zhou, Z. Mao, D. Yu, B. Wang and C. Gao, *Soft Matter*, **2012**, 8, 9235-9245.
197. J. Dausend, A. Musyanovych, M. Dass, P. Walther, H. Schrezenmeier, K. Landfester and V. Mailänder, *Macromolecular Bioscience*, **2008**, 8, 1135-1143.
198. F. Thielbeer, E. M. V. Johansson, S. V. Chankeshwara and M. Bradley, *Macromolecular Bioscience*, **2013**, 13, 682-686.
199. Y. Zhang, M. Yang, N. G. Portney, D. Cui, G. Budak, E. Ozbay, M. Ozkan and C. S. Ozkan, *Biomedical Microdevices*, **2008**, 10, 321-328.
200. A. Topaçli and S. Akyüz, *Spectrochimica Acta Part A: Molecular and Biomolecular Spectroscopy*, **1995**, 51, 633-641.

201. L. Ould-Moussa, O. Poizat, M. Castellà-Ventura, G. Buntinx and E. Kassab, *The Journal of Physical Chemistry*, **1996**, 100, 2072-2082.
202. Z. Zhuang, X. Shi, Y. Chen and M. Zuo, *Spectrochimica Acta Part A: Molecular and Biomolecular Spectroscopy*, **2011**, 79, 1593-1599.
203. Renishaw, TM14 Multi-file data analysis (univariate), inVia User Guide, 2014.
204. Renishaw, TM15 Multi-file data analysis (multivariate), inVia User Guide, 2014.
205. J. Kneipp, H. Kneipp, A. Rajadurai, R. W. Redmond and K. Kneipp, *Journal of Raman Spectroscopy*, **2009**, 40, 1-5.
206. N. J. Everall, *Applied Spectroscopy*, **2000**, 54, 773-782.
207. N. Everall, *Journal of Raman Spectroscopy*, **2014**, 45, 133-138.
208. I. Notingher, *Sensors*, **2007**, 7, 1343-1358.
209. N. M. S. Sirimuthu, C. D. Syme and J. M. Cooper, *Analytical Chemistry*, **2010**, 82, 7369-7373.
210. X. Su, J. Zhang, L. Sun, T.-W. Koo, S. Chan, N. Sundararajan, M. Yamakawa and A. A. Berlin, *Nano Letters*, **2004**, 5, 49-54.
211. M. Yang, T. Chen, W. S. Lau, Y. Wang, Q. Tang, Y. Yang and H. Chen, *Small*, **2009**, 5, 198-202.
212. D. Graham, G. McAnally, J. C. Jones and W. Ewen Smith, *Chemical Communications*, **1998**, 1187-1188.
213. G. McAnally, C. McLaughlin, R. Brown, D. C. Robson, K. Faulds, D. R. Tackley, W. E. Smith and D. Graham, *Analyst*, **2002**, 127, 838-841.
214. C. J. McHugh, F. T. Docherty, D. Graham and W. E. Smith, *Analyst*, **2004**, 129, 69-72.
215. A. Enright, L. Fruk, A. Grondin, C. J. McHugh, W. E. Smith and D. Graham, *Analyst*, **2004**, 129, 975-978.
216. K. Faulds, R. Jarvis, W. E. Smith, D. Graham and R. Goodacre, *Analyst*, **2008**, 133, 1505-1512.
217. R. J. Stokes, A. Macaskill, P. J. Lundahl, W. E. Smith, K. Faulds and D. Graham, *Small*, **2007**, 3, 1593-1601.
218. R. J. Stokes, A. Ingram, J. Gallagher, D. R. Armstrong, W. E. Smith and D. Graham, *Chemical Communications*, **2008**, 567-569.
219. F. McKenzie, A. Ingram, R. Stokes and D. Graham, *Analyst*, **2009**, 134, 549-556.
220. J. Hu, B. Zhao, W. Xu, B. Li and Y. Fan, *Spectrochimica Acta Part A: Molecular and Biomolecular Spectroscopy*, **2002**, 58, 2827-2834.

221. A. Matschulat, D. Drescher and J. Kneipp, *ACS Nano*, **2010**, 4, 3259-3269.
222. J. C. Banford, D. H. Brown, A. A. McConnell and W. E. Smith, *Inorganica Chimica Acta*, **1981**, 56, L15-L16.
223. B. O. Skadtchenko and R. Aroca, *Spectrochimica Acta Part A: Molecular and Biomolecular Spectroscopy*, **2001**, 57, 1009-1016.
224. R. A. Alvarez-Puebla, D. S. Dos Santos Jr and R. F. Aroca, *Analyst*, **2004**, 129, 1251-1256.
225. A. Michota and J. Bukowska, *Journal of Raman Spectroscopy*, **2003**, 34, 21-25.
226. Y. Yan, K. T. Gause, M. M. J. Kamphuis, C.-S. Ang, N. M. O'Brien-Simpson, J. C. Lenzo, E. C. Reynolds, E. C. Nice and F. Caruso, *ACS Nano*, **2013**, 7, 10960-10970.
227. C. J. Orendorff, A. Gole, T. K. Sau and C. J. Murphy, *Analytical Chemistry*, **2005**, 77, 3261-3266.
228. Invitrogen, alamarBlue®—Rapid & Accurate Cell Health Indicator - http://www.lifetechnologies.com/uk/en/home/brands/molecular-probes/key-molecular-probes-products/alamarblue-rapid-and-accurate-cell-health-indicator.html#what, Accessed 25/06/2014, 2014.
229. Invitrogen, SYTOX® Green Nucleic Acid Stain - http://tools.lifetechnologies.com/content/sfs/manuals/mp07020.pdf, Accessed 25/06/2014, 2014.
230. B. R. Lutz, C. E. Dentinger, L. N. Nguyen, L. Sun, J. Zhang, A. N. Allen, S. Chan and B. S. Knudsen, *ACS Nano*, **2008**, 2, 2306-2314.
231. Z. Liu, S. Tabakman, S. Sherlock, X. Li, Z. Chen, K. Jiang, S. Fan and H. Dai, *Nano Research*, **2010**, 3, 222-233.
232. M. S. Bergholt, W. Zheng, K. Lin, K. Y. Ho, M. Teh, K. G. Yeoh, J. B. Yan So and Z. Huang, *International Journal of Cancer*, **2011**, 128, 2673-2680.
233. Y. Oshima, H. Shinzawa, T. Takenaka, C. Furihata and H. Sato, *Journal of Biomedical Optics*, **2010**, 15, 017009-017009.
234. F. C. Pascut, H. T. Goh, N. Welch, L. D. Buttery, C. Denning and I. Notingher, *Biophysical Journal*, **2011**, 100, 251-259.
235. J. J. Einspahr and P. M. Voyles, *Ultramicroscopy*, **2006**, 106, 1041-1052.
236. H. Jiang, C. Song, C.-C. Chen, R. Xu, K. S. Raines, B. P. Fahimian, C.-H. Lu, T.-K. Lee, A. Nakashima, J. Urano, T. Ishikawa, F. Tamanoi and J. Miao, *Proceedings of the National Academy of Sciences*, **2010**, 107, 11234-11239.

237. W. Gu, L. D. Etkin, M. A. Le Gros and C. A. Larabell, *Differentiation*, **2007**, 75, 529-535.
238. J. A. W. Heymann, D. Shi, S. Kim, D. Bliss, J. L. S. Milne and S. Subramaniam, *Journal of Structural Biology*, **2009**, 166, 1-7.
239. R. Schmidt, C. A. Wurm, A. Punge, A. Egner, S. Jakobs and S. W. Hell, *Nano Letters*, **2009**, 9, 2508-2510.
240. L. Schermelleh, P. M. Carlton, S. Haase, L. Shao, L. Winoto, P. Kner, B. Burke, M. C. Cardoso, D. A. Agard, M. G. L. Gustafsson, H. Leonhardt and J. W. Sedat, *Science*, **2008**, 320, 1332-1336.
241. X. Michalet, F. F. Pinaud, L. A. Bentolila, J. M. Tsay, S. Doose, J. J. Li, G. Sundaresan, A. M. Wu, S. S. Gambhir and S. Weiss, *Science*, **2005**, 307, 538-544.
242. N. J. Everall, *Analyst*, **2010**, 135, 2512-2522.
243. W.-T. Cheng, M.-T. Liu, H.-N. Liu and S.-Y. Lin, *Microscopy Research and Technique*, **2005**, 68, 75-79.
244. R. J. Lakshimi, V. B. Kartha, C. M. Krishna, J. G. R. Solomon, G. Ullas and P. Uma Devi, *Radiation Research*, **2002**, 157, 175.
245. N. M. S. Sirimuthu, C. D. Syme and J. M. Cooper, *Chemical Communications*, **2011**, 47, 4099-4101.
246. S. Nie and S. R. Emory, *Science*, **1997**, 275, 1102-1106.
247. K. Lau, A. Hobro, T. Smith, T. Thurston and B. Lendl, *Vibrational Spectroscopy*, **2012**, 60, 34-42.
248. R. Malini, K. Venkatakrishma and J. Kurien, *Biopolymers*, **2006**, 81, 179-193.
249. G. Shetty, C. Kedall, N. Shepherd, N. Stone and H. Barr, *British Journal of Cancer*, **2006**, 94, 1460-1464.
250. D.-H. Kim, R. M. Jarvis, Y. Xu, A. W. Oliver, J. W. Allwood, L. Hampson, I. N. Hampson and R. Goodacre, *Analyst*, **2010**, 135, 1235-1244.
251. I. Notingher, C. Green and C. Dyer, *Journal of the Royal Society Interface*, **2004**, 1, 79-90.
252. Z. Huang, A. McWilliams, M. Lui, D. I. McLean, S. Lam and H. Zeng, *International Journal of Cancer*, **2003**, 107, 1047-1052.
253. N. Stone, C. Kendell, N. Shepherd, P. Crow and H. Barr, *Faraday Discussions*, **2004,** 126, 141-157.
254. A. J. Ruiz-Chica, M. A. Medina, F. Sanchez-Jimenez and F. J. Ramirez, *Journal of Raman Spectroscopy*, **2004**, 35, 93-100.

255. J. W. Chan, D. S. Taylor, T. Zwerdling, S. M. Lane, K. Ihara and T. Huser, *Biophysical Journal*, **2006**, 90, 648-656.
256. C. J. Frank, R. L. McCreecy and D. C. B. Redd, *Analytical Chemistry*, **1995**, 67, 777-783.
257. L. Hosta-Rigau, I. Olmedo, J. Arbiol, L. J. Cruz, M. J. Kogan and F. Albericio, *Bioconjugate Chemistry*, **2010**, 21, 1070-1078.
258. Z. Krpetić, S. Saleemi, I. A. Prior, V. Sée, R. Qureshi and M. Brust, *ACS Nano*, **2011**, 5, 5195-5201.
259. R. Lévy, N. T. K. Thanh, R. C. Doty, I. Hussain, R. J. Nichols, D. J. Schiffrin, M. Brust and D. G. Fernig, *Journal of the American Chemical Society*, **2004**, 126, 10076-10084.
260. G. R. Chamberlain, D. V. Tulumello and S. O. Kelley, *ACS Chemical Biology*, **2013**, 8, 1389-1395.
261. D. M. Copolovici, K. Langel, E. Eriste and Ü. Langel, *ACS Nano*, **2014**, 8, 1972-1994.
262. C. M. Feldherr and D. Akin, *The Journal of Cell Biology*, **1990**, 111, 1-8.
263. Invitrogen, ER-Tracker™ Green (BODIPY® FL Glibenclamide), for live-cell imaging http://tools.lifetechnologies.com/content/sfs/manuals/mp12353.pdf, Accessed 11/06/2014, 2014.
264. Invitrogen, NBD and BODIPY Dye Labeled Sphingolipids http://tools.lifetechnologies.com/content/sfs/manuals/mp01154.pdf, Accessed 11/06/2014, 2014.
265. M. Zheng, F. Davidson and X. Huang, *Journal of the American Chemical Society*, **2003**, 125, 7790-7791.
266. M. Hanauer, S. Pierrat, I. Zins, A. Lotz and C. Sönnichsen, *Nano Letters*, **2007**, 7, 2881-2885.
267. R. K. Dukor, *Biomedical Applications*, **2002**, 5, 3335-3359.
268. C. Krafft, L. Neudert, T. Simat and R. Salzer, *Spectrochimica Acta Part A: Molecular and Biomolecular Spectroscopy*, **2005**, 61, 1529-1535.
269. D. P. Lau, Z. Huang, H. Lui, D. W. Anderson, K. Berean, M. D. Morrison, L. Shen and H. Zeng, *Lasers in Surgery and Medicine*, **2005**, 37, 192-200.
270. J. Binoy, J. P. Abraham, I. H. Joe, V. S. Jayakumar, G. R. Pettit and O. F. Nielsen, *Journal of Raman Spectroscopy*, **2004**, 35, 939-946.

271. G. I. Dovbeshko, N. Y. Gridina, E. B. Kruglova and O. P. Pashchuk, *Talanta*, **2000**, 53, 233-246.
272. G. van Meer, D. R. Voelker and G. W. Feigenson, *Nature Reviews Molecular Cell Biology*, **2008**, 9, 112-124.
273. N. Demaurex, W. Furuya, S. D'Souza, J. S. Bonifacino and S. Grinstein, *Journal of Biological Chemistry*, **1998**, 273, 2044-2051.
274. N. Leopold and B. Lendl, *The Journal of Physical Chemistry B*, **2003**, 107, 5723-5727.
275. T. Ung, L. M. Liz-Marzán and P. Mulvaney, *Langmuir*, **1998**, 14, 3740-3748.
276. Renishaw, TM11 - 3D Imaging, inVia User Guide, 2014.

Appendices

Appendix I: Representative SERS spectra for small molecule labelled nanotags – 532 nm

Appendix II: Representative SERS spectra for small molecule/PEG labelled nanotags – 532 nm

Appendix III: Representative SERS spectra for small molecule labelled nanotags – 785 nm

Appendix IV: Representative SERS spectra for small molecule/PEG labelled nanotags – 785 nm

Appendix V: Representative SERS spectra for the components used in the study.

Appendix VI: MALDI-MS of the unconjugated dye Texas-Red.

Appendix VII: MALDI-MS of the unconjugated ER peptide.

Appendix VIII: MALDI-MS of the unconjugated TGN peptide.

Appendix IX: MALDI-MS of the ER peptide and Texas-Red dye conjugate.

Appendix X: MALDI-MS of the TGN peptide and Texas-Red dye conjugate.

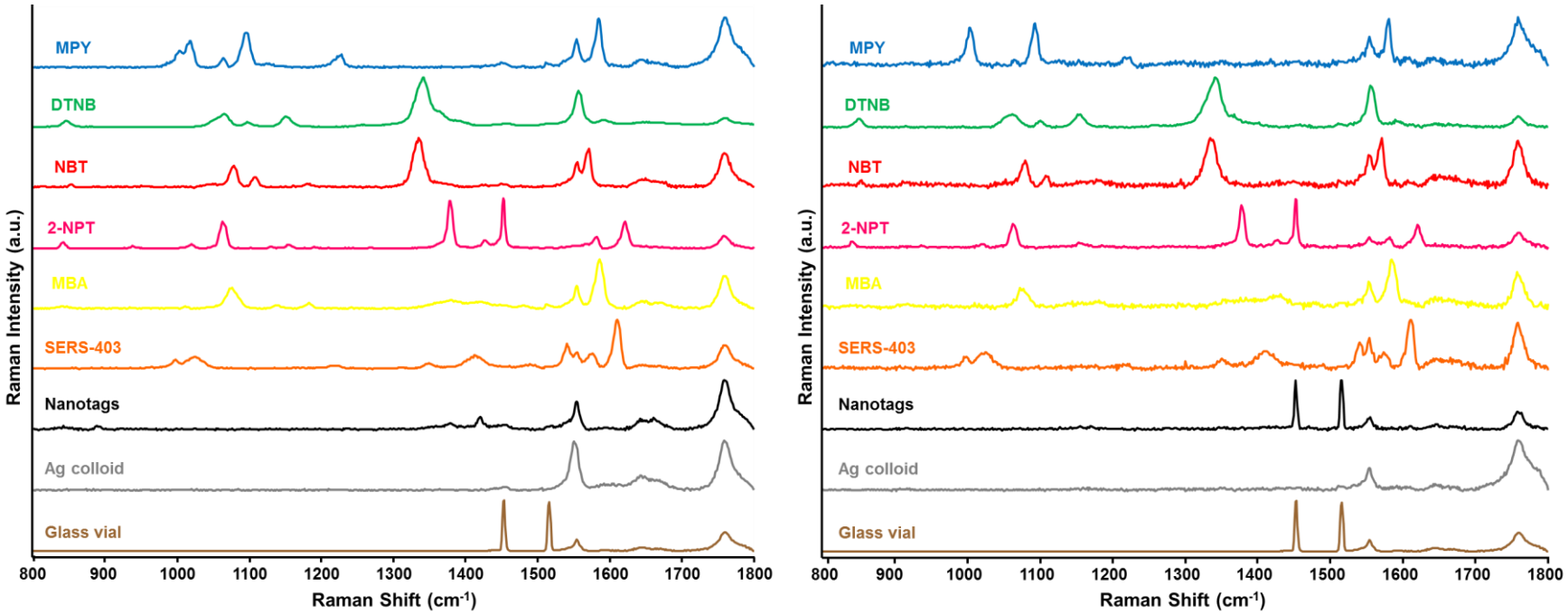

Appendix I: Representative SERS spectra for each of the small molecule labelled nanotags. Spectra were offset for illustrative purposes and as no major peaks used for identification were observed below 800 cm^{-1} or above 1800 cm^{-1} the spectra were truncated accordingly. The left spectra represent the nanotags in water and the right in cell media (λ_{ex} = 532 nm edge, 1 % (0.159 mW), extended scan, 800-1800 cm^{-1}, 10 s).

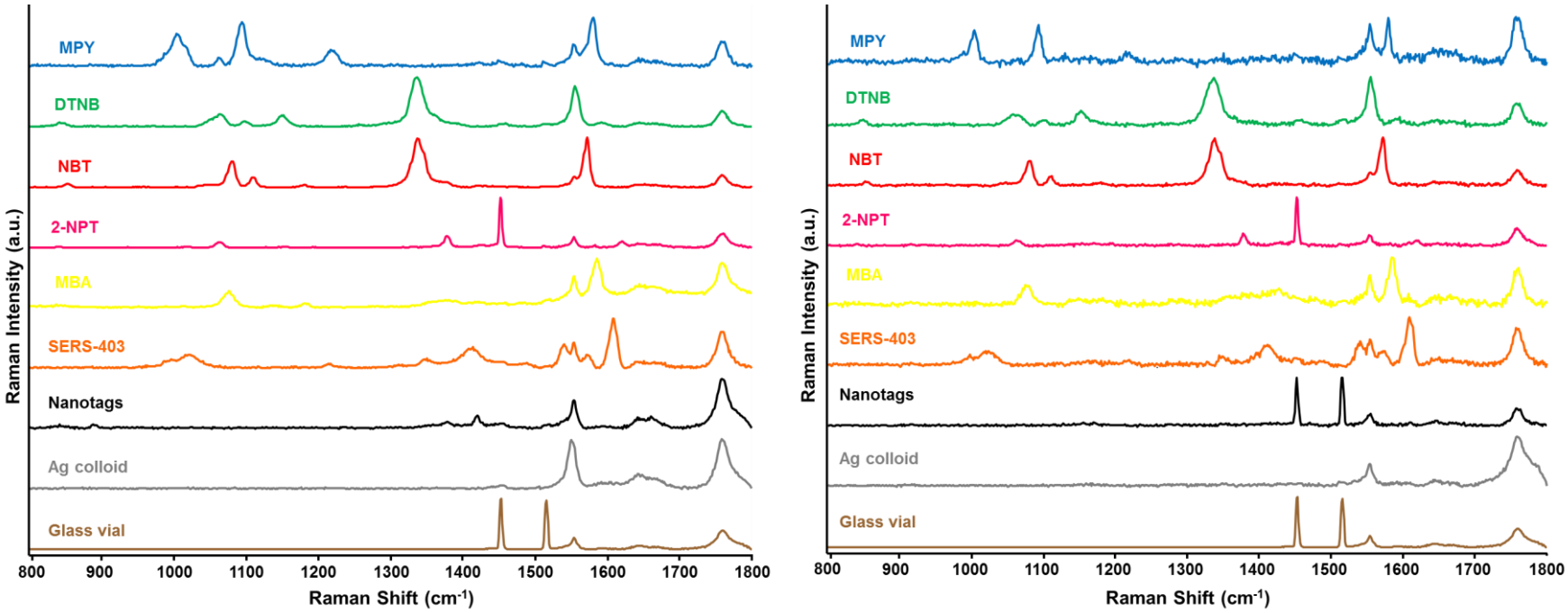

Appendix II: Representative SERS spectra for each of the small molecule/PEG labelled nanotags. Spectra were offset for illustrative purposes and as no major peaks used for identification were observed below 800 cm^{-1} or above 1800 cm^{-1} the spectra were truncated accordingly. The left spectra represent the nanotags in water and the right in cell media (λ_{ex} = 532 nm edge, 1 % (0.159 mW), extended scan, 800-1800 cm^{-1}, 10 s).

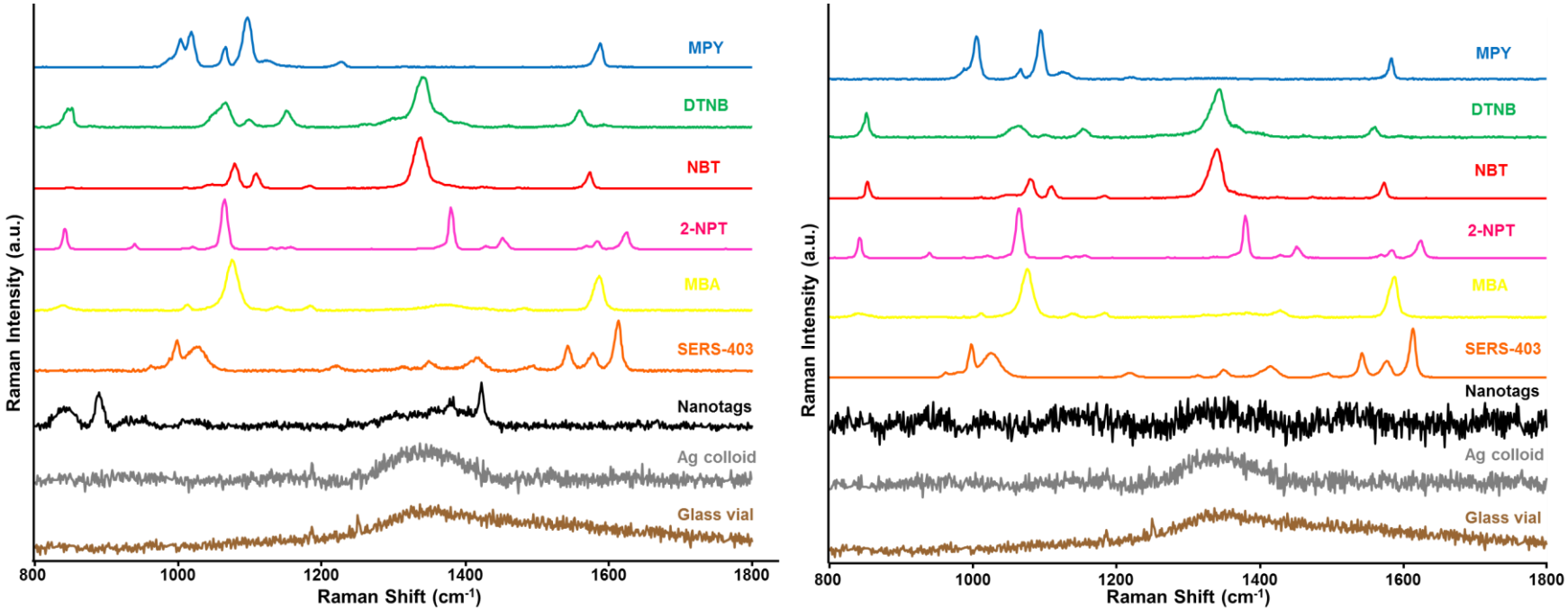

Appendix III: Representative SERS spectra for each of the small molecule labelled nanotags. Spectra were offset for illustrative purposes and as no major peaks used for identification were observed below 800 cm^{-1} or above 1800 cm^{-1} the spectra were truncated accordingly. The left spectra represent the nanotags in water and the right in cell media (λ_{ex} = 785 nm edge, 10 % (45 mW), extended scan, 800-1800 cm^{-1}, 10 s).

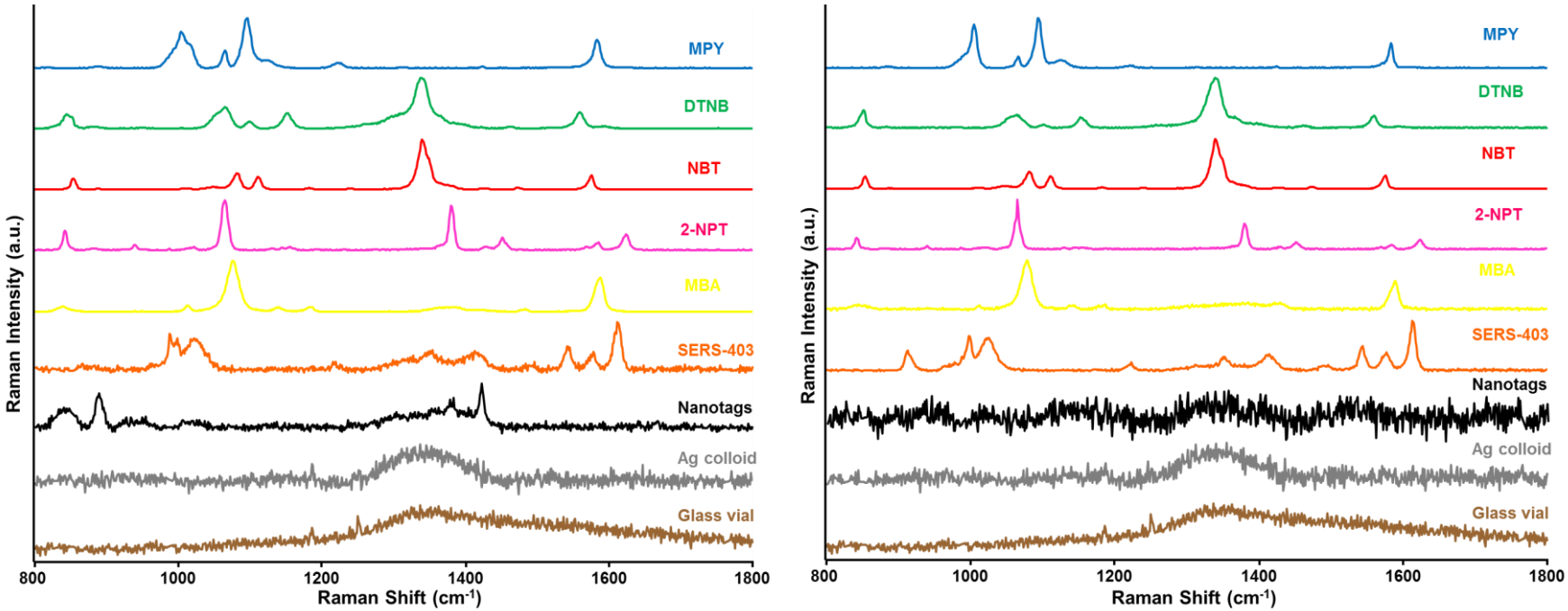

Appendix IV: Representative SERS spectra for each of the small molecule/PEG labelled nanotags. Spectra were offset for illustrative purposes and as no major peaks used for identification were observed below 800 cm^{-1} or above 1800 cm^{-1} the spectra were truncated accordingly. The left spectra represent the nanotags in water and the right in cell media (λ_{ex} = 785 nm edge, 10 % (45 mW), extended scan, 800-1800 cm^{-1}, 10 s).

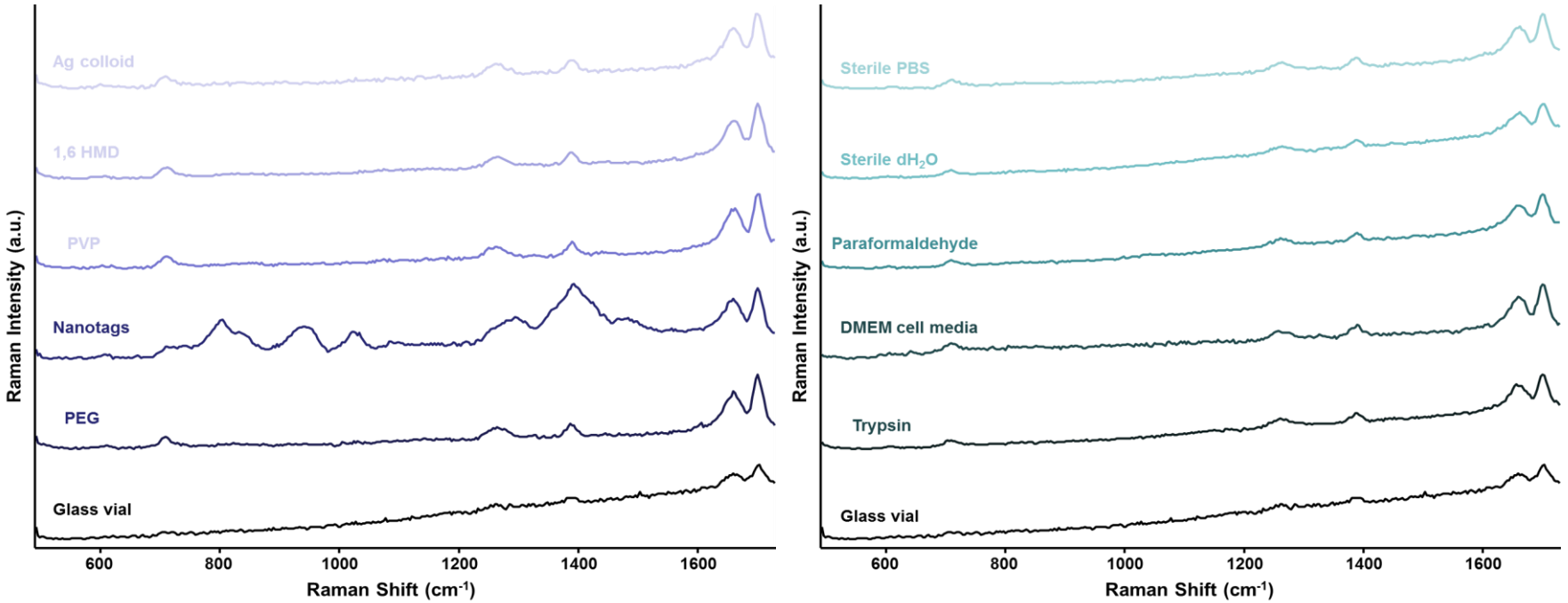

Appendix V: Representative SERS spectra for each of the components used in the synthesis of the nanotags and in the culture of cells. Spectra were offset for illustrative purposes and as no major peaks used for identification were observed below 500 cm^{-1} or above 1700 cm^{-1} the spectra were truncated accordingly. The left spectra represent the nanotag components and the right the components used in cell culture (λ_{ex} = 633 nm edge, 100 % (6.6 mW), static scan, 492-1728 cm^{-1}, 1 s).

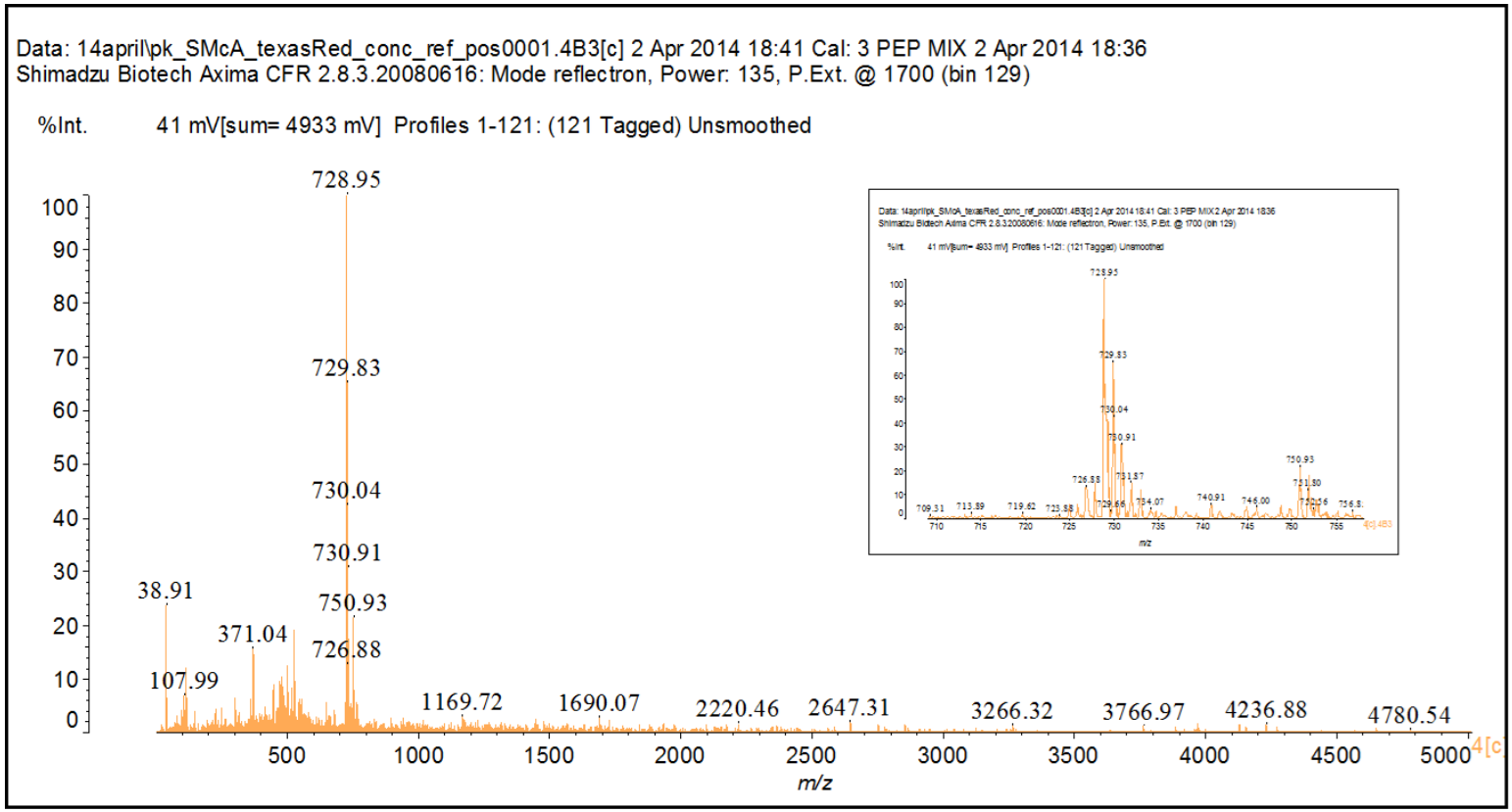

Appendix VI: MALDI-MS of the unconjugated dye Texas-Red.

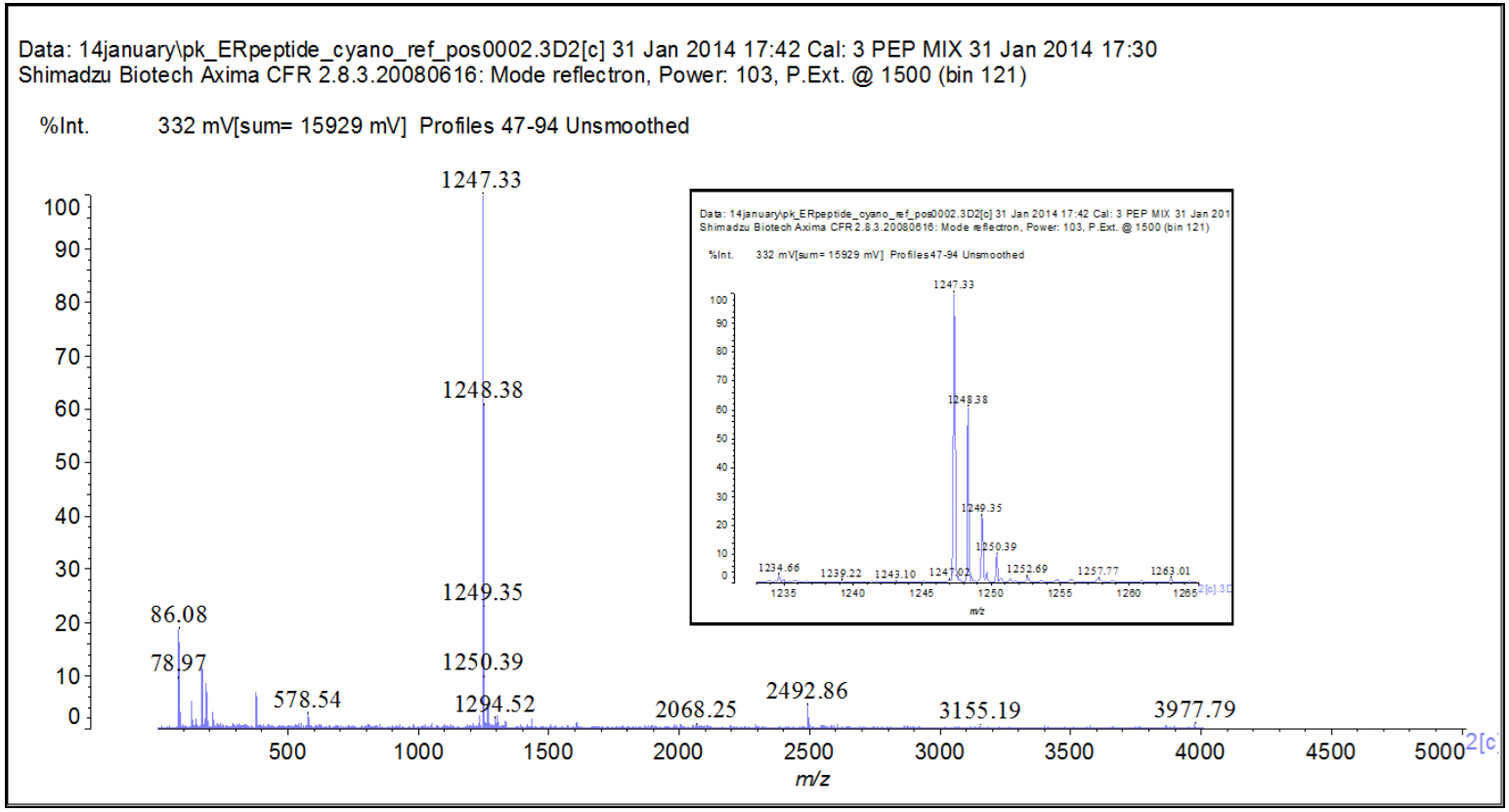

Appendix VII: MALDI-MS of the unconjugated ER peptide.

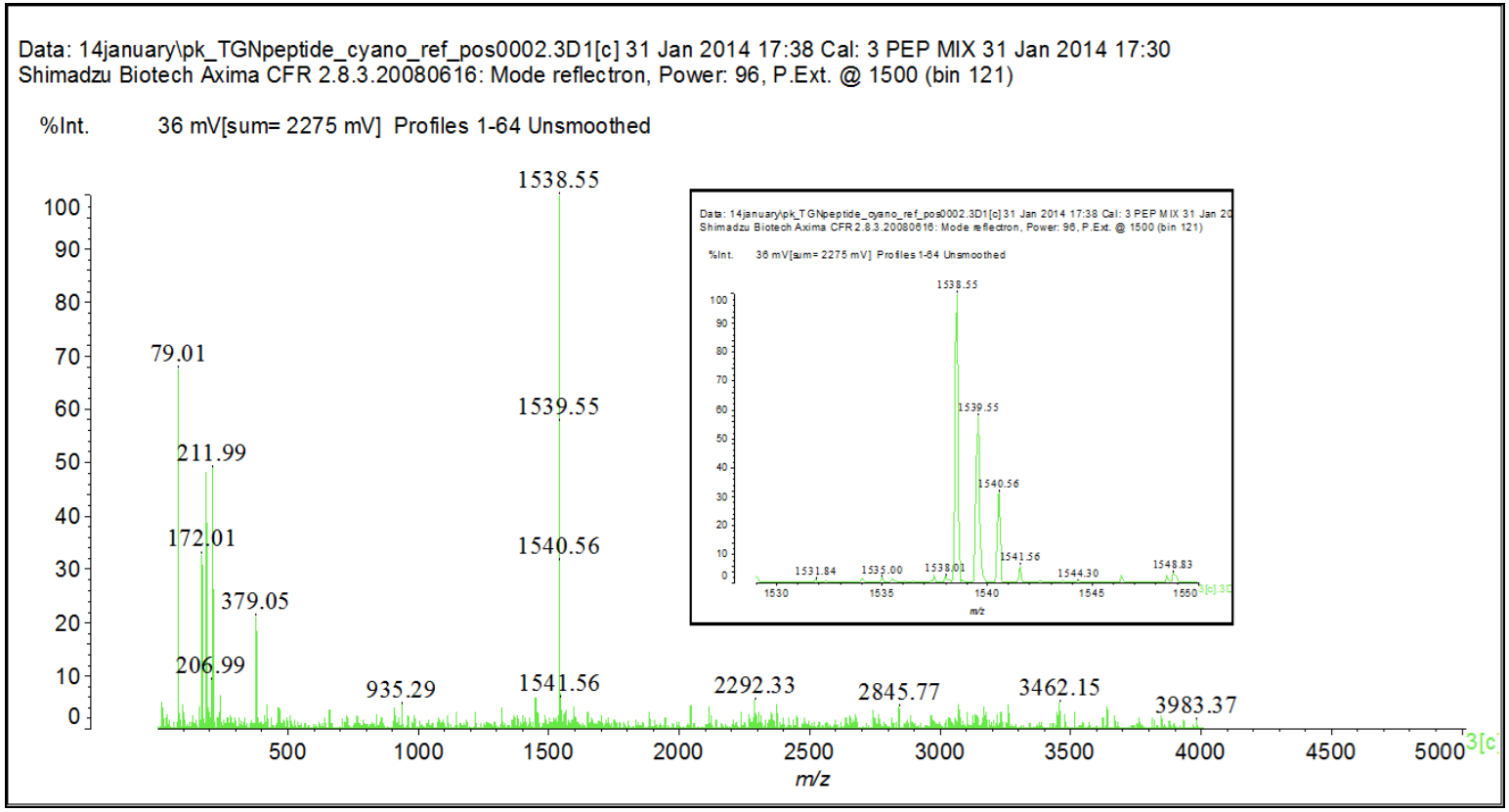

Appendix VIII: MALDI-MS of the unconjugated TGN peptide.

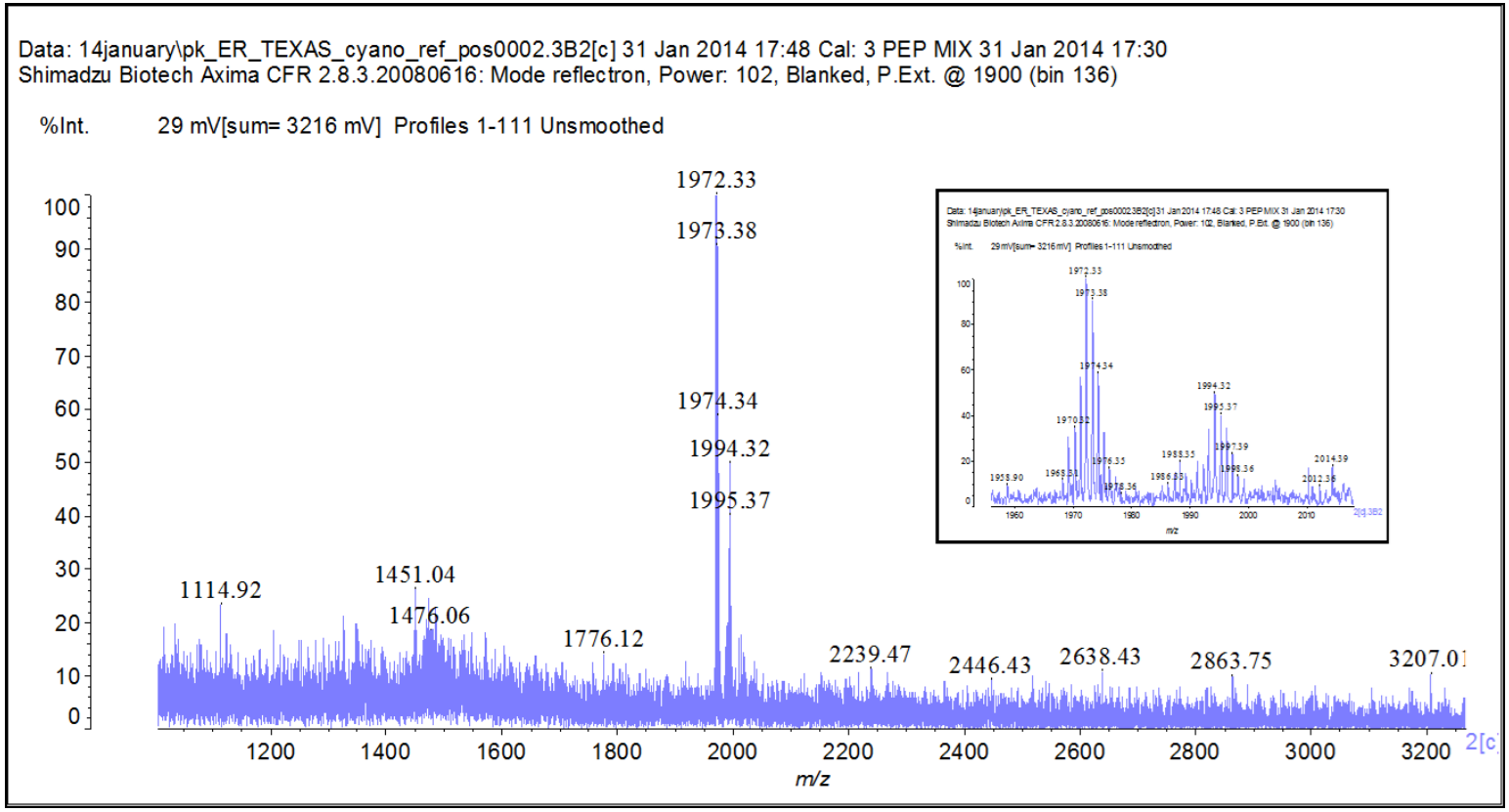

Appendix IX: MALDI-MS of the ER peptide and Texas-Red dye conjugate.

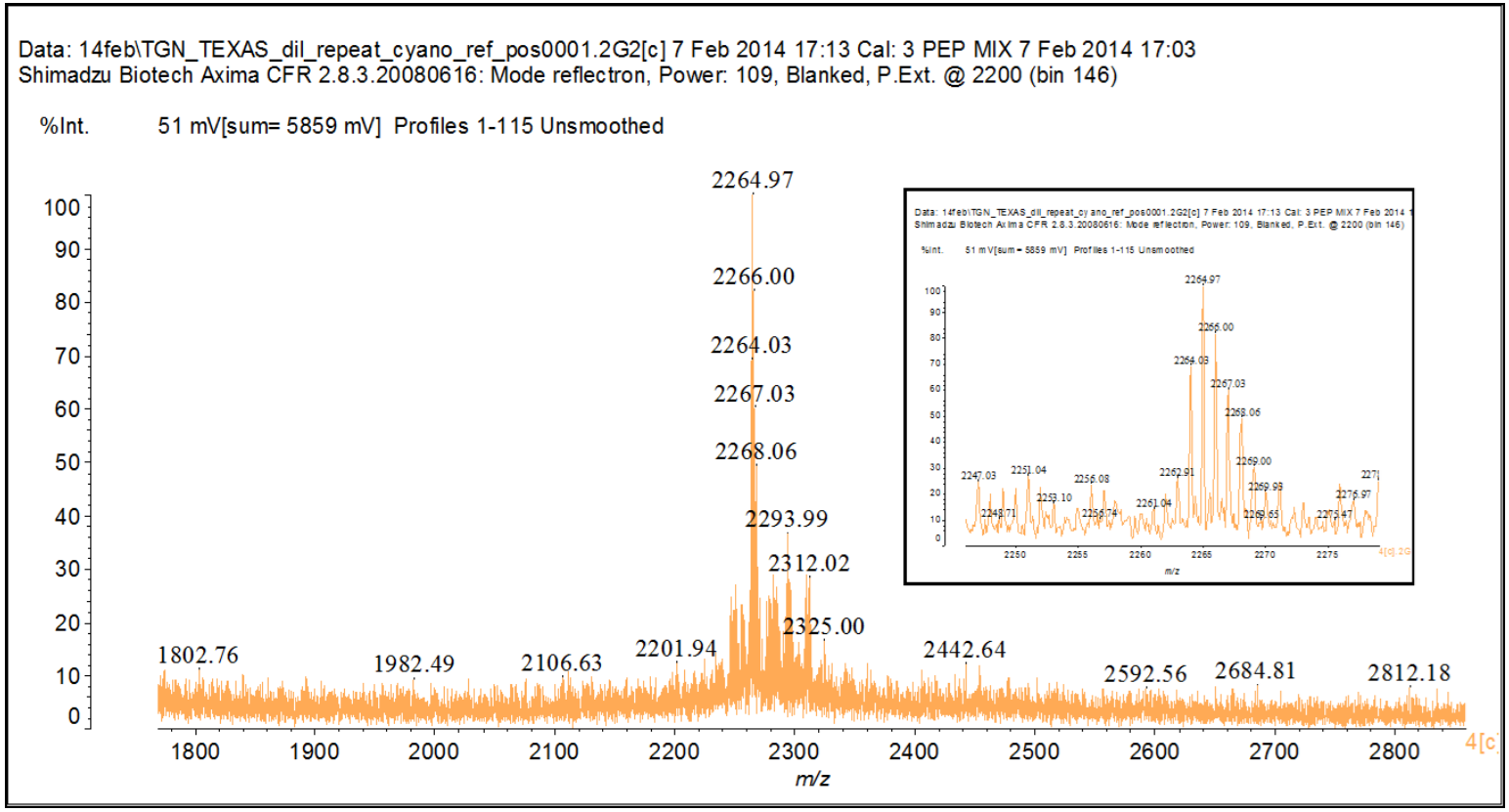

Appendix X: MALDI-MS of the TGN peptide and Texas-Red dye conjugate.

Publications

Chemical Science

RSC Publishing

EDGE ARTICLE

View Article Online
View Journal | View Issue

3D optical imaging of multiple SERS nanotags in cells†

Cite this: *Chem. Sci.*, 2013, **4**, 3566

Sarah McAughtrie,‡[a] Katherine Lau,‡[b] Karen Faulds[a] and Duncan Graham*[a]

Recent studies have clearly demonstrated that Raman and surface enhanced Raman scattering (SERS) spectroscopies are information rich, non-destructive techniques for the monitoring of subtle intracellular changes. However, despite the demonstrated and sophisticated applications of these techniques in cell studies there still remains a lack of accompanying 3D images. Herein we demonstrate for the first time combined 3D Raman and SERS imaging for the simultaneous confirmation of the cellular inclusion and multiple component detection of SERS nanotags. We also report on the 3D elucidation of the cell nuclei by multivariate analysis methods. Imaging in 3D will be critical to understanding architectural changes between diseased and healthy cells, and tissues. It will also provide non-destructive definitive proof of cellular uptake whilst simultaneously confirming targeting of SERS nanotags to their intended destinations.

Received 22nd May 2013
Accepted 10th July 2013

DOI: 10.1039/c3sc51437d

www.rsc.org/chemicalscience

Introduction

The application of Raman and surface enhanced Raman scattering (SERS) spectroscopies to complex biological and medical samples has increased dramatically in recent years. This is due in part to improvements in instrument sensitivity but also because both represent a non-destructive method by which considerable information can be gained. Raman spectroscopy also has the added advantage of being a non-invasive analysis method. Whilst the Raman spectra of biological samples are often complex, subtle changes between samples can be readily elucidated by the incorporation of multivariate analysis methods. For example, Raman spectroscopy has been used to identify cell components[1] and to discriminate between cancerous and normal cells,[2] cancer cells with differing phenotype[3] and distinguishing human embryonic stem cells from differentiated cells.[4] In the case of SERS, unfunctionalised nanoparticles have been used to obtain information about cell compartments,[5] endocytosis,[6] as well as cell health[7] and viability.[8] Function specific SERS nanotags have also been designed for the molecular profiling of single cells,[6] intracellular pH sensing[9] and *in vivo* tumour targeting and detection.[10,11]

Despite the advanced applications of both Raman and SERS spectroscopies there are limited examples of sophisticated 3D imaging within the literature to accompany these applications.[12] Imaging in 3D by Raman spectroscopy can be relatively simple to achieve using depth profiling in the *z* direction and software packages such as ImageJ (National Institutes of Health (NIH)) and Volocity™ (Perkin Elmer®). 3D imaging has the potential to provide a wealth of information which could be critical to the detection of disease states. For example, 3D Raman imaging of cells and tissues which results in the resolution of cell organelles represents a non-invasive technique for studying cell construction[12] and this could be extremely beneficial when investigating changes in cellular architecture between diseased and healthy cells. If 3D Raman were combined with 3D SERS imaging it may be possible to track nanotags functionalised with specific organelle targeting moieties or drug molecules. Imaging in this manner would not only demonstrate non-destructive evidence of cellular uptake but it would provide evidence that the tags are being directed to their intended targets.

Indeed one of the most notable difficulties when using SERS nanotags for intracellular imaging is in determining cellular inclusion. Whilst it is straightforward to track the 'uptake' and localisation of the nanotags by SERS mapping in two dimensions,[13,14] it provides no real evidence of uptake and thus cellular inclusion. Traditionally, internalisation has been confirmed by transmission electron microscopy (TEM) or depth-profiling in the *z*-direction. However, TEM imaging requires convoluted sample preparation, the images are often expensive to obtain and therefore the approach is not open to all. In addition, obtaining a SERS map of the same cell examined by TEM is very challenging and results in the destruction of the cell rendering it unsuitable for live cell analysis. Whilst conventional TEM imaging can provide evidence of cellular inclusion confocal scanning transmission electron microscopy (STEM)[15] as well as X-ray diffraction[16] and topography,[17] and ion-abrasion scanning electron microscopy (SEM)[18] can be used to generate 3D cell images. Although these techniques provide

[a]*Centre for Molecular Nanometrology, WestCHEM, Department of Pure and Applied Chemistry, University of Strathclyde, Glasgow, G1 1XL, UK. E-mail: duncan.graham@strath.ac.uk; Fax: +44 (0)141 5520876; Tel: +44 (0)141 5484701*

[b]*Renishaw plc, Spectroscopy Products Division, Old Town, Wotton-Under-Edge, GL12 7DW, UK*

† Electronic supplementary information (ESI) available: Full preparation details for the nanoparticles, nanotags and cells are included. The procedures for analysing the cell samples and characterisation data for the nanotags are also included. See DOI: 10.1039/c3sc51437d

‡ Both authors contributed equally.

excellent resolution (nm range *cf.* μm range for Raman spectroscopy), comparable acquisition times (hours) and the deduction of cell organelles in 3 dimensions no biochemical information is gained and some of these techniques can result in cellular destruction. The generation of the 3D images also relies on the post collection processing of stacked 2D images. With regards to fluorescence microscopy for the generation of 3D cell images resolution has been greatly enhanced (~30 nm in the *x*, *y* and *z* directions *cf.* μm)[19] with the advent of approaches such as stimulated emission depletion (STED) microscopy[19] and structured illumination microscopy (SIM).[20] Acquisition times are considerable faster since the collection of a full vibrational spectrum is not required, however, as with the other techniques fluorescence microscopy is limited in that it prohibits biochemical imaging of the cell contents and the 3D images are again generated from 2D stacks. In addition fluorophores, unlike Raman active labels, can be prone to photobleaching which is problematic if they are to be used for 3D imaging where the acquisition of successive *z*-sections is necessary and where any bleaching could compromise the correct reconstruction of 3D structures.[21] As fluorophores exhibit broad absorption and emission bands the detection of multiple components within a sample can be compromised. This is not an issue when employing Raman or SERS active labels since sharp (nm width)[22] molecularly specific bands are produced. Furthermore, the use of SERS active labels can confer picomolar sensitivity *in vivo* as opposed to nanomolar sensitivity when quantum dots and conventional fluorescence microscopy are employed.[23] Here, we demonstrate for the first time the concept of 3D Raman and SERS imaging for the simultaneous confirmation of cellular inclusion and multiple component detection, thus avoiding the need for expensive TEM images. Novelty therefore arises from the fact that specific molecular information can be garnered and from the fact, unlike many of the techniques mentioned, the entire volume is collected at once, all the collected data can be processed and analysed as one data set, and both uni-variate and multivariate analyses can be applied to the volume. The advantage of applying statistical evaluation to the entire volume is that the trends in the data are explained in the *x*, *y* and *z* directions simultaneously, as opposed to applying multivariate analysis to each plane and reassembling plane images as a block which takes only trends in the *x* and *y* directions into account.[12]

Results and discussion

A multiple component suspension of four nanotags[24] (nanotag characterisation data – Fig. S1 and 2 and Table S1 and 2†) (4-mercaptopyridine (MPY), 5′5-dithiobis(2-nitrobenzoic acid) (DTNB), 4-nitrobenzenethiol (NBT) and 2 naphthalenethiol (2-NPT) labelled nanotags – ESI†) was applied to Chinese Hamster Ovarian (CHO) cells according to the standard protocol (ESI†). Cell samples were then mapped in 2D (StreamLine™, StreamLineHR™ – Renishaw inVia Raman spectrometer/Leica DM 2500 microscope, Renishaw plc, Gloucestershire, UK.) to rapidly identify cells which had taken up the suspension and in which all four or multiple components could be identified (data not shown). The nanotags were selected on the basis that aggregated systems formed following the addition of 1,6-hexamethylenediamine (HMD) to the silver citrate nanoparticles.[24] Small clusters such as this are ideal scaffolds for the formation of hotspots[24,25] and thus enhanced SERS.[25] Previous investigations (data not shown) have also shown that signals can decrease 10–100 fold following cell uptake so an aggregated system is necessary if the nanotags are to be detected intracellularly. However, in order to ensure that aggregation is slowed and to retard the formation of excessively large clusters which would not be suitable for cellular uptake[26,27] polyvinylpyrrolidone (PVP) was added to quench the aggregation.[24] The polymer layer stabilises the hot spots[24] whilst still allowing the small molecule reporters to infiltrate these zones.[24] The small molecule reporters (MPY, DTNB, NBT and 2-NPT) were selected on the basis that no synthesis was required, they like the other nanotag materials, are inexpensive, are readily available, give strong SERS signals, nanoparticle conjugation – *via* terminal thiol groups or disulfide linkages – is extremely straightforward and their chemical structures are such that subsequent functionalisation with biomolecules for the targeting of specific cell components is relatively straightforward. In addition to this the small molecule reporters[9,13,14,24,28] have been widely used in intracellular investigations demonstrating the suitability of the nanotags for cellular uptake. Nanotag identification was a two-fold process whereby each of the components was identified from their unique peaks (Fig. S2†) and direct classical least squares (DCLS) multivariate analysis. This method is typically employed when reference spectra are available for all of the components and involves fitting the unknown data (collected during mapping) to a linear combination of the specified component spectra (standard suspension spectra). If a match was found to occur between the standard and the collected spectra a false colour was assigned and separate false colour images were created for each component. The contributions were normalised to a value of between 0 and 1 where values close to 1 indicate areas within the image with high similarities in shape to that of the reference spectrum. Once a cell containing all four or multiple components had been identified, it was imaged in 3D.

To successfully image a multiple component positive cell in 3D and therefore verify the uptake of the nanotags, the cell was mapped using volume mapping, a confocal configuration which allows layers of Raman and SERS images to be rapidly collected. When this method is employed the step sizes in the *x* and *y* directions can be defined independently from the step size in the *z* direction. Here the step sizes in the *x* and *y* directions were set at 0.8 μm and 0.5 μm for the cell and nanotag maps respectively, and in the *z* direction it was set at 1 μm. The *z*-range was defined as ±3 μm from the point of focus when the cell was observed under white light illumination (set as $z = 0$). The cell sample was imaged under immersion in a saline solution using an Olympus 60× (N.A. 1) water immersion objective. In order to volume map both the cells and the SERS nanotags two different laser excitations were required – one where the intrinsic Raman signals of the cell dominate and there is minimal interference from the SERS nanotags, and one

where the SERS signals from the nanotags are most prevalent. The total acquisition times for the cell (0.8 μm step size, 2 s acquisition) and the nanotag (0.5 μm step size, 0.5 s acquisition) maps were 3.24 h and 4.7 h respectively. This is comparable with other Raman studies[12] and unlike the depth profiling methods there is no need for the post collection processing of 2D stacks to generate 3D images.[12] Additionally, in comparison to other methods although the overall collection time is

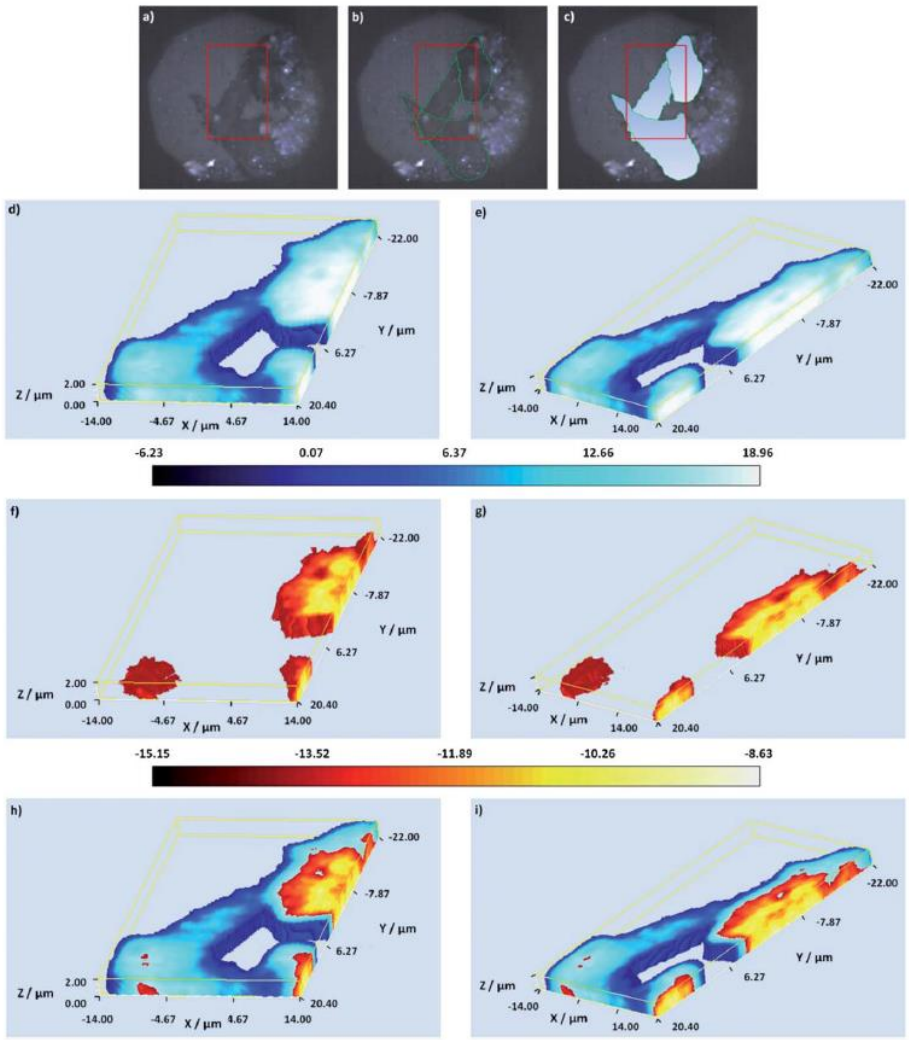

Fig. 1 White light and false colour volume 3D Raman images of the mapped cells – (a) white light image of the mapped cells, the cells are outlined in green in (b) and the mapped cell areas are distinguished with a gradient fill in blue in (c). In (a)–(c) the red box indicates the complete 3D Raman analysed area. (d and e) A false colour 3D Raman cell image generated using PC 2 displayed at different angles. (f and g) A false colour 3D Raman nuclei image generated using PC 1 displayed at different angles. (h and i) Combined false colour 3D Raman cell and nuclei images presented at different angles. In (d)–(g) the false colour scale bar is shown below the images.

somewhat greater this is offset by the biochemically specific information obtained. The 3D volume Raman cell map was generated (Fig. 1d–i) by mapping the highlighted cells (Fig. 1a–c) using 532 nm excitation.

At this wavelength intrinsic Raman signals from cell components such as proteins, amino acids, lipids and DNA can be readily visualised.[5,6] Following data collection, the false colour Raman 3D images were constructed by performing univariate analysis based on signal to baseline maps (the integrated intensities of selected bands), and multivariate analysis based on principal component analysis (PCA). A signal to baseline map was generated specifically from the ring breathing mode of the amino acid phenylalanine (998–1008 cm^{-1}, ~1004 cm^{-1})[5,6] (data not shown) and this was found to clearly define the cell structure.

Phenylalanine is found ubiquitously in the cell hence it is an excellent marker for its delineation. However, as we also wished to determine the location of the SERS nanotags in relation to the cell organelles, PCA was applied to the data (normalised, not mean centred) to determine if there were any spectral variations, which could be ascribed to specific cell organelles.[29] The main principles of PCA have been previously described[29,30] but for this particular data set the PCA conditions included spectrum centring and normalisation. Mean centring was not applied since the band positions were sufficiently different to distinguish the two PCs chemically (Fig. 2). The main advantages of these conditions are that the loadings reflect the baseline offset, the background and the appearance of a typical spectrum. For the mapped cells two principal components (PCs) explained 86.5% of the variance in the data set with PCs 1 and 2 representing the cell contents (Fig. 2a–d). When comparing the PC loadings (Fig. 2d) and the band assignments (Table 1) PC 2 is characterised collectively by Raman bands attributed to protein, lipid and nucleic acids but most notably by peaks at 1004 cm^{-1}, 1245 cm^{-1} and 1451 cm^{-1} assigned to phenylalanine,[31,32] amide III (protein) band[33] and the CH_2CH_3 deformation of protein and lipid.[34] PC2 therefore represents the general cellular regions. This is consistent with the raw Raman spectra (Fig. 2c) and the PC2 image clearly defines the structure of the mapped cells (Fig. 1d, e, h and i).

The PC1 domain contains negative scores and is thus characterised by the negative peaks in the loadings. PC1 is characterised by a combination of peaks ascribed to nucleic acids, nucleotides, amino acids and protein. These include phenylalanine peaks[31,32] at 1004 cm^{-1} and the CH_2CH_3 deformation of protein at 1451 cm^{-1} (Fig. 2b).[34] The PC loadings suggest that PC1 represents domains which are biochemically distinct from the main cell structure and based on these loadings we propose that PC1 represents the cell nuclei (Fig. 1f–i). This is consistent with the raw Raman spectra from the nuclei, specifically DNA peaks at 751 cm^{-1} and 788 cm^{-1} (Fig. 2a).[30,35]

The 3D volume SERS nanotag map was generated by mapping the same volume as highlighted (Fig. 1b and c) but with 633 nm excitation instead. However, because of the smaller step size used (0.5 μm *cf.* 0.8 μm) the SERS image was collected at 0.5 μm higher in the *y* direction than the Raman cell image.

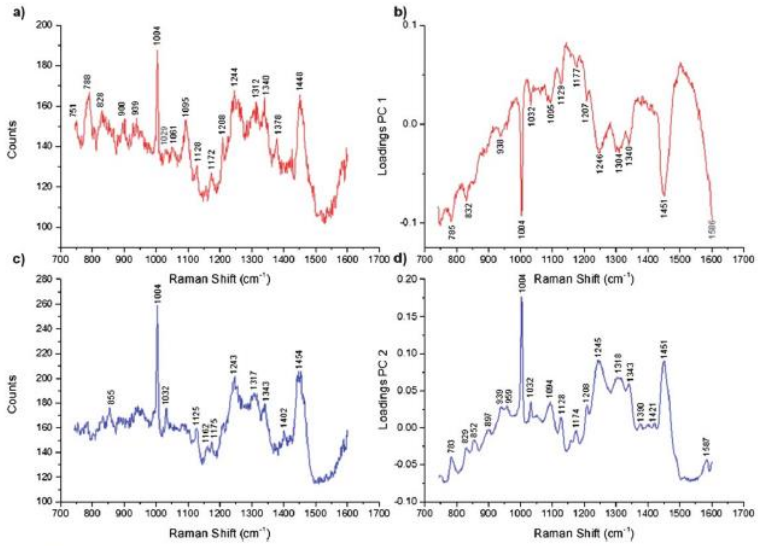

Fig. 2 Representative Raman spectra and the corresponding PC loadings for the cells and the nuclei. (a) A representative Raman spectrum measured from the nuclei, (b) PC 1 loadings which distinguish the nuclei, (c) representative Raman spectrum measured from the cells and (d) PC 2 loadings which distinguish the cells.

Table 1 Peak position and tentative assignments of the main peaks found in the principal component (PC) loadings for each PC shown in the volume 3D cell map.[30–41]

Peak position (cm^{-1})	Assignment
783	DNA
785	νO–P–O stretch DNA
829	O–P–O stretch DNA/RNA ring breathing tyrosine
832	Tyrosine, ν_{asym}O–P–O
852	Proline/tyrosine
897	—
938/939	νC–C, peptide
959	—
1004	Phenylalanine
1032	CH_2CH_3 collagen and phospholipids, phenylalanine
1094/1095	DNA, νC–N lipid
1128	C–N (proteins), C–O (carbohydrates)
1174	Phenylalanine, tyrosine
1177	Tyrosine, cytosine, guanine
1207/1208	Phenylalanine
1245/1246	Amide III
1304	CH_2 deformation (lipid) adenine/cytosine
1318	Guanine (DNA/RNA)
1340	—
1421	Adenine, guanine ring breathing modes of DNA/RNA
1451	CH_2CH_3 deformation
1586/1587	Phenylalanine

This has been corrected for in the final 2D images (ESI†). At this wavelength the signals from the small molecule reporters can be readily visualised and using the employed laser power intrinsic Raman signals from the cells is minimal. Following data collection the false colour SERS 3D images were constructed by performing multivariate data analysis in the form of component DCLS.

The two independently collected 3D data sets (cells and nanotags) were then combined in 2 dimensions for the determination of cellular uptake and multiple component detection (Fig. 3). The z range was defined as ±3 μm from the point of focus for both the cell and the nanotag maps. However, when the volume 3D cell map was collected (data not shown) it was found that only certain z-slices were of relevance. This was ascertained by viewing the 3D volume cell map along the z-direction. From this angle it was apparent that the spectra from above z-slice +2.00 and below z-slice +0.00 were not of relevance. In light of this the 3D cell map was recollected from z-slice +2.00 to +0.00 but the 3D nanotag map was collected from the entire z-range previously mentioned. Despite this it was still possible to combine the relevant z-slices in 2D to ascertain cellular uptake, and the combined cell and nanotag z-slices are presented in Fig. 3d–f.

On close inspection of the combined z-slices we can instantly determine that three out of the four nanotags, MPY, DTNB and NBT labelled nanotags, which are shown in blue, green and red respectively, within the multiple component suspension are located within the cells (Fig. 3d–f). In z-slice +2.00 only NBT labelled nanotags were observed (Fig. 3d), whilst in z-slice +1.00 only NBT and DTNB labelled nanotags were found (Fig. 3e) and in z-slice +0.00 three out of the four nanotags, MPY, DTNB and NBT, were observed (Fig. 3f). The reasons as to why 2-NPT labelled nanotags were not observed intracellularly are unclear but if 2-NPT remains extracellularly the possibility of using this nanotag as an external standard exists. On the basis of these images (Fig. 3d–f) it is quite difficult to observe the three nanotags located within the cells because there is a degree of co-localisation. In theory, co-localisation may be expected since the suspension applied to the cell population contained equal proportions of the four individually labelled tags which were well mixed. Thus there was an equal probability of each nanotag within the suspension being internalised simultaneously. As such z-slice +0.00 has been enlarged (Fig. 4a–c) for ease of observation and the combined SERS z-slice image for the three nanotags and for each of the individually labelled nanotags located intracellularly are also shown (Fig. 4d).

Each of the components was identified by their unique peak and component DCLS analysis. Unique peaks were found at ~1004 cm^{-1}, 1150 cm^{-1}, 1084 cm^{-1} and 1450 cm^{-1} for MPY, DTNB, NBT and 2-NPT respectively (Fig. S2†). With the component DCLS a 'false' colour was assigned if a match was found to

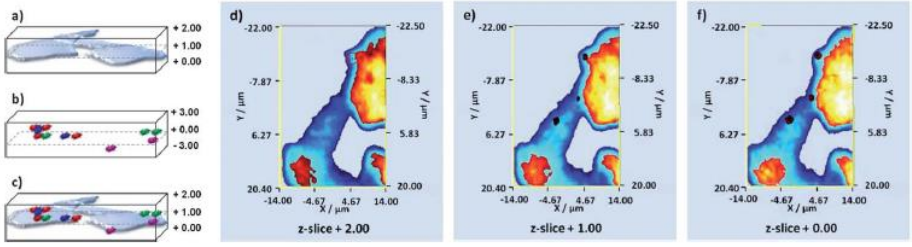

Fig. 3 Schematic of how the two volume 3D data sets are combined. (a) Schematic of volume 3D Raman cell map, (b) schematic of volume 3D SERS nanotag map, (c) combined 3D volume Raman cell and SERS nanotag map. Images from each plane of the 3D volume Raman cell and SERS nanotag maps can be extracted and these can be combined in 2D – (d) z-slice nanotags and cell +2.00, in this z-slice the signal is considerably weaker than those obtained from the other z-slices and as such the corresponding false colour is considerably smaller hence it has been highlighted with an appropriately coloured circle, (e) z-slice nanotags and cell +1.00 and (f) z-slice nanotags and cell +0.00. MPY, DTNB and NBT labelled nanotags are shown in blue, green and red respectively.

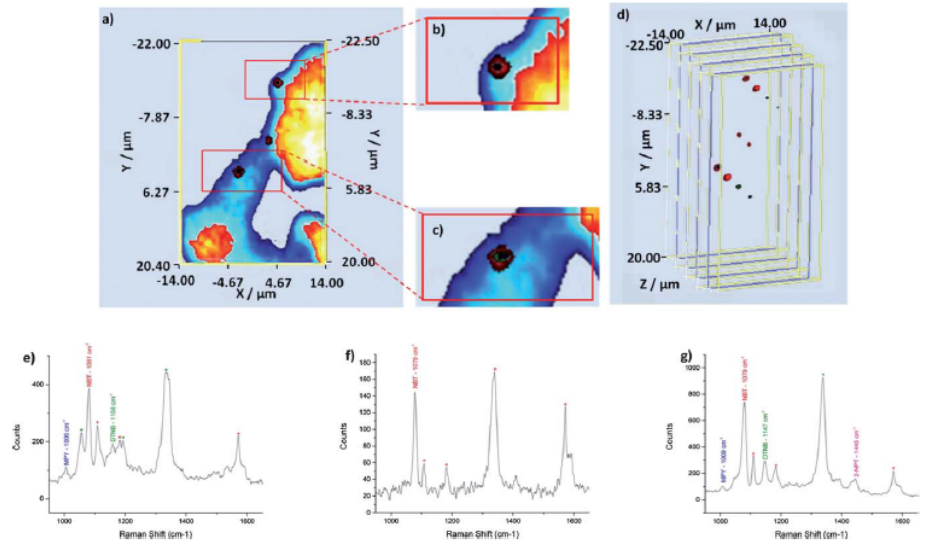

Fig. 4 Enlarged image of *z*-slice +0.00 and the corresponding SERS spectra for each of the three false colour clusters. (a) 2D *z*-slice nanotags and cell +0.00, (b) and (c) enlarged areas from the top and bottom clusters respectively, *z*-slice +0.00 which shows three of the four nanotags within a single area and a single cell and (d) exploded 3D SERS *z*-slice image for the three nanotags combined and for each of the individual nanotags. In the enlarged image it is difficult to identify the three false colours because they overlap but in the exploded image each can be clearly visualised. (e–g) Representative SERS spectra obtained for the top, middle and bottom false colour clusters.

occur between the reference and the collected data. In order to further confirm the spatial positioning of the components, the data was viewed on moveable plane slices within the volume. When viewed in this way the corresponding spectra for a selected position are also displayed and these can be extracted and visually compared with standard spectra from the nanotag suspensions.

For *z*-slice +0.00 representative SERS spectra have been extracted for each of the three locations where the nanotags were found (Fig. 4e–g). In accordance with the co-localisation observed, cumulative SERS signals concomitantly arise from the nanotags. That is, we observe SERS signals from all of the nanotags which are found within a specified location (Fig. 4e–g). The unique peak for the appropriate nanotag has been labelled with the corresponding abbreviation and peak position. The minor peaks have also been tentatively assigned to a small molecule reporter and labelled with an asterisk of corresponding colour (Fig. 4e–g). For the top spot in *z*-slice +0.00 MPY, NBT and DTNB were identified at ~1006 cm^{-1}, ~1081 cm^{-1} and ~1158 cm^{-1} respectively. For the middle spot, NBT was identified at ~1079 cm^{-1}. MPY, NBT and DTNB were identified at ~1008 cm^{-1}, ~1079 cm^{-1}, ~1147 cm^{-1} in the bottom cluster. 2-NPT was also identified at ~1445 cm^{-1} in the bottom spot although no false colour has been assigned to 2-NPT at that particular location.

It should also be noted that none of the nanotags penetrated the nuclei (Fig. 3 and 4) and they presumably resided in the cytoplasm or endosome compartments. This is to be expected since the nanotags were not functionalised with targeting moieties specific for this or any other cell organelle. Based on this information these unfunctionalised nanotags could be used as controls to distinguish between targeting and non-targeting nanotags when targeting of the nucleus is attempted. This will be investigated further in later studies.

Conclusions

In conclusion, volume 3D Raman and SERS imaging represents a non-destructive technique for the simultaneous confirmation of cellular inclusion and multiple component detection. Three of the four components of the suspension were detected, and by extracting and combining 2D *z*-slices from the 3D images it was possible to determine the intracellular location of the nanotags without the need for expensive and destructive TEM imaging. This study is also the first to report on the generation of true 3D Raman and 3D SERS images. Although, other studies have reported the production of 3D images[12] these have been constructed using depth profiling methods. In the current study the entire volume was analysed at once reflecting the novelty of the technique. It was also possible to define a subcellular compartment without the need for any special sample preparation (*i.e.* staining). The resolution of further cell organelles[12] is expected and the ability to detect such structures whilst

maintaining the integrity of the cell will undoubtedly be of benefit to the detection of disease process in which the architecture of the cell changes considerably. The adoption of a multi-marker approach is also critical if disease states are to be fully characterised or multiple cell organelles are to be targeted. Hence, the ability to detect these multi-markers in 3 dimensions is of huge importance for a whole host of applications including cellular disease or tumour detection and the delivery of drugs and their subsequent fate within the cells. This work also has implications for the application of combined 3D Raman and SERS imaging to living cells.

Acknowledgements

SMcA acknowledges Renishaw plc for funding. DG acknowledges support from Royal Society Wolfson Trust Research Merit Award.

References

1 C. Krafft, T. Knetschke, A. Siegner, R. H. W. Funk and R. Salzer, *Vib. Spectrosc.*, 2003, **32**, 75–83.
2 M. S. Bergholt, W. Zheng, K. Lin, K. Y. Ho, M. Teh, K. G. Yeoh, J. B. Yan So and Z. Huang, *Int. J. Cancer*, 2011, **128**, 2673–2680.
3 Y. Oshima, H. Shinzawa, T. Takenaka, C. Furihata and H. Sato, *J. Biomed. Opt.*, 2010, **15**, 017009.
4 F. C. Pascut, H. T. Goh, N. Welch, L. D. Buttery, C. Denning and I. Notingher, *Biophys. J.*, 2011, **100**, 251–259.
5 K. Kneipp, A. S. Haka, H. Kneipp, K. Badizadegan, N. Yoshizawa, C. Boone, K. E. Shafer-Peltier, J. T. Motz, R. R. Dasari and M. S. Feld, *Appl. Spectrosc.*, 2002, **56**, 150–154.
6 J. Kneipp, H. Kneipp, M. McLaughlin, D. Brown and K. Kneipp, *Nano Lett.*, 2006, **6**, 2225–2231.
7 S. C. Pînzaru, L. M. Andronie, I. Domsa, O. Cozar and S. Astilean, *J. Raman Spectrosc.*, 2008, **39**, 331–334.
8 H.-W. Tang, X. B. Yang, J. Kirkham and D. A. Smith, *Appl. Spectrosc.*, 2008, **62**, 1060–1069.
9 A. Pallaoro, G. B. Bruan, N. O. Reich and M. Moskovits, *Small*, 2010, **6**, 618–622.
10 X. Qian, X.-H. Peng, D. O. Ansari, Q. Yin-Goen, G. Z. Chen, D. M. Shin, L. Yang, A. N. Young, M. D. Wang and S. Nie, *Nat. Biotechnol.*, 2008, **26**, 83–90.
11 C. L. Zavaleta, B. R. Smith, I. Walton, W. Doering, G. Davis, B. Shojaei, M. J. Natan and S. S. Gambhir, *Proc. Natl. Acad. Sci. U. S. A.*, 2009, **106**, 13511–13516.
12 K. Majzner, A. Kaczor, N. Kachamakova-Trojanowska, A. Fedorowicz, S. Chlopicki and M. Baranska, *Analyst*, 2013, **138**, 603–610.
13 M. K. Gregas, J. P. Scaffidi, B. Lauly and T. Vo-Dinh, *Appl. Spectrosc.*, 2010, **64**, 858–866.
14 M. K. Gregas, F. Yan, J. Scaffidi, H.-N. Wang and T. Vo-Dinh, *Nanomedicine*, 2011, **7**, 115–122.
15 J. J. Einspahr and P. M. Voyles, *Ultramicroscopy*, 2006, **106**, 1041–1052.
16 H. Jiang, C. Song, C.-C. Chen, R. Xu, K. S. Raines, B. P. Fahimian, C.-H. Lu, T.-K. Lee, A. Nakashima, J. Urano, T. Ishikawa, F. Tamanoi and J. Miao, *Proc. Natl. Acad. Sci. U. S. A.*, 2010, **107**, 11234–11239.
17 W. Gu, L. D. Etkin, M. A. Le Gros and C. A. Larabell, *Differentiation*, 2007, **75**, 529–535.
18 J. A. W. Heymann, D. Shi, S. Kim, D. Bliss, J. L. S. Milne and S. Subramaniam, *J. Struct. Biol.*, 2009, **166**, 1–7.
19 R. Schmidt, C. A. Wurm, A. Punge, A. Egner, S. Jakobs and S. W. Hell, *Nano Lett.*, 2009, **9**, 2508–2510.
20 L. Schermelleh, P. M. Carlton, S. Haase, L. Shao, L. Winoto, P. Kner, B. Burke, M. C. Cardoso, D. A. Agard, M. G. L. Gustafsson, H. Leonhardt and J. W. Sedat, *Science*, 2008, **320**, 1332–1336.
21 X. Michalet, F. F. Pinaud, L. A. Bentolila, J. M. Tsay, S. Doose, J. J. Li, G. Sundaresan, A. M. Wu, S. S. Gambhir and S. Weiss, *Science*, 2005, **307**, 538–544.
22 J. A. Dougan and K. Faulds, *Analyst*, 2012, **137**, 545–554.
23 S. Keren, C. Zavaleta, Z. Cheng, A. de la Zerda, O. Gheysens and S. S. Gambhir, *Proc. Natl. Acad. Sci. U. S. A.*, 2008, **105**, 5844–5849.
24 G. B. Braun, S. J. Lee, T. Laurence, N. Fera, L. Fabris, G. C. Bazan, M. Moskovits and N. O. Reich, *J. Phys. Chem. C*, 2009, **113**, 13622–13629.
25 R. Jin, *Angew. Chem., Int. Ed.*, 2010, **49**, 2826–2829.
26 F. Zhao, Y. Zhao, Y. Liu, X. Chang, C. Chen and Y. Zhao, *Small*, 2011, **7**, 1322–1337.
27 L. Y. T. Chou, K. Ming and W. C. W. Chan, *Chem. Soc. Rev.*, 2011, **40**, 233–245.
28 N. M. S. Sirimuthu, C. D. Syme and J. M. Cooper, *Chem. Commun.*, 2011, **47**, 4099–4101.
29 K. Lau, A. Hobro, T. Smith, T. Thurston and B. Lendl, *Vib. Spectrosc.*, 2012, **60**, 34–42.
30 D.-H. Kim, R. M. Jarvis, Y. Xu, A. W. Oliver, J. W. Allwood, L. Hampson, I. N. Hampson and R. Goodacre, *Analyst*, 2010, **135**, 1235–1244.
31 W.-T. Cheng, M.-T. Liu, H.-N. Liu and S.-Y. Lin, *Microsc. Res. Tech.*, 2005, **68**, 75–79.
32 R. Malini, K. Venkatakrishma and J. Kurien, *Biopolymers*, 2006, **81**, 179–193.
33 G. Shetty, C. Kedall, N. Shepherd, N. Stone and H. Barr, *Br. J. Cancer*, 2006, **94**, 1460–1464.
34 R. J. Lakshimi, V. B. Kartha, C. M. Krishna, J. G. R. Solomon, G. Ullas and P. Uma Devi, *Radiat. Res.*, 2002, **157**, 175.
35 I. Notingher, C. Green and C. Dyer, *J. R. Soc., Interface*, 2004, **1**, 79–90.
36 Z. Huang, A. McWilliams, M. Lui, D. I. McLean, S. Lam and H. Zeng, *Int. J. Cancer*, 2003, **107**, 1047–1052.
37 N. Stone, C. Kendell, N. Shepherd, P. Crow and H. Barr, *Faraday Discuss.*, 2004, **126**, 141–157.
38 A. J. Ruiz-Chica, M. A. Medina, F. Sanchez-Jimenez and F. J. Ramirez, *J. Raman Spectrosc.*, 2004, **35**, 93–100.
39 J. W. Chan, D. S. Taylor, T. Zwerdling, S. M. Lane, K. Ihara and T. Huser, *Biophys. J.*, 2006, **90**, 648–656.
40 C. J. Frank, R. L. McCreecy and D. C. B. Redd, *Anal. Chem.*, 1995, **67**, 777–783.
41 J. Binoy, J. P. Abraham, I. H. Joe, V. S. Jayakumar, G. R. Pettit and O. F. Nielsen, *J. Raman Spectrosc.*, 2004, **35**, 939–946.

Analyst

RSC Publishing

PAPER

View Article Online
View Journal | View Issue

Cite this: *Analyst*, 2013, **138**, 6331

Analysis of intracellular enzyme activity by surface enhanced Raman scattering†

Ross Stevenson,[a] Sarah McAughtrie,[a] Laura Senior,[a] Robert J. Stokes,[a] Helen McGachy,[b] Laurence Tetley,[c] Paola Nativo,[a] James M. Brewer,[c] James Alexander,[b] Karen Faulds[a] and Duncan Graham*[a]

Received 11th April 2013
Accepted 28th August 2013

DOI: 10.1039/c3an00729d

www.rsc.org/analyst

Dysfunctional intracellular enzymatic activity is believed to be an underlying cause of a myriad of diseases. We present the first use of surface enhanced Raman scattering (SERS) as a detection technique capable of reporting intracellular activity of a specific enzyme. Careful choice of reagents allowed the preparation of high resolution cellular activity maps highlighting the specific conversion of the commonly used ELISA reagent 5-bromo-4-chloro-3-indolyl β-D-galactopyranoside (X-Gal), by wild type β-galactosidase enzymes. Further, through co-addition of X-Gal substrate and inhibitors we were able to demonstrate that intracellular substrate conversion occurred predominantly through an enzymatically specific pathway. The data presented therefore supports the application of SERS probes as sensitive, specific sensors of biochemical activity and demonstrates the use of SERS probes for the first time as beacons capable of high resolution subcellular localisation of native enzymes.

Introduction

The functional integrity of individual cells and organisms is crucially dependent upon the activity of cohorts of intracellular enzymes. Dysfunctional activity, localisation or the absence of specific enzymes is invariably associated with significant diseases including cystic fibrosis.[1] As a result the ability to measure the activity and localisation of specific enzymes within a cellular environment is critical to life science research. A variety of methods exist for this purpose however, most are based on fluorescence or colorimetric detection which are limited in terms of either sensitivity or multiplexing capability.[2] In addition, the reagents used for such analyses tend to provide uniform coverage across the cell which is acceptable when looking at populations but inadequate when trying to observe the sub-cellular compartmentalisation of enzymatic activities. Herein, we provide the first description of the use of surface enhanced Raman scattering (SERS) to detect galactosidase enzymes within cells in a non-destructive manner. SERS was facilitated by nanoparticle enhancement of the coloured hydrolysis product generated from the colorimetric substrate, 5-bromo-4-chloro-3-indolyl β-D-galactopyranoside (X-Gal), a commonly used marker for galactosidase enzymes.

SERS requires the detection of light inelastically scattered from an analyte adsorbed onto a metal surface.[3] Raman scattering is an inherently weak process prone to interference from fluorescence however, the development of SERS has led to a range of superior probes that show improved sensitivity and which can quench fluorescence.[4,5] The main condition required to obtain SERS is the adsorption of the analyte onto a suitable enhancing surface, typically electrodes or specifically designed metal surfaces or nanoparticles.[6] Gold or silver nanoparticles, as used in the study, can be coupled with different excitation sources to match the plasmon frequency of either unaggregated or aggregated nanoparticles.[7] A further enhancement can also be obtained by using an analyte which has an electronic transition coincident with the Raman excitation frequency.[8]

In our approach, β-galactosidase was studied as an intracellular target to test the enzymatic generation of a SERS signal. We have previously shown that conversion of typical ELISA dye substrates, bromochloroindolylphosphate (BCIP) and 2,2-azinobis(3-ethylbenzothiazoline-6-sulfonic acid) (ABTS), can be monitored by SERS in a sensitive and quantitative manner, however, this was never extended into a biological environment.[9,10] β-galactosidase enzymes are stable and have the ability to hydrolyse dye substrates making them ideal for use in ELISAs and for testing cell senescence.[11] *In vitro* β-galactosidase levels can currently be measured using the Miller technique[12] however, this approach requires the destructive permeabilisation of the cell membrane. Herein, we report the first use of SERS to detect the activity of galactosidase enzymes from

[a]*Centre for Molecular Nanometrology, WestCHEM, Pure and Applied Chemistry, University of Strathclyde, 295 Cathedral Street, Glasgow, G1 1XL, UK. E-mail: duncan.graham@strath.ac.uk; Fax: +44 (0)1415520876; Tel: +44 (0)1415484701*
[b]*Strathclyde Institute of Pharmacy and Biomedical Sciences, University of Strathclyde, 161 Cathedral Street, Glasgow, G4 0RE, UK*
[c]*Institute of Infection, Immunity and Inflammation, University of Glasgow Sir Graeme Davies Building, 120 University Place, Glasgow, G12 8TA, UK*
† Electronic supplementary information (ESI) available. See DOI: 10.1039/c3an00729d

specific locations within cells by monitoring the conversion of X-Gal.

Materials and methods

Materials

All materials purchased were from Sigma-Aldrich except β-galactosidase (Calbiochem, UK) and gold nanoparticles, 40 nm (British Biocell International, UK).

Measurements

Plate based spectroscopy was carried out using Renishaw inVia Raman spectrometers using different excitation wavelengths. An Ar-ion laser was used for work using a 514.5 nm (7.30 mW) incident wavelength, 632.8 nm (2.43 mW) was provided by a He–Ne laser and 785 nm utilised a laser diode (5.41 mW). An Olympus 20× LWD objective (N.A. 0.4) was used and the spectrometer grating was centred at 600 cm^{-1} and 10 s acquisitions were used. The specific experiment being carried out dictated what volumes of reagents were present in the sample wells.

SERS mapping was performed using Renishaw inVia Raman spectrometers fitted with inverted and upright microscope systems equipped with a 100× LWD objective (N.A. 0.75) (~6 mW power at the sample). Line mapping was performed using a StreamLine™ Raman mapping system (Renishaw plc, UK). SERS maps were coloured by integrating the area under the characteristic peak at 598 cm^{-1}. A grating of 1200 l mm^{-1} was used with a *RenCam* CCD. Mapping was also performed with a WiTec alpha 300R (100× objective, N.A. 0.95) confocal Raman spectrometer (WiTec, Germany) (~5 mW power at the sample). Both utilised a He–Ne 632.8 nm laser. The Renishaw spectrometer grating was centred at 600 cm^{-1} and used 10 s acquisitions. The WiTec system recorded spectra in the range 0–3000 cm^{-1} with 0.1 s acquisitions.

Sample preparation

Colloid. 50 mg of sodium tetrachloroaurate and 500 mL of distilled water were added to a round-bottomed flask (which had previously been cleaned using aqua regia) and heated until boiling. A solution of 75 mg of sodium citrate in 7.5 mL distilled water was added and the mixture was then allowed to boil for 15 min with continuous stirring. After cooling, the quality of the colloid was confirmed using UV-Vis spectroscopy (λmax = 521 nm) and transmission electron microscopy (TEM). The nanoparticle diameter was recorded for over one hundred of the gold nanoparticles and the average value recorded was 19.66 ± 2.65 nm.

X-Gal/inhibitor solutions. 5 mg of X-Gal was dissolved in 100 μL of dimethylformamide (DMF) before being added gradually to phosphate buffered saline (PBS) to reach the required concentrations. 5 mg of each inhibitor was also dissolved in DMF before dilution to the desired concentrations in PBS. For *in vitro* studies the solutions were diluted in Roswell Park Memorial Institute (RPMI) media instead of PBS.

Cell preparation. Bone marrow macrophages were obtained from Balb/C mice. Femurs were flushed with 5 mL of Dulbecco's Modified Eagle Media (DMEM) and the cells were cultured in a 9 cm Petri dish with 20% heat inactivated fetal calf serum (FCS), 30% cell culture supernatant from L929 cell line, 1% L-glutamine (2 mM) and 1% penicillin/streptomycin solution (100 μg mL^{-1}). On day 4 and 8 fresh media was added before harvesting the cells on day 10. Cells were counted and plated out onto 13 mm cover slips in a 24 well tissue culture plate at 5×10^5 cells per well in RPMI with 10% FCS, 1% L-glutamine and 1% penicillin/streptomycin solution. To ensure the cells were fixed to the cover slips they were left overnight at 37 °C, 5% CO_2. Solutions were prepared in RPMI (serum free) and were sterilized before use in an appropriate tissue culture hood under UV light for 30 min. The appropriate volumes and concentrations of nanoparticles, X-Gal and inhibitor were made up to an overall volume of 300 μL and were added to the cells to incubate for 24 h at 37 °C, 5% CO_2. Upon completion the media was removed and the cells were washed twice with serum free RPMI. The cells were fixed with 1% glutaraldehyde for 15 min before washing with PBS then rinsing with ddH_2O. Cover slips were removed from the plate and allowed to air dry for 2 h before mounting onto a slide using DPX mountant.

Transmission electron microscopy (TEM). Cells were grown to confluence on Thermanox® (Agar Scientific, UK) coverslips and incubated overnight with X-Gal (10 mM) and gold nanoparticles (0.1 nM). The cells were then washed (×3) with PBS before being fixed for 2 h with 3% (v/v) glutaraldehyde in 0.1 M sodium cacodylate buffer. Cells were washed a further 3 times with sodium cacodylate buffer before a post-fixation with 1% (v/v) osmium tetroxide in 0.1 M sodium cacodylate buffer. After a further wash the cells were dehydrated with acetone before being infiltrated and embedded in epoxy resin, allowing ultra-thin sections to be taken by a diamond knife. Sections were positioned on TEM grids and stained with 2% aqueous uranyl acetate and the grids were examined and photographed at an accelerating voltage of 80 keV in a CM120 Biotwin (Philips) TEM with a digital camera.

Results and discussion

Prior to *in vitro* analysis the idealised SERS response was investigated using nanoparticles and different excitation frequencies (514.5 nm, 632.8 nm and 785 nm) under buffer conditions (10 mM phosphate buffer, pH 7.4). X-Gal itself yields a minimal SERS signal however, the dimerised hydrolysis product gives a strong peak at 598 cm^{-1} due to a skeletal vibration from the newly formed *trans*-alkene (Fig. 1 and S1, S2†).[13] A comparison between several different, commonly used, nanoparticle suspensions namely citrate reduced gold and silver and EDTA reduced silver was carried out to compare the surface enhancement achieved. The combination of 632.8 nm excitation and gold nanoparticles (20 nm) provided the highest SERS signal in the shortest time (Fig. S2†). Smaller particles are inherently more stable and reliable and high signal intensity is achieved since the X-Gal product produces a strong blue colour with an absorbance maxima at ~635 nm, putting it directly in resonance with both the surface plasmon of the aggregated gold nanoparticles (521 nm unaggregated, 630 nm aggregated) and

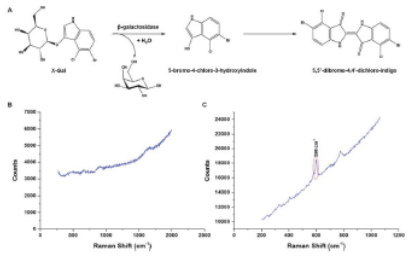

Fig. 1 SERS detection to monitor the conversion of X-Gal. The conversion of the colourless X-Gal to the blue coloured (λ_{max} = 635 nm) 5,5′-dibromo-4,4′dichloro-indigo by galactosidase (A) can be monitored by SERS. The product gives a new sharp vibrational Raman peak at 598 cm^{-1} as illustrated in the comparison of (B) and (C).

the excitation frequency (632.8 nm). In order to prove that the reaction could be affected by known enzyme inhibitors two commercially available competitive inhibitors of β-galactosidase, phenylethyl-β-D-galactopyranoside (PEG) and phenylethyl-β-D-thiolgalactopyranoside (PETG)[14] were used to investigate the inhibition of the enzyme and the resulting reduction of the SERS signal. The X-Gal and nanoparticle concentrations were maintained at 1 mM and 0.1 nM respectively. The inhibitor concentration was varied from 10 mM to 0.1 mM and a dose dependent response was observed (Fig. S3†). The inhibitors themselves gave minimal Raman signal and therefore did not influence the signal obtained from the hydrolysis of the X-Gal.

A primary cell line, bone marrow-derived macrophages, was chosen to study the measurement of β-galactosidase activity by SERS. Macrophages naturally express β-galactosidase and readily endocytose metallic nanoparticles therefore eliminating the issue of cellular uptake of the nanoparticle substrates to obtain the enhancement of the Raman scattering.[15] Suspensions of nanoparticles (0.1 nM) and X-Gal with various concentrations (10–0.1 mM) were added to macrophage cells grown on cover slips. Following 48 h of incubation the cells were washed, harvested and the cover slips attached to slides. The Raman spectra obtained from the cells are shown (Fig. 2A and B). The map is produced by taking the signal to baseline area (570–620 cm^{-1}) of the major peak centred at 598 cm^{-1} at each individual pixel across the area. The StreamLine mapping system on the Renishaw inVia system utilizes line mapping, allowing large areas to be mapped rapidly whilst minimising tissue damage. A typical map would be a complete 150 micron by 100 micron area where Raman signals were collected every 2 microns in the *X* co-ordinate and 1.1 microns in the *Y* co-ordinate. The streamline mapping approach was limited to approximately 5–6 scans across the cell. Data can also be observed from a larger population (~120 cells) using a 20× objective as shown in Fig. 2C. The data presented is representative of this type of experiment which has been repeated many times. It was also possible to produce a dose dependant response from the cells by varying the concentration of X-Gal substrate added to the cells (10 mM to 0.1 mM) as shown in Fig. S4.†

In order to test the specificity of this enzymatic transformation the two galactosidase inhibitors previously used in the optimisation of the conditions were applied to the cells. If the transformation was unique to the galactosidase then the inhibitors would reduce the enzymatic activity resulting in a lower SERS signal from the product of the X-Gal hydrolysis. In this set of experiments the X-Gal and gold nanoparticle concentrations were maintained at 10 mM and 0.1 nM respectively and the inhibitor concentrations diluted from 10 mM to 0.1 mM. The results, as shown in Fig. 2D, clearly indicate that there is a significant difference in the response measured by SERS when looking at the various concentrations of the two different inhibitors applied to the cells. In addition, it also indicates that PEG appears to be more effective than PETG 10 at inhibiting the β-galactosidase and that this is a biomolecularly specific interaction which is being measured using the gold nanoparticles and SERS within the cells. The same false colour scale was used throughout all maps.

TEM images taken of cell sections confirm that the nanoparticles were indeed inside the cell (Fig. 3A). The TEM images indicate that the nanoparticles are contained within endosomes and not simply adsorbed onto the cell membrane. Upon isolation of the nanoparticle containing intracellular compartments it was possible to characterise them as LAMP-1 expressing but transferrin receptor negative suggesting these were late endosomes or lysosomes (Fig. S5†).[16,17]

In order to prepare higher definition maps to observe spectra every 100 nm in the *X* and *Y* co-ordinates, a point mapping approach was taken whereby the stage was moved by 400 μm^2 in combination with a 100× objective (N.A. 0.9) to provide approximate lateral resolution of 461 nm optically. The results, shown in Fig. 3B, are in agreement with the TEM image indicating that sub-cellular localisation of the nanoparticles can be observed by SERS. Furthermore, this is the first demonstration of the potential to measure enzyme activity at nanometre dimensions using SERS. Also, as shown in Fig. 3C, it was possible to screen a larger area of cells with the same high resolution screening.

These results are the first to demonstrate that SERS can be used to detect enzyme activity in an intracellular environment and that SERS provides several important advantages over conventional approaches. Firstly, detection of the substrate X-Gal with a commonly studied enzyme has been reported using gold nanoparticles and SERS. The formation of a substrate product which offers a strong unique SERS fingerprint has been monitored over a standard ELISA timeframe allowing the observation of the increasing levels of enzyme turned-over product. This aspect of the work is novel yet runs parallel to some of our groups' earlier studies where we analysed the suitability of SERS as a detection method with commonly used ELISA reagents.[9,10,18] Our results also show that the measurement is specific to β-galactosidase enzymes since the addition of β-galactosidase inhibitors reduces the observed SERS signal and that the SERS response is dependent on inhibitor concentration proving that we are not observing non-specific hydrolysis. The inhibitors used both contain a galactopyranoside moiety and compete with X-Gal for the active site of the enzyme.

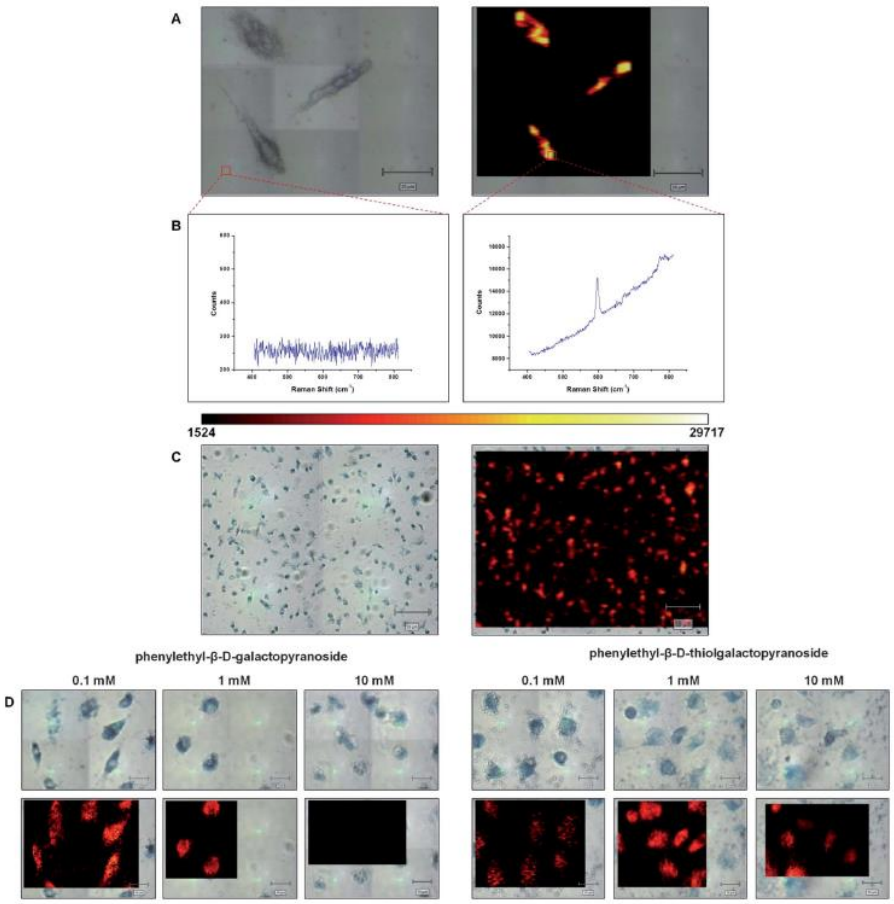

Fig. 2 Intracellular SERS detection. The bright field (A) and false colour image (B) of three treated cells mapped by SERS using a 100× objective are shown. Spectra associated with specific mapped pixels are shown below each figure and the scale bar in (A) and (B) represents 20 μm. A false colour scale bar was used throughout and this is also shown below (A) and (B). Areas with no Raman signal appear black and areas with increasing peak intensity at 598 cm^{-1} are represented by increasing brightness. (C) Uses the same technique but looks at a larger area with use of a 20× objective. (D) Demonstrates the effect of inhibitor concentration on the cellular SERS response for both phenylethyl-β-o-galactopyranoside (PEG) and phenylethyl-β-o-thiolgalactopyranoside (PETG). The X-Gal and nanoparticle concentrations were 10 mM and 0.1 mM respectively.

Turnover of X-Gal yields an indole/indigo dye with a large vibrational Raman cross-section whereas the inhibitors produce phenylethyl groups with negligible Raman responses.

By combining this chemical innovation with high resolution SERS mapping it was possible to localise nanoparticles within specific cellular sites and measure biomolecular activity. Indeed, the ability to measure enzyme activity specifically in the endolysosome compartment allows the use of our approach in a wide variety of biological systems and in particular is significant for major pathophysiological conditions associated with lysosomal enzyme disorders such as Parkinson's and Alzheimer's.[16,17] Differential quantification of galactosidase enzyme activities in these subcellular compartments during different disease states or inflammatory processes will provide clear insights as to how best to manipulate these biological systems therapeutically. These studies strongly support the application

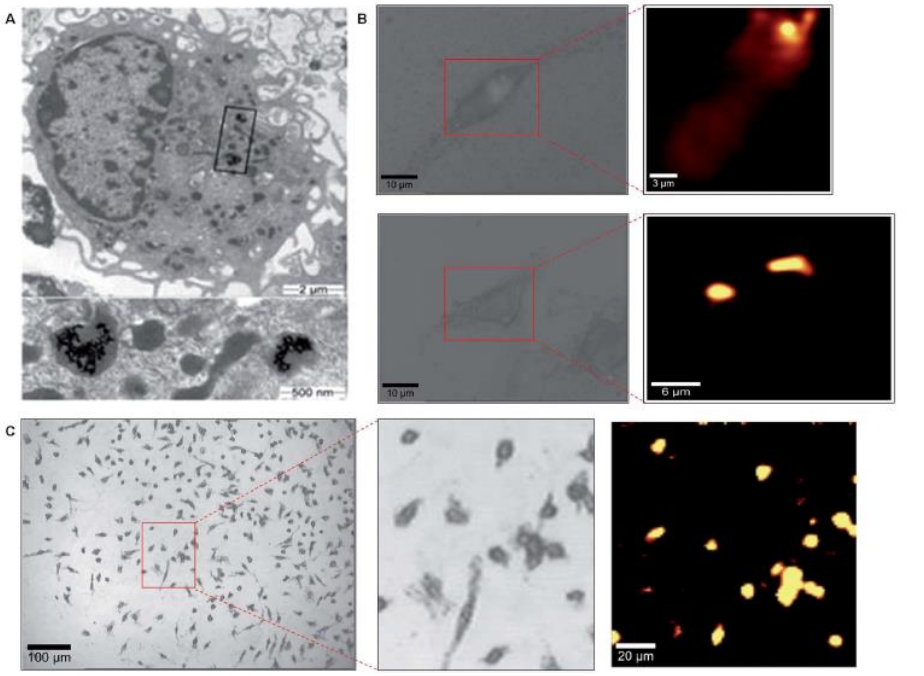

Fig. 3 Localisation of nanopartides within cells. Macrophages treated with gold nanoparticles are show in (A). A magnified version of the highlighted area is shown in the lower figure. (B) High resolution mapping of two individual macrophage cells and their associated false colour Raman images. (C) High resolution mapping of a cell population using a 20× objective.

of SERS approaches to quantify and localise specific multiparameter biochemical activities within cells which will have a significant impact on functional biochemical imaging and analysis of a variety of biological samples.

Conclusions

The application of nanoparticles to cells has been a field of intense research and here we show that by combining the innovative detection of the X-Gal product with high resolution SERS mapping it becomes possible to localise the nanoparticles to specific cellular sites. It should be noted that SERS has previously been used in intracellular studies to measure pH and to detect 11 individual cellular components.[19-22] However, these earlier studies have either delivered SERS active nanoparticles into cells[22] or have relied on the cellular components to offer modest Raman gains.[21] In this particular study metallic nanoparticles were employed to selectively enhance the molecular vibrations of a molecule which only becomes Raman active upon interaction with the target enzyme and this is the first documented intracellular Raman enzyme detection method. It is worth raising the point that we only observe signals from specific areas within the cell where both the nanoparticles and the turned-over product are present. However, this may not represent the true location of the enzymes. Further, it is possible that an area with a high Raman signal could be indicative of either a high concentration of nanoparticles or high enzyme concentration as it is well established that aggregated nanoparticles yield greater SERS signal. Although fluorescence spectroscopy has traditionally been the technique of choice for the monitoring of such enzyme activity it is clear that the SERS method confers numerous advantages over fluorescence namely the ability to obtain specific molecular information and its multiplexing capability. Indeed the potential to detect and measure the activity and location of multiple enzymes exists as a direct result of the sharp molecularly specific spectral bands produced by SERS. In addition, it is hoped that with the introduction of live cells, ultrafast Raman imaging, careful temporal analysis and complementary TEM analysis SERS approaches may be able to definitively ascribe enzymes to specific cellular locations. These studies strongly support the application of SERS approaches to quantify and

localise specific multiparameter biochemical activities within cells. This will have a significant impact on functional biochemical imaging and the analysis of a variety of biological samples.

Acknowledgements

The authors acknowledge the EPSRC platform grant EP/E000584/1 for supporting this work and the Royal Society for a Wolfson Research Merit Award to DG.

Notes and references

1 S. Holland, *Clin. Rev. Allergy Immunol.*, 2010, **38**, 3–10.
2 R. M. Yates, A. Hermetter, G. A. Taylor and D. G. Russell, *Traffic*, 2007, **8**, 241–250.
3 M. Fleischmann, P. J. Hendra and A. J. McQuillan, *Chem. Phys. Lett.*, 1974, **26**, 163–166.
4 X. Zhang, J. Zhao, A. V. Whitney, J. W. Elam and R. P. Van Duyne, *J. Am. Chem. Soc.*, 2006, **128**, 10304–10309.
5 K. Kneipp, Y. Wang, H. Kneipp, L. T. Perelman, I. Itzkan, R. R. Dasari and M. S. Feld, *Phys. Rev. Lett.*, 1997, **78**, 1667–1670.
6 K. Hering, D. Cialla, K. Ackermann, T. Dörfer, R. Möller, H. Schneidewind, R. Mattheis, W. Fritzsche, P. Rösch and J. Popp, *Anal. Bioanal. Chem.*, 2008, **390**, 113–124.
7 R. J. Stokes, A. Macaskill, P. J. Lundahl, W. E. Smith, K. Faulds and D. Graham, *Small*, 2007, **3**, 1593–1601.
8 K. Faulds, R. P. Barbagallo, J. T. Keer, W. E. Smith and D. Graham, *Analyst*, 2004, **129**, 567–568.
9 R. Stevenson, A. Ingram, H. Leung, D. C. McMillan and D. Graham, *Analyst*, 2009, **134**, 842–844.
10 F. M. Campbell, A. Ingram, P. Monaghan, J. Cooper, N. Sattar, P. D. Eckersall and D. Graham, *Analyst*, 2008, **133**, 1355–1357.
11 V. Bassaneze, A. A. Miyakawa and J. E. Krieger, *Anal. Biochem.*, 2008, **372**, 198–203.
12 J. H. Miller, *Experiments in Molecular Genetics*, Cold Spring Harbor Laboratory Press, USA, 1972.
13 D. A. Long, *J. Raman Spectrosc.*, 2004, **35**, 905.
14 D. H. Juers, S. Hakda, B. W. Matthews and R. E. Huber, *Biochemistry*, 2003, **42**, 13505–13511.
15 R. Shukla, V. Bansal, M. Chaudhary, A. Basu, R. R. Bhonde and M. Sastry, *Langmuir*, 2005, **21**, 10644–10654.
16 T. E. Tjelle, B. Saigal, M. Froystad and T. Berg, *J. Cell Sci.*, 1998, **111**, 141–148.
17 C. Bellettato and M. Scarpa, *J. Inherited Metab. Dis.*, 2010, **33**, 347–362.
18 S. Laing, A. Hernandez-Santana, J. R. Sassmannshausen, D. L. Asquith, I. B. McInnes, K. Faulds and D. Graham, *Anal. Chem.*, 2010, **83**, 297–302.
19 C. E. Talley, L. Jusinski, C. W. Hollars, S. M. Lane and T. Huser, *Anal. Chem.*, 2004, **76**, 7064–7068.
20 H.-W. Tang, X. B. Yang, J. Kirkham and D. A. Smith, *Anal. Chem.*, 2007, **79**, 3646–3653.
21 J. Kneipp, H. Kneipp, M. McLaughlin, D. Brown and K. Kneipp, *Nano Lett.*, 2006, **6**, 2225–2231.
22 J. Kneipp, H. Kneipp, W. L. Rice and K. Kneipp, *Anal. Chem.*, 2005, **77**, 2381–2385.

analytical chemistry

Article

pubs.acs.org/ac

Confocal SERS Mapping of Glycan Expression for the Identification of Cancerous Cells

Derek Craig,[†] Sarah McAughtrie, Jonathan Simpson, Corinna McCraw, Karen Faulds, and Duncan Graham*

Centre for Molecular Nanometrology, WestCHEM, Pure and Applied Chemistry, University of Strathclyde, 295 Cathedral Street, Glasgow G1 1XL, U.K.

Supporting Information

ABSTRACT: Lectin-functionalized silver nanoparticles have been successfully designed for use as molecular imaging agents to investigate carbohydrate−lectin interactions at the surface of mammalian cells, using surface-enhanced Raman scattering (SERS). Carbohydrate-lectin interactions are key to many cellular processes and are responsible for controlling an array of cellular interactions. In this study, lectin-functionalized silver nanoparticles were used to detect the expression of carbohydrate species at the cellular interface. The carbohydrate−lectin interactions were demonstrated using three different lectin species for three distinct cell types. Due to the known difference between the expressions of glycans in cancerous versus noncancerous cells of the same origin, this approach has been expanded to study both cancerous and noncancerous prostate cells. This has been achieved via confocal SERS mapping of the expression of the key glycan, sialic acid, on the surface of each of these cell types. In achieving such discrimination, a novel method has been created by which glycan expression can be reproducibly monitored. Comparative studies were performed using both fluorescence and SERS. SERS provided an increased discrimination over fluorescence when analyzing cell subsets to discriminate between cancerous and noncancerous cells. The success of this method means that it could be used to complement the current gold standard histopathological techniques.

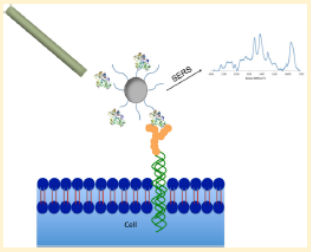

Global cancer fatalities account for millions of people each year and with the number of new cases expected to increase annually to 22 million by 2030, the importance of early disease identification and treatment has never been such a pertinent issue.[1] The identification of a substantial number of cancer biomarkers has led to the development of new therapeutics and novel techniques to map cancer pathways and to combat the disease.[2−5] One of the key biomarkers identified has been a family of glycans (carbohydrates) known as sialoglycans.[6,7] These glycans are present on the surface of mammalian cells and play key roles in the regulation of molecular and cellular interactions.[8] The elevated expression of sialic acid containing glycoproteins is symptomatic of disease and cancer progression. Herein, a study is reported by which the sialic acid composition of mammalian cells has been used to discriminate between noncancerous and cancerous cell tissue.

Histopathology is the current gold standard technique for cancerous tissue identification.[9] A study of histological features such as irregular stratification, loss of intercellular adherence, and polarity alongside changes in nuclear size and miotic activity are currently used to evaluate cancer cell development.[10] Highly trained individuals perform these analyses, however, as these evaluations are deemed to be subjective and cross correlation analyses are required.[11,12] A more robust chemical analysis based approach would not only significantly improve histological classification and lower costs, but most importantly, it would reduce the time taken for a patient to receive a diagnosis.

Typical chemical analysis methods including mass spectrometry (MS), nuclear magnetic resonance (NMR), and high-performance liquid chromatography (HPLC) are not amenable to cellular interrogation, therefore, a spectroscopic approach is required.[13] Recently, advances in this field by technologies such as magnetic resonance imaging (MRI), Fourier-transform infrared (FT-IR), and fluorescence spectroscopy have revolutionized research in cancer detection.[14−16] Raman spectroscopy has also been utilized for cellular interrogation; however, due to the many chemical components present in each cell and the limitation on the laser power able to be used in order to prevent cellular degradation, it is an inherently weak technique.[17] A significant disadvantage of each of these techniques are the high levels of background fluorescence achieved during cellular analysis.[18] By using surface-enhanced Raman spectroscopy (SERS), inherent background fluorescence can be overcome by using metallic nanoparticles, which quench any fluorescence via nonradiative decay channels.[17] In comparison to the other techniques available, SERS permits the simultaneous analysis of multiple components in a single

Received: November 28, 2013
Accepted: April 19, 2014

dx.doi.org/10.1021/ac4038762 | Anal. Chem. XXXX, XXX, XXX−XXX

sample; it provides a unique vibrational fingerprint spectrum and has been show to consistently afford a significant increase in sensitivity.[19−22] SERS has shown its versatility as a technique which can be used sensitively for a number of purposes, including the detection of microorganisms, the monitoring of biological interactions both in solution and on surfaces, and also as a key cancer cell detection technique when used in both in vivo and ex vivo studies.[23−26] Recent advances in the use of SERS for biological detection have displayed the capability to create two-dimensional (2D) and three-dimensional (3D) cellular images, which could be crucial toward identifying key disease states.[27] By creating such images, subtle chemical and morphological changes in the composition of cells can be monitored with high accuracy.[28] Therefore, it is essential to identify suitable biomarkers in order to follow disease development and to create new therapeutics.

As the disease state of cancer progresses, the sialoglycan composition of the cell changes in order to prevent cell coagulation and ensure rapid entry into the bloodstream in order to facilitate cancer metastasis.[29] In order to facilitate the detection of these changes in carbohydrate composition, specific proteins known as lectins can be used.[30] Lectins are carbohydrate specific proteins that can display either single or multiple specificities.[31] The interaction of lectins and carbohydrates are known to be key to the mediation of a variety of biological processes, including cell signaling, molecular recognition, and immunity.[32−34] However, as these interactions are typically very weak, multivalent platforms are typically created in order to improve the occurrence of such events.[35] Through the use of nanomaterials, such platforms can be created. Previous studies in solution have exploited these interactions using a range of spectroscopic techniques.[36,37] Studies have shown the use of fluorescence microscopy to discriminate between cell types via the use of lectin conjugated quantum dots.[38] Although this was a successful approach, issues surrounding the toxicity of quantum dots and the inherent advantages of SERS over fluorescence spectroscopy still remain (i.e., a fingerprint spectrum of the reporter molecule is produced, multiplexing is much easier, and it has been shown that SERS can provide an increase in sensitivity over fluorescence). Recently, the first use of SERS for the detection of carbohydrate−lectin interactions was reported.[39] This study identified that by conjugating silver nanoparticles with carbohydrate species, these interactions could be detected with unparalleled sensitivity.

Herein, we report a method for the functionalization of nanoparticles with lectins to elucidate the composition of carbohydrate species at the cellular interface. This method has also been expanded to facilitate the discrimination between noncancerous and cancerous prostate cells.

■ EXPERIMENTAL SECTION

All solvents were of laboratory grade. Chemicals were obtained from commercial sources. Water used in the preparation of colloid and all solutions was obtained from a triply distilled deionized water system.

Linker Synthesis. Wang resin (1 g), succinic anhydride (0.336 g, 3 equiv), and 4-dimethylaminopyridine (DMAP) (0.397 g, 3 equiv) were refluxed for 6 h in dichloromethane (DCM) at 90 °C. The resin was allowed to cool overnight before being filtered and washed five times in the following sequence: (1) DCM, (2) methanol (MeOH), (3) DCM, (4) MeOH, and (5) DCM. The resin was then mixed with Jeffamine ED-2001 (PEG-41) (6 g, 3 equiv) and diisopropylcarbodiimide (DIC) (0.378 g, 3 equiv) overnight at room temperature. The resin was then filtered and washed in sequence as before. The resin was then mixed overnight with CDI (0.454 g, 2 equiv) and the benzotriazole dye (0.417 g) at room temperature in DMF. The resin was then filtered and washed in sequence as before. A light red colored product was produced. The target compound was then cleaved from the resin. The resin was placed in a 10% trifluoroacetic acid (TFA) in DCM solution and stirred for 3 h. This resulted in a dark red/brown-colored solution and a red solid residue around the inside of the flask. The mixture was then filtered and washed as before. The resin solid was removed, and to the filtrate, a spatula full of morphino-methyl polystyrene was added to remove any excess TFA; the resin was then filtered. The solvent was removed under reduced pressure and a red solid was obtained.

^{1}H NMR were recorded on a Bruker DPX 400 MHz spectrometer with the appropriate solvent peak as a reference. J coupling values are quoted in Hertz. High-resolution FAB MS was recorded on JEOL AX505 spectrometer in methanol and nitrobenzyl alcohol/glycerol matrices. ^{1}H: ∂H (400 MHz $CDCl_3$): 1.06 (2H, t, J 4.0, CH_2), 1.12 (2H, d, J 4.0, CH_2), 2.13 (6H, d, J 7.3, CH_3), 2.65 (2H, t, J 8.1, CH_2), 3.43 (2H, t, J 8.0, CH_2), 3.62 (m, CH_2), 5.4 (1H, s, NH), 7.20 (1H, d, J 12.0, ArH), 7.28 (1H, s, ArH), 7.60 (1H, d, J 8.0, ArH), 10.51 (1H, s, OH), 12.04 (1H, s, BT NH). MS: $C_{112}H_{206}N_8O_{47}$. MW: 2416, MALDI *m/z*: 2417

Nanoparticle Preparation. Citrate reduced silver (Ag) colloid was prepared via a modified version of the Lee and Meisel method, whereby 90 mg of silver nitrate was added to 500 mL of distilled water (dH_2O) and heated until boiling.[40] Once boiling, a 1% aqueous solution of sodium citrate (100 mg in 10 mL dH_2O) was added and boiling was maintained for 15 min. The solution was then allowed to cool, and continuous stirring was maintained throughout.

Lectin-Functionalized Nanoparticle Preparation. The following lectins were purchased from Sigma-Aldrich Wheat Germ Agglutinin, *Lens culinaris*, and Concanavalin A. Each lectin species was suspended in a 10 mM Tris buffer to achieve a final concentration of 1 μM. Prior to nanoparticle attachment, each lectin was attached to the linker molecule via EDC·HCl and sulfo NHS coupling chemistry. Ten microliters of the lectin was added to a solution containing 10 μL of linker (1 mM stock), 10 μL of EDC·HCl (2 mg/mL stock), 10 μL of sulfo NHS (2 mg/mL stock), and 50 μL of 10 mM Tris buffer. These solutions were reacted for 3 h at room temperature prior to purification to remove any unattached lectin by centrifugation, using molecular weight spin columns where the solutions underwent 3 cycles of centrifugation at 13000 rpm for 5 min with 50 μL of 10 mM Tris buffer added between cycles. The columns were then inverted, and the purified lectin-linker solution was obtained via a final centrifugation cycle at 2000 rpm for 5 min. To a solution of 450 μL silver citrate nanoparticles, 50 μL of the corresponding lectin-linker species were added and shaken overnight to facilitate lectin-linker functionalization of the nanoparticle surface. A further purification step was undertaken to remove any unattached linker species, with each solution undergoing centrifugation at 6000 rpm in triplicate with resdispersion in 500 μL of a 10 mM Tris buffer following each purification cycle.

Cell Preparation. Chinese Hamster Ovarian (CHO) cells were stored in an incubator at 37 °C with 5% CO_2. CHO cells

dx.doi.org/10.1021/ac4038762 | Anal. Chem. XXXX, XXX, XXX−XXX

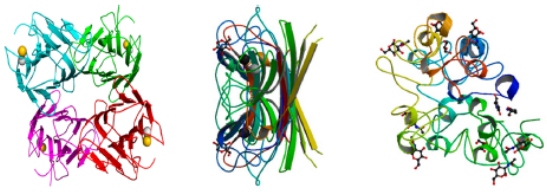

Lectin Type	Carbohydrate Specificity
Con A	α-*D*-mannosyl and α-*D*-glucosyl groups
Lens culinaris	α-Mannose
Wheat Germ Agglutinin (WGA)	$(GlcNAc)_2$ (N-acetylglucosamine), NeuNAc (N-acetylneuramic acid)

Figure 1. Three lectins chosen for conjugation to the silver nanoparticles and the carbohydrate specificities of each species. Images obtained from the Protein Data Bank (PDB). Con A PDB: 3CNA; *Lens culinaris*, PDB: 1LEM; wheat germ agglutinin PDB: 2UVO.

were cultured in HAM F12 media supplemented with 10% fetal calf serum, 1% penicillin/streptomycin (10 mg/mL). Cells were grown to confluence prior to harvesting, using trypsin/EDTA. HeLa cells were stored in an incubator at 37 °C with 5% CO_2. HeLa cells were cultured in minimum essential medium eagle (MEME) media supplemented with 10% fetal calf serum, streptomycin, and L-glutamine. Cells were grown to confluence prior to harvesting, using trypsin/EDTA.

PNT2A (noncancerous) and PC-3 (cancerous) cells were stored in an incubator at 37 °C with 5% CO_2. Each of these cell lines were cultured in RPMI 1640 Medium supplemented with HEPES, 10% fetal calf serum, 1% of both penicillin/streptomycin, and 1% fungizone. Cells were grown to confluence prior to harvesting, using trypsin/EDTA.

Once harvested, 300 μL of the cells were seeded, at 4×10^6 cells/mL, on glass coverslips and incubated at 37 °C for 24 h with 5% CO_2. Following this period of incubation, 30 μL of the lectin-functionalized nanomaterials were added to each coverslip and again incubated for 1 h at 37 °C with 5% CO_2. The coverslips were then washed in triplicate with 1× PBS prepared in sterile distilled water prior to fixing the cells to the coverslips using a 4% paraformaldehyde for 15 min. Following this period, the coverslips were again washed with 1× PBS followed by washing with sterile water before allowing to air-dry for 2 h. The coverslips were then mounted to glass slides using DPX mountant prior to analysis.

Analysis of Cell Samples using SERS. *633 nm Excitation.* Fixed CHO and HeLa cell samples were imaged in 2D (StreamLine-Renishaw inVia Raman spectrometer/Leica DMI 5000 M microscope, Renishaw plc, Gloucestershire, U.K.), using a 633 nm laser (HeNe) excitation source. Samples were imaged using a 20× long working distance (LWD) objective lens. A grating of 1800 lines/mm was used with a RenCam charge-coupled device (CCD) (1040 × 256 pixels). Line mapping was performed with a StreamLine Raman mapping system, and the following conditions were used: ~633 nm line focus, spectral range of 934.7–1720.8 cm^{-1}, ~8 mW laser power, and an acquisition time of 5 s.

532 nm Excitation. WITec Alpha 300 R confocal microscope (WITech, Ulm, Germany) with a 532 nm excitation wavelength. Mapping of samples was performed using 100 lines and 100 points per line for each 25 × 25 μm sample area using an integration time of 0.1 s at 5% laser power, using a 10× long working distance objective lens.

Cell Sample Preparation for Fluorescence Imaging. PNT2A and PC3 cultures were grown to confluence and harvested in Trypsin/EDTA as before. Once harvested, 300 μL of the cells were seeded, at 4×10^6 cells/mL, on glass coverslips and incubated at 37 °C for 24 h with 5% CO_2. Following this period of incubation, 30 μL of the FITC-tagged WGA lectin was added to each coverslip and again incubated for 1 h at 37 °C with 5% CO_2. The coverslips were then washed in triplicate with a 1× PBS prepared in sterile distilled water prior to fixing the cells to the coverslips using 4%-paraformaldehyde at 37 °C for 2 min. Following this period, the coverslips were again washed with 1× PBS followed by washing with sterile water before allowing it to air-dry for 2 h. The coverslips were then mounted to glass slides using DPX mountant prior to analysis.

Fluorescence Imaging. Images of WGA-FITC-tagged PNT2A and PC3 cells were obtained using a Nikon Eclipse LV100 microscope using a Photometrics CoolSNAP HQ camera with a SEMROCK BRIGHTLINE FITC 350B-NTE filter cube. Images were processed using Metamorph.

RESULTS AND DISCUSSION

Glycans form a layered coating around mammalian cells known as the glycocalyx, which is the first point of contact for approaching cells or pathogens. The glycans present are derived from combinations of a small number of common monosaccharides that include *N*-acetyl neuraminic acid, glucose, galactose, mannose, fucose, xylose, glucorinic acid, iduronic acid, *N*-acetyl glucosamine, and *N*-acetyl galactosamine.[41] To investigate the carbohydrate composition of the cell lines being studied, three different lectin species were identified, with each displaying a variety of carbohydrate specificities. These lectins are shown in Figure 1.

To facilitate the binding of these lectins to the appropriate glycan species, a multivalent platform was created via the tethering of each lectin species to functionalized silver nanoparticles. Silver nanoparticles were used in this study, as they have an increased Raman scattering cross section in comparison to gold nanoparticles.[42] To tether the lectin species to the surface of the silver nanoparticles, a novel heterobifunctional poly(ethylene glycol) linker species was designed, which

had been functionalized at one terminus with a benzotriazole dye for surface attachment and at the other with a carboxylic acid residue for lectin attachment. Benzotriazole dyes have been used routinely in SERS analysis due to the strong covalent bonding achieved between the triazole group and the silver nanoparticle surface, which enables reproducible SERS analyses to be obtained.[43−45] Poly(ethylene glycol) was incorporated into the linker design to prevent nonspecific interactions between the functionalized nanoparticles and other cellular components.[46] The synthesis of this ligand was performed on a functionalized resin support for ease of recovery and to improve the reaction yield. The synthetic scheme for the linker construction is shown in Scheme 1.

Scheme 1. Synthesis of Linker Performed on a Wang Resin Support[a]

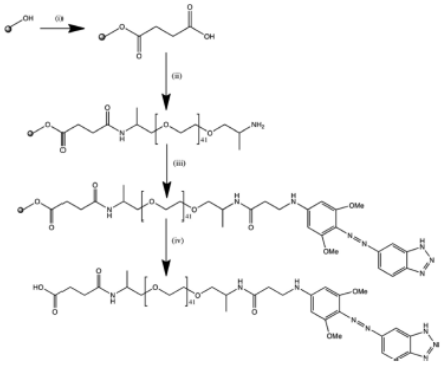

[a]The following conditions were used: (i) succinic anhydride, DMAP, DCM, 90 °C, 6 h; (ii) PEG-41, DIC, DCM, r.t., 14 h; (iii) benzotriazole dye, CDI, DCM, r.t., 14 h; and (iv) 10% TFA in DCM, r.t., 3 h. Yield 42%.

Following the successful synthesis of this ligand, three different functionalized lectin silver nanoparticle species were prepared, containing the individual lectin species shown in Figure 1. Each lectin species was coupled to the linker via common 1-ethyl-3-[3-(dimethylamino)propyl] carbodiimide hydrochloride (EDC) and *N*-hydroxysulfosuccinimide (sulfo-NHS) coupling chemistry prior to the attachment of the linker species to the nanoparticle surface. These nanoparticles were then analyzed using extinction spectroscopy and gel electrophoresis to confirm successful functionalization. A slight characteristic red shifting of 1−2 nm of the plasmon resonance band of the silver nanoparticles was witnessed, indicating that a change in the surface dielectric environment had occurred following the attachment of each lectin-linker species to the nanoparticle surface. The gel electrophoresis study confirmed these results via comparison of the distance moved by the nanoparticle conjugates within the gel in comparison to unmodified nanoparticles (Figure S-1 of the Supporting Information). Scanning electron microscopy images were also obtained to analyze the size of the nanoparticle species prior to and post functionalization. From these analyses, an appreciable size difference was apparent (Figure S-2 of the Supporting Information). For the nonfunctionalized nanoparticles, an average diameter of 40 nm was obtained and this increased to 48 nm, following the attachment of the lectin-linker species to the nanoparticle surface.

Preliminary cellular studies were performed using the commonly available Henrietta Lacks (HeLa) and chinese hamster ovarian (CHO) cell lines. These cell lines were chosen due to their availability and because of their routine use in nanoparticle imaging studies. Initial experiments were performed on each of these cell sets to identify if the carbohydrate composition of the cell surface could be mapped using the lectin-functionalized silver nanoparticles. Prior to analysis, each lectin species were individually incubated with each cell line for an optimized period of 3 h. Following the incubation period, cell viability analysis was performed using 0.1% Trypan blue, which is a commonly used stain for dead cells. Trypan blue identifies cells in which the membrane has ruptured following necrosis. These results indicated that following nanoparticle incubation, no significant cell necrosis had occurred.

SERS analyses were performed using a confocal Raman microscope with a laser excitation wavelength of 532 nm. This system enabled individual Raman spectra to be collected at each pixel of the imaging area selected for each cell. This gives rise to thousands of individual Raman spectra, which can be used to construct an intensity map profile of each cell to determine the localization of a particular chemical species. Monitoring the most intense peak of the SERS signature at 1619 cm^{-1}, which is the aromatic quadrant stretch of the benzotriazole dye attached at the nanoparticle surface, generated intensity profile maps. Following the incubation of each lectin species with each cell line for an optimized period of 3 h SERS analyses were performed. HeLa cell line analysis proved successful, significant interactions between each lectin species, and the carbohydrates present on the cell surface were observed. The results for the CHO cell line showed that no significant carbohydrate−lectin interactions were occurring, as shown in Figure 3. Therefore, this can be explained in terms of the carbohydrate expression on the surface of the CHO cells, which must be significantly reduced in comparison to the HeLa cell line.

SERS analyses were also performed using a confocal Raman microscope with a 633 nm excitation source. Following repeated analyses, it was not possible to ascertain data which would suggest the nanoparticles had bound to the outermost glycan species on the CHO line, as shown in Figure S-3 of the Supporting Information. However, a small level of localized binding of low intensity was observed for the HeLa cell line at this wavelength. This binding was not reproducible through repeated analysis, and out of the sample set analyzed, only a small number of cells displayed such binding, as shown in Figure S-3 of the Supporting Information. The low levels of detection of lectin−carbohydrate interactions at this wavelength are to be expected due to the excitation wavelength being significantly shifted from the surface plasmon resonance extinction band of the silver nanoparticles (400−410 nm) and of the benzotriazole dye present on the nanoparticle surface (440 nm) as a result 532 nm was chosen as the laser excitation wavelength for subsequent experiments.

The SERS fingerprint spectra obtained for analysis of the WGA-AgNPs from the HeLa cell line displayed a correlation to the fingerprint spectrum obtained for the samples prior to cell incubation, as shown in Figure 2. The peaks of each respective spectra are slightly offset due to the software used to record each spectra and chromatic aberrations due to changes in

dx.doi.org/10.1021/ac4038762 | Anal. Chem. XXXX, XXX, XXX−XXX

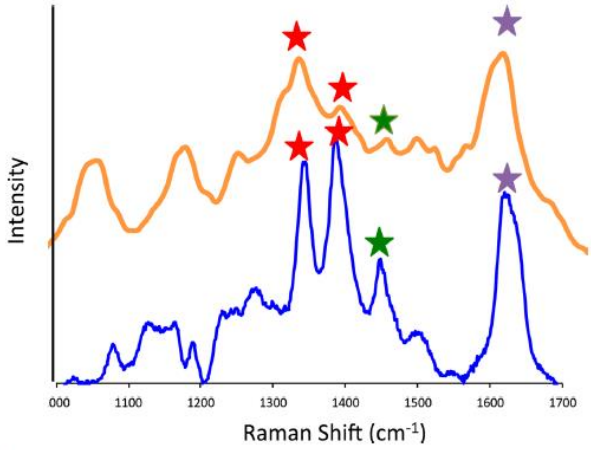

Figure 2. Blue spectra-solution phase SERS spectra of WGA-AgNPs using a 532 nm excitation wavelength and a 1 s exposure with 10 accumulations. Orange spectra—SERS spectra obtained from HeLa cells of WGA-AgNPs using 532 nm excitation wavelength, 1 s exposure with 10 accumulations. Peaks correlated to the SERS signature of the benzotriazole dye have been identified with stars.

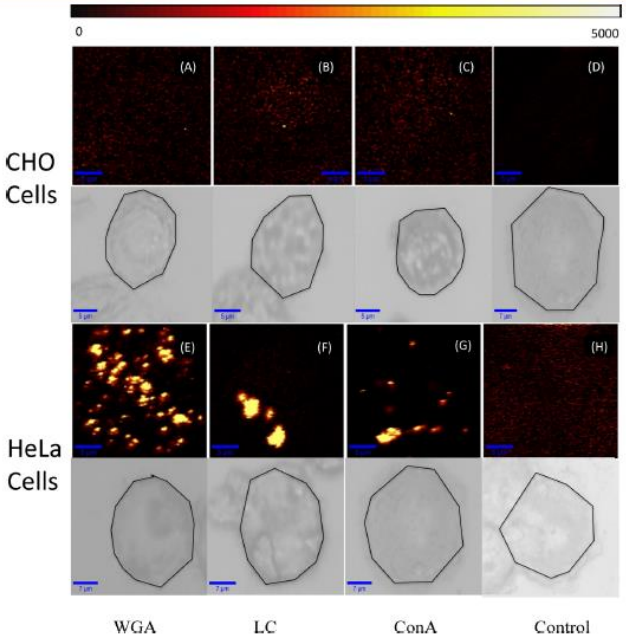

Figure 3. Analysis of (A–D) CHO and (E–H) HeLa cells incubated with lectin-functionalized nanoparticles using a confocal Raman microscope with a 532 nm laser excitation. Control spectra for both the CHO and HeLa cell lines were obtained following incubation of the cells with nano particles with no lectin attached.

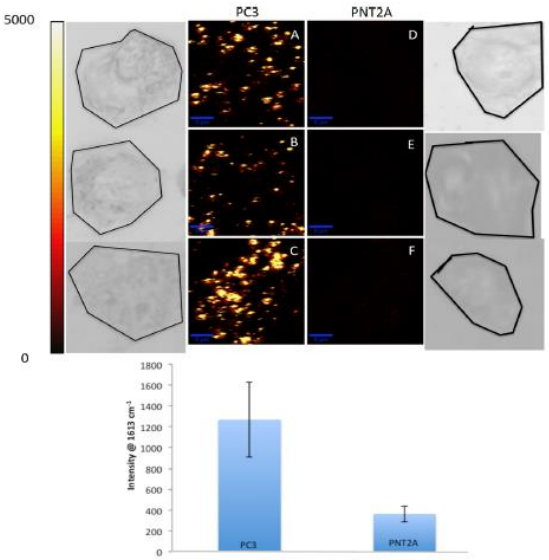

Figure 4. Comparison of sialic acid residue composition between noncancerous (PNT2A, images D–F) and cancerous prostate cells (PC3, images A–C). Bar graph represents the average intensity of the 1619 cm^{-1} peak for the PC3 (cancerous) and PNT2A (noncancerous) cells. Fifteen cells were analyzed to generate the intensity measurements, and the error bars represent the standard deviations of these measurements.

refractive index. The significant intensity of the aromatic quadrant stretch of the reporter molecule at 1619 cm^{-1} following repeated analyses resulted in this peak being chosen for the generation of the false color intensity profiles for each cell line.

Figure 3 shows the false color intensity profiles generated from the SERS spectra obtained from each individual lectin-conjugated nanoparticle species upon separate cells of the HeLa cell line. The results shown are a representative sample of the SERS analysis, which was undertaken for 15 cells for each lectin-AgNP configuration.

As shown in Figure 3e, the WGA bound nanoparticles provide the most intense profile, indicating an increased level of binding in comparison to the nanoparticles functionalized with both LC and ConA, respectively.

These results highlight that the lectin-functionalized nanoparticles are an ideal scaffold for monitoring the changes in carbohydrate expression in different cells and, in particular, the increased expression in cancerous cells.

■ PROSTATE CANCEROUS CELL DETECTION

Following on from the successful analysis of the carbohydrate composition of HeLa cells using the lectin-functionalized nanoparticle species, the next step was to expand this approach to prostate cancer cell detection. As stated previously, an increased sialic acid expression occurs on malignant prostate cells. Using the sialic acid specific WGA-AgNPs, it was proposed that discrimination could be achieved between noncancerous (PNT2A) and cancerous (PC3) prostate cells due to the difference in expression of sialic acid residues on each cell type. To confirm this hypothesis, both noncancerous and cancerous prostate cells were obtained. WGA-AgNPs were incubated with each cell type and analyzed using a confocal Raman microscope with a 532 nm excitation source. Representative samples of each cell type are shown in Figure 4. For comparison purposes, the false color intensity profiles shown in Figure 4 were set to the same intensity scales. It is clearly shown that a comparison between the cell types shows a significant difference between the sialic acid residue compositions detected. It is also important to note that the expression of sialic acids on the PC3 (cancerous) cell type occurs across the entire length and breadth of the cells, indicating that following their elevated expression, the localization of the sialic acid residues becomes more widespread. The use of confocal fluorescence imaging for the discrimination between fluorescently tagged cells has been a pioneering technique in the field of cell discrimination. For the purpose of a control experiment, FITC tagged WGA was also incubated with both cell types, and the resulting images obtained are shown in Figure 5.

Figures 4 and 5 explicitly show qualitative differences between the PNT2A and PC3 cell lines. As a result of this, the distinct difference, which exists in the sialo-glycan composition of both cell types, can be distinguished in both figures. However, the fluorescence control images only display a slight differential between the PNT2A and PC3 cells in regard to the sialo-glycan composition, while the SERS imaging provides a greater contrast between both cell types, permitting more sensitive and quicker detection than by using fluorescence microscopy. Using the SERS approach also means that this methodology could be extended with ease to a multiplexed

dx.doi.org/10.1021/ac4038762 | Anal. Chem. XXXX, XXX, XXX–XXX

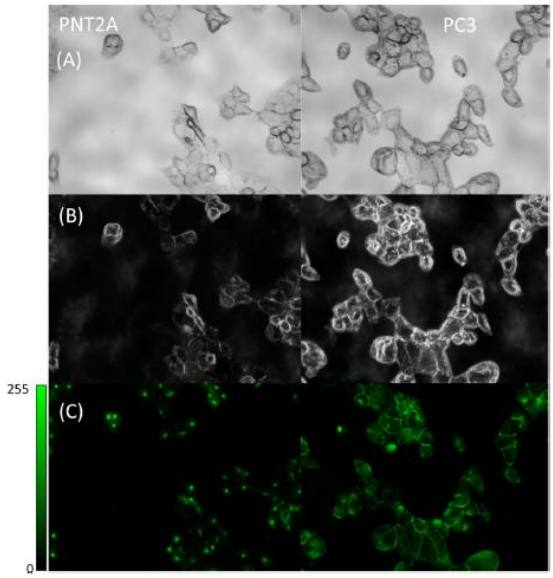

Figure 5. Fluorescence control images of WGA-FITC incubated with PNT2A and PC3 cells. (A) Bright field cell images, (B) dark field cell images, and (C) fluorescence images of WGA-FITC tagged cells.

approach for glycan sensing, due to the distinct vibrational spectra obtained when using SERS in comparison to fluorescence.

■ CONCLUSION

This study has described the first use of SERS as a molecular imaging technique to discriminate between cancerous and noncancerous cells using lectin-functionalized imaging agents. A clear strategy was undertaken to show the use of SERS to identify interactions between the lectin-functionalized nanoparticles and the carbohydrates existing on the cell surface. The success of this approach resulted in the use of SERS to discriminate between two types of prostate cell and to enable the identification of an increased sialo-glycan expression of one over the other. Comparative studies using fluorescence microscopy only established a slight difference between the two cell subsets and the discrepancies between both in terms of glycan expression were much more clearly resolved using SERS imaging. The success of this method has established a novel approach, by which the glycan expression can be correlated to cancer cell detection using SERS. The implementation of SERS in the field of biomedical diagnosis has grown rapidly over recent years due to the robust nature of the analysis achieved, of which this is another key example of a possible use for this technique. The use of SERS in both ex vivo, in vitro, and in vivo studies has shown that in the years to come SERS shall be an invaluable tool in the medical toolbox with the ability to be used as a rapid screening tool or to provide real-time surgical analyses being distinct possibilities.

■ ASSOCIATED CONTENT

Supporting Information

Additional information as noted in text. This material is available free of charge via the Internet at http://pubs.acs.org.

■ AUTHOR INFORMATION

Corresponding Author

*E-mail: duncan.graham@strath.ac.uk.

Present Address

†University of St. Andrews, JF Allen Building, North Haugh, Fife, KY16 9SS, U.K.

Notes

The authors declare no competing financial interest.

■ ACKNOWLEDGMENTS

D.C. would like to acknowledge the EPSRC for funding. D.G. acknowledges support from the Royal Society Wolfson Trust Research Merit Award.

■ REFERENCES

(1) Bray, F.; Jemal, A.; Grey, N.; Ferlay, J.; Forman, D. *Lancet Oncol.* **2012**, *13*, 790–801.

(2) Andersen, J. N.; Sathyanarayanan, S.; Di Bacco, A.; Chi, A.; Zhang, T.; Chen, A. H.; Dolinski, B.; Kraus, M.; Roberts, B.; Arthur, W.; Klinghoffer, R. A.; Gargano, D.; Li, L.; Feldman, I.; Lynch, B.; Rush, J.; Hendrickson, R. C.; Blume-Jensen, P.; Paweletz, C. P. *Sci. Transl. Med.* **2010**, *2*, 43ra55.

(3) Bischel, V. E.; Liotta, L. A.; Petricoin, E. F., 3rd *Cancer J.* **2001**, *7*, 69–78.

dx.doi.org/10.1021/ac4038762 | *Anal. Chem.* XXXX, XXX, XXX–XXX

(4) Garnett, M. J.; Edelman, J.; Heidorn, S. J.; Greenman, C. D.; Dastur, A.; Lau, K. W.; Greninger, P.; Thompson, I. R.; Luo, X.; Soares, J.; Liu, Q. S.; Iorio, F.; Surdez, D.; Chen, L.; Milano, R. J.; Bignell, G. R.; Tam, A. T.; Davies, H.; Stevenson, J. A.; Barthorpe, S.; Lutz, S. R.; Kogera, F.; Lawrence, K.; McLaren-Douglas, A.; Mitropoulos, X.; Mironenko, T.; Thi, H.; Richardson, L.; Zhou, W. J.; Jewitt, F.; Zhang, T. H.; O'Brien, P.; Boisvert, J. L.; Price, S.; Hur, W.; Yang, W. J.; Deng, X. M.; Butler, A.; Choi, H. G.; Chang, J.; Baselga, J.; Stamenkovic, I.; Engelman, J. A.; Sharma, S. V.; Delattre, O.; Saez-Rodriguez, J.; Gray, N. S.; Settleman, J.; Futreal, P. A.; Haber, D. A.; Stratton, M. R.; Ramaswamy, S.; McDermott, U.; Benes, C. H. *Nature* **2012**, *483*, 570−U587.
(5) Hait, W. N. *Cancer Res.* **2009**, *69*, 1263−1267.
(6) Toyoda, M.; Ito, H.; Matsuno, Y. K.; Narimatsu, H.; Kameyama, A. *Anal. Chem.* **2008**, *80*, 5211−5218.
(7) Raval, G. N.; Parekh, L. J.; Patel, M. M.; Patel, P. S.; Rawal, R. M.; Balar, D. B.; Patel, D. D. *Int. J. Biol. Markers* **1997**, *12*, 61−67.
(8) Varki, A. *Nature* **2007**, *446*, 1023−1029.
(9) Baker, M. J.; Gazi, E.; Brown, M. D.; Shanks, J. H.; Clarke, N. W.; Gardener, P. *J. Biophotonics* **2009**, *2*, 104−113.
(10) Bakker Schut, T. C.; Witjes, M. J. H.; Sterenborg, H. J. C. M.; Speelman, O. C.; Roodenburg, J. L. N.; Marple, E. T.; Bruining, H. A.; Puppels, G. J. *Anal. Chem.* **2000**, *72*, 6010−6018.
(11) Maru, D.; Harpaz, N.; Potack, J.; Muldoon, T. J.; Richards-Kortum, R.; Thekkek, N.; Anandasabapathy, S.; Roblyer, D. *Biomedicine* **2010**, *15*, 026027.
(12) Deolekar, M.; Morris, J. A. *Histopathology* **2003**, *42*, 227−232.
(13) Forsberg, L. S.; Carlson, R. W. *J. Biol. Chem.* **2008**, *283*, 16037−16050.
(14) El-Boubbou, K.; Huang, X. F. *Curr. Med. Chem.* **2011**, *18*, 2060−2078.
(15) Wu, J. G.; Xu, Y. Z.; Sun, C. W.; Soloway, R. D.; Xu, D. F.; Wu, Q. G.; Sun, K. H.; Weng, S. F.; Xu, G. X. *Biopolymers* **2001**, *62*, 185−192.
(16) Lee, J. H.; Jung, M. J.; Hwang, Y. H.; Lee, Y. J.; Lee, S.; Lee, D. Y.; Shin, H. *Biomaterials* **2012**, *33*, 4861−4871.
(17) Kneipp, K.; Haka, A. S.; Kneipp, H.; Badizadegan, K.; Yoshizawa, N.; Boone, C.; Shafer-Peltier, K. E.; Motz, J. T.; Dasari, R. R.; Field, M. S. *Appl. Spectrosc.* **2002**, *56*, 150−154.
(18) Dochow, S.; Bergner, N.; Krafft, C.; Clement, J.; Mazilu, M.; Praveen, B. B.; Ashok, P. C.; Marchington, R.; Dholakia, K.; Popp, J. *Anal. Methods* **2013**, *5*, 4608−4614.
(19) Ni, J.; Lipert, R. J.; Dawson, G. B.; Porter, M. D. *Anal. Chem.* **1999**, *71*, 4903−4908.
(20) Cialla, D.; Marz, A.; Bohme, R.; Theil, F.; Weber, K.; Schmitt, M.; Popp, J. *Anal. Bioanal. Chem.* **2012**, *403*, 27−54.
(21) Maiti, K. K.; Dinish, U. S.; Samanta, A.; Vendrell, M.; Soh, K. S.; Park, S. J.; Olivo, M.; Chang, Y. T. *Nano Today* **2012**, *7*, 85−93.
(22) Dougan, J. A.; Faulds, K. *Analyst* **2012**, *137*, 545−554.
(23) Craig, A. P.; Franca, A. S.; Irudayaraj, J. *Annu. Rev. Food Sci. Technol.* **2013**, *4*, 369−380.
(24) Guerrini, L.; Pazos, E.; Penas, C.; Vázquez, M. V.; Mascareñas, J. L.; Alvarez-Puebla, R. A. *J. Am. Chem. Soc.* **2013**, *135*, 10314.
(25) Huefner, A.; Kuan, W. L.; Barker, R. A.; Mahajan, S. *Nano Lett.* **2013**, *13*, 2463−2470.
(26) Neng, J.; Harpster, M. H.; Zhang, H.; Mecham, J. O.; Wilson, W. C.; Johnson, P. A. *Biosens. Bioelectron.* **2010**, *26*, 1009−1015.
(27) McAughtrie, S.; Lau, K.; Faulds, K.; Graham, D. *Chemical Science* **2013**, *4*, 3566−3572.
(28) van Manen, H. J.; Kraan, Y. M.; Roos, D.; Otto, C. *PNAS USA* **2005**, *102*, 10159−10164.
(29) Varki, N. M.; Varki, A. *Lab. Invest.* **2007**, *87*, 851−857.
(30) Reuel, N. F.; Mu, B.; Zhang, J.; Hinckley, A.; Strano, M. S. *Chem. Soc. Rev.* **2012**, *41*, 5744−5779.
(31) Hirabyashi, J. *J. Biochem.* **2008**, *144*, 139−147.
(32) Gabius, H. J. *Angew. Chem., Int. Ed.* **1988**, *27*, 1267−1276.
(33) Monsigny, M.; Roche, A. C.; Kieda, C.; Midoux, P.; Obrénovitch, A. *Biochimie* **1988**, *70*, 1633−1649.
(34) Ambrosi, M.; Cameron, N. R.; Davis, B. G. *Org. Biomol. Chem.* **2005**, *3*, 1593−1608.
(35) Sato, Y.; Yoshioka, K.; Murakami, T.; Yoshimoto, S.; Niwa, O. *Langmuir* **2011**, *28*, 1846−1851.
(36) Schofield, C. L.; Mukhopadhyay, B.; Hardy, S. M.; McDonnell, M. B.; Field, R. A.; Russell, D. A. *Analyst* **2008**, *133*, 626−634.
(37) Sanchez-Pomales, G.; Morris, T. A.; Falabella, J. B.; Tarlov, M. J.; Zangmeister, R. A. *Biotechnol. Bioeng.* **2012**, *109*, 2240−2249.
(38) Zhelev, Z.; Ohba, H.; Bakalova, R.; Jose, R.; Fukuoka, S.; Nagase, T.; Ishikawa, M.; Baba, Y. *Chem. Commun.* **2005**, 1980−1982.
(39) Craig, D.; Simpson, J.; Faulds, K.; Graham, D. *Chem. Commun.* **2013**, *49*, 30−32.
(40) Lee, P. C.; Meisel, D. *J. Phys. Chem.* **1982**, *86*, 3391−3395.
(41) Varki, A.; Cummings, R. D.; Esko, J. D.; Freeze, H. F.; Hart, G. W.; Marth, J. D. *Essentials of Glycobiology*; Cold Spring Harbor Laboratory Press: Plainview, NY, 1999.
(42) Yguerabide, J. Y. *Anal. Biochem.* **1998**, *262*, 137.
(43) Wilson, H.; Smith, W. E. *J. Raman. Spectrosc.* **1994**, *25*, 899.
(44) Ling, Y.; Guan, Y.; Han, K. N. *Corros. Sci.* **1995**, *51*, 367.
(45) McAnally, G.; McLaughlin, C.; Brown, R.; Robson, D. C.; Faulds, K.; Tackley, D. R.; Smith, W. E.; Graham, D. *Analyst* **2002**, *127*, 838.
(46) Otsuka, H.; Nagasaki, Y.; Kataoka, K. *Adv. Drug Delivery Rev.* **2003**, *55*, 403.

G Model
JPR-207; No. of Pages 14
ARTICLE IN PRESS

Journal of Photochemistry and Photobiology C: Photochemistry Reviews xxx (2014) xxx–xxx

Contents lists available at ScienceDirect

Journal of Photochemistry and Photobiology C: Photochemistry Reviews

journal homepage: www.elsevier.com/locate/jphotochemrev

Invited Review

Surface enhanced Raman spectroscopy (SERS): Potential applications for disease detection and treatment

Sarah McAughtrie, Karen Faulds, Duncan Graham*

Centre for Molecular Nanometrology, WestCHEM, Department of Pure and Applied Chemistry, University of Strathclyde, Glasgow G1 1XL, UK

ARTICLE INFO

Article history:
Received 10 June 2014
Received in revised form 2 September 2014
Accepted 11 September 2014
Available online xxx

Keywords:
Raman
SERS
Disease
Mapping
Imaging
In vivo

ABSTRACT

The implementation of Raman and surface enhanced Raman spectroscopy (SERS) for the detection of disease has increased in recent years. The reasons for their increased implementation have often been attributed to their well-known advantages, including the production of narrow spectral bands, which are characteristic of the molecular components present, their non-destructive method of analysis and the sensitivity and specificity which they can confer. This review analyses a range of diseases which can be detected by Raman or SERS, particularly those *in vitro*, *ex vivo* and *in vivo*. The sophistication of the investigated systems varied widely but the suitability of Raman and SERS for medical diagnostics and future implementation in a clinical environment is clearly demonstrated.

Contents

* Corresponding author. Tel.: +44 0141 5484701; fax: +44 0141 5520876.
E-mail address: duncan.graham@strath.ac.uk (D. Graham).

http://dx.doi.org/10.1016/j.jphotochemrev.2014.09.002
1389-5567/

Please cite this article in press as: S. McAughtrie, et al., Surface enhanced Raman spectroscopy (SERS): Potential applications for disease detection and treatment, J. Photochem. Photobiol. C: Photochem. Rev. (2014), http://dx.doi.org/10.1016/j.jphotochemrev.2014.09.002

Sarah McAughtrie is currently a PhD student at the Centre for Molecular Nanometrology at the University of Strathclyde, Glasgow. She is due to complete her PhD this summer. Her current interests involve implementing Raman and SERS spectroscopy for the detection of disease and sensing applications. Her research has additionally involved combined 3D Raman and SERS imaging in order to determine cellular uptake and localisation of SERS nanotags. She was awarded the RSC Ronald Belcher Award in 2014 for her work on combined 3D Raman and SERS imaging.

Karen Faulds obtained her PhD from the University of Strathclyde in 2003. She then started a postdoctoral position in 2003 before being appointed as a lecturer in 2006. She was awarded Nexxus young life scientist of the year in 2009 and promoted to Senior Lecturer in 2010 and Reader in 2012. Most recently she was awarded the RSC Joseph Black Award 2013. She is a founding member of Renishaw Diagnostics Ltd. which spun out of Strathclyde in 2007. She is a member of the Royal Society of Edinburgh Young Academy of Scotland, Analyst editorial advisory board and a committee member of the Infrared and Raman Discussion Group (IRDG). Her main interests are in creating new methods of bioanalysis using SERS and in particular, the development of molecular diagnostic SERS based assays and nanoparticle biosensors.

Duncan Graham is Research Professor of Chemistry and director of the Centre for Molecular Nanometrology at the University of Strathclyde in Glasgow. He is currently Deputy Director of WestCHEM and he has been awarded numerous awards for his research including the RSCs SAC Silver medal (2004), Corday Morgan prize (2009), a Royal Society Wolfson Research Merit award (2010), Coblentz Society Craver Award (2012) and was elected to the fellowship of the Royal Society of Edinburgh (2008). He is also a cofounder and director of Renishaw Diagnostics Ltd. (2007). He completed a PhD in organic chemistry at the University of Edinburgh (1996) and now his interests are in using synthetic chemistry to produce nanosensors that respond to a specific biological species or event as measured by surface enhanced Raman scattering.

1. Introduction

When the pioneers of Raman spectroscopy initially conceived the technique in 1923 [1] and latterly demonstrated it in 1928 [2] it is unlikely that they had any inclination of the future impact or bio-diagnostic applications [3–5]. In particular, the use of Raman spectroscopy for *in vitro*, *ex vivo* and *in vivo* disease detection has proliferated over the last decade. This is unsurprising when considering the non-invasive nature of the technique and the provision of molecularly specific spectra which allow for the identification of disease targets [6]. However, the obvious disadvantage with its implementation is that it can be quite insubstantial, especially considering that approximately only one in every million photons are Raman scattered [6].

This weak effect was negated by successive developments of the original technique most notably surface enhanced Raman spectroscopy (SERS) [7–9] and surface enhanced resonance Raman spectroscopy (SERRS) [10], where signal enhancements of the order of 10^{10} [8,9,11] and 10^{14} [10] were observed respectively. The incorporation of a roughened metal surface (metal electrodes, coatings, surfaces and nanostructures) [11] is essential for manipulation of the SERS enhancement, which is widely believed within the community to arise through a combined electromagnetic and chemical effect [6,11,12]. SERRS, whilst manipulating the enhancement conferred by a roughened metallic scaffold, additionally exploits excitation with a laser line that corresponds to an electronic transition of the interrogated analyte to further augment the enhancement effect [10].

The introduction of nanostructures can render these techniques invasive however; this can be offset by the conferred enhancement. As with the original method, the employment of SERS for disease detection *in vitro*, *ex vivo* and *in vivo* has increased exponentially, again a direct consequence of the molecularly definitive spectra which allow for confident identification of disease biomarkers. However, as clinical medicine strives towards a personalised approach, there is further need to increase the sensitivity and specificity by which diseases are detected and the simultaneous requirements of comprehensive characterisation and detection of multiple pathosis [13]. SERS is ideally suited to fulfil these requirements since the observed enhancement can satisfy the sensitivity criteria whilst functionalisation with specific targeting moieties allows for disease recognition with a high degree of specificity. The sharp bands produced within a SERS spectrum lend the technique to multiplexed detection satisfying the demand to diagnose multiple aspects of a single disease or a myriad of disorders [13].

This review will examine the application of SERS for disease detection. A range of formats will be discussed, including *in vitro* analysis of simple matrices to more sophisticated analysis *in vivo* but with the predominant focus on mapping/imaging applications. The review will additionally highlight the progression of the technique from a simple lab based analytical method to a contender for the interrogation and discernment of clinical samples. The advancement of SERS as a diagnostic imaging method is developing at a ferocious pace and if maintained at this level, there is huge potential to revolutionise the ability to detect, treat and manage disease.

2. Raman spectroscopy and disease detection

While this review will predominantly concentrate on SERS it is worth highlighting the parallel advancements occurring with Raman spectroscopy. The obvious advantage of Raman spectroscopy over SERS is that it is non-invasive so there is no requirement for the introduction of nanostructures to observe a response. In terms of *in vitro*, *ex vivo* and *in vivo* analysis, this is particularly beneficial since minimal sample preparation is involved, toxicity trials are not required as adulterants have not been introduced and more importantly for *in vivo* studies there is no need to consider the distribution and localisation of nanoscaffolds for effective analysis. However, consideration must be given to the employed laser power, acquisition time and sample format to prohibit sample degradation and auto-fluorescence.

2.1. Raman spectroscopy and in vitro cell analysis

The interrogation of single cells and cell populations may not have the same allure and glamour of *in vivo* studies but, in terms of indicators of disease, they can be equally important. The architecture of the cell can be altered considerably during processes such as differentiation [14], mitosis and apoptosis [15]. Uncontrolled division and cell death can be indicative of pathosis, including tumour growth, inflammation, HIV infection and neurodegeneration diseases such as Parkinson's and Alzheimer's [16]. Monitoring the cell composition and architecture permits a viable method for the detection of disease and, with the advent of 3D Raman imaging, the resolution of cell organelles may be more representative of the disease led changes that can occur intracellularly [17,18]. Cell health can also be directly monitored *via* Raman spectroscopy and it is possible to distinguish between live and dead cells [19], and cells that are stressed [20], conditions which can arise as a result of infection or disease. Cells can also be readily distinguished on the basis of their phenotypic differences and this has been used to discriminate between bone [21] and lung cells [22], and more importantly in terms of disease diagnosis between cancerous and non-cancerous

Please cite this article in press as: S. McAughtrie, et al., Surface enhanced Raman spectroscopy (SERS): Potential applications for disease detection and treatment, J. Photochem. Photobiol. C: Photochem. Rev. (2014), http://dx.doi.org/10.1016/j.jphotochemrev.2014.09.002

cells [23,24]. This was not completed with a clinical sample but the authors highlighted the desire to extend analysis into urine [23]. In a clinical setting, this has the potential to provide cancer diagnosis non-invasively *via* an excretory product.

2.2. Raman spectroscopy and ex vivo/in vivo applications for the detection of disease

As a diagnostic tool, Raman spectroscopy is forging ahead in the cancer field providing a method by which to detect breast [25–27], skin [28,29], prostate [30–32], bladder [33–35], cervical [36–38], colorectal [39,40] and oesophageal cancer [41,42]. With bladder [34,35], cervical [37,38], colorectal [43] and oesophageal cancer [42] all being detected *in vivo*. The incidence of breast cancer in the UK accounts for the greatest proportion of all cancer diagnosis and like all forms of the disease there is demand for sensitive, selective and non-invasive detection [44]. A subsequent adaptation of the original Raman technique led to the development of spatially offset Raman spectroscopy (SORS) which has a demonstrated ability to differentiate between calcifications associated with cancerous and non-cancerous tissues and at a reported depth of ~8.7 mm [26]. The authors reported that this could be used to complement the current clinical method of detection, mammography, whilst simultaneously demonstrating the potential to minimise the number of invasive biopsies [26]. Successive developments and the implementation of a transmission Raman setup increased the thickness of tissue through which cancerous and non-cancerous samples could be differentiated [27]. The depth of detection was increased to 27 mm with anything above 20 mm being classified as clinically significant for *in vivo* detection, further highlighting the applicability and relevance of implementing the technique in a clinical environment [27]. A proof of concept study also investigated the possibility of detecting brain tumours *in vivo* in mice models [45]. The authors reported that the tumours could be located with an accuracy of approximately 250 μm and while principally a demonstration of what could be achieved, the authors emphasised the possibility of using Raman spectroscopy for brain analysis and tumour detection in a live subject [45].

Raman spectroscopy is not limited to the detection of cancer and research has postulated that the method could be used for the characterisation and monitoring of atherosclerotic plaques [46]. In the UK alone coronary heart disease and the conditions which stem from it cost an estimated £19 billion [47]. This is clearly an extensive and significant problem and Raman was found to be a suitable method by which plaque deposits could be distinguished and their size determined [46]. The effects of statin drug treatment were also tracked, and in mice that were provided a cholesterol rich diet, the statins successfully minimised plaque formation [46]. Whilst this remains a proof-of-principal study there is potential for extension to studies in man and although not demonstrated remote sensing could be achieved by coupling *via* a fibre optic probe [46].

Similarly, Raman spectroscopy has been implemented to monitor organ rejection in patients following transplant procedures [48,49]. While not directly involving the detection of disease, it is possible that the processes which led to transplant were the result of disease, for example, coronary heart or chronic kidney disease. This demonstrates the application of Raman for monitoring subsequent disease effects. In the particular instances of heart and kidney transplant the confirmation of rejection requires an invasive biopsy procedure and the observation of an elevated serum creatinine level, respectively [48]. However, the rejection of heart tissues can be characterised by serotonin biomarkers, which can be detected using Raman, presenting a viable non-invasive alternative to biopsy [49]. While the methods for monitoring kidney rejection do not require the same invasive procedures, by the time detection of serum creatinine is confirmed significant deterioration of the organ can have occurred [48]. Raman spectroscopy was employed as a method to differentiate between T-cells which were produced in response to different stimuli (*i.e.* in response to rejection and under normal circumstances) [48]. These were selected as biomarkers for monitoring the rejection response since the process is primarily characterised by T-cells. The technique was found to be suitable for differentiating between normal cells and those which are characteristic of a rejection response [48]. It should be noted that the T-cells were not directly obtained from a patient undergoing rejection but rather the cells were artificially modelled to be representative. Raman spectroscopy therefore represents a viable alternative by which rejection could be monitored.

This is in no way an exhaustive review of the methods by which Raman spectroscopy can be employed to detect disease or monitor health, however, it does emphasise the vast array of medically related applications. For further discussion regarding the employment and advancements of Raman spectroscopy in medicine, readers are encouraged to review literature from the Stone [44] and Goodacre groups [50,51]. However, it is clear that with instrumental improvements and careful consideration of the employed laser power and acquisition time, vast amounts of information can be yielded by Raman spectroscopy. Central to all of these applications is the employment of chemometric methods. Raman spectra are often similar in appearance and discerning any differences by eye are difficult, but by implementing chemometric analysis subtle differences can be extracted and conclusions drawn with statistical significance. However, in order to make the leap from bench to body, further analysis must be completed in physiologically representative media, clinical samples and *in vivo* [52]. While diagnostic information can be extracted using chemometrics clinicians require simple yes/no answers to dispense a diagnosis or prognosis. Therefore, any transition to a clinical environment will require coupling of the data collection and analysis so that single definitive answers can be provided.

3. Surface enhanced Raman spectroscopy (SERS)

The advantages of SERS over conventional Raman were briefly discussed in the introduction but are worth re-iterating since these benefits in conjunction with the shortcomings of Raman are responsible for the proliferation of the technique. Although, non-invasivity is a key attraction of Raman spectroscopy, the overall outcome is that the technique is reliant on spectral signatures from the intrinsic components of the interrogated system, which in biological matrices tend to be weak, inefficient scatterers and spectrally similar [53], such that subtle differences must be discerned by the incorporation of chemometric methods. SERS unlike Raman is not reliant on native chromophores and a vast array of efficient scattering molecules [54–59], with large Raman cross sections, can be conjugated to metallic scaffolds for the provision of distinct, optically strong, spectral signatures. By capitalising on this conferred enhancement, through the implementation of a metal surface and superior reporting moieties, the measured spectral intensities can be significantly enhanced [8,9,11]. The key advantages of this enhancement are that a reduced laser power and acquisition time can be incorporated for the analysis of fragile samples with minimal loss of the spectral sensitivity whereas with conventional Raman some compromise must be made between the laser power and measurement time to obtain sufficiently distinct spectra without incurring sample damage. The sharp molecularly specific spectra produced by SERS also promote the technique for use in multiplexed scenarios including multiple disease detection and in many instances differences can be determined by eye without the need for the incorporation of chemometric methods [13].

Please cite this article in press as: S. McAughtrie, et al., Surface enhanced Raman spectroscopy (SERS): Potential applications for disease detection and treatment, J. Photochem. Photobiol. C: Photochem. Rev. (2014), http://dx.doi.org/10.1016/j.jphotochemrev.2014.09.002

Conventional Raman is unlikely to be employed in such a manner since the spectral differences between healthy and diseased samples are extremely subtle, let alone between multiple diseases in a single sample, and generally require the implementation of statistical methods for their differentiation [53].

As discussed above exploitation of the SERS effect requires the incorporation of a roughened metal surface [6,11]. The forms which this can take are vast and can include metal electrodes [10], coatings, surfaces [60,61] and nanostructures [62,63]. *In vitro* examples have employed unfunctionalised nanoparticles for simple sensing applications, for example, monitoring enzyme activity [62] or the determination of intracellular components [64]. To actively image and/or target and detect disease *in vitro*, *ex vivo* and *in vivo* the sophistication of the implemented systems varies. Ranging from metallic nanoparticles labelled with reporter molecules [65–69] to more complicated systems with mixed reporter monolayers [70], dually functionalised systems consisting of reporter molecules and membrane penetrating or targeting antibodies [71–73], peptides [65,74,75] or oligomers. To minimise or prohibit degradation from the surrounding environment nanostructures can be afforded a certain degree of stability by silica [13,76] or polymer encapsulation [71,77,78]. The incorporation of polyethylene glycol (PEG) again offers protection from the chemical and physical environment, minimisation of non-specific binding [79] and, depending on the terminal functionality, PEG is readily amenable for bioconjugation to a range of targeting ligands [80].

3.1. SERS and in vitro applications for the detection of disease

SERS based nanotags have been used with a variety of different sample formats for the *in vitro* detection of disease. In some of the earliest examples, functionalised nanoparticles and nanotags were not employed for the detection of disease. Instead metallic surfaces were used to exploit the SERS effect. In one such system used for the detection of glucose, spheres were coated in a layer of silver for the provision of the SERS enhancement and they were subsequently functionalised with both decanethiol and mercaptohexanol [60]. Dual functionalisation with molecules of varying chain length results in hole formation between the different chains actively providing a region into which the glucose molecules can enter and the response can be measured *via* SERS [60]. With the implementation of the system it was possible to quantitatively detect glucose and the majority of the measurements were detected within levels which were considered to be medically relevant [60]. The authors also reported that the system worked effectively even when interfering analytes were present [60]. Detecting glucose in real-time is of huge importance for diabetes sufferers who currently check their levels *via* pin prick blood tests. With this method of monitoring huge variations in glucose levels are often missed and in order to improve disease management, there is a real need for accurate continuous monitors [60]. Later work by the same group has strived to further develop this method for *in vivo* sensing [81–83]. In the initial stages the sensors (as described above) were implanted into animal models and the glucose levels were successfully measured *via* SERS and surface enhanced spatially offset Raman spectroscopy (SESORS) respectively [81–83] (SESORS shall be discussed further in Section 3.3). In the most recent developments, the same sensor has been investigated *via* animal implementation [83]. The device was found to actively work over 17 days and more importantly the authors reported that between days 6 and 17, the glucose levels measured were found to lie within the clinically relevant levels [83]. This elegant and sophisticated example is a significant step forward in the development of a method by which diabetes sufferers could monitor and control their condition more accurately [83]. A similar format was also used to monitor lactate quantitatively [61]. Variations in lactate levels can be indicative of trauma in a number of medical conditions and as with glucose monitoring the ability to measure lactate in real time would further improve the clinical care offered to patients suffering from a range of conditions [61].

In other examples, the SERS enhancement was achieved using metallic nanoparticles. Using this format and a nanofluidic device Chou et al. demonstrated the detection of the β-amyloid peptide, which is a key component in plaques in sufferers of Alzheimer disease [63]. β-Amyloid detection was achieved by concentrating the nanoparticles and target molecules within the device, irradiating with a laser and monitoring the SERS signal [63]. To demonstrate the sensitivity of the detection system the author's added additional proteins of similar and different conformations. Analysis of the SERS signals found that it was possible to discriminate between the different protein forms [63], in particular, α-helices could be discriminated from β-sheets and between the different β-sheet forms discrimination was also possible [63]. Having a method by which to characterise the disease process is hugely beneficial and it could be used as a method to monitor disease development [63].

Unfunctionalised nanoparticles have also been used to monitor enzyme activity intracellularly [62]. This is relevant in terms of disease detection since some notable diseases, including cystic fibrosis, Parkinson's and Alzheimer's are all characterised by some form of abnormal enzyme activity [62]. In the study Au nanoparticles were incorporated by cell populations alongside the colourless substrate X-Gal, where upon internalisation it was enzymatically transformed by β-galactosidase enzymes to 5,5′-dibromo-4,4′-dichloroindigo. This transformation was characterised by the appearance of a peak in the SERS spectra at 598 cm^{-1} and a blue colour which was indicative of the turnover of the substrate by the enzyme (Fig. 1) [62]. The conversion was specific to the enzyme as confirmed when known enzyme inhibitors were introduced (Fig. 1) and the corresponding reduction in the measured SERS signal [62]. High resolution analysis of single cells and cell populations suggested that enzyme action was localised in specific cellular compartments which were proposed to be endosomes [62]. The authors expressed a desire to quantify enzyme levels within these compartments, particularly in response to different disease stimuli and states. It is hoped that such knowledge will facilitate the development of suitable treatments [62].

More recently systems for disease detection have looked at functionalised nanotags [84–86]. In one immunoassay, the detection of the carcinoembryonic antigen (CEA), a marker frequently used for the detection of lung cancer, was achieved using a combination of hollow gold nanospheres (HGNs) and magnetic beads [86]. Porter et al. also implemented an immunoassay format for the detection of the pancreatic cancer marker, MUC4 [84]. This marker is suitable for detecting cancer since it appears to be absent in healthy and pancreatitis-suffering populations [84]. Detection was achieved using SERS *via* gold nanoparticles which were labelled with a reporter molecule and an antibody specific for the marker. SERS was critical for the detection of disease, especially as the authors noted that conventional immunoassay formats had failed to detect the protein in human sera [84]. In an extension of this initial work Porter et al. developed an immunoassay system which could simultaneously detect two markers of pancreatic cancer [85]. The detection of multiple disease markers is a key step in the future of disease diagnosis since it is rare for disease processes to be represented or characterised by a single indicator [13]. In addition, the detection of multiple aspects of a disease will undoubtedly lead to better personalised medicine and immunoassays could be extended to detect a plethora of diseases simultaneously.

Cell based detection is a vast field and in particular research has centred on detecting breast cancer [87,88]. One of the earliest studies employed SERS dots (a form of silica encapsulated nanotags) functionalised with breast cancer (HER2) or leukaemia specific

Please cite this article in press as: S. McAughtrie, et al., Surface enhanced Raman spectroscopy (SERS): Potential applications for disease detection and treatment, J. Photochem. Photobiol. C: Photochem. Rev. (2014), http://dx.doi.org/10.1016/j.jphotochemrev.2014.09.002

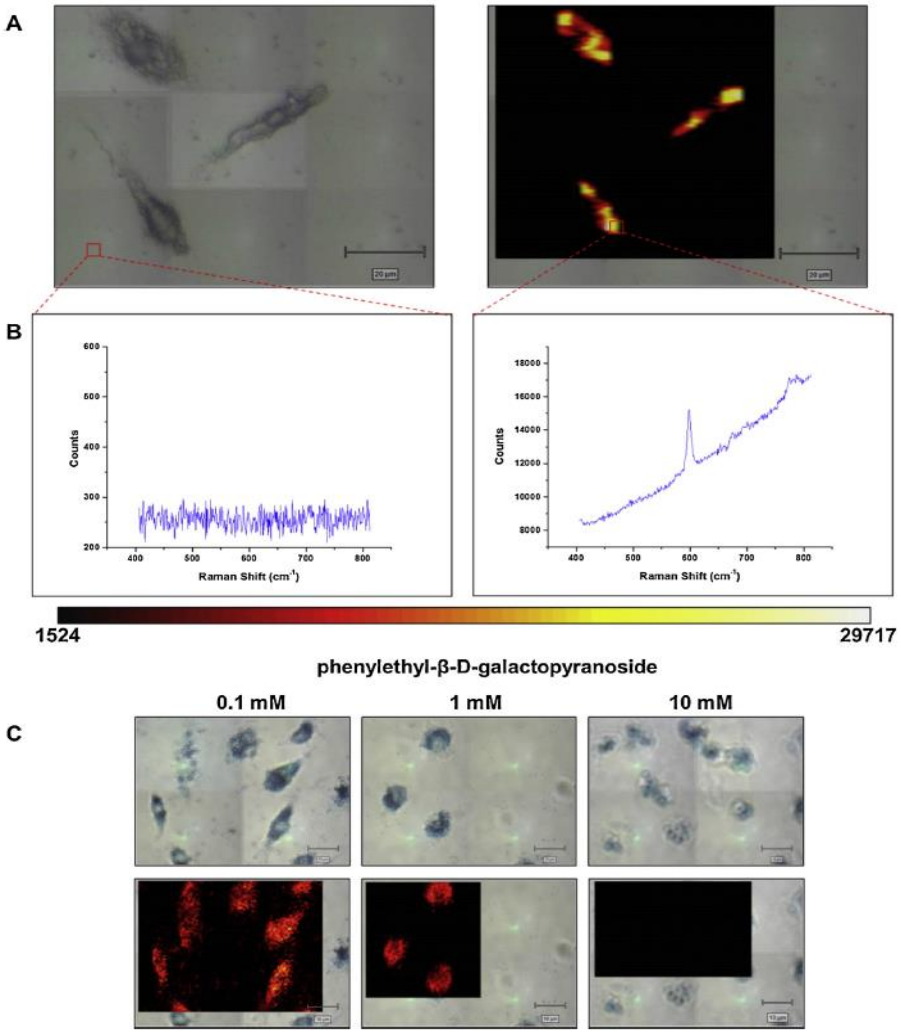

Fig. 1. Intracellular conversion of X-Gal to the blue coloured product 5,5′-dibromo-4,4′-dichloro indigo by the enzyme β-galactosidase – (A) white light and false colour image based on the 5,5′-dibromo-4,4′-dichloro indigo peak at 598 cm^{-1}, (B) corresponding spectra from the highlighted areas and the associated false colour LUT bar and (C) the effect of an enzyme inhibitor on the measured SERS signals [62].
Modified and reproduced by permission of the RSC.

antibodies (CD10) [87]. Antibody functionalisation was required so that the dots would bind specifically to the corresponding cell line and when the conjugates were incubated with different cell populations this specificity was observed [87]. HER2-functionalised dots only bound to the breast cancer cells and similarly the CD10 functionalised dots bound only to the leukaemia cells [87]. SERS signals were not observed when either of the antibody functionalised nanotags was incubated with the control cell population [87]. This initial study highlighted the possibility of screening cell populations for cancerous and non-cancerous cells and, provided that

Please cite this article in press as: S. McAughtrie, et al., Surface enhanced Raman spectroscopy (SERS): Potential applications for disease detection and treatment, J. Photochem. Photobiol. C: Photochem. Rev. (2014), http://dx.doi.org/10.1016/j.jphotochemrev.2014.09.002

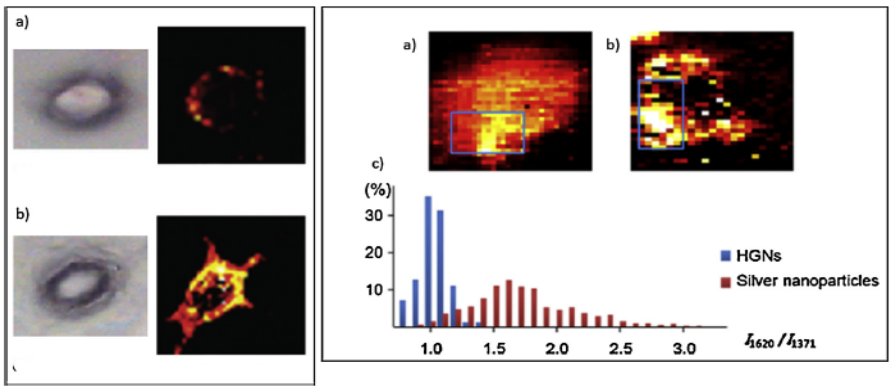

Fig. 2. Left panel – differential levels of binding between (a) gold nanospheres and (b) rods functionalised with HER2 antibody and exposed to MCF7 cells overexpressing HER2 [90]. Modified and reproduced from [90] with permission from the PCCP owner societies. Right panel – differential levels of binding between (a) HGNs and (b) silver nanoparticles functionalised with HER2 antibody and exposed to MCF7 cells overexpressing HER2, (c) intensity ratios for the peaks at I_{1620}/I_{1371} for the crystal violet reporter [89].
Reprinted with permission from Elsevier.

each subset of dots was labelled with a distinct reporter and an antibody, a range of diseases could be detected simultaneously. The authors also reported that the method could potentially be implemented as an alternative to the radioactive tagging of cells and tissues [87].

Later, studies took advantage of the same binding relationship between HER2 antibodies and the corresponding receptors on cell membranes [89,90]. However, rather than focusing on spherical shaped nanostructures rods and HGNs were investigated as alternative imaging scaffolds [89,90]. In both instances, recognition *via* the specific antibody–antigen interaction was achieved and brighter images were observed (Fig. 2) [89,90]. The increased SERS intensity in the false colour images were not the result of any improvement in the binding efficiency but were a direct result of the enhanced optical properties demonstrated by both the rods and HGNs (Fig. 2) [89,90]. The authors suggested that both systems are extremely sensitive imaging agents and when designing a disease detection system consideration should also be given to the imaging scaffold especially if the disease target is present at low concentrations [89,90].

In a recent study antibody–antigen interactions were studied as means for differentiating between disease states [72]. The development of the nanostructures involved the labelling of silver nanoparticles with reporter molecules, and HER2 antibodies were subsequently conjugated *via* the terminal carboxylic acid group on the reporter [72]. The functionalised nanostructures were then exposed to two cell lines (SKBR3 and MCF7) which demonstrated a differential level of HER2 expression [72]. In the SKBR3 cell line which exhibits a high level of HER2 expression the SERS signal was observed by the authors to be 3–4 times greater than in MCF7 cells, which have a low level of expression [72]. Although significantly greater levels of data would need to be collected from cells, at a number of different disease stages, this preliminary study highlights the implementation of SERS nanotags for the categorisation of cancerous disease states. The principles of the study are not limited to cancer and any other condition which exhibits differential levels in the expression of disease markers could be analysed and graded in an analogous manner.

In the most recent study, implementing breast cancer cell lines, the cell phenotype was determined from specific antibody antigen interactions occurring between nanostructures labelled with antibodies and antigen receptors present on cell surfaces [91]. This was achievable because each of the nanostructures was labelled with a different reporter molecule and thus different SERS signals were measured (Fig. 3) [91]. The false colour SERS maps were subsequently used as a method to quantify the level of biomarker expression since the SERS intensity is a direct measure of the concentration of biomarker [91].

Biomarker or protein expression can also be used to differentiate cancerous from non-cancerous cells [92]. In prostate cancer cells neuropilin-1 is overexpressed and, on the basis of this knowledge, selective SERS nanotags were constructed for differentiating between cell lines [92]. To actively target cancerous cells or more specifically the receptors, nanotags were functionalised with a peptide with a specific affinity for neuropilin [92]. Control nanotags were functionalised with the HIV transactivator of transcription (TAT) peptide sequence and these nanotags had the ability to bind to both cells lines [92]. In order to positively identify the cancerous cells, the ratio of the SERS signal from each of the reporters was calculated [92]. The cancerous cells should have a high contribution from the reporter on the specific targeting nanotags whilst the non-cancerous cells should have a high contribution from the reporter on the control system [92]. This was found to represent a viable method for differentiating between the two cell lines [92]. Prostate cancer cells can also be positively identified from interactions between imaging agents and surface carbohydrates [93]. For example, PC3 cancerous cells exhibit elevated levels of sialic acid residues on their surface [93]. These can be actively targeted with nanostructures functionlised with the lectin, *Triticum vulgaris*, which is known to have a specific affinity for these glycans [93]. Craig et al. demonstrated this lectin–glycan interaction and in doing so successfully distinguished cancerous PC3 cells from the non-cancerous PNT2A cells [93].

Further applications involving the detection of cancerous cells have centred on circulating tumour cells (CTCs). Unlike other applications, which might be concerned with the primary detection of

Please cite this article in press as: S. McAughtrie, et al., Surface enhanced Raman spectroscopy (SERS): Potential applications for disease detection and treatment, J. Photochem. Photobiol. C: Photochem. Rev. (2014), http://dx.doi.org/10.1016/j.jphotochemrev.2014.09.002

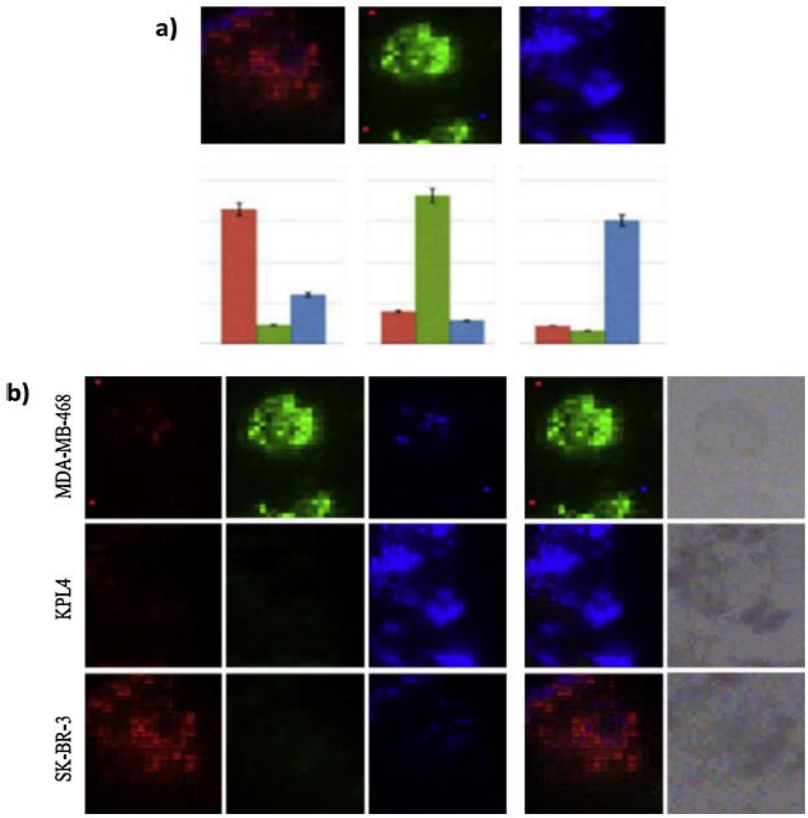

Fig. 3. Silica encapsulated hollow gold nanoshells (SEHGNs) used to phenotypically identify cancerous cell lines and determine the level of antigen expression in each cell line – (a) SEHGNs were applied to the different cell lines and each of the cell types were identified based on the signal from the specific reporter molecules and (b) SERS mapping images of the corresponding cell lines were measured at 1650 cm^{-1} (RBITC), 1619 cm^{-1} (MGITC) and 1490 cm^{-1} (RuITC) for the SK-BR-3, KPL4 and MDA-MB-468 cell line specific reporter molecules [91].
Modified and reprinted with permission from Elsevier.

cancer, CTCs are particularly aggressive and are associated with the initiation of further cancerous growth [73,94]. During an initial study the CTCs were exposed to antibody functionalised nanotags and magnetic beads. The nanotags whilst simultaneously binding to the CTCs acted as the reporter component and similarly, the magnetic beads whilst capable of binding to the cancer cells were incorporated so that the samples could be concentrated *via* a magnet [73]. The implementation of this method has resulted in successful detection of CTCs *via* SERS [73]. Detection was also achievable with high sensitivity and specificity when whole blood was employed [73]. In a subsequent study by Wang et al. a similar method was employed but the incorporation of magnetic beads was substituted for a physical separation step [94]. Initially, the blood was separated by centrifugation and, because of their low density, CTCs were removed from the upper portion of the container with relative ease [94]. CTCs were then incubated with nanotags for a specified period and after this any unbound nanotags were also removed by centrifugation prior to the SERS analysis [94]. Both methods allow for sensitive and selective detection of CTCs [73,94].

In a final example of SERS based disease detection *in vitro*, targeting of stem cells was investigated. Although this is not strictly a method for the detection of disease, stem cells have an important role in disease research [95]. In this study nuclear targeting SERS nanotags were deployed to ascertain the differences between differentiated and undifferentiated stem cell populations [95]. The cells were analysed by SERS and spectral information was extracted. Principal component analysis (PCA) was employed and it revealed that there were distinct differences between the two stem cell forms with regards to the organisation of the nucleus. These changes were suitably distinct and allowed for cell identification [95].

Please cite this article in press as: S. McAughtrie, et al., Surface enhanced Raman spectroscopy (SERS): Potential applications for disease detection and treatment, J. Photochem. Photobiol. C: Photochem. Rev. (2014), http://dx.doi.org/10.1016/j.jphotochemrev.2014.09.002

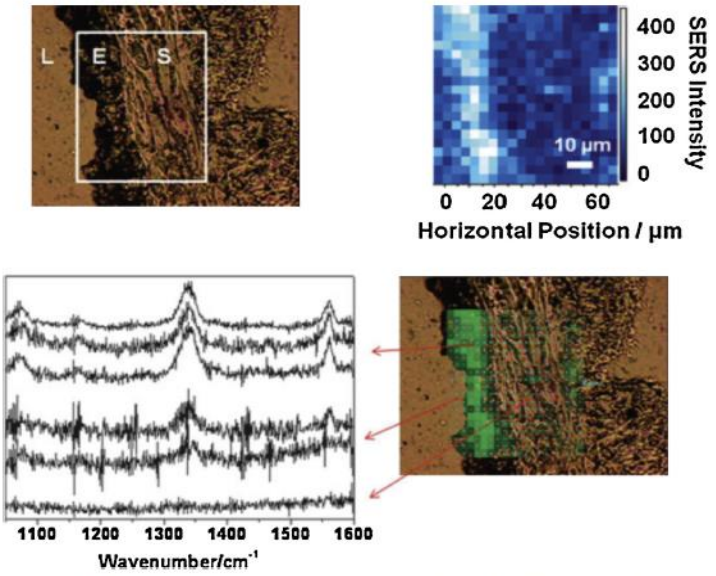

Fig. 4. Detection of PSA *ex vivo* – top: bright field microscope image of a prostate tissue section. The grid shows the locations at which Raman spectra were acquired in a point mapping experiment. The false colour SERS image shows that the characteristic signal of the SERS-labelled antibody is observed selectively in the epithelium. Reproduced from [80] with permission from the PCCP Owner Societies.

3.2. SERS and ex vivo/in vivo applications for the detection of disease

3.2.1. Tissue imaging and disease detection

The use of SERS for disease related tissue imaging was initially performed by Schlucker et al. in 2006 [96]. The SERS based detection system consisted of gold nanoparticles conjugated to an antibody *via* a small molecule reporter and this was used to actively detect prostate specific antigen (PSA) in tissue samples [96]. In a later study the same group extended this to monitor PSA expression in tissues [80]. This predominantly occurs in the epithelium of the prostate and, when incubated with functionalised nanoshells, the localised expression was confirmed by SERS signals arising from the specific nanoshell antibody–tissue antigen interaction and it was particularly evident in the false colour SERS maps (Fig. 4) [80]. Determining the localisation of other components within the tissues is not isolated to biomarkers of disease and the group successfully determined the localisation of the tumour suppressor p63, in non-cancerous tissue [97]. Elucidation of this was again determined by SERS signals arising from the specific interaction between the detection system and tissue [97].

Whilst detection systems like this might seem trivial, they are actually of huge importance for the characterisation of disease in tissue. In all of the examples discussed, the measured signals arise from the SERS reporters. However, a second laser line could be employed at a frequency where the nanotags are not SERS active but where intrinsic Raman signals from the tissues dominate. This would allow biochemically characteristic information to be obtained from the tissues and the false colour SERS images could be used to delineate the boundaries between the regions where, for example, PSA expression is high and low. This would provide further information which is biochemically representative of the disease biomarkers. Whilst areas of protein expression can be imaged using traditional immunohistochemical methods, no biochemical information is obtained. Additionally, conventional fluorophores have broad absorption and emission bands so the staining of multiple areas is difficult. However, when employing either Raman and/or SERS imaging, the spectral bands are narrow thus they are not limited in terms of the number of tissue regions or receptors which could be targeted simultaneously. This is particularly important as the documentation of disease processes progresses towards the detection of multiple markers [13].

Manipulation of the antibody–antigen interaction has also been exploited for the determination of nasopharyngeal cancer in tissue samples [98]. As with most of the discussed samples, antibody functionalised SERS nanotags were exposed to tissues [98]. Clinical samples were analysed and directly compared with the tissue, which had been analysed *via* a traditional immunohistochemical method. SERS analysis was found to considerably exceed the conventional method [98]. In total, there were 34 cancerous and 20 non-cancerous tissue samples and the SERS detection method correctly identified 33 of the cancerous samples whilst the traditional method only identified 22 [98]. Negative samples were correctly identified by both methods [98]. As with the previous examples all of the above discussed advantages of the SERS method are equally applicable to this study [98].

SORS has been previously discussed as a method for disease detection in Section 2.2. SORS has also been developed to incorporate a surface enhanced method known as surface enhanced spatially offset Raman spectroscopy (SESORS) [99]. The key feature and main advantage of this technique is that it can measure Raman or SERS signals through medically relevant tissue depths [99]. This

Please cite this article in press as: S. McAughtrie, et al., Surface enhanced Raman spectroscopy (SERS): Potential applications for disease detection and treatment, J. Photochem. Photobiol. C: Photochem. Rev. (2014), http://dx.doi.org/10.1016/j.jphotochemrev.2014.09.002

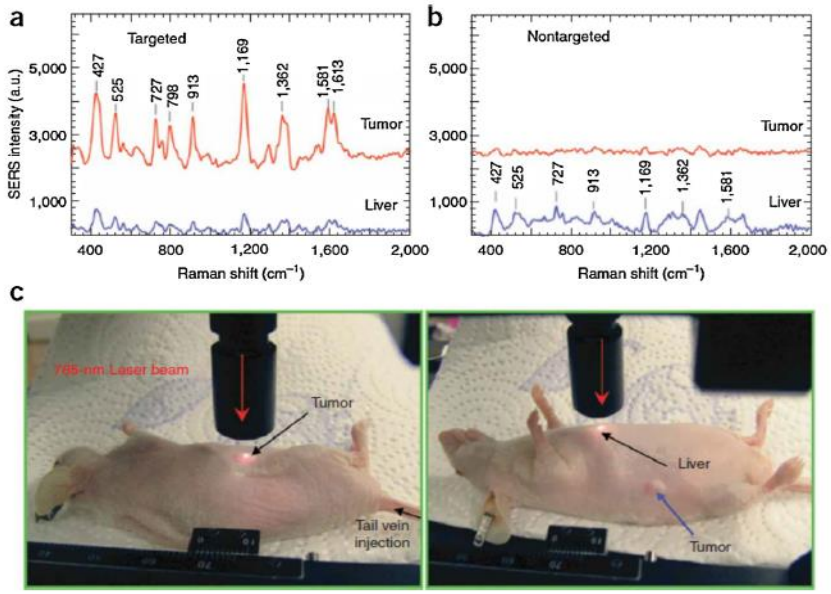

Fig. 5. *In vivo* cancer targeting and surface enhanced Raman detection by using ScFv-antibody conjugated gold nanoparticles that recognise the tumour biomarker EGFR. (a and b) SERS spectra obtained from the tumour and the liver locations by using targeted (a) and nontargeted (b) nanoparticles. Two nude mice bearing human head-and-neck squamous cell carcinoma (Tu686) xenograft tumour (3-mm diameter) received 90 μL of ScFv EGFR-conjugated SERS tags or pegylated SERS tags (460 pM). The particles were administered *via* tail vein single injection. SERS spectra were taken 5 h after injection. (c) Photographs showing a laser beam focusing on the tumour site or on the anatomical location of liver. *In vivo* SERS spectra were obtained from the tumour site (red) and the liver site (blue) with 2-s signal integration and at 785 nm excitation. The spectra were background subtracted and shifted for better visualisation. The Raman reporter molecule is malachite green, with distinct spectral signatures as labelled in (a) and (b). Laser power, 20 mW.
Reprinted by permission from Macmillan Publishers Ltd. Nature Biotechnology, [101] (2008).

is of huge importance since it actively demonstrates non-invasive detection of disease [99]. In one of the latest studies cumulative SERS signals were measured from four different SERS nanotags which were located within tissue at a depth of 20 mm [99]. Even more significantly, it was possible to measure SERS signals through 50 mm of tissue [99]. This study highlights the possibility of implementing SERS and their nanotags for use *in vivo*.

In a subsequent study the method was investigated in specific relation to a disease process [100]. Osteoporosis is a progressive bone disease which can be treated with drugs known as bisphosphonates [100]. The disease itself was not investigated but rather the study was designed to replicate drug distribution and investigate its localisation [100]. In order to do this, the drug was conjugated to SERS nanotags and subsequently incubated with representative bone samples. The bones were then transplanted into a tissue mass and the samples were analysed [100]. It was possible to detect the drug-nanotag conjugates at a depth of 20 mm [100]. Although this study did not involve the direct detection of the disease it is nonetheless important because it actively demonstrates the ability to monitor drug distribution non-invasively [100]. This therefore highlights the suitability of SERS as a key process in the treatment of disease.

3.2.2. *In vivo* imaging and disease detection

One of the most recognisable and well documented examples of *in vivo* SERS imaging is undoubtedly the study by Qian et al. [101], where tumours were successfully targeted with an antibody functionalised gold nanoparticle system *in vivo* [101]. The nanotag conjugates were introduced into the mice model *via* tail injection and they were successfully translocated to tumour locations [101]. Successful targeting was demonstrated *via* monitoring of the SERS signals and those measured from the tumour regions of the mouse were found to be representative of the reporter from the SERS nanotags (Fig. 5) [101]. This study actively demonstrated that the nanoparticles were able to travel through the animal model and reach their targets [101]. It was also critical for demonstrating the success and application of SERS for monitoring such interactions *in vivo*.

In vivo imaging of SERS nanotags has also been applied for the observation of inflammation and again, while not a disease process, it is of relevance since any change can be indicative of infection and underlying disease conditions [102]. Nanotags were functionalised with antibodies which have a specific affinity for the identified inflammation biomarker, intracellular adhesion molecule 1 – (ICAM-1-). The nanotags specifically targeted inflammation *in vitro*, *ex vivo* and *in vivo* [102]. When the effectiveness of the SERS approach was directly compared with the conventional fluorescence method it was found to be significantly more sensitive [102].

Whilst the previous examples have demonstrated active *in vivo* disease targeting, a multi marker approach is considered to be beneficial, especially if multiple disease aspects are to be detected

Please cite this article in press as: S. McAughtrie, et al., Surface enhanced Raman spectroscopy (SERS): Potential applications for disease detection and treatment, J. Photochem. Photobiol. C: Photochem. Rev. (2014), http://dx.doi.org/10.1016/j.jphotochemrev.2014.09.002

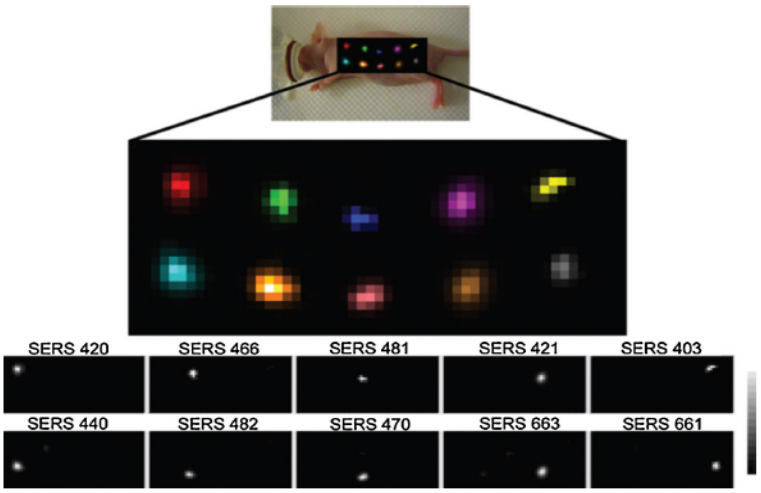

Fig. 6. Evaluation of multiplexing 10 different SERS nanoparticles *in vivo*. Raman map of 10 different SERS particles injected subcutaneously in a nude mouse. Grayscale bar to the right depicts the Raman intensity, where white represents the maximum intensity and black represents no intensity [13].

simultaneously [13]. It is hoped that by analysing disease processes or even multiple different diseases it will lead to better characterisation and personalised medicine.

With the advent of superior nanotag systems, which display excellent stability and are optically 'hot', the possibility of multiplexed imaging *in vivo* has become a real possibility [13,76]. In the initial stages it was possible to simultaneously detect two different nanotags within a live subject but this was latterly extended to include the simultaneous detection of 10 different nanotags (Fig. 6) [13,76]. This was a crucial step forward for multiplexed detection *in vivo*, actively demonstrating the potential to detect multiple pathosis or different elements of disease simultaneously [13]. In a further extension of the work, in terms of true multiplexing and the confident identification of nanotags present within a specified location, it was possible to positively identify four nanotags in a multiplexed scenario [13].

Further *in vivo* applications have been demonstrated by Maiti et al. [103–105]. In the first of their *in vivo* experiments nanotags were injected into a mouse model and successfully imaged using SERS [103]. The only difference being that the antibody functionalised nanotags were actively bound to cancerous cells prior to their introduction, highlighting the opportunity to successfully image the nanotags *in vivo* even after participation in a disease recognition event [103]. In an extension to this work nanotags functionalised with antibodies which had a specific affinity for the receptors in the xenograft were found to translocate to the xenograft site following introduction into the animal [104]. Thus the conjugates participated in antibody–antigen recognition and signals representative of the reporter molecule were measured at the xenograft site [104]. However, when nanotags were introduced into mice bearing xenografts of the non-cancerous cell population SERS signals were not measured in accordance with the absence of a specific binding event [104].

In the most recent of their work, the group elegantly demonstrated the selectivity of their targeting nanotags [105]. In this study the xenograft was composed of oral squamous cell carcinoma (OSCC) cells which exhibit a differential level of expression of EGFR and HER2. EGFR receptors are present at a much higher level than HER2 receptors on the surface of the OSCC cells [105]. In accordance with the expressed receptors three nanotags were injected into the tail of the animal subject, two of which had been functionalised with the EGFR specific antibody and the remaining nanotag was functionalised with the HER2 antibody [105]. The signals which were measured from the site of the xenograft were in accordance with the two nanotags functionalised with the specific antibody and two different reporter molecules. There was no contribution from the nanotag functionalised with the HER2 antibody (Fig. 7). This study represents one of the first true targeted *in vivo* multiplexing examples and this is an important step forwards in terms of striving towards the deliverable of comprehensively characterising and detecting multiple aspects of disease [105].

4. SERS as a method for disease treatment

The idea of implementing nanoscaffolds for disease treatment is not a new concept and nanostructures in many different forms (*i.e.* nanorods, nanoshells and nanoparticles), predominantly gold based, have been utilised for the destruction of cancerous cells [53,106–111]. This occurs because nanostructures absorbing the interrogating laser light experience localised heating and this heat is subsequently dissipated to the cell resulting in destruction [53,106,107,112,113]. It is widely believed that an increase in temperature is responsible for this effect but recent studies have shown that cellular damage can result without a significant temperature increase [114]. The method must therefore elicit some of form of damage which can ultimately result in cell death [114,115]. While there are many examples highlighting the use of nanomaterials for therapeutic purposes, there are no demonstrated applications where SERS has been employed as a treatment method. However, its use has recently been critical in determining the localisation of nanostructures so that treatment can be targeted to a specific position. SERS is therefore becoming a key step in treatment processes.

The detection of bacteria which are drug resistant is one such field where this method might be beneficial. Fan et al. described

Please cite this article in press as: S. McAughtrie, et al., Surface enhanced Raman spectroscopy (SERS): Potential applications for disease detection and treatment, J. Photochem. Photobiol. C: Photochem. Rev. (2014), http://dx.doi.org/10.1016/j.jphotochemrev.2014.09.002

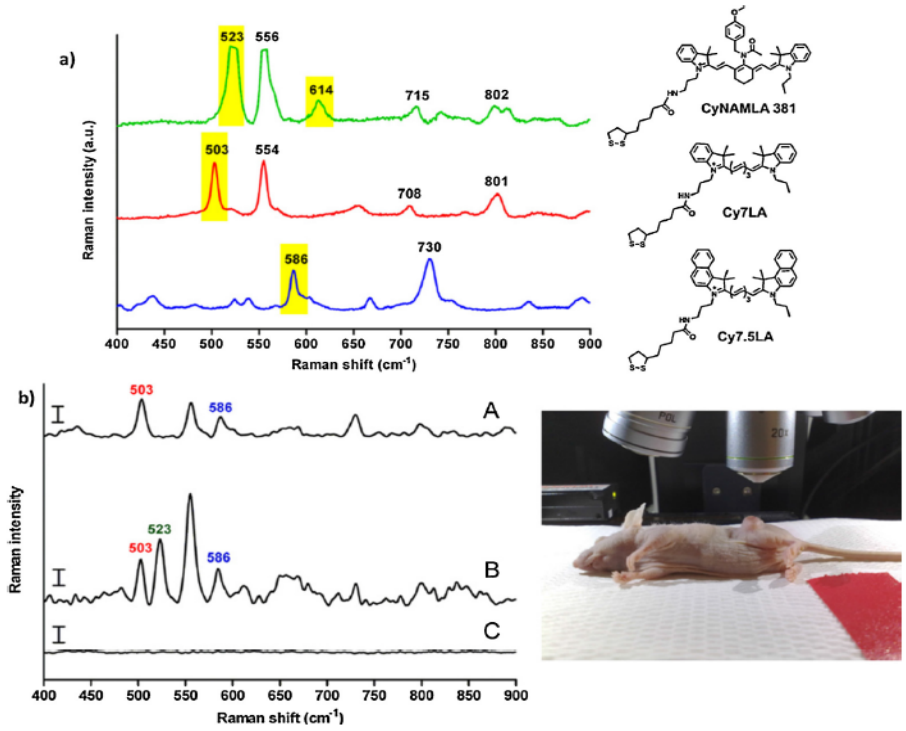

Fig. 7. *In vivo* multiplex detection in xenograft tumour – (a) normalised SERS spectra of CyNAMLA-381, Cy7LA and Cy7.5LA after chemisorption of AuNPs and (b) – (A) SERS spectra from tumour site (peaks obtained at 503 and 586 cm^{-1} from two EGFR positive nanotags, Cy7LA and Cy7.5LA), (B) SERS spectra from liver site (peaks obtained at 503, 523 and 586 cm^{-1}) from two EGFR nanotag Cy7LA, Cy7.5 and anti-HER2 nanotag CyNAMLA-381) and (C) SERS spectra from dorsal region [105].
Modified and reprinted with permission from Elsevier.

the generation of popcorn shaped magnetic nanoparticles which consisted of an iron core and a gold shell [116]. The nanostructures were further labelled with an antibody with affinity for *Salmonella* DT104 [116]. In the study the nanoparticles were found to bind to the *Salmonella* cells with high affinity and, because of their magnetic properties, cells could be extracted from the bulk solution [116]. Cells were then destroyed by illuminating with a therapeutic light source [116]. As with several of the studies which will be discussed, SERS was not directly involved in the treatment process, but it was essential for determining that the nanoparticle conjugates had successfully bound to the target cells and without these conjugates treatment would not have been successful [116]. While this remains a preliminary study the method is postulated as an alternative to drug based treatment methods for bacterial infections and disease, and this has important consequences since drug resistance continues to increase [116].

Implementation in the detection of lung cancer is another field where these SERS based detection methods might be beneficial, especially since lung cancer is often diagnosed beyond a stage of effective treatment [113]. In a study by Wu et al. aptamer conjugated silver shell gold core nanoparticles labelled with rhodamine 6G were used for the specific targeting of A549 lung cancer cells. The specificity of the system was tested against six cell lines (two generic cancer and four lung cancer cell lines) and the aptamer conjugates were not found to give a significant SERS response, suggesting that the conjugates did not bind to any other cell lines except those which were specifically targeted [113]. Implementation of the aptamer system allowed for considerable levels of aggregation between the cancer cells to occur since aptamers on a single shell could bind to different cells within the exposed population [113]. This was beneficial since it created concentrated areas of the conjugates and cells, ideal preparation for SERS detection and treatment with the irradiating laser. During the study it was found that a laser power of 0.2 W cm^{-1} applied for 60 min was sufficient to kill the cancerous cells [113]. The SERS response was also observed to decline following application of the treatment laser and it was postulated that this could be used as a measure of treatment efficacy [113]. When the same procedure was performed with the conjugates and the remaining cell lines, cell damage or death was not observed. The authors highlighted that this method could be applied for the medical treatment of cancer since differentiation between the cancerous cells was both selective and specific [113]. In this particular application SERS has been implemented to confirm the binding reaction and the possibility exists for it

Please cite this article in press as: S. McAughtrie, et al., Surface enhanced Raman spectroscopy (SERS): Potential applications for disease detection and treatment, J. Photochem. Photobiol. C: Photochem. Rev. (2014), http://dx.doi.org/10.1016/j.jphotochemrev.2014.09.002

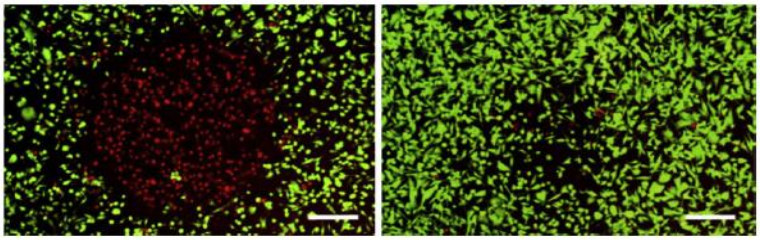

Fig. 8. Viability staining of cells incubated with AuNS-DTDC@SiO_2-PpIX-TAT (left) and AuNS-DTDC@SiO_2-TAT (right) after 30 s of light irradiation. Live cells are stained green and dead cells are stained red. Scale bars are 250 μm.
Reprinted with permission from [117]. Copyright (2013) American Chemical Society.

to be used as an indicator of treatment progression. Although not directly responsible for the treatment the implementation of SERS was critical to the overall therapeutic procedure and success of the system.

Such procedures are not isolated to the treatment of lung cancer and a similar scenario was developed for breast cancer cells (BT-549) [117]. In this procedure gold nanostars which had been previously pegylated were labelled with the reporter molecule 3,3′-diethylthiadicarbocyanine (DTDC) before silica encapsulation and further labelling with the phototherapeutic drug protoporphyrin IX (PpIX) and the cell penetrating peptide TAT [117]. In the study SERS was employed to monitor the uptake of the nanostars by breast cancer cells. When functionalised with the TAT peptide considerable SERS signals were observed. However, when the peptide sequence was removed from the conjugate, SERS signals were significantly reduced or not detected [117]. This is consistent with observations that functionalisation with the TAT peptide aids in the cellular uptake of nanomaterials [117–119]. In this particular study, TAT functionalisation was critical for the successful treatment of cancerous cells using PpIX. PpIX is used as an initiator for the production of damaging oxygen species which in turn continues the cascade of reactions initiating cellular damage and death [117]. Following exposure to the therapeutic light source, cell death was apparent in those cells which had been subject to the TAT functionalised conjugates whilst no significant effect was observed in those exposed to the TAT or PpIX free nanostructures (Fig. 8) [117]. The use of SERS in this study was again critical for determining the successful targeting of the conjugates, and whilst it is not directly responsible for the therapeutic effects observed, without it, treatment delivery could not be confirmed [117].

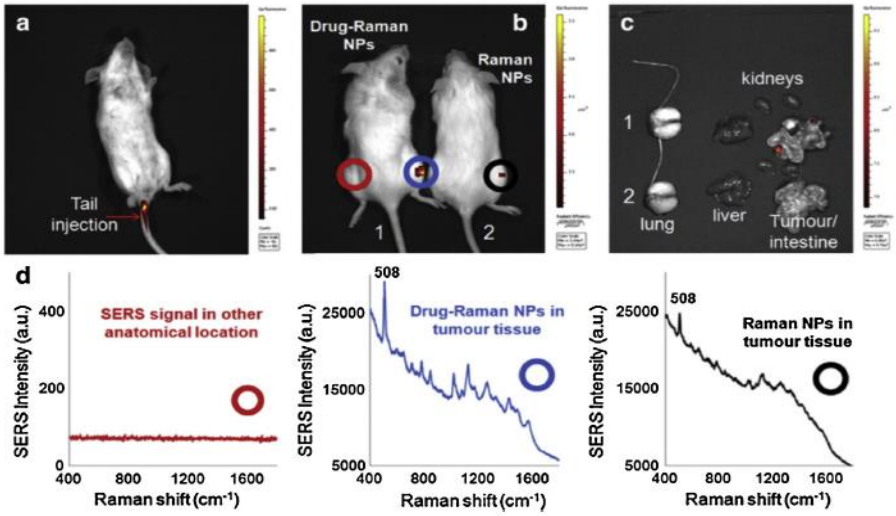

Fig. 9. Drug-Raman NP uptake and bio-distribution in whole body mice. Representative imaging of individual mice from each group (n = 10 animals) is shown, with the same scale of epi-fluorescence (a and b) indicating emission signal from the Raman reporter, DTTC (emission = 780–800 nm). (c) Evaluation of nanoparticles distribution in mice organs treated with Raman- and drug-Raman NPs. (d) SERS spectra of the tumour site, measured through the tumour tissues excised from the mice, of drug-Raman NPs (blue line), Raman NPs only (black line) and other anatomical locations (i.e., the opposite leg, red line). Characteristic SERS peak at 508 cm^{-1} [121].
Reprinted with permission from Elsevier.

Please cite this article in press as: S. McAughtrie, et al., Surface enhanced Raman spectroscopy (SERS): Potential applications for disease detection and treatment, J. Photochem. Photobiol. C: Photochem. Rev. (2014), http://dx.doi.org/10.1016/j.jphotochemrev.2014.09.002

In a further example silver nanotriangles encapsulated in chitosan and labelled with a reporter molecule and folic acid were used for the treatment of ovarian cancer cells (NIH-OVCAR-3) [120]. Folic acid was essential for transporting the conjugates across the cell membrane *via* a receptor mediated targeting strategy [120]. SERS was again implemented to confirm the transport of the nanostructures to their specified targets. Treatment with the therapeutic laser lead to cell death and the levels of cellular destruction were correlated with nanostructure concentration [120]. This method could be used to deliver therapeutics specifically to a diseased cell population since nanotriangle uptake between the cancerous and non-cancerous cells should vary in accordance with the expression of cancer related receptors [120]. SERS was again a vital step in the overall treatment process.

While cell based examples are undoubtedly interesting and stimulate further research this ultimately must be translated to *in vivo* applications. Conde et al. developed gold nanoparticle conjugates which were labelled with a reporter molecule and the antibody–drug conjugate Cetuximab (Erbitux®) for targeted detection and treatment of tumours *in vivo*. [121] Mice models were implanted with cancerous cells to generate xenografts [121] and mice were then treated with nanostructures *via* tail injection, while the tumours were located in the right leg [121]. The conjugates were successfully translocated to the tumour site and resulted in a reduction of further tumour development by the inhibition of cellular division [121]. Active targeting of the tumour was monitored *via* SERS and large SERS signals were observed in mice treated with the drug conjugates whilst minimal signals were observed from those treated with drug-free nanostructures (Fig. 9) [121]. The authors reported that the signals measured from drug labelled nanoparticles at the xenograft were 4.5 times higher than those of the drug free system as measured from a key identification peak at 508 cm^{-1} [121]. The variation in the SERS signal between the two sites and samples presumably arises because the drug-free conjugates were not specifically targeting the tumour site [121]. The SERS studies were performed *ex vivo* but the method further highlights the implementation of SERS based conjugates and SERS as a method for the successful targeting and treatment of disease *in vivo* [121].

5. Conclusion

The rich and varied applications of Raman and more significantly SERS for the detection of diseases are direct consequences of the numerous advantages that they confer. Unlike their fluorescent counterparts, sharp molecularly specific spectra are obtained, which instantly and readily lends the techniques to multiplexed disease detection opportunities. As demonstrated in some of the examples discussed, detection *via* these methods is often more sensitive and selective. In addition, the possibility exists for combined Raman and SERS imaging of cells and tissues so that in the advent of implementing SERS active nanotags, biochemical and characteristic information relating to the disease process can be simultaneously obtained. In order for SERS to achieve and remain at the forefront of disease diagnostics further studies are required in physiological representative media, clinical samples and *in vivo*. When these applications fully demonstrate their robustness, reliability, repeatability, sensitivity and selectivity *in vivo*, the technique will make the full transition from the laboratory to a clinical setting. Presently, the techniques are strong contenders for revolutionising our ability to detect disease.

Acknowledgments

SMcA acknowledges Renishaw plc for funding. D.G. acknowledges support from Royal Society Wolfson Trust Research Merit Award.

References

[1] A. Smekal, Naturwissenschaften 11 (1923) 873–875.
[2] C.V. Raman, K.S. Krishnan, Nature 121 (1928) 501–502.
[3] M.S. Bergholt, W. Zheng, K. Lin, K.Y. Ho, M. Teh, K.G. Yeoh, J.B. Yan So, Z. Huang, Int. J. Cancer 128 (2011) 2673–2680.
[4] Y. Oshima, H. Shinzawa, T. Takenaka, C. Furihata, H. Sato, J. Biomed. Opt. 15 (2010) 017009.
[5] F.C. Pascut, H.T. Goh, N. Welch, L.D. Buttery, C. Denning, I. Notingher, Biophys. J. 100 (2011) 251–259.
[6] E. Smith, G. Dent, Modern Raman Spectroscopy – A Practical Approach, John Wiley & Sons Ltd, Chichester, West Sussex, England, 2004.
[7] M. Fleischmann, P.J. Hendra, A.J. McQuillan, Chem. Phys. Lett. 26 (1974) 163–166.
[8] D.L. Jeanmaire, R.P. Van Duyne, J. Electroanal. Chem. 84 (1977) 1–20.
[9] M.G. Albrecht, J.A. Creighton, J. Am. Chem. Soc. 99 (1977) 5215–5217.
[10] A.A. Stacy, R.P. Van Duyne, Chem. Phys. Lett. 102 (1983) 365–370.
[11] E.C. Le Ru, P.G. Etchegoin, Principles of Surface-Enhanced Raman Spectroscopy, 1st ed., Elsevier, Oxford, England, 2009.
[12] K. Faulds, A. Hernandez-Santana, W.E. Smith, The inorganic chemistry of surface enhanced Raman scattering (SERS), in: J. Yarwood, R. Douthwaite, S. Duckett (Eds.), Spectrosc. Prop. Inorg. Organomet. Compd., The Royal Society of Chemistry, Cambridge, 2010, pp. 1–21.
[13] C.L. Zavaleta, B.R. Smith, I. Walton, W. Doering, G. Davis, B. Shojaei, M.J. Natan, S.S. Gambhir, Proc. Natl. Acad. Sci. U. S. A. 106 (2009) 13511–13516.
[14] C. Krafft, T. Knetschke, R.H.W. Funk, R. Salzer, Vib. Spectrosc. 38 (2005) 85–93.
[15] C. Matthäus, T. Chernenko, J.A. Newmark, C.M. Warner, M. Diem, Biophys. J. 93 (2007) 668–673.
[16] K. Klein, A.M. Gigler, T. Aschenbrenner, R. Monetti, W. Bunk, F. Jamitzky, G. Morfill, R.W. Stark, J. Schlegel, Biophys. J. 102 (2012) 360–368.
[17] S. McAughtrie, K. Lau, K. Faulds, D. Graham, Chem. Sci. 4 (2013) 3566–3572.
[18] K. Majzner, A. Kaczor, N. Kachamakova-Trojanowska, A. Fedorowicz, S. Chlopicki, M. Baranska, Analyst 138 (2013) 603–610.
[19] I. Notingher, S. Verrier, S. Haque, J.M. Polak, L.L. Hench, Biopolymers 72 (2003) 230–240.
[20] C. Krafft, T. Knetschke, R.H.W. Funk, R. Salzer, Anal. Chem. 78 (2006) 4424–4429.
[21] I. Notingher, G. Jell, U. Lohbauer, V. Salih, L.L. Hench, J. Cell. Biochem. 92 (2004) 1180–1192.
[22] R.J. Swain, S.J. Kemp, P. Goldstraw, T.D. Tetley, M.M. Stevens, Biophys. J. 98 (2010) 1703–1711.
[23] E. Gazi, A.D. Ward, N.W. Clarke, T.J. Harvey, R.D. Snook, P. Gardner, E.C. Faria, M.D. Brown, A. Henderson, J. Biomed. Opt. 13 (2008) 064004–064012.
[24] T.J. Harvey, C. Hughes, A.D. Ward, E.C. Faria, A. Henderson, N.W. Clarke, M.D. Brown, R.D. Snook, P. Gardner, J. Biophotonics 2 (2009) 47–69.
[25] K.E. Shafer-Peltier, A.S. Haka, M. Fitzmaurice, J. Crowe, J. Myles, R.R. Dasari, M.S. Feld, J. Raman Spectrosc. 33 (2002) 552–563.
[26] N. Stone, R. Baker, K. Rogers, A.W. Parker, P. Matousek, Analyst 132 (2007) 899–905.
[27] N. Stone, P. Matousek, Cancer Res. 68 (2008) 4424–4430.
[28] M. Calin, S. Parasca, R. Savastru, M. Calin, S. Dontu, J. Cancer Res. Clin. Oncol. 139 (2013) 1083–1104.
[29] H. Lui, J. Zhao, D. McLean, H. Zeng, Cancer Res. 72 (2012) 2491–2500.
[30] P. Crow, N. Stone, C.A. Kendall, J.S. Uff, J.A.M. Farmer, H. Barr, M.P.J. Wright, Br. J. Cancer 89 (2003) 106–108.
[31] P. Crow, B. Barrass, C.A. Kendall, M. Hart-Prieto, M. Wright, R. Persad, N. Stone, Br. J. Cancer 92 (2005) 2166–2170.
[32] P. Crow, A. Molckovsky, N. Stone, J.S. Uff, B. Wilson, L.-M. WongKeeSong, Urology 65 (2005) 1126–1130.
[33] P. Crow, J.S. Uff, J.A. Farmer, M.P. Wright, N. Stone, BJU Int. 93 (2004) 1232–1236.
[34] M.C.M. Grimbergen, C.F.P. van Swol, R.O.P. Draga, P. van Diest, R.M. Verdaasdonk, N. Stone, J.H.L.R. Bosch, Bladder cancer diagnosis during cystoscopy using Raman spectroscopy, 2009, pp. 716114–716116.
[35] R.O.P. Draga, M.C.M. Grimbergen, P.L.M. Vijverberg, C.F.P.v. Swol, T.G.N. Jonges, J.A. Kummer, J.L.H. Ruud Bosch, Anal. Chem. 82 (2010) 5993–5999.
[36] A. Mahadevan-Jansen, M.F. Mitchell, N. Ramanujamf, A. Malpica, S. Thomsen, U. Utzinger, R. Richards-Kortumt, Photochem. Photobiol. 68 (1998) 123–132.
[37] U. Utzinger, D.L. Heintzelman, A. Mahadevan-Jansen, A. Malpica, M. Follen, R. Richards-Kortum, Appl. Spectrosc. 55 (2001) 955–959.
[38] A. Robichaux-Viehoever, E. Kanter, H. Shappell, D. Billheimer, H. Jones III, A. Mahadevan-Jansen, Appl. Spectrosc. 61 (2007) 986–993.
[39] E. Widjaja, W. Zheng, Z. Huang, Int. J. Oncol. 32 (2008) 653–662.
[40] A. Beljebbar, O. Bouché, M.D. Diébold, P.J. Guillou, J.P. Palot, D. Eudes, M. Manfait, Crit. Rev. Oncol./Hematol. 72 (2009) 255–264.
[41] C. Kendall, N. Stone, N. Shepherd, K. Geboes, B. Warren, R. Bennett, H. Barr, J. Pathol. 200 (2003) 602–609.
[42] M.S. Bergholt, W. Zheng, K. Lin, K.Y. Ho, M. Teh, K.G. Yeoh, J.B.Y. So, Z. Huang, Technol. Cancer Res. Treat. 10 (2011) 103–112.
[43] A. Molckovsky, L.M. Wong Kee Song, M.G. Shim, N.E. Marcon, B.C. Wilson, Gastrointest. Endosc. 57 (2003) 396–402.
[44] C. Kallaway, L.M. Almond, H. Barr, J. Wood, J. Hutchings, C. Kendall, N. Stone, Photodiagn. Photodyn. Ther. 10 (2013) 207–219.
[45] M. Kirsch, G. Schackert, R. Salzer, C. Krafft, Anal. Bioanal. Chem. 398 (2010) 1707–1713.

Please cite this article in press as: S. McAughtrie, et al., Surface enhanced Raman spectroscopy (SERS): Potential applications for disease detection and treatment, J. Photochem. Photobiol. C: Photochem. Rev. (2014), http://dx.doi.org/10.1016/j.jphotochemrev.2014.09.002

[46] S.W.E. van de Poll, T.J. Römer, O.L. Volger, D.J.M. Delsing, T.C. Bakker Schut, H.M.G. Princen, L.M. Havekes, J.W. Jukema, A. van der Laarse, G.J. Puppels, Arterioscler. Thromb. Vasc. Biol. 21 (2001) 1630–1635.
[47] B.H. Foundation, Cardiovascular Disease Statistics http://www.bhf.org.uk/heart-health/heart-statistics.aspx
[48] K.L. Brown, O.Y. Palyvoda, J.S. Thakur, S.L. Nehlsen-Cannarella, O.R. Fagoaga, S.A. Gruber, G.W. Auner, Cytometry A 75A (2009) 917–923.
[49] Y.G. Chung, Q. Tu, D. Cao, S. Harada, H.J. Eisen, C. Chang, Clin. Transl. Sci. 2 (2009) 206–210.
[50] D.I. Ellis, R. Goodacre, Analyst 131 (2006) 875–885.
[51] D.I. Ellis, D.P. Cowcher, L. Ashton, S. O'Hagan, R. Goodacre, Analyst 138 (2013) 3871–3884.
[52] P.D. Howes, S. Rana, M.M. Stevens, Chem. Soc. Rev. 43 (2014) 3835–3853.
[53] C. Loo, A. Lin, L. Hirsch, M.-H. Lee, J. Barton, N. Halas, J. West, R. Drezek, Technol. Cancer Res. Treat. 3 (2004) 33–40.
[54] D. Graham, G. McAnally, J.C. Jones, W. Ewen Smith, Chem. Commun. (1998) 1187–1188.
[55] G. McAnally, C. McLaughlin, R. Brown, D.C. Robson, K. Faulds, D.R. Tackley, W.E. Smith, D. Graham, Analyst 127 (2002) 838–841.
[56] C.J. McHugh, F.T. Docherty, D. Graham, W.E. Smith, Analyst 129 (2004) 69–72.
[57] A. Enright, L. Fruk, A. Grondin, C.J. McHugh, W.E. Smith, D. Graham, Analyst 129 (2004) 975–978.
[58] R.J. Stokes, A. Macaskill, P.J. Lundahl, W.E. Smith, K. Faulds, D. Graham, Small 3 (2007) 1593–1601.
[59] R.J. Stokes, A. Ingram, J. Gallagher, D.R. Armstrong, W.E. Smith, D. Graham, Chem. Commun. (2008) 567–569.
[60] O. Lyandres, N.C. Shah, C.R. Yonzon, J.T. Walsh, M.R. Glucksberg, R.P. Van Duyne, Anal. Chem. 77 (2005) 6134–6139.
[61] N.C. Shah, O. Lyandres, J.T. Walsh, M.R. Glucksberg, R.P. Van Duyne, Anal. Chem. 79 (2007) 6927–6932.
[62] R. Stevenson, S. McAughtrie, L. Senior, R.J. Stokes, H. McGachy, L. Tetley, P. Nativo, J.M. Brewer, J. Alexander, K. Faulds, D. Graham, Analyst 138 (2013) 6331–6336.
[63] I.H. Chou, M. Benford, H.T. Beier, G.L. Coté, M. Wang, N. Jing, J. Kameoka, T.A. Good, Nano Lett. 8 (2008) 1729–1735.
[64] K. Kneipp, A.S. Haka, H. Kneipp, K. Badizadegan, N. Yoshizawa, C. Boone, K.E. Shafer-Peltier, J.T. Motz, R.R. Dasari, M.S. Feld, Appl. Spectrosc. 56 (2002) 150–154.
[65] M.K. Gregas, J.P. Scaffidi, B. Lauly, T. Vo-Dinh, Appl. Spectrosc. 64 (2010) 858–866.
[66] M.K. Gregas, F. Yan, J. Scaffidi, H.-N. Wang, T. Vo-Dinh, Nanomed. Nanotechnol. 7 (2011) 115–122.
[67] J. Kneipp, H. Kneipp, B. Wittig, K. Kneipp, Nanomed. Nanotechnol. 6 (2010) 214–226.
[68] D.C. Kennedy, K.A. Hoop, L.L. Tay, J.P. Pezacki, Nanoscale 2 (2010) 1413–1416.
[69] N.M.S. Sirimuthu, C.D. Syme, J.M. Cooper, in: T. Vo-Dinh, J.R. Lakowicz (Eds.), Intracellular Multiplex Detection and Imaging of Stable Chemisorbed Labels by SERS Spectroscopy, SPIE, San Francisco, California, USA, 2012, pp. 82340F-82347.
[70] M. Gellner, K. Kömpe, S. Schlücker, Anal. Bioanal. Chem. 394 (2009) 1839–1844.
[71] G.B. Braun, S.J. Lee, T. Laurence, N. Fera, L. Fabris, G.C. Bazan, M. Moskovits, N.O. Reich, J. Phys. Chem. C 113 (2009) 13622–13629.
[72] J. Yang, Z. Wang, S. Zong, C. Song, R. Zhang, Y. Cui, Anal. Bioanal. Chem. 402 (2012) 1093–1100.
[73] M.Y. Sha, H. Xu, M.J. Natan, R. Cromer, J. Am. Chem. Soc. 130 (2008) 17214–17215.
[74] W. Xie, L. Wang, Y. Zhang, L. Su, A. Shen, J. Tan, J. Hu, Bioconj. Chem. 20 (2009) 768–773.
[75] A.G. Tkachenko, H. Xie, D. Coleman, W. Glomm, J. Ryan, M.F. Anderson, S. Franzen, D.L. Feldheim, J. Am. Chem. Soc. 125 (2003) 4700–4701.
[76] S. Keren, C. Zavaleta, Z. Cheng, A. de la Zerda, O. Gheysens, S.S. Gambhir, Proc. Natl. Acad. Sci. U. S. A. 105 (2008) 5844–5849.
[77] X. Tan, Z. Wang, J. Yang, C. Song, R. Zhang, Y. Cui, Nanotechnology 20 (2009) 445102.
[78] A.F. McCabe, C. Eliasson, R. Arun Prasath, A. Hernandez-Santana, L. Stevenson, I. Apple, P.A.G. Cormack, D. Graham, W.E. Smith, P. Corish, S.J. Lipscomb, E.R. Holland, P.D. Prince, Faraday Discuss. 132 (2006) 303–308.
[79] S. Yu, S.B. Lee, M. Kang, C.R. Martin, Nano Lett. 1 (2001) 495–498.
[80] C. Jehn, B. Kustner, P. Adam, A. Marx, P. Strobel, C. Schmuck, S. Schlucker, Phys. Chem. Chem. Phys. 11 (2009) 7499–7504.
[81] D.A. Stuart, J.M. Yuen, N. Shah, O. Lyandres, C.R. Yonzon, M.R. Glucksberg, J.T. Walsh, R.P. Van Duyne, Anal. Chem. 78 (2006) 7211–7215.
[82] J.M. Yuen, N.C. Shah, J.T. Walsh, M.R. Glucksberg, R.P. Van Duyne, Anal. Chem. 82 (2010) 8382–8385.
[83] K. Ma, J.M. Yuen, N.C. Shah, J.T. Walsh, M.R. Glucksberg, R.P. Van Duyne, Anal. Chem. 83 (2011) 9146–9152.
[84] G. Wang, R.J. Lipert, M. Jain, S. Kaur, S. Chakraboty, M.P. Torres, S.K. Batra, R.E. Brand, M.D. Porter, Anal. Chem. 83 (2011) 2554–2561.
[85] J.H. Granger, M.C. Granger, M.A. Firpo, S.J. Mulvihill, M.D. Porter, Analyst 138 (2013) 410–416.
[86] H. Chon, S. Lee, S.W. Son, C.H. Oh, J. Choo, Anal. Chem. 81 (2009) 3029–3034.
[87] J.-H. Kim, J.-S. Kim, H. Choi, S.-M. Lee, B.-H. Jun, K.-N. Yu, E. Kuk, Y.-K. Kim, D.H. Jeong, M.-H. Cho, Y.-S. Lee, Anal. Chem. 78 (2006) 6967–6973.
[88] K.K. Maiti, A. Samanta, M. Vendrell, K.-S. Soh, M. Olivo, Y.-T. Chang, Chem. Commun. 47 (2011) 3514–3516.
[89] S. Lee, H. Chon, M. Lee, J. Choo, S.Y. Shin, Y.H. Lee, I.J. Rhyu, S.W. Son, C.H. Oh, Biosens. Bioelectron. 24 (2009) 2260–2263.
[90] H. Park, S. Lee, L. Chen, E.K. Lee, S.Y. Shin, Y.H. Lee, S.W. Son, C.H. Oh, J.M. Song, S.H. Kang, J. Choo, Phys. Chem. Chem. Phys. 11 (2009) 7444–7449.
[91] S. Lee, H. Chon, J. Lee, J. Ko, B.H. Chung, D.W. Lim, J. Choo, Biosens. Bioelectron. 51 (2014) 238–243.
[92] A. Pallaoro, G.B. Braun, M. Moskovits, Proc. Natl. Acad. Sci. 108 (2011) 16559–16564.
[93] D. Craig, S. McAughtrie, J. Simpson, C. McCraw, K. Faulds, D. Graham, Anal. Chem. 86 (2014) 4775–4782.
[94] X. Wang, X. Qian, J.J. Beitler, Z.G. Chen, F.R. Khuri, M.M. Lewis, H.J.C. Shin, S. Nie, D.M. Shin, Cancer Res. 71 (2011) 1526–1532.
[95] A. Huefner, W.-L. Kuan, R.A. Barker, S. Mahajan, Nano Lett. 13 (2013) 2463–2470.
[96] S. Schlücker, B. Küstner, A. Punge, R. Bonfig, A. Marx, P. Ströbel, J. Raman Spectrosc. 37 (2006) 719–721.
[97] M. Schutz, D. Steinigeweg, M. Salehi, K. Kompe, S. Schlucker, Chem. Commun. 47 (2011) 4216–4218.
[98] Y.P. Chen, X.W. Zheng, G. Chen, C. He, W.F. Zhu, S.Y. Feng, G. Xi, R. Chen, F.H. Lan, H.S. Zeng, Int. J. Nanomed. 2012 (2011) 73–82.
[99] N. Stone, M. Kerssens, G.R. Lloyd, K. Faulds, D. Graham, P. Matousek, Chem. Sci. 2 (2011) 776–780.
[100] H.-N. Xie, R. Stevenson, N. Stone, A. Hernandez-Santana, K. Faulds, D. Graham, Angew. Chem. Int. Ed. 51 (2012) 8509–8511.
[101] X. Qian, X.-H. Peng, D.O. Ansari, Q. Yin-Goen, G.Z. Chen, D.M. Shin, L. Yang, A.N. Young, M.D. Wang, S. Nie, Nat. Biotechnol. 26 (2008) 83–90.
[102] R. McQueenie, R. Stevenson, R. Benson, N. MacRitchie, I. McInnes, P. Maffia, K. Faulds, D. Graham, J. Brewer, P. Garside, Anal. Chem. 84 (2012) 5968–5975.
[103] K.K. Maiti, U.S. Dinish, C.Y. Fu, J.-J. Lee, K.-S. Soh, S.-W. Yun, R. Bhuvaneswari, M. Olivo, Y.-T. Chang, Biosens. Bioelectron. 26 (2010) 398–403.
[104] A. Samanta, K.K. Maiti, K.-S. Soh, X. Liao, M. Vendrell, U.S. Dinish, S.-W. Yun, R. Bhuvaneswari, H. Kim, S. Rautela, J. Chung, M. Olivo, Y.-T. Chang, Angew. Chem. Int. Ed. 50 (2011) 6089–6092.
[105] K.K. Maiti, U.S. Dinish, A. Samanta, M. Vendrell, K.-S. Soh, S.-J. Park, M. Olivo, Y.-T. Chang, Nano Today 7 (2012) 85–93.
[106] X. Huang, M.A. El-Sayed, J. Adv. Res. 1 (2010) 13–28.
[107] L.R. Hirsch, R.J. Stafford, J.A. Bankson, S.R. Sershen, B. Rivera, R.E. Price, J.D. Hazle, N.J. Halas, J.L. West, Proc. Natl. Acad. Sci. 100 (2003) 13549–13554.
[108] C. Loo, A. Lowery, N. Halas, J. West, R. Drezek, Nano Lett. 5 (2005) 709–711.
[109] A.M. Gobin, M.H. Lee, N.J. Halas, W.D. James, R.A. Drezek, J.L. West, Nano Lett. 7 (2007) 1929–1934.
[110] I.H. El-Sayed, X. Huang, M.A. El-Sayed, Cancer Lett. 239 (2006) 129–135.
[111] X. Huang, I.H. El-Sayed, W. Qian, M.A. El-Sayed, J. Am. Chem. Soc. 128 (2006) 2115–2120.
[112] L.K. Bogart, G. Pourroy, C.J. Murphy, V. Puntes, T. Pellegrino, D. Rosenblum, D. Peer, R. Lévy, ACS Nano 8 (2014) 3107–3122.
[113] P. Wu, Y. Gao, Y. Lu, H. Zhang, C. Cai, Analyst 138 (2013) 6501–6510.
[114] M. Creixell, A.C. Bohórquez, M. Torres-Lugo, C. Rinaldi, ACS Nano 5 (2011) 7124–7129.
[115] R. Lévy, N.T.K. Thanh, R.C. Doty, I. Hussain, R.J. Nichols, D.J. Schiffrin, M. Brust, D.G. Fernig, J. Am. Chem. Soc. 126 (2004) 10076–10084.
[116] Z. Fan, D. Senapati, S.A. Khan, A.K. Singh, A. Hamme, B. Yust, D. Sardar, P.C. Ray, Chem. – Eur. J. 19 (2013) 2839–2847.
[117] A.M. Fales, H. Yuan, T. Vo-Dinh, Mol. Pharm. 10 (2013) 2291–2298.
[118] J.M. de la Fuente, C.C. Berry, Bioconj. Chem. 16 (2005) 1176–1180.
[119] Z. Krpetić, S. Saleemi, I.A. Prior, V. Sée, R. Qureshi, M. Brust, ACS Nano 5 (2011) 5195–5201.
[120] S. Boca-Farcau, M. Potara, T. Simon, A. Juhem, P. Baldeck, S. Astilean, Mol. Pharm. 11 (2013) 391–399.
[121] J. Conde, C. Bao, D. Cui, P.V. Baptista, F. Tian, J. Controlled Release 183 (2014) 87–93.

Please cite this article in press as: S. McAughtrie, et al., Surface enhanced Raman spectroscopy (SERS): Potential applications for disease detection and treatment, J. Photochem. Photobiol. C: Photochem. Rev. (2014), http://dx.doi.org/10.1016/j.jphotochemrev.2014.09.002